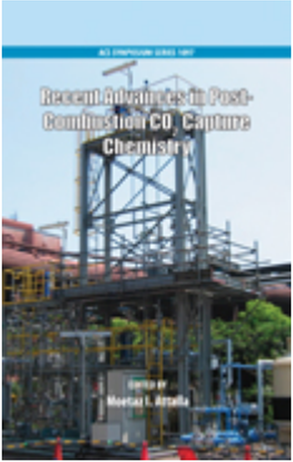

ACS SYMPOSIUM SERIES 1097

Recent Advances in Post-Combustion CO_2 Capture Chemistry

EDITED BY

Moetaz I. Attalla

Downloaded by 89.163.35.42 on June 14, 2012 | http://pubs.acs.org
Publication Date (Web): May 3, 2012 | doi: 10.1021/bk-2012-1097.fw001

Recent Advances in Post-Combustion CO_2 Capture Chemistry

Downloaded by 89.163.35.42 on June 14, 2012 | http://pubs.acs.org
Publication Date (Web): May 3, 2012 | doi: 10.1021/bk-2012-1097.fw001

ACS SYMPOSIUM SERIES **1097**

Recent Advances in Post-Combustion CO_2 Capture Chemistry

Moetaz I. Attalla, Editor
CSIRO Energy Technology

American Chemical Society, Washington, DC

Distributed in print by Oxford University Press, Inc.

Downloaded by 89.163.35.42 on June 14, 2012 | http://pubs.acs.org
Publication Date (Web): May 3, 2012 | doi: 10.1021/bk-2012-1097.fw001

Downloaded by 89.163.35.42 on June 14, 2012 | http://pubs.acs.org
Publication Date (Web): May 3, 2012 | doi: 10.1021/bk-2012-1097.fw001

Library of Congress Cataloging-in-Publication Data

Recent advances in post-combustion CO2 capture chemistry / Moetaz I. Attalla, editor.
p. cm. -- (ACS symposium series ; 1097)
Includes bibliographical references and index.
ISBN 978-0-8412-2621-0 (alk. paper)
1. Carbon dioxide--Absorption and adsorption. 2. Combustion gases. 3. Carbon sequestration. I. Attalla, Moetaz I.
QD181.C1R398 2012
546'.6812--dc23
2012011235

The paper used in this publication meets the minimum requirements of American National Standard for Information Sciences—Permanence of Paper for Printed Library Materials, ANSI Z39.48n1984.

Copyright © 2012 American Chemical Society

Distributed in print by Oxford University Press, Inc.

All Rights Reserved. Reprographic copying beyond that permitted by Sections 107 or 108 of the U.S. Copyright Act is allowed for internal use only, provided that a per-chapter fee of $40.25 plus $0.75 per page is paid to the Copyright Clearance Center, Inc., 222 Rosewood Drive, Danvers, MA 01923, USA. Republication or reproduction for sale of pages in this book is permitted only under license from ACS. Direct these and other permission requests to ACS Copyright Office, Publications Division, 1155 16th Street, N.W., Washington, DC 20036.

The citation of trade names and/or names of manufacturers in this publication is not to be construed as an endorsement or as approval by ACS of the commercial products or services referenced herein; nor should the mere reference herein to any drawing, specification, chemical process, or other data be regarded as a license or as a conveyance of any right or permission to the holder, reader, or any other person or corporation, to manufacture, reproduce, use, or sell any patented invention or copyrighted work that may in any way be related thereto. Registered names, trademarks, etc., used in this publication, even without specific indication thereof, are not to be considered unprotected by law.

PRINTED IN THE UNITED STATES OF AMERICA

Downloaded by 89.163.35.42 on June 14, 2012 | http://pubs.acs.org
Publication Date (Web): May 3, 2012 | doi: 10.1021/bk-2012-1097.fw001

Foreword

The ACS Symposium Series was first published in 1974 to provide a mechanism for publishing symposia quickly in book form. The purpose of the series is to publish timely, comprehensive books developed from the ACS sponsored symposia based on current scientific research. Occasionally, books are developed from symposia sponsored by other organizations when the topic is of keen interest to the chemistry audience.

Before agreeing to publish a book, the proposed table of contents is reviewed for appropriate and comprehensive coverage and for interest to the audience. Some papers may be excluded to better focus the book; others may be added to provide comprehensiveness. When appropriate, overview or introductory chapters are added. Drafts of chapters are peer-reviewed prior to final acceptance or rejection, and manuscripts are prepared in camera-ready format.

As a rule, only original research papers and original review papers are included in the volumes. Verbatim reproductions of previous published papers are not accepted.

ACS Books Department

Downloaded by 89.163.35.42 on June 14, 2012 | http://pubs.acs.org
Publication Date (Web): May 3, 2012 | doi: 10.1021/bk-2012-1097.pr001

Preface

Carbon dioxide has become a major target for emission reduction strategies due to its rapidly increasing atmospheric levels. The dominant driving force is anthropogenic carbon dioxide emissions from fossil fuel combustion and industrial processes. It is for this reason aqueous amine based carbon capture technologies of carbon dioxide generated from these sources has been identified as a crucial part of the global solution to mitigating these greenhouse gas emissions.

The selective removal of acid gases, such as carbon dioxide, from gas streams using aqueous amines is a well established technology. It was first patented in the 1930's as a gas purification process and used since in the removal of carbon dioxide and other sour gases from small-scale industrial processes such as ammonia production, sweetening of natural gas and enhanced oil recovery. It wasn't until the 1980's that the prospect of utilising this established technology to reduce carbon dioxide emissions from much larger point sources, such as coal fired power stations, emerged. However, none of the established gas purification processes were specifically developed for application at such a large scale and in the presence of flue gas contaminates such as oxygen, oxides of sulphur and nitrogen and trace elements associated with ash and fly ash.

Since the 1980's, amine-based post combustion carbon dioxide capture has become widely recognized as the most viable and near-ready technology to reduce carbon dioxide emissions in the midterm. However, the large scale roll-out of the technology has been hindered by a number of technical challenges, several of which are addressed in the chapters of this monograph, including i) cost of scale-up; ii) energy efficiency penalty for solvent regeneration; iii) solvent degradation in the presence of the various flue gas constituents; and iv) the potential environment impacts of solvents and solvent degradation products released to the environment. In line with this resurgence in the technology a considerable amount of research was undertaken in an attempt to further understand the chemistry involved in the capture of carbon dioxide from flue gas streams using aqueous amines.

In developing amine-based post combustion carbon dioxide capture as a commercially viable solution for the reduction of carbon dioxide emissions in a carbon-constrained future, researchers worldwide are addressing all challenges to the technology to accelerate its implementation while maintaining a realistic approach to the economics of the process and its environmental impacts. Over the past 6-7 years there has been an intense global resurgence in developing a deeper understanding of the chemistry of post combustion carbon dioxide capture in an endeavor to reduce the cost of the process and determine the environmental footprint of this technology to make it a practical option for mitigating carbon dioxide emissions from coal-fired power stations.

In Recent Advances in Post-Combustion CO2 Capture Chemistry; Attalla, M.;
ACS Symposium Series; American Chemical Society: Washington, DC, 2012.

The chapters in this monograph are contributions from the *Chemistry of Post-Combustion Carbon Dioxide Capture* symposium held at the Pacifichem 2010, International Chemical Congress of Pacific Basin Societies. The symposium was dedicated to capturing snapshots of the most recent advances in carbon dioxide capture using solvent-based post combustion carbon dioxide capture technology. I am certain that readers interested in forefront developments in this field will find this book of great value and a nice addition to the scientific literature. I wish to thank all the authors of the chapters for their contributions to the ACS book and symposium.

Dr. Moetaz I. Attalla

CSIRO Energy Technology
P.O. Box 330
Newcastle NSW 2300
Australia
+61(0) 249606083 (telephone)
+61(0) 417225938 (fax)

Downloaded by 89.163.35.42 on June 14, 2012 | http://pubs.acs.org
Publication Date (Web): May 3, 2012 | doi: 10.1021/bk-2012-1097.pr001

In Recent Advances in Post-Combustion CO2 Capture Chemistry; Attalla, M.;
ACS Symposium Series; American Chemical Society: Washington, DC, 2012.

Downloaded by PENNSYLVANIA STATE UNIV on June 14, 2012 | http://pubs.acs.org
Publication Date (Web): May 3, 2012 | doi: 10.1021/bk-2012-1097.ot001

Editor's Biography

Moetaz I. Attalla

Moetaz Attalla is currently a Principal Research Scientist with the Australian Commonwealth Scientific and Industrial Research Organisation (CSIRO). Dr Attalla has been with the CSIRO for over 25 years. He is the leader of the Solvent Development Research Project for the CSIRO Post Combustion Capture program. Dr Attalla is a chemist with extensive research experience in the energy technology sector. Dr Attalla was awarded a doctorate in physical chemistry and catalysis from Macquarie University, Sydney, NSW Australia.

Dr Attalla has over 25 years research experience that spans many scientific disciplines from development of novel direct coal liquefaction catalyst and chemistry to trace element behaviour in combustion processes from coal fired power stations. More recently he has undertaken major projects in environmental chemistry and monitoring science for the Australian Coal Association as well as amine solvent development for post combustion CO_2 capture.

In Recent Advances in Post-Combustion CO2 Capture Chemistry; Attalla, M.;
ACS Symposium Series; American Chemical Society: Washington, DC, 2012.

Downloaded by 89.163.35.42 on June 14, 2012 | http://pubs.acs.org
Publication Date (Web): May 3, 2012 | doi: 10.1021/bk-2012-1097.ch001

Chapter 1

The Effect Molecular Structural Variations Has on the CO_2 Absorption Characteristics of Heterocyclic Amines

K. Robinson,[1,2] A. McCluskey,[2] and M. I. Attalla[1,*]

[1]Energy Transformed Flagship, CSIRO Energy Technology,
10 Murray-Dwyer CCT, Mayfield West NSW 2300, Australia
[2]Chemistry, School of Environmental & Life Sciences, The University of Newcastle, Callaghan NSW 2308, Australia
[*]e-mail: Moetaz.attalla@csiro.au

This chapter details the novel application of in-situ Attenuated Reflectance Fourier Transform Infrared (ATR FT-IR) spectroscopy to investigate the effect molecular structural variation has on the CO_2 absorption characteristics of heterocyclic amines. The reaction between CO_2 and a subset of structurally variant amines were analyzed including piperidine, as well as commercially available functionalized piperidine derivatives, for example, those with methyl-, hydroxyl- and hydroxyalkyl- substituents. This new technique uses an ATR probe optically coupled to an FT-IR spectrometer to monitor the reaction species evolving in solution as CO_2 is being absorbed into solution. The effect of molecular structural variations on CO_2 absorption was then assessed in relation to the IR identifiable ionic reaction products, CO_2 absorption capacity and the mass-transfer coefficient at zero loading.

Introduction

At present, aqueous amine-based PCC is viewed as the most promising and near ready technology for the reduction of CO_2 emissions from coal-fired power stations. The technology is industrially proven for absorbents such as aqueous monoethanolamine (MEA), and has been used for decades to remove CO_2 from gas streams in small-scale commercial processes such as ammonia production

In Recent Advances in Post-Combustion CO2 Capture Chemistry; Attalla, M.;
ACS Symposium Series; American Chemical Society: Washington, DC, 2012.

Downloaded by 89.163.35.42 on June 14, 2012 | http://pubs.acs.org
Publication Date (Web): May 3, 2012 | doi: 10.1021/bk-2012-1097.ch001

and natural gas processing (*1*, *2*). Despite being an established technology, deployment of current industry standard technology (30 wt % aqueous MEA system) on a large scale would come at the expense of the efficiency of the power generation process. The absorbent regeneration stage of the PCC process is energy intensive (*3*) requiring a substantial input of heat to re-release the CO_2 and as such anything from a 25-30% reduction in the net efficiency of a coal-fired power plant is expected (*4*, *5*). The reactivity of the amine-based absorbent towards CO_2, i.e. its CO_2 absorption capacity and absorption rate, will also largely determine the economics and feasibility of the process. One approach to reduce the energy requirements and cost of the process is through the development of more cost-effective and superior-performing amines.

The chemical reactions involved in CO_2 absorption/desorption by aqueous amine-based absorbents are continually being investigated to identify potential for and make improvements in efficiency. When CO_2 reacts with amines in an aqueous environment, carbamate, bicarbonate (HCO_3^-) and protonated amine are generated. Briefly, primary (R_1NH_2) and secondary (R_1R_2NH) amines, such as MEA and diethanolamine (DEA), respectively, typically react with CO_2 in an aqueous environment to form a carbamate derivative, $R_1R_2NCOO^-$ (a carboxylate moiety), as shown in Scheme 1. The 2:1 stoichiometry of the reaction limits the absorption capacity of primary and secondary amines to a theoretical upper limit of 0.5 moles of CO_2 per mole of amine. Generally this reaction pathway is kinetically and thermodynamically favoured for primary and secondary amines (*6*). The carbamate species may undergo hydrolysis to produce HCO_3^- and regenerate a free amine (*7–9*) (Scheme 1). A certain amount of carbamate hydrolysis is anticipated to occur with most amines (*10*), however it has yet to be observed, and given the chemical stability of the carbamate derivative of primary and secondary amines, it does not occur at a readily appreciable rate (*7*).

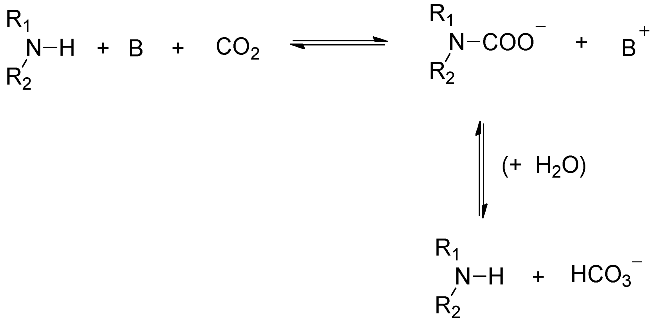

Scheme 1. Reaction mechanism leading to carbamate formation for the reaction of CO_2 with primary (R_1R_2NH, where R_2=H) and secondary (R_1R_2NH) amines (27).

Tertiary amines ($R_1R_2R_3N$) do not react directly with CO_2 to form the carbamate species, as in the case of primary and secondary amines. The lack of a free proton on the nitrogen atom of these amines inhibits carbamate formation (*9*, *11*, *12*). Instead, tertiary amines are thought to behave as a catalyst, facilitating the hydrolysis of CO_2 to generate HCO_3^- (base-catalyzed reaction pathway) (*9*, *11*, *13*).

The degree of carbamate versus HCO_3^- formation will impact on the CO_2 absorption capacity, absorption rate and regeneration energy of amine-based absorbents. Amines that form a stable carbamate derivative tend to exhibit faster reaction rates (*14*), however their absorption capacity is limited (*11*) due to the 2:1 stoichiometry of the reaction, and a larger input of energy is required for regeneration (*9*). On the other hand, amines that form more HCO_3^- than carbamate exhibit slower reaction rates, higher absorption capacities and require less energy for regeneration (*9–11*, *15*). The HCO_3^- reaction pathway is kinetically and thermodynamically less favourable than that of carbamate formation (*6*).

Amines and their ionic reaction products (carbamate, HCO_3^- and protonated amine) absorb radiation in the mid-infrared frequency range. Fourier Transform Infrared (FT-IR) spectroscopy is therefore capable of detecting these absorbing species (*16–19*). Recent advances in Attenuated Total Reflectance (ATR) FT-IR spectroscopy have allowed for the convenient and rapid analysis of these chemical species to be carried out *in-situ* as CO_2 is absorbed into an aqueous amine solution. *In-situ* FT-IR analysis in particular is a valuable tool as it can provide an insight into the reaction mechanism and pathway that is difficult to otherwise observe and measurements can be achieved without disturbing the system. Having this insight into the reaction pathway allows us to identify certain structural features of amines that give rise to more favorable characteristics for the absorption of CO_2, making it possible to tailor amine structures for enhanced CO_2 absorption capacities and rates.

Recently, heterocyclic amines such as piperazine and piperidine have attracted considerable attention due to their increased activity for CO_2 absorption. Piperazine in particular has been found to exhibit significantly enhanced CO_2 absorption rates (53,000 m^3/ kmol s), along with an increased absorption capacity, compared to other primary and secondary amines, such as MEA (7,000 m^3/ kmol s) and DEA (1,200 m^3/ kmol s) (*20*). This increased reactivity towards CO_2 has been attributed to the cyclic and diamine structure of piperazine (*20*). The second amine moiety offers the potential for enhanced CO_2 absorption capacity either in the form of a second reactive site for carbamate formation or proton acceptance, in the catalysis of bicarbonate formation or in modifying/enhancing the reactivity of the first amine site. However, the low aqueous solubility of piperazine (1.7 mol/ L (146 g/ L) at 20°C) (*21*) and piperazine carbamate (1.3 mol/ L (170 g/ L) before precipitation) (*22*) limits its use as a sole CO_2 capture absorbent (*22*). Rather, piperazine is commonly used in catalytic quantities as an absorption accelerator in aqueous solutions of sterically-hindered or tertiary amines (*22–26*). In contrast, piperidine, the monoamine analogue of piperazine, does not suffer the same limitations with improved aqueous solubility.

In light of this, ATR FT-IR spectroscopy has been applied to investigating the reaction between CO_2 and a subset of structurally variant heterocyclic amines. We believe studying the reaction between CO_2 and piperidine, as well as commercially available functionalized piperidine derivatives, e.g. those with methyl, hydroxyl and hydroxyalkyl substituents, will provide valuable insight into the effect molecular structural variation has on CO_2/amine reactivity

Downloaded by 89.163.35.42 on June 14, 2012 | http://pubs.acs.org
Publication Date (Web): May 3, 2012 | doi: 10.1021/bk-2012-1097.ch001

of heterocyclic amines and their enhanced activity compared to conventional primary and secondary amines. This chapter herein reports our findings.

Characterizing the Effect Molecular Structural Variation Has on CO_2/Amine Reactivity

To characterize the effects of molecular structural variation on CO_2/ amine reactivity, the CO_2 absorption characteristics of a series of functionalized piperidines were investigated. Figure 1 provides the structures of the subset of amines analyzed. The chemical reactions between CO_2 and the functionalized piperidines were followed in-situ using ATR FT-IR spectroscopy. The effect of the structural variations on CO_2 absorption was then assessed in relation to the:

- IR identifiable ionic reaction products i.e. carbamate versus HCO_3^- absorbance, with time and CO_2 absorption.
- CO_2 absorption capacity - moles of CO_2 absorbed per mole of amine in solution (mol CO_2/ mol amine), and
- mass transfer coefficient at zero loading - initial rate of CO_2 absorption.

The CO_2 absorption capacity was measured simultaneously with the IR spectral data during a typical CO_2 absorption/ FT-IR experiment with an aqueous amine solution. Briefly, a typical absorption experiment involved bubbling a 13% (v/v) CO_2 in nitrogen (N_2) gas stream through an aqueous amine solution (3 mol/ L) situated in a glass reaction vessel. The difference between the CO_2 concentration of the reactor gas inflow and gas outflow (measured using a Horiba VA 3000 CO_2 analyzer) was used to determine the amount of CO_2 absorbed by the amine solution (mol CO_2/ mol amine). Each experiment was run until the percent CO_2 concentration of the gas outflow returned to its original value (13%), i.e. chemical equilibrium had been reached and a maximum CO_2 loading was achieved. Depending on the amine a typical run lasted between 45-90 minutes. A diamond tip ATR probe, optically coupled to an FT-IR spectrometer (all supplied by Mettler Toledo), was immersed in the aqueous amine solution for the duration of the experiment and in-situ IR measurements were obtained simultaneously with the CO_2 absorption measurements. The FT-IR spectrometer was set to continuously collect spectra over the spectral range of 4000-650 cm^{-1}. Prior to analysis of the amine/ CO_2/ H_2O spectra, the baseline was adjusted to zero. For more details on the experimental technique see Robinson *et al* (*27*).

A wetted-wall column (WWC) apparatus was used to analyze the absorption rate of CO_2 into aqueous solutions of the functionalized piperidines (1 mol/ L). Briefly, the process involves counter-contacting a 1 mol/ L aqueous amine thin liquid film (170 ml/ min flow rate), with a N_2/ CO_2 gas stream (5 L/ min flow rate) on the surface of a stainless steel rod with a known surface area (effective height 8.21 cm, diameter 1.27 cm). The CO_2/ N_2 composition (v/v) was varied to achieve CO_2 partial pressures in the range of 0 to 20 kPa. The difference between the CO_2 concentration of the reactor gas inflow and gas outflow (measured using a Horiba VA-3000 CO_2 analyzer), along with the known experimental parameters

Downloaded by 89.163.35.42 on June 14, 2012 | http://pubs.acs.org
Publication Date (Web): May 3, 2012 | doi: 10.1021/bk-2012-1097.ch001

including gas flow rate and contact area for reaction, were used to determine the flux and mass transfer coefficient (K_g) at zero loading (*27*).

All experiments were carried out at 40°C, which is the current standard operating temperature for the absorption step of the PCC process.

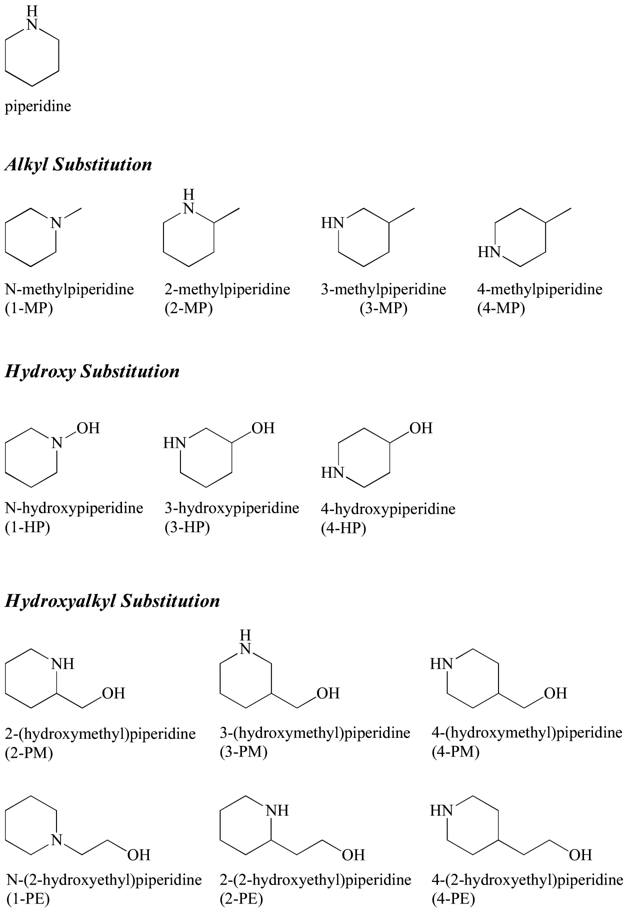
piperidine
Alkyl Substitution
N-methylpiperidine (1-MP)
2-methylpiperidine (2-MP)
3-methylpiperidine (3-MP)
4-methylpiperidine (4-MP)
Hydroxy Substitution
N-hydroxypiperidine (1-HP)
3-hydroxypiperidine (3-HP)
4-hydroxypiperidine (4-HP)
Hydroxyalkyl Substitution
2-(hydroxymethyl)piperidine (2-PM)
3-(hydroxymethyl)piperidine (3-PM)
4-(hydroxymethyl)piperidine (4-PM)
N-(2-hydroxyethyl)piperidine (1-PE)
2-(2-hydroxyethyl)piperidine (2-PE)
4-(2-hydroxyethyl)piperidine (4-PE)

Figure 1. Structures of the subset of functionalized piperidines examined in this study.

Infrared Spectral Analysis

The IR spectral window 1800-900 cm^{-1} was focused on for monitoring the chemical species evolving in solution as CO_2 was being absorbed into solution. The region above 1800 cm^{-1} and below 900 cm^{-1} contained no valuable information. Above 1800 cm^{-1} is the broad O-H stretch of water (3700 – 2500 cm^{-1}) and a 'blind spot' were the diamond sensor on the ATR probe absorbs IR radiation (2250 – 1950 cm^{-1}). Below 900 cm^{-1} is the superimposition of a number of absorbing species in the system.

Downloaded by 89.163.35.42 on June 14, 2012 | http://pubs.acs.org
Publication Date (Web): May 3, 2012 | doi: 10.1021/bk-2012-1097.ch001

Downloaded by 89.163.35.42 on June 14, 2012 | http://pubs.acs.org
Publication Date (Web): May 3, 2012 | doi: 10.1021/bk-2012-1097.ch001

Piperidine

Figure 2 shows the IR spectral changes that occur in the 1800-900 cm^{-1} region as CO_2 is absorbed by an aqueous piperidine (3 mol/ L) solution. Five major FT-IR peaks are shown to evolve with CO_2 absorption in the 1800-900 cm^{-1} region and hence can be related to the vibrational modes of the potential ionic reaction products, including:

- piperidine-carbamate (piperidine-1-carboxylate) of the form $R_1R_2NCOO^-$,
- protonated piperidine (piperidine-H$^+$), and
- bicarbonate (HCO_3^-).

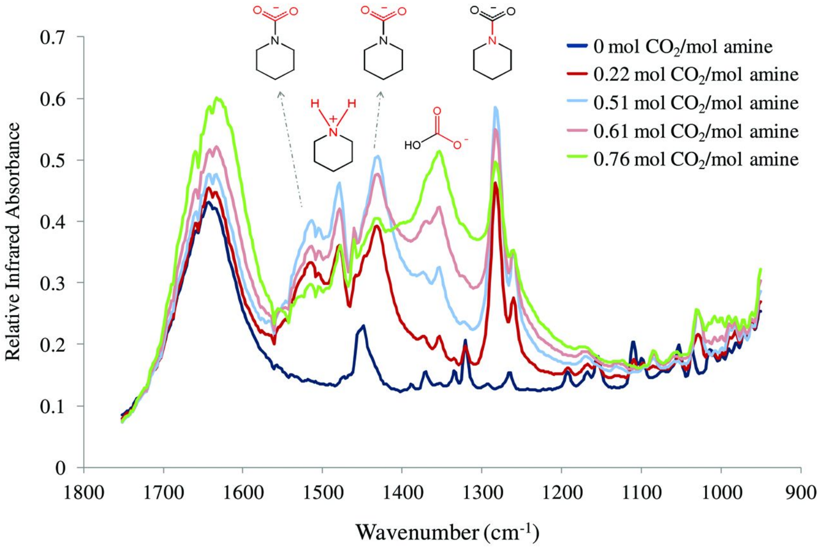

Figure 2. IR spectra of aqueous piperidine (3 mol/ L) as CO_2 is absorbed to a maximum loading of 0.76 mol CO_2/ mol amine, collected during a typical CO_2 absorption/ FT-IR experiment (27). (see color insert)

Piperidine, being a secondary amine should typically react with CO_2 in solution to form a carbamate derivative. Specific assignment of the spectral peaks that emerged is detailed below.

The broad peak at 1640 cm^{-1} present in the original aqueous piperidine spectra and subsequent spectra was also found to be present in the spectrum of pure water and has been assigned to the O-H bending mode of water (*28*, *29*).

Three main peaks have been assigned to the vibrational modes of piperdine-1-carboxylate, as shown in Figure 2:

i. **1514 cm^{-1} -** asymmetric COO^- stretching vibration ($V_{as}COO^-$)
ii. **1434 cm^{-1} -** symmetric COO^- stretching vibration (V_sCOO^-)
iii. **1283 cm^{-1} -** N-COO^- stretching vibration (VN-COO^-).

The carbamate species analyzed in this study are a deprotonated carboxylic acid derivative, or carboxylate (anionic), and do not give rise to the typical strong carbonyl (C=O) absorbance band expected to evolve at around 1700 cm^{-1}. The electron distribution of the negatively charged COO^- group in the depronated carboxylic acid becomes spread out across both C-O bonds equivalently to stabilize the carboxylate moiety (i.e. resonance stabilization). The two oxygen atoms become coupled, giving rise two absorbance bands, an asymmetric and symmetric COO^- stretch, at lower frequencies compared to that of the VC=O of carboxylic acids. The $V_{as}COO^-$ and V_sCOO^- of carboxylates have been found to generally give rise to two absorbance bands in the 1650-1540 cm^{-1} and 1450-1360 cm^{-1} region, depending on the molecular constituents (*29*).

To guide in the assignment of the vibrational modes of piperdine-1-carboxylate, in particular VN-COO^-, gas phase harmonic frequency (and intensity) calculations were performed for optimized geometries of the piperidine carbamate species (characterized by a gradient < 0.001), at both the B3LYP/ 6-31+G** and MP2/ 6-31+G** level of theory using *'Spartan 08'* (*30*) software. Density functional theory (DFT) calculations (B3LYP) were employed as they are computationally economical and thus applicable to larger molecules such as that investigated in this study. DFT is also commonly used and has been reported to yield accurate geometries and reasonable vibration frequencies (*31*, *32*). *Ab initio* calculations (MP2) were also performed for comparative purposes.

VN-COO^- was predicted to give rise to a sharp intense band at 1289 cm^{-1} (B3LYP, no scaling) and 1287 cm^{-1} (MP2, no scaling), similar in shape to that emerging at 1283 cm^{-1} in Figure 2. The theoretical results were in good agreement with the experimental results with regards to VN-COO^-, despite the exclusion of anharmonic effects and solvent corrections in the calculations, confirming our assignment of the 1283 cm^{-1} absorbance band. With regards to the $V_{as}COO^-$ and V_sCOO^-, the calculations were unable to match the assigned vibrational frequencies of the carboxylate moiety, predicting the frequency of $V_{as}COO^-$ at 1694 cm^{-1} (very intense) and V_sCOO^- at 1402 cm^{-1} (very weak). Both the symmetric and asymmetric C-O stretching modes are appreciably affected by anharmonicity and solvation effects (*33*), as opposed to VN-COO^-, which would account for the large differences between the experimental solution phase and calculated gas phase values. All calculated frequencies herein are reported with no scaling.

The absorbance band that appears at 1477 cm^{-1} has been assigned to the NH_2^+ bending mode of piperidine-H^+. To confirm this assignment spectral data was collected during the gradual acidification of the original 3 mol/ L piperidine solution using concentrated HCl acid (Figure 3). Figure 3 shows a small peak evolving at around 1477 cm^{-1} on protonation of the amine functionality. The theoretical calculations predicted piperidine-H^+ to have two NH_2^+ bending modes, one at 1661 cm^{-1} (B3LYP) or 1675 cm^{-1} (MP2) (scissoring) and another at 1437 cm^{-1} (B3LYP) or 1465 cm^{-1} (MP2) (twisting). An absorbance band in the

Downloaded by 89.163.35.42 on June 14, 2012 | http://pubs.acs.org
Publication Date (Web): May 3, 2012 | doi: 10.1021/bk-2012-1097.ch001

1700-1620 cm^{-1} region (*8*) was expected to evolve, however as can been seen from Figure 2, this region is obscured by the dominant broad water absorbance band at 1643 cm^{-1}. The calculated NH_2^+ bending mode at 1437 cm^{-1} (B3LYP) or 1465 cm^{-1} (MP2), depending on the level of theory, is in reasonably good agreement with the experimental value of 1477 cm^{-1}.

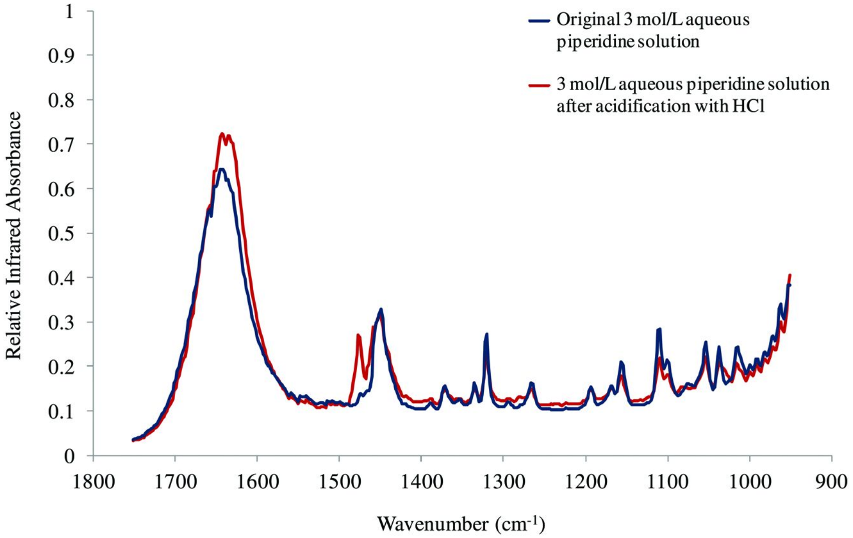

Figure 3. IR spectra of a 3 mol/ L aqueous piperidine solution before and after acidification with concentrated HCl. (see color insert)

Figure 4 shows that an almost identical relationship exists between IR peak absorbance and cumulative CO_2 absorption for the spectral peaks assigned to both piperidine-1-carboxylate (VN-COO^-, $V_{as}COO^-$ and V_sCOO^-) and piperidine-H^+. Peak absorbance is observed to increase at the rate of carbamate formation at the reaction onset and decrease after a loading of about 0.5 mol CO_2/ mol amine. This decrease in peak absorbance was not only observable in the peak absorbance versus cumulative CO_2 absorption curve presented in Figure 4, but it was also clearly evident in the raw sequential IR spectral data presented in Figure 2. This change in peak absorbance at high CO_2 loadings (> 0.5 mol CO_2/ mol amine) may be attributed to the sequential onset of a new reaction pathway such as the hydrolysis of the carbamate derivative to HCO_3^-. The relationship identified above, with regards to the absorbance bands assigned to both piperidine-1-caboxylate and piperidine-H^+, can be distinguished from that observed for the broad absorbance band that evolves at 1354 cm^{-1}, which shows a corresponding increase in peak absorbance after a loading of about 0.5 mol CO_2/ mol amine. This band has been assigned to the $V_sC\text{-}O^-$ of HCO_3^-, which is in good agreement with literature values for aqueous HCO_3^- (*16*, *28*). Falk and Miller (*16*) investigated the IR spectrum of CO_2 in aqueous solution, reporting carbonate (CO_3^{2-}) and HCO_3^- to give rise to bands at around 1385 cm^{-1} and 1360

Downloaded by 89.163.35.42 on June 14, 2012 | http://pubs.acs.org
Publication Date (Web): May 3, 2012 | doi: 10.1021/bk-2012-1097.ch001

cm^{-1}, respectively. The IR absorbance of HCO_3^- in an aqueous amine/ CO_2 system was established by separate experiments that are detailed below.

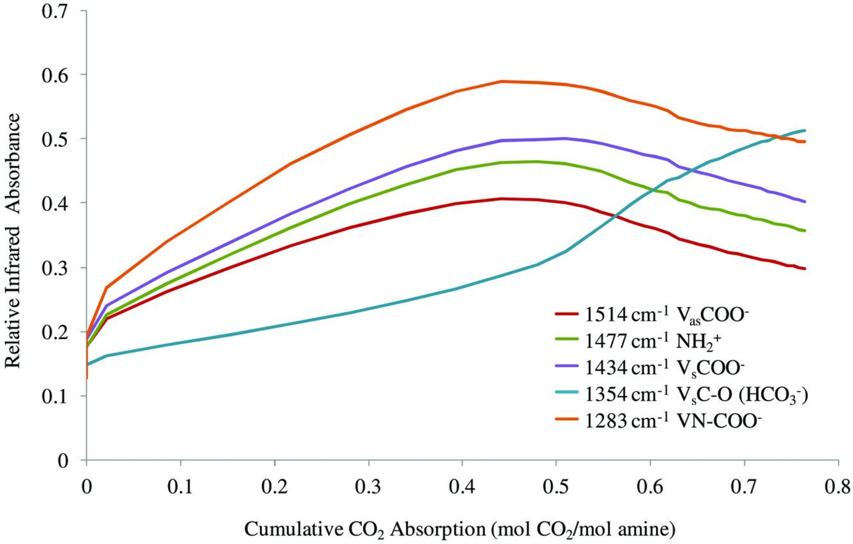

Figure 4. The relationship between the cumulative CO_2 absorption of aqueous piperidine (3 mol/ L) and IR peak absorbance for the bands assigned to the vibrational modes of piperidine-1-carboxylate, piperidine-H^+ and HCO_3^- (27). (see color insert)

There are two possible reaction pathways that can lead to the formation of HCO_3^- in an aqueous amine environment i.e. via the

i. hydrolysis of the carbamate species (equation 1 and 2, where base 'B' is a second amine molecule or molecule of water) or
ii. direct nucleophilic attack of OH- on dissolved CO_2 (base-catalyzed reaction pathway, typical of tertiary amines) (equation 3 and 4).

$$R_1R_2NH + CO_2 + B \rightleftharpoons R_1R_2NCOO^- + BH^+ \quad (1)$$

$$R_1R_2NCOO^- + H_2O \rightleftharpoons R_1R_2NH + HCO_3^- \quad (2)$$

$$R_1R_2R_3N + H_2O \rightleftharpoons R_1R_2R_3NH^+ + OH^- \quad (3)$$

$$OH^- + CO_2 \rightleftharpoons HCO_3^- \quad (4)$$

The IR spectral data presented in Figure 2 and 4, for the aqueous piperidine/ CO_2 system, is illustrative of the first of these two pathways (equation 1 and 2) with the simultaneous decline in absorbance of the $V_{as}COO^-$, V_sCOO^- and VN-COO$^-$ of piperidine-1-carboxylate and increase in HCO_3^- absorbance.

In Recent Advances in Post-Combustion CO2 Capture Chemistry; Attalla, M.;
ACS Symposium Series; American Chemical Society: Washington, DC, 2012.

Downloaded by 89.163.35.42 on June 14, 2012 | http://pubs.acs.org
Publication Date (Web): May 3, 2012 | doi: 10.1021/bk-2012-1097.ch001

To demonstrate further that the trend in peak absorbance identified above is indicative of a carbamate derivative undergoing hydrolysis, IR spectral data was collected during a typical CO_2 absorption experiment with aqueous piperazine (PZ) (1.5 mol/ L). PZ is the diamine analogue of piperidine and is believed to form a stable carbamate derivative, as well as a dicarbamate species (*20*, *34*).

Piperazine

The IR spectral profile presented in Figure 5 for the aqueous PZ/ CO_2 system closely resembles that of the monoamine analogue piperidine (Figure 2), with regards to peak positioning (PZ frequencies are slightly shifted). The aqueous PZ/ CO_2 system (Figure 5) exhibits the $V_{as}COO^-$ (1524 cm^{-1} and shifts to 1546 cm^{-1} as CO_2 is absorbed), V_sCOO^- (1425 cm^{-1}) and $VN\text{-}COO^-$ (1276 cm^{-1} and shifts to 1289 cm^{-1}) of the PZ-carbamate derivative (1-piperzinium-4-carboxylate ($^+H\text{-}HNR_1R_2NCOO^-$) or piperazine-1-carboxylate ($HNR_1R_2NCOO^-$)); and the NH_2^+ vibration of the PZ-H^+ species (1470 cm^{-1}, including piperazinium, piperazine-1,4-diium and 1-piperzinium-4-carboxylate).

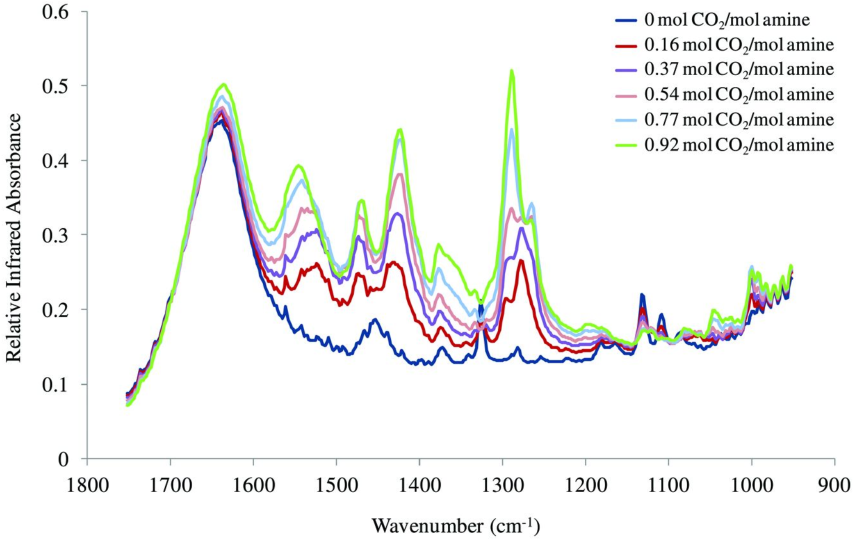

Figure 5. IR spectra of aqueous PZ (1.5 mol/ L) as CO_2 is absorbed to a maximum loading of 0.92 mol CO_2/ mol amine, collected during a typical CO_2 absorption/FT-IR experiment. (see color insert)

As expected, an almost identical relationship exists between IR peak absorbance and cumulative CO_2 absorption (Figure 6) for the spectral peaks assigned to the $V_{as}COO^-$ and V_sCOO^- of the PZ-carbamate species and PZ-H^+. Peak absorbance is observed to increase at the rate of carbamate formation at

Downloaded by 89.163.35.42 on June 14, 2012 | http://pubs.acs.org
Publication Date (Web): May 3, 2012 | doi: 10.1021/bk-2012-1097.ch001

the reaction onset and level off as a maximum CO_2 loading of 0.92 mol CO_2/ mol amine is approached. However, this trend can be differentiated from that observed for the VN-COO^- absorbance bands that evolve at 1276 cm^{-1} and 1294 cm^{-1} (Figure 5). Figures 5 and 6 show the peak emerging at 1276 cm^{-1} to be the dominant absorbance band, increasing with initial CO_2 absorption up to a loading of about 0.4 - 0.5 mol CO_2/ mol amine at which point it ceases to increase in intensity, and a corresponding sharp increase in intensity of the absorbance band at 1294 cm^{-1} is observed, along with a shift in frequency to 1289 cm^{-1}. The emergence of the intense VN-COO^- absorbance band at 1289 cm^{-1} may be attributed to the formation of PZ-dicarbamate ($^-$OOC-PZ-COO^-). This trend in peak absorbance was not observed for the heterocyclic monoamine piperidine (Figure 2) or for the remaining subset of secondary heterocyclic amines analyzed in this study.

Downloaded by 89.163.35.42 on June 14, 2012 | http://pubs.acs.org
Publication Date (Web): May 3, 2012 | doi: 10.1021/bk-2012-1097.ch001

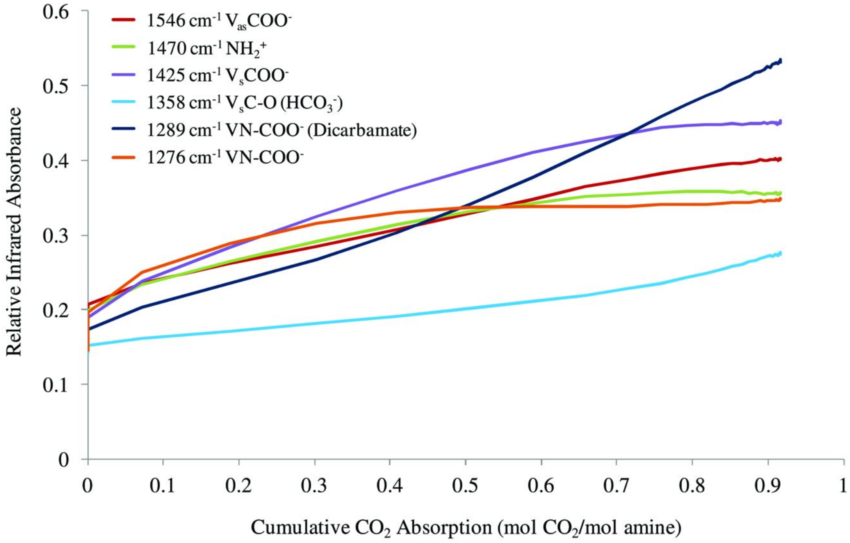

Figure 6. The relationship between the cumulative CO_2 absorption of aqueous PZ (1.5 mol/ L) and IR peak absorbance for the bands assigned to the vibrational modes of the PZ-carbamate species, PZ-H^+ and HCO_3^-. (see color insert)

The weak broad absorbance band beginning to emerge in the 1350-1360 cm^{-1} region of the aqueous PZ/ CO_2 IR spectral profile (Figure 5) may be assigned to the V_sC-O of HCO_3^-. This absorbance band is far less prominent then that observed for the aqueous piperidine/ CO_2 system (Figure 2) and does not illustrate the same trend in peak absorbance, i.e. the simultaneous decline in $V_{as}COO^-$, V_sCOO^- and VN-COO^- and increase in HCO_3^- absorbance bands, at high CO_2 loadings (> 0.5 mol CO_2/ mol amine) (Figure 5 and 6). Based on the IR spectral data presented in Figure 5 and 6, PZ forms a stable carbamate derivative that does not undergo hydrolysis as readily as the piperidine-carbamate derivative.

Downloaded by 89.163.35.42 on June 14, 2012 | http://pubs.acs.org
Publication Date (Web): May 3, 2012 | doi: 10.1021/bk-2012-1097.ch001

Effect of N-Methyl, -Hydroxyl and -Hydroxyalkyl Substituents

Tertiary amines, such as the N -methyl, -hydroxyl and -hydroxyalkyl substituted piperidines (1-MP, 1-HP and 1-PE, respectively) analyzed in this study, form HCO_3^- on absorption of CO_2. The lack of a free proton on the nitrogen atom of these amines inhibits carbamate formation. For this reason their activity will not be compared to the subset of secondary amines being analyzed. However, the IR spectra collected for these amines will be used as a standard for HCO_3^- formation in an aqueous amine/ CO_2 system. Furthermore, the results obtained for these amines illustrate the effect different N-substituents have on CO_2 absorption via the base-catalyzed reaction pathway.

The IR spectral profile presented in Figure 7 for aqueous 1-PE (3 mol/ L) shows the evolution of a characteristic broad HCO_3^- absorbance band in the 1350-1360 cm^{-1} region, with CO_2 absorption. Further confirmation of this assignment is provided in Figure 8, which shows the evolution of a similar broad absorbance band in the 1360-1350 cm^{-1} region with the gradual addition of ammonium bicarbonate to an aqueous piperidine (3 mol/ L) solution. The same broad absorbance band was also observed in the IR spectral data collected for the aqueous 1-MP/ CO_2 system. 1-HP was an exception, the IR spectral data collected for this amine showed no spectral changes for the duration of the experiment. The tertiary amine 1-HP did not absorb any CO_2, as opposed to 1-MP and 1-PE. It seems that the hydroxyl substituent directly bonded to the amino nitrogen in 1-HP, as opposed to the alkyl or hydroxyalkyl substituent in 1-PM and 1-PE, respectively, inhibits a tertiary amine's role as a catalyst in the base-catalyzed hydrolysis of CO_2 to generate HCO_3^-.

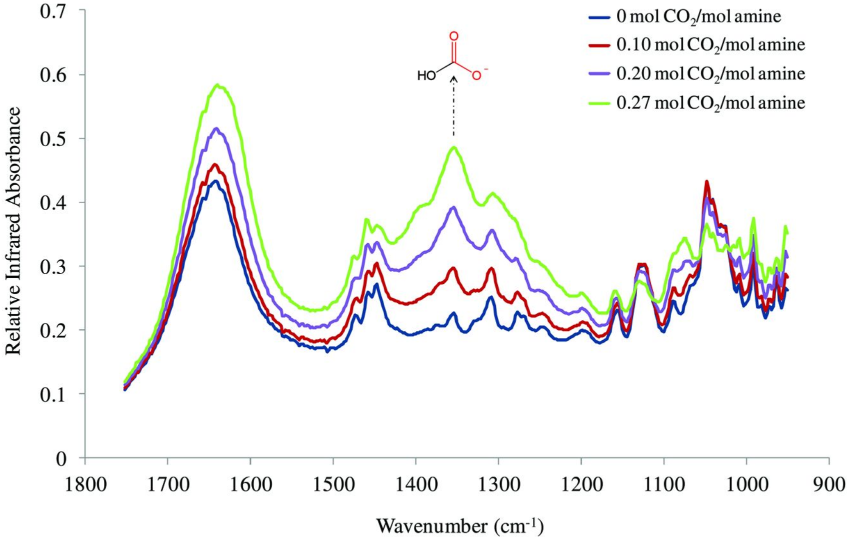

Figure 7. IR spectral profile obtained for aqueous 1-PE (3 mol/ L), collected during a typical CO_2 absorption/ FT-IR experiment (27). (see color insert)

Downloaded by 89.163.35.42 on June 14, 2012 | http://pubs.acs.org
Publication Date (Web): May 3, 2012 | doi: 10.1021/bk-2012-1097.ch001

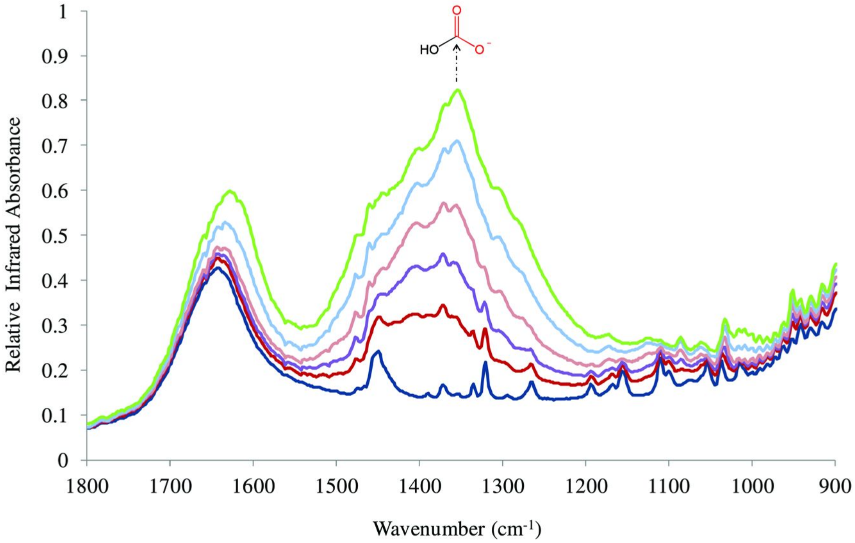

Figure 8. IR spectra of an aqueous piperidine solution (3mol/ L) with the gradual addition of ammonium bicarbonate (27). (see color insert)

Effect of 2-Methyl and -Hydroxyalkyl Substituents

The 2-MP, 2-PM and 2-PE compounds analyzed in this study, all share a common structural feature, that being either an alkyl or hydroxyalkyl substituent on the carbon alpha (Cα) to the amino nitrogen. The IR spectral data collected for these amines differs significantly from that obtained for the aqueous piperidine system. Their spectra however, are very similar to that of the tertiary amines 1-MP and 1-PE (though much more intense), with the evolution of the characteristic broad absorbance band in the 1360-1350 cm^{-1} region, indicative of HCO_3^- formation. Figure 6 illustrates this similarity, presenting sequential IR spectral data collected during a typical CO_2 absorption/ FT-IR experiment with aqueous solutions (3 mol/ L) of 2-MP (Figure 9) and 2-PE (Figure 10).

A common misconception for amines with one or more substituents at the α-carbon (e.g. conventional absorbent 2-amino-2-methyl-1-propanol (AMP)), or in this study the 2-methyl (2-MP), 2-hydroxymethyl (2-PM) and 2-hydroxyethyl (2-PE) substituted piperidines, is the notion that they are sterically-hindered and unable to form the carbamate species. Recently, a theoretical study undertaken by Ismael *et al* (*35*) suggested that the carbamate reaction pathway is kinetically unfavorable for these amines, rather the reaction proceeds directly to HCO_3^- formation via a base-catalyzed reaction mechanism, similar to that of tertiary amines. However, in an even more recent theoretical and experimental study undertaken by Jackson *et al.* (*36*), direct observation of the carbamate derivatives of the C_α-substituted amines AMP and tris(hydroxymethyl)amino methane (THAM) were made based on negative-ion electrospray ionization mass spectrometry (ESI-MS) data and the reaction of these amines with sodium bicarbonate ($NaHCO_3$) to form a carbamate species in an aqueous environment.

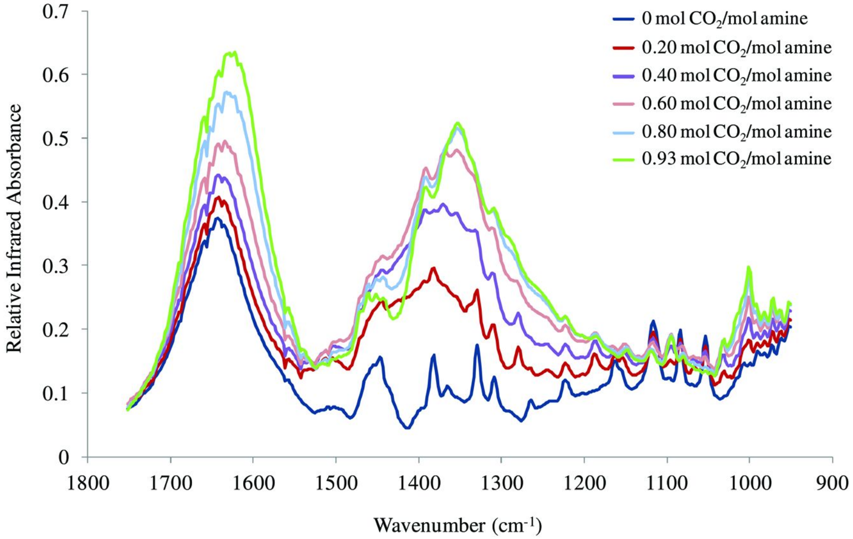

Figure 9. IR spectra of aqueous 2-MP (3 mol/ L) as CO_2 is absorbed to a maximum loading of 0.93 mol CO_2/ mol amine, collected during a typical CO_2 absorption/ FT-IR experiment (27). (see color insert)

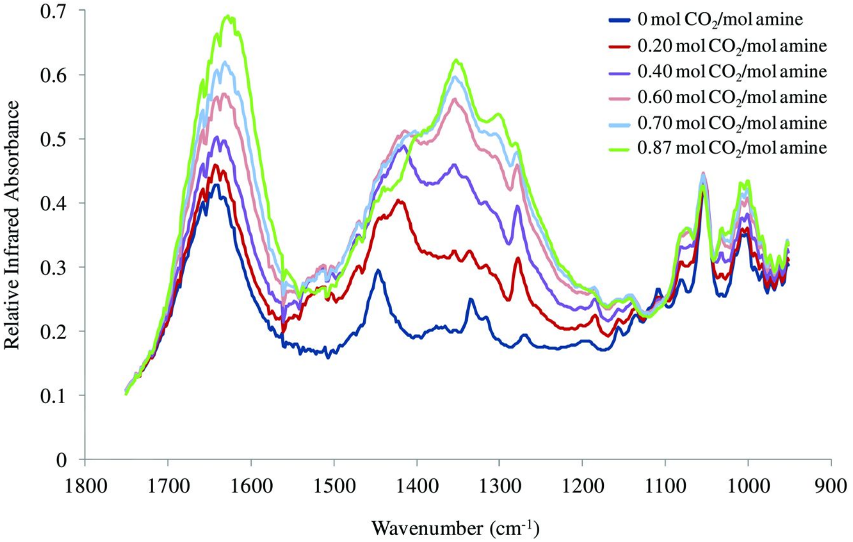

Figure 10. IR spectra of aqueous 2-PE (3 mol/ L) as CO_2 is absorbed to a maximum loading of 0.87 mol CO_2/ mol amine, collected during a typical CO_2 absorption/ FT-IR experiment (27). (see color insert)

Downloaded by 89.163.35.42 on June 14, 2012 | http://pubs.acs.org
Publication Date (Web): May 3, 2012 | doi: 10.1021/bk-2012-1097.ch001

In an attempt to observe the carbamate derivatives of 2-MP, 2-PM and 2-PE in real time as a result of the reaction with gaseous CO_2 (at low partial pressures i.e. 13 % CO_2 (v/v) in N_2 @ 1 atm) and using *in-situ* ATR FT-IR spectroscopy, spectral data was collected during CO_2 absorption experiments with amine/ hexanol solutions. In a non-aqueous environment, HCO_3^- formation via the CO_2 or carbamate hydrolysis pathway should be suppressed. To confirm this inhibition of HCO_3^- formation, spectral data was collected during a typical CO_2 absorption with a tertiary amine (1-PE)/ hexanol solution. Figure 11a shows there to be no spectral changes in the 1800-900 cm^{-1} region, for the duration of the experiment (run time = 20 mins), as would be expected with an aqueous 1-PE/ CO_2 system (Figure 7). The 1-PE/ hexanol solution did not absorb any CO_2 due to the inhibition of HCO_3^- formation. For comparison and to establish the formation of carbamate species in a non-aqueous environment, spectral data was also collected during a typical CO_2 absorption experiment with a piperidine/ hexanol solution. The piperidine/ hexanol solution absorbed CO_2 to an upper limit of 0.5 mol CO_2/ mol amine, as opposed to the upper limit of 0.76 mol CO_2/ mol amine obtained for the aqueous piperidine solution (Figure 2). The spectra presented in Figure 11b shows the evolution of piperidine-1-carboxlylate and piperidine-H^+ absorbance bands including $V_{as}COO^-$ (1540 cm^{-1}), V_s COO^- (1425 cm^{-1}) and $VN\text{-}COO^-$ (1279 cm^{-1}); and one of the NH_2^+ bending modes (scissoring) at 1643 cm^{-1} (this mode was not observed in the piperidine/ CO_2/ H_2O system due to the broad H_2O absorbance band in this region). The NH_2^+ bending mode (wagging) identified as being responsible for the evolution of the absorbance band at 1477 cm^{-1} in the IR spectral data collected for the aqueous piperidine/ CO_2 system is not observable in the spectral data presented in Figure 11b for the piperidine/ CO_2/ hexanol system. This is due to the coinciding strong absorbance of the original piperidine/ hexanol solution in this region.

The Cα-substituted piperidines, including 2-MP, 2-PM and 2-PE, were found to absorb a small amount of CO_2 in a non-aqueous environment, as opposed to the tertiary amine 1-PE. This in itself is indicative of these amines being able to form a carbamate species, one that it is inherently susceptible to hydrolysis in an aqueous environment and subsequently HCO_3^- formation. The IR spectral profiles presented in Figure 12a and b for the 2-PE and 2-MP/ CO_2/ hexanol solutions, shows the evolution of the same absorbance bands as that observed for the piperidine/ CO_2 /hexanol system, although somewhat weaker, including the NH_2^+ bending mode of protonated 2-PE and 2-MP (1639 and 1638 cm^{-1}, respectively); and the $V_{as}COO^-$ (1536 cm^{-1}), V_SCOO^- (1416 and1417 cm^{-1}) and $VN\text{-}COO^-$ (1276 and 1278 cm^{-1}) of 2-(2-hydroxyethyl)piperidine-1-carboxylate and 2-methylpiperdine-1-carboxylate, respectively (carbamate derivatives of 2-PE and 2-MP, respectively). Because the intensity of these absorbance bands is weak, further clarification of the existence of these elusive anions was established based on ESI-MS data (*37*) and the method utilized by Jackson *et al.* in their detection of carbamate anions (*36*).

Downloaded by 89.163.35.42 on June 14, 2012 | http://pubs.acs.org
Publication Date (Web): May 3, 2012 | doi: 10.1021/bk-2012-1097.ch001

Downloaded by 89.163.35.42 on June 14, 2012 | http://pubs.acs.org
Publication Date (Web): May 3, 2012 | doi: 10.1021/bk-2012-1097.ch001

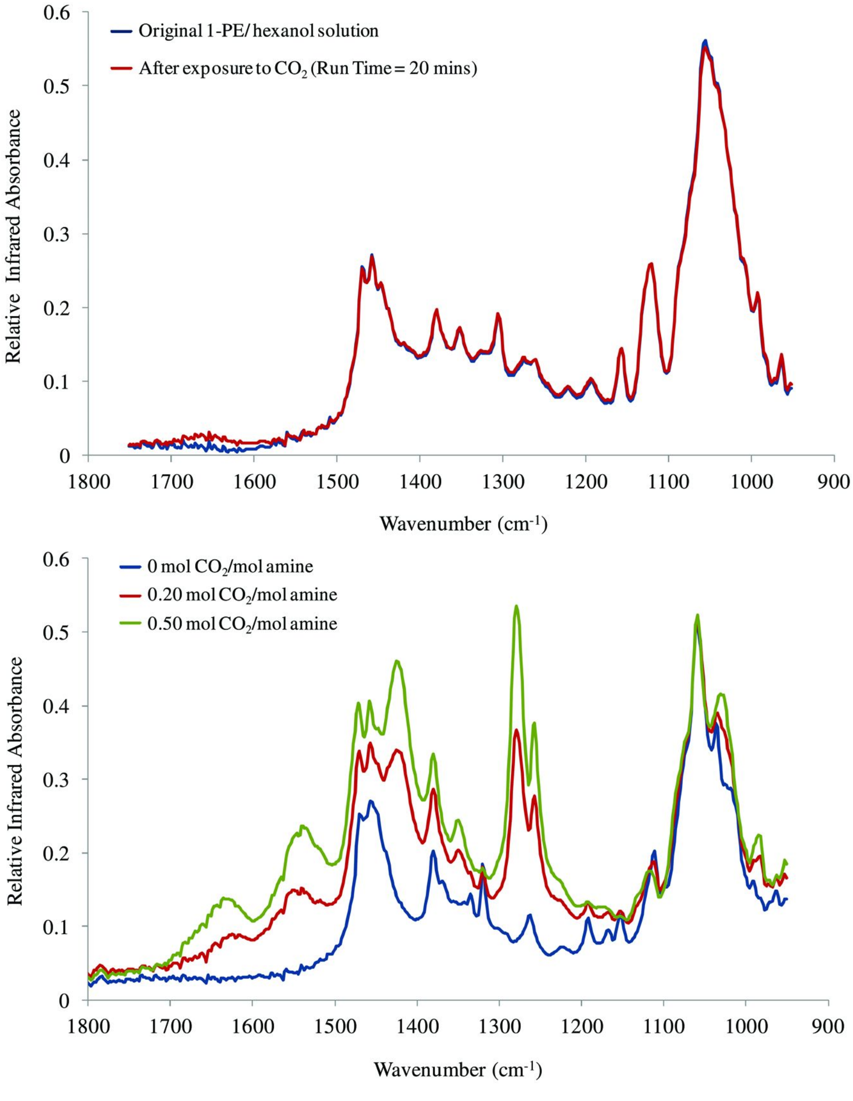

*Figure 11. The IR spectra collected as CO_2 was bubbled through **a)** a 1-PE / hexanol solution (3 mol/ L) and **b)** a piperidine/ hexanol solution (3 mol/ L) (27). (see color insert)*

Downloaded by 89.163.35.42 on June 14, 2012 | http://pubs.acs.org
Publication Date (Web): May 3, 2012 | doi: 10.1021/bk-2012-1097.ch001

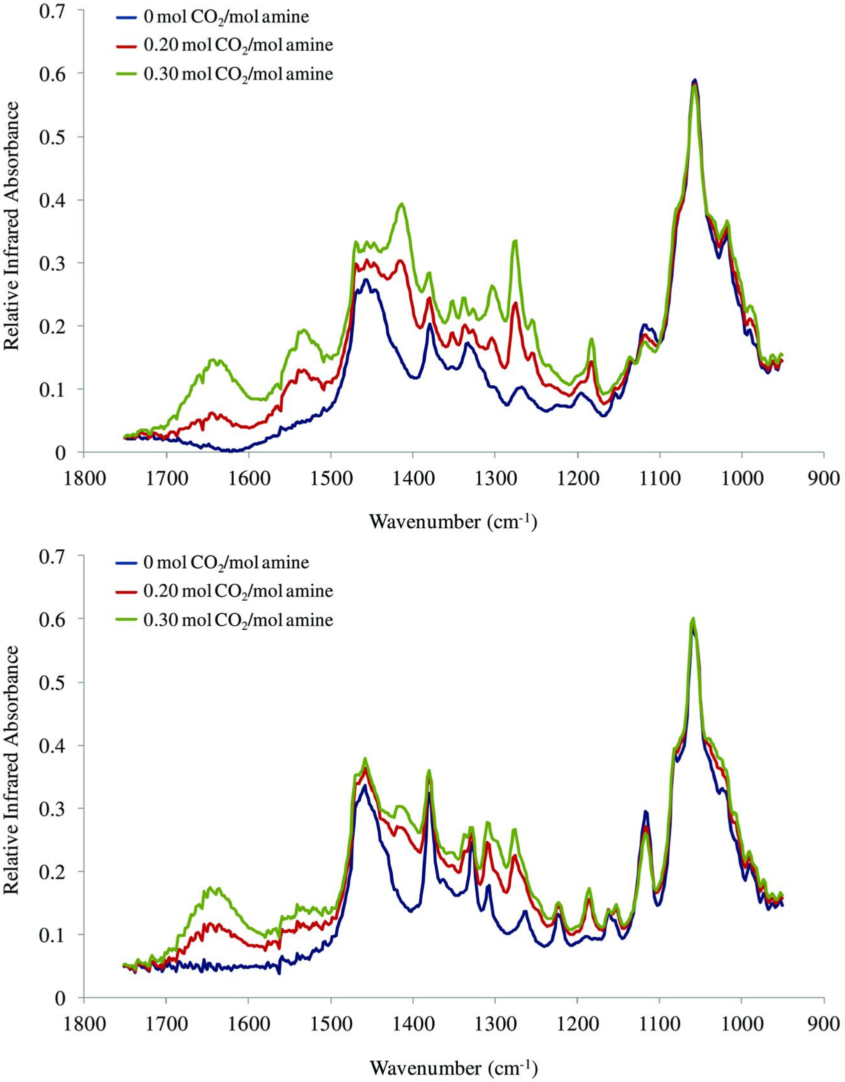

*Figure 12. The IR spectra collected as CO_2 was bubbled through **a)** a 2-PE/ hexanol solution (3 mol/ L) and **b)** a 2-MP/ hexanol solution (3 mol/ L) (27). (see color insert)*

Table 1. Comparison of the frequencies assigned to $V_{as}COO^-$, V_sCOO^-, $VN\text{-}COO^-$ and NH_2^+ for piperidine and the 3- and 4- methyl, hydroxyl and hydroxyalkyl substituted piperidines.

Amine/ CO_2/H_2O System	*Infrared Vibrational Modes and Frequencies (cm^{-1})*			
	$V_{as}COO^-$	*V_sCOO^-*	*$VN\text{-}COO^-$*	*NH_2^+*
piperidine	1514	1434	1283	1477
3-MP	1519	1429	1276	1474
4-MP	1519	1429	1261 shifts to 1272	1477
3-HP	1521	1429	1278	1477
4-HP	1521	1432	1276	1478
3-PM	1516	1430	1276	1477
4-PM	1516	1434	1274	1477
4-PE	1520	1432	1281	1477

Briefly, the method involved the addition of $NaHCO_3$ (50-70 µg/ ml) to aqueous solutions of 2-MP, 2-PM and 2-PE (130-150 µg/ ml), followed by analysis in a Waters Acquity HPLC-MS system. The carbamate derivatives of 2-MP (m/z= 141.9), 2-PM (m/z= 158.0) and 2-PE (m/z= 172.0) were observable in the negative ion ESI-MS broad scan spectrum. A dissociation peak corresponding to the mass loss of CO_2 (m/z= 44) was also evident in the multiple collision-induced dissociation (CID) spectrum of the 2-MP-carbamate parent ion (2-methylpiperidine-1-carboxylate) (*37*). However, in the case of the 2-PM and 2-PE carbamate parent ions (2-(hydroxylmethyl)piperidine-1-carboxylate and 2-(2- hydroxyethyl)piperidine-1-carboxylate, respectively), a dissociation peak corresponding to the mass loss of m/z= 46 was evident in their CID spectrum. A mass loss of m/z= 46 was also observed by Jackson *et al.* (*36*) in the CID spectrum they obtained for the carbamate derivative of secondary amine DEA. The carbamate derivatives of 2-PM and 2-PE, as well as DEA, both have exchangeable hydrogens on the hydroxyl group of the alkyl side chain that is within close proximity of the carboxylate moiety, similar to that of the anions of α-hydroxy carboxylic acids. These anions are known to dissociate by eliminating a mass loss of m/z= 46, corresponding to the loss of formic acid (*38*).

Effect of 3- and 4-Methyl, Hydroxyl and Hydroxyalkyl Subsituents

The IR spectral data collected for aqueous solutions of the 3- and 4- alkyl (3-MP and 4-MP), hydroxyl (3-HP and 4-HP) and hydroxyalkyl (3-PM, 4-PM and 4-PE) substituted piperidines illustrate a high degree of similarity with that of aqueous piperidine on absorption of CO_2, in terms of peak positioning and the relationship between peak absorbance and cumulative CO_2 absorption for the spectral peaks assigned to carbamate, protonated amine and HCO_3^- formation.

Downloaded by 89.163.35.42 on June 14, 2012 | http://pubs.acs.org
Publication Date (Web): May 3, 2012 | doi: 10.1021/bk-2012-1097.ch001

Table 1 provides a brief summary of the frequencies assigned to the carbamate vibrational modes $V_{as}COO^-$, V_sCOO^-, and $VN\text{-}COO^-$, as well as the protonated amine (NH_2^+) vibrational mode, for the 3- and 4- substituted piperidines. For comparison the vibrational frequencies of piperidine-1-carboxylate and piperidine-H^+ have also been included. From Table 1 it can be seen that the difference in frequencies corresponding to the vibrational modes of protonated amine and the carbamate derivatives of piperidine and the 3- and 4-substituted piperidines, do not exceed 7 cm^{-1}. There are a few differences in the IR spectral data collected, particularly with regards HCO_3^- formation and carbamate hydrolysis in the aqueous 3-HP and 4-HP/ CO_2 systems, which are discussed below.

With regards to the 3- and 4- methyl and hydroxyalkyl substituted piperidines, Figures 13-15 highlight the similarity in the spectral data collected for these amines, presenting a) a partial profile of the sequential IR spectral data collected for aqueous 3-MP (3 mol/ L), 3-PM (3 mol/ L) and 4-PE (3 mol/ L), respectively; and b) the corresponding relationship between peak absorbance and cumulative CO_2 absorption for the spectral peaks assigned to carbamate, protonated amine and HCO_3^- formation. The IR spectral data obtained for 4-MP and 4-PM have not been included as they closely resemble that of the IR spectral data presented in Figures 13-15.

Both the sequential IR spectral data and the peak absorbance versus cumulative CO_2 absorption curve, presented in Figures 13-15 for 3-MP, 3-PM and 4-PE, respectively, clearly illustrate the hydrolysis of the carbamate species (3-methylpiperidine-1-carboxylate, 3-(hydroxymethyl)piperidine-1- carboxylate and 4-(2-hydroxyethyl)piperidine-1-carboxylate, respectively) at high CO_2 loadings (> 0.5 mol CO_2/ mol amine) to generate HCO_3^-.

With regards to the 3- and 4- hydroxyl substituted piperidines (3-HP and 4-HP) hydrolysis of the carbamate species (3-hydroxypiperidine-1-carboxylate and 4-hydroxypiperidine-1-carboxylate, respectively) was not as evident in the IR spectral data collected for these amines, compared to piperidine, 3-MP, 4-MP, 3-PM, 4-PM and 4-PE. Figure 16 presents a) a partial profile of the sequential IR spectral data collected for aqueous 3-HP (3 mol/ L); and b) the relationship between peak absorbance and cumulative CO_2 absorption for the spectral peaks assigned to 3-hydroxypiperidine-1-carboxylate, 3-hydroxypiperidine-H^+ and HCO_3^- formation. From Figure 16a it can be seen that the evolution of the broad HCO_3^- absorbance band in the 1360-1350 cm^{-1} is not as prominent as that observed to evolve in the IR spectra collected for piperidine (Figure 2), or the 3- and 4- methyl and hydroxyalkyl substituted piperidines (Figures 13-15). The absorbance of the original aqueous 3-HP solution in this region, contributes to the intensity of the absorbance band seen to evolve, as well as the odd shape of this band compared to previously assigned HCO_3^- absorbance bands. The peak absorbance versus cumulative CO_2 absorption curve presented in Figure 16b also does not show to the same extent the decline in intensity of the carbamate absorbance bands as that observed for piperidine or the other 3- and 4- substituted piperidines. Further evidence with regards to the carbamate derivatives of 3-HP and 4-HP being less susceptible to hydrolysis is discussed below in terms of their absorption capacity.

Downloaded by 89.163.35.42 on June 14, 2012 | http://pubs.acs.org
Publication Date (Web): May 3, 2012 | doi: 10.1021/bk-2012-1097.ch001

Downloaded by 89.163.35.42 on June 14, 2012 | http://pubs.acs.org
Publication Date (Web): May 3, 2012 | doi: 10.1021/bk-2012-1097.ch001

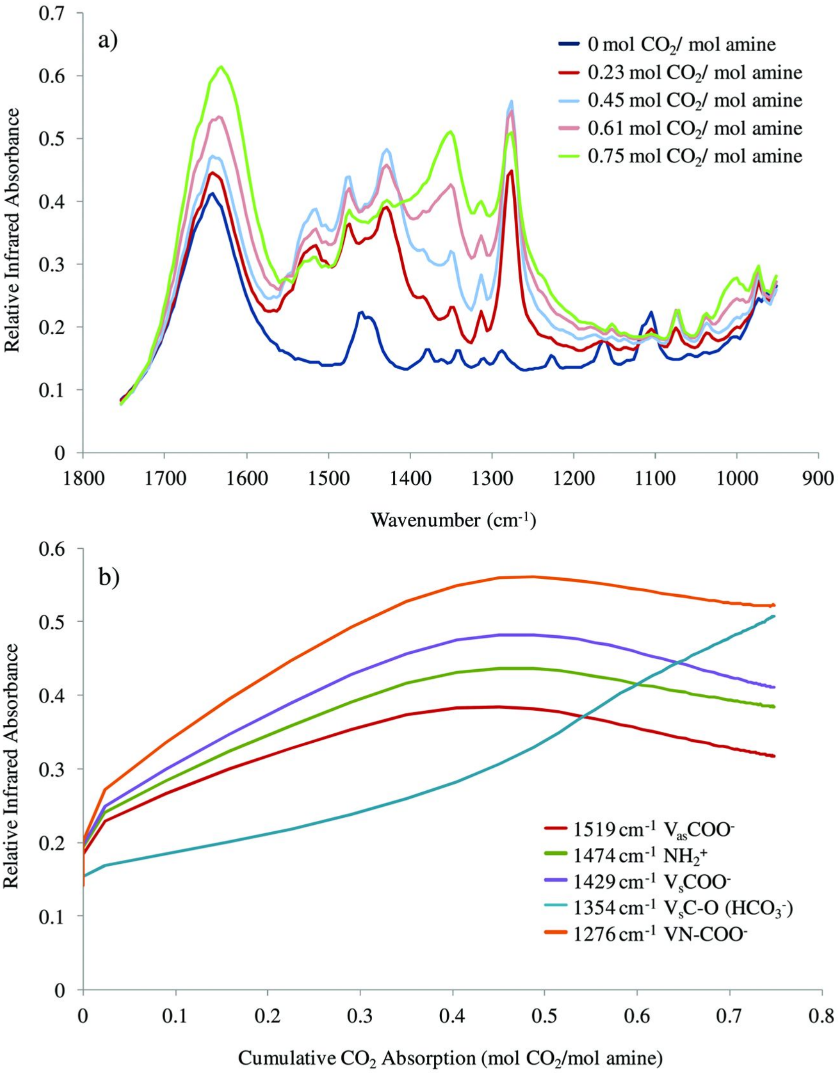

Figure 13. ***a)*** *IR spectra of aqueous 3-MP (3 mol/ L) as CO_2 is absorbed to a maximum loading of 0.75 mol CO_2/ mol amine, collected during a typical CO_2 absorption/ FT-IR experiment; and* ***b)*** *the relationship between the cumulative CO_2 absorption of 3-MP and IR peak absorbance for the bands assigned to 3-methylpiperidine-1-carboxylate, 3-methylpiperidine-H^+ and HCO_3^-. (see color insert)*

Downloaded by 89.163.35.42 on June 14, 2012 | http://pubs.acs.org
Publication Date (Web): May 3, 2012 | doi: 10.1021/bk-2012-1097.ch001

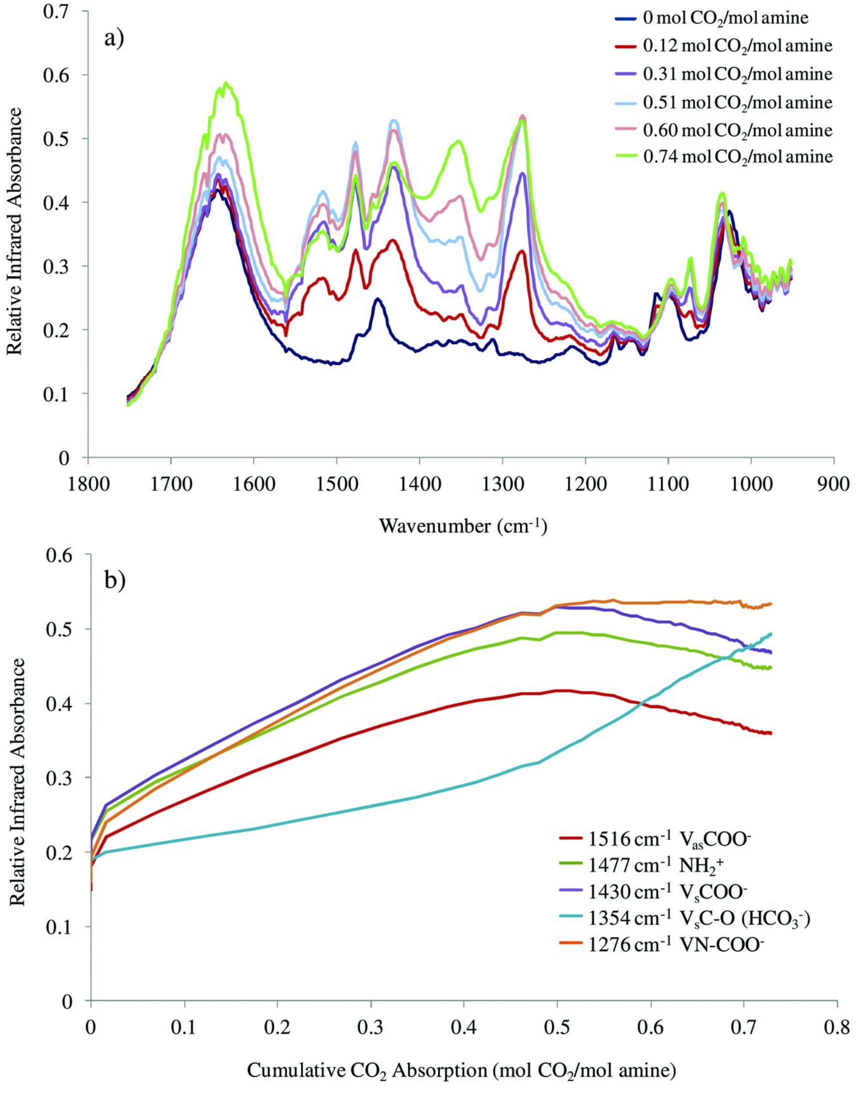

Figure 14. ***a)*** *IR spectra of aqueous 3-PM (3 mol/ L) as CO_2 is absorbed to a maximum loading of 0.74 mol CO_2/ mol amine, collected during a typical CO_2 absorption/ FT-IR experiment; and* ***b)*** *the relationship between the cumulative CO_2 absorption of 3-PM and infrared peak absorbance for the bands assigned to 3-(hydroxymethyl)piperidine-1-carboxylate, 3-(hydroxymethyl)piperidine-H^+ and HCO_3^-. (see color insert)*

Downloaded by 89.163.35.42 on June 14, 2012 | http://pubs.acs.org
Publication Date (Web): May 3, 2012 | doi: 10.1021/bk-2012-1097.ch001

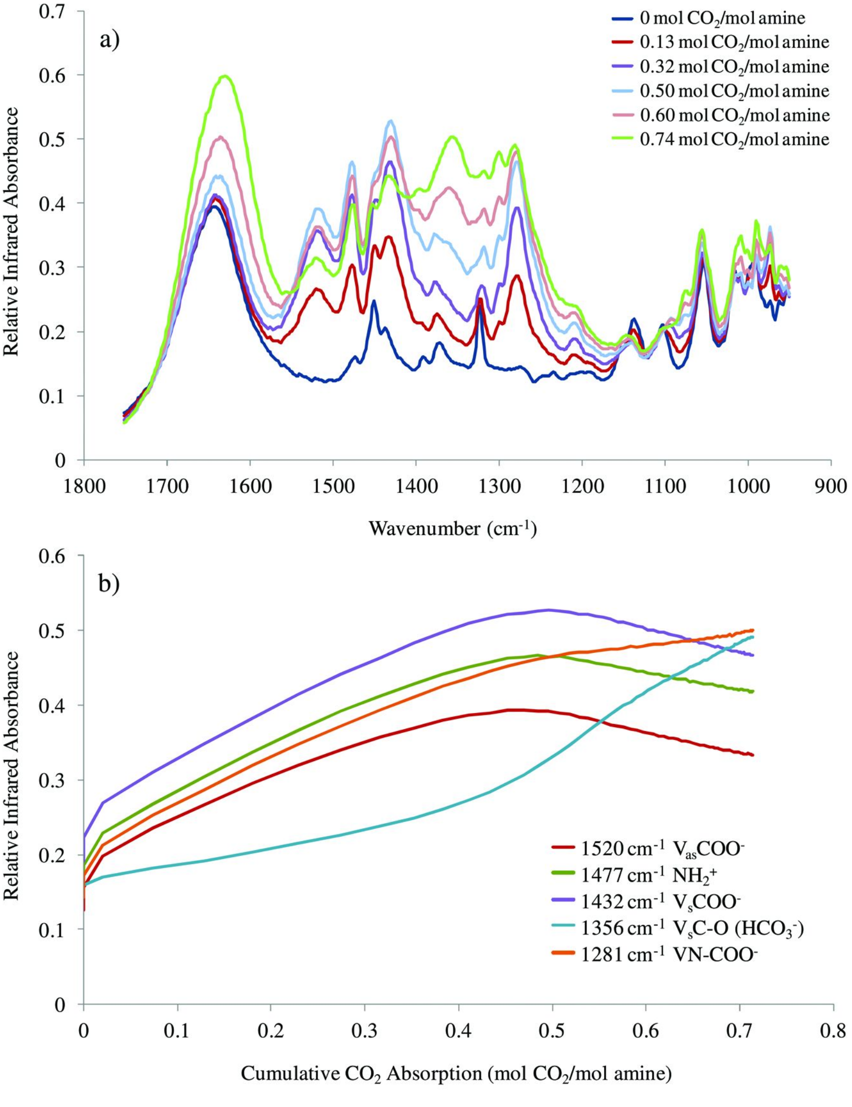

Figure 15. ***a)*** *IR spectra of aqueous 4-PE (3 mol/ L) as CO_2 is absorbed to a maximum loading of 0.74 mol CO_2/ mol amine, collected during a typical CO_2 absorption/ FT-IR experiment; and* ***b)*** *the relationship between the cumulative CO_2 absorption of 4-PE and infrared peak absorbance for the bands assigned to 4-(2-hydroxyethyl)piperidine-1-carboxylate, 4-(2-hydroxymethyl)piperidine-H^+ and HCO_3^-. (see color insert)*

Downloaded by 89.163.35.42 on June 14, 2012 | http://pubs.acs.org
Publication Date (Web): May 3, 2012 | doi: 10.1021/bk-2012-1097.ch001

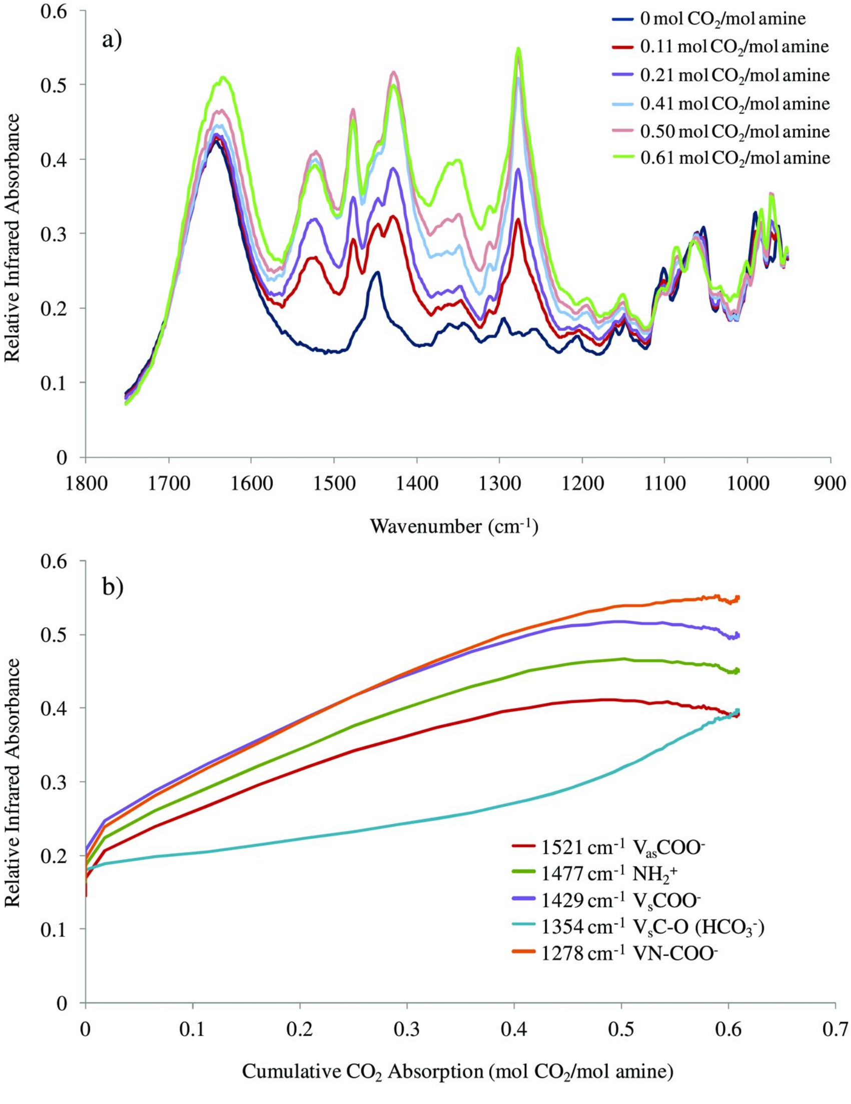

*Figure 16. **a)** IR spectra of aqueous 3-HP (3 mol/ L) as CO_2 is absorbed to a maximum loading of 0.61 mol CO_2/ mol amine, collected during a typical CO_2 absorption/ FT-IR experiment; and **b)** the relationship between the cumulative CO_2 absorption of 3-HP and IR peak absorbance for the bands assigned to 3-hydroxypiperidine-1-carboxylate, 3-hydroxypiperidine-H^+ and HCO_3^-. (see color insert)*

Downloaded by 89.163.35.42 on June 14, 2012 | http://pubs.acs.org
Publication Date (Web): May 3, 2012 | doi: 10.1021/bk-2012-1097.ch001

Absorption Capacity and Absorption Rate

To quantify the effect of the alkyl, hydroxy and hydroxyalkyl substitutents on the relative reactivity of the amino nitrogen, the CO_2 absorption capacity (C_A) and initial absorption rate (mass transfer coefficient (K_g) at zero loading) was determined for each individual amine.

The measured absorption capacity (C_A) and mass transfer coefficient (K_g) for the subset of alkyl, hydroxyl and hydroxylalkyl substituted piperidines analyzed in this study are presented in Table 2. For comparison of reactivity, the C_A and K_g values obtained for conventional amine-based absorbents MEA, DEA and AMP (di-methyl substituted analogue of MEA) have been included in Table 2.

The C_A and K_G results presented in Table 2 highlight the significant increase in reactivity of cyclic secondary amines compared to conventional straight chain aliphatic primary and secondary amines MEA and DEA, respectively. Particularly noteworthy is the increase in initial absorption rates of the α-substituted cyclic amines 2-MP, 2-PM and 2-PE compared to that of the Cα -substituted aliphatic amine AMP, given the similarity in structure (i.e. they are considered sterically-hindered). The K_G values obtained for 2-MP, 2-PM and 2-PE are even comparable/higher compared to that of MEA.

The 3- and 4- alkyl and hydroxyalkyl substituted piperidines exhibited similar absorption capacities (0.74 - 0.76) to that of piperidine (0.76) (Table 1). This similarity in C_A values is consistent with the interpretation of the IR spectral data collected for these amines, that being they react with CO_2 to form a relatively stable carbamate derivative, which at higher CO_2 loadings (> 0.5 mol CO_2/ mol amine) begins to hydrolyze forming HCO_3^-. The hydrolysis of the carbamate species permits the CO_2 loading of these amines to well exceed 0.5 mol CO_2/ mol amine, despite the 2:1 stoichiometry of the carbamate reaction pathway. However, on absorption of CO_2 the formation of the carbamate derivatives of the 3- and 4-hydroxymethyl substituted piperidines were found to be kinetically less favorable than the carbamate derivatives of piperidine and the 3 and 4-methyl substituted piperdines. In terms of K_g values or initial rates of CO_2 absorption, methyl substitution at the 3- and 4- position of the piperidine ring had a relatively small effect, as opposed to the 3- and 4- hydroxyalkyl substituents. As shown in Table 1, the K_g values obtained for 3-MP (3.73) and 4-PM (3.75) were comparable to that of piperidine (3.85), where as the values obtained for 3-PM (2.32) and 4-PM (1.86) were much smaller. The initial CO_2 absorption rate of 4-PE was not measured due to the availability of the amine.

Hydroxyl substitution in 3-HP (0.61, 2.24) and 4-HP (0.64, 2.28) lead to both reduced C_A and K_g values, respectively, compared to piperidine, as well as its methyl substituted analogues. The lower C_A values obtained for these amines is consistent with the interpretation of the IR spectral data, that being their carbamate derivatives are less susceptible to hydrolysis at higher CO_2 loadings compared to the carbamate derivatives of piperidine or the methyl and hydroxyalkyl substituted piperidines. These amines still however exhibited higher initial absorption rates than MEA and DEA, but with similar C_A values. Both 3-HP and 4-HP share a structural similarity with MEA and DEA that being a hydroxyl group 2-3 carbon removed from the amino nitrogen. It should also be noted that presence of an

In Recent Advances in Post-Combustion CO2 Capture Chemistry; Attalla, M.;
ACS Symposium Series; American Chemical Society: Washington, DC, 2012.

Table 2. Measured absorption capacity (C_A) at 40°C and 3 mol/ L amine concentrations; and mass transfer coefficient (K_g) at 40°C, zero loading and 1 mol/ L amine concentrations, for aqueous solutions of the alkyl, hydroxyl and hydroxyalkyl substituted piperidines. For comparison the reactivity of conventional absorbents such as MEA, DEA and AMP have been included at the bottom of the table (*27*).

Amine	C_A *(mol CO_2/ mol amine)*	K_g *(mol/s.cm^{2}Pa) (x10^{-10})*
piperidine	0.76	3.85
2-methylpiperidine (2-MP)	0.93	2.38
3-methylpiperidine (3-MP)	0.75	3.73
4-methylpiperidine (4-MP)	0.76	3.75
3-hydroxypiperidine (3-HP)	0.61	2.24
4-hydroxypiperidine (4-HP)	0.64	2.28
2-(hydroxymethyl)piperidine (2-PM)	0.85	1.07
3-(hydroxymethyl)piperidine (3-PM)	0.74	2.32
4-(hydroxymethyl)piperidine (4-PM)	0.74	1.86
2-(2-hydroxyethyl)piperidine (2-PE)	0.87	1.27
4-(2-hydroxyethyl)piperidine (4-PE)	0.74	Nm[a]
Tertiary Amines		
N-methylpiperidine (1-MP)	0.31	Nm[a]
N-hydroxypiperidine (1-HP)	0	Nm[a]
N-(2-hydroxyethyl)piperidine (1-PE)	0.27	Nm[a]
Conventional Absorbents		
monoethanolamine (MEA)	0.56	1.48
diethanolamine (DEA)	0.60	0.61
2-amino-2-methyl-1-propanol (AMP)	0.84	0.61

[a] Nm= Not measured

oxygen atom directly bonded to the nitrogen atom in the tertiary amine 1-HP (Table 2) completely hindered CO_2 absorption, as opposed to the methyl or hydroxyethyl substitution in 1-MP and 1-PE. The IR data collected for 1-HP showed no spectral changes in the 1800-900 cm^{-1} region, where as the IR data collected for 1-MP and 1-PE showed the evolution of HCO_3^-.

The tendency of the 2-methyl and 2-hydroxyalkyl substituted piperidines to favor HCO_3^- formation over carbamate formation, as indicated by the IR spectral data, is reflected in the higher C_A and lower K_g values reported in Table 2, for 2-MP, 2-PM and 2-PE.

In Recent Advances in Post-Combustion CO2 Capture Chemistry; Attalla, M.;
ACS Symposium Series; American Chemical Society: Washington, DC, 2012.

Downloaded by 89.163.35.42 on June 14, 2012 | http://pubs.acs.org
Publication Date (Web): May 3, 2012 | doi: 10.1021/bk-2012-1097.ch001

In terms of C_A and K_g values 2-MP (0.93, 2.38, respectively) stands out from the rest of the amines. Whilst the amine has been identified in this study as forming predominantly HCO_3^- on absorption of CO_2, it showed a significant improvement in the K_g value, as well as C_A value, compared to 2-PM (0.85, 1.07) and 2-PE (0.87, 1.27). This may be accounted for by the less bulky methyl substituent on the Cα of 2-MP, compared to the hydroxymethyl or hydroxyethyl substituent in 2-PM and 2-PE, respectively. Based on the IR spectral data the ability of these amines to form a carbamate derivative, inherently susceptible to hydrolysis, was established. A plausible explanation for the difference in reactivity may be that the increased exposure of the amino nitrogen in 2-MP, compared to 2-PM and 2-PE, facilitates the initial uptake of CO_2 to form an unstable carbamate derivative. The electronic effect exerted by the neighboring methyl group (electron donating) (*27*) facilitates the destabilization of the carbamate derivative, which is then readily hydrolyzed to HCO_3^-. The electronic and/or steric effect of the substituents present on the α-carbon of these amines play a large role in destabilizing the carbamate derivative and increasing its susceptibility to hydrolysis (*27*).

Downloaded by 89.163.35.42 on June 14, 2012 | http://pubs.acs.org
Publication Date (Web): May 3, 2012 | doi: 10.1021/bk-2012-1097.ch001

References

1. Gielen, D.; Podkanski, J.; Unander, F. *Energy Technology Analysis: Prospects for CO_2 Capture and Storage*; International Energy Agency (IEA): France, 2004.
2. Blomen, E.; Hendriks, C.; Neele, F. *Energy Procedia* **2009**, *1*, 1505–1512.
3. Wang, M.; Lawal, A.; Stephenson, P.; Sidders, J.; Ramshaw, C. *Chem. Eng. Res. Des.* **2011**, *89*, 1609–1624.
4. Davison, J. *Energy* **2007**, *32*, 1163–1176.
5. Finkenrath, M. *Cost and Performance of Carbon Dioxide Capture from Power Generation*; IEA Energy Papers, No. 2011/05; 2011.
6. Versteeg, G. F.; Van Dijck, L. A. J.; Van Swaaij, W. P. M. *Chem. Eng. Commun.* **1996**, *144*, 113–158.
7. Fauth, D. J.; Filburn, T. P.; Gray, M. L.; Hedges, S. W.; Hoffman, J.; Pennline, H. W.; Filburn, T. Development of Novel CO_2 Adsorbents for Capture of CO_2 from Flue Gas. *Air & Waste Management Association 100th Annual Conference & Exhibition*; Air & Waste Management Association: Pittsburgh, PA, 2007.
8. Colthup, N.; Daly, L.; Wiberley, S. *Introduction to Infrared and Raman Spectroscopy*, 3rd ed.; Academic Press Inc.: San Diego, CA, 1990.
9. Vaidya, P. D.; Kenig, E. Y. *Chem. Eng. Technol.* **2007**, *30*, 1467–1474.
10. Sartori, G.; Savage, D. W. *Ind. Eng. Chem. Fundam.* **1983**, *22*, 239–249.
11. Bonenfant, D.; Mimeault, M.; Hausler, R. *Ind. Eng. Chem. Res.* **2003**, *42*, 3179–3184.
12. da Silva, E. F.; Svendsen, H. F. *Ind. Eng. Chem. Res.* **2006**, *45*, 2497–2504.
13. Donaldson, T. L.; Nguyen, Y. N. *Ind. Eng. Chem. Fundam.* **1980**, *19*, 260–266.
14. da Silva, E. F.; Svendsen, H. F. *Int. J. Greenhouse Gas Control* **2007**, *1*, 151–157.

15. Hook, R. J. *Ind. Eng. Chem. Res.* **1997**, *36*, 1779–1790.
16. Falk, M.; Miller, A. G. *Vibrat. Spectrosc.* **1992**, *4*, 105–108.
17. Khanna, R.; Moore, M. *Spectrochim. Acta, Part A* **1999**, *55*, 961–967.
18. Park, H.; Jung, Y. M.; You, J. K.; Hong, W. H.; Kim, J. N. *J. Phys. Chem. A* **2008**, *112*, 6558–6562.
19. Rogers, W. J.; Bullin, J. A.; Davison, R. R.; Frazier, R. E.; Marsh, K. N. *AIChE J.* **1997**, *43*, 3223–3231.
20. Bishnoi, S.; Rochelle, G. T. *Chem. Eng. Sci.* **2000**, *55*, 5531–5543.
21. Muhammad, A.; Mutalib, M. I. A.; Murugesan, T.; Shafeeq, A. *J. Chem. Eng. Data* **2009**, *54*, 2317–2321.
22. Appl, M.; Wagner, U.; Henrici, H. J.; Kuessner, K.; Volkamer, F.; Ernst Neust, N. U.S. Patent 4336233, 1982.
23. Xu, G.-W.; Zhang, C.-F.; Qin, S.-J.; Gao, W.-H.; Liu, H.-B. *Ind. Eng. Chem. Res.* **1998**, *37*, 1473–1477.
24. Sun, W.-C.; Yong, C.-B.; Li, M.-H. *Chem. Eng. Sci.* **2005**, *60*, 503–516.
25. Bishnoi, S.; Rochelle, G. T. *Ind. Eng. Chem. Res.* **2002**, *41*, 604–612.
26. Bishnoi, S.; Rochelle, G. T. *AIChE J.* **2002**, *48*, 2788–2799.
27. Robinson, K.; McCluskey, A.; Attalla, M. *ChemPhysChem* **2011**, *12*, 1088–1099.
28. Dobson, K. D.; McQuillan, A. J. *Langmuir* **1997**, *13*, 3392–3396.
29. Smith, B. *Infrared Spectral Interpretation: A systematic Approach*; CRC Press LLC: Boca Raton, FL, USA, 1999.
30. Wavefunction Inc; Q-chem Inc. *Spartan '08 for Windows, Macintosh and Linux*; 2008.
31. Jung, D.; Chen, C.-J.; Bozzelli, J. W. *J. Phys. Chem. A* **2000**, *104*, 9581–9590.
32. Scott, A. P.; Radom, L. *J. Phys. Chem.* **1996**, *100*, 16502–16513.
33. Tafipolsky, M.; Schmid, R. *J. Chem. Theory Comput.* **2009**, *5*, 2822–2834.
34. Ermatchkov, V.; Pérez-Salado Kamps, Á.; Maurer, G. *J. Chem. Thermodyn.* **2003**, *35*, 1277–1289.
35. Ismael, M.; Sahnoun, R.; Suzuki, A.; Koyama, M.; Tsuboi, H.; Hatakeyama, N.; Endou, A.; Takaba, H.; Kubo, M.; Shimizu, S.; Del Carpio, C. A.; Miyamoto, A. *Int. J. Greenhouse Gas Control* **2009**, *3*, 612–616.
36. Jackson, P.; Fisher, K.; Attalla, M. *J. Am. Soc. Mass Spectrom.* **2011**, *22*, 1420–1431.
37. Jackson, P. Personal Communication. May, 2010.
38. Bialecki, J. B.; Axe, F. U.; Attygalle, A. B. *J. Mass Spectrom.* **2008**, *44*, 252–259.

Downloaded by 89.163.35.42 on June 14, 2012 | http://pubs.acs.org
Publication Date (Web): May 3, 2012 | doi: 10.1021/bk-2012-1097.ch001

Downloaded by UNIV OF DELAWARE MORRIS LIB on June 15, 2012 | http://pubs.acs.org
Publication Date (Web): May 3, 2012 | doi: 10.1021/bk-2012-1097.ch002

Chapter 2

Influence of Amine Chemical Structures to Amine Capacities in CO_2 Capture

Qi Yang,* **Susan James, Mathew Ballard, and Mark Bown**

CSIRO Materials Science and Engineering, Bag 10, Clayton South MDC,
Vic 3169, Australia
***Corresponding author (qi.yang@csiro.au)**

The chemical structure of an amine has a strong impact on the amine's capacity to capture CO_2. We have studied the effect of varying the carbon chain length from 2 to 6 methylene "spacers" between the two functional groups in primary and secondary alkanolamines and diamines, using quantitative ^{13}C NMR techniques to examine their speciation during the absorption and desorption of CO_2. Each group of amines was affected differently. A replacement of methyl by hydroxyethyl has a greater impact on tertiary amines than secondary amines in their capacity decrease during CO_2 absorption. The steric hindrance of 2-amino-2-methypropane-1,3-diol significantly increases the amine's capacity for absorbing CO_2. Structural change to an amine molecule can result in complicated changes in its characteristics and properties and hence need to be considered, along with other factors, when trying to design the most suitable amine for CO_2 capture.

Keywords: CO_2; absorption; desorption; amines; structures

Introduction

Amine based solvent systems are a credible means of implementing carbon capture and storage (CCS) on a commercial scale in the time frame required to reduce CO_2 emissions globally. Aqueous amines, e.g. monoethanolamine (MEA), have been applied to CO_2 capture/separation in the oil and natural gas industries for decades and are promising solvents for removal of CO_2 from flue gases (*1*,

Published 2012 by American Chemical Society
In Recent Advances in Post-Combustion CO2 Capture Chemistry; Attalla, M.;
ACS Symposium Series; American Chemical Society: Washington, DC, 2012.

2). However, the application of aqueous amines in CO_2 capture from flue gases still has many challenges, and continued development of amines is required to improve efficacy, stability and safety in CO_2 capture (*3*, *4*). CO_2 capture from flue gases requires more efficient amines that react with CO_2 rapidly to high loading during absorption from flue gases that have low CO_2 partial pressures. These amines are also required to release CO_2 rapidly and efficiently during thermally driven desorption with low energy consumption. Greater chemical stability of amines is also required as flue gas contains other acidic and oxidative gases, such NO_x, SO_x and O_2, and amines are cyclically heated and cooled, which make amine degradation a serious operational problem, and can also cause corrosion problems. All these characteristics and properties of amines can potentially be improved through amine structural modification. In our research to find or design more suitable amines for CO_2 capture, we have studied the influence of amine structural factors on amine capacity in CO_2 absorption and desorption. Some of these results are presented in this work.

The influence of amine structure on the amine's capacity to capture CO_2 has been studied by different researchers. Hook (*5*) published a study on sterically hindered amines in CO_2 absorption and desorption. The change of amine structures from MEA to 2-amino-2-methylpropanol (AMP) (Figure 1) increased the steric hindrance at the α-carbon and hence promoted bicarbonate formation, which resulted in higher CO_2 loading in absorption. At the same time this amine structural change decreased the absorption rate.

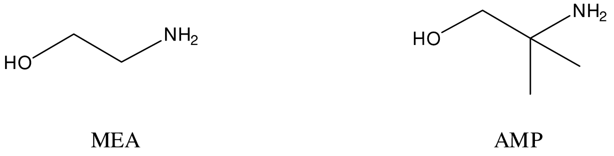

Figure 1. Structures of MEA and AMP

This same amine structural change increased both the CO_2 release rate and amount in desorption, resulting a leaner solvent. A leaner solvent has a more favourable reaction rate and CO_2 loading when reused in CO_2 absorption. Hook also studied CO_2 absorption and desorption with different potassium salts of amino acids with different steric hindrance on the nitrogen and/or on the adjacent carbon atom. He showed that the extent of the influence of various steric factors is highly dependent on CO_2 partial pressure in the reactions, for example two methyl substituents on the α-carbon decreased the rate of absorption of AMP compared with that of MEA when CO_2 partial pressure was reduced. Hence, AMP is better suited for absorbing CO_2 from gases with higher CO_2 partial pressure. This informative paper demonstrates that structural alterations strongly affect amine characteristics in reactions and can be used to improve the required reaction properties.

Bonenfant *et al.* (*6*) examined the absorption and desorption of a number of primary, secondary and tertiary amines containing up to three amino groups, under conditions of low concentration (5 wt%), high gas flow rates (1-3 dm^3 min^{-1}), and

Downloaded by UNIV OF DELAWARE MORRIS LIB on June 15, 2012 | http://pubs.acs.org
Publication Date (Web): May 3, 2012 | doi: 10.1021/bk-2012-1097.ch002

short reaction times (up to 120 s for absorption and 210 s for desorption). They observed an order of magnitude variation in the rate of reaction, the maximum loading, and the maximum desorption after refluxing for 210 s.

More recently, Singh and Versteeg (*7*) published the study results of the influence of major structural aspects, including side chain length, cyclic and steric hindrance, and number of nitrogen atoms, on CO_2 desorption capacities via screening a range of amines. Puxty *et al.* (*8*) also published a screening study of 76 structurally diverse amines for their CO_2 absorption by isothermal gravimetric analysis (IGA). This paper presented CO_2 absorption capacity results from a wide range of amines and showed the influence of amine structures on amine capacity in CO_2 absorption.

The influence of structural change on the activities of amines in CO_2 capture is very complicated since many factors, such as amine structure, reaction conditions and process techniques affect each other dynamically. A better understanding of the impact of structures of amines on their behaviours in CO_2 capture is important for scientists to improve amine characteristics to suit the demands in CO_2 capture applications. This work presents speciation study results on a range of amines in CO_2 absorption and desorption using quantitative ^{13}C NMR spectroscopy. It provides useful information to improve the understanding of structural effects on CO_2 absorption and to achieve higher efficiency amine solvent in CO_2 capture through amine structure modification.

Downloaded by UNIV OF DELAWARE MORRIS LIB on June 15, 2012 | http://pubs.acs.org
Publication Date (Web): May 3, 2012 | doi: 10.1021/bk-2012-1097.ch002

Experimental

Reaction Apparatus and Chemicals

Reactions were carried out in a 50 ml jacketed, 2-necked, pear-shaped flask maintained at a constant temperature with a Ratek Thermoregulator thermostatted water bath. A non-jacketed flask of the same size and shape was also used in some absorption experiments in which a preheated oil bath was used as a heating source. A condenser was connected to the flask through a Claisen adapter, and an electronic thermometer introduced to monitor the temperature of the amine solution. During absorption experiments the side neck of the flask was used to introduce CO_2 gas into the amine solution through a Teflon tube (0.71 mm ID) at a flow rate of 5 ml/min. In desorptions, the CO_2 gas was voided through the condenser with the flask side neck sealed with a stopper. Reactions were stirred with an egg-shaped stirring bean (15 x 6 mm) at 900 rpm.

Primary amines, diamines, *N*-methylethanolamine and piperizine are commercially available and were purchased from Sigma-Aldrich or Merck and used in experiments without further purification. The remaining *N*-methyl secondary amines, $MeNH(CH_2)_nOH$, n = 3, 4, 5 and 6, were synthesised using the method of Sheldrake *et al.* (*9*) from the corresponding chloroalcohol.

^{13}C NMR Spectroscopy

^{13}C NMR experiments were performed at 25°C using Bruker Av400 spectrometer. Samples were taken from reactions at designated times and placed

Downloaded by UNIV OF DELAWARE MORRIS LIB on June 15, 2012 | http://pubs.acs.org
Publication Date (Web): May 3, 2012 | doi: 10.1021/bk-2012-1097.ch002

into a 5 mm NMR tube with an external standard of 1,4-dioxane (δ_C 67.18 ppm, calibrated with an external TMS/$CHCl_3$ solution). Relaxation times (T_1) of carbon atoms were measured using the standard inversion recovery ("Null") method. The NMR interscan recycle time ($AQ + D1$) was chosen as 70 seconds which is equal or longer than 5xT_1 for all carbon signals to ensure that accurate quantification of signals is obtained. Data were processed with experiential multiplication with a line broadening of 3.0 Hz before Fourier transformation.

CO_2 Absorption with Aqueous Amines

The concentrations of amine solutions were 4M for most amines and 2M for those of lesser solubility or where product precipitation occurred. Amine solutions were prepared in volumetric flasks by dissolving a weighed amount of the corresponding amine in deionised water. The stock solution (15 ml) was dispensed to a 50 ml jacketed two-necked pear-shaped flask and warmed with thermostatted water at 40°C, or to a non-jacketed flask of the same shape and size and warmed with an oil bath at 40°C. After the amine solution reached and stabilised at 40°C, CO_2 gas was introduced to the reaction above the stirring bean at a flow rate of 5 ml/min. Samples of the reaction mixture were taken at 10 min, 30 min, 1 h, 2 h, 3 h, 4 h, 5 h, 6 h and 7 hours. Each sample was then analysed at the end of the day using the general NMR method above.

Many of the absorption experiments were kept under the same reaction conditions for 23 hours to ensure the maximum CO_2 loading. Most reached or were close to saturation before 7 hours of reaction time hence the data obtained at 23 hours of reaction time were similar to that of 7 hours time.

The amines in table 1 were used in CO_2 absorption experiments using the general method above. The concentration of each amine solution used and the reaction time are also listed.

CO_2 Desorption

A CO_2-rich amine stock solution (10 ml) was prepared in a 50 ml jacketed two-necked pear-shaped flask by either: (1) using the remaining CO_2-loaded amine solution from the CO_2 absorption method described above after a further 16 hours of absorption time (the total volume of the final solution was approximately 10 ml); or (2) CO_2 was bubbled through 10 ml of lean amine solution for 23 hours in the same manner.

For desorption, the CO_2 bubbler was removed and the side neck of the flask was sealed by a stopper. The solution was stirred by a stirring bean at 900 rpm. The reaction start was recorded when preheated, thermostatted water of 90°C was introduced to the heating jacket. Samples of the reaction mixture were taken at 5 min, 10 min, 30 min and 60 min for NMR analysis as described in the general method above.

The amines in table 2 were used in CO_2 desorption experiments using the general method above. The concentration of each amine solution used and the reaction time are also listed.

Downloaded by UNIV OF DELAWARE MORRIS LIB on June 15, 2012 | http://pubs.acs.org
Publication Date (Web): May 3, 2012 | doi: 10.1021/bk-2012-1097.ch002

Table 1. Amines, their concentrations and reaction time in CO_2 absorption study

	Amines	Conc.	Time (h)
Primary amine	$H_2N(CH_2)_nOH$		
	n=2	4M & 2M	7
	n=3	4M	7
	n=4	4M	7
	n=5	4M	7
	n=6	4M	7
	AMPD (2-amino-2-methyl-propan-1,3-diol)	2M	6
Secondary amine	$MeNH(CH_2)_nOH$		
	n=2	4M	7
	n=3	4M	7
	n=4	4M	7
	n=5	4M	7
	n=6	4M	7

	Amines	Conc.	Time (h)
Diamines	$H_2N(CH_2)_nNH_2$		
	n=2	4M & 2M	7
	n=3	4M	7
	n=4	4M	7
	n=5	4M & 2M	7
	n=6	4M	5
	Piperazine	2M	7
Other Amines	$R^1R^2N(CH_2)_2OH$		7
	DEA (R^1=H; R^2=Me)	4M	7
	DMEA (R^1= R^2=Me)	4M	7
	MDEA [R^1=Me; R^2=$(CH_2)_2OH$]	4M	7
	TEA [(R^1= R^2=$(CH_2)_2OH$]	4M	7

Table 2. Amines used in desorption study, their concentration and reaction time

	Amines	Con.	Time (h)
Primary	$H_2N(CH_2)_nOH$		
	n=2	4M	1
	n=3	4M	1
	n=4	4M	1
	n=5	4M	1
	n=6	4M	1
Secondary amine	$MeNH(CH_2)_nOH$		
	n=2	4M	1
	n=3	4M	1
	n=4	4M	1
	n=5	4M	1
	n=6	4M	-

	Amines	Con.	Time (h)
Diamines	$H_2N(CH_2)_nNH_2$		
	n=2	4M	1
	n=3	4M	1
	n=4	4M	1
	n=5	4M	1
Other Amines	$R^1R^2N(CH_2)_2OH$		
	DEA (R^1=H; R^2=Me)	4M	1
	DMEA (R^1= R^2=Me)	4M	1
	MDEA [R^1=Me; R^2=$(CH_2)_2OH$]	4M	1
	TEA [(R^1= R^2=$(CH_2)_2OH$]	4M	1

Results and Discussion

These experiments were designed to study the speciation of the amine solutions following CO_2 absorption and desorption. Liquid samples taken at different reaction times were analysed by quantitative ^{13}C NMR spectroscopy to identify the carbonyl species in solution and to quantify them by comparison of their integrals against the sum of the integrals of all amine species. The results are presented as the molar ratio of carbonyl species (mol CO_2 / mol amine, Y-axis) versus the reaction time (X-axis). The absorption results up to 7 hours of reaction time are presented as there is little change for most amines after this time.

Primary alkanolamines of 4M concentration with different chain lengths between amino and hydroxyl groups, $H_2N(CH_2)_nOH$, where n was 2, 3, 4, 5 and 6, were studied during CO_2 absorption at 40°C and desorption at 90°C. Their speciation results and total CO_2 loading in amine solutions are displayed in Figure 2. Figure 2a displays the carbamate formation in the reaction; Figure 2b the bicarbonate formation and total CO_2 loading, which is the sum of carbamate and bicarbonate in these results; Figure 2c and d are the respective results of their desorption study.

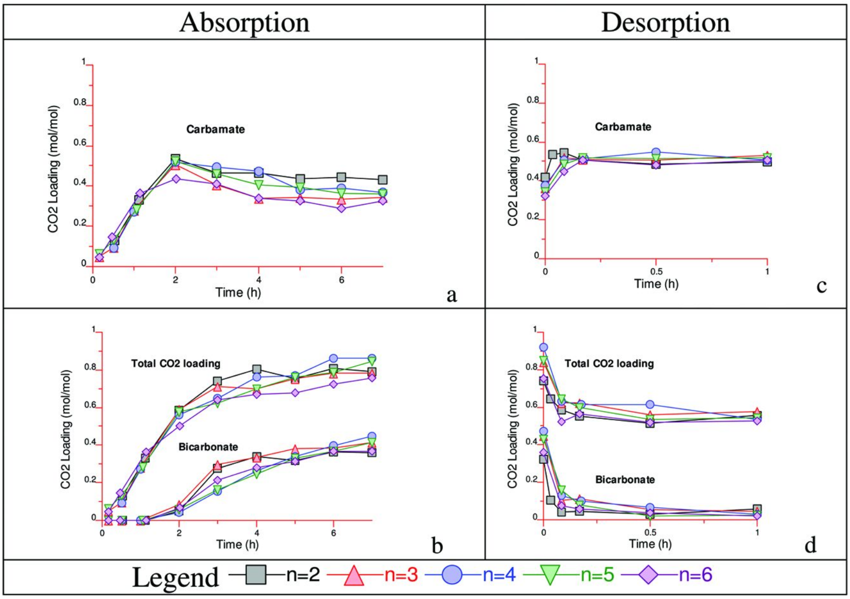

Figure 2. CO_2 absorption and desorption of primary amines, $H_2N(CH_2)_nOH$ (a) and (c) carbamate in reactions; (b) and (d) bicarbonate and total CO_2 loading in reactions.

The chain length change of this group of primary alkanolamines made little difference on carbamate and bicarbonate formation in absorption, and resulted in the similar total CO_2 loading. At early times (< 3 h) the total CO_2 loading was roughly in order of chain length, while at extended times 4-aminobutan-1-ol (n=4) has the highest total absorption and absolute desorption. In contrast, the longest chain, 6-aminohexan-1-ol (n=6), has the lowest loading and desorption. These small variations are within the analytical error and the chain length alone does not make an obvious impact on the CO_2 absorption and desorption in this group of amines. This agrees with the results of Singh and Versteeg (*7*) for a similar group of primary alkanolamines.

Downloaded by UNIV OF DELAWARE MORRIS LIB on June 15, 2012 | http://pubs.acs.org
Publication Date (Web): May 3, 2012 | doi: 10.1021/bk-2012-1097.ch002

These results indicate that the alkyl chain length in a straight chain primary alkanolamine has little impact on absorption and desorption in the CO_2 capture process.

Secondary *N*-methylalkanolamines of 4M concentration with different chain lengths, $CH_3NH(CH_2)_nOH$, where n is 2, 3, 4, 5 and 6, were also studied in CO_2 absorption and desorption (Figure 3). Under the reaction conditions, amines of shorter chains in this group behave similarly, but *N*-methylhexanol (n=6) has lower bicarbonate concentration, and hence the lowest total CO_2 loading, even more so than 6-aminohexan-1-ol in the alkanolamines series. This group of secondary amines have an extra methyl group on their nitrogen atoms compared to the above primary amines, and this structural change contributes to a higher total CO_2 loading via the more favourable bicarbonate formation in the reaction. The higher concentration of bicarbonate from the absorption gives these amines the ability to achieve higher net CO_2 absorption than the above primary amines.

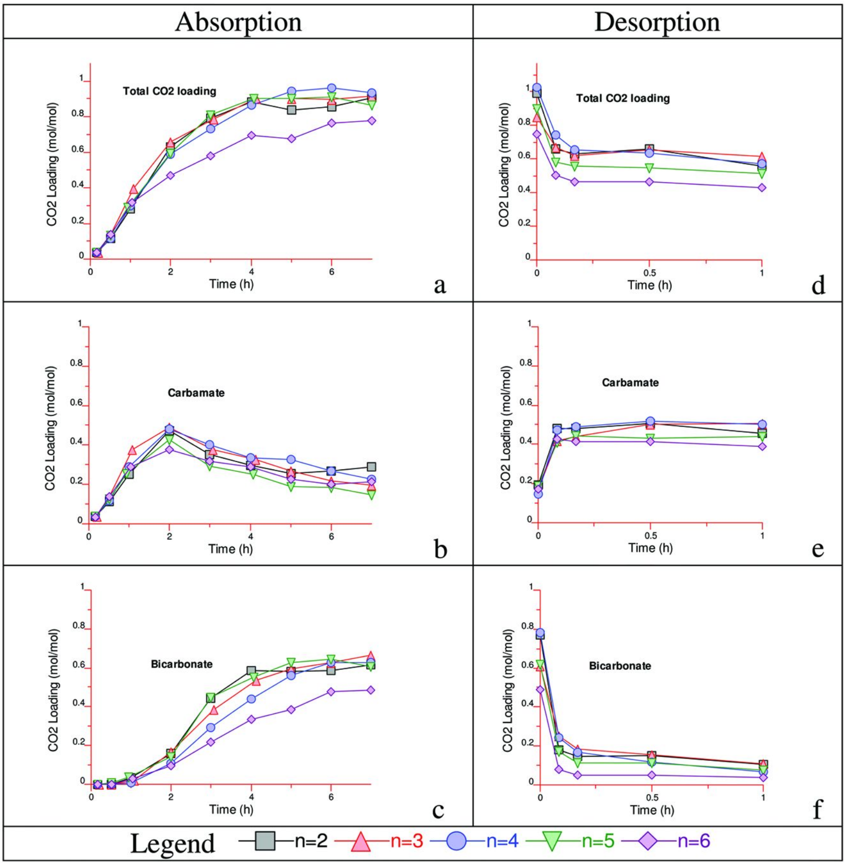

Figure 3. CO_2 absorption and desorption of secondary amines, $MeNH(CH_2)_nOH$

Downloaded by UNIV OF DELAWARE MORRIS LIB on June 15, 2012 | http://pubs.acs.org
Publication Date (Web): May 3, 2012 | doi: 10.1021/bk-2012-1097.ch002

Figure 4 shows the results of CO_2 absorption and desorption for a series of diamines of 4M concentration. It should be noted that the concentrations of the amino group of diamines are twice that of their molecular concentrations (8 M), and so the theoretical maximum CO_2 loading should be 2 mol CO_2/ mol amine (assuming complete conversion to bicarbonate). 1,6-Diaminohexane formed a precipitate before 6 hours of reaction time during CO_2 absorption, hence its absorption data are only shown to 5 hours and its desorption was not studied.

Downloaded by UNIV OF DELAWARE MORRIS LIB on June 15, 2012 | http://pubs.acs.org
Publication Date (Web): May 3, 2012 | doi: 10.1021/bk-2012-1097.ch002

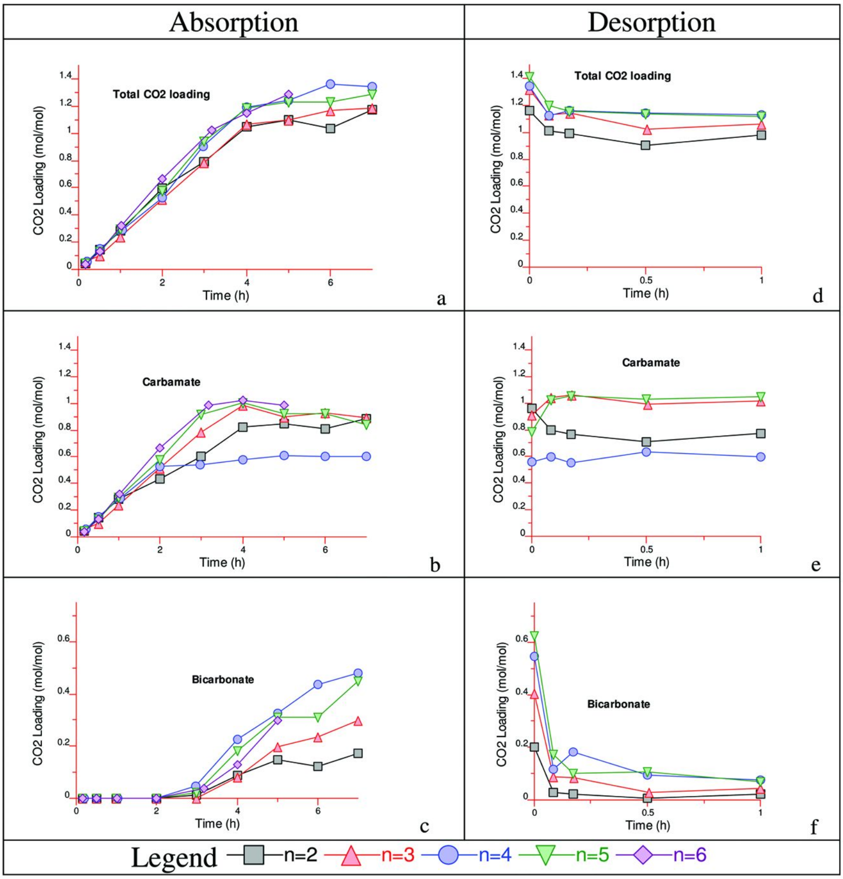

Figure 4. CO_2 absorption and desorption of primary diamines, $NH_2(CH_2)_nNH_2$

Downloaded by UNIV OF DELAWARE MORRIS LIB on June 15, 2012 | http://pubs.acs.org
Publication Date (Web): May 3, 2012 | doi: 10.1021/bk-2012-1097.ch002

Figure 4c shows that the bicarbonate formation depends strongly on alkyl chain length, with a minimum for n=2 (1,2-diaminoethane, DAE) and a maximum for n=4 and 5 (DAB and DAP). Not only did DAB (n=4) have the highest bicarbonate formation, it also had the highest total CO_2 loading of all of these amines.

Theoretically, diamines can form more species of carbamates and bicarbonates/carbonates than mono-amines in CO_2 absorption, including intra-molecular and inter-molecular carbamates (Figure 5a and 5b). The formation of more than one carbamate is observed on the ^{13}C NMR spectra of some amines, especially in the case of 1,2-diaminoethane. However, the chemical shift differences of these carbamate signals are very small and it is difficult to identify carbamate structural types based on the obtained NMR results. Therefore, the total carbamate loading is used in Figure 4b. It is noticeable that 1,2-diaminoethane has the lowest bicarbonate formation among all studied diamines (Figure 4c). The intra-molecular carbamate of 1,2-diaminoethane (Figure 5a, n = 1) chould have contributed to this as the 6-membered ring structure could provide extra stability.

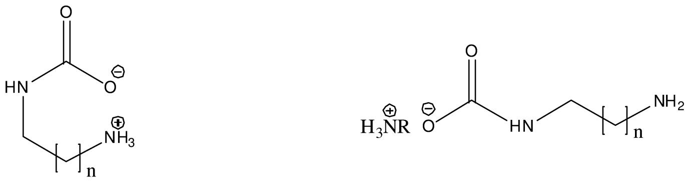

(a) (b)

Figure 5. Some carbamate species of diamines in CO_2 absorption (n = 1, 2, 3, 4, 5)

While absorption capacities of these diamines are fairly high, particularly on a weight basis, they desorb significantly less than the alkanolamines above. Among these diamines, 1,5-diaminopentane (DAP) has the highest total CO_2 absorption (1.41 mol CO_2 / mol amine) and absolute CO_2 release (0.29 mol CO_2 / mol amine at 1 hour of desorption time) (Figure 4a and 4d). The next is 1,4-diaminobutane (DAB) with total absorption and absolute desorption of 1.34 and 0.21 mol CO_2 / mol amine respectively. However, both of these two amines achieve the same absolute CO_2 release at 5 minutes of desorption time at 90°C, 0.22 and 0.21 mol CO_2 / mol amine for DAB and DAP respectively.

Figures 6a and 6b show a brief comparison of the CO_2 absorption of a common cyclic diamine, piperazine (Pz), with DAE and DAP. The results show that Pz and DAE have similar total CO_2 loading (6a) and bicarbonate formation (6b), while DAP has a much higher capacity. Pz, like DAE above (Figure 5a), is able to form a stable intra-molecular carbamate (Figure 6c) that can reduce the conversion of carbamate to bicarbonate. Diamine concentrations of 2 M were chosen for this comparison because it is close to the saturation concentration of aqueous Pz at room temperature. These absorptions are also carried out at 40°C.

Downloaded by UNIV OF DELAWARE MORRIS LIB on June 15, 2012 | http://pubs.acs.org
Publication Date (Web): May 3, 2012 | doi: 10.1021/bk-2012-1097.ch002

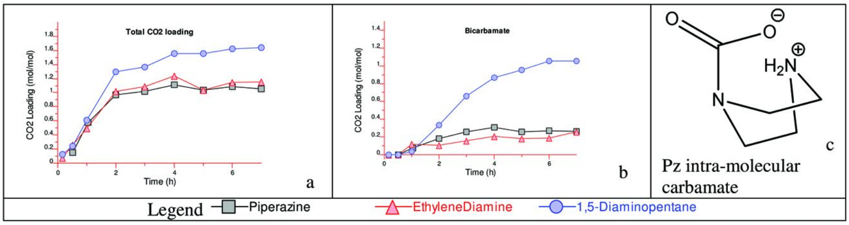

Figure 6. (a) and (b) CO_2 absorption (40°C) of Pz and $H_2N(CH_2)_nNH_2$ (n=2 and 5) and (c) Pz intra-molecular carbamate

It should also be noted that the total CO_2 loading of DAP with the lower concentration of 2M is higher (1.64 mol CO_2 / mol amine) than that of DAP at 4M concentration (1.29 mol CO_2 / mol amine) while this molar ratio has a smaller change in the case of DAE of the same dilution (1.15 and 1.03 mol CO_2 / mol amine respectively to 2M and 4M concentration). The major contribution to the increase of total loading in the diluted DAP case is from a higher conversion of carbamate to bicarbonate, which changes from 0.44 to 1.06 when the amine concentration decreases from 4M to 2M. This phenomenon also supports the formation of stable intra-molecular DAE carbamate (Figure 5a) which would be affected less by dilution.

Replacement of the methyl group by hydroxyethyl group also makes for an interesting impact on an amine's CO_2 absorption capacity. Figure 7 show the results of CO_2 absorptions and desorptions of simple chain secondary and tertiary amines, in which monoethanolamine is successively substituted on the nitrogen with methyl ($-CH_3$) and hydroxyethyl ($-CH_2CH_2OH$) groups. All of these amines are of 4M concentration, and absorptions are carried out at 40°C and desorptions at 90°C.

The structural difference between diethanolamine (DEA) and *N*-methyl-ethanolamine (MMEA) is the replacement of a methyl group in MMEA by hydroxyethyl group in DEA. The larger and more polar hydroxyethyl substituent increases the boiling point and makes DEA more polar than MMEA, and also increases the steric hindrance to its amino nitrogen. The CO_2 absorption and desorption results of these two amines (Figure 7) indicate that MMEA has a higher amount of bicarbonate formed in the absorption and this leads to a higher total CO_2 loading. The higher bicarbonate formation for MMEA in absorption also helps it achieve larger absolute CO_2 release during desorption than DEA.

As the level of hydroxyethyl substitution increases in tertiary amines from *N*,*N*-dimethylethanol-amine (DMEA), to *N*-methyl-diethanolamine (MDEA) then to triethanolamine (TEA), so too do their polarities and boiling points. The experimental results illustrate that bicarbonate formation and total CO_2 loading decrease as more hydroxyethyl groups are introduced to the molecule, and the absolute CO_2 release in desorption also follows the same trend (Figure7). The results displayed in Figure 7 also demonstrate that the replacement of a methyl by hydroxyethyl substituent has greater impact on tertiary amines than on secondary amines in their CO_2 absorbing capacities.

In Recent Advances in Post-Combustion CO2 Capture Chemistry; Attalla, M.;
ACS Symposium Series; American Chemical Society: Washington, DC, 2012.

Downloaded by UNIV OF DELAWARE MORRIS LIB on June 15, 2012 | http://pubs.acs.org
Publication Date (Web): May 3, 2012 | doi: 10.1021/bk-2012-1097.ch002

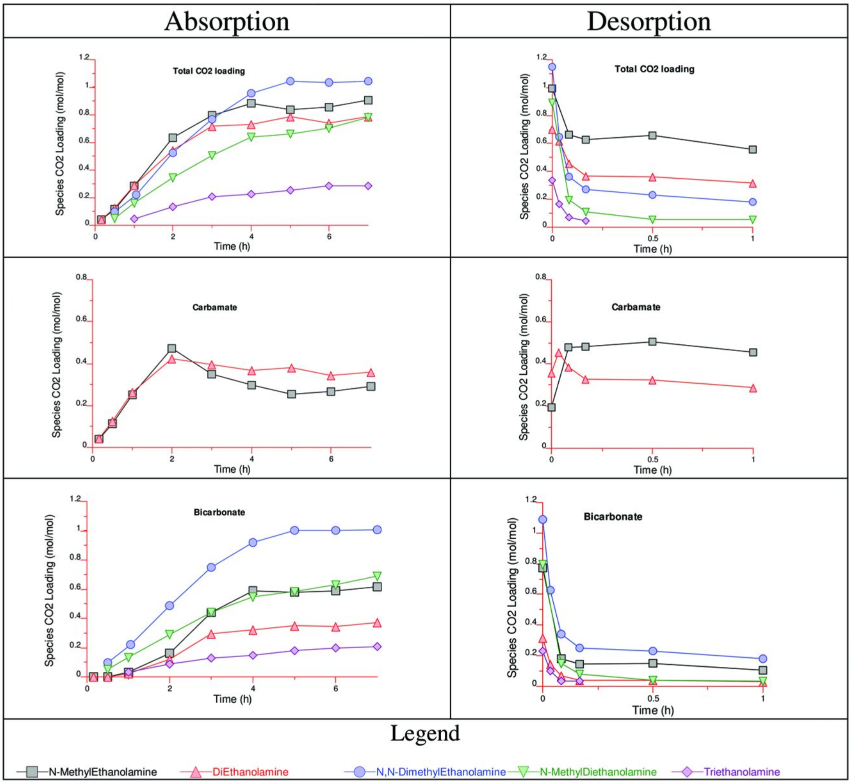

Figure 7. CO_2 absorption and desorption of secondary and tertiary amines of different level of hydroxyethyl substitutes

Both primary (R^1=R^2=H) and secondary amines (R^1=H; R^2≠H) act as nucleophiles towards CO_2 to form carbamates (eq. 1) which can convert to bicarbonate/carbonate in the reaction. Tertiary amines cannot form carbamates, and so instead just form bicarbonates when they absorb CO_2 (eq. 2 and 3).

$$2R^1R^2NH + CO_2 \rightleftharpoons R^1R^2N\text{-}C\overset{\ominus}{O}_2\ \ R^1R^2\overset{\oplus}{N}H_2 \qquad (1)$$

$$R^1R^2R^3N + H_2O \rightleftharpoons R^1R^2R^3\overset{\oplus}{N}H\ \ \overset{\ominus}{O}H \qquad (2)$$

$$\overset{\ominus}{O}H + CO_2 \rightleftharpoons HC\overset{\ominus}{O}_3 \qquad (3)$$

These results illustrate that amines with more hydroxyethyl groups are less reactive towards CO_2, and the greater steric hindrance in these amines does not enhance CO_2 capture either. A further study using different alkyl groups (especially the propyl group which has a similar size and shape to the

Downloaded by UNIV OF DELAWARE MORRIS LIB on June 15, 2012 | http://pubs.acs.org
Publication Date (Web): May 3, 2012 | doi: 10.1021/bk-2012-1097.ch002

hydroxyethyl group), rather than hydroxyethyl group to replace methyl, would help to separate the effects caused by steric hindrance and polarity changes.

Steric hindrance in an amine can promote amine absorption of CO_2 under some circumstances. The CO_2 absorption results of MEA and 2-methyl-2-aminopropanyl-1,3-diol (AMPD) in Figure 8a show that while AMPD absorbs more CO_2 than MEA, it does not form carbamate. This result is consistent with that found by Hook (*5*) for AMP, although AMPD contains an extra hydroxyl group in the molecule. The concentrations of these two amines are of 2M in this study as AMPD of 4M concentration forms a precipitate during CO_2 absorption.

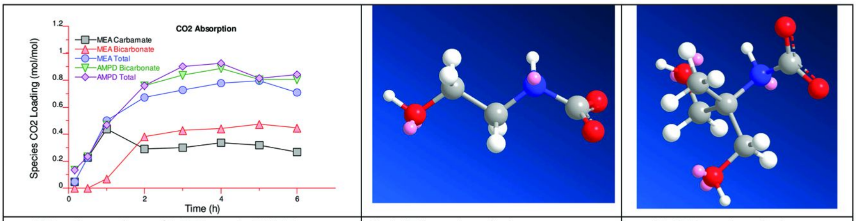

a. CO_2 absorption of MEA and AMPD | b. MEA carbamic ion | c. AMPD carbamic ion

Figure 8. (a) CO_2 absorption of MEA (b) and (c) AMPD and structure of their carbamic ions

Figure 8a indicates that AMPD and MEA have similar total CO_2 loading at early reaction time, and AMPD reaches a higher level for its total CO_2 loading after one hour of reaction time. Compared to the structure of MEA carbamic ion (Figure 8b), AMPD carbamic ion has a much higher steric hindrance (Figure 8c) that could cause a fast decomposition of its carbamate resulting in the rapid formation of bicarbonate and contributing to the higher total CO_2 loading. The replacement of hydrogen atoms on the α-carbon of MEA in this case not only increases the steric hindrance at the nitrogen center of AMPD, but also changes other properties including polarity and basicity. These characteristic changes also contribute to amine activity in the reaction with CO_2. Therefore, the observed difference in these reactions is the overall contribution of all factors (e.g. polarity, basicitiy, steric) originating from the amine structural alteration.

There are additional structural aspects which have not been included in this study, such as ring factors, that significantly affect amine characteristics in CO_2 capture. The above results demonstrate that all structural aspects do not simply affect the amine reactions as a single factor but that they often interact with each other, and also with the reaction conditions and process methods. At present it is not possible to propose clear rules to predict the entire complex of structural effects on amine efficacy to CO_2 capture. Further study is needed to more fully understand the effect of structure on the reaction between amines and CO_2.

Conclusion

The present study revealed some of the results of structural changes on a series of amines during CO_2 absorption and desorption:

- Variation of chain lengths from two to six carbons between two functional groups has different impact on the studied primary and secondary alkanolamines and diamines. The chain length variation has stronger impact on diamines and weak influence on primary alkanolamines to their CO_2 capture;
- *N*-methylalkanolamines with chain length of four or five carbons have better results during absorption and desorption whilst the amine containing a six carbon chain forms a precipitate during absorption;
- Diamines display a trend of increased bicarbonate formation when the carbon-chain between the two amino-groups is more than three carbons; this results in a higher total loading in the CO_2 absorption experiments studied;
- The replacement of a methyl group by hydroxyethyl group has a negative effect on both the secondary and tertiary amines studied;
- Steric hindrance of AMPD contributes to its high CO_2 loading in absorption via rapid formation of bicarbonate.

This study also demonstrates that structural factors interact with many other factors in a complicated way, and a comprehensive consideration of all possible aspects should be considered when a new amine is designed for CO_2 capture application.

Acknowledgments

We acknowledge the assistance of Dr Roger Mulder and Dr Jo Cosgriff for their help in NMR analysis. This project was carried out within the Research stream on Post-Combustion Capture in CSIRO’s Coal Technology Portfolio. It received funding from the Australian Government as part of the Asia-Pacific Partnership on Clean Development and Climate. The views expressed herein are not necessarily the views of the Commonwealth, and the Commonwealth does not accept responsibility for any information or advice contained herein.

References

1. International Energy Agency. *CO_2 Capture and Storage*; 2004.
2. Rochelle, G. T. Amine Scrubbing for CO_2 Capture. *Science* **2009**, *325*, 1652–1654.
3. Figueroa, J. D.; Fout, T.; Plasynski, S.; McIlvried, H.; Srivastava, R. Advances in CO_2 capture technology - The U.S. Department of Energy’s Carbon Sequestration Program. *Int. J. Greenhouse Gas Control* **2008**, *2*, 9–20.
4. Shao, R.; Stangeland, A. *Amines Used in CO_2 Capture – Health and Environmental Impacts*; The Bellona Foundation: 2009.
5. Hook, R. J. An investigation of some sterically hindered amines as potential carbon dioxide scrubbing compounds. *Ind. Eng. Chem. Res.* **1997**, *36*, 1779–1790.

Downloaded by UNIV OF DELAWARE MORRIS LIB on June 15, 2012 | http://pubs.acs.org
Publication Date (Web): May 3, 2012 | doi: 10.1021/bk-2012-1097.ch002

6. Bonenfant, D.; Mimeault, M.; Hausler, R. Determination of the structural features of distinct amines important for the absorption of CO_2 and regeneration in aqueous solution. *Ind. Eng. Chem. Res.* **2003**, *42*, 3179–3184.
7. Singh, P.; Versteeg, G. F. Structure and activity relationships for CO_2 regeneration from aqueous amine-based absorbents. *Process Saf. Environ. Prot.* **2008**, *86*, 347–359.
8. Puxty, G.; Rowland, R.; Allport, A.; Yang, Q.; Bown, M.; Burns, R.Maeder, M.; Attalla, M. Carbon Dioxide Postcombustion Capture: A Novel Screening Study of the Carbon Dioxide Absorption Performance of 76 Amines. *Env. Sci. Technol.* **2009**, *43*, 6427–6433.
9. Sheldrake, P.; Tyrrell, E.; Mintias, S.; Shahid, I. The Anion of 3-Methyl-2-pyridin-4-yl-1,3-oxazine. *Synth. Commun.* **2003**, *33*, 2263–2268.

Downloaded by UNIV OF DELAWARE MORRIS LIB on June 15, 2012 | http://pubs.acs.org
Publication Date (Web): May 3, 2012 | doi: 10.1021/bk-2012-1097.ch002

Downloaded by STANFORD UNIV GREEN LIBR on June 14, 2012 | http://pubs.acs.org
Publication Date (Web): May 3, 2012 | doi: 10.1021/bk-2012-1097.ch003

Chapter 3

Kinetics and Dissociation Constants (*pK_a*) of Polyamines of Importance in Post-Combustion Carbon Dioxide (CO_2) Capture Studies

**F. Khalili,[†] A. V. Rayer,[†] A. Henni,[*,†] A. L. L. East,[‡]
and P. Tontiwachwuthikul[†]**

[†]Industrial Systems Engineering and Applied Science, (International Test Centre for Carbon Capture), University of Regina, Regina, SK S4S 0A2, Canada
[‡]Department of Chemistry and Biochemistry, University of Regina, Regina, SK S4S 0A2, Canada
[*]E-mail: amr.henni@uregina.ca

Pseudo-first-order overall rate constants for the loss of CO_2 via reaction with different types of amines were measured using a stopped-flow technique at 298.15 K. Polyamines and cyclic amines were found to have higher reaction rates than linear primary and secondary amines. Therefore, six aqueous cyclic polyamine solutions were studied at (298.15 to 313.15) K over a concentration range of (20 to 120) $mol{\cdot}m^{-3}$ using. The overall reaction orders were calculated using the empirical power law kinetics and were found to be fractional in order, for practically all studied cyclic polyamines. The overall rate constants were fitted with the Crooks-Donnellan termolecular rate expression to determine elementary rate constants. In addition, the dissociation constants (pK_a) were determined using the potentiometric titration method at (298, 303, 313 and 323) K, and predicted using quantum chemistry techniques (IEFPCM continuum solvation model). A trend was found for the variation of the pK_a with the addition of different radical groups to the cyclic base molecules. Computational techniques tested for the prediction of pK_a involved *B3LYP* and MP2 levels of electronic structure theory, the addition of an explicit water molecule inside the continuum cavity, and a special scaling of

In Recent Advances in Post-Combustion CO2 Capture Chemistry; Attalla, M.;
ACS Symposium Series; American Chemical Society: Washington, DC, 2012.

the cavity radii for the ions. The procedure developed in this study reduced the error found in a previous technique for cyclic amines by 62%.

1. Introduction

In order to satisfy environmental combustion standards, acid gases such as CO_2 and H_2S must be removed from gaseous streams in refining, and in chemical and gas associated production plants. Natural gas and synthetic fuels such as coal gasification and shale oil cover broad ranges of both acid gas composition and pressure (*1*). The most common solvents used to capture CO_2 are the alkanolamines such as the monoethanolamine (MEA), diethanolamine (DEA) and n-methyldiethanol amine (MDEA). These amines are used commercially in post-combustion CO_2 capture as aqueous solution or in aqueous organic medium or in combination with aqueous potassium carbonate solutions (*2*).

CO_2 capture by chemical absorption using aqueous solution of amine uses absorper abd stripper units. This technology needs to overcome the challenge of reducing the energy, the environmental impact and the capture cost. Finding a better solvent is the path to solve these issues. High cyclic capacity, fast absorption rate, high equilibrium temperature sensitivity and low enthalpy of absorption are some of the factors to be considered in the selection of the best solvent. Both capital and capture costs of CO_2 removal depend on the CO_2 absorption and desorption rates. Solvents with fast reaction rates can reduce the height of the packing required in both the absorber and stripper. Energy in the stripper can be saved by faster solvents and by achieving a closer equilibrium in the absorber (*3*). Since 1960, various primary, secondary and tertiary amines were studied for their reaction rate with CO_2 to find out faster solvents and many studies were published in the literature, and reviewed by Blauwhoff et al. (*4*), Versteeg et al. (*5*), and more recently by Vaidya et al. (*6*) In this work, a screening study was performed on different types of amines (primary, secondary, tertiary, cyclic and polyamines) using a well established stopped-flow procedure in order to find the best solvents based on their kinetics rates at 298.15 K. Six cyclic aqueous polyamines were studied at (298.15 to 313.15) K over a concentration range of (20 to 120) $mol \cdot m^{-3}$.

The bascity of the solvent, quantified by the pK_a of its conjugate acid, is an important fundamental property which affects the kinetics and possibly the mechanism of the capture process (*3–6*). A linear relationship between the pK_a of an acid or base with its catalytic effect on the reaction rate was reported by Brønsted et al. (*4*) Many literature studies reported on a Brønsted relationship between the rate constant of the reaction of amines with CO_2 and the basicity of such amines (*4–8*). The following Brønsted relationship was reported by Versteeg et al. (*5*)for aqueous primary and secondary alkanolamines:

$$\ln k_2 = pK_a + 17.60 - \left(\frac{7188}{T}\right) m^3 \cdot mol^{-1} \qquad (1)$$

and for tertiary amines (*5*):

In Recent Advances in Post-Combustion CO2 Capture Chemistry; Attalla, M.;
ACS Symposium Series; American Chemical Society: Washington, DC, 2012.

Downloaded by STANFORD UNIV GREEN LIBR on June 14, 2012 | http://pubs.acs.org
Publication Date (Web): May 3, 2012 | doi: 10.1021/bk-2012-1097.ch003

$$\ln k_2 = 1.3pK_a + 11.48 - \left(\frac{8270}{T}\right) m^3 \cdot mol^{-1} \quad (2)$$

Because of the essential need for pK_a values, it would be useful to predict the aqueous pK_a of new amines by a prior means. One direct way is the calculation of such values using a widely popular quantum chemistry program (Gaussian 03) with a continum solvation model, in which the solvent is approximated as a dielectric continuum. A study of this kind was reported by da Silva and Svendsen (*9*), and improved by our previous work to predict the aqueous pK_a values within ± 1 (*10*). The procedure and the choice of conformers for the studied alkanolamines were recently published.

2. Experimental Setup

2.1. Determination of Chemical Kinetics

A stopped flow technique was used for the direct measurement of pseudo first-order kinetics, k_0, for different aqueous and non-aqueous diamines, as well as primary, secondary and tertiary alkanolamines. The experimental setup is a standard SF-51 stopped flow unit from Hi-Tech Scientific Ltd., UK. It is an assembly of four major units; a sample-handling unit, a conductivity-detection cell, an A/D converter and a microprocessor. The sample-handling unit is comprised of a stainless steel case which provides support and an enclosure for the sample flow circuit. Schematics of the sample handling unit is shown in Figure 1. The entire flow circuit, with the exception of the stop/waste syringe, is enclosed in a thermostat and maintained at a constant temperature by an external water bath within ± 0.1 K. The front panel of the sample handling unit displays a temperature indicator with a resolution of 0.1 K and an air pressure indicator. A pneumatic air supply is used to control the movement of drive plate located at the bottom of the internal syringes that contains the CO_2 solution and amine solution. During an experimental run, a fresh solution of CO_2 is loaded into one syringe and a fresh solution of amine is loaded into the other.

CO_2 solutions were prepared by bubbling research grade CO_2 for at least half an hour through the desired medium with water for an aqueous solution and methanol or ethanol for a non-aqueous solution. The concentration of CO_2 in the liquid medium was measured in a gas chromatograph (GC-6890 from Agilent). It was then diluted with the chosen media to keep the CO_2 solution at least 10 times lower than the amine solution in order to achieve pseudo first-order conditions. The pseudo first-order rate constants of the aqueous solution of EDA obtained for different concentrations are compared with previously published data (*11*) in Figure 2. A reproducibility of 4% (absolute average deviation of 15 sets of k_0 values from their mean value) and an estimated uncertainty of 5% (absolute average deviation of the obtained value from the literature value) were observed when compared to published data. By fitting the empirical power-law kinetics to the data of the experimentally found pseudo first order constants for CO_2 as shown in Figure 2, the reaction order of the amine was determined.

Downloaded by STANFORD UNIV GREEN LIBR on June 14, 2012 | http://pubs.acs.org
Publication Date (Web): May 3, 2012 | doi: 10.1021/bk-2012-1097.ch003

Downloaded by STANFORD UNIV GREEN LIBR on June 14, 2012 | http://pubs.acs.org
Publication Date (Web): May 3, 2012 | doi: 10.1021/bk-2012-1097.ch003

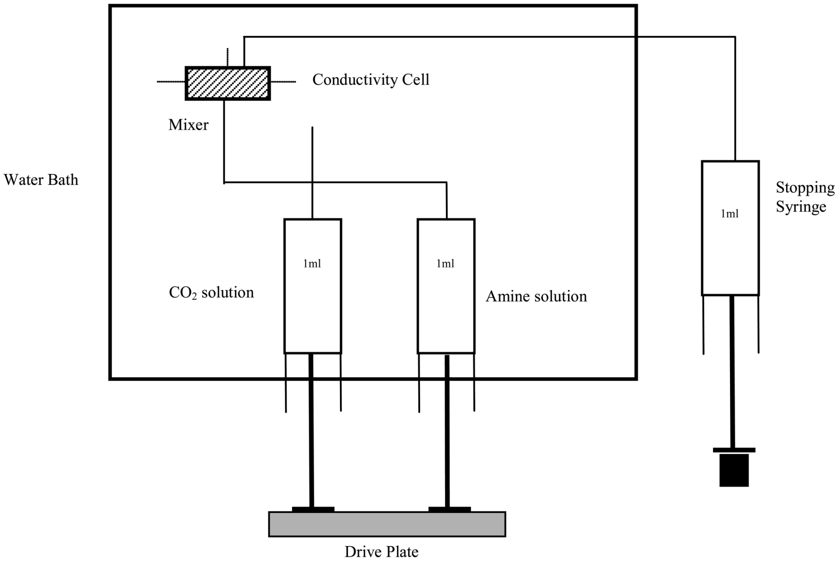
Conductivity Cell
Mixer
Water Bath
1ml
Stopping
Syringe
1ml
1ml
CO$_2$ solution
Amine solution
Drive Plate

Figure 1. Schematic diagram of stopped flow instrument

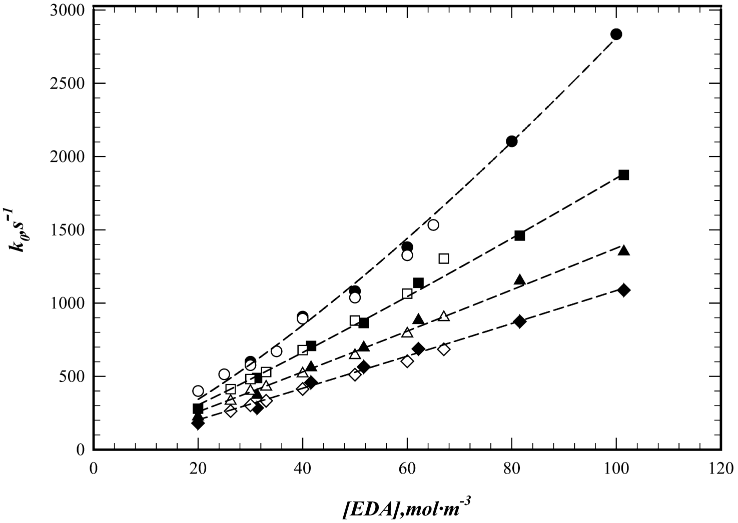

Figure 2. Pseudo first order reaction for (EDA + H_2O) solution. ♦, 298.15 K; ◊, 298.15 K[11]; ▴, 303.15 K; ▵, 303.15 K[11]; ▪, 308.15 K; □, 308.15 K[11]; ●, 313.15 K; ○, 313.15 K[11]; --- Power law kinetics.

2.2. Determination of the Dissociation Constant (*pK_a*)

0.01 M aqueous solutions of amines were prepared using deionized double distilled water. The solution was maintained at the experimental temperature and blanketed with a slow stream of nitrogen. The amine solutions (50 mL) were titrated with 0.1M HCl. Twenty equal portions (0.5 mL) of the titrant were added to the solution and the *pH* value was read when the equilibrium was reached. The pK_a values were determined using the Albert and Serjeant procedure (*12*). pK_a values of piperazine (PZ), from the experimental work are discussed and the same procedure was used to calculate the pK_a values of other cyclic amines.

PZ is a diacidic base and it ionizes in aqueous solution as follows:

$$PZ + H_3O^+ \xleftrightarrow[K_{a(1)}]{} PZH^+ + H_2O \tag{3}$$

$$PZH^+ + H_3O^+ \xleftrightarrow[K_{a(2)}]{} PZH_2^{2+} + H_2O \tag{4}$$

where PZH^+ represents the monoprotonated piperazine, and PZH_2^{2+} denotes the piperazinium ion. Considering the mole fraction of water as unity and expressing the concentration of hydronium ion, $[H_3O^+]$, as $[H^+]$, the pK_a values of *PZ* can be written as:

$$pK_{a(1)} = pH + \log\frac{[PZH^+]}{[PZ]} - \frac{Az^2I^{1/2}}{1+Bk_iI^{1/2}} \tag{5}$$

$$pK_{a(2)} = pH + \log\frac{[PZH_2^+]}{[PZH^+]} - \frac{1.5276I^{1/2}}{1+1.5I^{1/2}} \tag{6}$$

The last terms in equations (5) and (6) are the thermodynamic corrections. The calculation procedures were explained in Albert and Serjeant (*12*). 0.5 ml of the titrant HCl was added to 50 mL solution of 0.01 M *PZ* in 10 parts (5ml) to calculate the ratios of $[PZH^+]/[PZ]$ and the next 10 parts of 0.5 ml were added to find the ratios of $[PZH_2{}^{2+}]/[PZH^+]$. The corresponding *pH* values after each addition of titrant were recorded. These ratios were used in equations 5 and 6 to find $pK_{a(1)}$ and $pK_{a(2)}$ values. Thermal corrections were subtracted from the $pK_{a(1)}$ values and the average values were calculated as the first pK_a of *PZ*. Correspondingly thermal corrections for the second dissociation constants ($pK_{a(2)}$) were deducted to find the average value as the second pK_a. The Debye-Hückel equation was used to calculate the activity coefficients:

$$-\log(\gamma_i) = \frac{Az_i^2I^{1/2}}{1+Bk_iI^{1/2}} \tag{7}$$

Downloaded by STANFORD UNIV GREEN LIBR on June 14, 2012 | http://pubs.acs.org
Publication Date (Web): May 3, 2012 | doi: 10.1021/bk-2012-1097.ch003

Downloaded by STANFORD UNIV GREEN LIBR on June 14, 2012 | http://pubs.acs.org
Publication Date (Web): May 3, 2012 | doi: 10.1021/bk-2012-1097.ch003

where the terms *A* and *B* are called the Debye-Hückel equation constants and vary with the dielectric constant and the temperature of the solvent. z_i is the ion valance and the term k_i is the ionic size parameter, i.e. the mean distance of approach of the ions. *I* represents the ionic strength and depends on the concentration of the solution. The values of *A* and *B* for different temperatures were taken from Manov et al. (*13*) The ionic size parameters (k_i) values were also obtained from the literature (*14*). The calculation of the ionic strength follows different procedures for the first and second pK_as as shown in the work of Albert and Serjeant (*13*).

3. Reaction Kinetics and Mechanism

The reaction kinetics of CO_2 with primary, secondary and sterically hindered amines HXYN (H, X, and Y bonded to N) can be explained with either the zwitterion mechanism or the so-called “termolecular” mechanism, whereas the reaction with tertiary amines is interpreted using a mechanism described by the base-catalyzed hydration of CO_2.

3.1. Zwitterion Mechanism

The zwitterion mechanism was proposed by Danckwerts (*15*) for alkanolamines, drawing upon an earlier idea for pure amines. This two-step mechanism assumes a formation of an intermediate zwitterion which then undergoes a deprotonation by basic molecules resulting in carbamate formation:

$$HXYN + CO_2 \underset{k_b}{\overset{k_2^Z}{\rightleftarrows}} H^+XYNCOO^- \qquad (8)$$

$$H^+XYNCOO^- + B \xrightarrow{k_B} XYNCOO^- + BH^+ \qquad (9)$$

Applying the steady-state principle to the intermediate zwitterion, the rate of reaction of CO_2 (r_{CO2}) in aqueous solutions can be described as:

$$r_{CO_2} = k_{ov}[CO_2] = \frac{[HXYN]}{\frac{1}{k_2^Z} + \frac{1}{\sum K_B[B]}}[CO_2] \qquad (10)$$

where k_{ov} is the overall reaction rate constant for CO_2 loss, $K_B = k_2^Z k_B/k_b$, and k_2^Z, k_b (b = backwards) and k_B (*B* = base) are the elementary rate constants in steps (8) and (9). *B* denotes any proton-accepting species present; if one considers $\{H_2O, OH^-, HXYN\}$, then one has elementary rate constants $k_B = \{k_W, k_{OH-}, k_{HXYN}\}$ and the corresponding composites K_B in equation (10).

Equation (10) is very general and should cover most cases. Fitting this equation to experimental data would give values for the three K_B’s as well as k_2^Z, but this 4-parameter function often has indeterminacy problems. Danckwerts (*15*) pointed out two limiting cases, arising if $k_b << \sum_B k_B[B]$ [equation (11)] or $k_b >> \sum_B k_B[B]$ [equation (12)]:

Downloaded by STANFORD UNIV GREEN LIBR on June 14, 2012 | http://pubs.acs.org
Publication Date (Web): May 3, 2012 | doi: 10.1021/bk-2012-1097.ch003

$$r_{CO_2} = k_2^Z [CO_2][HXYN] \tag{11}$$

$$r_{CO_2} = \sum_B K_B [B][CO_2][HXYN] \tag{12}$$

Equation (12), like (10), allows for fractional orders of the amine between 1 and 2.

3.2. "Termolecular" Mechanism

It turns out that the limiting rate law in equation (12) is identical to the Crooks-Donnellan expression, which arose from assuming that the mechanism consists of one elementary termolecular step (*16*):

$$B + HXYN + CO_2 \rightarrow BH^+ + XYNCOO^- \tag{13}$$

There are theoretical objections to termolecular elementary steps, as any step which requires simultaneous collision of 3 entities is very rare. It is more likely that the single step starts with two of the three reactants initially complexed, either as $B.HXYN$, $HXYN.CO_2$ (Crooks-Donnellan (*16*)), or the zwitterion $H^+XYNCOO^-$ (Danckwerts (*15*)). Hence, the use of equation (12) does *not* confirm or deny the existence of any one of these supposed initial complexes. The label "termolecular" for the rate law in [equation (12)] should be taken to mean that this rate law arises in the limit that the intermediate, regardless of its nature, is in a sufficiently rapid equilibrium with reactants as to make the two-step reaction appear to be one step. Note that it would be incorrect practice to equate equation (12) with equation (11).

Some workers (e.g. Blauwhoff et al. (*4*)) have assumed the zwitterion mechanism and derived values for its elementary rate constants. Values for the k_W and k_{OH-} rate constants, for the uncatalyzed reaction between CO_2 and either water or the hydroxide ions, can be determined by the correlations proposed by Pinsent et al. many years ago (*17*). In the current work, results published in ref. (*4*) for primary and secondary amines were used in determining the intial guesses for K_W and K_{OH-} in fits of equations (10) and (12). Calculations without proper intial guesses can lead to erroneous results in estimating the rate constants (K_a, K_W and K_{OH-}).

3.3. Base Catalysis Mechanism

This mechanism seems important only for tertiary amines, which were not studied in this work, but the theory is presented here for completeness. Donaldson and Nguyen (*18*) proposed a different termolecular mechanism for the reaction of CO_2 with tertiary amine:

$$Am + CO_2 + H_2O \rightarrow AmH^+ + HCO_3^- \tag{14}$$

Again, a true termoleculecular elementary step is unlikely, and the mechanism is more likely to have an initial rapid equilibrium inconsequential to rate:

In Recent Advances in Post-Combustion CO2 Capture Chemistry; Attalla, M.;
ACS Symposium Series; American Chemical Society: Washington, DC, 2012.

Downloaded by STANFORD UNIV GREEN LIBR on June 14, 2012 | http://pubs.acs.org
Publication Date (Web): May 3, 2012 | doi: 10.1021/bk-2012-1097.ch003

$$Am + CO_2 + H_2O \rightleftarrows \text{intermediate complex} \tag{15}$$

$$\text{intermediate complex} \rightarrow AmH^+ + HCO_3^- \tag{16}$$

An additional possibility for the CO_2 loss rate could be the uncatalyzed reaction:

$$CO_2 + OH^- \rightleftarrows HCO_3^- \tag{17}$$

but this was deemed unimportant by Littel, Versteeg, and van Swaaij (*19*). They went on to straightforwardly derive the rate expression from the termolecular mechanism (14):

$$r_{CO_2} = k_{ov}\left[CO_2\right] = k_3[H_2O][CO_2][Am] = k_2^B[CO_2][Am] \tag{18}$$

where $k_2^B = k_3[H_2O]$ should be independent of amine concentration.

Blauwhoff et al. (*4*) studied the kinetics of several amines and concluded that an increase in amine pK_a increases the rate of CO_2 loss for primary,secondary, and tertiary amines. In this work, $[OH^-]$ ions contributions are calculated using the relations given by Astarita et al. (*20*):

$$[OH^-] = \sqrt{\frac{K_W}{K_p}[Am]} \quad , \quad \alpha < 10^{-3} \tag{19}$$

$$[OH^-] = \frac{K_W}{K_p}\left[\frac{1-\alpha}{\alpha}\right] \quad , \quad \alpha \geq 10^{-3} \tag{20}$$

where α is the CO_2 loading in amine solution (always low in stopped-flow experiments), and K_p is the equilibrium constant for:

$$Am + H_2O \rightleftarrows AmH^+ + OH^- \tag{21}$$

The value of K_W was estimated based on the correlation of Barth et al. (*21*) and the values of K_p for each amine were estimated using the experimental pK_a values. pK_a values were measured using the experimental set-up described in our previous work (*22*). Depending upon the order of the reactions, all experimental data for the studied aqueous cyclic amines were tested with equations (10), (11), or (12). The equation with the better AAD % (Percentile Absolute Average Deviation) and R^2 was chosen to interpret the mechanism of reactions.

4. Results and Discussion

4.1. Screening of Different Types of Amines

Using the stopped-flow technique, kinetic (pseudo-first order) rate constants (k_0) were determined for different types of amines (Primary amines: 1-amino-

In Recent Advances in Post-Combustion CO2 Capture Chemistry; Attalla, M.;
ACS Symposium Series; American Chemical Society: Washington, DC, 2012.

Downloaded by STANFORD UNIV GREEN LIBR on June 14, 2012 | http://pubs.acs.org
Publication Date (Web): May 3, 2012 | doi: 10.1021/bk-2012-1097.ch003

propanol (1-AP), 3-amino-propanol(3-AP), ethyl aminoethanol (EAE); Secondary amines: ethylene diamine (EDA), 1, 3-diaminopropane (DAP), 2-(amino ethyl) ethanol amine (AEEA);Cyclic amine:piperazine; Polyamine: n-(2-aminoethyl)-1,3-propane diamine (NAEDP)) at 298.15 K over a concentration range of (20 to 120) mol·m^{-3}. It was observed (Fig. 3) that polyamines and cyclic amines have higher reaction rates than linear primary and secondary amines: the trend of the rates of reaction followed by the amines was polyamines > cyclic amines > secondary amines > primary amines. The CO_2 absorption rate increased with the increase in -NH groups in the amines. Increase in –OH groups in amines decreased the rate of the reaction due to their electron withdrawing effect and a tendency to form intramolecular hydrogen bonding (*21*). Increase in the number of $–CH_3$ and $–CH_2$ groups increases the rate of the reaction due to their electron donor effect to the nitrogen atom.

The order of the reaction in amine (n) was found by fitting the data with a power law expression. To mimic Rochelle et al. (*23*), the second-order reaction constants k_2 from equation (11) were determined at 298.15 K and E_a value was calculated using the Arrhenius plot (ln k_2 vs. $1/T$) for the temperature range (298.15-313.15) K. The screening results are similar to the results of Rochelle et al. (*23*) obtained from Brønsted plot (Figure 4) by comparing the second order reaction rate constant (k_2) of various amines with respect to their pK_a (*23*). From Figures 3 and 4, it is notable that there was a considerable reduction in the reaction rates when the primary –OH group was exchanged with a secondary –OH group (example 3-AP to 1-AP).

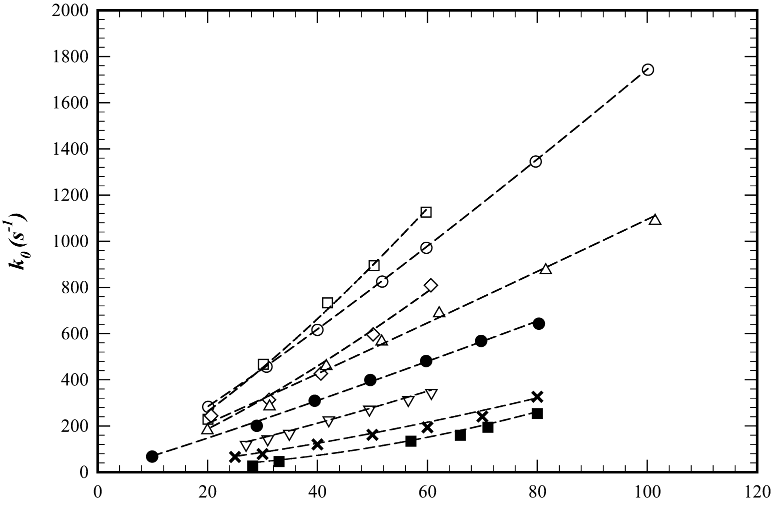

Figure 3. Comparison of pseudo-first order rate constants (k_0) for CO_2 absorptionreaction of various amines at 298.15 K: □, NAEDP; ○, PZ; ◊, DAP; ▵, EDA; ▿, 3-AP; ×, 1-AP; ▪, EAE; --- Eq. 11.

Downloaded by STANFORD UNIV GREEN LIBR on June 14, 2012 | http://pubs.acs.org
Publication Date (Web): May 3, 2012 | doi: 10.1021/bk-2012-1097.ch003

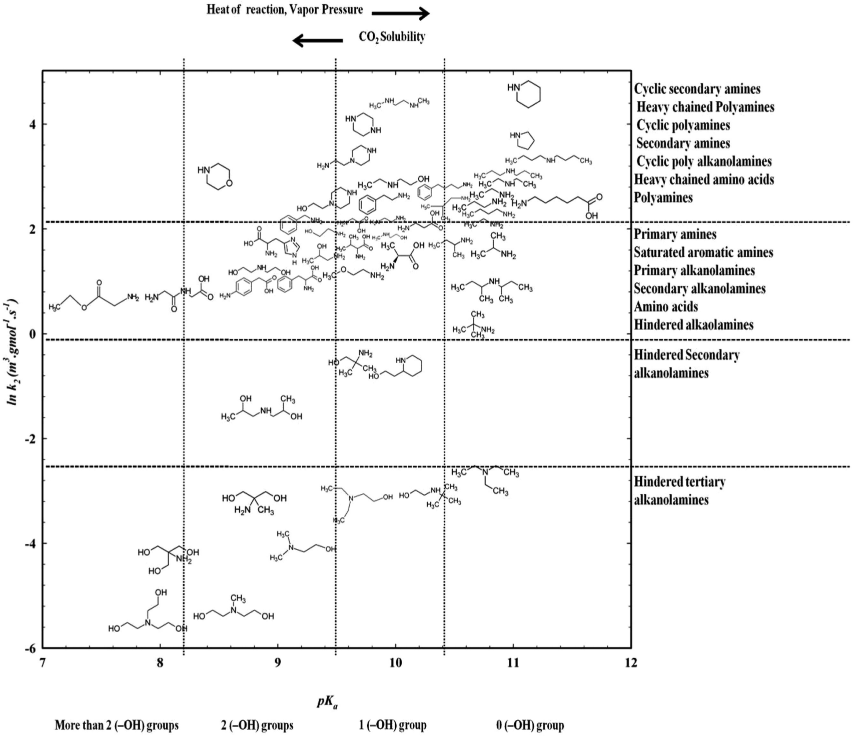

Figure 4. Brønsted correlation of CO_2 reaction rates with amines. (data in this figure was adapted from Rochelle et al. (23))

Both stopped-flow experiment and pK_a studies concluded that cyclic amines are more suitable for CO_2 capture than other amines due to their high absorption rates. Higher second order rate constants for polyamines and cyclic amines mean that the deprotonation reaction of carbamates was very fast in these amines. By comparing EDA, AEEA and EEA, it can be observed that the steric hindrance effect for the reaction kinetics offered by the –OH group is greater than the effect caused by the $–CH_3$ group. The order of the reaction increased in the case of EEA and decreased in the case of AEEA. The temperature sensitivity of the amine can be noted from the activation energies derived from the rate constants. Among the amines studied, PZ has the lowest activation energy and EEA has the highest activation energy. This implies that the highest hindrance effect in EEA for –NH group is the reason for its high activation energy and it decreases as the hindrance effect is reduced. Two –NH groups in PZ contribute to its low activation energy, indicating that the reaction proceeds very fast by forming zwitterion ions. Similar conclusion was made by Bishnoi and Rochelle (*24*) for the increase in the zwitterion formation rate by a reduction in steric hindrance around the amine group.

4.2. Screening of Cyclic Amines

The second order reaction rate constants (k_2) of the cyclic amines are higher than those of other types of amines, which was confirmed by both the stopped-flow experiment with the same concentrations, and the Brønsted plot of the amines with similar pK_a (Figure 4). Rochelle et al. (*23*) reviewed the kinetic studies for the cyclic amines studied by other researchers using different equipments for different concentrations and temperatures. Graeme et al. (*25*) and Singh et al. (*26*) conducted screening studies for several cyclic amines from their capacity for CO_2 solubility and their absorption rate with CO_2. Singh et al. (*26*) investigated the effect of different substituted saturated and unsaturated cyclic amines using an absorbent vessel. The conclusion derived from that work was, an amine group substitution in a saturated cyclic ring increases the protonation reaction, thus increasing the absorption rate and increases the absorption capacity. A substitution of one methyl group increased the absorption rate by increasing the basicity of the compounds to provide faster protonation reaction. But the absorption capacity varied depending on the position of the substitution of methyl group. All unsaturated cyclic amines showed poor absorption rate and capacity.

Graeme et al. (*25*) concluded in their screening experiment that amines that exhibited the fastest initial absorption rate were all polyamines with well separated amine functionality in structurally similar environments. The distance of the hydroxyl functionality (–OH) from the amine and the structural features around it had a significant effect on the solubility of CO_2 capacity by formation of intramolecular hydrogen bond between amine and hydroxyl groups. There are four cyclic amines among the top six solvents screened by Graeme et al. (*25*) They were ranked as follows: homopiperazine > piperazine > 1,4,7-triazacyclohexnae > tans-N-hydroxyethyl-1 and 4-diaminocyclohexane. Piperidine and piperazine which are heterocycles have faster reaction rate toward carbamate formation (*27*).

Among the cyclic amines, PZ is considered to be the best solvent and an accelerator in many CO_2 capture studies, because of its high loading capacity (mol_{CO2}/mol_{PZ}) and fast absorption rate (*24*, *28*). MDEA activated with PZ is being used as a solvent for high capacity CO_2 removal and found major application in ammonia and synthesis gas production (*29*). PZ has an ability to be effective at very low activator concentration with MDEA and provides a fast rate and high capacity to remove $CO_2$from industrial gases. Therefore, the kinetics of the reaction of CO_2 with six cyclic amines (derivatives of PZ) in aqueous solutions have been studied at (298.15-313.15) K over a concentration range of (20-120) $mol{\cdot}m^{-3}$ using the stopped-flow technique. (piperazine (PZ), 1-methyl piperazine (1-MPZ), 2-methyl piperazine (2-MPZ), 1-ethyl piperazine (1-EPZ), N-(2-hydroxyethyl) piperazine (1-HEPZ) and 3-morpholino propyl amine (3-MOPA). Their molecular structures and other details are given in Table 1.

The measured pseudo first-order rate constants (k_0) are plotted against the concentration ($mol{\cdot}m^{-3}$) in Figure 5 showing an expected increase in pseudo first-order rate constant (k_0) with concentration as well as temperature i.e. the reaction is favored by a rise in temperature and concentration. Figure 5 represents the pseudo-first order rate constants (k_0) for the six studied cyclic amines at 298.15 K. All

Downloaded by STANFORD UNIV GREEN LIBR on June 14, 2012 | http://pubs.acs.org
Publication Date (Web): May 3, 2012 | doi: 10.1021/bk-2012-1097.ch003

Downloaded by STANFORD UNIV GREEN LIBR on June 14, 2012 | http://pubs.acs.org
Publication Date (Web): May 3, 2012 | doi: 10.1021/bk-2012-1097.ch003

cyclic amines were found to have fractional reaction order with respect to amine varying from 1 to 2 (Except PZ). PZ has the highest reaction rate and 1-MPZ the lowest. The trend of reaction rates are given as (PZ > 2-MPZ > 1-EPZ > 3-MOPA > HEPZ > 1-MPZ). Aqueous 2-MPZ has an absorption rate similar to aqueous piperazine, but both PZ and 2-MPZ are solid in nature at room temperature.

Table 1. Details of the studied cyclic amines

Structure	Symbols	Purity (mass)	CAS. No
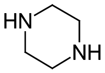	PZ	99%	110-85-0
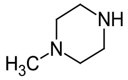	1-MPZ	99%	109-01-3
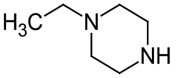	1-EPZ	98%	5308-25-8
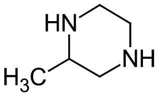	2-MPZ	≥ 98%	109-07-9
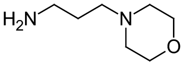	3-MOPA	99%	123-00-2
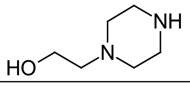	HEPZ	98%	103-76-4

Downloaded by STANFORD UNIV GREEN LIBR on June 14, 2012 | http://pubs.acs.org
Publication Date (Web): May 3, 2012 | doi: 10.1021/bk-2012-1097.ch003

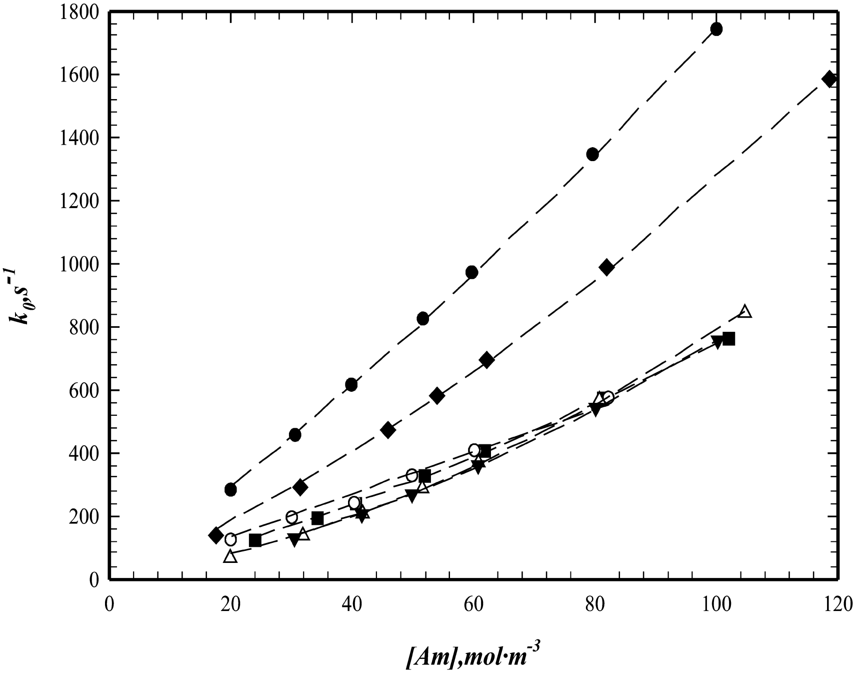

Figure 5. Comparison of pseudo-first order rate constants for CO_2 absorption in aqueous cyclic amines at 298.15 K: ●, PZ ; ▪, 1-MPZ; ♦, 2-MPZ; ▵, HEPZ; ▾, 3-MOPA; ○, 1-EPZ; --- Eq. 12.

All experimental data for the aqueous six cyclic amines were fitted with a power law kinetics to determine the order of the reaction (n) and fitted with equations (10), (11) or (12) to determine the second order rate and the mechanism of the reaction with CO_2. An Arrhenius rate equation was used to obtain the value of the activation energy for the reactions. The calculated second order reaction constants for all the six amines are listed in Tables (2-7) with their statistical anaylsis. pK_a values were taken from Khalili et al. (*22*) in order to calculate the $[OH^-]$ contribution (pK_a value of 3-MOPA was measured in this work and the values listed in Table 8). The temperature dependent correlations for these dissociation constants were also derived. Equation (12) corresponding to the termolecular mechanism fitted the data better than equations (10) and (11). This confirms that the zwitterion deprotonation is the rate-determining step and it is slow compared to the reverse reaction. According to Blauwhoff et al. (*4*), this indicates that the larger part of the zwitterion is reverted to CO_2 and amine and that only a small part is converted to carbamate. Second-order reaction constant (k_2) was calculated from equation (11) to estimate E_a using the Arrhenius plot (ln k_2 vs. $1/T$) for the temperature range (298.15-313.15) K. But it should be noted that the order of the reaction was taken as unity. Cyclic amines 2-MPZ, 3-MOPA and HEPZ showed poor fitting with equation (11), because the reaction orders for these amines were far greater than unity.

In Recent Advances in Post-Combustion CO2 Capture Chemistry; Attalla, M.;
ACS Symposium Series; American Chemical Society: Washington, DC, 2012.

Downloaded by STANFORD UNIV GREEN LIBR on June 14, 2012 | http://pubs.acs.org
Publication Date (Web): May 3, 2012 | doi: 10.1021/bk-2012-1097.ch003

Table 2. Second order reaction constants for (PZ + H_2O) solution

Parameters *(Eq. 12)*	***T /K***			
	298.15	***303.15***	***308.15***	***313.15***
K_a ($m^6 \cdot mol^{-2} \cdot s^{-1}$)	0.0353	0.0234	0.011	1.296E-14
K_w ($m^6 \cdot mol^{-2} \cdot s^{-1}$)	2.53E-04	3.05E-04	3.47E-04	4.11E-04
K_{OH^-}($m^6 \cdot mol^{-2} \cdot s^{-1}$)	1.89E-02	9.20E-03	4.66E-03	4.18E-01
Order (*n*) {Actual}	0.961	1.076	1.134	1.028
R^2	0.9997	0.9999	1.0000	0.9456
AAD%	1.4	0.8	0.3	1.6
k_2^Z ($m^3 \cdot mol^{-1} \cdot s^{-1}$) (Eq. 11)	16.7 ± 0.33	18.61 ± 0.21	19.95 ± 0.09	22.65 ± 0.93
Order (*n*) {Assumed}	1	1	1	1
R^2	0.9896	0.9962	0.9994	0.9447
AAD%	7.5	4.2	1.5	1.7

Table 3. Second order reaction constants for (1-MPZ + H_2O) solution

Parameters *(Eq. 12)*	***T /K***			
	298.15	***303.15***	***308.15***	***313.15***
K_a ($m^6 \cdot mol^{-2} \cdot s^{-1}$)	0.0259	0.0269	0.026	3.310E-02
K_w ($m^6 \cdot mol^{-2} \cdot s^{-1}$)	8.87E-05	1.01E-04	1.19E-04	1.27E-04
K_{OH^-}($m^6 \cdot mol^{-2} \cdot s^{-1}$)	4.64E-02	3.33E-05	3.32E-02	2.83E-01
Order (*n*) {Actual}	1.231	1.197	1.236	1.252
R^2	0.9994	0.9995	0.9995	0.9995
AAD%	1.9	1.8	1.6	1.8
k_2^Z ($m^3 \cdot mol^{-1} \cdot s^{-1}$) (Eq. 11)	6.90± 0.25	7.65± 0.26	8.56 ± 0.24	9.55 ± 0.32
Order (*n*) {Assumed}	1	1	1	1
R^2	0.9675	0.9708	0.9782	0.9717
AAD%	14	13	10	12

Downloaded by STANFORD UNIV GREEN LIBR on June 14, 2012 | http://pubs.acs.org
Publication Date (Web): May 3, 2012 | doi: 10.1021/bk-2012-1097.ch003

Table 4. Second order reaction constants for (1-EPZ + H_2O) solution

Parameters *(Eq. 12)*	***T /K***			
	298.15	***303.15***	***308.15***	***313.15***
K_a **($m^6 \cdot mol^{-2} \cdot s^{-1}$)**	1.50E-10	2.05E-10	2.13E-10	1.23E-10
K_w **($m^6 \cdot mol^{-2} \cdot s^{-1}$)**	1.22E-04	1.40E-04	1.59E-04	1.77E-04
K_{OH^-}**($m^6 \cdot mol^{-2} \cdot s^{-1}$)**	4.21E-02	1.92E-02	1.00E-02	1.65E-02
Order (*n*) {Actual}	1.066	1.036	1.069	1.084
R^2	0.9860	0.9778	0.9821	0.9959
AAD%	5.9	7.4	6.7	7.9
k_2^Z **($m^3 \cdot mol^{-1} \cdot s^{-1}$)** (Eq. 11)	6.74 ± 0.13	7.73 ± 0 .19	8.77 ± 0.19	9.74 ± 0.11
Order (*n*) {Assumed}	1	1	1	1
R^2	0.9846	0.9760	0.9805	0.9717
AAD%	5.6	7.1	6.5	7.8

Table 5. Second order reaction constants for (2-MPZ + H_2O) solution

Parameters *(Eq. 12)*	***T /K***			
	298.15	***303.15***	***308.15***	***313.15***
K_a **($m^6 \cdot mol^{-2} \cdot s^{-1}$)**	4.43E-02	6.13E-02	1.36E-01	2.09E-01
K_w **($m^6 \cdot mol^{-2} \cdot s^{-1}$)**	5.78E-05	5.95E-05	9.02E-06	1.38E-11
K_{OH^-}**($m^6 \cdot mol^{-2} \cdot s^{-1}$)**	1.12E-02	3.69E-03	1.07E-02	4.89E-01
Order (*n*) {Actual}	1.522	1.389	1.288	1.273
R^2	0.9995	0.9995	0.9998	0.9821
AAD%	1.8	1.8	2.2	2.7
k_2^Z **($m^3 \cdot mol^{-1} \cdot s^{-1}$)** (Eq. 11)	12.18 ± 0.52	14.71 ± 0.79	18.23 ± 1.56	23.63 ± 3.09
Order (n) {Assumed}	1	1	1	1
R^2	0.9846	0.9760	0.8906	0.7994
AAD%	19	23	38	59

Downloaded by STANFORD UNIV GREEN LIBR on June 14, 2012 | http://pubs.acs.org
Publication Date (Web): May 3, 2012 | doi: 10.1021/bk-2012-1097.ch003

Table 6. Second order reaction constants for (3-MOPA + H_2O) solution

Parameters *(Eq. 12)*	***T /K***			
	298.15	***303.15***	***308.15***	***313.15***
K_a ($m^6 \cdot mol^{-2} \cdot s^{-1}$)	4.29E-02	6.49E-02	1.28E-01	0.240
K_w ($m^6 \cdot mol^{-2} \cdot s^{-1}$)	1.52E-04	1.63E-04	1.25E-04	4.45E-05
K_{OH^-}($m^6 \cdot mol^{-2} \cdot s^{-1}$)	6.45E-03	1.10E-02	4.29E-03	3.21E-02
Order (*n*) {Actual}	2.257	1.880	1.551	1.477
R^2	0.9992	0.9995	0.9996	0.9983
AAD%	3.6	2.2	3.7	10.3
k_2^Z ($m^3 \cdot mol^{-1} \cdot s^{-1}$) (Eq.11)	6.62 ± 0.44	8.03 ± 0.60	11.08 ± 1.35	15.88 ± 2.68
Order (n) {Assumed}	1	1	1	1
R^2	0.9121	0.8936	0.7993	0.7097
AAD%	23	27	51	87

Table 7. Second order reaction constants for (HEPZ + H_2O) solution

Parameters *(Eq. 12)*	***T /K***			
	298.15	***303.15***	***308.15***	***313.15***
K_a ($m^6 \cdot mol^{-2} \cdot s^{-1}$)	4.91E-02	4.56E-02	4.88E-02	5.28E-02
K_w ($m^6 \cdot mol^{-2} \cdot s^{-1}$)	5.44E-05	7.51E-05	8.44E-05	9.68E-05
K_{OH^-}($m^6 \cdot mol^{-2} \cdot s^{-1}$)	1.00E-02	4.74E-02	7.29E-04	5.96E-04
Order (*n*) {Actual}	1.392	1.406	1.418	1.517
R^2	0.9993	0.9992	0.9992	0.9992
AAD%	3.9	3.6	3.5	3.4
k_2^Z ($m^3 \cdot mol^{-1} \cdot s^{-1}$) (Eq.11)	6.89 ± 0.49	7.76 ± 0.46	11.08 ± 1.35	15.88 ± 2.68
Order (n) {Assumed}	1	1	1	1
R^2	0.9121	0.933	0.9357	0.9390
AAD%	36	27	26	25

Downloaded by STANFORD UNIV GREEN LIBR on June 14, 2012 | http://pubs.acs.org
Publication Date (Web): May 3, 2012 | doi: 10.1021/bk-2012-1097.ch003

Table 8. Dissociation constants for aqueous 3-MOPA

	pK_a				***$lnK_p=A+B/T$***		***K_p (298.15 K)***
T/K	***298.15***	***303.15***	***308.15***	***313.15***	***A***	***B***	
3-MOPA	9.98	9.73	9.58	9.51	-0.307	-6730	1.16E-10

Table 9 lists the order of the reactions, the second order reaction rate constants and the activation energies of the studied cyclic amines derived by assuming the rate to be unity. Activation energies and the temperature dependence of the second order reaction rate constants were calculated using an Arrhenius- relation.

Figure 6 represents the Brønsted-plot for the studied amines at different temperatures. For all cyclic amines, a linear relationship exists between ln k_2 and pK_a. As the pK_a increases the second order rate constants for the cyclic amines decreases. This indicates that the alkalinity of the solution influences the rate of the reaction between CO_2 and the amine. From this plot, the effect of methyl group ($-CH_3$) can also be observed. The basicity of the piperazine molecule decreases when it is hindered by the position of methyl group, thereby reducing the reaction rate with CO_2.

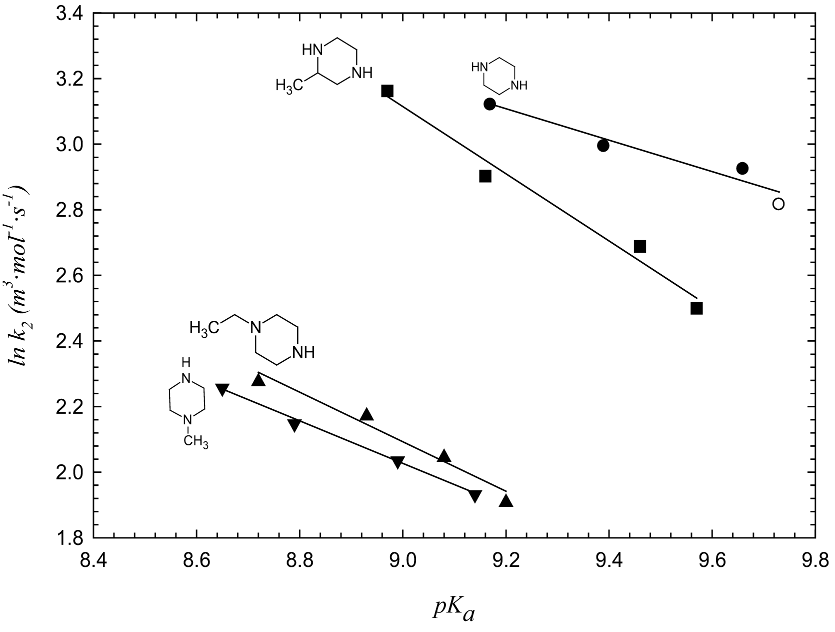

Figure 6. Brønsted plot for the studied cyclic amines.

Downloaded by STANFORD UNIV GREEN LIBR on June 14, 2012 | http://pubs.acs.org
Publication Date (Web): May 3, 2012 | doi: 10.1021/bk-2012-1097.ch003

Table 9. Second order reaction constants and order of the reaction with CO_2 for aqueous cyclic amine solutions

Amine	*Order (n)*	k_2^Z *($m^3 \cdot mol^{-1} \cdot s^{-1}$) (Eq. 11)*	E_a *($kJ \cdot mol^{-1}$)*
PZ	0.96 - 1.1	$k_2 = 7.84 \times 10^4 * \exp\left[\frac{-1833}{T}\right]$	15.24
1-MPZ	1.19 - 1.25	$k_2 = 6.20 \times 10^3 * \exp\left[\frac{-2027}{T}\right]$	16.85
1-EPZ	1.20 - 1.25	$k_2 = 1.51 \times 10^4 * \exp\left[\frac{-2297}{T}\right]$	19.10
2-MPZ	1.27 - 1.93	$k_2 = 1.14 \times 10^7 * \exp\left[\frac{-4104}{T}\right]$	34.13
3-MOPA	1.0 - 2	$k_2 = 6.23 \times 10^8 * \exp\left[\frac{-5486}{T}\right]$	45.61
HEPZ	1.27 - 1.37	$k_2 = 3.63 \times 10^8 * \exp\left[\frac{-5321}{T}\right]$	44.24

5. Dissociation Constants (pK_a) of Cyclic Amines

The dissociation constant is one of the main factors in the choice of a chemical solution for acid gas removal or in the interpretation of the kinetic mechanism for the absorption of the acid gas in the solution (*30*). Information available from the dissociation constants are mainly a measure of the basic strength of the chemical solution (amine) at a specific temperature. Information about a temperature dependent dissociation constant provides the change in the reaction enthalpy by indicating the change of the basic strength of the absorbent within a given temperature range in the absorption/desorption and cooling/ heating cycle for a conventional acid gas removal plant (*31*). pK_a is defined as the negative of the logarithm of the equilibrium constant (K_a) for the reaction:

$$HA \xleftrightarrow[K_a]{} H^+ + A^- \qquad (22)$$

$$K_a = \frac{[H^+][A^-]}{[HA]} \qquad (23)$$

where $[H^+]$,$[A^-]$ and $[HA]$ represent the concentrations of the solution species in $mol \cdot L^{-1}$. Then, pK_a will be derived as:

$$pK_a = pH + \log[HA] - \log[A^-] \tag{24}$$

It implies that a solution with 50% dissociation has a pH equal to the pK_a of the acid. For bases, the dissociation constants are reported as pK_a values for the conjugate acid (*32*):

$$BH^+ \underset{K_a}{\longleftrightarrow} H^+ + B \tag{25}$$

An ionization constant K_b was used for the reaction:

$$B + H_2O \underset{K_b}{\longleftrightarrow} BH^+ + OH^- \tag{26}$$

and pK_b is related to pK_a by:

$$pK_a + pK_b = pK_{water} = 14 \text{ at } (T = 298.15 \text{ K}) \tag{27}$$

The basicity of the solvent, quantified by the pK_a of its conjugate acid, is a key factor for the reaction rate and absorption capacity of the solvent in the process (*22*). A linear relationship between the pK_a of an acid or a base and its reaction rate was derived by Brønsted et al. (*7*) In a previous section, a Brønsted relationship between the rate constant of the reaction of amines with CO_2 and the basicity of such amines was discussed. pK_a values of alkanolamines are available in the open literature at different temperatures (*22*, *32–35*). The experimental determination of the pK_a values for five cyclic diamines have been reported in our work at different temperatures. The experimental set-up and its details were reported in our previous work (*20*).

5.1. Results and Discussion

Table 10 shows the first and second pK_a values of cyclic amines. As observed in these tables, the pK_a values of PZ calculated in our work, are in good agreement (± 0.05) with the data reported by Hetzer et al. (*36*) Among the cyclic amines studied in this work PZ and 2-MPZ have the highest pK_a values and DMPZ has the lowest value. Secondary amines are stronger bases than tertiary amines. Therefore, DMPZ, with two tertiary amine groups, is the weakest base, and PZ and 2-MPZ, with two secondary amine groups, are the most basic amines. Due to the steric effect, 2-MPZ is a weaker base than PZ. The methyl ($-CH_3$) group on α carbon in this amine causes steric hindrance to the solvation on cation formation which lowers the basicity. Intramolecular hydrogen bonding also lowers the basicity. HEPZ, an alkanolamine with an intramolecular hydrogen bonding tendency has as a lower pK_a value than 1-EPZ (*37*).

Downloaded by STANFORD UNIV GREEN LIBR on June 14, 2012 | http://pubs.acs.org
Publication Date (Web): May 3, 2012 | doi: 10.1021/bk-2012-1097.ch003

Downloaded by STANFORD UNIV GREEN LIBR on June 14, 2012 | http://pubs.acs.org
Publication Date (Web): May 3, 2012 | doi: 10.1021/bk-2012-1097.ch003

Table 10. First and second pK_a values of amines at different temperatures

Amine	$pK_{a(1)}$			
	T/K			
	298	***303***	***313***	***323***
PZ	9.78	9.66	9.39	9.17
2-MPZ	9.57	9.46	9.16	8.97
1-MPZ	9.14	8.99	8.79	8.65
1-EPZ	9.20	9.08	8.93	8.72
HEPZ	9.09	8.95	8.75	8.63
DMPZ	8.38	8.27	8.06	7.84
Amine	$pK_{a(2)}$			
	T/K			
	298	***303***	***313***	***323***
PZ	5.35	5.27	5.02	4.93
2-MPZ	5.24	5.19	4.92	4.84
1-MPZ	4.63	4.40	4.31	4.18
1-EPZ	4.76	4.58	4.48	4.31
HEPZ	3.92	3.89	3.74	3.60
DMPZ	3.81	3.70	3.64	3.45

To sum up and present a clear picture for the change of pK_a with the addition of different radicals to PZ, we suggest the following rules. Starting with the PZ molecule with two secondary amines, the addition of a methyl group (-CH_3) on any carbon of the ring introduces a hindrance effect and lowers the pK_a. The addition of an ethyl group (CH_3-CH_2) to PZ further lowers the pK_a. The addition of a methyl group lowers the pKa more than in the case of an ethyl group. The addition of a hydroxyl group (-OH) to 1-EPZ or a hydroxyl group to PZ reduces the pK_a further than any previous addition (hydrogen bonding). Finally, the addition of a methyl radical (-CH_3) to each secondary amine of PZ to form tertiary amines (DMPZ) leads to the lowest pK_a. These conclusions are valid for the first and second pK_a of the studied amines. In the present study, the calculated ΔS° values from the Van'f Hoff equation were almost negiligible compared to the contribution of the $(-\Delta H^\circ/T)$ term. The higher the value of $-\Delta H^\circ$, the larger is the shift in basicity from low temperature (high basicity leading to better absorption of CO_2) to the higher temperature (low basicity leading to better regeneration of CO_2). Accordingly, 2-MPZ and PZ should be the most attractive amines for gas swettening in terms of cyclic capacity.

Downloaded by STANFORD UNIV GREEN LIBR on June 14, 2012 | http://pubs.acs.org
Publication Date (Web): May 3, 2012 | doi: 10.1021/bk-2012-1097.ch003

5.2. pK_a Prediction Using Computational Chemistry

Aqueous pK_a of amines can be predicted by direct calculation using a popular quantum chemistry program (Gaussian 03) with a continuum solvation model, in which the solvent is approximated as a dielectric continuum. A computational study of some alkanolamines was reported by da Silva and Svendsen in 2003 (*9*), but they deemed their results too inaccurate and it was improved by Khalili et al. (*10*) in 2009. In this work, we are reporting that technique to calculate aqueous pK_a values to ± 1 pK_a accuracy for the substituted PZs which were used in the kinetic screening experiment. The amines studied are listed in Table 11 with their experimental pK_a values. The improvents provided in our work are (i) reduction of cavities around cations (an electrostriction technique) and the use of explicit solvent molecules inside the cavities (a semicontinuum technique); (ii) the equations to calculate pK_a were developed through the continuum salvation methods; (iii) to formalize an approximation for the entropy of multiple conformers; (iv) historical problems involved in ab initio pK_a calculations to improve the predictions in future.

Table 11. Experimental pK_a values of the bases investigated in our work

Base	*Name or Abbreviation*	*pK_a (298.15 K)*	*Ref*
$C_4H_9N_2(CH_3)$	2-methylpiperazine	9.57	(*10*)
$C_4H_9N_2(C_2H_5)$	1-ethylpiperazine	9.20	(*10*)
$C_4H_9N_2(CH_3)$	1-methylpiperazine	9.14	(*10*)
$C_4H_9N_2(C_2H_4OH)$	1-(2-hydroxyethyl)piperazine	9.09	(*10*)
$C_4H_8N_2(CH_3)_2$	1,4-dimethylpiperazine	8.38	(*10*)
$O(CH_2CH_2)_2NH$	morpholine	8.50	(*37*)
$HN(CH_2CH_2)_2NH$	piperazine	9.73	(*37*)

5.3. Theory of pK_a Calculation

The pK_a of a base B is a scaled version of $\Delta_r G_{(aq)}$, the free energy change of the acid-dissociation reaction:

$$BH^{+}(aq) \rightarrow B_{(aq)} + H^{+}_{(aq)} \tag{28}$$

$$pK_a = \frac{\Delta_r G_{(aq)}}{RT \ln 10} \tag{29}$$

where R is the gas constant and T is temperature. Basicity increases with $\Delta_r G_{(aq)}$ and hence with pK_a. $\Delta_r G_{(aq)}$ can be expressed as:

$$\Delta_r G_{(aq)} \rightarrow \Delta_h G_{(aq)}(BH^+ \rightarrow B) + G_{(aq)}(H^+) \tag{30}$$

The half-reaction energy $\Delta_h G_{(aq)}(BH^+ \rightarrow B)$ is the quantity of interest in this work. It is computed as the difference of two free energies of compounds in solution:

$$\Delta_h G_{(aq)} = G_{(aq)}(B) - G_{(aq)}(BH^+) \tag{31}$$

$G_{(aq)}(H+)$, is independent of base and is difficult to determine, aqueous H^+ exists in several forms, like H_3O^+, H_5O^{2+}, and H_9O^{4+} (*38*). The best value for $G_{(aq)}(H^+)$ is -270.3 kcal·mol^{-1} ($G_{(g)}(H^+)$ = -6.3 kcal·mol^{-1}(1 atm) (*39*) + $\Delta_{solv}G(H^+)$ = -264.0 kcal·mol^{-1} (1 atm gas → 1 mol·L^{-1} aqueous solution) (*40*)). Semicontinuum technique was used to determine the free energies of the compounds in the solution. In order to reduce pK_a-proportional error with a semicontinuum technique an explicit water molecule was added inside the solute cavity (*40*). An empirical approach was used to eliminate the known systematic error for predictive uses by different researchers (*41–43*).

$$pK_{a(\exp t)} = m \times pK_{a(theo)} + b \tag{32}$$

Adam (*44*) and Tao (*45*), have found phenomenal accuracy (± 0.2) for a single class of compounds by taking this approach further, replacing $pK_{a(theo)}$ in equation (32) with some other computable property of the solute molecule. Of the direct pK_a computation studies (i.e. not based on linear regressions like equation (32), the few that have reported computed pK_a accuracy of better than ±1 were studies of a handful of compounds within a single class and small pK_a ranges (*46–49*), where the slope errors were hard to observe and constant-shift errors might have cancelled them. A good example would be the work of da Silva et al. (*50*), whose results for carboxylic acids looked very good, but whose ensuing results for three other classes of compounds showed large class-dependent errors (*51*). Similar results can be achieved for PZ of *pH* range 8-11.

5.4. Computational Procedures

All calculations were done using the Gaussian 03 software program and the *6-311++G*** basis set. Solvent effects were computed using the continuum solvation method IEFPCM (*52*) with *UA0* radii for spherical cavities. Theelectronic structure levels of theory tested for IEFPCM calculations (including geometry optimization) were *B3LYP* and *MP2*. Geometry optimizations with IEFPCM minimize $E_{elec} + \Delta G_{el}$. All $E_{nuc}(0)^{g@g}$ terms were computed only with *B3LYP* at *B3LYP* gas-phase-optimized geometries. For neutral amine, a hydrogen atom of the explicit water molecule was hydrogen-bonded to the nitrogen atom in amine, while for protonated amine the new proton attached to nitrogen atom was hydrogen-bonded to the oxygen of water molecule. The use of one explicit water molecule was named as *Model II*, to distinguish from *Model I*, where no explicit water is used. The utility of a constant scale factor to contract the radii of charged “united atoms” was tested to accommodate electrostriction. Instead of the default

Downloaded by STANFORD UNIV GREEN LIBR on June 14, 2012 | http://pubs.acs.org
Publication Date (Web): May 3, 2012 | doi: 10.1021/bk-2012-1097.ch003

factor of 1.0 for the NH_x groups of protonated amines, 0.9 was used. This was referred to as “special scaling”. Conformer choices and entropy calculations are explained in our previous work (*10*). The conformers used were the ones with lowest in energy from IEFPCM/*B3LYP* calculations.

5.5. *pK_a* Results

In order to calculate the pK_a values using equation (29), we must convert $\Delta G_{(aq)}$ to $\Delta_r G_{(aq)}$ via equation (30), by adding the contribution $G_{(aq)}(H^+)$. In this work, empirical choices for $G_{(aq)}(H^+)$ was taken. This parameter was fitted by minimizing the root mean square (rms) of calculated pK_a values versus experimental values. Fitting was done for each model and level of theory. It was also done to convert the results of da Silva and Svendsen (*9*) from relative $\Delta G_{(aq)}$ values into best possible pK_a values. The results are shown in Table 12. The rms errors reveal that the best results are obtained from Model II with default radii scaling. The best two techniques of Table 12 were used to compute the pK_a values in Table 11. This included refitting of $G_{(aq)}(H^+)$ to minimize rms error. This resulted in two fitting parameters for each modelling technique, and improved the rms errors by 42-45% compared to single-parameter results (Table 13). Our most accurate procedure for the calculation of the pK_a of bases studied in this work is *Model II* with the explicit water technique employing IEFPCM/MP2/6-311++G** for the optimized geometries and ensuing energies, with $E_{nuc}(0)^{g@g}$ terms computed with *B3LYP*/6-311++G** at a C_1-symmetry gas-phase conformer geometry, statistical entropy corrections and $G_{(aq)}(H^+)$ values of -266.96 kcal/mol for acyclic bases and -269.63 kcal/mol for cyclic bases. It produced an rms error of 0.68 for the pK_a of the 17 compounds studied here. The best experimental value for $G_{(aq)}(H^+)$ is -270.3 kcal/mol. Interestingly, the fitted values in our computational work are close to this value for the cyclic molecules with no electrostriction scaling, and a chemically meaningful *ab initio* procedure in which the empirical fitting of $G_{(aq)}(H^+)$ is replaced by properly fixing its experimental value will be pursued in future work.

Downloaded by STANFORD UNIV GREEN LIBR on June 14, 2012 | http://pubs.acs.org
Publication Date (Web): May 3, 2012 | doi: 10.1021/bk-2012-1097.ch003

Table 12. Comparison of Theoretical and Experimental *pK_a* Results

	B3LYP Model I	*B3LYP Model I*	*B3LYP Model II*	*MP2 Model II*	*B3LYP Model II*	*MP2 Model II*	
Base	*Ref (9)*	*Def. sc.*[a]	*Sp. sc.*[a]	*Sp. sc.*[a]	*Def. sc.*[a]	*Def. sc.*[a]	*expt*[b]
morpholine	10.97	9.61	9.21	8.97	9.81	9.56	8.50
piperazine[c]	12.49	12.21	11.26	10.87	12.02	11.61	9.73
rms error	1.79	1.85	1.47	1.30	1.22	1.00	

[a] “Def. sc.” means default radii scaling, “Sp. sc.” means special scaling; [b] For references see Table 11; [c] $pK_{a(1)}$

Downloaded by STANFORD UNIV GREEN LIBR on June 14, 2012 | http://pubs.acs.org
Publication Date (Web): May 3, 2012 | doi: 10.1021/bk-2012-1097.ch003

Table 13. Comparison of theoreticaland experimental *pK_a* results, including extra piperazines

	one fitting parameter		*two fitting parameters*		
Base	*B3LYP*	*MP2*	*B3LYP*	*MP2*	*Expt*[a]
Morpholine	9.13	9.04	7.65	7.89	8.50
Piperazine[b]	11.34	11.10	9.86	9.95	9.73
2-methylpiperazine[b]	11.01	10.46	9.53	9.31	9.57
1-ethylpiperazine[b]	10.95	10.60	9.47	9.45	9.20
1-methylpiperazine[b]	10.40	10.02	8.92	8.87	9.14
1-(2-hydroxyethyl)piperazine[b]	10.49	10.08	9.01	8.93	9.09
1,4-dimethylpiperazine[b]	10.65	10.37	9.17	9.21	8.38
rms error	1.48	1.18	0.81	0.68	

[a] For references see Table 11; [b] $pK_{a(1)}$

6. Conclusion

Screening of primary, secondary, poly and cyclic amines was performed using a stopped-flow technique at 298.15 K over a concentration range of (20 to 120) mol·m^{-3}. Polyamines and cyclic amines have higher pseudo first order reaction rates compared to linear secondary and primary amines. Consequently, six cyclic amines were studied between (298.15 and 313.15) K over a concentration range of (20 to 120) mol·m^{-3}. PZ had the highest reaction rate and 1-MPZ the lowest. At the same temperature, the trend of reaction rates is given as (PZ > 2-MPZ > 1-EPZ > 3-MOPA > HEPZ > 1-MPZ). The termolecular mechanism was used for calculating the rate parameters by fitting the experimental data. Higher second order rate constants for polyamines and cyclic amines mean that the deprotonation reactions of carbamates were very fast for these amines. The dissociation constants of the conjuagate acids of six cyclic diamines (PZ, 1-MPZ, 2-MPZ, 1-EPZ, HEPZ and DMPZ) were meaured using a potentiometric titration method at (298, 303, 313 and 323) K. A trend is proposed relating the variation of pK_a with the addition of different radical groups to the base PZ molecule. pK_a values of piperazines were computed using quantum chemistry techniques and the IEFPCM continuum solvation model. Of several techniques tested, the best one involved the incorporation of an explicit water molecule inside the continuum cavity (Model II). Proper entropy corrections, often neglected in pK_a studies, were also included. The use of a second fitting parameter for these compounds dramatically lowered the overall rms error by 42-45%. Our best technique reduced the errors found in a previous technique (*9*) for similar compounds by 62% (*10*).

References

1. Satori, G.; Ho, W. S.; Savage, D. W. Sterically-Hindered Amines for Acid-Gas Absorption. *Sep. Purif. Methods* **1987**, *16* (2), 171–200.
2. Rao, A. B. *Technologies: Separation and capture inCarbon Capture and Sequestration*; Wilson, E. J.Gerard, D., Eds.; Blackwell: Ames, IA, 2007.
3. Rayer, A. V.; Sumon, K. Z.; Henni, A.; Tontiwachwuthikul, P. Kinetics of the reaction of Carbon Dioxide (CO_2) with Cyclic Amines Using the Stopped-Flow Technique. *Energy Procedia* **2011**, *4*, 140–147.
4. Blauwhoff, P. M. M.; Versteeg, G. F.; van Swaaij, W. P. M. A Study on theReaction Between CO_2 and Alkanolamines in Aqueous Solutions. *Chem. Eng. Sci.* **1984**, *39*, 207–225.
5. Versteeg, G. F.; van Dijck, L. A. J.; van Swaaij, W. P. M. On the Kinetics Between CO_2 and Alkanolamines both in Aqueous and Non-Aqueous Solution, An Overview. *Chem. Eng. Commun.* **1996**, *144*, 113–158.
6. Vaidya, P. D.; Kenig, E. Y. CO_2-Alkanolamines Reaction Kinetics: A Review of Recent Studies. *Chem. Eng. Technol.* **2007**, *30* (11), 1467–1474.
7. Brønsted, J. N.; Guggenheim, E. A. Contribution to the Theory of Acid and Basic Catalysis. The Mutarotation of Glucose. *J. Am. Chem. Soc.* **1927**, *49*, 255–2584.
8. Penny, D. E.; Ritter, T. J. Kinetic Study of the Reaction Between Carbon Dioxide and Primary Amines. *J. Chem. Soc., Faraday Trans I* **1983**, *79*, 2103–2109.
9. da Silva, E. F.; Svendsen, H. F. Prediction of the pK_a Values of Amines Using Ab-initio Methods and Free-Energy Perturbations. *Ind. Eng. Chem. Res.* **2003**, *42*, 4414–4421.
10. Khalili, F.; Henni, A.; East, A. L. L. Entropy Contributions in pK_a computation: Application to Alkanolamines and Piperazines. *J. Mol. Struct. THEOCHEM* **2009**, *916*, 1–9.
11. Li, J.; Henni, A.; Tontiwachwuthikul, P. Reaction Kinetics of CO_2 in Aqueous Ethylenediamine, Ethyl ethanolamine and Diethyl monoethanolamineSolutions in the Temperature Range of 298-313 K Using the Stopped–Flow Technique. *Ind. Eng. Chem. Res.* **2007**, *46* (13), 4426–4434.
12. Albert, A.; Serjeant, E. P. *The Determination of Ionization Constants; A Laboratory Manual*, 3rd ed.; Chapman and Hall: 1984.
13. Manov, G. G.; Bates, R. G.; Hamer, W. J.; Acree, S. F. Values of the Constants inthe Debye-Hückel Equation for Activity Coefficients. *J. Am. Chem. Soc.* **1943**, *65*, 1765–1767.
14. Kielland, J. Individual Activity Coefficients of Ions in Aqueous Solutions. *J. Am. Chem. Soc.* **1937**, *59* (9), 1675–1678.
15. Danckwerts, P. V. The Reaction of CO_2 with Ethanolamines. *Chem. Eng. Sci.* **1979**, *34*, 443–446.
16. Crooks, J. E.; Donnellan, J. P. Kinetics of the Formation of N,N-Diakylcarbamate from Diethanolamine and Carbon Dioxide in Anhydrous Ethanol. *J. Chem. Soc., Perkin Trans.* **1988**, *2*, 191–194.

Downloaded by STANFORD UNIV GREEN LIBR on June 14, 2012 | http://pubs.acs.org
Publication Date (Web): May 3, 2012 | doi: 10.1021/bk-2012-1097.ch003

17. Pinsent, B. R. W.; Pearson, L.; Roughton, F. W. J. The Kinetics of combination of Carbon Dioxide with Hydroxyl Ions. *J. Chem. Soc., Faraday Trans.* **1956**, *52*, 1512–1520.
18. Donaldson, T. L.; Nguyen, N. Y. Carbon Dioxide Reaction Kinetics and Transport in Aqueous Amine Membranes. *Ind. Eng. Chem. Fundam.* **1980**, *19*, 260–266.
19. Littel, R. J.; Versteeg, G. F.; van Swaaij, W. P. M. Kinetics of Carbon Dioxidewith Primary and Secondary Amines in Aqueous Solutions. I. ZwitterionDeprotonation Kinetics for DEA and DIPA in Aqueous Blends of Alkanolamines. *Chem. Eng. Sci.* **1992**, *47*, 2027–2035.
20. Astarita, G.; Savage, D. W.; Bisio, A. *Gas Treating with Chemical Solvents*; John Wiley & Sons: New York, 1983.
21. Barth, D.; Tondre, C.; Delpuech, J. J. Stopped-Flow Investigations of the Reaction Kinetics of Carbon Dioxide with Some Primary and Secondary Alkanolamines in Aqueous solutions. *Int. J. Chem. Kinet.* **1986**, *18* (4), 445–457.
22. Khalili, F.; Henni, A.; East, A. L. L. pK_a values of some piperazine at 298, 303, 313 and 323 K. *J. Chem. Eng. Data* **2009**, *54*, 2914–2917.
23. Rochelle, G. T.; Bishnoi, S.; Chi, S.; Dang, H.; Snatos, J. Final report for P. O. No. DEAF26-99FT01029, U.S. Department of Energy, Federal Energy Technology Center, Sept. 26, 2000.
24. Bishnoi, S.; Rochelle, G. T. Absorption of Carbon Dioxide into Aqueous Piperazine: Reaction Kinetics, Mass Transfer and Solubility. *Chem. Eng. Sci.* **2000**, *55*, 5531–5543.
25. Graeme, P.; Rowland, R.; Allport, A.; Yang, Q.; Bown, M.; Burns, R.; Maeder, M.; Attalla, M. Carbon Dioxide Post Combustion Capture: A Novel Screening Study of the Carbon Dioxide Absorption Performance of 76 Amines. *Environ. Sci. Technol.* **2009**, *43* (16), 6427–6433.
26. Singh, P.; John, P. M. N.; Versteeg, G. F. Structure and Activity Relationships for Amine-based CO_2 Absorbents — II. *Chem. Eng. Res. Des.* **2008**, *87*, 135–144.
27. Sharma, M. M. Kinetics of Reactions of Carbonyl Sulphide and Carbon Dioxide with Amines and Catalysis by Brønsted Bases of the Hydrolysis of COS. *Trans. Faraday Soc.* **1965**, *61*, 681–687.
28. Kadiwala, S.; Rayer, A. V.; Henni, A. High Pressure Solubility of Carbon Dioxide (CO_2) in Aqueous Piperazine Solutions. *Fluid Phase Equilibria* **2010**, *292* (1−2), 20–28.
29. Appl, M.; Wagner, U.; Henrici, H. J.; Kuessner, K.; Voldamer, K.; Furest, E. Removal of CO_2 and/or H_2S and/or COS from Gases Containing These Constituents. U.S. Patent 4336233, 1982.
30. Kohl, A.; Riesenfeld, F. *Gas Purification*, 4th ed.; Gulf Publ. Co.: Houston, 1985.
31. Hamborg, E. S.; Versteeg, G. F. Dissociation Constants and Thermodynamic Properties of Amines and Alknaolamines from (293 to 353) K. *J. Chem. Eng. Data* **2009**, *54*, 1318–1328.
32. Perrin, D. D. *Dissociation Constants of Organic Bases in Aqueous Solution*; Butterworths: London, 1965. Supplement, 1972.

Downloaded by STANFORD UNIV GREEN LIBR on June 14, 2012 | http://pubs.acs.org
Publication Date (Web): May 3, 2012 | doi: 10.1021/bk-2012-1097.ch003

33. Hamborg, E. S.; Versteeg, G. F. Dissociation Constants and Thermodynamic Properties of Amines and Alknaolamines from (293 to 353) K. *J. Chem. Eng. Data* **2009**, *54*, 1318–1328.
34. Xu, S.; Otto, F. D.; Mather, A. E. Dissociation Constants of Some Alkanolamines. *Can. J. Chem.* **1993**, *71*, 1048–1050.
35. Littel, R. J.; Bos, M.; Knoop, G. J. Dissociation Constants of Some Alkanolamines at 293, 303, 318, and 333 K. *J. Chem. Eng. Data* **1990**, *35*, 276–277.
36. Hetzer, H. B.; Robinson, R. A.; Bates, R. G. Dissociation Constants of Piperazinium Ion and Related Thermodynamic Quantities from 0 to 50°C. *J. Phys. Chem.* **1968**, *72*, 2081–2086.
37. Perrin, D. D.; Dempsey, B.; Serjeant, E. P. *pK_a Prediction for Organic Acids and Bases*; Chapman and Hall: 1981.
38. Woutersen, S.; Bakker, H. J. Ultrafast Vibrational and Structural Dynamics of the Proton in Liquid Water. *Phys. Rev. Lett.* **2006**, *96*, 138305–138309.
39. Liptak, M. D.; Shields, G. C. Experimentation with Different Thermodynamic Cycles Used for pK_a Calculations on Carboxylic Acids Using Complete Basis Set and Gaussian- nModels Combined with CPCM Continuum Solvation Methods. *Int. J. Quantum Chem.* **2001**, *85*, 727–741.
40. Tissandier, M. D.; Cowen, K. A.; Feng, W. Y.; Gundlach, E.; Cohen, M. H.; Earhart, A. D.; Coe, J. V.; Tuttle, T. R., Jr. The Proton's Absolute Aqueous Enthalpy and Gibbs Free Energy of Solvation from Cluster-Ion Solvation Data. *J. Phys. Chem. A* **1998**, *102*, 7787–7794.
41. Rick, S. W.; Berne, B. J. The Aqueous Solvation of Water: A Comparison of Continuum Methods with Molecular Dynamics. *J. Am. Chem. Soc.* **1994**, *116*, 3949–3954.
42. Kallies, B.; Mitzner, R. pK_a Values of Amines in Water from Quantum Mechanical Calculations Using a Polarized Dielectric Continuum Representation of the Solvent. *J. Phys. Chem. B* **1997**, *101*, 2959–2967.
43. Schüürmann, G.; Cossi, M.; Barone, V.; Tomasi, J. Prediction of the pK_a of Carboxylic Acids Using *ab Initio* Continuum-Solvation Model PCM-UAHF. *J. Phys. Chem. A* **1998**, *102*, 6706–6712.
44. Adam, K. R. New Density Functional and Atoms in Molecules Method of Computing Relative pK_aValues in Solution. *J. Phys. Chem. A* **2002**, *106*, 11963–11972.
45. Tao, L.; Han, J.; Tao, F.-M. Correlations and Predictions of Carboxylic Acid pK_a Values Using Intermolecular Structure and Properties of Hydrogen-Bonded Complexes. *J. Phys. Chem. A* **2008**, *112*, 775–782.
46. da Silva, E. F.; Svendsen, H. F. *Ab Initio* Study of the reaction of carbamate formation from CO_2 and alkanolamines. *Ind. Eng. Chem. Res.* **2004**, *43*, 3413–3418.
47. Bryantsev, V. S.; Diallo, M. S.; Goddard, W. A., III. pK_aCalculations of Aliphatic Amines, Diamines, and Aminoamides via Density Functional Theory with a Poisson-Boltzmann Continuum Solvent Model. *J. Phys. Chem. A* **2007**, *111*, 4422–4430.

Downloaded by STANFORD UNIV GREEN LIBR on June 14, 2012 | http://pubs.acs.org
Publication Date (Web): May 3, 2012 | doi: 10.1021/bk-2012-1097.ch003

48. Liptak, M. D.; Shields, G. C. Accurate pK_a Calculations for Carboxylic Acids Using Complete Basis Set and Gaussian-n Models Combined with CPCM Continuum Solvation Methods. *J. Am. Chem. Soc.* **2001**, *123*, 7314–7319.
49. Smith, B. J. Calculation of Aqueous Proton Dissociation Constants of Quinoline and Hydroxyquinolines: A Comparison of Solvation Models. *Phys. Chem. Chem. Phys.* **2000**, *2*, 5383–5388.
50. da Silva, C. O.; da Silva, E. C.; Nascimento, M. A. C. *Ab Initio* Calculations of Absolute pK_a Values in Aqueous Solution I. Carboxylic Acids. *J. Phys. Chem. A* **1999**, *103*, 11194–11199.
51. da Silva, C. O.; da Silva, E. C.; Nascimento, M. A. C. *Ab Initio* Calculations of Absolute pK_a Values in Aqueous Solution II. Aliphatic Alcohols, Thiols, and Halogenated Carboxylic Acids. *J. Phys. Chem. A* **2000**, *104*, 2402–2409.
52. Woutersen, S.; Bakker, H. J. Ultrafast Vibrational and Structural Dynamics of the Proton in Liquid Water. *Phys. Rev. Lett.* **2006**, *96*, 138305–138309.

Downloaded by STANFORD UNIV GREEN LIBR on June 14, 2012 | http://pubs.acs.org
Publication Date (Web): May 3, 2012 | doi: 10.1021/bk-2012-1097.ch003

Downloaded by OHIO STATE UNIV LIBRARIES on June 15, 2012 | http://pubs.acs.org
Publication Date (Web): May 3, 2012 | doi: 10.1021/bk-2012-1097.ch004

Chapter 4

CO_2 Absorption Characteristics of 2-Isopropylaminoethanol (IPAE) Aqueous Solution

K. Goto,* F. A. Chowdhury, S. Kodama, H. Okabe, and Y. Fujioka

Chemical Research Group, Research Institute of Innovative Technology for the Earth (RITE), 9-2 Kizugawadai, Kizugawashi, Kyoto 619-0292, Japan
***goto.ka@rite.or.jp**

This chapter reports on the characteristics of aqueous amine solutions for post-combustion CO_2 capture (PCC), especially 2-Isopropylaminoethanol (IPAE) aqueous solution. The laboratory experiments, which were gas scrubbing test, vapor-liquid equilibrium measurement, reaction calorimetry and ^{13}C NMR spectroscopy, were conducted in order to obtain fundamental information on aqueous amine solutions. Also, the effects of IPAE concentration and Piperazine (PZ) addition into the IPAE aqueous solution on CO_2 capture behavior were examined. The results show that the IPAE aqueous solution has excellent characteristics, such as a moderately high absorption rate, a large cyclic capacity of CO_2 capture and low heat of reaction. That is, IPAE has a great potential to reduce a required energy of CO_2 capture and to be used as a novel absorbent in CO_2 scrubbing system.

1. Introduction

CCS (Carbon Capture and Storage) is one of realistic countermeasures against issues of greenhouse gases, especially carbon dioxide (CO_2), However, the CCS is not a process of a consumer product and currently needs inevitable cost, which is strongly related to regeneration energy in CO_2 capture process. Therefore, it is strongly required to develop state-of-the-art technologies of wet scrubbing system for CO_2 capture.

In Recent Advances in Post-Combustion CO2 Capture Chemistry; Attalla, M.;
ACS Symposium Series; American Chemical Society: Washington, DC, 2012.

Characteristics of aqueous amine solutions is one of research subjects in the field of CO_2 capture for the CCS. Signigficant characteristics focused on in the previous papers could be listed as absorption rate, CO_2 solubility, a heat of reaction and so on. For example, Bonefant et al. (*1*) and Hook (*2*) carried out gas scrubbing tests to investigate the relation between absorption behavior and molecular structure. Mimura et al (*3*) and Ma'mum et al (*4*) evaluated aqueous amine solutions using vapor-liquid equilibrium (VLE) measurement. Some researchers (*5–7*) analyzed aqueous amine solutions to make reaction mechanism clear. In aqueous amine solutions, CO_2 is absorbed by the formation of carbamate or bicarbonate anions:

$$2B + CO_2 \leftrightarrow B'COO^- + BH^+$$

$$B + CO_2 + H_2O \leftrightarrow HCO_3^- + BH^+$$

where B is amine and B' implies the deprotonation of the neutral amino group. In the case of CO_2 absorption by bicarobonate anion, there is an advantage of stoichiometric loading capacity. Calorimetry was also essential to design unit operations of chemical absorption process. Mathonat et al (*8*) measured heat of reaction for an aqueous 2-Aminoethanol (Monoethanolamine, MEA) solution. Kim et al (*9*) determined the heat of reaction of CO_2 absorption in the aqueous 2-((2-Aminoethyl)amino)ethanol (AEEA) solutions.

Other research subject is formulation of chemical compounds in an aqueous amine solution. In order to investigate high amine concentration and enhancement of cyclic capacity of CO_2 capture, Aboudheir et al (*10*) carried out the pilot plant studies on CO_2 capture using aqueous MEA solutions up to 54wt%. The results showed that increasing the MEA concentration contributed to enhancement of removal efficiency. The addition of an activator to an aqueous amine solution is other formulation technique. Several papers reported on the characteristics and performance of PZ activated solvents. Bishonoi and Rochelle (*11*) and Xu et al. (*12*) investigated PZ activated aqueous MDEA solution. Seo and Hong (*13*) focused on PZ activated aqueous AMP solutions.

The authors and our group have been also interested in a CO_2 scrubbing solvent for CCS technology. A lot of amine compounds were evaluated concerning relative absorption rate, cyclic capacity of CO_2 capture and heat of reaction (*14–16*). New novel amine solvents were developed in the COCS project (*17*).

In this study, gas scrubbing test, VLE measurement, reaction calorimetry and ^{13}C NMR spectroscopy are used for analysis of aqueous amine solutions. Then, CO_2 capture characteristics of 2-Isopropylaminoethnol (IPAE) are discussed in comparison with the MEA, Diethanolamine (DEA) and MDEA. Also, in order to obtain the clues of solvent development, the effects of IPAE concentration and PZ addition on the CO_2 capture behaviors are investigated.

Downloaded by OHIO STATE UNIV LIBRARIES on June 15, 2012 | http://pubs.acs.org
Publication Date (Web): May 3, 2012 | doi: 10.1021/bk-2012-1097.ch004

Downloaded by OHIO STATE UNIV LIBRARIES on June 15, 2012 | http://pubs.acs.org
Publication Date (Web): May 3, 2012 | doi: 10.1021/bk-2012-1097.ch004

2. Experiments

2.1. Tested Amines

Single amine compounds and a mixture shown in Table 1 were investigated in this study. MEA is a primary amine, which is a well-known CO_2 capture solvent for atmospheric pressure gas such as combustion gas. DEA and IPAE are secondary amines. MDEA is a tertiary amine, which is suitable to CO_2 capture from high-pressure gas such as production process of natural gas. IPAE was also tested in the conditions of a mixture solution with PZ.

Table 1. Aqueous amine solutions tested in this study

	Amine, Molecular weight	*Concentration (wt%)*
Single component	2-Aminoethanol (MEA), 61 Diethanolamine (DEA), 105 2-Isopropylaminoethnolamine (IPAE), 113 Methyldiethanolamine (MDEA), 119	30 30 10, 20, 30, 40, 50 30
Mixture	IPAE-PZ[a]	49-1, 45-5, 30-20

[a] PZ: Piperazine

All amine compounds, except for IPAE, were purchased from Sigma Aldrich Chemical Co. and Tokyo Kasei Kogyo Co. Ltd. and were used without further purification. IPAE was prepared using hydroxyalkylation reaction between Isopropylamine and 2-Bromoethanol. After rectification, the purity of the synthesized IPAE was established by gas chromatography and mass spectroscopy.

For each amine compound, a 30wt% aqueous solution was prepared for gas scrubbing test, vapor-liquid equilibrium measurement, reaction calorimetry and ^{13}C NMR spectroscopy. In addition, aqueous IPAE solutions and IPAE-PZ mixture solutions were prepared to clarify the effect of amine concentration and additives on CO_2 absorption. The range of IPAE concentration was from 10wt% to 50wt%. The IPAE-PZ mixtures were formulated at three conditions in composition.

2.2. Experimental Procedures

2.2.1. Gas Scrubbing Test

Gas scrubbing test was an initial-stage attempt to figure out solution characteristics of CO_2 absorption and desorption. 50ml of an aqueous amine solution was put into a 250ml glass scrubbing bottle and a gas mixture (CO_2/N_2 =20/80vol%) was supplied to the bottle at a flow rate 700 ml/min. For the first 60 minutes, the bottle was placed in a water bath of 40°C to investigate CO_2 absorption, and for the following 60 minutes the bottle was placed in a water bath of 70°C for a desorption test.

The schematic diagram of a scrubbing system for a gas scrubbing test is shown in Figure 1. The flow rate and CO_2 concentration of the feed gas were controlled

Downloaded by OHIO STATE UNIV LIBRARIES on June 15, 2012 | http://pubs.acs.org
Publication Date (Web): May 3, 2012 | doi: 10.1021/bk-2012-1097.ch004

by mass flow controllers (SEC E-40, Horiba). The outlet gas from the bottle was analyzed with a carbon dioxide analyzer (VA-3001, Horiba). The equipment consists of six units of scrubbing system, which can simultaneously carry out a number of gas scrubbing tests at the same condition in low and high temperature water baths. Vaporized aqueous solution generated during the test was returned as a condensate from a downstream gas condenser. That is, amine concentration of the solution in the system was constant during the test without any device of a humidity control.

Figure 2 shows a typical result obtained from a gas scrubbing test. An amount of absorbed CO_2 in the aqueous amine solution, "CO_2 loading", was estimated from the measured CO_2 concentration of the outlet gas flow. The curve of CO_2 loading with time showed CO_2 loading at 40ºC and 70ºC clearly. A gradient of the curve at a half point of the 60-minute CO_2 loading was calculated as an absorption rate. The absorption rate is not chemical reaction rate but CO_2 transfere rate from gas phase to liquid phase. This reference index was used to understand the relative behavior of an amine aqueous solution for others. The difference of CO_2 loading between 40ºC and 70ºC defined as cyclic capacity between 40ºC and 70ºC.

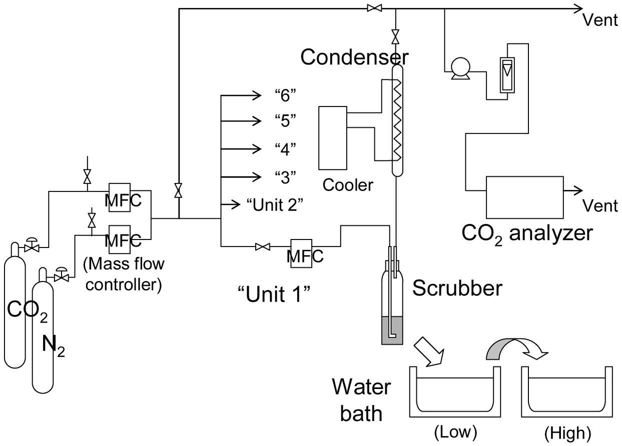

Figure 1. Schematic diagram of a scrubbing system for gas scrubbing test

Downloaded by OHIO STATE UNIV LIBRARIES on June 15, 2012 | http://pubs.acs.org
Publication Date (Web): May 3, 2012 | doi: 10.1021/bk-2012-1097.ch004

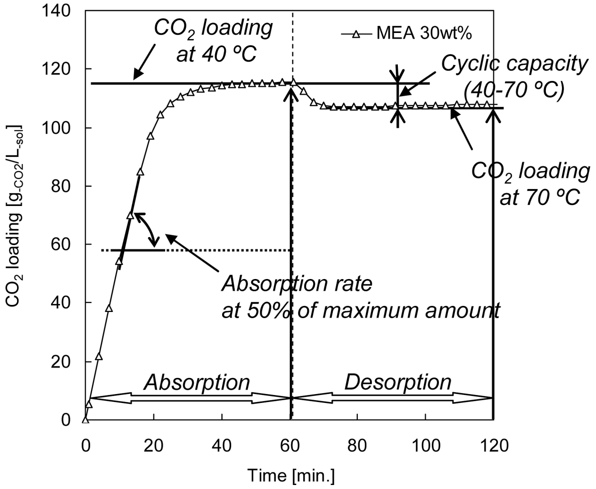

Figure 2. Characteristics obtained from a gas scrubbing test

2.2.2. Vapor-Liquid Equilibrium (VLE) Measurement

Figure 3 shows a schematic diagram of the experimental apparatus used for a vapor-liquid equilibrium measurement. It consists of a 700-cm^3 crystal glass cylindrical reactor vessel (TEM-V1000N, Taiatsu Techno Corp.), a steam-saturator, a CO_2 analyzer (VA-3001, Horiba) and so on. The reactor vessel was filled with a test solvent and heated with an electric heater. The gas mixture controlled to a specific CO_2 concentration was supplied to the reactor vessel after flowing through a steam saturator. The equilibrium condition was determined when the CO_2 analyzer of the outlet gas indicated same CO_2 concentration of the inlet gas. Tests were conducted between 40ºC and 120ºC in temperature and between 1kPa and 200kPa in CO_2 partial pressure.

To analyze the equilibrium condition, the CO_2 concentrations in both gas and liquid phase were measured. The CO_2 partial pressure was derived from the temperature, total pressure and the measured CO_2 concentration. For the liquid phase, a sample was taken from the reactor vessel and the amount of absorbed CO_2 in the sample was measured with a Total Organic Carbon analyzer (TOC-VCH, Shimadzu).

Downloaded by OHIO STATE UNIV LIBRARIES on June 15, 2012 | http://pubs.acs.org
Publication Date (Web): May 3, 2012 | doi: 10.1021/bk-2012-1097.ch004

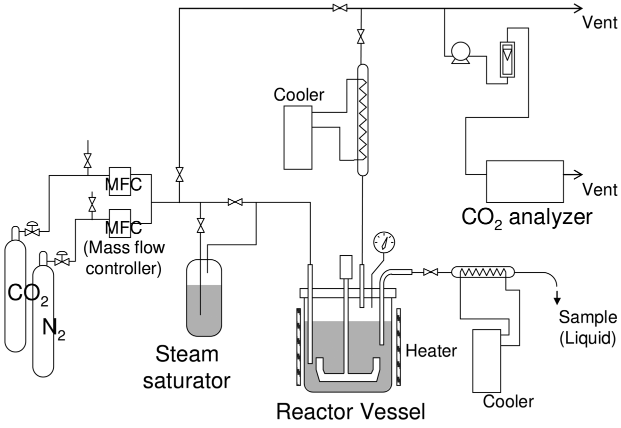

Figure 3. Schematic diagram of VLE measurement

2.2.3. Reaction Calorimetry

The heat of reaction for aqueous amine solutions was measured with Differential Reaction Calorimeter (DRC, SETARAM) at 40ºC in temperature. This instrument works on the principle of differential thermal analysis which simultaneously measures values in temperature of a sample reactor and a reference reactor. The solvent volume was 150 ml and the injected gas was 99.9% CO_2 gas. Non-CO_2-loaded solvent was prepared and CO_2 was injected into it from 0.0 to around 0.5 $mol_{\text{-CO2}}/mol_{\text{-amine}}$ in CO_2 loading. The amount of absorbed CO_2 in the solvent was then measured with the Total Organic Carbon analyzer (TOC-VCH, Shimadzu). A heat of reaction was estimated by dividing the total generated heat obtained from DRC by the CO_2 amount absorbed into the solvent during CO_2 injection.

2.2.4. NMR Spectroscopy

^{13}C NMR spectroscopy was used to analyze the CO_2-absorbed amine solvents and to determine the amounts of carbamate and bicarbonate anions produced by CO_2 absorption in the solvent. The method of the NMR analysis was same as that of the previous paper (*5*). Solvent samples, Amine-CO_2-H_2O mixtures, were prepared at the same condition of gas scrubbing test. That is, 20% CO_2 gas balanced with N_2 was supplied for 60 minutes at a rate of 700 ml/min into 50ml of a 30wt% aqueous solution of single-component amines using a glass scrubbing bottle controlled at 40ºC. The CO_2 loading of the amine solution was estimated by monitoring the outlet gas with a carbon dioxide analyzer (VA-3001, Horiba). The measurements of the ^{13}C NMR were performed at 289-299K using JEOL JNM-ECA400 spectrometer. Quantitative spectra were obtained with a delay of 30s, a pulse width of 9μs, and 400 scans. The measurement frequency was

100MHz. In order to confirm the accuracy of measurement, CO_2 loadings of a sample were measured by both TOC anaysis and NMR spectra. The rmsd (root mean square deviation) of the CO_2 loadings between TOC and NMR was about 0.05 mol_{-CO2}/mol_{-amine}. It was good enough quantitatively to compare different types of amines in this study.

3. Results

3.1. Solvent Characteristics

3.1.1. Gas Scrubbing Test

Figure 4 shows the results of gas scrubbing tests. The result of MEA shows that both CO_2 loading at 40ºC and CO_2 loading at 70C were high. Consequently, the cyclic capacity between 40ºC and 70ºC was small. CO_2 absorption rate of MDEA was relatively low and CO_2 loading after 60 minutes did not reach to the saturated condition and still went up. The chart shows that the CO_2 loading at both 40ºC and 70ºC followed the order MDEA<DEA<IPAE<MEA. The main reason of the high CO_2 loading for the aqueous MEA solution was that MEA was small in molecular weight and the molar concentration of aqueous amine solution was higher than the other amine solutions. As for IPAE, CO_2 loading at 40ºCwas relatively high and the cyclic capacity of CO_2 capture was larger than the other amine aqueous solutions.

Downloaded by OHIO STATE UNIV LIBRARIES on June 15, 2012 | http://pubs.acs.org
Publication Date (Web): May 3, 2012 | doi: 10.1021/bk-2012-1097.ch004

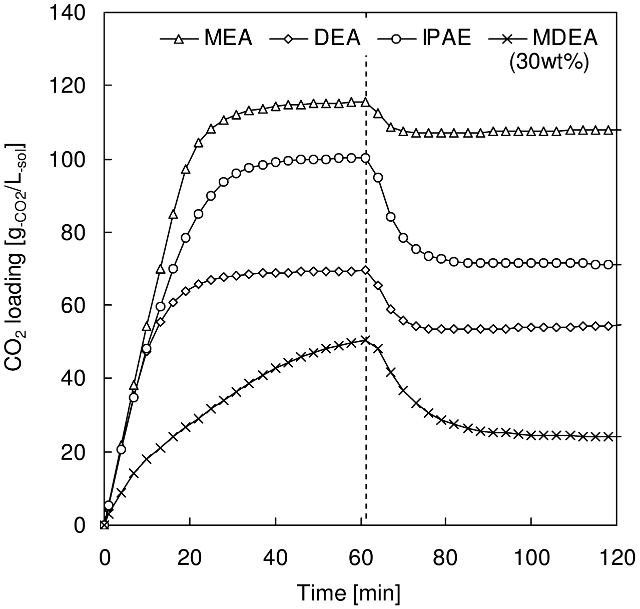

Figure 4. Absorption and desorption behavior of gas scrubbing tests

In Recent Advances in Post-Combustion CO2 Capture Chemistry; Attalla, M.;
ACS Symposium Series; American Chemical Society: Washington, DC, 2012.

3.1.2. Vapor-Liquid Equilibrium (VLE) Measurement

Figures 5, 6 and 7 show the VLE of MEA, IPAE and MDEA, respectively. In the Figures 5 and 6, the results of previous papers are plotted (120ºC data of MEA: Jou et. al (*18*), 40ºC data of MEA: Ma'mum et al (*19*), 40ºC and 100ºC data of MDEA: Jou et al (*20*)). The results of this study had a good agreement with those results.

As shown in Figure 5, influence of CO_2 partial pressure on CO_2 loading of aqueous MEA solution was small for all the temperature. Figure 6 shows that CO_2 loading of aqueous MDEA solution in the condition of 40ºC was strongly dependent on CO_2 partial pressure. In the high temperature condition, 100ºC and 120ºC, CO_2 loading was less than 0.1 mol/mol. As shown in Figure 7, IPAE's VLE chart was similar to MDEA's. In the low temperature condition, 40ºC, CO_2 loading of IPAE was larger than MEA and MDEA. In the case of 40ºC and 20kPa$_{\text{-CO2}}$, CO_2 loading reached to over 0.7 mol/mol. In addition, because of the low solubility at high temperature, cyclic capacity of CO_2 capture seems to be larger than that of the other amine solution.

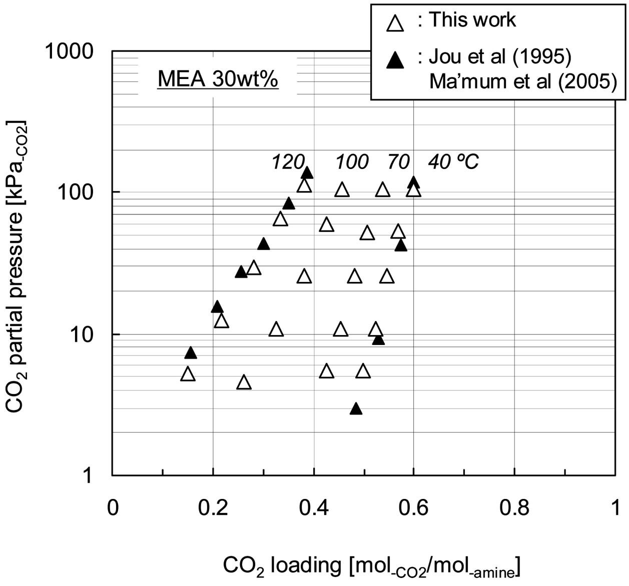

Figure 5. CO_2 solubility of 30wt% MEA aqueous solution

Downloaded by OHIO STATE UNIV LIBRARIES on June 15, 2012 | http://pubs.acs.org
Publication Date (Web): May 3, 2012 | doi: 10.1021/bk-2012-1097.ch004

Downloaded by OHIO STATE UNIV LIBRARIES on June 15, 2012 | http://pubs.acs.org
Publication Date (Web): May 3, 2012 | doi: 10.1021/bk-2012-1097.ch004

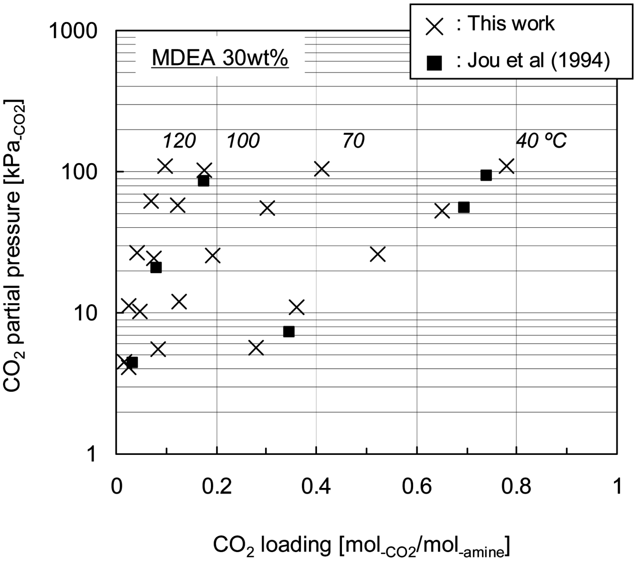

Figure 6. CO_2 solubility of 30wt% MDEA aqueous solution

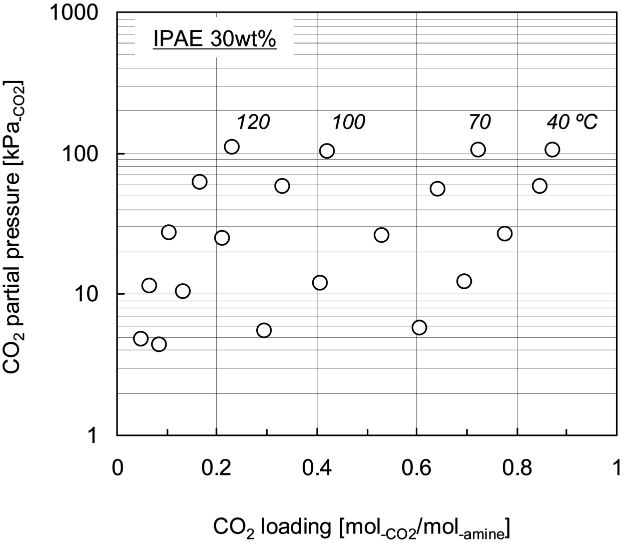

Figure 7. CO_2 solubility of 30wt% IPAE aqueous solution

3.1.3. Heat of Reaction

Table 2 shows the results of reaction calorimetry. “Heat of reaction” means the enthalpy difference between fresh aqueous amine solution and CO_2-loaded solution. The experimental results for MEA and MDEA were almost same as the values presented in the paper by Feron (*21*). The order of the heat of reaction in this study was MEA>DEA>IPAE>MDEA. Heat of reaction of the aqueous IPAE solution was 68 kJ/mol$_{-CO2}$.

Table 2. Results of reaction calorimetry

Amines (30wt%)	*MEA*	*DEA*	*IPAE*	*MDEA*
Heat of reaction [kJ/mol$_{-CO2}$]	88.2	69.0	68.1	60.0

3.1.4. ^{13}C NMR Spectroscopy

Figure 8 shows the results of ^{13}C NMR spectroscopy. This bar chart shows the absorption amount in a aqueous amine solution after 60 minutes absorption and amount of carbamate and bicarbonate anions in the solution. For primary and secondary amines, there is a possibility to generate both carbamate and bicarbonate anions in the reaction with CO_2, but the ratio of the bicarbonate anion and carbamate anion is different for each amine compound. IPAE mainly absorbed CO_2 as bicarbonate anion and CO_2 loading to one amine molecule was higher than the other amines. As mentioned by Yamada (*5*), steric hinderance of molecular structure interrupts the generation of carbamate anion for CO_2 absorption by IPAE. In addition, CO_2 loading to one IPAE molecule was high, around 0.7 mol$_{-CO2}$/mol$_{-amine}$. MDEA is the tertiary amine and absorbed CO_2 as only bicarbonate, however MDEA needed more time for saturate condition and the CO_2 loading of the prepared sample of aqueous MDEA solution was small.

3.2. IPAE-Based Aqueous Solution

Figure 9 shows the experimental results of the absorption and desorption behavior for the different concentration solvents. CO_2 loading at 40ºC was increasing with amine concentration. However, CO_2 loadings at 70ºC for 30, 40 and 50wt% were almost same. Consequently, cyclic capacity of CO_2 capture of 50wt% IPAE aqueous solution became larger.

Figure 10 shows the effect of PZ addition on the absorption and desorption behaviors of IPAE-PZ mixture solvents. By the addition of PZ, a relative absorption rate and CO_2 loading became high, but the CO_2 loading at 70ºC became high, too. That is, high concentration of PZ decreased a cyclic capacity of CO_2 capture.

Downloaded by OHIO STATE UNIV LIBRARIES on June 15, 2012 | http://pubs.acs.org
Publication Date (Web): May 3, 2012 | doi: 10.1021/bk-2012-1097.ch004

Downloaded by OHIO STATE UNIV LIBRARIES on June 15, 2012 | http://pubs.acs.org
Publication Date (Web): May 3, 2012 | doi: 10.1021/bk-2012-1097.ch004

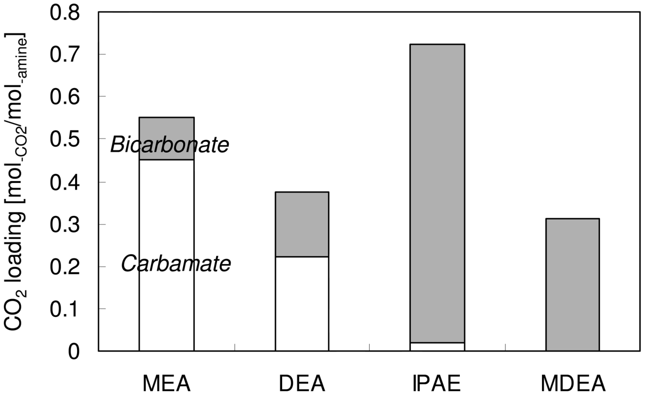

Figure 8. CO_2 absorption mechanisms for single-component solvents

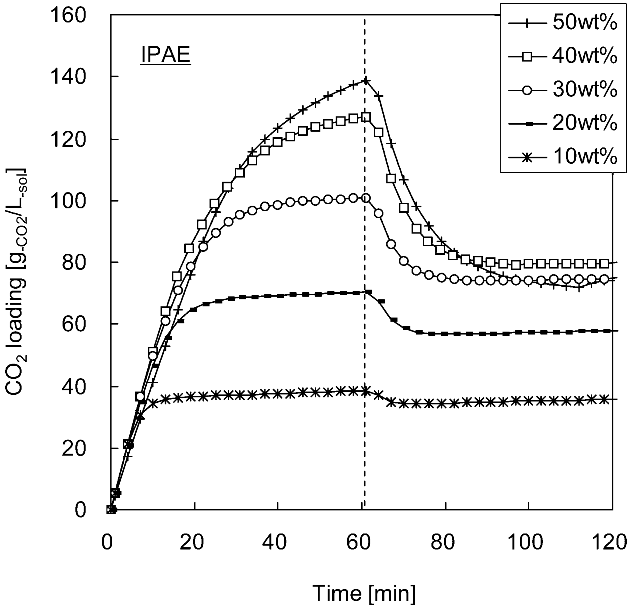

Figure 9. Effect of amine concentration on CO_2

Downloaded by OHIO STATE UNIV LIBRARIES on June 15, 2012 | http://pubs.acs.org
Publication Date (Web): May 3, 2012 | doi: 10.1021/bk-2012-1097.ch004

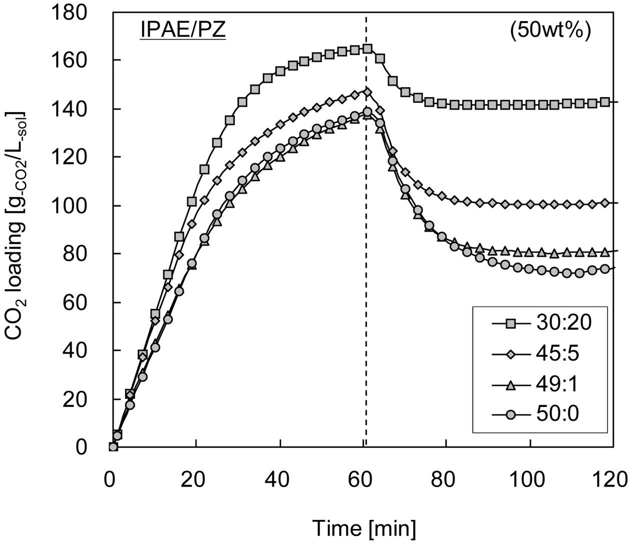

Figure 10. Effect of Piperazine on CO_2 absorption and desorption

4. Discussions

Table 3 shows the result summary of laboratory experiments. Absorption rate is the gradient of the half point of CO_2 loading at 40ºC. MEA is higher than the others but IPAE was superior to DEA. CO_2 loading of IPAE is high because of CO_2 absorption by bicarbonate anion. Both the cyclic capacity between 40ºC and 70ºC, which was obtained from gas scrubbing test, and the cyclic capacity between 40ºC and 120ºC, which was obtained from VLE measurement, indicated a similar tendency that the aqueous IPAE solution was larger than the other amine solutions. That means that it is possible to evaluate the CO_2 capture ability concerning plant process by a simple gas scrubbing test. To sum up the experimental results, IPAE had an advantage of large cyclic capacity and there is high possibility to use it efficiently for CO_2 capture from atmospheric pressure gas.

Table 4 shows the effect of IPAE concentration on absorption behaviors. The evaluation items of both CO_2 loading at 40ºC and cyclic capacity of CO_2 loading increased with IPAE concentration. However, absorption rate declined with IPAE concentration. The reason is that the "absorption rate" is not chemical reaction rate but CO_2 transfer rate from gas phase to liquid phase. Therefore, increase of solvent viscosity with IPAE concentration could affect the absorption rate. The result show that IPAE should be used at high concentration condition with improvement of absorption rate.

Table 5 shows the effect of piperazine on the CO_2 absorption characteristics. Absorption rate and CO_2 loading increase with PZ concentration. However, the cyclic capacity between 40ºC and 70ºC decrease with the PZ concentration. That means IPAE-PZ mixture solvent should be formulated in proper mixture ratio.

Table 3. CO_2 absorption characteristics of single amine aqueous solutions

Amines (30wt%)	*Absorption rate [g-$_{CO_2}$/L/min]*	*CO_2 loading at 40 ℃ [g-$_{CO_2}$/L]*	*Cyclic capacity 40-70 ℃ [g-$_{CO_2}$/L]*	*Cyclic capacity 40-120 ℃ [g-$_{CO_2}$/L]*	*Heat of Reaction [kJ/mol-$_{CO_2}$]*
MEA	5.3	115.5	7.4	36.9	88.2
DEA	4.0	69.4	14.8	41.8	69.0
IPAE	4.5	100.3	29.1	66.0	68.1
MDEA	0.9	50.4	26.3	40.9	60.0

Table 4. Summary of gas scrubbing test for different concentration IPAE solvents

IPAE concentration [wt%]	*Absorption rate [g-$_{CO_2}$/L/min]*	*CO_2 loading at 40℃ [g-$_{CO_2}$/L]*	*Cyclic capacity 40-70 ℃ [g-$_{CO_2}$/L]*
10	5.2	38.6	3.0
20	4.6	70.3	12.6
30	4.5	100.9	26.0
40	4.2	127.0	48.0
50	3.8	138.7	64.3

Table 5. Summary of gas scrubbing test for PZ addition

Concentration IPAE/PZ [wt%]	*Absorption rate [g-$_{CO_2}$/L/min]*	*CO_2 loading at 40℃ [g-$_{CO_2}$/L]*	*Cyclic capacity 40-70 ℃ [g-$_{CO_2}$/L]*
50/0	3.8	138.7	64.3
49/1	3.6	137.4	56.4
45/5	4.6	146.6	45.7
30/20	5.3	164.9	22.0

5. Conclusion

The IPAE aqueous solution could reduce a required energy of CO_2 capture. The laboratory-scale experiments were introduced in this chapter and their results were discussed from the perspective of the characteristics of the IPAE aqueous solution for post-combustion CO_2 capture. IPAE produces a bicarbonate anion much rather than carbamate anion in the reaction with CO_2. Owing to this reaction mechanism, CO_2 loading to one IPAE molecule becomes high and cyclic

Downloaded by OHIO STATE UNIV LIBRARIES on June 15, 2012 | http://pubs.acs.org
Publication Date (Web): May 3, 2012 | doi: 10.1021/bk-2012-1097.ch004

In Recent Advances in Post-Combustion CO2 Capture Chemistry; Attalla, M.;
ACS Symposium Series; American Chemical Society: Washington, DC, 2012.

capacity of the aqueous solution for CO_2 capture is large. Also, its absorption rate is moderately high and the heat of reaction is low. These characteristics can make the required energy of CO_2 capture low.

Also, the IPAE aqueous solution has a potential to be used as a novel absorbent in the formulation of CO_2 scrubbing solvents, although further research is necessary to seek optimimum condition of concentration and PZ addition. Increase of IPAE concentration makes cyclic capacity of CO_2 capture large and PZ addition makes absorption rate high.

Downloaded by OHIO STATE UNIV LIBRARIES on June 15, 2012 | http://pubs.acs.org
Publication Date (Web): May 3, 2012 | doi: 10.1021/bk-2012-1097.ch004

Acknowledgments

This research was conducted in the COCS Project, which was financially supported by the Ministry of Economy, Trade and Industry (METI), Japan.

References

1. Bonenfant, D.; Mimeault, M.; Hausler, R. *Ind. Eng. Chem. Res.* **2003**, *42*, 3179–3184.
2. Hook, R. J. *Ind. Eng. Chem. Res.* **1997**, *36*, 1779–1790.
3. Mimura, T.; Yagi, Y.; Takashina, T.; Yoshiyama, R.; Honda, A. *Kagaku Kogaku Ronbunshu* **2005**, *41* (4), 237–242.
4. Ma'mum, S.; Svendsen, H. F.; Hoff, K. A.; Juliussen, O. *Energy Convers. Manage.* **2007**, *48*, 251–258.
5. Yamada, H.; Shimizu, S.; Okabe, H.; Matsuzaki, Y.; Chowdhury, F. A.; Fujioka, Y. *Ind. Eng. Chem. Res.* **2010**, *49*, 2449–2455.
6. Böttinger, W.; Maiwald, M.; Hasse, H. *Fluid Phase Equilib.* **2008**, *263*, 131–143.
7. Park, J. Y.; Yoon, S. J.; H. Lee, H. *Environ. Sci. Technol.* **2003**, *37* (8), 1670–1675.
8. Mathonat, C.; Major, V.; Mather, A. E.; Grolier, J. P. E. *Ind. Eng. Chem. Res.* **1998**, *37*, 4136–4141.
9. Kim, I.; Ma'mum, S.; Tobiesen F. A.; Svendsen, H. F. *8th International conference on greenhouse gas control technologies*, Trondheim, Norway, June 19−22, 2006; Elsevier Ltd.: Oxford, UK, 2006; paper P01_01_07.PDF (CD-ROM).
10. Aboudheir A.; Tontiwachwuthikul, P.; Chakma, A. In *5th Int. Conf. Greenhouse Gas Control Technologies*, Cairns, Queensland, Australia, June 13−16, 2000; Williams, D. J., Durie, R. A., McMullan, P., Paulson, C. A. J., Smith, A., Eds.; CSIRO Publishing: Collingwood, Victoria, Australia, 2001; pp 217−222.
11. Bishonui, S.; Rochelle, G. T. Absorption of Carbon Dioxide in Aqueous Piperazine/Methyldiethanolamine. *AIChE J.* **2002**, *48* (12), 2788–2799.
12. Xu, G. W.; Zhang, C. F.; Qin, A. J.; Wang, Y. W. *Ind. Eng. Chem. Res.* **1992**, *31*, 921–927.
13. Seo, D. J.; Hong, W. H. *Chem. Eng. Sci.* **2000**, *60*, 503–516.

14. Shimizu, S.; Onoda, M.; Goto, K.; Yamada, K.; Mimura, T. *8th Int. Conf. Greenhouse Gas Control Technologies*, Trondheim, Norway, June 19−22, 2006; Elsevier Ltd.: Oxford, UK; paper P01_06_03.pdf.
15. Chowdhury, F. A.; Okabe, H.; Shimizu, S.; Onoda, M.; Fujioka, Y. *Energy Procedia* **2009**, *1*, 1241–1248.
16. Chowdhury, F. A.; Okabe, H.; Yamada, H.; Onoda, M.; Fujioka, Y. *Energy Procedia* **2011**, *4*, 201–208.
17. Goto, K.; Okabe, H.; Chowdhury, F. A.; Shimizu, S.; Fujioka, Y.; Onoda, M. *Int. J. Greenhouse Gas Control* **2011**, *5*, 1214–1219.
18. Jou, F. Y.; Mather, A. E.; Otto, F. D. *Can. J. Chem. Eng.* **1995**, *73*, 140–147.
19. Ma'mum, S.; Nielsen, R.; Svendsen, H. F.; Juliussen, O. *J. Chem. Eng. Data* **2005**, *50*, 630–634.
20. Jou, F. Y.; Otto, F. D.; Mather, A. E. *Ind. Eng. Chem. Res.* **1994**, *33*, 2002–2005.
21. Feron, P. H. M. *Energy Procedia* **2009**, *1*, 1067–1074.

Downloaded by OHIO STATE UNIV LIBRARIES on June 15, 2012 | http://pubs.acs.org
Publication Date (Web): May 3, 2012 | doi: 10.1021/bk-2012-1097.ch004

Downloaded by OHIO STATE UNIV LIBRARIES on June 14, 2012 | http://pubs.acs.org
Publication Date (Web): May 3, 2012 | doi: 10.1021/bk-2012-1097.ch005

Chapter 5

Novel Amine Solution Development for High Pressure CO_2 Capture and Application Examination to IGCC Gas

**Shin Yamamoto,*[,1] Hiroshi Machida,[2] Yuichi Fujioka,[3]
Takayuki Higashii,[1] and Shingo Kazama[1]**

**[1]Chemical Research Group, Research Institute of Innovative Technology for the Earth (RITE), 9-2 Kizugawadai, Kizugawa-shi, Kyoto, 619-0292, Japan
[2]Department of Chemical Engineering, Graduate School of Engineering, Nagoya University, Furo-cho, Chikusa-ku, Nagoya, 464-8601, Japan
[3]Department of Environmental Sciences, International College of Arts and Sciences, Fukuoka Women's University, 1-1-1 Kasumigaoka, Higashi-ku, Fukuoka, 813-8529, Japan
*E-mail: yamashin@rite.or.jp**

To develop a novel chemical CO_2 solvent showing high efficiency for the separation of CO_2 from high-pressure exhaust gases, such as integrated gasification combined cycle (IGCC) produced gases, tertiary amine solutions were evaluated from CO_2 absorption and desorption rates, and CO_2 recovery under the pressure of 1.6 MPa-CO_2. Our novel developed solvent RH-2b shows a high CO_2 recovery and high CO_2 absorption and desorption rates; these values are approximately three times higher than those with a methyldiethanolamine solution, thus meaning that our solvent can recover CO_2 with low energy under high pressure. The total energy for CO_2 separation and capture including the compression process, was calculated using the measured values of CO_2 recovery and reaction heat of RH-2b. RH-2b is able to reduce the total energy by approximately 19% from that with a methyldiethanolamine solution. Additionally, the pressurized desorption process to 4.0 MPa-CO_2 is estimated to reduce the total energy for CO_2 separation and capture including the compression process to 1.6 GJ/t-CO_2.

In Recent Advances in Post-Combustion CO2 Capture Chemistry; Attalla, M.;
ACS Symposium Series; American Chemical Society: Washington, DC, 2012.

Downloaded by OHIO STATE UNIV LIBRARIES on June 14, 2012 | http://pubs.acs.org
Publication Date (Web): May 3, 2012 | doi: 10.1021/bk-2012-1097.ch005

Introduction

CO_2 separation technology has received much attention as a measure to prevent global warming, and there are many studies for CO_2 capture and storage. The chemical absorption method utilising an amine solution is well-known and one of the most important industrial methods used in CO_2 capture processes, and many investigations have been undertaken on the CO_2 solubility of amine solutions (*1–7*) and the modeling simulations of CO_2 solubility mechanisms (*8–14*).

High pressure gas containing high concentration of CO_2 is known to be exhausted from IGCC power plants (*15–17*), and thus amine solutions would be expected to provide high performances for CO_2 capture under high pressure conditions. Methyldiethanolamine (MDEA) and Selexol are well known as high-pressure CO_2 solvents. However, the CO_2 separation processes with these solvents commonly include a depressurization process for desorption of the absorbed CO_2. The depressurization process increases the total energy for CO_2 separation and capture including compression owing to repressurizing the captured CO_2 for transportation and storage.

We know that tertiary amines have relatively low performances for CO_2 absorption despite relatively high performances for CO_2 desorption. Therefore, the tertiary amines such as MDEA are thought to be suitable for high pressure conditions because high pressure enhances the CO_2 absorption process, although primary and secondary amines such as monoaminoethanol (MEA) are unsuitable. Chowdhury et al. examined several tertiary amines under a low pressure condition to determine the effect of the tertiary amine structure on the CO_2 absorption and desorption properties (*18*). Under low pressure conditions, the CO_2 absorption rates of the examined tertiary amines were relatively low. Some activators such as piperazine are added to the tertiary amine solutions to increase the absorption rates (*3*, *5*), although these additives increase the reaction heat. Tomizaki et al. reported the high performances of cyclic tertiary amines for CO_2 capture under a high pressure condition, that imidazole-based amines and hydroxyethylmorpholine show high CO_2 recovery under the condition of 1.6 MPa-CO_2 and very low reaction heats (*19–21*).

In this study, we have measured the CO_2 absorption and desorption rates and CO_2 recoveries of several tertiary amine solutions, which have been prepared in a concentration of 3.0 M in water, under a high pressure condition for screening the high pressure CO_2 solvents. For the developed CO_2 solvents, their total energies for CO_2 separation and capture, including compression process, have been calculated using the measured values of CO_2 recoveries and reaction heats. Additionally, the developed solvents have been evaluated with the coal gasification gas supplied from an IGCC pilot-plant.

Downloaded by OHIO STATE UNIV LIBRARIES on June 14, 2012 | http://pubs.acs.org
Publication Date (Web): May 3, 2012 | doi: 10.1021/bk-2012-1097.ch005

Experimental

Apparatus

A high pressure CO_2 absorption-desorption apparatus (Figure 1) was used in this study for the screening measurement of tertiary amine solutions. This apparatus consists of CO_2 and N_2 compressed gas cylinders, CO_2 and N_2 mass flow controllers, a high pressure vessel to absorb and desorb CO_2, a condenser, back pressure regulator, a gas flow meter, and a CO_2 meter. The amine solution temperature in the high pressure vessel was controlled by circulation of heating oil-mediums adjusted to the CO_2 absorption and desorption temperatures.

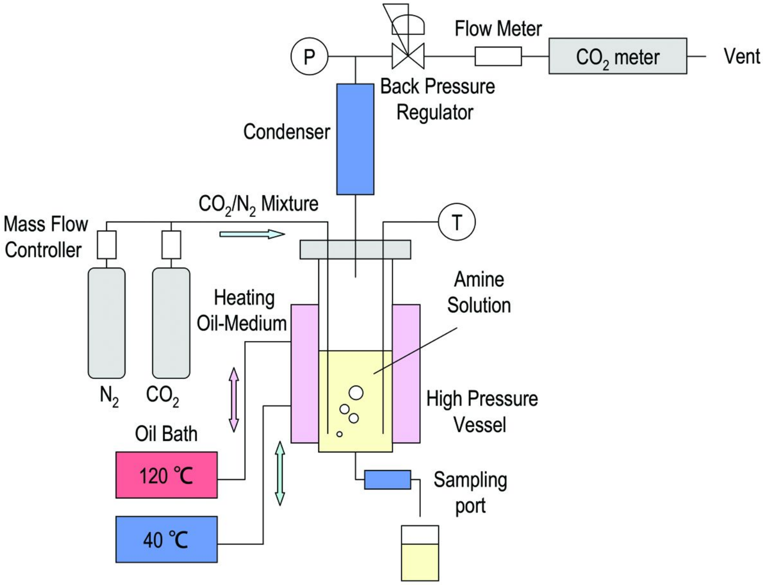
P
Flow Meter
CO2 meter
Vent
Back Pressure Regulator
Condenser
CO2/N2 Mixture
T
Mass Flow Controller
Amine Solution
Heating Oil-Medium
N2
CO2
High Pressure Vessel
Oil Bath
120 °C
40 °C
Sampling port

Figure 1. High Pressure CO_2 Absorption-Desorption Apparatus

Measurement

An amine solution (300 ml) was added to the high pressure vessel. N_2 gas flowed into the high pressure vessel and the pressure in the vessel was controlled with the back pressure regulator at the absorption temperature of 40 °C. After the pressure reached 3.5 MPa, an amine solution (3.0 l/min) was aerated with CO_2/N_2 mixture (46 vol%) and the CO_2 absorption process was started under the pressure of 1.6 MPa-CO_2. Two hours after the beginning of the CO_2 absorption process, the oil-medium, adjusted to 120 °C, was started to circulate in the CO_2 desorption process for two hours. The CO_2 solubility S_c (g/l) was calculated from the CO_2 concentration C (vol%) and the supplied gas flow rates of CO_2 F_{cs} (l/min) and N_2 F_{ns} (l/min) in the following equation.

$$S_c = \frac{44.0}{22.4} \int \left(F_{cs} - F_{ns} \frac{C}{100 - C} \right) dt \frac{1}{0.3}$$

Data Analysis

For example of temporal change in CO_2 solubility, the result of CO_2 absorption-desorption test with the MDEA solution is shown in Figure 2. The CO_2 absorption and desorption rates were defined as the slopes of a CO_2 solubility curve at the beginnings of absorption and desorption. The CO_2 recovery was defined as a difference in the CO_2 solubility between the absorption process and the desorption process.

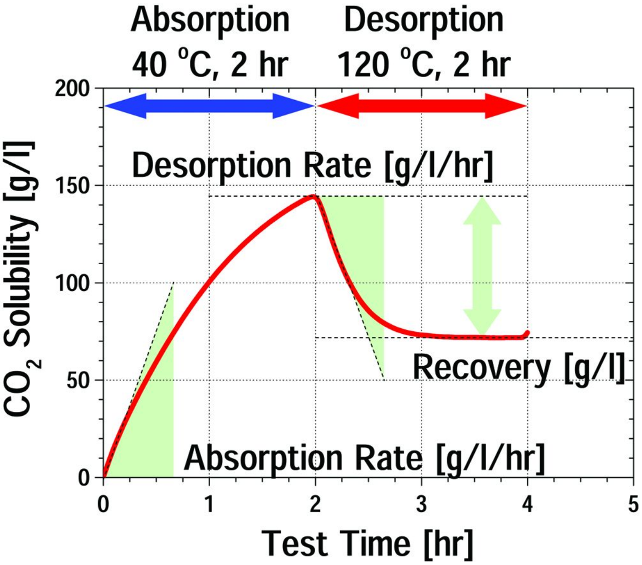

Figure 2. Example for Temporal Change in CO_2 Solubility

Downloaded by OHIO STATE UNIV LIBRARIES on June 14, 2012 | http://pubs.acs.org
Publication Date (Web): May 3, 2012 | doi: 10.1021/bk-2012-1097.ch005

Reaction Heats

The reaction heats of each solvent were measured with a differential reaction calorimeter at 40 °C under 0.1 MPa-CO_2; this data is summarized in Table 1.

Stability tests

Our novel solvents were evaluated with coal gasification gas supplied through water-shift reaction within an IGCC pilot-plant as stability tests. The mean composition of the supplied gas was 44% of H_2, 36% of CO_2, 1.2% of CO, 0.7% of CH_4, and containing N_2 and Ar. The mean total pressure was 2.2 MPa. The stability tests were carried out with the high pressure CO_2 absorption-desorption apparatus at the temperature of 40 °C for absorption and 120 °C for desorption, under 0.67 MPa-CO_2.

Results and Discussion

Screening of Tertiary Amine Solutions

We selected some tertiary amines as candidates for a high pressure CO_2 solvent, namely, imidazole type, alkanolamine type, diamine type, ether type, and cyclic-amine type. We carried out CO_2 absorption-desorption tests with the CO_2 absorption-desorption apparatus for screening of the candidate tertiary amine solutions. Figures 3 and 4 show the results of the CO_2 absorption-desorption tests, respectively, the relationship between CO_2 absorption rate and CO_2 desorption rate and the relationship between CO_2 recovery and reaction heat. The marks plotted in these figures indicate each results of the candidate solutions. An amine solution having higher absorption and desorption rates, and higher recovery, with lower reaction heat is better as a high pressure CO_2 solvent, because high recovery and low reaction heat reduce the energy for the CO_2 separation and capture process, and high CO_2 absorption and desorption rates downsize CO_2 capture plants. These results indicate that RH-1 has a higher desorption rate and a lower reaction heat, and RH-2a has higher CO_2 absorption and desorption rates and a higher CO_2 recovery, in comparison to the MDEA solution.

Downloaded by OHIO STATE UNIV LIBRARIES on June 14, 2012 | http://pubs.acs.org
Publication Date (Web): May 3, 2012 | doi: 10.1021/bk-2012-1097.ch005

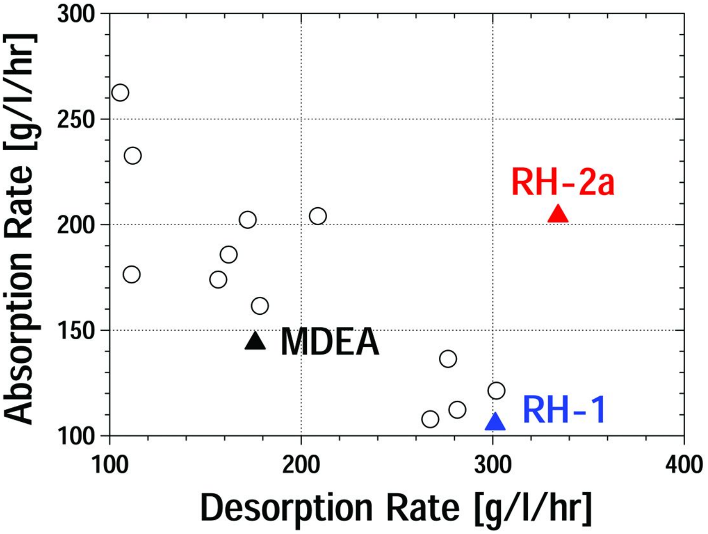

Figure 3. Relationship between CO_2 Absorption Rate and CO_2 Desorption Rate

Downloaded by OHIO STATE UNIV LIBRARIES on June 14, 2012 | http://pubs.acs.org
Publication Date (Web): May 3, 2012 | doi: 10.1021/bk-2012-1097.ch005

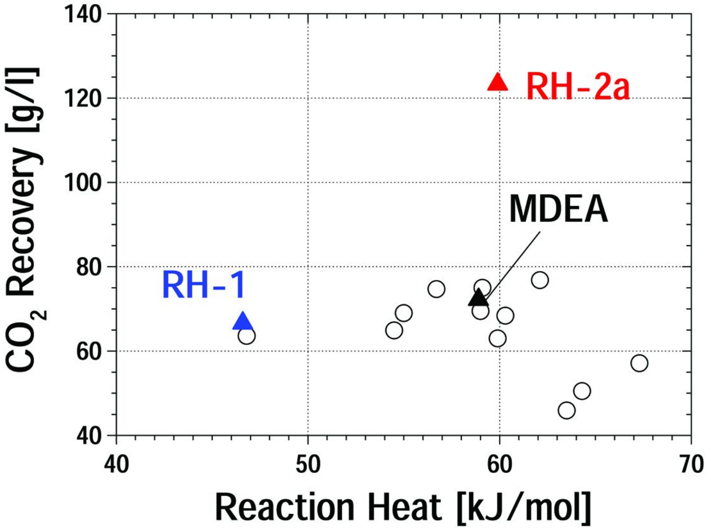

Figure 4. Relationship between CO_2 Recovery and Reaction Heat

Optimization of Amine Concentration

The effects of amine concentrations on CO_2 solubility profiles are shown in Figures 5a and 5b. The tertiary amine used in RH-2a shows a dynamic change in the CO_2 solubility profile with changing concentration, while that of the MDEA solution shows very little change. Thus, we have developed RH-2b by optimization of the amine concentration of RH-2a.

The results of the absorption-desorption tests and the reaction heats of RH2b, RH-2a, RH-1, and the MDEA solution are arranged in Table 1. RH-2b shows 2.8 times higher CO_2 absorption and desorption rates, and 3 times higher recovery with lower reaction heat than the MDEA solution.

Table 1. CO_2 Separation Performances of the novel solvents

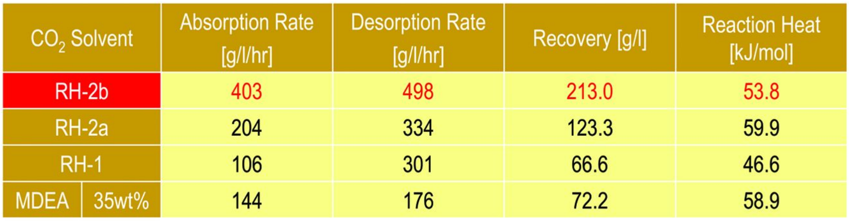

CO_2 Solvent		Absorption Rate [g/l/hr]	Desorption Rate [g/l/hr]	Recovery [g/l]	Reaction Heat [kJ/mol]
RH-2b		403	498	213.0	53.8
RH-2a		204	334	123.3	59.9
RH-1		106	301	66.6	46.6
MDEA	35wt%	144	176	72.2	58.9

Vapor-Liquid Equilibria

CO_2 pressure-solubility relationships at 40 °C and 120 °C were measured with a high pressure CO_2 vapor-liquid equilibrium apparatus to obtain CO_2 loading-differences under a given CO_2 partial pressure. The measurement procedure and the apparatus have been closely described in the previous paper (*20*). Figures 6a, 6b and 6c show the CO_2 pressure-solubility relationships of RH-2b, RH-1, and the MDEA solution, respectively. The developed CO_2 solvents, RH-2b and RH-1, show larger loading-differences under higher CO_2 partial pressure. In particular, the loading-difference of RH-2b shows more than three times that of the MDEA solution under the CO_2 partial pressure above 1 MPa-CO_2.

Downloaded by OHIO STATE UNIV LIBRARIES on June 14, 2012 | http://pubs.acs.org
Publication Date (Web): May 3, 2012 | doi: 10.1021/bk-2012-1097.ch005

Estimation of Total Energy

For RH-2b, RH-2a, RH-1, and the MDEA solution, their total energies for CO_2 separation and capture including compression process were estimated with the CO_2 recoveries and the reaction heats. The total energy consists of reaction heat that is heat absorbed through the CO_2 desorption reaction, solvent sensible heat that is to maintain the solvent at the desorption temperature of 120 °C, vaporization latent heat that is heat taken away through solvent vaporization, and compression energy that is a energy for compressing the recovered CO_2 to the pressure of 7.2 MPa required for CO_2 transportation. The estimated total energies are shown in Figure 7. RH-2b is estimated to reduce the total energy for CO_2 separation and capture including compression process to 1.9 GJ/t-CO_2, which is a 19% reduction from that with the MDEA solution. RH-1 is also able to reduce the total energy to 2.0 GJ/t-CO_2 because of its low reaction heat.

Additionally, RH-2b is able to desorb CO_2 under a higher pressure than the absorption pressure. An application of the pressurized desorption process to 4.0 MPa-CO_2 is estimated to reduce the total energy for CO_2 separation and capture including compression process to 1.6 GJ/t-CO_2, meaning a 32% reduction from that with the MDEA solution.

Stability Test with Coal Gasification Gas

Figure 8 shows the temporal changes in CO_2 solubilities on the stability tests of one-cycle, which is the absorption process for 4 hours and the desorption process for 2 hours. It has been found, even for the coal gasification gas, that RH-2b shows a higher CO_2 recovery and higher CO_2 absorption and desorption rates than those of the MDEA solution.

Figure 9 shows the result of 12-cycle stability test, which is 12 times that of the absorption processes for 1 hour and the desorption processes for 1 hour, on RH-2b. Little change in the performance of RH-2b was observed through the stability test of 12-cycle for 4 days.

Downloaded by OHIO STATE UNIV LIBRARIES on June 14, 2012 | http://pubs.acs.org
Publication Date (Web): May 3, 2012 | doi: 10.1021/bk-2012-1097.ch005

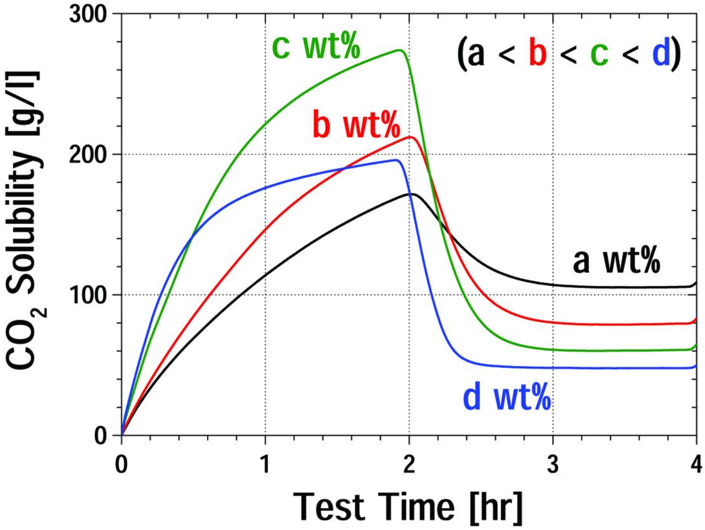

(a) Amine of RH-2a

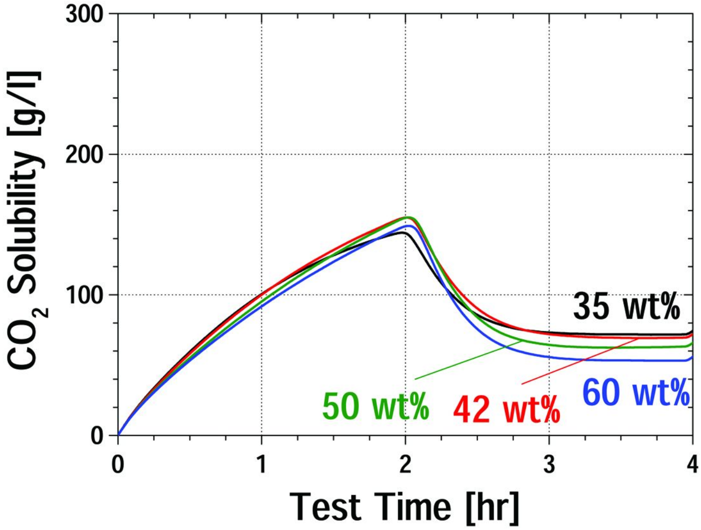

(b) MDEA

Figure 5. Effects of Amine Concentration on CO_2 Solubility Profiles

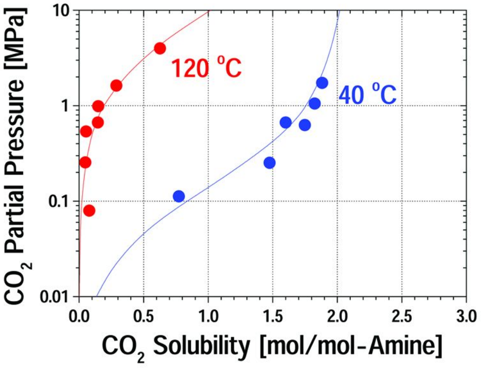

(a) RH-2b

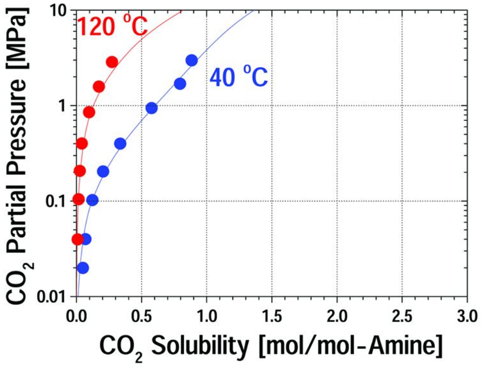

(b) RH-1

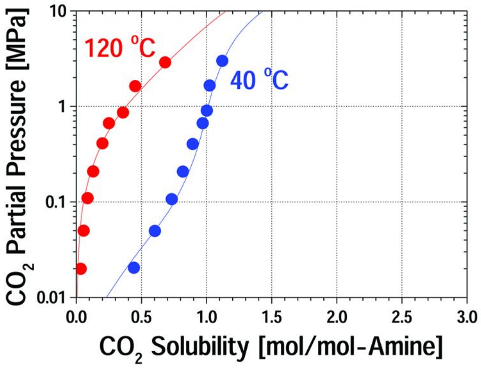

(c) MDEA

Figure 6. CO_2 Pressure-Solubility Relationships

Downloaded by OHIO STATE UNIV LIBRARIES on June 14, 2012 | http://pubs.acs.org
Publication Date (Web): May 3, 2012 | doi: 10.1021/bk-2012-1097.ch005

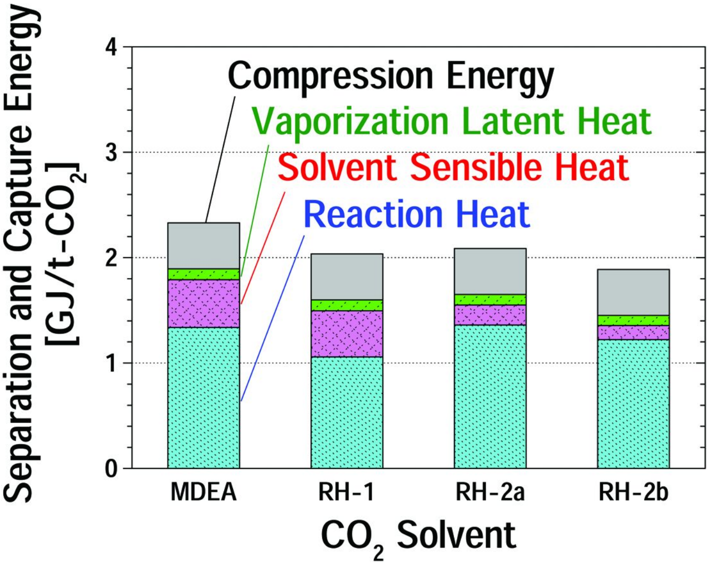

Figure 7. Estimation CO_2 Separation and Capture Energies

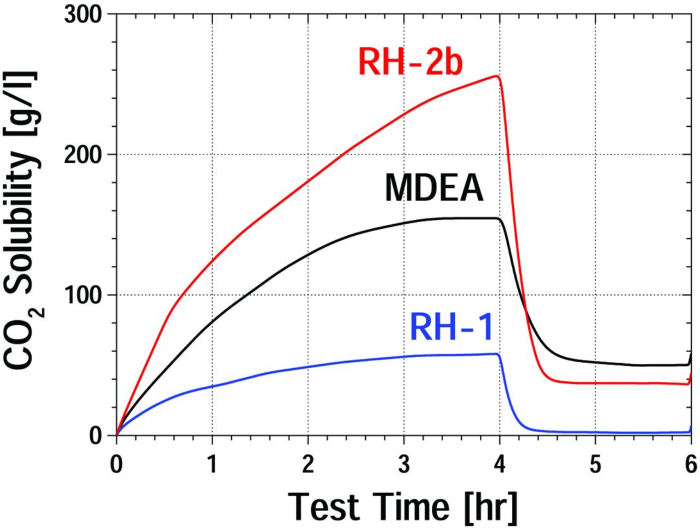

Figure 8. Temporal Changes in CO_2 Solubilities on the One-Cycle Stability Tests

Downloaded by OHIO STATE UNIV LIBRARIES on June 14, 2012 | http://pubs.acs.org
Publication Date (Web): May 3, 2012 | doi: 10.1021/bk-2012-1097.ch005

Downloaded by OHIO STATE UNIV LIBRARIES on June 14, 2012 | http://pubs.acs.org
Publication Date (Web): May 3, 2012 | doi: 10.1021/bk-2012-1097.ch005

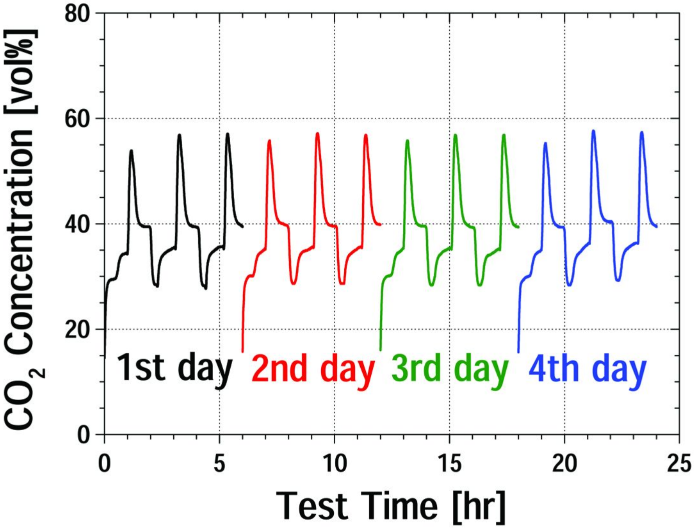

Figure 9. Result of the 12-Cycle Stability Test on RH-2b

Additionally, we carried out analyses of these amine solutions before and after the stability tests with a gas-chromatography flame ionization detector. Any new peaks attributed to amine degradation have not been observed in the result of the 12-cycle stability test for RH-2b, while some new peaks have been observed in the result of one-cycle stability test for the MDEA solution. It means that RH-2b has relatively high durability to the coal gasification gas.

Conclusions

The novel amine solution developed as a high pressure CO_2 solvent, RH-2b, shows high CO_2 absorption and desorption rates and a high CO_2 recovery under high pressure conditions; these values are approximately three times higher than those with the MDEA solution. RH-2b is estimated to reduce the total energy for CO_2 separation and capture including compression process to 1.9 GJ/t-CO_2, which is a 19% reduction from that with the MDEA solution. Additionally, the pressurized desorption process to 4 MPa-CO_2 is estimated to reduce the total energy to 1.6 GJ/t-CO_2. RH-2b has been found to have a relatively high durability to the actual coal gasification gas, as well as high performances as a high pressure CO_2 solvent.

References

1. Rinker, E. B.; Ashour, S. S.; Sandall, O. C. *Ind. Eng. Chem. Res.* **2000**, *39*, 4346–4356.
2. Park, J. *Greenhouse Gas Control Technol., Proc. Int. Conf., 7th* **2004**, *202*, 359–366.

3. Closmann, F.; Nguyen, T.; Rochelle, G. T. *Energy Procedia* **2009**, *1*, 1351–1357.
4. Dave, N.; Do, T.; Puxty, G.; Rowland, R.; Feron, P. H. M.; Attalla, M. I. *Energy Procedia* **2009**, *1*, 949–954.
5. Mondal, M. K. *J. Chem. Eng. Data* **2009**, *54*, 2381–2385.
6. Puxty, G.; Allport, A.; Attalla, M. *Energy Procedia* **2009**, *1*, 941–947.
7. Kadiwala, S.; Rayer, A. V.; Henni, A. *Fluid Phase Equilib.* **2010**, *292*, 20–28.
8. Haji-Sulaiman, M. Z.; Haji-Sulaiman, M. K.; Aroua, A. B. *Chem. Eng. Res. Des.* **1998**, *76*, 961–968.
9. Gabrielsen, J.; Michelsen, M. L.; Stenby, E. H.; Kontogeorgis, G. M. *Ind. Eng. Chem. Res.* **2005**, *44*, 3348–3354.
10. Vrachnos, A.; Kontogeorgis, G.; Voutsas, E. *Ind. Eng. Chem. Res.* **2006**, *45*, 5148–5154.
11. McCann, N.; Maeder, M.; Attalla, M. *Ind. Eng. Chem. Res.* **2008**, *47*, 2002–2009.
12. Mac Dowell, N.; Llovell, F.; Adjiman, C. S.; Jackson, G.; Galindo, A. *Ind. Eng. Chem. Res.* **2009**, *49*, 1883–1899.
13. Plaza, J. M.; Van Wagener, D.; Rochelle, G. T. *Energy Procedia* **2009**, *1*, 1171–1178.
14. Plaza, J. M.; Van Wagener, D.; Rochelle, G. T. *Int. J. Greenhouse Gas Control* **2010**, *4*, 161–166.
15. Chen, C.; Rubin, E. S. *Energy Policy* **2009**, *37*, 915–924.
16. Renzenbrink, W.; Ewers, J.; Keller, D.; Wolf, K. J.; Apel, W. *Energy Procedia* **2009**, *1*, 615–622.
17. Klara, J. M.; Plunkett, J. E. *Int. J. Greenhouse Gas Control* **2010**, *4*, 112–118.
18. Chowdhury, F. A.; Okabe, H.; Shimizu, S.; Onoda, M.; Fujioka, Y. *Energy Procedia* **2009**, *1*, 1241–1248.
19. Tomizaki, K.-Y.; Kanakubo, M.; Nanjo, H.; Shimizu, S.; Onoda, M.; Fujioka, Y. *Ind. Eng. Chem. Res.* **2010**, *49*, 1222–1228.
20. Tomizaki, K.-Y.; Shimizu, S.; Onoda, M.; Fujioka, Y. *Ind. Eng. Chem. Res.* **2010**, *49*, 1214–1221.
21. Yamada, H.; Shimizu, S.; Okabe, H.; Matsuzaki, Y.; Chowdhury, F. A.; Fujioka, Y. *Ind. Eng. Chem. Res.* **2010**, *49*, 2449–2455.

Downloaded by OHIO STATE UNIV LIBRARIES on June 14, 2012 | http://pubs.acs.org
Publication Date (Web): May 3, 2012 | doi: 10.1021/bk-2012-1097.ch005

Downloaded by STANFORD UNIV GREEN LIBR on June 15, 2012 | http://pubs.acs.org
Publication Date (Web): May 3, 2012 | doi: 10.1021/bk-2012-1097.ch006

Chapter 6

The Kinetics and Thermodynamics of CO_2 Capture by Aqueous Ammonia Derived Using Meta-GGA Density Functional Theory and Wavefunction-Based Model Chemistry Methods

P. Jackson,[1] A. Beste,[2] and M. I. Attalla[1,*]

[1]CSIRO Energy Technology, PO Box 330, Newcastle, NSW 2300 Australia
[2]Computer Science and Mathematics, Oak Ridge National Laboratories, P.O. Box 2008 MS6367, Oak Ridge, TN 37831-6164
***Moetaz.attalla@csiro.au**

A meta GGA-DFT study of CO_2 activation in aqueous ammonia solutions, with an emphasis on the reaction barrier and molecularity, has been undertaken using the M06-2X functional with an augmented triple-zeta split-valence basis set (6-311++G(d,p)). Up to five base molecules were treated explicitly in order to establish the effects of solvent catalysis in the chemical capture process. Aqueous free energies of solvation were determined for optimised reactant and transition structures using SM8/M06-2X/6-311++G(d,p). The concept of the solvent pre-complex as presented by Dixon and coworkers (Nguyen, M. T.; Matus, M. H.; Jackson, V. E.; Ngan, V. T.; Rustad, J. R.; Dixon, D. A. *J. Phys. Chem.* A **2008**, *112*, 10386−10398) was exploited to account for the energetics of disruption of the hydrogen-bonding solvent nano-network prior to the CO_2 activation step. Selected gas- and aqueous-phase thermodynamic quantities have also been derived.

Background

Global ammonia production peaked in 2009 at 153 million metric tonnes (*1*). Most commercial production of ammonia is converted into fertiliser

In Recent Advances in Post-Combustion CO2 Capture Chemistry; Attalla, M.;
ACS Symposium Series; American Chemical Society: Washington, DC, 2012.

Downloaded by STANFORD UNIV GREEN LIBR on June 15, 2012 | http://pubs.acs.org
Publication Date (Web): May 3, 2012 | doi: 10.1021/bk-2012-1097.ch006

(ammonium bicarbonate, ammonium phosphate), explosives (ammonium nitrate), or nitrous oxide (medical applications) via the degradation of the nitrate salt. Another significant application is in the manufacture of synthetic fibres (e.g. polyurethanes, nylon) and resins.

In 2010, ammonia was sold on global markets at an average price of USD$390/ton (*2*). In comparison, 2-aminoethanol (ethanolamine, MEA), the most widely used and intensively studied functionalised alkanolamine for post-combustion capture, was sold at a price of USD$1631/ton in May 2010 (*3*). Aside from the obvious cost benefits of using water/ammonia as a CO_2 capture solvent, laboratory-based studies of this system have demonstrated that:

(i) it has a higher loading capacity than MEA on a per weight basis (*4–6*),
(ii) regeneration of CO_2-loaded ammonia solutions requires as little as one-sixth the energy of loaded MEA solutions (*7*),
(iii) there is the potential for the single-step removal of NO_x, SO_x, HCl, HF as well as CO_2 from pulverised fuel flue gas
(iv) heat-stable salts in the form of $(NH_4)_2SO_4$ and NH_4NO_3 can be separated from other process solids produced during carbon capture and on-sold as fertiliser to help recoup any costs associated with solvent loss.

In general, the degradation products of ammonia, and ammonia itself, are not as corrosive to pipes and reaction vessels as the degradation products of MEA (MEA degradation products are described in References (*8–11*)). Oxalic acid is one of many oxidative degradation products of MEA (*12*) – its conjugate base (oxalate) has excellent metal chelating properties which undoubtedly contribute to the acceleration of corrosion in plants operating with this solvent.

Our group has recently demonstrated that organic amines, in particular secondary amines such as piperazine, can react in an alkaline aqueous environment with nitrogen oxides to produce nitrosamines (*13–15*). Secondary amines, including oxazolidinone and bis-N,N′-(2-hydroxyethyl)urea, are potential nitrosamine or nitrosamide precursors that have been identified as significant degradation products in spent MEA capture liquors (for example, see Strazisar *et. al.* (*9*), and Jackson *et. al.* (*16*)). In addition, the synthesis of MEA from ethylene oxide and ammonia results in the generation of mono-, di- and tri-ethanolamine species; the synthesis of ethanolamines is kinetically controlled to favour whichever of these products is desired, and separation is usually achieved by distillation. As a result, low-grade MEA sometimes contains traces of diethanolamine (DEA), a stable secondary alkanolamine which readily nitrosates. To date, there is no evidence to indicate that the putative nitroso derivatives of ammonia i.e. either nitrosoamine (H_2NNO) or nitroamine (H_2NNO_2), have significant lifetimes in either the condensed- or gas phases.

While there are many advantages associated with the use of aqueous ammonia as a CO_2 capture system (*5*, *8*, *17–20*) there are also some disadvantages, which include:

(i) the need for refrigeration to limit solvent losses via slip, and
(ii) slower reaction rates which translate to the need for larger absorption towers and plant capital costs.

Significantly degraded ammonia solvents can also impact pumping system performance if measures to reduce slurry formation/viscosity are not adopted.

A complete understanding of the kinetics and thermodynamics of the ammonia/water/carbon dioxide system is an obvious goal for improving the efficiency of the overall process. One particular aspect that has received recent experimental attention is the transient nature of carbamate ($NH_2CO_2^-$) in ammonia capture solutions. Carbamates usually increase the regeneration energy of CO_2 capture solvents, as their formation is usually significantly exoergic. It is also not clear what role – if any – carbamic acid might play. For a process which performs optimally at low temperatures (0-10 °C), it is desirable to minimise or even eliminate carbamate formation via the manipulation of solvent equilibria. You Jeong Kim *et. al.* (*5*) report that, while carbamate formation is prevalent in the early stages of CO_2 capture by ammonia solutions, it is either unstable with respect to the reactants, or it is particularly susceptible to hydrolysis. In this study, the authors observed a rapid increase in $[HCO_3^-]$ and an associated decrease in $[NH_2CO_2^-]$ as the solution pH fell to 9.14, very close to $pK_a(NH_4^+) = 9.23$ (*21*). The co-existence of $NH_2CO_2^-$ ($\delta = 166$ ppm) and HCO_3^--CO_3^{2-} ($\delta = 161.5$-165.2 ppm) is clear in a ^{13}C NMR study of ammonia solutions sparged with CO_2 (*22*). In an excess of NH_3, ^{13}C NMR results suggests the following equilibria apply:

$$2NH_3 + CO_2 \leftrightarrow NH_2CO_2^- + NH_4^+ \qquad K\ (293\ K) = 3.68 \times 10^3$$

$$2NH_3 + CO_2 + H_2O \leftrightarrow CO_3^{2-} + 2NH_4^+ \qquad K\ (293\ K) = 1.06 \times 10^2$$

When the ratio of CO_2 and NH_3 is closer to 1, the molecularity of the dominant CO_2 capture process is:

$$NH_3 + H_2O + CO_2 \leftrightarrow HCO_3^- + NH_4^+ \qquad K\ (293\ K) = 1.02 \times 10^3$$

HoSeok Park *et. al.* (*23*) have used two-dimensional IR spectroscopy to demonstrate that both the solution pH and bicarbonate concentration profoundly affect carbamate abundance, and are strongly interdependent. Brooker and Wen (*24*) used both Raman and ^{13}C NMR spectroscopies to study the $NH_2CO_2^-/HCO_3^-/CO_3^{2-}/NH_4^+/NH_3$ aqueous system. These authors used peak integration (after an appropriate scattering correction) to quantify the species of interest, and found that in 2.00 mol/kg unbuffered solutions of ammonium bicarbonate, 16 % of the CO_2 was in the form $NH_2CO_2^- + CO_3^{2-}$, whereas for an unbuffered solution of sodium carbonate and ammonia, there were no detectable quantities of either carbamate or bicarbonate. The weight of experimental evidence suggests that, as the pH of the solution falls during CO_2 capture, conditions become favourable for carbamate hydrolysis and bicarbonate formation.

Downloaded by STANFORD UNIV GREEN LIBR on June 15, 2012 | http://pubs.acs.org
Publication Date (Web): May 3, 2012 | doi: 10.1021/bk-2012-1097.ch006

Downloaded by STANFORD UNIV GREEN LIBR on June 15, 2012 | http://pubs.acs.org
Publication Date (Web): May 3, 2012 | doi: 10.1021/bk-2012-1097.ch006

Arstad *et. al.* (*25*) have used composite (G3MP2B3) and density functional (B3LYP) computational methods to examine the effects of base catalysis on the activation energies of the CO_2 capture reactions involving NH_3, MEA, and DEA. Energies were adjusted using the polarisable continuum models IPCM and SCIPCM, however the authors report reaction enthalpies at 0 K, rather than free energies at 298 K. Nonetheless, their results confirm the importance of a second base molecule acting directly as a proton transfer catalyst to reduce the activation energy. For MEA, they also found that the mechanism which produced the best activation energy estimate involved a second alkanolamine molecule acting as the proton transfer catalyst. For carbamic acid formation catalysed by a single water molecule plus ammonia, they obtained activation energies ranging from 52-87 kJ mol^{-1} (52 kJ mol^{-1} = IPCM(g)//B3LYP/6-31G**, 87 kJ mol^{-1} = SCIPCM+MP2/6-31G**//B3LYP/6-31G**). These authors also suggest that there is insufficient theoretical information to completely discount a zwitterion type mechanism, at least for MEA. Kim *et. al.* (*26*) have used coupled cluster calculations with an augmented correlation consistent double-zeta basis set to investigate:

(i) ammonia-catalysed CO_2 capture to form carbamate, and
(ii) the reaction between CO_2 and water, producing (short-lived) carbonic acid.

The best activation energy estimate for CO_2 capture leading to carbamic acid is 74.9 kJ mol^{-1}, with the inclusion of isodensity polarisable continuum model (IPCM) solvation effects lowering this energy to ~ 30 kJ mol^{-1}. The activation energy for the formation of carbonic acid is ~ 47.0 kJ mol^{-1} according to these calculations. These authors propose that the direct conversion of carbamate/carbamic acid to bicarbonate/carbonic acid does not take place, but instead a step-wise hydrolytic process generates aqueous CO_2 which in turn reacts separately with an aqueous ammonia molecule.

The calculations presented in this chapter have been performed in an attempt to describe the CO_2 activation reaction in aqueous ammonia as accurately as possible, with an emphasis on:

(i) heats and free energies of formation for $NH_2CO_2^-$ and NH_2CO_2H in the condensed phase,
(ii) reproducing these and other condensed phase thermodynamic quantities (including activation energies) for NH_3/CO_2 capture products using combined *ab initio* and semi-empirical methods,
(iii) a better understanding of the molecularity of the CO_2 capture reaction, and
(iv) identifying the trigger for the observed carbamate decomposition in experiments at ~ pH 9-10.

There are experimental difficulties associated with measurements of the CO_2/ammonia system, which is evident in the wide variation in literature reaction rates and mass transfer values (*27*).

Downloaded by STANFORD UNIV GREEN LIBR on June 15, 2012 | http://pubs.acs.org
Publication Date (Web): May 3, 2012 | doi: 10.1021/bk-2012-1097.ch006

Computational Methods

We have relied on the Minnesota 2006 meta-density functional (*28*) in conjunction with an augmented triple-zeta split-valence basis set (M06-2X/ 6-311++G(d,p)) for the calculation of relative isomer energies and activation energies. Others have demonstrated that the M06 meta-density functional outperforms the widely-used B3LYP hybrid functional in most areas, and in many cases performs as well as CCSD(T) calculations with similar-sized basis sets for reaction energies and barrier heights (*29*). All M06-2X calculations were performed with the GAMESS Revision 1 software package (*30*). The MacMolPlt 7.0 program (*31*) was used for visualization. To assess the accuracy of the meta-GGA DFT calculations, the model chemistry method CBS-QB3 (*32*, *33*), as implemented in the Gaussian software suite (*34*), was also used to derive gas-phase heats of formation for NH_2CO_2H and $NH_2CO_2^-$. This method can produce thermochemical quantities to within 4-8 kJ of experiment.

Meta-DFT gas-phase geometry optimisations were performed using a Newton-Raphson steepest descent algorithm until a stationary point was located, characterised by a gradient less than 0.0001. We have used the software author's recommended density of grid points to reduce integration errors in the DFT exchange-correlation quadrature to less than 1 microhartree per atom, namely NRAD = 96, NTHE = 36 and NPHI = 72, producing 248832 grid points per atom. Vibrational analysis was performed for all stationary points. All transition structures located exhibit a single imaginary vibrational frequency (NIMAG =1). Gas-phase molar heat capacities (C_p, C_v), entropies, enthalpies and free energies at specified temperatures for both molecules and ions were provided by the GAMESS program using standard statistical mechanical equations applicable to the rigid rotor-harmonic oscillator approximation (*35*).

When combined with SM8 solvation free energies (SM8/M06-2X/6-311++G(d,p)) and appropriate thermodynamic cycles, aqueous free energies of formation can be obtained and various thermodynamic properties determined for solvated species with reasonable accuracy (within 12 kJ mol^{-1}).

SM8 single-point calculations for optimised gas-phase geometries, as well as optimisations in the liquid phase, were performed using the GAMESSPLUS software (*36*). ΔG_{soln} within the SM8 theory is defined as:

$$\Delta G_{soln} = \Delta G_{EP} + G_{CDS}$$

where ΔG_{EP} is an electrostatic component accounting for solute-solvent interactions (solvent rearrangement and solute electrostatic adjustment energies), and G_{CDS} is a term dependent on atomic surface tensions and solvent-exposed solute surface area. In certain instances e.g. the evaluation of aqueous enthalpies of formation, the temperature dependence of ΔG_{soln} over the temperature range 273.15-373.15 K was evaluated; the effect of temperature is accounted for in the ΔG_{EP} term by a quadratic equation describing the variation in the dielectric conductivity of water with temperature, whereas the heat capacity and entropy changes in solution are accounted for with parametrized surface tensions. Class IV atomic charges were chosen for these calculations, and the recommended

In Recent Advances in Post-Combustion CO2 Capture Chemistry; Attalla, M.;
ACS Symposium Series; American Chemical Society: Washington, DC, 2012.

Downloaded by STANFORD UNIV GREEN LIBR on June 15, 2012 | http://pubs.acs.org
Publication Date (Web): May 3, 2012 | doi: 10.1021/bk-2012-1097.ch006

fraction of Hartree-Fock exchange was used in the charge- and solvation parts of the SM8/M06-2X calculations (HFE = 0.54). Standard thermodynamic parameters for the solvent water were used throughout.

Results

NH_2CO_2H Isomers

The M06-2X/6-311++G(d,p) and CBS-QB3 results confirm the earlier MP2 results of Remko *et. al.* (*37*) for the relative energetics of the *syn-* versus *anti-* conformers of gas-phase carbamic acid, i.e. the *syn-* isomer (Scheme 1) is the most stable conformer with free energy differences ΔG_{298} (*syn*/*anti*) = +37.6 kJ/mol (M06-2X) and ΔG_{298} (*syn*/*anti*) = +30.8 kJ/mol (CBS-QB3).

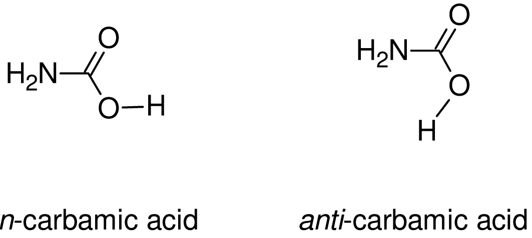
syn-carbamic acid *anti*-carbamic acid

Scheme 1. Syn- and anti- carbamic acid structures.

Gas Phase Energetics: Carbamic Acid and Carbamate

The hypothetical isodesmic reaction presented in Scheme 2 was used to evaluate ΔH_f NH_2CO_2H (g):

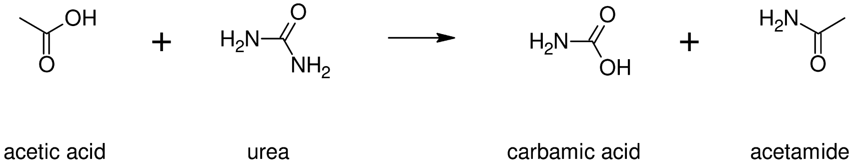
acetic acid urea carbamic acid acetamide

Scheme 2. Hypothetical isodesmic reaction producing carbamic acid from acetic acid and urea.

With the exception of carbamic acid, the experimental gas phase enthalpies of formation for all species in Scheme 2 are known with reasonable accuracy (< 1 kcal mol^{-1} error, see Table I); a theoretical reaction enthalpy at 298 K can be used to ascertain ΔH_f $NH_2CO_2H(g)$ according to Equation 1:

$$\begin{aligned}\Delta H_f\ NH_2CO_2H = {} & \Delta H_r\ (\text{theory}) + \Delta H_f\ CH_3COOH + \\ & \Delta H_f\ NH_2CONH_2 - \Delta H_f\ (CH_3CONH_2) \qquad (1)\end{aligned}$$

Downloaded by STANFORD UNIV GREEN LIBR on June 15, 2012 | http://pubs.acs.org
Publication Date (Web): May 3, 2012 | doi: 10.1021/bk-2012-1097.ch006

The M06-2X and CBS-QB3 reaction enthalpies plus experimental formation enthalpies relevant to the evaluation are presented in Table I.

The value determined using M06-2X is: ΔH_f NH_2CO_2H (g) = -438.3 ± 9 kJ mol^{-1}. The error incorporates a reasonable estimate of 4 kJ for the uncertainty in the theoretical reaction enthalpy. To confirm the accuracy of the M06-2X approach, the reaction enthalpy was also calculated using the CBS-QB3 model chemistry method. The result is almost identical: CBS-QB3 ΔH_f NH_2CO_2H (g) = -438.1 ± 9 kJ mol^{-1}. It was noted that the B3LYP frequency calculation in the CBS-QB3 evaluation for *syn*-NH_2CO_2H produced an imaginary frequency of 118i cm^{-1}, which affects the CBS enthalpy via the zero point and internal energy contributions. Nonetheless, the good correspondence between the two values supports the ostensible accuracy of M06-2X for thermochemical values.

Table I. Thermochemical values relevant to Scheme 2 for the neutral and corresponding anion reactions.

R(g) =	*ΔH_f R (g) 298 K, kJ mol^{-1}*
CH_3COOH, acetic acid[a]	-433 ± 3
CH_3COO^-, acetate[b]	-503.7 ± 12
NH_2CONH_2, urea[a]	-235.5 ± 1.2
CH_3CONH_2, acetamide[a]	-238.33 ± 0.78
ΔH_r (Scheme 2) M06-2X	-8.1
ΔH_r (Scheme 2) CBS-QB3	-7.9
ΔH_r (Scheme 2, anion) M06-2X[c]	-8.3
ΔH_r (Scheme 2, anion) CBS-QB3[c]	-6.2
PA(CH_3COO^-), M06-2X	1453.4
PA(CH_3COO^-), CBS-QB3	1459.5

[a] From (*38*); [b] From (*39*); [c] Corresponding values for the anionic equivalent (conjugate base) of Scheme 2

When the following substitutions are made: acetate for acetic acid and carbamate for carbamic acid in Scheme 2, and acetate for acetic acid in Equation 1, the gas phase enthalpy of formation of carbamate anion ($NH_2CO_2^-$) at can also be determined in the same way. Values obtained are: M06-2X, ΔH_f, $NH_2CO_2^-$(g) = -509.2 ± 21 kJ mol^{-1}, CBS-QB3, ΔH_f $NH_2CO_2^-$ (g) = -507.1 ± 21 kJ mol^{-1}. The large uncertainties (21 kJ mol^{-1}) are predominantly due to the experimental uncertainty for ΔH_f CH_3COO^- (see Table I). Substituting the experimental heat of formation of acetate with a theoretically-computed value should substantially reduce the associated error in ΔH_f $NH_2CO_2^-$(g). The theoretical values for ΔH_f $CH_3CO_2^-$ (g) are M06-2X: -509.6 ± 7 kJ mol^{-1}, CBS-QB3: -503.5 ± 7 kJ mol^{-1}, as determined using the M06-2X and CBS-QB3 proton affinities (PA's) together with experimental heats of formation for H^+ (g) and CH_3COOH (g). Experimentally,

ΔH_f H^+ (g) is known accurately to three decimal places (*38*). From this: M06-2X ΔH_f $NH_2CO_2^-$(g) = -515.1 ± 13 kJ mol^{-1}, CBS-QB3 ΔH_f $NH_2CO_2^-$(g) = -506.9 ± 13 kJ mol^{-1}.

The gas-phase frequencies of NH_2CO_2H and $NH_2CO_2^-$ can be used to calculate theoretical entropies using standard statistical mechanical equations: $S_{298\,K}$ NH_2CO_2H (g) = 289 J mol^{-1} K^{-1} and $S_{298\,K}$ $NH_2CO_2^-$ (g) = 269 J mol^{-1} K^{-1}. This leads to M06-2X gas phase free energies of formation: ΔG_f NH_2CO_2H (g) = -524.4 ± 9 kJ mol^{-1}, and ΔG_f $NH_2CO_2^-$ (g) = -595.4 ± 13 kJ mol^{-1}. These values will be used in the subsequent derivation of thermodynamic properties pertaining to the aqueous ammonia/CO_2 capture system. Other thermochemical quantities derived from the M06-2X/6-311++G(d,p) calculations include $\Delta_{acid}G(NH_2CO_2H)$ = 1426.6 kJ mol^{-1}, and $\Delta_{acid}H(NH_2CO_2H)$ = PA($NH_2CO_2^-$) = 1453.3 kJ mol^{-1}.

Downloaded by STANFORD UNIV GREEN LIBR on June 15, 2012 | http://pubs.acs.org
Publication Date (Web): May 3, 2012 | doi: 10.1021/bk-2012-1097.ch006

Solvation Free Energies

To establish the best values for ion and neutral solvation free energies, single point SM8 calculations were performed for each optimised gas phase structure in Scheme 2 (neutrals and ions). As the ΔG_{soln} values obtained in this fashion (denoted $\Delta_{soln}(1)$ in Table II) do not account for relaxation of the gas phase structure in solution, optimisations were also performed in the polarised continuum. The ΔG_{soln} values calculated with the optimised solution structures correspond to the true or relaxed ΔG_{soln} values for the level of theory employed, and are denoted $\Delta G_{soln}(2)$; these values *may not* agree as well with experiment, but this needs to be assessed. Both sets of values were corrected for the reference standard state of 1 mole/litre in the gas phase and are presented in Table II. Values have been calculated across the temperature range 273-373 K in order to apply the van't Hoff equation to determine aqueous reaction enthalpies.

The relaxed free energies of solvation predicted by SM8 theory ($\Delta G_{soln}(2)$) are typically within 6 kJ mol^{-1} of the experimental values, with the notable exception of acetic acid, for which the error appears to be almost 14 kJ mol^{-1}. Note that the experimental value presented for urea was derived using the experimental value for acetone (-16.1 kJ mol^{-1}, (*42*)) together with Helmholtz energies produced by Monte Carlo simulations of acetone/water, acetamide/water and urea/water (*41*). Relaxed free energies of solvation, as described above ($\Delta G_{soln}(2)$, see Table II) are used in subsequent evaluations. In order to evaluate a reaction enthalpy for carbamic acid and carbamate, standard enthalpies of solvation are needed for all the reactants and products in Scheme 2, together with an aqueous reaction enthalpy. Experimental enthalpies of solution are available for acetone (*42*): ΔH_{soln} = -40.9 ± 0.9 kJ mol^{-1}, urea: ΔH_{soln} = -72.2 kJ mol^{-1} (no uncertainty stated, (*42*)), and acetic acid: ΔH_{soln} = -52.8 ± 1 kJ mol^{-1} (*42*). The experimental enthalpy of solution for acetate anion is: ΔH_{soln} = -423 kJ mol^{-1} (*43*). Using appropriate thermodynamic cycles and the isodesmic reaction presented in Scheme 3, a value for the enthalpy of solvation of acetamide, and thus ΔH_f CH_3CONH_2 (aq), was determined. A van't Hoff plot of lnK vs 1/T using the free energies of reaction over the temperature range 273-373 K was used in this evaluation. The relevant energies are presented in Table III.

Downloaded by STANFORD UNIV GREEN LIBR on June 15, 2012 | http://pubs.acs.org
Publication Date (Web): May 3, 2012 | doi: 10.1021/bk-2012-1097.ch006

Table II. Free energy of solvation (ΔG_{soln}) for the neutral and anionic participants in the isodesmic reactions (Scheme 2) involving carbamate and carbamic acid. $\Delta G_{soln}(1)$ denotes a value determined with the optimised gas phase geometry, whereas $\Delta G_{soln}(2)$ denotes the true value obtained using the solution-optimised structure. All values in kJ mol^{-1}.

Temp. (K)	*acetamide* CH_3CONH_2		*urea* $(NH_2)_2CO$		*acetic acid* CH_3COOH		*acetate* CH_3COO^-		*syn-carbamic acid* NH_2COOH		*carbamate* NH_2COO^-	
	$\Delta G_{soln}(1)$	$\Delta G_{soln}(2)$	$\Delta G_{soln}(1)$	$\Delta G_{soln}(2)$	$\Delta G_{soln}(1)$	$\Delta G_{soln}(2)$	$\Delta G_{soln}(1)$	$\Delta G_{soln}(2)$	$\Delta G_{soln}(1)$	$\Delta G_{soln}(2)$	$\Delta G_{soln}(1)$	$\Delta G_{soln}(2)$
273.15	-31.4	-37.5	-50.1	-55.5	-16.2	-17.2	-318.8	-321.7	-43.5	-46.1	-345.2	-352.5
283.15	-30.1	-36.2	-48.7	-54.1	-15.0	-16.1	-317.8	-320.7	-42.2	-44.7	-344.0	-351.3
298.15	-28.3	-34.4	-46.7	-52.1	-13.4	-14.5	-316.4	-319.3	-40.2	-42.7	-342.1	-349.4
303.15	-27.7	-33.8	-46.0	-51.4	-12.9	-14.0	-315.9	-318.8	-39.5	-42.1	-341.5	-348.8
313.15	-26.5	-32.6	-44.6	-50.0	-11.9	-13.0	-314.9	-317.8	-38.2	-40.8	-340.2	-347.5
323.15	-25.4	-31.4	-43.2	-48.6	-10.9	-12.0	-314.0	-316.9	-36.9	-39.4	-338.9	-346.2
373.15	-19.8	-25.8	-36.2	-41.6	-6.5	-7.5	-309.5	-312.3	-30.3	-32.8	-332.1	-339.3
Expt. (298 K)		-40.6[a]		-58.7[b]		-28.03[c]		-322.2[c]		N/A		N/A

Temp. (K)	*Standard state correction values (1 bar → 1 mol L^{-1})*	*Temp. (K)*	*Standard state correction values (1 bar → 1 mol L^{-1})*
273.15	7.1	313.15	8.5
283.15	7.4	323.15	8.8
298.15	7.9	373.15	10.6
303.15	8.1		

[a] From (*40*); [b] Derived using data presented in (*41*); [c] From (*42*)

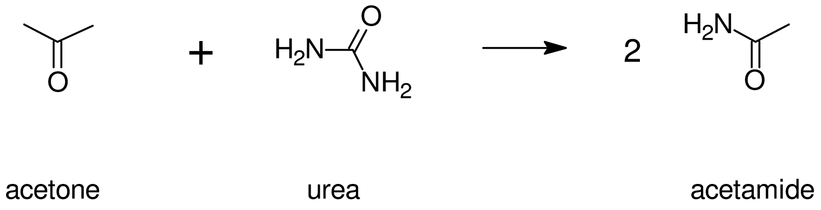

Scheme 3. Isodesmic reaction used to determine the aqueous solvation enthalpy (ΔH_{soln}) of acetamide.

Downloaded by STANFORD UNIV GREEN LIBR on June 15, 2012 | http://pubs.acs.org
Publication Date (Web): May 3, 2012 | doi: 10.1021/bk-2012-1097.ch006

The ΔG_{rxn} values in Table III were used to evaluate equilibrium constants for the reaction in Scheme 3. The van't Hoff plot yielded a straight line of slope +4843.9 (-ΔH(aq)/R), $r^2 = 1.00$. Thus, the aqueous reaction enthalpy for Scheme 3 determined in this fashion is -40.3 kJ mol^{-1}, and ΔH_f CH_3CONH_2 (aq) = -292.7 kJ mol^{-1}. We do not state uncertainties for these values, but it is worth noting that the experimental gas phase reaction enthalpy for Scheme 3 (ΔH_{rxn} (expt) = -44.7 kJ mol^{-1}), derived using values in the first data row of Table III, is approximately twice the value of the gas-phase reaction enthalpy predicted using CBS-QB3 (-21.3 kJ mol^{-1}), M06-2X/6-311++G(d,p) (-23.5 kJ mol^{-1}) and M06-HF/6-311++G(d,p) (-23.8 kJ mol^{-1}). The excellent agreement between the different theoretical reaction energies, which apply different mixtures of pure and approximated exchange energy, suggests that the DFT exchange approximation is not the cause of any error. Resonance structures for acetamide: $CH_3{-}C({-}O^-)({=}NH_2^+)$ and urea: $H_2N{-}C({-}O^-)({=}NH_2^+) \leftrightarrow H_2N^+{=}C({-}O^-)({-}NH_2)$ indicate that the problem could be related to the single reference description of these molecules. To assess this, the T1 diagnostics (*44*) for urea and acetamide were computed at the CCSD(T)/cc-pVTZ//M06-2X/6-311++G(d,p) level. Values of T1 > 0.02 suggest multi-reference character for the species in question. Results for urea (0.01375, largest amplitude 0.045) and acetamide (0.01417, largest amplitude 0.0257) identify a potential source of error. The GB1 diagnostic value (*45*) of 26.5 kcal mol^{-1} for urea (i.e. ΔE(B1LYP//BLYP – BLYP) > 10 kcal mol^{-1} for any reasonable basis set) confirms this situation, which will also apply to carbamic acid. Experimental energies have been used where possible, although the paucity of aqueous heats of formation makes the use of theoretical values unavoidable in the final determinations. Finally, we note that the M06-2X calculated proton affinity (PA) of urea is in excellent agreement with the value determined by Cooks (*46*) (M06-2X: 868.4 kJ mol^{-1}, Expt.: 873.5 ± 5.0 kJ mol^{-1}). The difference between the theoretical and experimental PA values for acetamide is slightly larger (M06-2X: 851.2 kJ mol^{-1}, Expt.: 863.6 kJ mol^{-1}), but this could be due to the method used for the determination of the experimental value.

We are now in a position to evaluate the aqueous heats of formation of carbamic acid and carbamate according to Scheme 2 and Equation 1. The theoretical free energies used for the van't Hoff plot determination of the aqueous reaction enthalpy (Scheme 2) are presented in Table IV.

Downloaded by STANFORD UNIV GREEN LIBR on June 15, 2012 | http://pubs.acs.org
Publication Date (Web): May 3, 2012 | doi: 10.1021/bk-2012-1097.ch006

Table III. Energies used in the determination of ΔH_f CH_3CONH_2 (aq).

	(1) Acetone CH_3COCH_3	(2) Urea $(NH_2)_2CO$	(3) Acetamide CH_3CONH_2	
ΔH_f (gas, 298 K) kJ mol^{-1}	-218.5 ± 0.6	-235.5 ± 1.2	-238.33 ± 0.78	
ΔH_{soln} (expt.)	-40.9 ± 0.9	-72.2	-	
Temp. (K)	M06-2X/6-311++G(d,p): solution energies (Hartree)			ΔG_{rxn} (1) + (2) → 2 × (3)
	Acetone	Urea	Acetamide	(kJ mol^{-1})
273.15	-193.0762450	-225.2433580	-209.1677121	-41.9
283.15	-193.0759113	-225.2429360	-209.1673497	-42.0
298.15	-193.0754389	-225.2422971	-209.1668151	-42.1
303.15	-193.0752887	-225.2420824	-209.1666392	-42.1
313.15	-193.0749994	-225.2416511	-209.1662910	-42.2
323.15	-193.0747247	-225.2412169	-209.1659478	-42.2
373.15	-193.0735683	-225.2390047	-209.1643091	-42.5

Table IV. Energies relevant to the determination of ΔH_f NH_2COOH (aq), refer to Scheme 2.

	(1)	(2)	(3)	(4)	
	acetic acid CH_3COOH	*urea* $(NH_2)_2CO$	*acetamide* CH_3CONH_2	*carbamic acid* NH_2COOH	
ΔH_f (aq, 298 K) kJ mol^{-1}	-486 ± 4	-307.7 ± 1.2	-292.7	-	
Temp. (K)	*M06-2X/6-311++G(d,p): solution energies (Hartree)*				ΔG_{rxn} (1) + (2) → (3) + (4)
	acetic acid	*urea*	*acetamide*	*carbamic acid*	(kJ mol^{-1})
273.15	-229.0475751	-225.2433580	-209.1677121	-245.1304901	-19.2
283.15	-229.0472424	-225.2429360	-209.1673497	-245.1311508	-22.0
298.15	-229.0467630	-225.2422971	-209.1668151	-245.1321702	-26.3
303.15	-229.0466085	-225.2420824	-209.1666392	-245.1325222	-27.7
313.15	-229.0463073	-225.2416511	-209.1662910	-245.1332326	-30.6
323.15	-229.0460167	-225.2412169	-209.1659478	-245.1339592	-33.6
373.15	-229.0447194	-225.2390047	-209.1643091	-245.1378305	-48.8

Downloaded by STANFORD UNIV GREEN LIBR on June 15, 2012 | http://pubs.acs.org
Publication Date (Web): May 3, 2012 | doi: 10.1021/bk-2012-1097.ch006

Downloaded by STANFORD UNIV GREEN LIBR on June 15, 2012 | http://pubs.acs.org
Publication Date (Web): May 3, 2012 | doi: 10.1021/bk-2012-1097.ch006

The plot yielded a straight line of slope -7380.4 (-ΔH(aq)/R, r^2 = 0.999) producing ΔH_{rxn} = 61.4 kJ mol^{-1}. From this, ΔH_f NH_2COOH (aq) = -439.6 kJ mol^{-1}. This value is very close to the gas phase heat of formation ΔH_f NH_2COOH (g) = -438.3 ± 9 kJ mol^{-1}, although the errors in the aqueous values used in the derivation (~ 20-30 kJ mol^{-1}) mean the enthalpies could in fact be quite different.

Using the same approach for the anion reaction (Scheme 2), a plot with slope 3128.2 (-ΔH(aq)/R, r^2 = 1.00) was obtained. The relevant acetate and carbamate energies are presented in Table V.

The slope corresponds to ΔH_{rxn} = -26 kJ mol^{-1} for the anionic isodesmic reaction in the aqueous phase. Using the values given in Table IV for aqueous heats of formation of acetamide and urea, together with the values for the enthalpy of solution (-423 kJ mol^{-1}) and the M06-2X gas phase heat of formation for acetate, ΔH_f NH_2COO^- (aq) = -973.6 kJ mol^{-1} is obtained.

We are interested in how this value compares with a direct evaluation of the aqueous heats of formation using ΔG_{soln}(2) values from Table II, together with an aqueous entropy evaluated using the frequencies from an "aqueous" hessian. As previously noted, the performance of M06-2X/6-311++G(d,p) in predicting gas phase enthalpies and free energies of reaction involving NH_2CO_2H and $NH_2CO_2^-$ is quite reasonable when measured against CBS-QB3 model chemistry values; the ΔG_{soln}(2) values introduce tolerable errors. Direct evaluation produces the following values: ΔG_f NH_2CO_2H (aq) = -567.1 ± 15 kJ mol^{-1}, and ΔG_f $NH_2CO_2^-$ (aq) = -944.8 ± 19 kJ mol^{-1}. A conservative error of 6 kJ mol^{-1} is included for the ΔG_{soln}(2) values. The entropies derived from the aqueous-hessians are: $S_{298\ K}$ NH_2CO_2H (aq) = 282.5 J mol^{-1} K^{-1} and $S_{298\ K}$ $NH_2CO_2^-$ (aq) = 268.9 J mol^{-1} K^{-1}. From ΔH = ΔG + TΔS: ΔH_f NH_2COOH (aq) = -482.9 ± 19 kJ mol^{-1} and ΔH_f $NH_2CO_2^-$ (aq) = -864.6 ± 23 kJ mol^{-1}. The van't Hoff values rely heavily on hypothetical isodesmic solution reaction energies (with attendant errors associated with the numerous theoretical ΔG_{soln} values used), whereas the values determined with the aqueous hessian primarily rely on the accuracy of gas-phase energies (usually good) and solution frequencies; we consider the latter values to be more reliable. We now turn our attention to pK_a (NH_2CO_2H).

pK_a of NH_2CO_2H

The experimental determination of this value is complicated by the existence of numerous coupled equilibria, as well as the instability of the acid species itself. The theoretical value at 298 K depends on the accuracy of the prediction of ΔG_{soln} for NH_2CO_2H and $NH_2CO_2^-$; an accurate experimental value for the free energy of solvation of the proton has been determined (-1112 ± 8 kJ mol^{-1}, (*47*)).

A cluster approach was taken for the evaluation of the pK_a of carbamic acid, in particular for the carbamate ion, because of the likelihood of strong localized ion-solvent interactions. In such instances treating additional solvent molecules explicitly can improve predicted pK_a values (*48*, *49*). The following reaction for the deprotonation of carbamic acid in solution was considered for a = 0-2:

$$NH_2CO_2H + aH_2O \rightarrow NH_2CO_2^-.(H_2O)_a + H^+$$

Table V. Energies relevant to the determination of ΔH_f NH_2COO^- (aq), refer to Scheme 2.

Temp. (K)	*M06-2X/6-311++G(d,p): solution energies (Hartree)*		*ΔG_{rxn} (kJ mol^{-1})*
	acetate	*carbamate*	*Scheme 2*
273.15	-228.6139251	-244.6978890	-22.0
283.15	-228.6136483	-244.6975008	-21.9
298.15	-228.6132359	-244.6969046	-21.7
303.15	-228.6130977	-244.6967006	-21.6
313.15	-228.6128239	-244.6962892	-21.5
323.15	-228.6125513	-244.6958703	-21.3
373.15	-228.6112124	-244.6936754	-20.6

The importance of the correct reference state has been outlined by Goddard and co-workers (*49*). Corrections are necessary when the number of moles of products and reactants differ in the gas-phase ($\Delta G^{\circ \to *} = nRT\ln(24.46)$) and when the concentration of water changes with solute addition i.e when water molecules are incorporated in the anion reaction product in Scheme 4. In this case, $\Delta G^{l \to *} = -nRT\ln(55.34)$, where $[H_2O(liq)] = 55.34$ mol L^{-1} and n = moles water consumed by the reaction. The optimised solvated anion structures used in the determinations are presented in Figure 1.

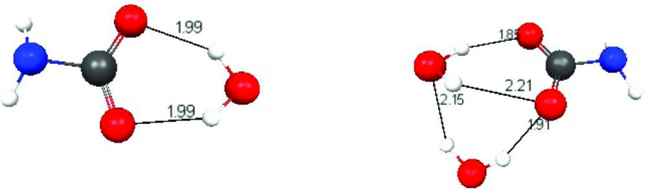

Figure 1. Carbamate anion solvated by one (left) and two (right) water molecules. White atoms = hydrogens; black = carbon; red = oxygens; blue = nitrogen. Hydrogen bond lengths in angstrom. (see color insert)

Using the relation $pK_a = \Delta G_{rxn}/RT\ln10$, and the experimental value $\Delta G_{soln}(H_2O) = -26.44$ kJ mol^{-1}, $pK_a(NH_2CO_2H)$ can be determined from the reaction given above. Table VI contains the data necessary for the calculation of these values using the clustered-anion approach.

Downloaded by STANFORD UNIV GREEN LIBR on June 15, 2012 | http://pubs.acs.org
Publication Date (Web): May 3, 2012 | doi: 10.1021/bk-2012-1097.ch006

Downloaded by STANFORD UNIV GREEN LIBR on June 15, 2012 | http://pubs.acs.org
Publication Date (Web): May 3, 2012 | doi: 10.1021/bk-2012-1097.ch006

Table VI. Gas-phase clustered-anion binding energies (ΔG_{bind} $NH_2CO_2^{-}.aH_2O_{(g)}$), clustered-anion free energies of solvation (ΔG_{soln} $NH_2CO_2^{-}.aH_2O$), gas- and liquid-phase standard state corrections and pK_a values for NH_2CO_2H.

	kJ mol⁻¹				
a =	ΔG_{bind} $NH_2CO_2^{-}.aH_2O_{(g)}$	ΔG_{soln} $NH_2CO_2^{-}.aH_2O$	$n\Delta G^{\circ\rightarrow *}$	$n\Delta G^{l\rightarrow *}$	SM8 pK_a
0	0.0	-333.0	7.9_3	0	5.7
1	44.9	-300.8	0	9.9_5	5.2
2	70.3	-290.6	-7.9_3	19.9	4.3

A minimum error of 1.5 pK_a units (the uncertainty in the experimental value for ΔG_{soln} H^+) is suggested for the theoretical pK_a values. The theory predicts that the pK_a of carbamic acid is similar to that of carbonic acid ($pK_a = 6.35$), and is much lower than the pH at which carbamate hydrolyses, which indicates carbamic acid isn't an important intermediate in the decomposition of carbamate during CO_2 capture. The experimental observation that carbamate hydrolyses readily near pH 9 lends support to the hypothesis that ammonium ions play a key role in the reversion of carbamate to $NH_{3(aq)}$ and $CO_{2(aq)}$. Supporting this, the authors of a recent coupled-cluster theoretical study (*26*) noted that the transition structures for the direct conversion of carbamate to bicarbonate – a reaction that must involve at least one water molecule – were associated with high activation energies. On the basis of this information, the conversion of carbamate to bicarbonate appears to occur in 3 distinct steps: ammonium ion formation, ammonium-catalysed decomposition of carbamate to NH_3 and CO_2, and the reaction of aqueous carbon dioxide with water to produce bicarbonate. The computed aqueous reaction free energy for *syn*-$NH_2CO_2H \rightarrow NH_3 + CO_2$ at the SM8/M06-2X/6-311++G(d,p) level is 23.7 kJ mol⁻¹; so at 298 K, the equilibrium lies towards the reactant ($K = 6.95 \times 10^{-5}$). For the equilibrium: $2NH_3 + CO_2 \leftrightarrow NH_2CO_2^- + NH_4^+$, the computed free energy change (from neutral to ionic products) is -73.3 kJ mol⁻¹, which gives $K = 7.03 \times 10^{12}$ (K (expt, 293 K) = 3.68×10^3 (*22*)). The large difference between the experimental and theoretical equilibrium constants may be attributed to a number of factors, including free energy of solvation errors and differences in the experimental and 'theoretical solution' ionic strengths. In spite of this, the parallels in the chemical behaviour of carbonic and carbamic acids are clear. The molecularity of the NH_3/CO_2 capture reaction and the role of ammonium ions is explored in the next section.

Transition Structures for the Activation of CO_2 by Water/Ammonia

In this section, we present transition structures (TS's) for the reactions given in Scheme 4:

$$aNH_3 + bH_2O + CO_2 \rightarrow (a\text{-}1)NH_3 + bH_2O + NH_2CO_2H$$

$$aNH_3 + bH_2O + CO_2 \rightarrow (a\text{-}2)NH_3 + NH_4^+ + bH_2O + NH_2CO_2^-$$

Scheme 4. The CO_2 activation reactions explored using SM8/M06-2X/6-311++G(d,p).

The premise of this study is as follows: the TS's are computed using M06-2X/6-311++G(d,p) in the gas phase for $a + b = n$, where $n \leq 4$ i.e. up to 3 catalyst molecules (plus ammonia and CO_2) are treated explicitly using DFT. Single-point aqueous free energies of solvation are then computed for the gas phase structures to approximate the long-range solvent effects. It is expected that, as the number of base (catalyst) molecules treated explicitly using DFT increases, the gas phase free energy of activation should converge to the aqueous free energy of activation. In other words, the contribution of the polarisable continuum to the free energy of activation becomes negligible as the electrostatic field of the reactant microdroplet swamps the continuum field.

Aqueous bicarbonate formation has been studied by Dixon and co-workers (*50*). They calculated the activation energies relative to a reactant pre-complex of base molecules. We have used the same approach for carbamate formation/decomposition, but instead of using coupled-cluster theory and the COSMO solvation models, we have used SM8(g)/M06-2X/6-311++G(d,p).

Bimolecular Activation of CO_2 (a = 1, b = 0)

The simplest aqueous ammonia capture reaction is bimolecular and corresponds to NH_3 reacting directly with CO_2; the gas-phase TS is presented in Figure 2 (ω_{im} = 1658i cm^{-1}). The final product of the reaction is *anti*-NH_2CO_2H. The OCO bond angle is 138°, and the principle motion of the reaction coordinate is hydrogen migration from the ammonia to one of the CO_2 oxygen atoms; the TS possesses C_s symmetry. The migrating hydrogen is 1.255 Å distant from its original nitrogen centre, and 1.295 Å from the nucleophilic oxygen; the bond that this oxygen makes with the carbon atom has also stretched to 1.274 Å (relative to 1.155$_6$ Å in free CO_2).

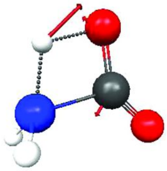

Figure 2. TS for NH_3+CO_2 gas phase reaction. White atoms = hydrogens; black = carbon; red = oxygens; blue = nitrogen. The red arrows describe the atomic motions associated with the reaction coordinate. (see color insert)

Downloaded by STANFORD UNIV GREEN LIBR on June 15, 2012 | http://pubs.acs.org
Publication Date (Web): May 3, 2012 | doi: 10.1021/bk-2012-1097.ch006

Downloaded by STANFORD UNIV GREEN LIBR on June 15, 2012 | http://pubs.acs.org
Publication Date (Web): May 3, 2012 | doi: 10.1021/bk-2012-1097.ch006

Termolecular Activation of CO_2 ($a = 1, 2$ and $b = 0, 1$; $a + b = 2$)

A base molecule - either water (*w*) or ammonia (*a*) - can act in a catalytic proton-acceptor/donor role to lower the activation energy of the capture reaction. The two gas-phase TS's located are presented in Figure 3. Note that a hydrogen atom from the solvent catalyst is incorporated in the carbamic acid product, rather than a hydrogen atom from the ammonia molecule which forms the N-C bond.

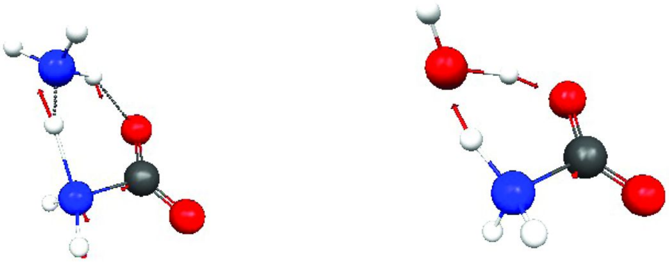

Figure 3. CO_2 activation by ammonia plus one other base molecule. Left: 'aa', (base = ammonia, ω_{im} = 661i cm^{-1}); right: 'aw' (base = water, ω_{im} = 1434i cm^{-1}). (see color insert)

The major differences in the structures are the orientation of the catalytic molecules relative to the product molecule (see Figure 4), and the relative distances of the migrating hydrogen atoms from their origins. Both migrating hydrogen atoms are close to the catalytic molecule and relatively 'distant' from their origins when CO_2 is activated by 2 ammonias in *aa* ($r_{Ncar\text{-}H}$ = 1.473 Å, $r_{H\text{-}O}$ = 1.697 Å); when the catalytic base molecule is water, the TS bond lengths are closer to those for direct or unassisted CO_2 activation by ammonia ($r_{Ncar\text{-}H}$ = 1.070 Å, $r_{H\text{-}O}$ = 1.249 Å). The imaginary frequencies associated with each TS are ω_{im} = 661i cm^{-1} (*aa*), ω_{im} = 1434i cm^{-1} (*aw*). The path followed by the migrating hydrogen atoms in the ammonia-catalysed reaction make angles of ~ 40° with the plane containing the N,C,O atoms incorporated in the product molecule, whereas the migrating atoms in the water-catalysed reaction are only slightly displaced from this plane (9°, 13.7°).

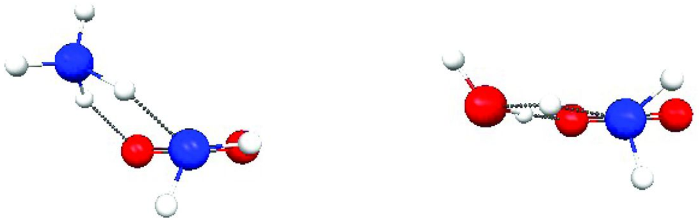

Figure 4. TS's for CO_2 capture by ammonia catalysed by: (left) an additional ammonia molecule, 'aa'; (right) a water molecule, 'aw'. The view is along the N-C bond that is forming between CO_2 and the ammonia molecule incorporated in the product (anti-carbamic acid). (see color insert)

Downloaded by STANFORD UNIV GREEN LIBR on June 15, 2012 | http://pubs.acs.org
Publication Date (Web): May 3, 2012 | doi: 10.1021/bk-2012-1097.ch006

a = 1-3 and b = 0-2; a + b = 3: Explicit Treatment of Two Catalyst Molecules

The addition of two or more catalyst molecule adds additional complexity to the activation reaction; the number of geometric arrangements is 2^N, where N = number of catalyst molecules, and this *only* concerns the order of catalyst molecules acting in a hydrogen "shuttling" capacity. For this study, we sought to locate transition structures in which all explicitly-modelled base molecules were involved directly in either transferring or solvating the migrating proton. The polarisable continuum should adequately account for any other energy contributions.

In total, four TS's were found for two base molecules catalysing the ammonia activation of CO_2. These are presented in Figure 5.

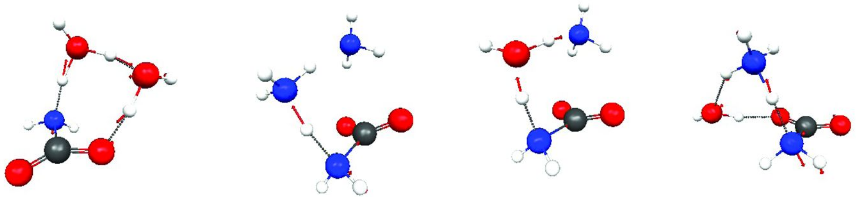

Figure 5. Transition structures for the base-catalysed activation of CO_2, a + b =3 in Equation 4. From left to right: a =1, b = 2, 'aww'; a = 3, b = 0, 'aaa'; a = 2, b = 1, 'awa'; a = 2, b = 1, 'aaw'. (see color insert)

From left to right in Figure 5, the imaginary frequencies associated with the hydrogen migration reactions are: 1096i cm^{-1}, 694i cm^{-1}, 1154i cm^{-1} and 278i cm^{-1}. Inspection of the TS's suggests that an ammonia molecule positioned near the CO_2 group acts as a terminal proton acceptor leading to an ammonium/carbamate ion pair, whereas a water molecule proximal to the CO_2 leads to *anti*-carbamic acid. This is supported by the C-O bond lengths: 1.263 and 1.206 Å for *aww*; 1.231 and 1.228 Å for *aaa*; 1.231 and 1.231 Å for *awa*; and 1.255 and 1.215 Å for *aaw*. A decreasing N-C bond length in the activated complex is another trend which emerges as the microsolvation of the transition structures increases i.e. for direct (unassisted) activation, r_{NC} = 1.573 Å; catalysis by one base molecule: r_{NC} = 1.536 Å (*aa*), r_{NC} = 1.547 Å (*aw*), and r_{NC} = 1.504-1.526 Å (2 catalyst molecules).

a = 1-4 and b = 0-3; a + b = 4: Explicit Treatment of Three Catalyst Molecules

There are 8 possible arrangements for 3 catalytic base molecules participating in CO_2 activation. The relevant TS's are presented in Figure 6.

Downloaded by STANFORD UNIV GREEN LIBR on June 15, 2012 | http://pubs.acs.org
Publication Date (Web): May 3, 2012 | doi: 10.1021/bk-2012-1097.ch006

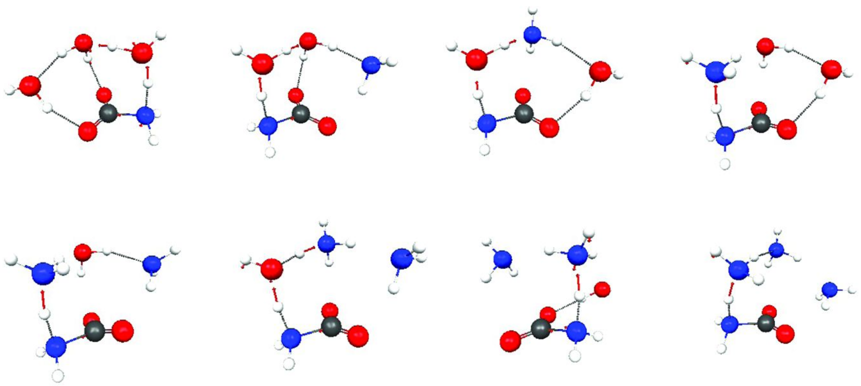

Figure 6. Transition structures for the base-catalysed activation of CO_2, a + b = 4 in Equation 4. From left to right; top row a =1, b = 3, awww; a = 2, b = 2, awwa, awaw and aaww; bottom row a = 3, b = 1 aawa, awaa and aaaw, and a = 4, b = 0, aaaa. (see color insert)

The imaginary frequencies associated with the structures presented in Figure 6 are 686i cm^{-1} (*awww*), 987i cm^{-1} (*awwa*), 1053i cm^{-1} (*awaw*), 712i cm^{-1} (*aaww*), 723i cm^{-1} (*aawa*), 1029i cm^{-1} (*awaa*) 593i cm^{-1} (*aaaw*) and 731i cm^{-1} (*aaaa*). Inspection of the TS's reveals that solvation of the proton is important when a water molecule is positioned near the ammonia molecule which forms the carbamate N-C bond (see *awww, awwa*, *awaw* and *awaa*). The water molecule in this position is involved in concerted proton accepting and donating (proton shuttling). Another feature of these TS's is that, in all instances, the fourth base molecule in the activating "chain" only appears to play a solvating role. When a second ammonia molecule is positioned near the carbamate-forming ammonia, it only acts as a proton acceptor, with the remaining bases solvating the TS. The values for rNC follow the bond-shortening trend identified previously, and ranges from 1.494 Å (*awww*) to 1.540 Å (*awaa* and *aaaa*), while the C-O bond lengths indicate carbamate (rather than carbamic acid) formation in all instances (r_{CO} = 1.22-1.24 Å).

Gas-Phase Activation Energies

The gas phase free energies of activation are plotted in Figure 7. This is highest for the direct reaction between CO_2 and one NH_3 molecule, 207.4 kJ mol^{-1}; there is a sharp decrease (av. ~ 70 kJ mol^{-1}) when the number of participating molecules increases by one (a + b = 2), another decrease of av. ~ 23 kJ mol^{-1} when 3 base molecules participate (a + b = 3), and a further decrease of av. ~ 17 kJ mol^{-1} when a + b = 4. '*aaww*' in Figure 6 corresponds to the reaction with the lowest gas-phase activation energy (86.9 kJ mol^{-1}). The effect of the continuum solvent field on the activation energies is discussed below.

Downloaded by STANFORD UNIV GREEN LIBR on June 15, 2012 | http://pubs.acs.org
Publication Date (Web): May 3, 2012 | doi: 10.1021/bk-2012-1097.ch006

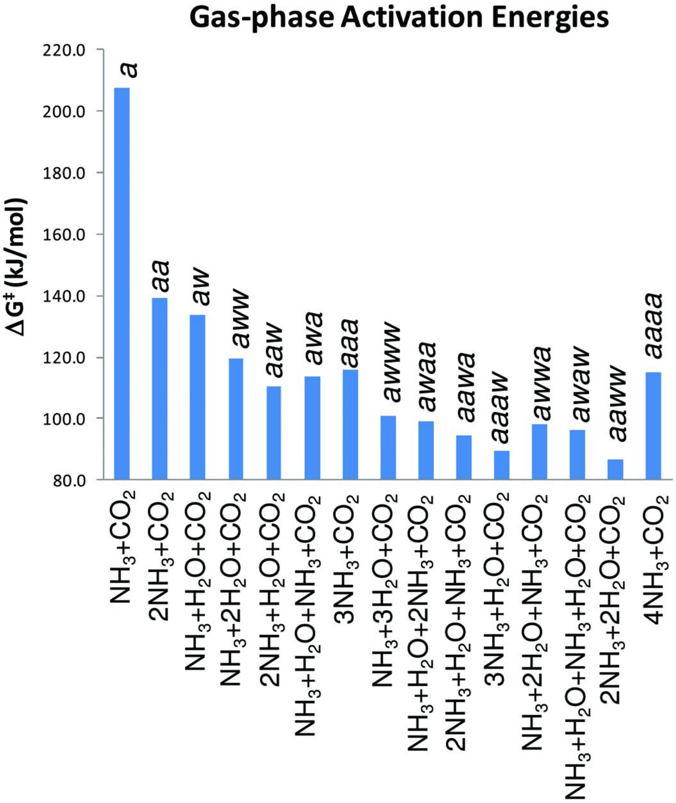

Figure 7. Variation of gas-phase activation energies with increasing numbers of participating base molecules.

Aqueous Activation Energies

The aqueous free energies of activation are plotted in Figure 8. The direct activation (*a*, bimolecular) is once again the least favourable pathway, however the termolecular reaction involving two ammonias (*aa*, ΔG‡ = 34.8 kJ mol^{-1}), and pathways involving ammonia molecules proximal to the carbamate-forming ammonia i.e. ammonia acting in a proton-accepting capacity e.g. *aaw* ΔG‡ = 35.9 kJ mol^{-1}, *aaa* ΔG‡ = 51.1 kJ mol^{-1}, act to lower the aqueous free energy of activation. The contrast is most clearly seen in the relative free energies for the termolecular pathways 'a + b = 2' (*aa* vs *aw*), and pathways 'a + b = 3' (*aaw*/*aaa* vs *awa*/*aww*), for which an additional water molecule markedly increases the activation energy. Water molecules only become important for 'a + b = 4', but only if an ammonia molecule is the primary proton acceptor in the activation "chain". We next explore the effects of solvent microstructures on the aqueous activation energies.

]

Downloaded by STANFORD UNIV GREEN LIBR on June 15, 2012 | http://pubs.acs.org
Publication Date (Web): May 3, 2012 | doi: 10.1021/bk-2012-1097.ch006

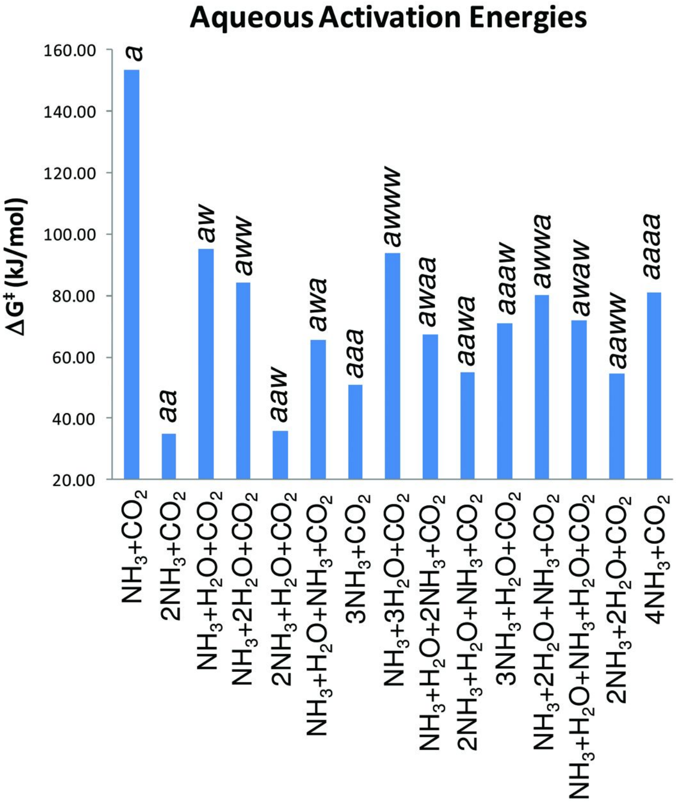

Figure 8. Variation of aqueous activation energies with increasing numbers of participating base molecules. 'aa' = activation by 2 NH_3 molecules, 'aww' = activation by NH_3 + $2H_2O$ molecules etc.

Solvent Microstructures

Following the example of Dixon and co-workers (*50*), base molecules participating in the activation of CO_2 should be considered the constituents of a hydrogen bonded nano-network in solution. Explicit quantum chemical treatment of solution structure should improve the estimated activation energies. The nano-network being considered is the solution-phase equivalent of a "thermally-equilibrated" gas-phase reactant pre-complex (dipole-dipole, charge-dipole etc.). The free energy required to disrupt the nano-network is: $\Delta G_{rxn,aq}$: $(NH_3)_a(H_2O)_b \rightarrow a.NH_3 + b.H_2O$ and is equal to the binding energy of the nano-network in the polarised continuum. The nano-network binding energy can be added to the overall energy of activation (resulting in a net increase in the free energy of activation).

The lowest energy nanostructures used in these calculations are presented in Figure 9. Their total energies ($E_{M06\text{-}2X}$ + ZPE + U + RT – T.S), solvation free energies and binding energies are presented in Table VII. Due to the average errors in the solvation free energies and binding energies (5-10 kJ mol^{-1}), conformational averaging was not considered for solvent nano-networks, with only the lowest energy conformation used. Also, the positive free energy of solvation for CO_2 (SM8(g)/M06-2X/6-311++G(d,p) = +15.7 kJ mol^{-1}) suggests that any nano-network including CO_2 will have a net lower binding energy than the corresponding pure solvent network without the CO_2 molecule; for this reason, we consider CO_2 to be bathed by the continuum only. The calculations also predict the dimer NH_3-H_2O is “unbound” in solution ($(NH_3)(H_2O)aq \rightarrow NH_3(aq) + H_2O(aq), \Delta G_{rxn}$ = -3.9 kJ mol^{-1}, so the free energy value for the water-assisted termolecular activation of CO_2 (Section (vii), Figure 3, right) stands at 95.3 kJ mol^{-1}. Revised activation energies are plotted in Figure 10.

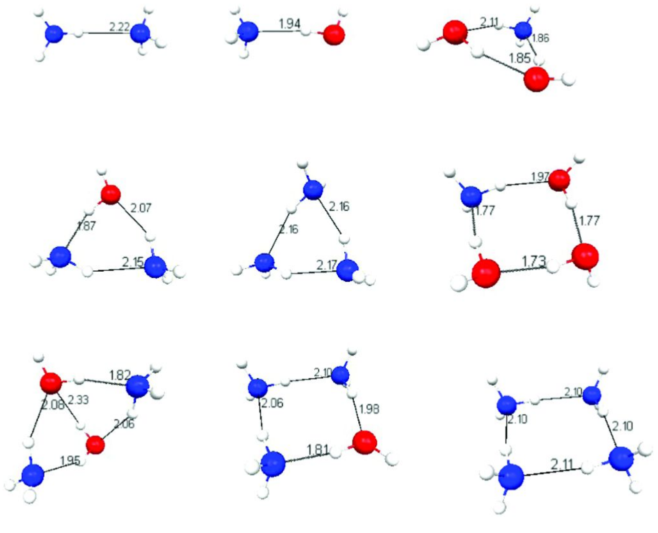

Figure 9. Lowest energy conformers for solvent nano-networks. Top row (L-R): $(NH_3)_2$, $NH_3(H_2O)$ and $NH_3(H_2O)_2$; centre row: $H_2O(NH_3)_2$, $(NH_3)_3$ and $(NH_3)(H_2O)_3$; bottom row: $(NH_3)_3H^+$; bottom row: $(NH_3)_2(H_2O)_2$, $(NH_3)_3H_2O$ and $(NH_3)_4$. Bond lengths between molecules in angstrom. Blue = nitrogen atoms, white = hydrogen atoms, red = oxygen atoms. (see color insert)

Downloaded by STANFORD UNIV GREEN LIBR on June 15, 2012 | http://pubs.acs.org
Publication Date (Web): May 3, 2012 | doi: 10.1021/bk-2012-1097.ch006

Table VII. M06-2X/6-311++G(d,p) gas phase energies (298.15 K, incl. thermal and entropy corrections, G_g), free energies of solvation and binding energies of solvent nano-networks (see Figure 9). Values are in kJ mol^{-1} unless stated otherwise.

$(NH_3)_a(H_2O)_b$ a,b =	G_g (Hartree)	G_{soln}	ΔG_{rxn} :$(NH_3)_a(H_2O)_b \rightarrow aNH_3 + bH_2O$	
			gas	aqueous
2,0	-113.055755	-26.2	19.1	14.4
0,2	-152.835912	-53.8	10.2	10.4
1,1	-132.950162	-44.9	3.2	-3.9
0,3	-229.256817	-48.3	7.5	40.2
1,2	-209.369460	-41.8	4.7	27.7
2,1	-189.476251	-31.3	17.4	34.7
3,0	-169.582486	-19.7	31.6	44.4
1,3	-285.790549	-55.4	1.50	37.9
2,2	-265.895412	-43.0	19.3	51.9
3,1	-246.004647	-38.6	25.6	46.4
4,0	-226.106579	-27.9	51.2	66.5

The termolecular activation of CO_2 by two ammonia molecules remains the most energetically favourable process. Pathways with an ammonia molecule accepting the proton from the carbamate-forming ammonia are consistently lower in energy than those with a water molecule playing this role i.e two proximal NH_3 molecules appears to be a key factor in the aqueous CO_2 activation process. Activation by four ammonia molecules is a notable exception (activation energy 147.7 kJ mol^{-1}); this may be due to the negative charge developing on the two oxygen atoms, and in this case water would be better at solvating these charged centres, whereas for the TS in question, this role is being fulfilled by ammonia. Ignoring the bimolecular process, the activation energies range from 49.2 kJ mol^{-1} (*aa*, termolecular) to 147.7 kJ mol^{-1} (carbamate formation catalysed by four ammonia molecules, *aaaa*).

Downloaded by STANFORD UNIV GREEN LIBR on June 15, 2012 | http://pubs.acs.org
Publication Date (Web): May 3, 2012 | doi: 10.1021/bk-2012-1097.ch006

Downloaded by STANFORD UNIV GREEN LIBR on June 15, 2012 | http://pubs.acs.org
Publication Date (Web): May 3, 2012 | doi: 10.1021/bk-2012-1097.ch006

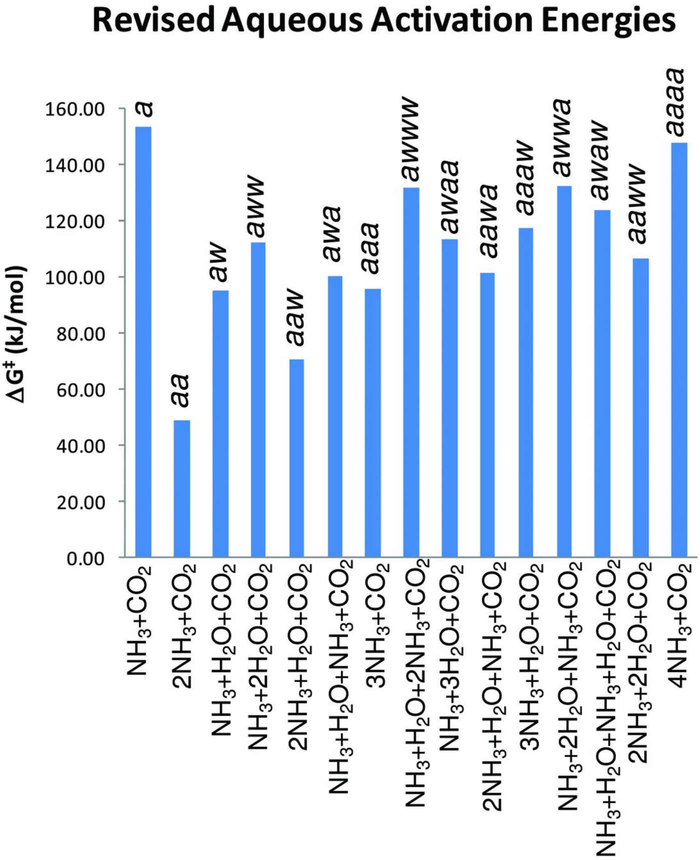

Figure 10. Variation of revised aqueous activation energies (taking solvent nano-networks into consideration) with increasing numbers of participating base molecules. 'aa' = activation by 2 NH_3 molecules, 'aww' = activation by NH_3 + $2H_2O$ molecules etc.

Carbamate Decomposition

The principle of microscopic reversibility dictates that carbamate decomposition to ammonia and CO_2 can follow the same pathway – but in the opposite direction – to the capture reaction. The major difficulty with modelling carbamate decomposition is that two of the reactants are charged; either NH_4^+ or H_3O^+, and $NH_2CO_2^-$. Because of charge redistribution, gas-phase geometry optimisation of carbamate/base-H^+ pairs produces a dipole-bonded neutral complex between either ammonia or water and carbamic acid. This also represents a problem when performing intrinsic reaction coordinate or path-following calculations on gas-phase transition structures. Although not an accurate reflection of the solution speciation, this problem can be skirted

Downloaded by STANFORD UNIV GREEN LIBR on June 15, 2012 | http://pubs.acs.org
Publication Date (Web): May 3, 2012 | doi: 10.1021/bk-2012-1097.ch006

by considering a separate nano-network for each of the charged reactants i.e. NH_4^+ and $NH_2CO_2^-$ separately solvated, with the number of reactants conserved according to the stoichiometry of the transition structure.

Each of the transition structures presented in Sections *(vi)-(ix)* correlates with one of the product sets identified in Equations 4(a) and 4(b). The bimolecular- and both termolecular TS's satisfy the stoichiometric requirements of 4(a), as does the transition structure for CO_2 activation by ammonia and 2 water molecules (*aww*). These TS's produce *anti*-carbamic acid, however it is unlikely that either *syn*- or *anti*-carbamic acids are long-lived at the high pH's operative in ammonia-based capture solvents – they will immediately deprotonate. We make the reasonable assumption that the acid deprotonation barrier is small compared to the barrier associated with the initial carbamic acid formation reaction. For these reasons, we only consider the ionic asymptotes ($NH_2CO_2^-$ plus either H^+ or H_3O^+/NH_4^+). The remaining TS's lead to carbamate and NH_4^+, with an obvious exception being the structure for CO_2 activation by ammonia and 3 waters, which instead produces carbamate and H_3O^+.

In order to find the most stable nano-network configuration, carbamate and ammonium interactions with both NH_3 and H_2O were modelled. The optimised (gas-phase) structures are presented in Figure 11 (for $NH_2CO_2^-.(H_2O)_{1,2}$ structures, see Figure 1). The gas phase and aqueous binding energies for the nano-networks in Figure 11 are presented in Table VIII. See Table VI for the gas phase binding energies of $NH_2CO_2^-.nH_2O$, n = 1,2.

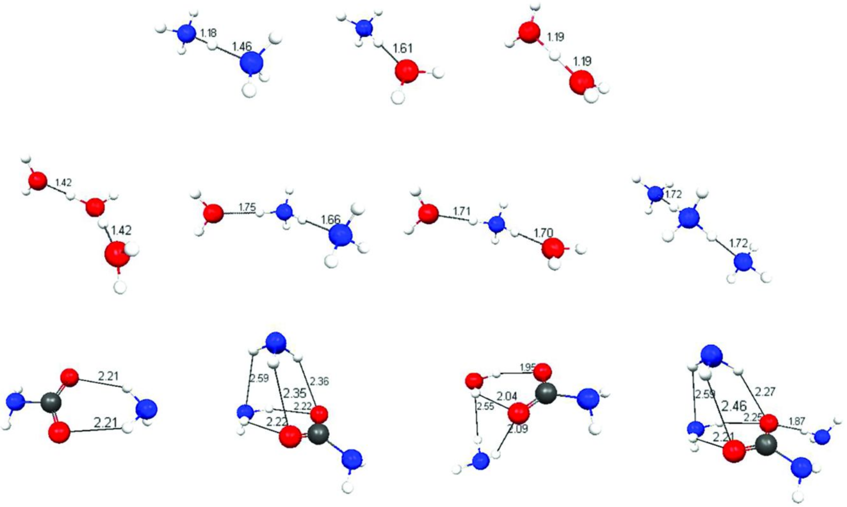

Figure 11. Optimised structures for charged nano-networks. Top row (L-R): $(NH_3)_2H^+$, $NH_3(H_2O)H^+$ and $(H_2O)_2H^+$; centre row: $(H_2O)_3H^+$, $(NH_3)_2(H_2O)H^+$, $(NH_3)(H_2O)_2H^+$ and $(NH_3)_3H^+$; bottom row: $(NH_2CO_2-)(NH_3)$, $(NH_2CO_2-)(NH_3)_2$, $(NH_2CO_2-)(NH_3)(H_2O)$, $(NH_2CO_2-)(NH_3)_3$. Bond lengths between molecules in angstrom. Blue = nitrogen atoms, white = hydrogen atoms, red = oxygen atoms. (see color insert)

Table VIII. M06-2X/6-311++G(d,p) gas phase energies (298.15 K, incl. thermal and entropy corrections, G_g), free energies of solvation and binding energies of charged solvent nano-networks (see Figure 11). Values are in kJ mol^{-1} unless stated otherwise.

Ion	*G_g (Hartree)*	*G_{soln}*	*ΔG_{rxn} :$(NH_3)_a(H_2O)_b \rightarrow aNH_3 + bH_2O$*	
			gas	*aqueous*
$NH_2CO_2^-.(NH_3)$	-301.0997145	-307.9	8.7	-19.2
$NH_2CO_2^-.(NH_3)(H_2O)$	-377.5326189	-289.9	43.2	-2.7
$NH_2CO_2^-.(NH_3)_2$	-357.6315583	-277.4	9.7	-59.6
$NH_2CO_2^-.(NH_3)_3$	-414.1624706	-266.0	8.2	-83.2
$(NH_4^+)(H_2O)$	-133.2948898	-327.3	53.8	0.3
$(NH_4^+)(NH_3)$	-113.4206639	-295.4	91.4	5.4
$(NH_4^+)(H_2O)_2$	-209.7296328	-295.2	93.2	-6.9
$(NH_4^+)(NH_3)(H_2O)$	-189.8476937	-274.5	110.3	7.5
$(NH_4^+)(NH_3)_2$	-169.9665172	-255.5	129.4	18.1
$(H_3O^+)(H_2O)$	-153.1514023	-333.0	128.7	41.7
$(H_3O^+)(H_2O)_2$	-229.5936102	-296.2	187.8	64.0

The results for ΔG_{bind} $NH_2CO_2^-(H_2O)_n$ (aq), n = 1-3, are -12.7 kJ mol^{-1}, -27.9 kJ mol^{-1} and -55.7 kJ mol^{-1}. These values, plus the results presented in Table VIII indicate that: (i) carbamate ions do not bind water or ammonia strongly in an aqueous environment, and (ii) ammonium ions bind ammonia molecules more strongly than water molecules. When considering aqueous reactants, the most stable nano-networks arise when ammonium is solvated by ammonia molecules, hydronium cation is solvated by water molecules and carbamate anion is bathed in the continuum. Optimisation within the polarised continuum may result in positive solution binding energies for some of these species with apparent 'negative' binding energies, but the effort required is not justified in this instance. The relative activation energies for carbamate decomposition are presented in Figure 12.

In the context of carbamate decomposition, it is worth discussing the relative aqueous free energies of the acid conformers. The theory predicts that *syn*-NH_2CO_2H is more stable than *anti*-NH_2CO_2H by 24.4 kJ mol^{-1}. The aqueous activation energy for the conversion *syn*-NH_2CO_2H → *anti*-NH_2CO_2H via rotation about the C-OH bond is +43.2 kJ mol^{-1}. This is noteworthy because the termolecular transition structure involving ammonia (*aa*) has an activation energy of 31.4 kJ mol^{-1} *with respect to the anti-carbamic acid reactant* (*anti*-NH_2CO_2H +

Downloaded by STANFORD UNIV GREEN LIBR on June 15, 2012 | http://pubs.acs.org
Publication Date (Web): May 3, 2012 | doi: 10.1021/bk-2012-1097.ch006

$(NH_3)_{catalyst} \rightarrow NH_3 + CO_2 + (NH_3)_{catalyst}$). We can conclude that *syn-anti* aqueous interconversion is plausible prior to decomposition to ammonia and CO_2, but it is more likely to be solvent-assisted, and only of importance at pH values which would hinder efficient CO_2 capture. With respect to the ionic reactants ($NH_2CO_2^- + NH_4^+ + (NH_3)_{catalyst}$), the *aa* pathway has an activation energy of 108.1 kJ mol^{-1}.

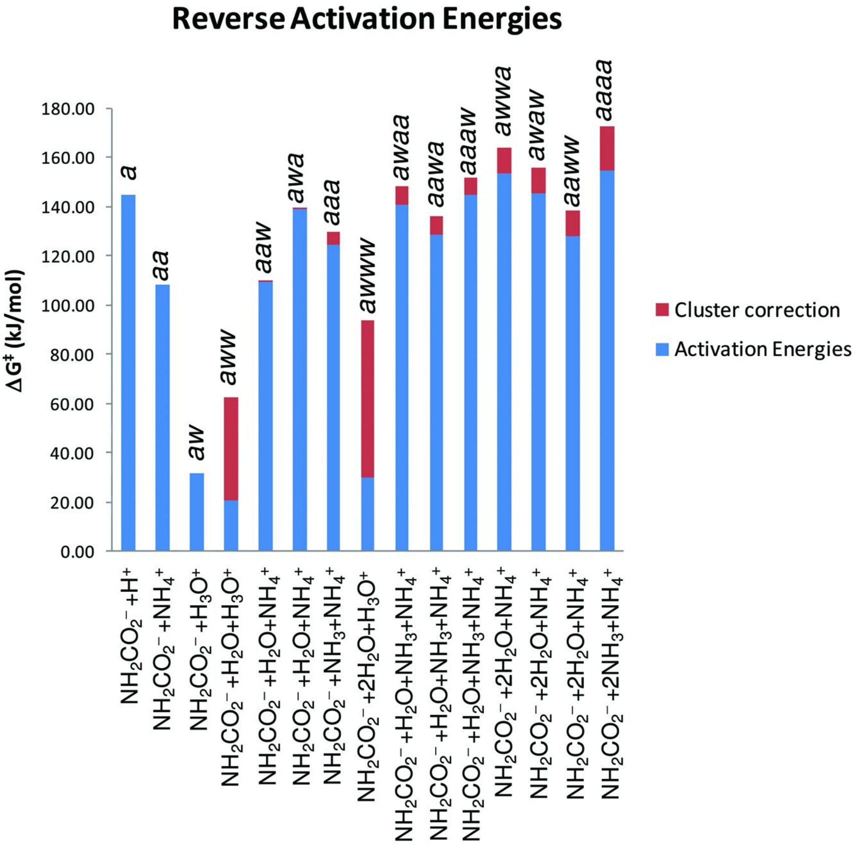

Figure 12. Reverse aqueous activation (carbamate decomposition) energies for the transition structures presented in Sections (vi)-(ix). Blue column = uncorrected activation energy; pink column = energy corrected for nano-network binding energies in solution. The x-axis labels indicate reactant stoichiometry, whereas the column label refers to the transition structures previously identified. (see color insert)

Downloaded by STANFORD UNIV GREEN LIBR on June 15, 2012 | http://pubs.acs.org
Publication Date (Web): May 3, 2012 | doi: 10.1021/bk-2012-1097.ch006

Downloaded by STANFORD UNIV GREEN LIBR on June 15, 2012 | http://pubs.acs.org
Publication Date (Web): May 3, 2012 | doi: 10.1021/bk-2012-1097.ch006

Not surprisingly, carbamate decomposition is thermodynamically more favourable when hydronium cation (H_3O^+) is involved i.e. activation via pathways with protons solvated only by water are less energy demanding, with the lowest free energy of activation corresponding to carbamate decomposition catalysed by a single water (*aw*, +31.7 kJ mol^{-1}). The theory is correctly predicting carbamate instability at low pH. The same situation has been verified experimentally for bicarbonate. At pH 9.2 - the pH at which carbamate hydrolysis has been observed (*7*) - few protons will be associated with water molecules, but the concentration of NH_4^+ will be increasing; the lowest activation energy for carbamate decomposition involving an ammonium ion (or its clustered variant) corresponds to NH_4^+ reacting directly with $NH_2CO_2^-$ to form $2NH_3 + CO_2$ (ΔG_{aq}‡ = 108.1 kJ mol^{-1}). Carbamate decomposition catalysed by both ammonium and water is almost degenerate (ΔG_{aq}‡ = 109.5 kJ mol^{-1}) and will be in competition. These values are believed to reflect the correct solution scenario for regeneration of NH_3 from $NH_2CO_2^-$ in loaded aqueous ammonia CO_2 capture solvents at high pH.

Summary

Using SM8/6-311++G(d,p)//M06-2X/6-311++G(d,p) and $SM8_{(g)}$//M06-2X/6-311++G(d,p) calculations, a number of thermodynamic values have been determined for $NH_2CO_2^-$ and NH_2CO_2H. The best values for these quantities are presented in Table IX. For comparison, $\Delta_{acid}G_{298}$ (H_2CO_3) = 1386.2 kJ mol^{-1} (*50*) and pK_a (H_2CO_3) = 5.7 (*50*). In short, the chemistry of carbamic acid will be similar to the chemistry of carbonic acid in both the gas- and solution-phases. The isolation of carbamic acid will pose experimental difficulties, and most likely will require cryogenic- or other techniques used for trapping and detecting transient species (molecular beams etc).

The most favourable energetic pathway for the capture of CO_2 by aqueous ammonia is termolecular in nature and is associated with an activation free energy of 49.2 kJ mol^{-1}, after explicit solvent nano-networks are taken into account. Further addition of either water or ammonia molecules does not lower the activation energy, which peaks at 147.7 kJ mol^{-1} when four ammonia molecules are involved. The best estimate obtained (49.2 kJ mol^{-1}) compares reasonably well with the value of 65.7 kJ mol^{-1} derived by Derks and Versteeg (*51*), but is almost twice the value (26.7 kJ mol^{-1}) derived by Diao *et. al.* (*52*).

The reaction order/molecularity in ammonia is 2 for the associated 'best estimate' TS. Note that the value determined in this work for water-catalysed (termolecular) carbamate formation is 95.3 kJ mol^{-1} (reaction order in ammonia = 1, the lowest energy pathway according to Arstad *et. al.* (*25*)). Using SM8(g)/M06-2X/6-311++G(d,p), two pathways have been identified which are energetically more favourable than water-catalysed carbamate formation (*aa* and *aaw*). Furthermore, the activation of CO_2 by three ammonia molecules represents an almost degenerate pathway (95.5 kJ mol^{-1}). This illustrates the importance of investigating as many possible pathways as is computationally feasible, even though the best estimate in this study is obtained with a synchronous Crooks-Donnellan type-transition structure involving only 3 molecules (*53*).

According to Kim *et. al.* (*26*), the best estimate (gas-phase: CCSD(T)/aug-cc-pVDZ//MP2/aug-cc-pVDZ) for the termolecular activation by two ammonias is 75.3 kJ mol^{-1}, while the water-assisted pathway is associated with an activation energy of 85.4 kJ mol^{-1} (this work: 95.3 kJ mol^{-1}). These authors claim solvation effects lower these values by ~ 45 kJ mol^{-1}, which yields $\Delta G^\ddagger$ ~ 30 kJ mol^{-1} for termolecular capture assisted by ammonia. Note that the SM8(g)//M06-2X/6-311++G(d,p) barrier in the absence of a hydrogen bonded nano-network is 34.8 kJ mol^{-1}, in reasonable agreement. It is our opinion that aqueous activation energies derived from gas-phase computations should be corrected - beyond single-point solvation free energies for participating molecules, ions and transition structures - for the disruption of the hydrogen-bonded solvent. Incorporating this correction is conceptually satisfying for either an aqueous reaction or a reaction at the gas-solution interface. Adding our hydrogen-bonding correction to Kim *et. al.*'s value produces an activation energy of 44.4 kJ mol^{-1}.

Downloaded by STANFORD UNIV GREEN LIBR on June 15, 2012 | http://pubs.acs.org
Publication Date (Web): May 3, 2012 | doi: 10.1021/bk-2012-1097.ch006

Table IX. Thermodynamic values for carbamic acid and carbamate derived from SM8 and M06-2X calculations with an augmented triple-zeta basis set.

Property	*NH_2CO_2H*	*$NH_2CO_2^-$*
H_{298} (gas)	-438.3 ± 9 kJ mol^{-1}	-515.1 ± 13 kJ mol^{-1}
S_{298} (gas)	289 J mol^{-1} K^{-1}	269 J mol^{-1} K^{-1}
G_{298} (gas)	-524.4 ± 9 kJ mol^{-1}	-595.4 ± 13 kJ mol^{-1}
$\Delta_{acid}G_{298}$	1426.6 kJ mol^{-1}	
$\Delta_{acid}H_{298}$	1453.3 kJ mol^{-1}	
PA	-	1453.3 kJ mol^{-1}
G_{soln}	-42.7 kJ mol^{-1}	-349.4 kJ mol^{-1}
G_{298} (aq)	-567.1 ± 15 kJ mol^{-1}	-944.8 ± 19 kJ mol^{-1}
H_{298} (aq)	-482.9 ± 19 kJ mol^{-1}	-864.6 ± 23 kJ mol^{-1}
$\Delta G_{syn\text{-}anti}$ (gas)	37.6 kJ mol^{-1}	
$\Delta G_{syn\text{-}anti}$ (aq)	24.4 kJ mol^{-1}	
pK_a	5.7-6.6	

Unlike CO_2 capture by pure water, the ammonia-water CO_2 capture system does not appear to rely on extensive proton shuttling by solvent catalysts to lower the activation energy. For CO_2 capture by pure water, the lowest activation energy was found for a TS involving 4 water molecules (~ 80 kJ mol^{-1} (*50*)). The results for ammonia-CO_2 capture also suggest that zwitterion models for ammonia-based CO_2 capture do not represent the true solution chemistry, and a termolecular mechanism according to Crook and Donnellan (*53*) appears to be correct for this reaction. The computation of transition structures *within* a dielectric continuum could indeed locate stable zwitterion structures, but such work is beyond the scope of this chapter.

After explicit consideration of solvent microstructure and the role of protons, the best estimate for the solvent regeneration activation free energy (carbamate reversion to ammonia and CO_2) is 108.1-109.5 kJ mol^{-1}. Acid-induced carbamate decomposition occur with much lower activation energies (31.4 kJ mol^{-1}). Carbamate activation at high pH values proceeds with proton transfer from ammonium to the -NH_2 group of carbamate (for both lowest energy pathways), confirming the crucial role of ammonium proximal to the -NH_2 group of carbamate for the decomposition process.

Downloaded by STANFORD UNIV GREEN LIBR on June 15, 2012 | http://pubs.acs.org
Publication Date (Web): May 3, 2012 | doi: 10.1021/bk-2012-1097.ch006

Acknowledgments

PJ and MIA would like to thank the Coal Portfolio and the Computational and Simulation Sciences Transformed Capability Platform (CSS-TCP) c/- Dr John Taylor, Centre for Mathematical and Information Sciences (CMIS, CSIRO) for financial support. We also would like to thank the NCI Facility (Canberra, Australia) for a generous allocation of computer time.

References

1. Chemical Industry News and Intelligence, Ammonia Uses and Market Data, 2010. URL http://www.icis.com.
2. Apodaca, L. E. U.S. Geological Survey, Mineral Commodity Summaries, January 2011. URL http://minerals.usgs.gov.
3. Chemical Market Associates Inc. Houston, Texas, USA, 2010. URL http://www.cmaiglobal.com
4. Huang, H.; Chang, S.-G.; Dorchak, T. *Energy Fuels* **2002**, *16*, 904–910.
5. Yeh, J. T.; Resnik, K. P.; Rygle, K.; Pennline, H. W. *Fuel Process. Technol.* **2005**, *86*, 1533–1546.
6. Bai, H.; Yeh, A. C. *Ind. Eng. Chem. Res.* **1997**, *36*, 2490–2493.
7. Yeh, A. C.; Bai, H. *Sci. Total Environ.* **1999**, *228*, 121–133.
8. Kim, Y. J.; You, J. K.; Hong, W. H.; Yi, K. B.; Ko, C. H.; Kim, J. N. *Sep. Sci. Technol.* **2008**, *43*, 766–777.
9. Strazisar, B. R.; Anderson, R. R.; White, C. M. *Energy Fuels* **2003**, *17*, 1034–1039.
10. Supap, T.; Idem, R.; Veawab, A.; Aroonwilas, A.; Tontiwachwuthikul, P.; Chakma, A.; Kybett, B. D. *Ind. Eng. Chem. Res.* **2001**, *40*, 3445–3450.

11. Chi, S.; Rochelle, G. T. *Ind. Eng. Chem. Res.* **2002**, *41*, 4178–4186.
12. Rooney, P. C.; DuPart, M. S.; Bacon, T. R. *Hydrocarbon Process.* **1998** (July), 109.
13. Jackson, P.; Attalla, M. I. *Rapid Commun. Mass Spectrom.* **2010**, *24*, 3567–3577.
14. Jackson, P.; Attalla, M. I. *Energy Procedia* **2011**, *4*, 2277–2284.
15. Jackson, P.; Robinson, K.; Attalla, M. I. The formation of nitrosamines in the presence of NO_x and O_2 under CO_2-capture conditions. *Proccedings of the 35th International Technical Conference on Clean Coal & Fuel Systems*; Coal Technology Association: Clearwater, FL, 2010; p 10.
16. Jackson, P.; Fisher, K. J.; Attalla, M. I. *J. Am. Soc. Mass Spectrom.* **2011**, *22*, 1420–1431.
17. Gal, E. *Chilled ammonia post-combustion CO_2 capture system – laboratory and economic evaluation results*; Report no. 1012797; EPRI: Palo Alto, CA, 2006.
18. Ciferno, J. P.; DiPietro, P.; Tarka, T. *An economic scoping study for CO_2 capture using aqueous ammonia*; Final Report; DoE/NETL, Advanced Resources International and Energetics Incorporated: Pittsburgh, PA, 2005.
19. Forward, K. Alstom and partners launch chilled ammonia capture project. *Carbon Capture J.* **2008** (2), 16.
20. You, J. K.; Park, H.; Yang, S. H.; Hong, W. H.; Shin, W.; Kang, J. K.; Yi, K. B.; Kim, J. N. *J. Phys. Chem. B* **2008**, *112*, 4323–4328.
21. Perrin, D. D. *Ionization Constants of Inorganic Acids and Bases in Aqueous Solution*, 2nd Edition; Pergamon: Oxford, UK, 1982.
22. Mani, F.; Peruzzini, M.; Stoppioni, P. *Green Chem.* **2006**, *8*, 995–1000.
23. Park, H.; Jung, Y. M.; You, J. K.; Hong, W. H.; Kim, J. N. *J. Phys. Chem. A* **2008**, *112*, 6558–6562.
24. Wen, N.; Brooker, M. H. *J. Phys. Chem.* **1995**, *99*, 359–368.
25. Arstad, B.; Blom, R.; Swang, O. *J. Phys. Chem. A* **2007**, *111*, 1222–1228.
26. Kim, D. Y.; Lee, H. M.; Min, S. K.; Cho, Y.; Hwang, I.; Han, K.; Kim, J. Y.; Kim, K. S. *J. Phys. Chem. Lett.* **2011**, *2*, 689–693.
27. Qin, F.; Wang, S.; Hartono, A.; Svendsen, H. F.; Chen, C. *Int. J. Greenhouse Gas Control* **2010**, *4*, 729–738.
28. Zhao, Y.; Truhlar, D. G. *Theor. Chem. Acc.* **2008**, *120*, 215–241.
29. Zhao, Y.; Truhlar, D. G. *Acc. Chem. Res.* **2008**, *41*, 157–167.
30. Schmidt, M. W.; Baldridge, K. K.; Boatz, J. A.; Elbert, S. T.; Gordon, M. S.; Jensen, J. H.; Koseki, S.; Matsunaga, N.; Nguyen, K. A.; Su, S. J.; Windus, T. L.; Dupuis, M.; Montgomery, J. A. *J. Comput. Chem.* **1993**, *14*, 1347–1363.
31. Bode, B. M.; Gordon, M. S. *J. Mol. Graphics Modell.* **1998**, *16*, 133–138.
32. Montgomery, J. A., Jr.; Frisch, M. J.; Ochterski, J. W.; Petersson, G. A. *J. Chem. Phys.* **1999**, *110*, 2822–2827.
33. Montgomery, J. A., Jr.; Frisch, M. J.; Ochterski, J. W.; Petersson, G. A. *J. Chem. Phys.* **2000**, *112*, 6532–6542.
34. Frisch, M. J.; Trucks, G. W.; Schlegel, H. B.; Scuseria, G. E.; Robb, M. A.; Cheeseman, J. R.; Montgomery, J. A., Jr.; Vreven, T.; Kudin, K. N.; Burant, J. C.; Millam, J. M.; Iyengar, S. S.; Tomasi, J.; Barone, V.; Mennucci, B.; Cossi, M.; Scalmani, G.; Rega, N.; Petersson, G. A.; Nakatsuji, H.;

Downloaded by STANFORD UNIV GREEN LIBR on June 15, 2012 | http://pubs.acs.org
Publication Date (Web): May 3, 2012 | doi: 10.1021/bk-2012-1097.ch006

Downloaded by STANFORD UNIV GREEN LIBR on June 15, 2012 | http://pubs.acs.org
Publication Date (Web): May 3, 2012 | doi: 10.1021/bk-2012-1097.ch006

Hada, M.; Ehara, M.; Toyota, K.; Fukuda, R.; Hasegawa, J.; Ishida, M.; Nakajima, T.; Honda, Y.; Kitao, O.; Nakai, H.; Klene, M.; Li, X.; Knox, J. E.; Hratchian, H. P.; Cross, J. B.; Bakken, V.; Adamo, C.; Jaramillo, J.; Gomperts, R.; Stratmann, R. E.; Yazyev, O.; Austin, A. J.; Cammi, R.; Pomelli, C.; Ochterski, J. W.; Ayala, P. Y.; Morokuma, K.; Voth, G. A.; Salvador, P.; Dannenberg, J. J.; Zakrzewski, V. G.; Dapprich, S.; Daniels, A. D.; Strain, M. C.; Farkas, O.; Malick, D. K.; Rabuck, A. D.; Raghavachari, K.; Foresman, J. B.; Ortiz, J. V.; Cui, Q.; Baboul, A. G.; Clifford, S.; Cioslowski, J.; Stefanov, B. B.; Liu, G.; Liashenko, A.; Piskorz, P.; Komaromi, I.; Martin, R. L.; Fox, D. J.; Keith, T.; Al-Laham, M. A.; Peng, C. Y.; Nanayakkara, A.; Challacombe, M.; Gill, P. M. W.; Johnson, B.; Chen, W.; Wong, M. W.; Gonzalez, C.; Pople, J. A. *Gaussian 03*, Revision C.02; Gaussian Inc: Wallingford, CT, 2004.

35. Irikura, K. K. In *Computational Thermochemistry: Prediction and Estimation of Molecular Thermodynamics*; Irikura, K. K., Frurip, D. J., Eds.; ACS Symposium Series 677; American Chemical Society: Washington DC, 1998; pp 402−418.
36. Higashi, M.; Marenich, A. V.; Olson, R. M.; Chamberlin, A.; Pu, J.; Kelly, C. P.; Thompson, J. D.; Xidos, J. D.; Li, J.; Zhu, T.; Hawkins, G. D.; Chuang, Y.-Y.; Fast, P. L.; Lynch, B. J.; Liotard, D. A.; Rinaldi, D.; Gao, J.; Cramer, C. J.; Truhlar, D. G. *GAMESSPLUS: A Module Incorporating Electrostatic Potential Hessians for Site–Site Electrostatic Embedding, QM/MM Geometry Optimization, Internal-Coordinate-Constrained Cartesian Geometry Optimization, Generalized Hybrid Orbital QM/MM Methods, the SM5.42, SM5.43, SM6, SM8, SM8AD, and SM8T Solvation Models, the Löwdin and Redistributed Löwdin Population Analysis Methods, and the CM2, CM3, CM4, and CM4M Charge Models into GAMESS*, Users Manual, Version 2010-2. URL http://comp.chem.umn.edu/gamessplus.
37. Remko, M.; Liedl, K. R.; Rode, B. M. *J. Chem. Soc., Faraday Trans.* **1993**, *89*, 2375–2379.
38. Linstrom, P. J., Mallard, W. G., Eds. *NIST Chemistry WebBook, NIST Standard Reference Database Number 69*; National Institute of Standards and Technology: Gaithersburg, MD, 2011. URL http://webbook.nist.gov.
39. Wenthold, P. G.; Squires, R. R. *J. Am. Chem. Soc.* **1994**, *116*, 11890–11897.
40. Meng, E. C.; Cieplak, P.; Caldwell, J. W.; Kollman, P. A. *J. Am. Chem. Soc.* **1994**, *116*, 12061–12062.
41. Jedlovszky, P.; Idrissi, A. *J. Chem. Phys.* **2008**, *129*, 164501–164507.
42. Cabani, S.; Gianni, P.; Mollica, V.; Lepori, L. *J. Solution Chem.* **1981**, *10*, 563–595.
43. Rashin, A. A.; Namboodiri, K. *J. Phys. Chem.* **1987**, *91*, 6003–6012.
44. Lee, T. J.; Taylor, P. R. *Int. J. Quantum Chem.* **1989**, *S23*, 199–207.
45. Zhao, Y.; Tischenko, O.; Gour, J. R.; Li, W.; Lutz, J. J.; Piecuch, P.; Truhlar, D. G. *J. Phys. Chem. A* **2009**, *113*, 5786–5799.
46. Wang, F.; Ma, S.; Zhang, D.; Cooks, R. G. *J. Phys. Chem. A* **1998**, *102*, 2988–2994.
47. Kelly, C. P.; Cramer, C. J.; Truhlar, D. G. *J. Phys. Chem. B* **2006**, *110*, 16066–16081.

48. Cramer, C. J.; Truhlar, D. G. *Acc. Chem. Res.* **2008**, *41*, 760–768.
49. Bryantsev, V. S.; Diallo, M. S.; Goddard, W. A., III. *J. Phys. Chem. B* **2008**, *112*, 9709–9719.
50. Nguyen, M. T.; Matus, M. H.; Jackson, V. E.; Ngan, V. T.; Rustad, J. R.; Dixon, D. A. *J. Phys. Chem. A* **2008**, *112*, 10386–10398.
51. Derks, P. W. J.; Versteeg, G. F. *Energy Procedia* **2009**, *1*, 1139–1146.
52. Diao, Y.-F.; Zheng, X.-Y.; He, B.-S.; Chen, C.-H.; Xu, X.-C. *Energy Convers. Manage.* **2004**, *45*, 2283–2296.
53. Crooks, J. E.; Donnellan, J. P. *J. Chem. Soc., Perkin Trans. 2* **1989**, *44*, 331–333.

Downloaded by STANFORD UNIV GREEN LIBR on June 15, 2012 | http://pubs.acs.org
Publication Date (Web): May 3, 2012 | doi: 10.1021/bk-2012-1097.ch006

Downloaded by STANFORD UNIV GREEN LIBR on June 14, 2012 | http://pubs.acs.org
Publication Date (Web): May 3, 2012 | doi: 10.1021/bk-2012-1097.ch007

Chapter 7

Theoretical Study of Optimal Conditions in Continuous CO_2 Capture Process Using Aqueous Ammonia Solution

S. Y. Park, C. H. Ko, J. H. Park, and J. N. Kim*

**Korea Institute of Energy Research, 102 Gajung-ro, Yuseong-gu, Kaejeon,
305- 343, Korea
*jnkim@kier.re.kr**

The mole fractions of CO_2, NH_3 and H_2O in vapor phase at equilibrium were calculated by AspenPlus. The simulation of vapor-liquid equilibrium of CO_2-NH_3-H_2O system was performed at atmospheric pressure and stripping temperature ranging from 80 to 97 °C. As a property method for thermodynamic calculation, electrolyteNRTL was used and a process library of flash was adopted for calculations of the mole fractions in vapor phase at vapor-liquid equilibrium state. Since the absorption of CO_2 depends on the regeneration of CO_2 rich absorbent, the mole fractions of CO_2, NH_3 and H_2O in vapor phase at regeneration condition were used for the selection of optimal conditions which consume lowest regeneration energy. The optimal operating conditions from theoretical studies were compared with the results of lab-scale continuous CO_2 absorption apparatus. The comparisons of theoretical study and lab-scale experiments showed that the optimal absorbent concentration was 12 wt%-NH_3 with CO_2 loading of rich absorbent below 0.4 mole-CO_2/mole-NH_3 and regeneration temperature of 90 °C.

Introduction

As global warming has become one of the most pressing issues globally, a lot of researchers has focused on CO_2 capture technologies. CO_2 capture technologies are classified into pre-combustion, oxy-combustion and post-combustion. Among

In Recent Advances in Post-Combustion CO2 Capture Chemistry; Attalla, M.;
ACS Symposium Series; American Chemical Society: Washington, DC, 2012.

Downloaded by STANFORD UNIV GREEN LIBR on June 14, 2012 | http://pubs.acs.org
Publication Date (Web): May 3, 2012 | doi: 10.1021/bk-2012-1097.ch007

various technologies for post-combustion, chemical absorption is known to be the most promising approach for the separation method of CO_2 from gas mixtures having a low partial pressure of CO_2, such as flue gas, and various studies in this area have been carried out. The most commonly used absorbents for CO_2 capture are aqueous solutions of alkanolamines such as monoethanolamine (MEA), diethanolamine (DEA), diisopropanolamine (DIPA) and methyldiethanolamine (MDEA) (*1*, *2*), and these single alkanolamines are competing with sterically hindered amines such as 2-amino-2-methyl-1-propanol (AMP) (*3*, *4*). Blends of alkanolamines and sterically hindered amines also have been widely studied, yielding data on solubility, mass transfer, and reaction kinetics (*5*, *6*).

Alternative process using aqueous NH_3 solution is known to offer notable advantages, such as low regeneration energy, cost and undesired material generation in absorbent, over conventional amine-based CO_2 capture technologies, and research on CO_2 capture has been actively conducted (*7–11*). Vapor-Liquid-Solid-Equilibrium (VLSE) and Vapor-Liquid-Equilibrium (VLE) of the CO_2-NH_3-H_2O system were studied under various conditions (*12–15*). The solubility of CO_2 and NH_3 in H_2O was modeled, correlated using the Pitzer model, and the interaction parameters were identified. Based on research of the CO_2-NH_3-H_2O system, the absorption and regeneration of CO_2 in a semi-batch reactor were studied, and researches on the reaction kinetics of CO_2 in an aqueous ammonia solution was carried out using various concentrations of aqueous ammonia solutions. Furthermore, various studies (*16–21*) on the development of a commercial CO_2 capture process using aqueous NH_3 solution have been conducted.

The objective of this study is to suggest a method for selection of optimal conditions such as CO_2 loading of a rich absorbent, regeneration temperature, and NH_3 concentration of the absorbent. In this work, CO_2 removal efficiency is measured in a continuous lab-scale CO_2 capture process with various operating conditions such as regeneration temperature and flow rates of feed gas and absorbent. The method is derived from a comparison of experimental results with a theoretical approach using mole fractions of CO_2, NH_3, and H_2O in the vapor phase at vapor-liquid equilibrium.

Experiments & Methods

This section describes experimental apparatus, materials, and method for preparation, operation and analysis.

Lab-Scale Continuous CO_2 Capture Apparatus

The experimental apparatus consists of CO_2 absorber, CO_2 stripper, washing columns for CO_2 absorber and stripper, wash water regenerator and heat exchangers for cooling and heat exchange. A schematic diagram of the continuous CO_2 capture apparatus is shown in Figure 1.

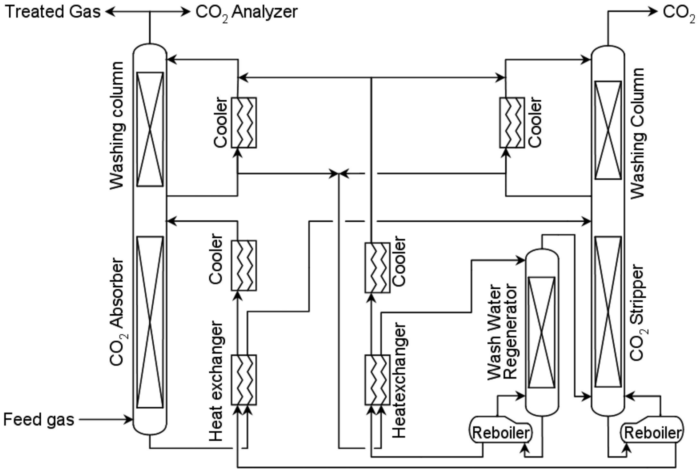

Figure 1. Schematic diagram of lab-scale continuous CO_2 capture apparatus. Reproduced from reference (22) .

Columns for CO_2 Absorber, Stripper and Wash Water Regenerator

The CO_2 absorber is made of polymethyl methacrylate (PMMA) with a diameter of 50 mm and a height of 1 m. The absorption column was directly connected to a washing column, which is made of PMMA with a diameter of 50 mm and a height of 0.5 m. In order to measure the temperature profile along the CO_2 absorber height, 10 thermocouples were installed at 10 cm intervals. The CO_2 stripper is made of glass with a diameter of 50 mm and a height of 0.5 m. It was also directly connected to a washing column, which is made of glass with a diameter of 50 mm and a height of 0.3 m. The wash water regenerator is made of glass with a diameter of 50 mm and a height of 0.3 m. All columns were packed with stainless steel wire gauze packing (Sulzer BX).

Reboilers and Heat Exchangers

Kettle type reboilers for the CO_2 stripper and the wash water regenerator are made of stainless steel and the temperatures were controlled by electric heaters immersed in liquid. The reboiler for CO_2 stripper was operated in a range of 75 to 97 °C and the reboiler for the wash water regenerator was operated at 100 °C. The liquid fed to reboiler was heated by electric heater and overflowed a weir installed beside heater and the liquid level in reboiler was controlled by level switch. When the liquid level is high, electric signal from level switch activates the solenoid valve and return the liquid to feed line. Through the action of level switch and solenoid valve, the liquid levels in absorber bottom and reboiler were kept within the interval of level switch activation.

Downloaded by STANFORD UNIV GREEN LIBR on June 14, 2012 | http://pubs.acs.org
Publication Date (Web): May 3, 2012 | doi: 10.1021/bk-2012-1097.ch007

Since the lean absorbent and wash water which generated in reboilers were hot, the heat of hot solution was recovered by the contact of rich absorbent and wash water using plate type heat exchangers (Alfanova 24-H). Also, the regenerated lean absorbent and wash water were cooled down using plate type heat exchangers (Alfanova 24-H).

Absorbent

The concentrations of the absorbent were adjusted to 3, 6, 12, 20, and 27 wt% NH_3 by mixing a commercial grade aqueous NH_3 solution (Samcheon, Korea) with distilled water. The fresh absorbent, which not contain CO_2 in liquid is circulated between absorber and stripper without reboiler heating at the flow rate of 100 mL/min until the experimental apparatus reach steady-state of flow rate and liquid level. After the steady-state of liquid stream, the flow rates were controlled to 50, 100, 150, 200 and 250 mL/min at 20 °C with supplying different flow rates of gas stream.

Feed Gas

The feed gas was prepared by mixing of pure CO_2 and dry air. The concentration of CO_2 was adjusted to 10 vol% by mass flow controllers (Brooks Instrument 5850E) and supplied to the absorber with flow rates of 1, 2, and 3 m_3/hr at ambient temperature.

The concentration of CO_2 in the gas stream was measured by a CO_2 gas analyzer (IR gas analyzer, Fuji Electronics). All used data were collected at a steady-state of continuous operation and the removal efficiencies of CO_2 were obtained from the following equation.

$$\eta_{CO_2} = \frac{\left(V_{CO_2,in} - V_{CO_2,out}\right) \times 100\ \%}{V_{CO_2,in}}$$

where, η_{CO_2} : CO_2 removal efficiency
$V_{CO_2,in}$: intlet volume of CO_2
$V_{CO_2,out}$: outlet volume of CO_2

Wash Water

Wash water for washing columns above the absorber and the stripper were continuously circulated with a flow rate of 150 mL/min. The temperature of circulated wash water was kept at 8 °C by wash water cooler. The wash water from wash water regenerator was supplied to the circulation loops, which are located above the absorber and stripper, with flow rates of 50 and 100 mL/min

Downloaded by STANFORD UNIV GREEN LIBR on June 14, 2012 | http://pubs.acs.org
Publication Date (Web): May 3, 2012 | doi: 10.1021/bk-2012-1097.ch007

Downloaded by STANFORD UNIV GREEN LIBR on June 14, 2012 | http://pubs.acs.org
Publication Date (Web): May 3, 2012 | doi: 10.1021/bk-2012-1097.ch007

at 8 °C, respectively. The same amount of wash water was separated from the circulation loop and returned to the wash water regenerator.

NH_3 Concentration and CO_2 Loading of Absorbent

The concentrations of NH_3 and CO_2 in liquids were measured by acid-base titration method. All chemicals used in the titration were reagent grade (SigmaAldrich). All liquid samples of 10 mL were mixed with 20 mL of 1 N NaOH and 1 N $BaCl_2$ aqueous solution as a pretreatment. The treated samples were analyzed by automatic titration facility (848 TitrinoPlus, Metrohm), which measures pH variance with the addition of aqueous solution of 1 N HCl at 2 °C.

The amounts of NH_3 and CO_2 in the liquid samples were calculated by the following equation and titration results.

$$m_{CO_2} = \frac{N_{HCl}\left(V_{HCl,2} - V_{HCl,1}\right)}{2000}$$

$$m_{NH_3} = \frac{N_{HCl} \times V_{HCl,2}}{1000} - \frac{N_{NaOH} \times V_{NaOH}}{1000}$$

where, m_{CO_2} and m_{NH_3} : moles of CO_2 and NH_3 in liquid
N_{HCl} and N_{NaOH} : normality of HCl and NaOH
$V_{HCl,1}$ and $V_{HCl,2}$: volume (mL) of HCl used for 1st and 2nd titration

Calculation of Mole Fractions of CO_2 and NH_3 in Vapor Phase at Vapor Liquid Equilibrium State

A method for selection of optimal regeneration temperature was studied by the comparison of experimental results and calculated mole fractions of CO_2 and NH_3 in vapor phase. The performance of a continuous CO_2 capture process depends on the regeneration of rich absorbents. In order to identify the behaviors of regeneration, the mole fractions of CO_2 and NH_3 in the vapor phase were calculated using AspenPlus.

Components

CO_2, NH_3 and H_2O were selected as the main components for simulation and the electrolytes formed in the reaction of main components were generated by “Elec Wizard” based on the stored reaction mechanisms of main components. Three molecules (CO_2, NH_3 and H_2O) and six electrolyte ions (NH_4^+, NH_2COO^-, HCO_3^-, CO_3^{2-}, H^+ and OH^-) were included as components for calculation.

Downloaded by STANFORD UNIV GREEN LIBR on June 14, 2012 | http://pubs.acs.org
Publication Date (Web): May 3, 2012 | doi: 10.1021/bk-2012-1097.ch007

Properties

Properties of components were calculated by the thermodynamic model which selected in input stage. “ELECNRTL” was selected as the property method for simulation. This property method uses ElectrolyteNRTL model which is an activity coefficient model for calculation of liquid phase and Redlich-Kwong model which is an EOS (equation of state model) for calculation of vapor phase.

Streams

Material streams were consists of liquid feed to “FLASH” unit operation, liquid and vapor streams from “FLASH” unit operation. The temperature and pressure of liquid feed were inputted as the same conditions of experiments at which calculate mole fractions of CO_2 and NH_3. Compositions of CO_2, NH_3 and H_2O were calculated by Excel solver and the constraints of solver were satisfying NH_3 concentration in solution and CO_2 loading of vapor-liquid equilibrium experimental data.

Blocks

The mole fractions of CO_2 and NH_3 at equilibrium were calculated using “Flash” unit operation in “Separators” process library. The temperature and pressure of experiments for vapor-liquid equilibrium were consists of the flash specification of unit operation. After running the unit operation of flash, the mole fractions of CO_2 and NH_3 shown in “Phase Equilibrium” were used in this study.

Results and Discussion

Experiments of continuous CO_2 absorption-desorption using lab-scale experimental apparatus were performed under various operating conditions, and a method to select the optimal regeneration temperature of continuous CO_2 capture system was studied by theoretical approach.

Continuous Operation of Lab-Scale CO_2 Capture Process

Effect of NH_3 Concentration

Figure 2 shows the effect of NH_3 concentration on CO_2 removal efficiency. The continuous experiments were performed under absorbent flow rates range from 50 to 250 mL/min and feed gas flow rate range from 1 to 3 m^3/hr. The rich absorbent which has high CO_2 loading after CO_2 absorption was regenerated at 85 °C. Depending on the flow rate of absorbent, CO_2 removal efficiencies rapidly increase up to the range from 45 to 93 % as the NH_3 concentration increases until 12 wt%. Under the same operating conditions, the removal efficiencies remained nearly constant above this concentration. Therefore, it can be said that the removal efficiency was not affected by NH_3 concentrations above 12 wt%.

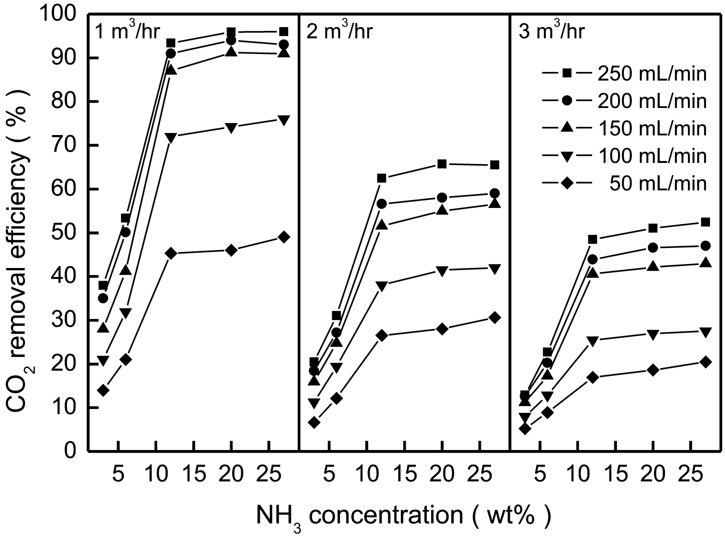

Figure 2. Effect of NH_3 concentration on CO_2 removal efficiency. Reproduced from reference (22).

Effect of Absorbent Flow Rate and Feed Gas Flow Rate

Figure 3 shows the effect of the absorbent flow rate on CO_2 removal efficiency. The removal efficiency increases as the absorbent flow rate increases. In the case of NH_3 concentration above 12 wt%, the removal efficiency increases until 150 mL/min and shows a relatively slow increase above this flow rate. A similar change of the removal efficiency occurs between 150 and 200 mL/min when the NH_3 concentration is below 6 wt%. For all absorbent flow rates, the removal efficiency is similar with NH_3 concentrations above 12 wt% and clearly different and lowered below this NH_3 concentration.

Based on the results in Figure 3, it can be said that the removal efficiency increases as the flow rate of absorbent increases. However, the increased absorbent flow rate needs the increased reboiler heat duty and consequently needs increased cooling heat duty for CO_2 stripper washing column. In the continuous operation using lab-scale experimental apparatus, the operation under absorbent flow rate above 250 mL/min was failed because of much more cooling duty than apparatus limit. In all other experiments, the flow rate of absorbent was maintained at 150 mL/min for stable operation. Figure 3 also shows the effect of feed gas flow rate on CO_2 removal efficiency. The results of experiments under feed gas flow rates of 2 and 3 m^3/hr reveal lowered removal efficiency than that at a feed rate of 1 m^3/hr, however, the same tendency of the removal efficiency is observed at the same NH_3 concentration and absorbent flow rate as those of 1 m^3/hr. These results

In Recent Advances in Post-Combustion CO2 Capture Chemistry; Attalla, M.;
ACS Symposium Series; American Chemical Society: Washington, DC, 2012.

Downloaded by STANFORD UNIV GREEN LIBR on June 14, 2012 | http://pubs.acs.org
Publication Date (Web): May 3, 2012 | doi: 10.1021/bk-2012-1097.ch007

Downloaded by STANFORD UNIV GREEN LIBR on June 14, 2012 | http://pubs.acs.org
Publication Date (Web): May 3, 2012 | doi: 10.1021/bk-2012-1097.ch007

indicate that the removal efficiency depends on the flow rate and is more dependent on NH_3 concentration reflecting the general behavior of gas absorption in a liquid. This means that NH_3 concentration higher than 12 wt% does not affect the removal efficiency. Therefore, the optimal NH_3 concentration is 12 wt% as shown in Figure 2 and 3.

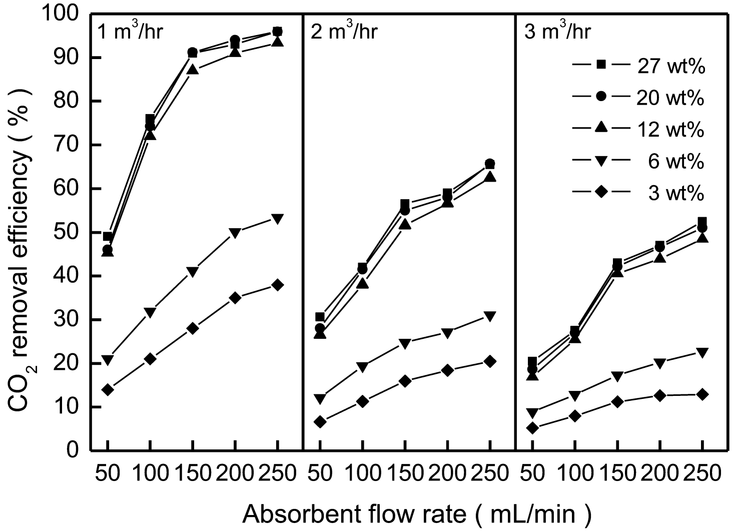

Figure 3. Effect of absorbent flow rate on CO_2 removal efficiency. Reproduced from reference (22).

Effect of Regeneration Temperature

CO_2 removal efficiency is directly depends on the absorption of CO_2 into CO_2 lean absorbent, which regenerated in CO_2 stripper. Therefore, the regeneration of CO_2 rich absorbent is directly related to generation of CO_2 lean absorbent and consequently to CO_2 removal efficiency.

In order to investigate the effect of regeneration temperature, CO_2 removal efficiencies were measured under various reboiler temperatures and NH_3 concentration, and showed in Figure 4.

As the regeneration temperature increases, the removal efficiency increases with a sigmoidal shape; it thereafter shows a rapid increase to the maximum value and remains nearly constant. The temperatures at which CO_2 removal efficiency changes from a rapid increase to a steady value were 87 °C for 15 wt%-NH_3, 90 °C for 12 wt%-NH_3, 93 °C for 9 wt%-NH_3, 95 °C for 6 wt%-NH_3 and 97 °C for 3 wt%-NH_3. This means that the temperature at which the removal efficiency reaches a nearly constant is the optimal regeneration temperature and it depends on NH_3 concentration

Downloaded by STANFORD UNIV GREEN LIBR on June 14, 2012 | http://pubs.acs.org
Publication Date (Web): May 3, 2012 | doi: 10.1021/bk-2012-1097.ch007

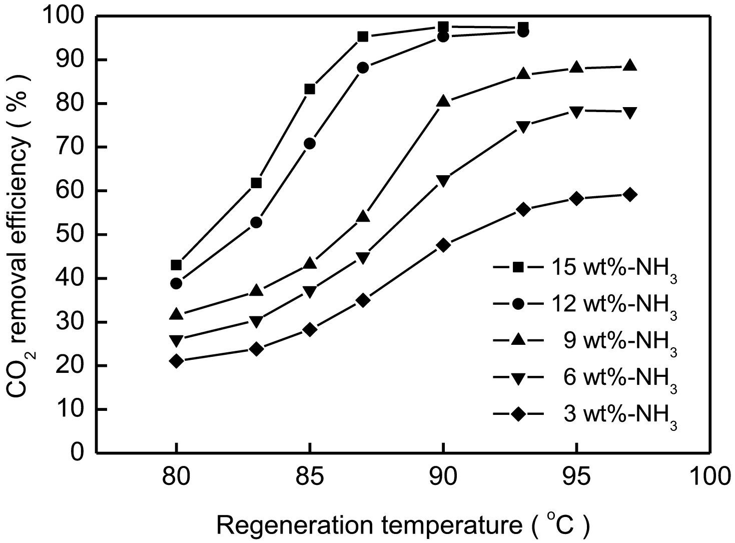

Figure 4. Effect of regeneration temperature on CO_2 removal efficiency. Reproduced from reference (22).

Considering the operation of continuous CO_2 capture in view of regeneration system, in can be said that the regeneration at higher than optimal temperature condition consumes additional energy than that for optimal regeneration. The operation using an absorbent of low NH_3 concentration for the prevention of NH_3 loss in treated gas reduces CO_2 absorption capacity and consequently increase the capital cost due to increased equipment size. Therefore, the selection of optimal NH_3 concentration and regeneration temperature is important for process design and efficient operation.

Effect of Regeneration Temperature on CO_2 Loading of Rich Absorbent

The effect of regeneration temperature on CO_2 loading was investigated by measuring the amount of CO_2 and NH_3 dissolved in the absorbent. Figure 5 shows the CO_2 loadings for lean and rich absorbents. The experiments were performed at feed gas flow rate of 1 m^3/hr, absorbent flow rate of 150 mL/min and NH_3 concentration of 12 wt%.

As the regeneration temperature increases, CO_2 loadings for lean and rich absorbents decrease but the difference in CO_2 loading increases. These results agree well with those in Figure 4. At regeneration temperature above 90 °C, the steady removal efficiency of 12 wt%-NH_3 and CO_2 loading of absorbents are nearly constant. This means that regeneration at low temperature produces a lean absorbent, of which CO_2 loading is relatively high. Furthermore, it leads to a small CO_2 loading difference between lean and rich absorbents and consequently low removal efficiency. CO_2 loadings for rich absorbents with other NH_3 concentrations range from 0.35 to 0.38 and are listed in Table I.

Downloaded by STANFORD UNIV GREEN LIBR on June 14, 2012 | http://pubs.acs.org
Publication Date (Web): May 3, 2012 | doi: 10.1021/bk-2012-1097.ch007

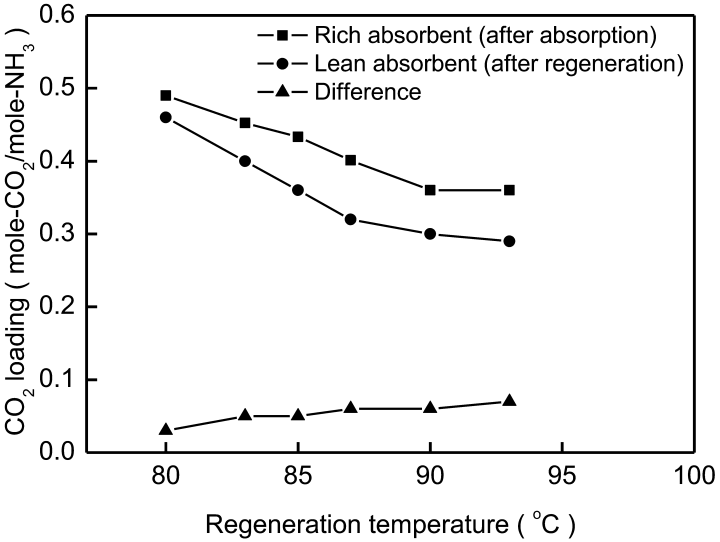

Figure 5. CO_2 loadings for lean and rich absorbents under various regeneration temperatures. Reproduced from reference (22).

Through the continuous CO_2 capture experiments, it was found that the removal efficiency depends on the operation parameters such as regeneration temperature, NH_3 concentration and CO_2 loadings for rich absorbents. A method to select the optimal operation parameters is theoretically studied in the following section.

Theoretical Approach for Optimal Operating Condition Selection

The selection of optimal condition is important for design and operation of CO_2 absorption process using aqueous NH_3 solution. Even optimal conditions for process could be selected from the actual operating experiences, these need a lot of operating cost and time consuming. Therefore, a method which can predict optimal conditions without actual operation will be useful for the saving of operation cost and efforts.

As a basis for the development of method which can be used for the selection of optimal operating conditions in continuous CO_2 absorption process using aqueous NH_3 solution, a theoretical approach was performed by the consideration of preferred regeneration condition and calculation of mole fractions of CO_2 and NH_3 in vapor phase at equilibrium.

Preferred Regeneration Condition

The preferred condition for better CO_2 absorption in continuous process which consists of absorption and desorption was considered in view of regeneration. In

Downloaded by STANFORD UNIV GREEN LIBR on June 14, 2012 | http://pubs.acs.org
Publication Date (Web): May 3, 2012 | doi: 10.1021/bk-2012-1097.ch007

continuous CO_2 capture process, CO_2 lean absorbent contacts with CO_2 containing gas stream and becomes CO_2 rich absorbent by the absorption of CO_2. CO_2 rich absorbent is transferred to CO_2 stripper where CO_2 is desorbed and CO_2 rich absorbent is regenerated to CO_2 lean absorbent. CO_2 rich absorbent is fed and flows downward to reboiler which installed at the bottom of CO_2 stripper. The regeneration of CO_2 rich absorbent is carried out during the flow down in CO_2 stripper at high temperature. The temperature needed for regeneration of CO_2 rich absorbent is kept by vapors at high temperature vapors, which evaporated from reboiler. The regeneration of CO_2 rich absorbent is directly related to the operating temperature of CO_2 stripper which derived by the vapors generated from reboiler. Therefore, the operation temperature of reboiler which generates high temperature vapor needed for the regeneration of CO_2 rich absorbent.

The estimation of regeneration temperature, that is operation temperature of regenerator, would be useful for the operation of continuous CO_2 capture process using an aqueous NH_3 solution. The basis for a theoretical method to estimate this operating condition was considered in view of the mole fractions of vapor components at equilibrium. The considerations were summarized in Figure 6. Figure 6 (a) describes the case that mole fraction of CO_2 in vapor phase at equilibrium state is larger than that of NH_3 and (b) describes the opposite case.

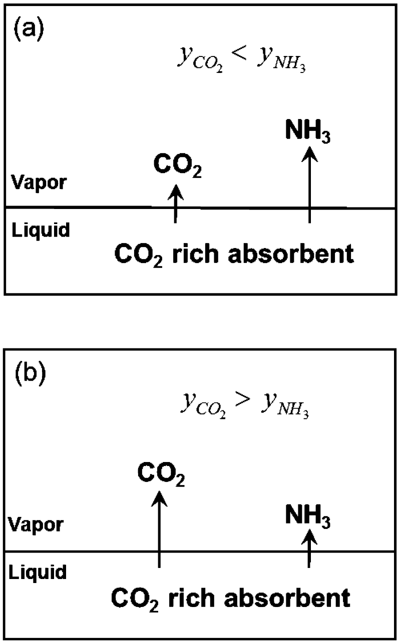

Figure 6. Schematic diagram for consideration of preferred regeneration condition.

Downloaded by STANFORD UNIV GREEN LIBR on June 14, 2012 | http://pubs.acs.org
Publication Date (Web): May 3, 2012 | doi: 10.1021/bk-2012-1097.ch007

When CO_2 rich absorbent is fed to CO_2 stripper and reboiler, the condition of rich absorbent changes until it reaches the equilibrium condition at the temperature of reboiler. The conditions of rich absorbent at actual operation are opposite conditions of rich absorbent at equilibrium. Therefore, the equilibrium condition at operating temperature determines the regeneration of rich absorbent and CO_2 desorption. In case that mole fraction of CO_2 in vapor phase at equilibrium is larger than that of NH_3 in vapor phase at equilibrium, the mole fraction of CO_2 in vapor phase at actual operating condition is smaller than that of NH_3 in vapor phase at actual operating condition. Since the mole fraction of CO_2 in vapor phase at actual operating condition is smaller than that of NH_3, the amount of CO_2 in vapor phase is larger than that of NH_3 at actual operating condition. This means that the amount of desorbed CO_2 is small to keep the mole fraction of CO_2 in vapor phase at actual operating condition is smaller than that of NH_3. As the amount of desorbed CO_2 is decreased, CO_2 loading of regenerated absorbent is increased and consequently, it reduces the amount of absorbed CO_2. In case that mole fraction of CO_2 in vapor phase at equilibrium state is smaller than that of NH_3, the regeneration operates to make that mole fraction of CO_2 in vapor phase at actual operating condition is smaller than that of NH_3. This means that proper desorption of CO_2 occurs and CO_2 absorption is increased by the decreased CO_2 loading of regenerated absorbent. It could be expected that the temperature, where mole fraction of NH_3 in vapor phase at equilibrium state is larger than that of CO_2, is preferred for the regeneration of rich absorbent.

Theoretical Study To Select the Optimal Operation Parameters

Figure 7 shows the calculated mole fractions of CO_2 and NH_3 in the vapor phase at vapor-liquid equilibrium of different CO_2 loadings and temperatures under atmospheric pressure. CO_2 loadings of 0.3, 0.36, 0.38 and 0.4 for Figure 7 (a), (b), (c) and (d) respectively. The calculations were performed using NH_3 concentration of 12 wt%, property method of ElectrolyteNRTL and process model of FLASH for vapor-liquid equilibrium.

As the temperature increases, the mole fractions of CO_2 and NH_3 decrease and then remain steady above 95 °C. The steady state mole fractions of CO_2 and NH_3 above this temperature can be explained by the evaporation of H_2O. Because the vapor pressure of H_2O is relatively small at low temperature, the mole fractions of CO_2 and NH_3 are high and become steady when the vapor pressure of H_2O is relatively high at high temperature. As shown in Figure 7 (a), the mole fraction of CO_2 in the vapor phase is higher than that of NH_3 until 84 °C. The temperature at which the mole fraction of CO_2 is higher than that of NH_3 increases as CO_2 loading increases. This temperature is 87 and 93 °C for CO_2 loading of 0.36 and 0.38 respectively, as shown in Figures 7 (b) and (c). The calculation results show the same behavior when CO_2 loading is below 0.4 and the mole fraction of CO_2 is higher than that of NH_3 when CO_2 loading is above 0.4 regardless of NH_3 concentration.

As the regeneration proceeds in continuous process, the rich absorbent moves to the equilibrium state of the regeneration system. In order to correlate the results in Figure 7 with the behavior of regeneration, the reactions of CO_2-NH_3-H_2O system are considered.

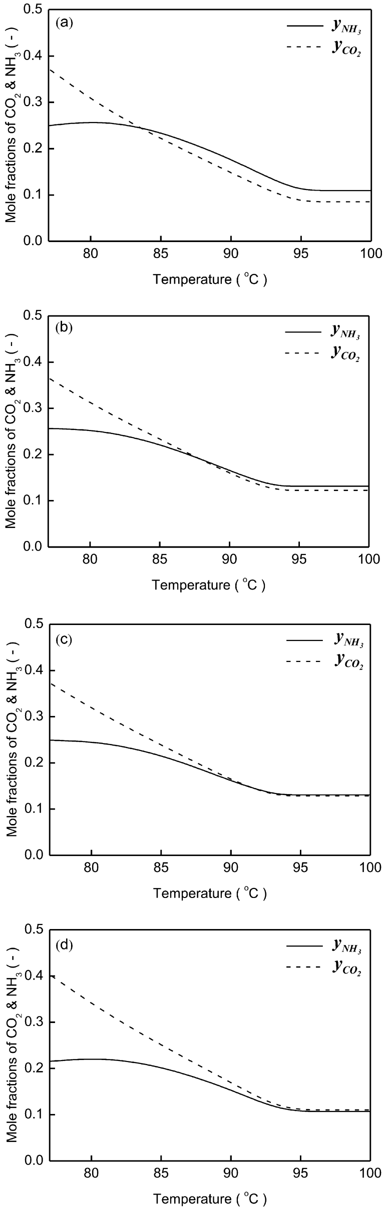

Figure 7. Calculated mole fractions of CO_2 and NH_3 in vapor phase at vapor-liquid equilibrium under CO_2 loading of (a) 0.3 and (b) 0.36. Calculated mole fractions of CO_2 and NH_3 in vapor phase at vapor-liquid equilibrium under CO_2 loading of (c) 0.38 and (d) 0.4. Reproduced from reference (22).

Downloaded by STANFORD UNIV GREEN LIBR on June 14, 2012 | http://pubs.acs.org
Publication Date (Web): May 3, 2012 | doi: 10.1021/bk-2012-1097.ch007

Downloaded by STANFORD UNIV GREEN LIBR on June 14, 2012 | http://pubs.acs.org
Publication Date (Web): May 3, 2012 | doi: 10.1021/bk-2012-1097.ch007

The electrolyte reactions are known to be very complicated and it is thus difficult to understand the overall behaviors of absorption and desorption simultaneously. Even though individual electrolyte reactions occur in a liquid phase, the reaction of CO_2 with aqueous NH_3 solution can be said to reversibly produce ammonium carbamate (NH_2COONH_4), ammonium carbonate ($(NH_4)_2CO_3$) and ammonium bicarbonate (NH_4HCO_3) through the formation of bicarbonate (HCO_3^-), and ammonium ions (NH_4^+).

For ease of understanding, the overall reversible reactions can be simplified as given in the following formulas:

$$\begin{aligned} NH_2COONH_4 &\longleftrightarrow 2NH_3 + CO_2 \\ (NH_4)_2CO_3 &\longleftrightarrow 2NH_3 + CO_2 + H_2O \\ NH_4HCO_3 &\longleftrightarrow NH_4^+ + HCO_3^- \\ &\longleftrightarrow NH_3 + CO_2 + H_2O \end{aligned}$$

Stoichiometrically, one mole of ammonium carbamate or carbonate produces two moles of NH_3 and one mole of CO_2, whereas one mole of ammonium bicarbonate produces one mole of NH_3 and CO_2. As CO_2 absorption proceeds, the amount of ammonium bicarbonate increases through the reaction of ammonium carbamate and carbonate which formed at low and medium CO_2 loading with additionally absorbed CO_2 at high CO_2 loading.

Considering the above reactions from the viewpoint of regeneration, the regeneration of a rich absorbent entails the decomposition of carbonated ammonia to CO_2, NH_3 and H_2O. Since regeneration begins after absorption, ammonium bicarbonate that formed at high CO_2 loading is regenerated with production of the same amount of NH_3 and CO_2, at which the mole ratio of NH_3 to CO_2 in the vapor phase is approximately unity.

In continuous operation, the produced NH_3 in the vapor phase is separated at the washing column installed above the CO_2 stripper and recovered from the wash water regenerator to CO_2 stripper. Through the recovery of NH_3, the concentration of NH_3 in the rich absorbent is maintained at a constant level and the amount of NH_3 in the vapor phase becomes larger than that of CO_2. Therefore, the mole ratio of NH_3 to CO_2 is larger than unity, and this also applies even to the case of regeneration with ammonium carbamate and carbonate. Although the amounts of carbonated ammonia species in the rich absorbent are difficult to quantify, the produced moles of NH_3 are at least larger than that of CO_2. Under proper regeneration of the rich absorbent, the mole ratio of NH_3 to CO_2 in the vapor phase should be larger than unity.

Based on the above stoichiometric consideration, the preferred regeneration temperature can be inferred from the mole fractions of CO_2 and NH_3 in the vapor phase at equilibrium. As shown in Figure 7 (c) and (d), the mole fractions of CO_2 and NH_3 cross over each other at different temperatures which depend on CO_2 loading. The regeneration behavior is explained for two cases of temperature at vapor-liquid equilibrium under constant CO_2 loading and pressure. In the case of the temperature at which the mole fraction of NH_3 in vapor phase is larger than that of CO_2, the mole ratio of NH_3 to CO_2 in the vapor phase at equilibrium is

Downloaded by STANFORD UNIV GREEN LIBR on June 14, 2012 | http://pubs.acs.org
Publication Date (Web): May 3, 2012 | doi: 10.1021/bk-2012-1097.ch007

larger than unity. Because the rich absorbent moves to the state of equilibrium at the regeneration condition, the mole ratio of NH_3 to CO_2 will be the same as that for proper regeneration. On the other hand, the stoichiometrically preferred regeneration condition is not satisfied when the mole fraction of NH_3 in the vapor phase is smaller than that of CO_2. Therefore, the theoretical approach based on the vapor-liquid equilibrium and simplified overall reactions of the CO_2-NH_3-H_2O system provides a means of estimating the proper regeneration temperature and CO_2 loading for a rich absorbent.

Selection of optimal operation conditions

Based on the consideration of theoretical approach for the preferred regeneration condition, the selection of optimal operating conditions was studied in this section.

Comparison with Experimental Results

Through consideration of the mole fractions of CO_2 and NH_3 in the vapor phase at equilibrium, the regeneration temperatures at which the removal efficiency is nearly constant are compared with the calculated temperature at which the mole fraction of NH_3 is higher than that of CO_2 in the vapor phase at equilibrium under the same NH_3 concentrations and CO_2 loadings as employed in the experiments.

Table I represents comparison of temperatures where complete regeneration starts with the calculated values under the same conditions as used in the experiment. As shown in Figure 4, the removal efficiency increases rapidly and slows down to near constant as the regeneration temperature increases. For simplicity, complete regeneration is defined such that it occurs at the temperature where the removal efficiency changes from a rapid increase to a steady value. The removal efficiency is proportionally increased from 55 to 95 % as the NH_3 concentration increases from 3 to 15 wt% but CO_2 loading of the rich absorbent is nearly the same, in a range from 0.35 to 0.38, regardless of the NH_3 concentration. The temperature of complete regeneration increases as the NH_3 concentration increases and the difference between the values obtained from the experiment and calculation is within ±2 °C. Therefore, the theoretical approach can be used for the selection of regeneration temperature within the same accuracy.

Behavior above Regeneration Temperature

In addition to selection of the temperature where complete regeneration occurs, the steady removal efficiency above the regeneration temperature is also considered using the above approach. As shown in Figure 5-7, since the mole fractions of CO_2 and NH_3 are affected by the evaporation of H_2O above the regeneration temperature, the mole fraction of H_2O in the vapor phase should be considered.

Downloaded by STANFORD UNIV GREEN LIBR on June 14, 2012 | http://pubs.acs.org
Publication Date (Web): May 3, 2012 | doi: 10.1021/bk-2012-1097.ch007

Table I. Comparison of the calculated optimal regeneration temperature with experimental results. Reproduced from reference (*22*).

NH_3 concentration (wt%)	*CO_2 loading*[a] $\left(\frac{\text{mole} - CO_2}{\text{mole} - NH_3}\right)$	*Removal efficiency (%)*	*Regeneration temperature*	
			Experiment[b] *(°C)*	*Calculation*[c] *(°C)*
3	0.38	> 55	97	98
6	0.35	> 75	95	93
9	0.35	> 85	93	92
12	0.36	> 95	90	90
15	0.37	> 95	87	88

[a] CO_2 loading for rich absorbent. [b] Temperature where CO_2 removal efficiency changes from a rapid increase to a steady value in Figure 5. [c] The lowest temperature where the mole fraction of NH_3 in the vapor phase is higher than that of CO_2 at equilibrium.

As shown in Figure 5-7, when the temperature is above the regeneration temperature where the mole fraction of NH_3 in the vapor phase is higher than that of CO_2, the mole fractions of NH_3 and CO_2 decrease due to the evaporation of H_2O. Therefore, the regeneration behavior can be more accurately understood by considering the mole fraction of H_2O in the vapor phase. The regeneration critical condition is introduced and defined as the following formula:

$$\zeta_{H_2O} = \frac{y_{NH_3} - y_{CO_2}}{1 - y_{H_2O}} = \frac{y_{NH_3} - y_{CO_2}}{1 - y_{NH_3} - y_{CO_2}}$$

where ζ_{H_2O} : regeneration critical condition including H_2O evaporation
y_{NH_3} : mole fraction of NH_3 in the vapor phase at equilibrium
y_{CO_2} : mole fraction of CO_2 in the vapor phase at equilibrium
y_{H_2O} : mole fraction of H_2O in the vapor phase at equilibrium

Figure 8 shows the critical condition for regeneration under different CO_2 loading and regeneration temperature. The calculations were performed using NH_3 concentration of 12 wt%, property method of ElectrolyteNRTL and process model of FLASH for vapor-liquid equilibrium.

Downloaded by STANFORD UNIV GREEN LIBR on June 14, 2012 | http://pubs.acs.org
Publication Date (Web): May 3, 2012 | doi: 10.1021/bk-2012-1097.ch007

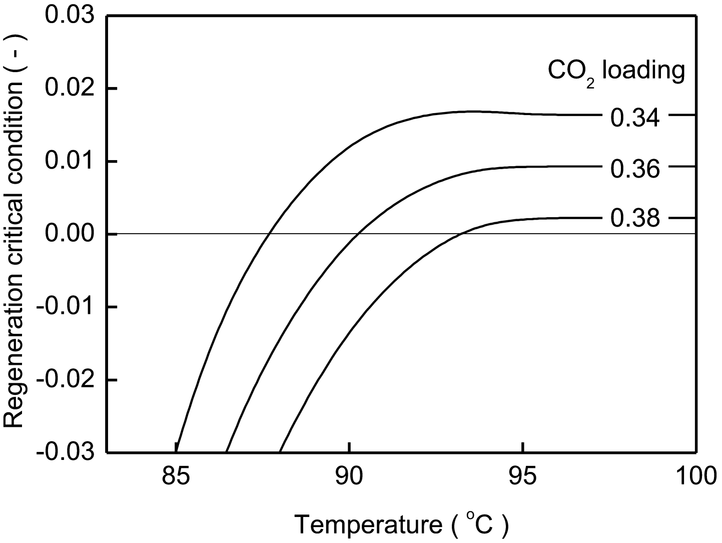

Figure 8. Calculated regeneration critical condition including H_2O evaporation. Reproduced from reference (22).

When the CO_2 loading is 0.36 for 12 wt% which is shown in Table I, the regeneration critical condition increases from negative to zero at 90 °C, 0.01 at 94 °C and remains steady above this temperature. Comparing the removal efficiency in Figure 5, the dependency of critical condition on temperature is in good agreement with that the removal efficiency. The same results are obtained for other NH_3 concentrations. This indicates that the regeneration with negative critical condition is incomplete and the regeneration with a critical condition above zero is complete. Since the regeneration is complete at high temperature but consumes extra energy by the evaporation of H_2O, the degree of regeneration and energy loss should be optimized. For this purpose, the regeneration critical condition is a useful parameter for estimation of the optimal regeneration temperature.

Selection of Optimal NH_3 Concentration

The calculation of regeneration critical condition using mole fractions of CO_2, NH_3 and H_2O is applied to select the optimal NH_3 concentration.

Figure 9 shows the calculated regeneration critical condition under different NH_3 concentrations and CO_2 loadings. The calculations were performed using regeneration temperature of 85°C, property method of ElectrolyteNRTL and process model of FLASH for vapor-liquid equilibrium.

Downloaded by STANFORD UNIV GREEN LIBR on June 14, 2012 | http://pubs.acs.org
Publication Date (Web): May 3, 2012 | doi: 10.1021/bk-2012-1097.ch007

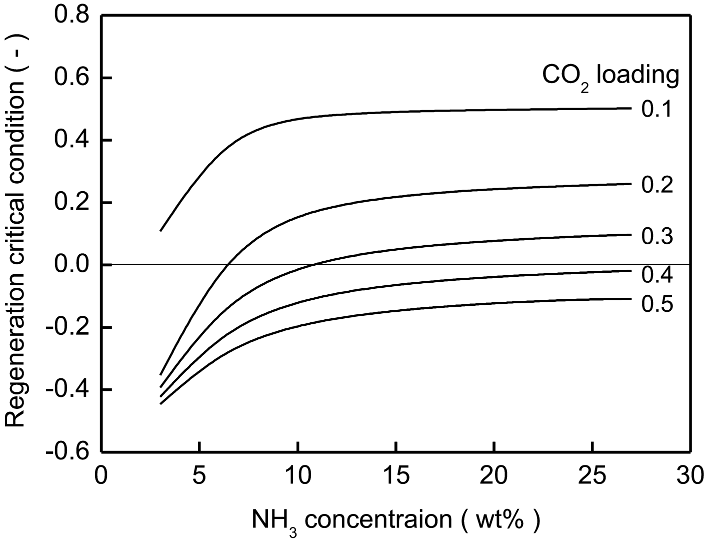

Figure 9. Calculated regeneration critical condition including H_2O evaporation at regeneration temperature of 85°C. Reproduced from reference (22).

As the NH_3 concentration increases, the regeneration critical condition increases rapidly up to 9 wt% and the rate of increase then slows down above this concentration regardless of CO_2 loading. In general, higher removal efficiency can be achieved with a higher absorbent concentration but use of a NH_3 concentration higher than a specific value does not increase the removal efficiency. In the present study, the experimental results shown in Figure 2 indicate that NH_3 concentrations above 12 wt% have little effect increasing the removal efficiency or the critical condition for regeneration. Although the dependency of the regeneration critical condition on NH_3 concentration does not precisely agree with that of the removal efficiency in Figure 2, the optimal NH_3 concentration for continuous operation can be estimated approximately by the regeneration critical condition.

Conclusions

This chapter summarizes the conclusions of the study performed. Through the continuous experiments using lab-scale CO_2 absorption-desorption apparatus and the calculations of mole fractions of CO_2 and NH_3 in vapor phase at equilibrium, a method to select the optimal operating conditions was developed.

The behaviors of continuous CO_2 capture process were studied by lab-scale experimental apparatus. CO_2 removal efficiencies using aqueous NH_3 solutions were proportionally dependent on the concentration of NH_3 in absorbent up to 12 wt% but remained nearly constant above this concentration. Although the removal efficiencies reveal proportional and disproportional dependency on flow rates of absorbent and gas respectively, the same outstanding dependency of removal efficiencies on NH_3 concentration was not observed. It could be concluded that the removal efficiency depends more on NH_3 concentration than flow rates and the optimal NH_3 concentration is 12 wt% because the removal efficiencies were not affected above this concentration. The effect of regeneration temperature on CO_2 removal efficiency and CO_2 loading were studied. As the regeneration temperature increased, the removal efficiencies were increased with sigmoidal shape. The regeneration temperatures at which CO_2 removal efficiency changes from a rapid increase to a steady value were increased as NH_3 concentration decreased and this temperature could be considered as optimal regeneration temperature, because the increased regeneration temperature without increase of CO_2 removal efficiency is only a consuming of additional energy. The optimal regeneration temperatures were 87 °C for 15 wt%-NH_3, 90 °C for 12 wt%-NH_3, 93 °C for 9 wt%-NH_3, 95 °C for 6 wt%-NH_3 and 97 °C for 3 wt%-NH_3. CO_2 loading of rich absorbent was higher than that of lean absorbent. As the regeneration temperature increase, CO_2 loadings of both absorbents were changed from rapid decrease to steady value and the increased differences of both CO_2 loadings explained increased CO_2 removal efficiencies. Through the continuous CO_2 capture experiments, it could be concluded that the removal efficiency depends on the operation parameters such as NH_3 concentration of absorbent, regeneration temperature and CO_2 loadings for rich absorbent. The optimal operating conditions were 12 wt% of NH_3 concentration, 90 °C of regeneration temperature with CO_2 loadings kept below 0.4.

A method based on behaviors of vapor components at the regeneration was developed and used for the selection of optimal operating condition for continuous CO_2 capture process using an aqueous NH_3 solution. Since the state of vapor and liquid at regeneration moves to the equilibrium state, the equilibrium conditions in regeneration determine the overall continuous CO_2 capture process. It could be understood that the regeneration of CO_2 rich absorbent prefers the condition that the mole fraction of NH_3 in vapor phase at equilibrium is larger than that of CO_2. In the preferred regeneration condition, the mole fractions of CO_2 and NH_3 in vapor phase at actual regeneration are opposite to those at equilibrium state and the mole fraction of CO_2 in vapor phase is larger than that of NH_3. The higher mole fraction of CO_2 in vapor phase at actual regeneration could be understood as better regeneration and consequently better CO_2 absorption. The regeneration of rich absorbent was reviewed in view of stoichiometry. The amounts of produced NH_3 by the decompositions of ammonium carbamate, carbonate and bicarbonate are larger than that of CO_2 and this was agreed well with the preferred regeneration condition that the mole fraction of NH_3 should be larger than those of CO_2 in vapor phase in vapor phase at equilibrium. The mole fractions of CO_2 and NH_3 in vapor phase at equilibrium were calculated using process library of “FLASH” in AspenPlus. The calculated optimal regeneration temperatures under different NH_3 concentrations were compared with those from the experimental results using continuous CO_2 capture process. The calculated optimal regeneration temperatures were agreed well with those from experimental results within ± 2 °C. The behavior of regeneration at above optimal regeneration temperature was expressed by regeneration critical condition. It showed well that the high regeneration temperature above optimal does not enhance CO_2 removal efficiency and cause additional energy consumption. It could be concluded that the method

Downloaded by STANFORD UNIV GREEN LIBR on June 14, 2012 | http://pubs.acs.org
Publication Date (Web): May 3, 2012 | doi: 10.1021/bk-2012-1097.ch007

based on calculation of mole fractions of vapor components at equilibrium agrees well with experimental results for selection of optimal operating conditions.

References

1. Chakma, A. *Energy Convers. Manage.* **1995**, *36* (6), 405–410.
2. Al-Ghawas, H. A.; Hagewiesche, D. P.; Ruiz-lbanez, G.; Sandall, O. C. *J. Chem. Eng. Data* **1989**, *34* (4), 385–391.
3. Saha, A.; Bandyopadhyay, S. *Chem. Eng. Sci.* **1995**, *50* (22), 3587–3598.
4. Bosch, H.; Versteeg, G. F.; van Swaaij, W. P. M. *Chem. Eng. Sci.* **1990**, *45* (5), 1167–1173.
5. Dey, A.; Aroonwilas, A. *Energy Procedia* **2009**, *1*, 211–215.
6. Mandal, B. P.; Bandyopadhyay, S. S. *Chem. Eng. Sci.* **2006**, *61* (16), 5440–5447.
7. Yeh, J. T.; Resnik, K. P.; Rygle, K.; Pennline, H. W. *Fuel Process. Technol.* **2005**, *86* (14−15), 1533–1546.
8. Lee, J. W.; Li, R. *Energy Convers. Manage.* **2003**, *44* (9), 1535–1546.
9. Huang, H.; Chang, S. G. *Energy Fuels* **2002**, *16* (4), 904–910.
10. Yeh, A. C.; Bai, H. *Sci. Total Environ.* **1999**, *228*, 121–133.
11. Hsunling, B.; An Chin, Y. *Ind. Eng. Chem. Res.* **1997**, *36* (6), 2490–2493.
12. Kurz, F.; Rumpf, B.; Maurer, G *Fluid Phase Equilib.* **1995**, *104*, 261–275.
13. Biling, V.; Rumpf, B.; Strepp, F.; Maurer, G G *Fluid Phase Equilib.* **1989**, *53*, 251–259.
14. Göppert, U.; Maurer, G. *Fluid Phase Equilib.* **1988**, *41* (1−2), 153–185.
15. Diao, Y. F.; Zheng, X. Y.; He, B. S.; Chen, C. H.; Xu, X. C. *Energy Convers. Manage.* **2004**, *45* (13−14), 2283–2296.
16. Darde, V.; Thomsen, K.; van Well, W. J. M.; Stenby, E. H. *Energy Procedia* **2009**, *1* (1), 1035–1042.
17. Kozak, F.; Petig, A.; Morris, E.; Rhudy, R.; Thimsen, D. *Energy Procedia* **2009**, *1* (1), 1419–1426.
18. Valenti, G.; Bonalumi, D.; Macchi, E. *Energy Procedia* **2009**, *1* (1), 1059–1066.
19. Koeijer, G.; Enge, Y. O.; Thebault, C.; Berg, S.; Lindland, J.; Overa, S. J. *Energy Procedia* **2009**, *1* (1), 1321–1326.
20. Derks, P. W. J.; Versteeg, G. F. *Energy Procedia* **2009**, *1* (1), 1139–1146.
21. Figueroa, J. D.; Fout, T.; Plasynski, S.; McIlvried, H.; Srivastava, R. D. *Int. J. Greenhouse Gas Control* **2008**, *2* (1), 9–20.
22. Park, S. Y.; Yi, K. B.; Ko, C. H.; Park, J. H.; Kim, J. N.; Hong, W. H. *Energy Fuel* **2010**, *24*, 3704–3709.

Downloaded by STANFORD UNIV GREEN LIBR on June 14, 2012 | http://pubs.acs.org
Publication Date (Web): May 3, 2012 | doi: 10.1021/bk-2012-1097.ch007

In Recent Advances in Post-Combustion CO2 Capture Chemistry; Attalla, M.;
ACS Symposium Series; American Chemical Society: Washington, DC, 2012.

Downloaded by CORNELL UNIV on June 15, 2012 | http://pubs.acs.org
Publication Date (Web): May 3, 2012 | doi: 10.1021/bk-2012-1097.ch008

Chapter 8

Tailoring Ionic Liquids for Post-Combustion CO_2 Capture

Hanming Liu,[1,2] Junhua Huang,[1,*] and Phillip Pendleton[2]

[1]Energy Technology, CSIRO, BOX 312, Clayton South, VIC 3169, Australia
[2]Center for Molecular and Materials Sciences, Sansom Institute, University of South Australia, Adelaide, South Australia 5000, Australia
[*]Corresponding author e-mail address: Jewel.Huang@csiro.au.

The anthropogenic carbon dioxide (CO_2) emissions from industries and power plants have been accepted as a dominant contributor to the recent changes in the global climate. One of the technologies that have been recently developed to tackle CO_2 emission is post-combustion capture. To meet the accelerated development in this technology, more effective absorbents are required to reduce energy consumption, capture cost, and equipment footprint in CO_2 capture processes. Ionic liquids (ILs) are regarded as potential alternative absorbents, due to their intrinsic properties, such as low volatility, low corrosivity, thermal stability, tunability, and high CO_2 affinity at elevated pressures. CO_2 solubilities in traditional ILs are relatively low under ambient conditions compared with amine-based absorbents, leading to the development of ILs bearing functional moieties or polymeric groups with improved and larger capacities for CO_2. These developments include amine groups, amino acid groups, superbases, aprotic heterocyclic anions as well as transition metal ions, promoting chemical interactions with CO_2. IL entities have also been tailored with polymerisable groups to create polymerised-ILs which are less energy intensive and highly selective in CO_2 capture processes. This chapter reviews the IL absorbents having different types of CO_2-philic groups, and discusses their reaction mechanisms with CO_2. Not all chemically modified ILs preserve the original advantageous properties of conventional ILs; some modified ILs become highly viscous

In Recent Advances in Post-Combustion CO2 Capture Chemistry; Attalla, M.;
ACS Symposium Series; American Chemical Society: Washington, DC, 2012.

while some become volatile, and some become moisture or air sensitive. Therefore, the benefits and drawbacks of using these IL absorbents for CO_2 capture are also addressed.

Introduction

Ionic liquids (ILs) are low-temperature melting salts comprising cations and anions. Owing to their exceptional properties, for example, reasonable chemical and thermal stability, relatively low corrosivity, low volatility, and physio/chemical tunability (*1–3*), ILs have become ubiquitous in the field of scientific and industrial research. Gas dissolution behaviour in ILs has constantly been an intriguing topic with great potential (*4–8*). The IL-gas phase behaviour has been studied extensively since it was reported that ILs show high solubility for CO_2 (*8*, *9*). ILs also exhibit a unique feature that gases can be dissolved in ILs selectively. In many cases, CO_2 and SO_2 can be dissolved in ILs substantially, while other gases, such as N_2, O_2, CH_4 and H_2, are poorly attracted (*10–16*). Since a great number of gas separation technologies are based on the high solubility and high selectivity of a certain gas into a liquid phase (*17*), a considerable increase in interest in ILs has occurred, whereby ILs have become a category of potential absorbents for post-combustion CO_2 capture technology.

There is a great scope for research into ILs due to the variety of cation and anion combinations (*4*, *6*). The structures of some typical cations and anions for ILs are shown in Figure 1; the list of structures shown is by no means complete. The physicochemical properties of ILs vary with their ionic structures and combinations. Gas solubilities and selectivities in ILs are important variables in their use as CO_2 absorbents. Table I shows the solubilities of different gases in some typical ILs. A low Henry's constant implies high solubility. The cationic structure of ILs has a minor effect on CO_2 absorption capacity, whereas the anions can interact with CO_2 to form a Lewis acid–base pair - the anions act as Lewis bases and CO_2 as the Lewis acid (*4*). Thus it makes anions, particularly the anions with fluorinated alkyl groups, the primay factor in determing CO_2 solubility in traditional ILs. As indicated in Table I and described elsewhere, the solubility of CO_2 follows an anion sequence of $[Tf_2N]^-$> $[PF_6]^-$> $[BF_4]^-$ (*4*, *6*, *7*). CO_2 absorption by traditional ILs follows a physical absorption mechanism where cavities between the ions accommodate the CO_2 molecules (*7*). These available cavities, which are also referred as "free volume" , determine the maximum CO_2 solubility that exhibits under extreme high pressure (*7*).

At ambient conditions, CO_2 solubility is relatively low in conventional ILs. For example, the absorption capacity for CO_2 in some favourable ILs, such as $[Emim][Tf_2N]$, $[Bmim][PF_6]$ and $[Bmim][BF_4]$, is only about 3.5 mol % (~0.4 wt %) at ambient pressure and temperature (*5*). This problem becomes especially important in post-combustion capture processes, where only 10-15 % of the flue gas is CO_2, and the CO_2 partial pressure is relatively low (*18*). Solubility can be increased by raising the pressure as ILs display considerable CO_2 absorption capacity at high pressure (*6*). This treatment however elevates capital costs.

Downloaded by CORNELL UNIV on June 15, 2012 | http://pubs.acs.org
Publication Date (Web): May 3, 2012 | doi: 10.1021/bk-2012-1097.ch008

Downloaded by CORNELL UNIV on June 15, 2012 | http://pubs.acs.org
Publication Date (Web): May 3, 2012 | doi: 10.1021/bk-2012-1097.ch008

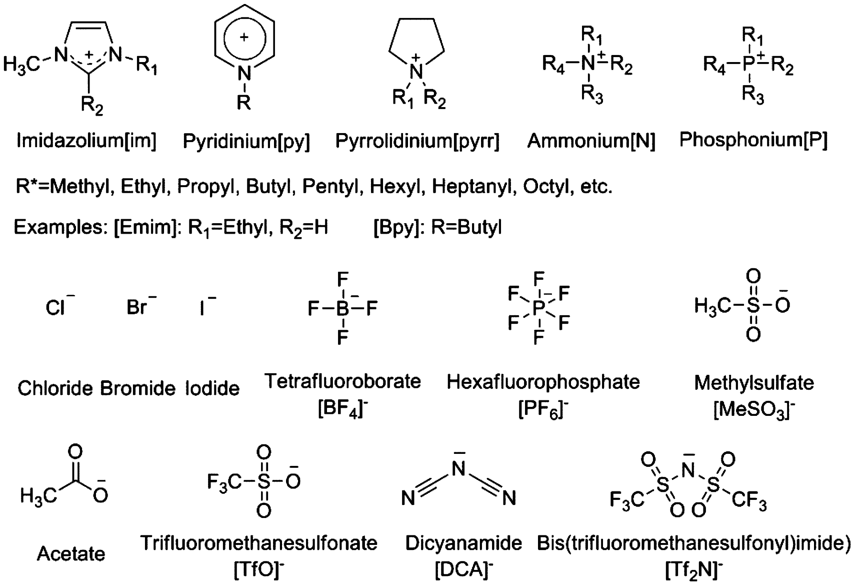
Imidazolium[im]
Pyridinium[py]
Pyrrolidinium[pyrr]
Ammonium[N]
Phosphonium[P]
R*=Methyl, Ethyl, Propyl, Butyl, Pentyl, Hexyl, Heptanyl, Octyl, etc.
Examples: [Emim]: R1=Ethyl, R2=H [Bpy]: R=Butyl
Chloride Bromide Iodide
Tetrafluoroborate [BF4]-
Hexafluorophosphate [PF6]-
Methylsulfate [MeSO3]-
Acetate
Trifluoromethanesulfonate [TfO]-
Dicyanamide [DCA]-
Bis(trifluoromethanesulfonyl)imide) [Tf2N]-

Figure 1. Cations and anions of common ionic liquids (1, 7)

Table I. Henry's Constant (bar) for gases in several traditional ILs at 25 °C

ILs	*CO_2*	*N_2*	*O_2*	*H_2*	*SO_2*	*CH_4*
[Emim][BF$_4$]] (*19*)	81.0	7194	—	8207	1.02	2938
[Emim][Tf$_2$N] (*19*)	39.5	1418	—	2634	—	587
[Bmim][BF$_4$] (*19, 20*)	59.0				1.04	2000
[Bmim][PF$_6$] (*19, 20*)	53.4	—	7190	—	1.12	1690
[Bmim][Tf$_2$N] (*19, 20*)	33.0	—	1730	—	1.10	560
[Hmim][Tf$_2$N] (*19–21*)	34.5	1013	623[a]	1824	1.64	329

[a] Data at 40 °C.

A more practical strategy is for IL structures to be altered to raise their affinity for CO_2 interactions. This approach could improve CO_2 absorption capacity and potentially make ILs, by combining with other advantageous properties, superior to the current state-of-art absorbents based on amines, such as monoethanolamine (MEA) (*22*, *23*), methyl diethanolamine (MDEA) (*22*), and diethanolamine (DEA) (*24*). One method is to incorporate, either physically or chemically, polymeric groups or functionalities exhibiting high CO_2 affinities, such as amine groups, amino acid groups, superbases, aprotic heterocyclic anions and transition metal ions (*25*). This chapter presents a review of the chemistry of CO_2 absorption by such tailored ILs, and discusses the benefits and disadvantages of these materials from a practical application's viewpoint.

Ionic Liquids Containing CO_2-philic Groups

Recently, a number of functionalised ILs bearing CO_2-philic groups showing increased CO_2 binding capacity have been reported. Unfortunately, not all of these reported absorbents can be considered as suitable for industrial applications (*7*, *26*) because ILs need to meet several important requirements for their commercial viability.

As illustrated in Figure 2, it is ideal that these functionalised ILs exhibit high CO_2 solubilities and reversible interactions with CO_2. From an energy consumption perspective, it would be appealing for functionalised ILs to interact with CO_2 through relatively weak interactions (characterised by a relatively low exothermic sorption enthalpy), so that subsequent regeneration of the absorbents can be achieved with a low energy input. This scenario would allow ILs to outperform conventional amine-based absorbents, especially since many have relatively high exothermic sorption enthalpies (> -50 $kJ \cdot mol^{-1}$) (*23*, *27*). Functionalised ILs should also exhibit high thermal stability over their operating temperature range. CO_2 desorption is an endothermic process usually requiring raised temperatures to remove the absorbed CO_2 from the absorbents (*7*). Since flue gases are emitted at elevated temperatures (*23*), it is also desirable that the absorbents possess reasonably high CO_2 solubilities even at high temperatures to avoid fuel-gas pre-cooling processes. The development of novel ionic liquids should address the above issues of current CO_2 absorption technology while retaining their advantageous properties.

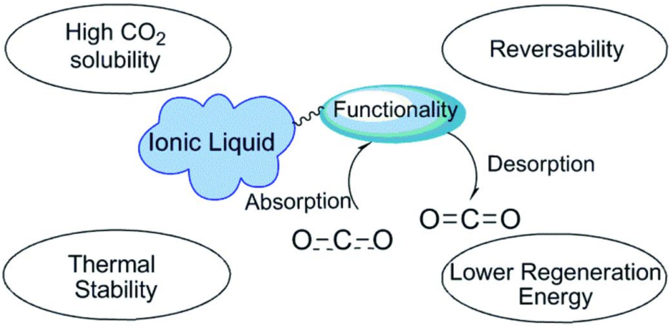

Figure 2. Requirements of ideal functionalised ILs for CO_2 capture

Amine Based Ionic Liquids

Owing to the high CO_2 solubility in amine-based solutions such as MEA (*22*), DEA (*24*), and MDEA (*22*), amine groups were one of the first reported functionalities incorporated into ILs (*28*). One simple preparation involves mixing together conventional ILs and amine. Noble et al. (*14*, *29*) demonstrated that

Downloaded by CORNELL UNIV on June 15, 2012 | http://pubs.acs.org
Publication Date (Web): May 3, 2012 | doi: 10.1021/bk-2012-1097.ch008

Downloaded by CORNELL UNIV on June 15, 2012 | http://pubs.acs.org
Publication Date (Web): May 3, 2012 | doi: 10.1021/bk-2012-1097.ch008

mixtures of room temperature ILs and commercial amines are capable of capturing CO_2 effectively. For example, a 1:1 mole ratio of MEA and [Hmim][Tf_2N] solutions absorbed 0.5 mole CO_2 per mole of MEA (≈ 4.2 wt %) at low CO_2 partial pressures, forming MEA-carbamate precipitates. A secondary amine DEA dissolved in an alcohol functionalised IL [EmimOH][Tf_2N] absorbed ≈ 0.25 mole CO_2 per mole DEA (≈ 2.2 wt %). In each case, the corresponding IL-amine solutions also absorbed CO_2 relatively quickly. These observations suggest simple physical mixing of the constituents leads to effective, functionalized ILs (*14*). However, these approaches only require high solubility of the amines in the ILs; no consideration has been taken for their thermal stability or volatility.

Other than the direct mixing, Bates et al. (*28*) were among the first to successfully incorporate amine groups with ILs by covalent bonding. They tethered a primary amine to the alkyl chain of an imidazolium cation to produce a 1-(3-aminopropyl)-3-n-butylimidazolium IL [aPbim][BF_4] for CO_2 capture, as shown in Figure 3. Based on the FT-IR and ^{13}C-NMR results, the absorption of CO_2 occurs by forming a carbamate through a reaction mechanism similar to that of primary amines (*30*), resulting in a ratio of nearly 0.5 mol CO_2 per mol IL reaction stoichiometry (*28*). The CO_2 solubility in this system was significantly increased to 7.4 wt % at 23 °C and 1 bar. The regeneration of this amine functionalised IL was made by heating under vacuum at 80-100 °C for several hours (*28*).

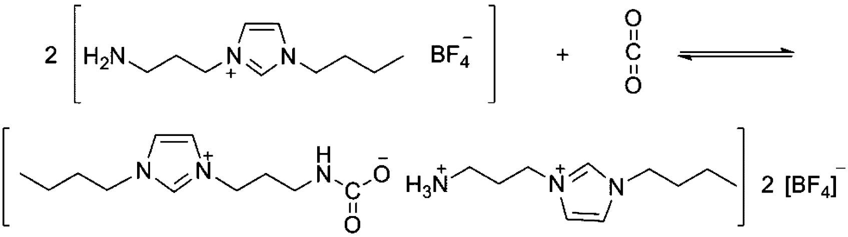

Figure 3. Proposed reaction mechanism in amine functionalised ILs with CO_2 (28)

Following this work, a series of primary and tertiary amine functionalised ILs were studied by Sanchez and coworkers (*31*). The structures of the ILs are shown in Figure 4. These amine functionalised ILs were compared with their unfunctionalised counterparts [Bmim][BF_4] and [Bmim][DCA]. The CO_2 absorption capacity for each functionalised and unfunctionalised IL increased with an increment of pressure or with a decrease of temperature. The CO_2 absorption behaviour varied significantly between the primary and the tertiary amine functionalised ILs (*31*). The primary amine tethered ILs exhibited a substantial rise in CO_2 solubility (0.16 mole CO_2 per IL, ~ 2.9 wt %) at low initial pressures (up to 1 bar), indicating a classical chemical absorption behaviour. For pressures above 1 bar, the absorption showed a linear increase with pressure, but with a reduced gradient, indicating physical absorption (*31*). In contrast, the tertiary amine functionalised ILs formed carbamates, but to a lesser extent (0.02

mole CO_2 per IL, < 0.3 wt %) due to the steric effects of the higher substituted amines.

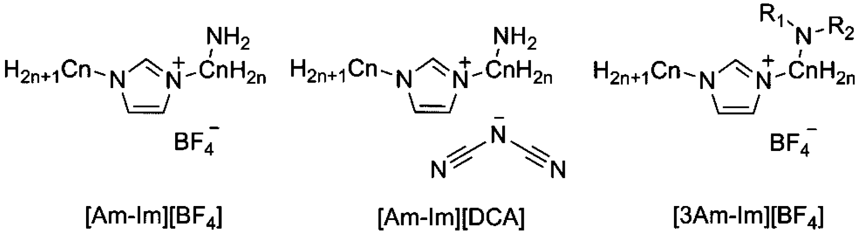

Figure 4. Functionalised ILs with amine tethered cations (31)

Downloaded by CORNELL UNIV on June 15, 2012 | http://pubs.acs.org
Publication Date (Web): May 3, 2012 | doi: 10.1021/bk-2012-1097.ch008

Amino Acid Based Ionic Liquids

The development of amino acid-derived ILs is another avenue for seeking desirable functionalised ILs for CO_2 capture. An amino acid functionality contains at least one amine group and one carboxylic group, together with various side groups and a chiral carbon atom (*32*). As illustrated in Figure 5, amino acid groups can act as cations or anions in ILs, depending on the system pH (*32*, *33*). Amino acids are natural, biodegradable, and relatively inexpensive, and have been reported to show a high affinity for CO_2 (*32*, *34*). These contributing parameters make amino acid functionalised ILs prospective candidates for CO_2 capture.

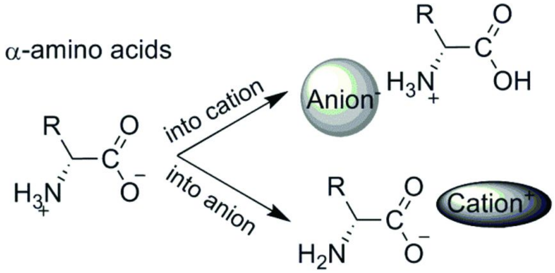

Figure 5. Design of amino acid functionalised ILs (32)

Studies have found that some amino acid-functionalised ILs tend to have more desirable CO_2 solubilities than amine functionalised ILs. Jiang et al. (*35*) incorporated amino acid anions with a symmetric tetraalkylammonium cation (Figure 6 (a)). They observed that some of these ILs, such as tetraethylammonium based $[N_{2222}]$[α–alanine] and $[N_{2222}]$[β–alanine], have viscosities of less than 200 mPa·s (*35*). A 0.43 mole ratio (8.6 wt %) of CO_2 solubility at ambient pressure and 40 °C was achieved with some of these materials. The absorption reaction mechanism is similar to that of amine functionalised ILs, i.e., nucleophilic attack onto the electrophilic carbon of CO_2 by the free base nitrogen producing a carbamic acid intermediate which requires a second amine to stabilise (*36*).

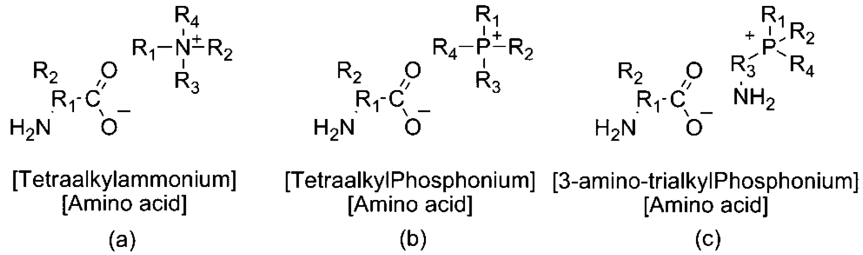

Figure 6. Functionalised ILs with amino acid anions (35–39), the selection of amino acid includes alanine, serine, glycine, lecine, valine etc.

Zhang et al. (*36*) combined natural amino acids into phosphonium ILs with their structures shown in Figure 6 (b). The amino acid IL was supported by porous silica gel in order to achieve higher CO_2 absorption/desorption rates. In the presence of approximately 1 wt % water, tetrabutylphosphonium-based [P_{4444}][glycine] IL was found to absorb up to 13.5 wt % CO_2, equivalent to a 1:1 mole ratio of CO_2:IL (*36*). The viscosity of each material was initially low. Reaction with CO_2 led to a gradual increase, resulting in highly viscous, cloudy gels (*36*). The FT-IR spectra showed a new peak at 1660 cm^{-1} in the reacted amino functionalised ILs, indicating the formation of a COOH group. As an explanation, the authors suggested that in the absence of water, the absorption occurs through carbamate formation mechanisms; in the presence of water carbonic acid forms from the reaction of H_2O and CO_2. The product is then stabilised by a proton transfer to an amine group, similar to the bicarbonate formation mechanism in amine aqueous solutions (*30*, *36*).

Zhang et al. (*37*) further explored a series of phosphonium ILs with dual amino acid groups where both the cation and the anion bear an amine moiety, as shown in Figure 6 (c). They chose (3-aminopropyl) tributylphosphonium [aP_{4443}]$^+$ as the cation since the corresponding [aP_{4443}] IL is thermally stable up to 281 °C (*37*). The CO_2 solubility in [aP_{4443}][aminoethanoic acid] ([aP_{4443}][Gly]) and [aP_{4443}][L-α-aminopropionic acid] ([aP_{4443}][Ala]) reach above 1 mol CO_2 per IL (13.9 wt%), twice that of mono amino acid functionalised ILs. The absorption by these dual amino acid functionalised ILs was reported to be repeatable up to 5 cycles without loss of absorption rate and capacity (*37*).

Recently, Gurkan et al. investigated a series of amino acid functionalised ILs with a trihexyl(tetradecyl)phosphonium [P_{66614}]$^+$ cation. The selection of amino acid anions is shown in Figure 7 (*38*, *39*). The CO_2 solubility in most of these functionalised ILs exceeded 0.5 mole ratio of CO_2 per IL at room temperature and 1 bar, approaching 1:1 mole ratio. The CO_2 solubility in [P_{66614}][Lys] and [P_{66614}][Gly] approached 1.3 mole CO_2 per IL (almost 9.1 wt %) under the same conditions (*39*). The amine group in the anion interacts with CO_2 to produce carbamate acid. The proton in the carbamate acid can either transfer to the amine group in a second amino acid anion, following a typical 1:2 carbamate formation mechanism, or it can be stabilised by a negatively charged carboxylate group. In the latter case, there is no involvement of a second anion and thus the reaction stochiometric ratio is 1:1 CO_2:IL (*39*).

Downloaded by CORNELL UNIV on June 15, 2012 | http://pubs.acs.org
Publication Date (Web): May 3, 2012 | doi: 10.1021/bk-2012-1097.ch008

Downloaded by CORNELL UNIV on June 15, 2012 | http://pubs.acs.org
Publication Date (Web): May 3, 2012 | doi: 10.1021/bk-2012-1097.ch008

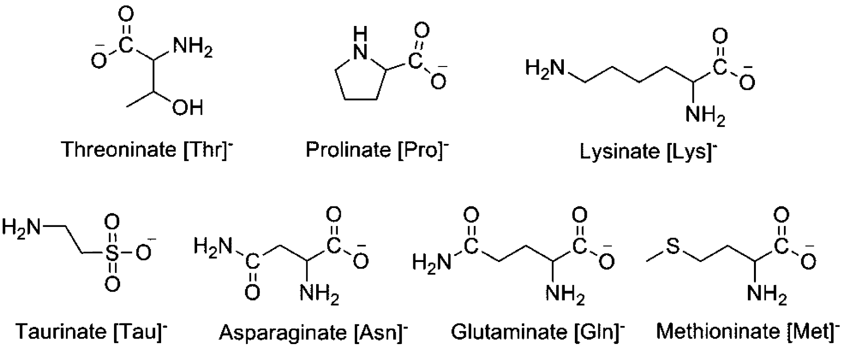
Threoninate [Thr]⁻ Prolinate [Pro]⁻ Lysinate [Lys]⁻

Taurinate [Tau]⁻ Asparaginate [Asn]⁻ Glutaminate [Gln]⁻ Methioninate [Met]⁻

Figure 7. Structures of amino acid anions used in the work by Gurkan et al. and Goodrich et al. (38, 39)

The ring structure blocks the active hydrogen atoms from generating a hydrogen bonding network and thus, the viscosity of [P_{66614}][Pro] only increases by approximately 2-fold upon complexation with almost 1:1 molar ratio of CO_2. In contrast, the viscosity of [P_{66614}][Lys] increases by 217 times to roughly 155,000 mPa·s after CO_2 absorption under the same conditions, and that of [P_{66614}][Methioninate] by 94 times, to about 30,000 mPa·s (*39*). Clearly, the results from the [P_{66614}][Pro] studies provide a valuable insight into structure development for new ILs with lower viscosities for CO_2-IL complexation.

Similar to amine functionalised ILs, all amino acid functionalised ILs mentioned above tend to have higher viscosities than their non-functionalised counterparts. The viscosity increases significantly upon complexation with CO_2, forming a gel-like substance (*40*). Additional examples include imidazolium-based amino acid functionalised ILs which have viscosities greater than 486 mPa·s (*33*), while [P_{4444}]$^+$ based amino acid functionalised ILs have viscosities higher than 344 mPa·s (*41*). From molecular simulations and *ab initio* calculations for 1-(aminoethyl)-3-methylimidazolium based [aEmim][BF_4] and [aEmim][PF_6], Yu and co-workers proposed that these inceases are due to the preferable interaction between the anion and the active –NH_2 group in the cation (*42*). This interaction forms strong ion-type hydrogen bonds, creating dense liquid structures where the motion of alkyl side chains reduces, and the interactions between cations and anions becomes ineffective (*42*). Gutowski and Maggin (*43*) further investigated [aEmim][Tf_2N] after CO_2 absorption using molecular simulation to explain the viscosity increase in CO_2-reacted amino acid functionalised ILs. Their results demonstrated that upon complexation with CO_2, the system forms a strong, compact, hydrogen-bonded network between ammonium (di-cation) and carbamate (zwitterion) species, also identified as a "salt-bridge network" (*43*). This salt-bridge network formation reduces the translational and rotational dynamics within the network, facts observed experimentally as the formation of glassy and/or gel-like materials upon contact with CO_2. Evidence of salt-bridge network formation between carbamate and ammonium tails has also been reported for other complexes (*40*, *44*).

Concerns have been raised regarding such highly viscous materials, because higher viscosities indicate lower diffusion (mass transport) efficiencies as well as extra capital costs for post-combustion CO_2 capture processes (*7*). To overcome this potential problem, selected amino acid-functionalised ILs have been coated as a thin layer of film on porous media, for example, porous silica gels (*36*, *37*) or polyethylene glycol 200 (PEG 200) (*45*). The resulting reduced gas diffusion distance significantly reduced their CO_2 absorption times.

An alternative approach is through tuning the chemical structures of ILs (*25*). For example, Jiang and co-workers (*35*) reported that the amino acid-functionalised ILs with small cations exhibited lower viscosities, e.g. 81 and 29 mPa·s for $[N_{2222}]$[α-alanine] and $[N_{2224}]$[α-alanine] at 25 °C, respectively.

Superbase Based Ionic Liquids

The effect of the basicity of ILs on CO_2 absorption was first reported by Han and co-workers (*46*). They measured the Hammett basicity function (H_-) for the four types of ILs shown in Figure 8. A higher H_--value corresponds to a higher basicity (*47*) Upon CO_2 absorption, the highly basic ILs [aEmim]$[BF_4]$ and choline chloride/urea (1:2 molar ratio) chemically interact with CO_2 to generate carbamates, accompanied by a drop in H_--values. In constrast, the less basic ILs [Bmim]$[BF_4]$ and [TMG]$[ClO_4]$ show only physical absorption (*46*). These reactions were demonstrated to be repeatable and reversible by bubbling alternately CO_2 and N_2 through the solutions.

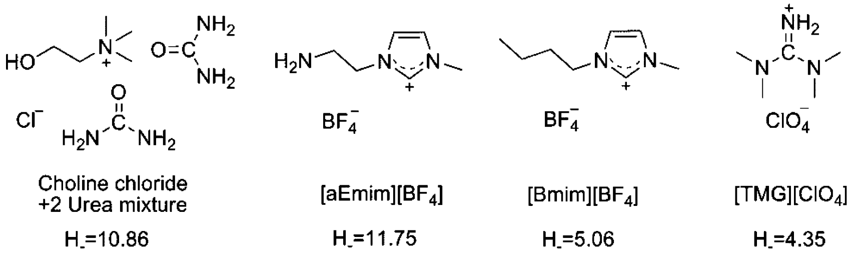

Figure 8. Structures of ILs and their basicities (46), [TMG] represents 1,1,3,3-tetramethylguanidinium

This work then led to the exploration of superbase-based ILs. A superbase is defined as a compound with an extremely high H_--value, with a high affinity for protons (*48*). Yu et al purged CO_2 through an aqueous solution containing an amino alcohol and an amidine superbase. The resulting reaction occured through a carbamate formation, with the superbase acting as the proton acceptor (Figure 9). The absorption product formed an IL which was readily separated from the aqueous phase (*49*). The CO_2 solubility in C8/LeuOH ($R1=C_8H_{17}$, ValOH=α-leucine OH in Figure 9) exceeded a 1:1 mole ratio of CO_2:amino alcohol, yielding > 16 wt % in a 60 min. contact time (*49*). This reaction was reported to be fully reversible upon exposure to a N_2 atmosphere or upon heating, with the IL reverting to its original form with minimal degradation (*49*). Although

Downloaded by CORNELL UNIV on June 15, 2012 | http://pubs.acs.org
Publication Date (Web): May 3, 2012 | doi: 10.1021/bk-2012-1097.ch008

Downloaded by CORNELL UNIV on June 15, 2012 | http://pubs.acs.org
Publication Date (Web): May 3, 2012 | doi: 10.1021/bk-2012-1097.ch008

such high absorption capacities are exciting, the amidine and amino alcohol systems retained their intrinsically high volatilities, a fact seriously limiting their commercial practicality.

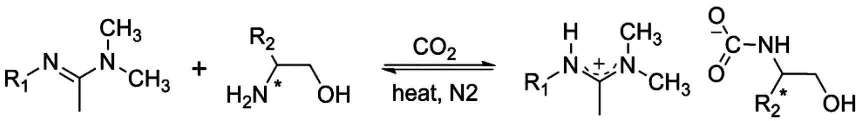

Figure 9. Reaction mechanism for amidines and chiral amino alcohols in CO_2 absorption, R_1 and R_2 are acyclic groups (49)

Dai and coworkers synthesised a family of protic ILs by mixing superbases and weak proton donors. Examples of weak proton donors used are alcohols, phenols, and imidazoles (*48*). Some of these examples are shown in Figure 10. The derived anions showed high reactivity towards CO_2 with most of these superbase-derived ILs absorbing 1 mole ratio of CO_2 (*50*). For example, the CO_2 solubility in [MTBDH][TFE] reached 1.13 mole ratio CO_2 per IL (19.6 wt %) at 1 bar and 23 °C, while [(P_2-Et)H][Pyrr] absorbed 0.92 mole ratio CO_2 (9.5 wt %). The two CO_2-reactive centres in the $[HEPD]^{2-}$ anion saw the $[MTBDH]_2[HEPD]$ system absorb > 2 mole CO_2 per IL (10.0 wt %). The reaction mechanisms for $[Im]^-$ and $[TFE]^-$ are described in Figure 11, forming carbamate or carbonate salt (*50*). Protic ILs also have significantly reduced viscosities, e.g. 9 mPa·s for [MTBDH][TFE] at room temperature. From the applications viewpoint, the high CO_2 absorption capacity and low viscosity represent a significant improvement over other modified ILs. On balance, however, these protic ILs suffer from relatively high volatility, as indicated by substantial mass loss at temperatures as low as 86 and 102 °C for [MTBDH][TFE] and [(P_2-Et)H][Pyrr], respectively (*50*).

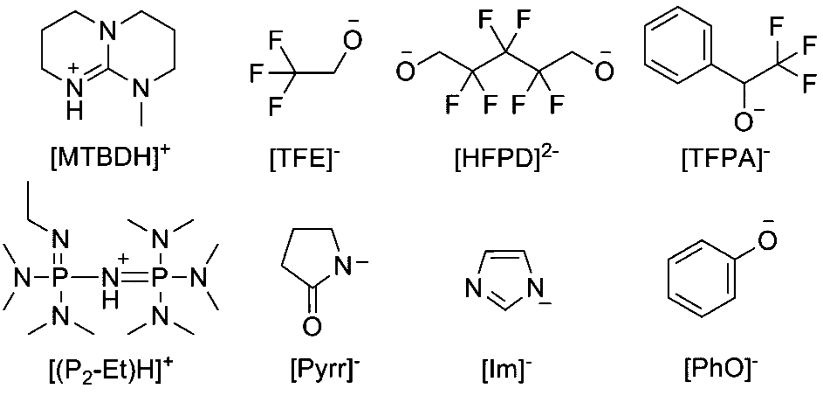

Figure 10. Structures of superbase-derived ILs (51)

Downloaded by CORNELL UNIV on June 15, 2012 | http://pubs.acs.org
Publication Date (Web): May 3, 2012 | doi: 10.1021/bk-2012-1097.ch008

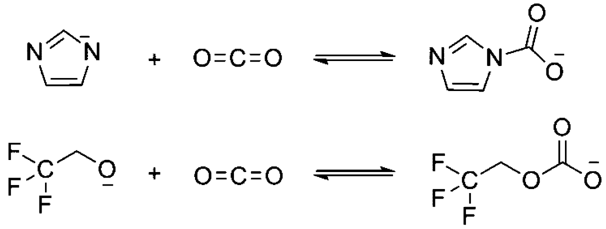

Figure 11. Reaction mechanisms of anions [Im]⁻ and [TFE]⁻ with CO_2 (50)

To address this high volatility problem, Wang et al. (*51*) firstly applied 1:1 mixtures of an alcohol-functionalised IL and a superbase for CO_2 absorption. Their selection of superbases is shown in Figure 12. These mixtures reached CO_2 equilibrium absorption capacity within 30 min., and CO_2 solubility approaching 1 mole ratio CO_2 per superbase at 1 bar and 20 °C (*51*). For example, the 1-(2-hydroxyethyl)-3-methylimidazolium Tf_2N ILs ([EmimOH][Tf_2N]) with equimolar DBU or MTBD absorbed approximately 1 mole ratio of CO_2 (8.2 and 8.0 wt % per DBU and MTBD, respectively). The alkylate derived from the alcohol group plays a key role by reacting with CO_2, forming amidinium alkylcarbonate salts during absorption, as shown in Figure 13 (*51*). In this case, CO_2 absorption was also repeatable and reversible, as the absorbents were readily regenerated by heating or on exposure to inert gases (*51*).

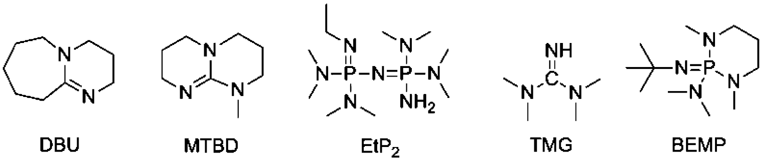

Figure 12. Structures of superbases for IL-superbase mixtures (51, 52)

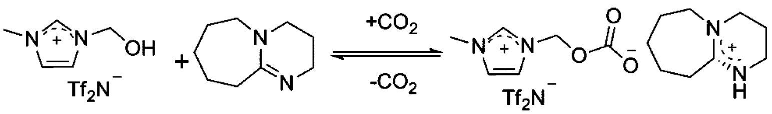

Figure 13. Reaction mechanism of [EmimOH][Tf_2N]+DBU 1:1 mixture with CO_2 (51)

Wang et al. (*52*) further demonstrated that conventional imidazolium-based IL and superbase mixtures can absorb CO_2 rapidly and reversibly. The proposed reaction mechanism is shown in Figure 14, indicating the formation of imidazolium carboxylate (*52*). The acidic nature of the C-2 position in the imidazolium (*5*, *53*) leads to carbene formation due to proton transfer to the superbase. The carbene then reacts with CO_2 to produce a carboxylate, as evidenced by a new IR peak at 1669 cm^{-1} and a new ^{13}C-NMR peak at 155.6 ppm. These authors also examined CO_2 absorption in mixtures of superbases and pyridinium-based ILs. While imidazolium based mixtures achieved 1 mole ratio of CO_2 solubilities at ambient pressure and 23 °C, equivalent to 7.5 and 7.6 wt % for [Bmim][Tf_2N]+DBU and [Emim][Tf_2N]+DBU mixtures, a pyridinium based mixture of [Bpy][Tf_2N]+DBU only absorbed 0.29 mole ratio of CO_2 (2.3 wt %) (*52*). This result further suggests the involvement of the imidazolium cation through the proton at C-2 position.

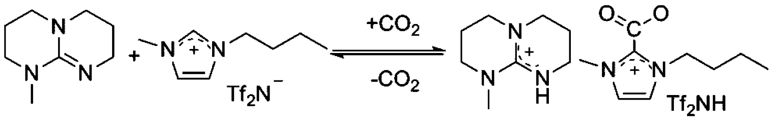

Figure 14. Reaction mechanism of [Bmim][Tf_2N]+MTBD 1:1 mixture with CO_2 (52)

Aprotic Heterocyclic Anion Based Ionic Liquids

To overcome the problem of high viscosity observed in CO_2 absoprtion products caused by strong hydrogen bonding, Brennecke and Dai explored, separately, the potential of aprotic heterocyclic anion-based ILs (*54*, *55*). Brennecke et al reported ILs based on a [P_{66614}]$^+$ cation combined with anions derived from pyrrolide or pyrazolide, as shown in Figure 15. These ILs showed a similar absorption capacity of nearly 1 mole CO_2 per IL at 1 bar and 22 °C, again forming carbamates (*54*). The viscosity for the CO_2 reacted [P_{66614}][2-CNpyr] or [P_{66614}][3-CF_3pyra] approached that of pure ILs, representing a significant improvement over the other tailored ILs. Equally interesting, the absorption enthalpy of these ILs is tunable. For example, the absorption enthalpy was lowered by substituting –CN or –CF_3 as electron-withdrawing groups in the anion, resulting in -53 kJ mol^{-1} for [P_{66614}][2-CNpyr] and -46 kJ mol^{-1} for [P^{66614}][3-CF_3pyra] (*54*).

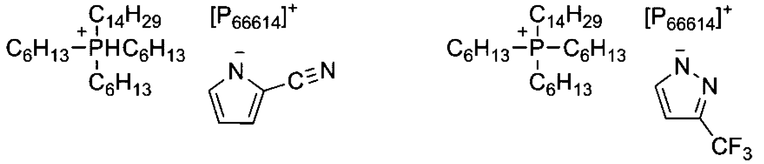

2-cyanopyrrolide [2-CNpyr]$^-$ 3-(trifluoromethyl)pyrazolide [3-CF_3pyra]$^-$

Figure 15. ILs with aprotic heterocyclic anion reported by Brennecke et al. (54)

Similarly, Dai et al. (*55*) investigated the tunability of the absorption enthalpy in aprotic heterocyclic anion-based ILs, as shown in Figure 16. They showed that by reducing the basicity of the anion, it is possible to decrease the CO_2-anion interaction energy, while maintaining a high CO_2 capacity. Trends in the bond strength between the anions and CO_2 can be elucidated using the proton affinity of the anion, i.e. the basicity and pKa values of the starting acids. This trend fits well as both H^+ and CO_2 share similar "hard" acidic characteristics (*56*). As strong

Downloaded by CORNELL UNIV on June 15, 2012 | http://pubs.acs.org
Publication Date (Web): May 3, 2012 | doi: 10.1021/bk-2012-1097.ch008

Downloaded by CORNELL UNIV on June 15, 2012 | http://pubs.acs.org
Publication Date (Web): May 3, 2012 | doi: 10.1021/bk-2012-1097.ch008

bases have a higher affinity for H^+, the same concept can be applied to the affinity of strong bases for CO_2. For example, [P_{66614}][Pyr], [P_{66614}][Im], [P_{66614}][Ind] and [P_{66614}][Triz] have pKa values in DMSO of 19.8, 18.6, 17.8, and 13.9, with absorption enthalpies of -91, -89.9, -63.1, and -56.4 $kJ{\cdot}mol^{-1}$, respectively (*55*). These ILs also show thermal stability up to 300 °C (*55*). Thus, this correlation provides an opportunity to achieve high CO_2 absorption with a relatively lower energy cost.

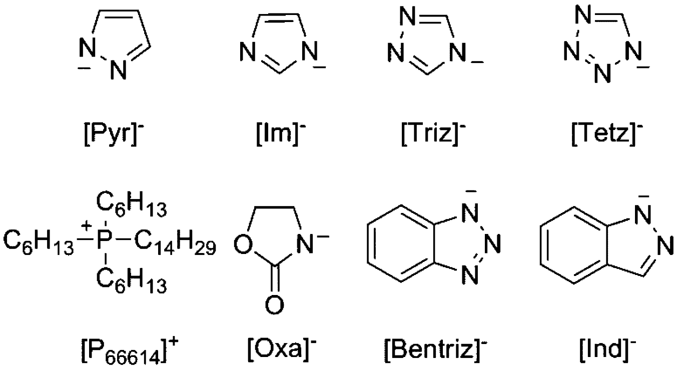

Figure 16. ILs with aprotic heterocyclic anions reported by Dai et al. (55)

Ionic Liquids with Transition Metal Ions

Huang and co-workers first reported the ILs containing transition metal ions as a different strategy to improve CO_2 solubility (*57*, *58*). As the coordination interaction between transition metals and CO_2 molecules is well understood, they investigated methods to improve CO_2 absorption capacity in ILs by incorporating transition metal ions. It is well established that the CO_2 molecule has two sets of filled π molecular orbitals and one vacant anti-bonding orbital (*59*). These orbitals can interact with transitional metal ions either by an η_1 or an η_2 bonding mode, as shown in Figure 17 (*60*).

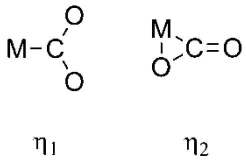

Figure 17. Structure types of η_1 and η_2 metal-CO_2 interaction (60)

Huang introduced transition metal salts bearing the same anion into ILs to form homo-anionic solutions for CO_2 absorption (*58*). The solubility of these homogenous transitional metals in ILs provided up to 1 mole ratio CO_2 absorbed. The absorption mechanism was interpreted as being due to a coordination sphere of anions formed around the transition metal centre, possibly in the form of $M[Tf_2N]_3^-$, acting as a reaction centre for CO_2 (*61*).

In previously reported work, the neat IL, [Emim][Tf_2N], showed only a small CO_2 absorption capacity of 0.39 wt % at 1 bar of CO_2 at 40 °C due to physical absorption (*21*). Mixing $Zn(Tf_2N)_2$ into [Emim][Tf_2N] in a 1:1 mole ratio, the CO_2 solubility in the IL increased to 8.2 wt % under the same conditions, interpreted as one Zn^{2+} ion binding > 1 CO_2 molecule through a coordination interaction in $[Emim]^+Zn^{2+}\cdot[Tf_2N]^-_3$. The coordination reaction mechanism analysis was later supported by FT-IR analyses. Other transition metals exhibited similar enhancement effects, but at different levels (*57*).

A disadvantage of mixing zinc salts with [Emim][Tf_2N] was the 43-fold increase in IL viscosity (*58*). Consequently, the CO_2 diffusion rate was slow, with the CO_2 diffusion coefficient evaluated in the range $10^{-13\ \sim\ -12}$ $m^2\cdot s^{-1}$, approximately three orders of magnitude lower than that in [Emim][Tf_2N]. These authors suggested that by altering the combination of the transition metal ions and the anions, the high viscosity problem could be solved.

Downloaded by CORNELL UNIV on June 15, 2012 | http://pubs.acs.org
Publication Date (Web): May 3, 2012 | doi: 10.1021/bk-2012-1097.ch008

Polymerised Ionic Liquids

Owing to the tunability of ILs, it is also appropriate to tailor monomeric groups onto the cation or anion of the ILs, forming IL monomers. Polymeric forms of ILs, poly(IL)s, can then be synthesised by polymerisation reactions (*62*). Studies found that poly(IL)s have relatively high CO_2 solubility and high selectivity, making them suitable candidates for gas separation processes. Tang et al. (*62*) first reported the application of poly(IL)s for CO_2 capture. Several examples of poly(IL)s synthesised in their work are shown in Figure 18 (*62*). They found that CO_2 solubilities in the polymerised tetraalkylammonium based ILs were 6- to 7.6-fold more than that in typical ILs. At 22 °C, P[VBTMA][PF_6], P[VBTMA][BF_4], P[MATMA][BF_4], P[VBTMA][Tf_2N] and P[VBTMA][Sac] ([Sac]: o-benzoicsulphimide) exhibited absorption capacities of 10.66 mol % (~1.34 wt %), 10.22 mol % (~1.53 wt %), 7.99 mol % (~1.43 wt %), 2.85 mol % (~0.27 wt %), and 2.67 mol % (~0.31 wt %). In comparison, the CO_2 absorption by [Bmim][BF_4] provided a capacity of 1.34 mol % (~ 0.26 wt %) (*62*, *63*). The CO_2 absorption by poly(IL)s have also been reported to be selective and reversible, with absorption equilibrium time up to 100 min. The absorption mechanism appears to be different from that in neat ILs, as the role of the fluorine atoms in poly(ILs) is not as important as in typical ILs. Poly(IL)s with non-fluorine anions (e. g. P[VBTMA][Sac]) exhibited similar CO_2 absorption capacities to P[VBTMA][Tf_2N] (*62*).

In Recent Advances in Post-Combustion CO2 Capture Chemistry; Attalla, M.;
ACS Symposium Series; American Chemical Society: Washington, DC, 2012.

Downloaded by CORNELL UNIV on June 15, 2012 | http://pubs.acs.org
Publication Date (Web): May 3, 2012 | doi: 10.1021/bk-2012-1097.ch008

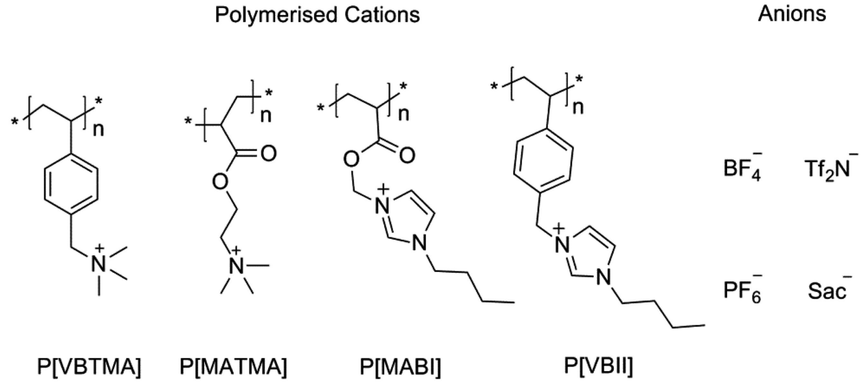

Figure 18. Structures of poly(IL)s synthesised by Tang et al. (62)

Samadi et al. (*64*) applied poly(IL)s, such as poly[(META)$^+$Cl$^-$], as a nanolayer of coating on a base support material. Poly[(META)$^+$Cl$^-$] showed no CO_2 uptake for pressures < 2.5 bar. However, by replacing [Cl]$^-$ anion with [BF_4]$^-$, [$MeSO_3$]$^-$ or [TfO]$^-$, as shown in Figure 19, these modified materials delivered linear CO_2 absorption behaviour with pressure. The CO_2 absorption capacity reached 2 mmol of CO_2 per gram (8.8 wt %) of poly(IL)s in [META][TfO] at 0.78 bar and 25 °C. These poly(IL)s materials also exhibited low absorption enthalpy, -26, -11, and -14 kJ·mol^{-1} for [BF_4]$^-$, [$MeSO_3$]$^-$, and [TfO]$^-$, respectively, clearly indicating a physical absorption mechanism and potentially facile regeneration capabilities (*64*).

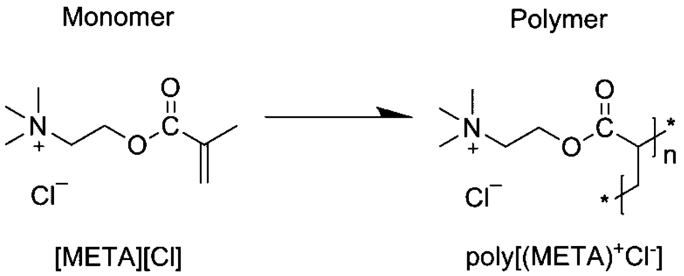

Figure 19. Structures for IL cation-monomer [META]$^+$and poly(IL) in the work reported by Samadi et al. (64)

In Recent Advances in Post-Combustion CO2 Capture Chemistry; Attalla, M.;
ACS Symposium Series; American Chemical Society: Washington, DC, 2012.

Bara et al. (*65*) synthesised several imidazolium based poly(IL)s with $[Tf_2N]^-$ as anions, as shown in Figure 20. These poly(IL)s were incorporated with ILs to form gel membranes for gas separation. The presence of 20 mol % free ILs in the polymer membranes improved the CO_2 permeability by 400 % and improved the CO_2/N_2 selectivity by 33 %, in comparison to the analogous membranes without free ILs (*65*).

Downloaded by CORNELL UNIV on June 15, 2012 | http://pubs.acs.org
Publication Date (Web): May 3, 2012 | doi: 10.1021/bk-2012-1097.ch008

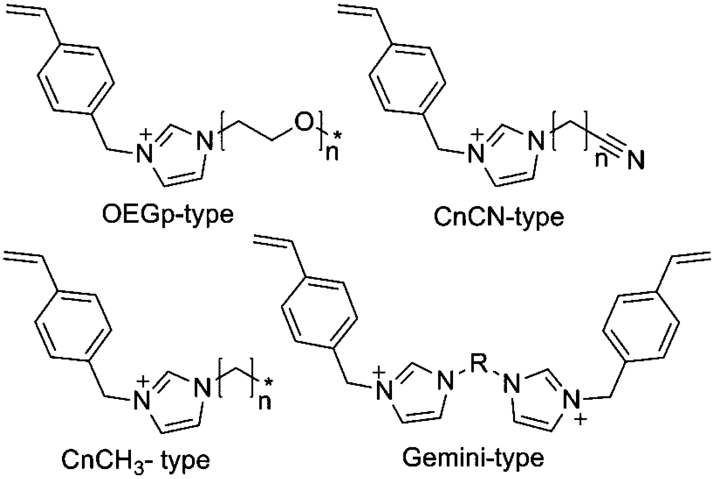

Figure 20. Types of polymerisable cationic-monomer synthesised by Bara et al. (65), $[Tf_2N]^-$ was used as the anion

Summary

As summarised in Table II and herein, a wide variety of methods have been explored in designing novel ILs specific for CO_2 capture. The primary goal for any new designs remains increased CO_2 absorption capacity, while, at the same time, retaining the attractive properties of the original ILs, such as their thermal stability, low volatility, and low corrosivity.

Downloaded by CORNELL UNIV on June 15, 2012 | http://pubs.acs.org
Publication Date (Web): May 3, 2012 | doi: 10.1021/bk-2012-1097.ch008

Table II. Summary of CO_2 absorption parameters in tethered ILs

IL absorbents	*CO_2 absorption capacity at RT and 1 bar*		*ΔH_{abs}*	*Viscosity at RT*	*Absorption Mechanism*	*Ref.*
	(mole CO_2 per IL)	*(wt %)*	*(kJ·mol^{-1})*	*(mPa·s)*		
ILs and amine mixtures						
[Hmim][Tf_2N]+MEA	$0.50^{40\ °C}$	$4.2^{40\ °C}$			carbamate	(*29*)
[EmimOH][Tf_2N]+DEA	$0.25^{40\ °C}$	$2.2^{40\ °C}$			formation	(*29*)
Amine functionalised ILs						
[aPbim][BF_4]	0.50	7.4				(*28*)
[Am-Im] [BF_4]	$0.16^{30\ °C}$	$2.9^{30\ °C}$				(*31*)
[3Am-Im][BF_4]	$0.02^{30\ °C}$				carbamate	(*31*)
[Am-Im] [Tf_2N]	$0.11^{30\ °C}$	$1.1^{30\ °C}$	-42		formation	(*31*)
[Am-Im] [PF_6]				195		(*66*)
Amino acid functionalised ILs						
[N_{2222}][α–alanine]	$0.43^{40\ °C}$	$8.6^{40\ °C}$		81	carbamate	(*35*)
[N_{2222}][β–alanine]	$0.43^{40\ °C}$	$8.6^{40\ °C}$	132		carbamate	(*35*)
[P_{4444}][glycine]	1.0	13.5		233	carbamate or bicarbonate	(*36*)
[aP_{4443}][Gly]	1.1	13.9		714	carbamate	(*37*)
[aP_{4443}][Ala]	1.1	13.9		758	carbamate	(*37*)

Continued on next page.

Downloaded by CORNELL UNIV on June 15, 2012 | http://pubs.acs.org
Publication Date (Web): May 3, 2012 | doi: 10.1021/bk-2012-1097.ch008

Table II. (Continued). Summary of CO_2 absorption parameters in tethered ILs

IL absorbents	*CO_2 absorption capacity at RT and 1 bar*		*ΔH_{abs}*	*Viscosity at RT*	*Absorption Mechanism*	*Ref.*
	(mole CO_2 per IL)	*(wt %)*	*(kJ·mol^{-1})*	*(mPa·s)*		
$[P_{66614}]$[Pro]	0.96	7.1	-80	720	carbamate	(*38*, *39*)
$[P_{66614}]$[Met]	0.9	6.3	-64	350	carbamate	(*38*, *39*)
$[P_{66614}]$[Lys]	1.3	9.1		730	carbamate	(*39*)
Superbase functionalised ILs						
C8/LeuOH	1.0	15.4		20	carbamate	(*49*)
[MTBDH][TFE]	1.1	19.6	-117	9	carbonate	(*50*)
[MTBDH][Im]	1.0	20.4	-85	32	carbamate	(*50*)
[MTBDH][PhO]	0.49	8.7	-42		carbonate	(*50*)
superbase and ILs mixtures						
[EmimOH][Tf_2N]+DBU	1.0	8.2			carbonate	(*51*)
[EmimOH][Tf_2N]+MTBD	1.0	8.0			carbonate	(*51*)
[Emim][Tf_2N]+DBU	0.93	7.5			carboxylate	(*52*)
[Bmim][Tf_2N]+DBU	0.99	7.6			carboxylate	(*52*)
[Bpy][Tf_2N]+DBU	0.29	2.3			-	(*52*)
Aprotic heterocyclic anion based ILs						
$[P_{66614}]$[2-CNpyr]	0.90	6.9	-53	420		(*54*)

Downloaded by CORNELL UNIV on June 15, 2012 | http://pubs.acs.org
Publication Date (Web): May 3, 2012 | doi: 10.1021/bk-2012-1097.ch008

IL absorbents	***CO_2 absorption capacity at RT and 1 bar***		***ΔH_{abs}***	***Viscosity at RT***	***Absorption Mechanism***	***Ref.***
	(mole CO_2 per IL)	***(wt %)***	***(kJ·mol^{-1})***	***(mPa·s)***		
$[P_{66614}]$[3-CF_3pyra]	0.90	6.4	-46	270	carbamate formation	(*54*)
$[P_{66614}]$[Pyr]	1.0	8.1	-91	245		(*55*)
$[P_{66614}]$[Im]	1.0	8.0	-90	810		(*55*)
$[P_{66614}]$[Ind]	0.98	7.2	-63			(*55*)
$[P_{66614}]$[Triz]	0.95	7.5	-56			(*55*)
ILs with transition metal ions						
[Emim][Tf_2N]+Zn(Tf_2N)$_2$	2.0 $^{40\ °C}$	8.2 $^{40\ °C}$		1758 $^{40\ °C}$	CO_2 - transition metal coordination	(*58*)
Polymerised ILs						
P[VBTMA][PF_6]	0.11	1.3			physical absorption	(*62*, *63*)
P[VBTMA][BF_4]	0.10	1.5				(*62*, *63*)
P[MATMA][BF_4]	0.08	1.4				(*62*, *63*)
P[VBTMA][Tf_2N]	0.03	0.3				(*62*, *63*)
P[VBTMA][Sac]	0.03	0.3				(*62*, *63*)
P[META][$MeSO_3$]	0.81	6.7	-11			(*64*)
P[META][BF_4]	0.42	7.1	-26			(*64*)
P[META][TfO]	0.41	11.1	-14			(*64*)

Downloaded by CORNELL UNIV on June 15, 2012 | http://pubs.acs.org
Publication Date (Web): May 3, 2012 | doi: 10.1021/bk-2012-1097.ch008

One of the approaches has been to physically mix additives, such as amines and superbases, with neat ILs. Equimolar amine-IL and superbase-IL mixtures were shown to absorb up to 0.5 and 1 mole of CO_2 per IL, respectively, representing a significant improvement over the traditional ILs. However, the implementation of additives brought their own complications into the systems. Volatile organic additives continue to contribute to considerable vapor pressure, and the reactive additives degrade on exposure to atmospheric environments. Despite their improved absorption capacities, these problems need to be further addressed before physical mixtures can be applied successfully to industrial-scale emissions control. ILs with transition metal ions are also classified as physically mixed systems where the transition metal salts and the ILs share the same anions. These materials contain coordination spheres embracing transition metals centred by anions, creating a different coordination framework. Although these materials are promising as CO_2 absorbents, the incorporated transitional metal ions significantly increases the system viscosity, with consequent reduction in absorption kinetics. Nonetheless, ample opportunities exist to overcome these drawbacks by altering the combination of ILs and transition metals.

The second IL design method involves chemically incorporating CO_2-philic groups into the system. In this strategy, different reactive moieties (i.e., amine, amino acid group) have been introduced into the structure of the constituent cations or anions leading to enhanced chemical absorption. In a similar way, polymeric groups have been tailored with ILs to improve the overall physical CO_2 absorption by the resulting poly(ILs), while maintaining relatively low absorption energy. Both reactive functionalities and polymeric groups undoubtedly endow the ILs with entirely different properties. However, poly(IL)s require further improvement in their CO_2 solubility capacity; nearly all amine and amino acid functionalised ILs present higher viscosity problems, further exacerbated on reaction with CO_2, and in some cases, resulting in precipitation problems. Supporting these amine and amino acid functionalised ILs on porous materials appears to go a long way in solving these physical property constraints.

The use of aprotic anions, which provide a deficiency of protons and act as CO_2-philic groups , mitigates the high viscocity issue caused by hydrogen bonding in the CO_2 adducts. The absorption capacity of some of these materials competes effectively with those of current commercially used amine-base absorbents, while the absorption equilibrium is reached in a relatively short time with little increase in the viscosity after CO_2 absorption. Despite some of the materials exhibiting high absorption energy, it is possible to reduce the anion-CO_2 interaction energies by tuning the chemical structures. These ILs however still exhibit relatively high viscosity. Industry adoption requires to further reduce the viscosity.

Overall, an increasing number of tailored ILs have been designed and explored in recent years. We anticipate that due to the high degree of tunability and the huge variety of the potential ILs, significant opportunities exist to further improve ILs to overcome the existing challenges for CO_2 capture.

Downloaded by CORNELL UNIV on June 15, 2012 | http://pubs.acs.org
Publication Date (Web): May 3, 2012 | doi: 10.1021/bk-2012-1097.ch008

References

1. Forsyth, S. A.; Pringle, J. M.; MacFarlane, D. R. *Aust. J. Chem.* **2004**, *57* (2), 113–119.
2. Dupont, J.; Suarez, P. A. Z. *Phys. Chem. Chem. Phys.* **2006**, *8* (21), 2441–2452.
3. Welton, T. *Chem. Rev.* **1999**, *99* (8), 2071–2083.
4. Maginn, E. J.; Anthony, J. L.; Anderson, J. L.; Brennecke, J. F. *J. Phys. Chem. B* **2005**, *109* (13), 6366–6374.
5. Cadena, C.; Anthony, J. L.; Shah, J. K.; Morrow, T. I.; Brennecke, J. F.; Maginn, E. J. *J. Am. Chem. Soc.* **2004**, *126* (16), 5300–5308.
6. Muldoon, M. J.; Aki, S. N. V. K.; Anderson, J. L.; Dixon, J. K.; Brennecke, J. F. *J. Phys. Chem. B* **2007**, *111* (30), 9001–9009.
7. Huang, J. H.; Ruther, T. *Aust. J. Chem.* **2009**, *62* (4), 298–308.
8. Blanchard, L. A.; Gu, Z. Y.; Brennecke, J. F. *J. Phys. Chem. B* **2001**, *105* (12), 2437–2444.
9. Blanchard, L. A.; Hancu, D.; Beckman, E. J.; Brennecke, J. F. *Nature* **1999**, *399* (6731), 28–29.
10. Meindersma, G. W.; Sanchez, L. M. G.; Hansmeier, A. R.; de Haan, A. B. *Monatsh. Chem* **2007**, *138* (11), 1125–1136.
11. Shiflett, M. B.; Niehaus, A. M. S.; Yokozeki, A. *J. Phys. Chem. B* **2011**, *115* (13), 3478–3487.
12. Shiflett, M. B.; Niehaus, A. M. S.; Yokozeki, A. *J. Chem. Eng. Data* **2010**, *55* (11), 4785–4793.
13. Baltus, R. E.; Counce, R. M.; Culbertson, B. H.; Luo, H. M.; DePaoli, D. W.; Dai, S.; Duckworth, D. C. *Sep. Sci. Technol.* **2005**, *40* (1−3), 525–541.
14. Bara, J. E.; Carlisle, T. K.; Gabriel, C. J.; Camper, D.; Finotello, A.; Gin, D. L.; Noble, R. D. *Ind. Eng. Chem. Res.* **2009**, *48* (6), 2739–2751.
15. Huang, J.; Riisager, A.; Berg, R. W.; Fehrmann, R. *J. Mol. Catal. A: Chem.* **2008**, *279* (2), 170–176.
16. Han, B. X.; Wu, W. Z.; Gao, H. X.; Liu, Z. M.; Jiang, T.; Huang, J. *Angew. Chem., Int. Ed.* **2004**, *43* (18), 2415–2417.
17. Astarita, G.; Savage, D. W.; Bisio, A. *Gas Treating with Chemical Solvents*; John Wiley & Sons Inc.: New York, 1983.
18. Perinline, H. W.; Luebke, D. R.; Jones, K. L.; Myers, C. R.; Morsi, B. I.; Heintz, Y. J.; Ilconich, J. B. *Fuel Process. Technol.* **2008**, *89* (9), 897–907.
19. Jiang, Y.-Y.; Zhou, Z.; Jiao, Z.; Li, L.; Wu, Y.-T.; Zhang, Z.-B. *J. Phys. Chem. B* **2007**, *111* (19), 5058–5061.
20. Anderson, J. L.; Dixon, J. K.; Brennecke, J. F. *Acc. Chem. Res.* **2007**, *40* (11), 1208–1216.
21. Shi, W.; Maginn, E. J. *J. Phys. Chem. B* **2008**, *112* (51), 16710–16720.
22. Lawal, A. O.; Idem, R. O. *Ind. Eng. Chem. Res.* **2006**, *45* (8), 2601–2607.
23. Arcis, H.; Ballerat-Busserolles, K.; Rodier, L.; Coxam, J. Y. *J. Chem. Eng. Data* **2011**, *56* (8), 3351–3362.
24. Paul, S.; Ghoshal, A. K.; Mandal, B. *Ind. Eng. Chem. Res.* **2007**, *46* (8), 2576–2588.
25. Giernoth, R. *Angew. Chem.* **2010**, *49* (16), 2834–2839.

26. Figueroa, J. D.; Fout, T.; Plasynski, S.; McIlvried, H.; Srivastava, R. D. *Int. J. Greenhouse Gas Control* **2008**, *2* (1), 9–20.
27. Svendsen, H. F.; Kim, I. *Ind. Eng. Chem. Res.* **2007**, *46* (17), 5803–5809.
28. Bates, E. D.; Mayton, R. D.; Ntai, I.; Davis, J. H. *J. Am. Chem. Soc.* **2002**, *124* (6), 926–927.
29. Camper, D.; Bara, J. E.; Gin, D. L.; Noble, R. D. *Ind. Eng. Chem. Res.* **2008**, *47* (21), 8496–8498.
30. Gibbons, B. H.; Edsall, J. T. *J. Biol. Chem.* **1963**, *238* (10), 3502–3507.
31. Sanchez, L. M. G.; Meindersma, G. W.; de Haan, A. B. *Chem. Eng. Res. Des.* **2007**, *85* (A1), 31–39.
32. Ohno, H.; Fukumoto, K. *Acc. Chem. Res.* **2007**, *40* (11), 1122–1129.
33. Fukumoto, K.; Yoshizawa, M.; Ohno, H. *J. Am. Chem. Soc.* **2005**, *127* (8), 2398–2399.
34. Hamborg, E. S.; Niederer, J. P. M.; Versteeg, G. F. *J. Chem. Eng. Data* **2007**, *52* (6), 2491–2502.
35. Jiang, Y. Y.; Wang, G. N.; Zhou, Z.; Wu, Y. T.; Geng, J.; Zhang, Z. B. *Chem. Commun.* **2008** (4), 505–507.
36. Zhang, J. M.; Zhang, S. J.; Dong, K.; Zhang, Y. Q.; Shen, Y. Q.; Lv, X. M. *Chem. Eur. J.* **2006**, *12* (15), 4021–4026.
37. Zhang, Y. Q.; Zhang, S. J.; Lu, X. M.; Zhou, Q.; Fan, W.; Zhang, X. P. *Chem. Eur. J.* **2009**, *15* (12), 3003–3011.
38. Gurkan, B. E.; de la Fuente, J. C.; Mindrup, E. M.; Ficke, L. E.; Goodrich, B. F.; Price, E. A.; Schneider, W. F.; Brennecke, J. F. *J. Am. Chem. Soc.* **2010**, *132* (7), 2116–2117.
39. Goodrich, B. F.; de la Fuente, J. C.; Gurkan, B. E.; Lopez, Z. K.; Price, E. A.; Huang, Y.; Brennecke, J. F. *J. Phys. Chem. B* **2011**, *115* (29), 9140–9150.
40. Soutullo, M. D.; Odom, C. I.; Wicker, B. F.; Henderson, C. N.; Stenson, A. C.; Davis, J. H. *Chem. Mater.* **2007**, *19* (15), 3581–3583.
41. Tao, G. H.; He, L.; Sun, N.; Kou, Y. *Chem. Commun.* **2005** (28), 3562–3564.
42. Yu, G.; Zhang, S.; Zhou, G.; Liu, X.; Chen, X. *AIChE J.* **2007**, *53* (12), 3210–3221.
43. Gutowski, K. E.; Maginn, E. J. *J. Am. Chem. Soc.* **2008**, *130* (44), 14690–14704.
44. Xu, H.; Rudkevich, D. M. *Chem. Eur. J.* **2004**, *10* (21), 5432–5442.
45. Li, X.; Hou, M.; Zhang, Z.; Han, B.; Yang, G.; Wang, X.; Zou, L. *Green Chem.* **2008**, *10* (8), 879–884.
46. Li, W.; Zhang, Z.; Han, B.; Hu, S.; Song, J.; Xie, Y.; Zhou, X. *Green Chem.* **2008**, *10* (11), 1142–1145.
47. Doskocil, E. J.; Bordawekar, S.; Davis, R. J. Catalysis by solid bases. In *Catalysis*; Spivey, J. J., Ed.; The Royal Society of Chemistry: 2000; Vol. 15, pp 40−72.
48. Luo, H. M.; Baker, G. A.; Lee, J. S.; Pagni, R. M.; Dai, S. *J. Phys. Chem. B* **2009**, *113* (13), 4181–4183.
49. Yu, T.; Yamada, T.; Gaviola, G. C.; Weiss, R. G. *Chem. Mater.* **2008**, *20* (16), 5337–5344.
50. Wang, C. M.; Luo, H. M.; Jiang, D. E.; Li, H. R.; Dai, S. *Angew. Chem., Int. Ed.* **2010**, *49* (34), 5978–5981.

Downloaded by CORNELL UNIV on June 15, 2012 | http://pubs.acs.org
Publication Date (Web): May 3, 2012 | doi: 10.1021/bk-2012-1097.ch008

51. Wang, C. M.; Mahurin, S. M.; Luo, H. M.; Baker, G. A.; Li, H. R.; Dai, S. *Green Chem.* **2010**, *12* (5), 870–874.
52. Wang, C. M.; Luo, H. M.; Luo, X. Y.; Li, H. R.; Dai, S. *Green Chem.* **2010**, *12* (11), 2019–2023.
53. Crowhurst, L.; Mawdsley, P. R.; Perez-Arlandis, J. M.; Salter, P. A.; Welton, T. *Phys. Chem. Chem. Phys.* **2003**, *5* (13), 2790–2794.
54. Gurkan, B.; Goodrich, B. F.; Mindrup, E. M.; Ficke, L. E.; Massel, M.; Seo, S.; Senftle, T. P.; Wu, H.; Glaser, M. F.; Shah, J. K.; Maginn, E. J.; Brennecke, J. F.; Schneider, W. F. *J. Phys. Chem. Lett.* **2010**, *1* (24), 3494–3499.
55. Wang, C.; Luo, X.; Luo, H.; Jiang, D.-e.; Li, H.; Dai, S. *Angew. Chem., Int. Ed.* **2011**, *50* (21), 4918–4922.
56. Pearson, R. G. *J. Am. Chem. Soc.* **1963**, *85* (22), 3533–3539.
57. Huang, J.; Ruether, T.; Feron, P.; Zhang, Z. WO2011011830-A1, 2010.
58. Liu, H.; Huang, J.; Pendleton, P. *Energy Procedia* **2011**, *4*, 59–66.
59. Stankevich, I. V.; Lysyak, T. V.; Aleksandrov, G. G.; Kolomnikov, I. S. *J. Struct. Chem.* **1979**, *19*, 777–800.
60. Gibson, D. H. *Chem. Rev.* **1996**, *96* (6), 2063–2095.
61. Chiappe, C.; Malvaldi, M.; Melai, B.; Fantini, S.; Bardi, U.; Caporali, S. *Green Chem.* **2010**, *12* (1), 77–80.
62. Tang, J.; Tang, H.; Sun, W.; Plancher, H.; Radosz, M.; Shen, Y. *Chem. Commun.* **2005** (26), 3325–3327.
63. Tang, J.; Tang, H.; Sun, W.; Radosz, M.; Shen, Y. *Polymer* **2005**, *46* (26), 12460–12467.
64. Samadi, A.; Kemmerlin, R. K.; Husson, S. M. *Energy Fuels* **2010**, *24* (10), 5797–5804.
65. Bara, J. E.; Hatakeyama, E. S.; Gin, D. L.; Noble, R. D. *Polym. Adv. Technol.* **2008**, *19* (10), 1415–1420.
66. Song, G.; Cai, Y.; Peng, Y. *J. Comb. Chem.* **2005**, *7* (4), 561–566.

Downloaded by CORNELL UNIV on June 15, 2012 | http://pubs.acs.org
Publication Date (Web): May 3, 2012 | doi: 10.1021/bk-2012-1097.ch008

Downloaded by CORNELL UNIV on June 14, 2012 | http://pubs.acs.org
Publication Date (Web): May 3, 2012 | doi: 10.1021/bk-2012-1097.ch009

Chapter 9

Silica/Polyethyleneimine Composite Adsorbent S-PEI for CO_2 Capture by Vacuum Swing Adsorption (VSA)

Gregory P. Knowles,[1] Paul A. Webley,[2] Zhijian Liang,[1]
and Alan L. Chaffee[1,*]

[1]CRC for Greenhouse Gas Technologies, P.O. Box 23, School of Chemistry,
Monash University, Vic 3800, Australia
[2]CRC for Greenhouse Gas Technologies, P.O. Box 36, School of Chemical
Engineering, Monash University, Vic 3800, Australia
***alan.chaffee@monash.edu**

SBA15 type mesoporous silica was combined with a pore volume equivalent of branched polyethyleneimine PEI (MW 1200) to prepare a high capacity adsorbent S-PEI for the selective capture of CO_2 from post combustion flue gas via pressure / vacuum swing adsorption (VSA). The adsorbent was characterized by helium pycnometry, N_2 adsorption / desorption at 77 K, powder X-ray diffraction XRD and thermogravimetric analysis. The potential of S-PEI for CO_2 capture via VSA was assessed by both CO_2 partial pressure swing adsorption (PPSA) studies via combined thermogravimetric analysis (TGA) / differential thermal analysis (DTA), and by CO_2 pressure / vacuum swing adsorption (VSA) studies via a custom bench gas sorption analyzer. The CO_2 sorption capacities determined by partial pressure swings were consistent with those determined by pressure / vacuum swings as expected by the Henry gas law and therefore demonstrate the validity of PPSA to estimate VSA process working capacities. S-PEI was found to exhibit greater working CO_2 capacity than zeolite 13X at 105 °C under key process conditions (0.05 – 0.15 atm CO_2) from either anhydrous or humidified (~1 % H_2O) process gas. The amine adsorbent was also found to exhibit a higher $H_{ads}(CO_2)$ (70-90 $kJ.mol^{-1}$ than zeolite 13X (30-40 $kJ.mol^{-1}$) as was expected

In Recent Advances in Post-Combustion CO2 Capture Chemistry; Attalla, M.;
ACS Symposium Series; American Chemical Society: Washington, DC, 2012.

for a chemisorption process. Zeolite 13X however was found to exhibit faster sorption kinetics under anhydrous process conditions consistent with its lower $H_{ads}(CO_2)$. Pelletized S-PEI exhibited the same good sorption kinetics as the powder, however with slightly reduced CO_2 working capacity, 2.5 wt% at 105 °C, and minimal void volume, equivalent to 29.3 g of CO_2 per L of sorbent bed. S-PEI was thus found to be attractive for CO_2 capture from post combustion flue gas via VSA.

Downloaded by CORNELL UNIV on June 14, 2012 | http://pubs.acs.org
Publication Date (Web): May 3, 2012 | doi: 10.1021/bk-2012-1097.ch009

Introduction

Scientific evidence suggests that the earth's climate is changing under the influence of anthropogenic greenhouse gas emissions causing an increase in the amount of infrared radiation (heat) trapped by the atmosphere (*1*). Left unabated this global warming will likely impact on humanity/society via the growing incidence of large scale crop failures, food/water shortages, diseases/epidemics, loss of habitats and environmental diversity, and mortalities (especially amongst infants, the elderly and the infirm) and a growing burden to our economies (*1*, *2*). Post combustion capture PCC and subsequent geosequestration of CO_2 is thus being considered as one of a number of strategies towards halting global warming (*3*). Absorption (*4*), adsorption (*5*) and membrane separation technologies (*5*) are being considered for CO_2 capture from major emission sources such as air fired fossil fuel power generators. The particular interest here is to assess the potential of an amine functionalized adsorbent to facilitate the PCC of CO_2 via pressure / vacuum swing adsorption (VSA), a prospective technology for reducing the parasitic energy requirement for CO_2 capture relative to current solvent based technologies (*6*).

Zeolite 13X (the sodium cation form of the faujasite type zeolite X) is being considered for CO_2 capture from post combustion flue gas via VSA (*7*) owing to its large reversible CO_2 capacity (*8*), poor affinity for N_2 (*8*), high thermal stability, low $H_{ads}(CO_2)$ of ~43kJ.mol^{-1} at 80-200 °C (*9*) (63 kJ.mol^{-1} at 120 °C (*8*)), and commercial availability. The selective working CO_2 capacity of zolite 13X is however compromised by preferential adsorption of water (*10*, *11*) (a major constituent of flue gas), such that the CO_2 capture cost from post combustion flue gas via VSA would be impacted by the additional requirement to carefully guard the 13X sorbent from this major constituent of post combustion flue gas (*12*).

Amine adsorbents are likewise known to exhibit high/reversible CO_2 capacities (*5*, *10*). They have negligible affinity for N_2 (for example TRI-PE-MCM-41 (*13*) and HMS -AP, -ED & -DT (*14*)), and are not particularly adversely affected by water. Indeed the presence of water has been found to enhance the CO_2 capacity of some amine adsorbents in some cases (for example, MONO-PE-MCM-41 (*15*), TRI-PE-MCM-41 (*13*), PEI/CARiACT (*16*), HMS-AP (*17*) and SBA15-ED (*18*)). They exhibit thermal stability in mildly oxygenated atmospheres (2 % O_2 / N_2) at elevated temperatures, up to 170 °C (HMS- AP, ED & DT (*14*)), and so are thought to present a potentially superior alternative for CO_2 capture. Aminosilica adsorbents comprising secondary amines

(MCF-DA and MCF-MAPS) however are reported to be particularly vulnerable to oxidative degradation in pure O_2 at elevated temperatures below 140 °C (*19*).

Such amine adsorbents have been prepared by the incorporation of amines either loaded into the mesoporous substrate [PEI (*20–26*) and tetraethylenepentamine (TEPA) (*27*)], grafted onto it [aminopropyltrimethoxysilane (APTS) (*17*, *28*)], co-polymerised with it [APTS (*29–31*), or polymerised within it [aziridine (*32*), diethylenetriaminopropyltrimethoxysilane (*33*)]. Amines have also been loaded into/onto other substrates such as polymethylmethacrylate (PMMA) (*16*) and glass fibre (*34*) and have also been prepared via the direct polycondensation of aminoalkysilanes (*35*).

High surface area substrates have been exploited to prepare high capacity surface functionalized adsorbents which retain substantial mesoporosity for good gas flux (*17*). Still higher capacity adsorbents, however, are prepared by more effectively utilizing the total pore volume of the substrates via pore filling techniques (*22*, *26*, *36*, *37*). Hence mesoporous materials with very large pore volumes such as SBA-15 (*26*), CARiACT silica (*38*), mesocellular siliceous foam (MCF) (*27*, *37*), pore expanded MCM-41 (PE-MCM-41) (*33*) and KIT-6 (*29*) have been considered. Such materials require higher temperature process conditions to overcome the additional limitation (pore filling) to gas diffusion (*25*, *36*), and as such are thought to be better suited to processing hot flue gas (100 – 150 °C) (*39*) avoiding the energy penalties to otherwise cool the flue gas. The co-incorporation of polyethyleneglycol (PEG) in the pores has been reported to enhance CO_2 adsorption/desorption kinetics of a PEI loaded PMMA adsorbent (*40*). Zeolite 13X loaded with isopropanol amine (IPA) and ethylenediamine (ED) (*41*) and monoethanolamine (MEA) (*41*, *42*) have also been considered.

PEI in particular has been loaded into MCM-41 (50 wt % PEI (*22*)), CARiACT (40 wt % PEI (*38*)), SBA-15 (50 wt% 423 $g.mol^{-1}$ linear PEI (*43*) and 50 wt% 1200 $g.mol^{-1}$ branched PEI (*25*)) and MCF (70 wt% 1200 $g.mol^{-1}$ branched PEI (*25*)) to prepare adsorbents with CO_2 capacities up to 112 (75 °C, 1 atm CO_2), 121 (80 °C, 1 atm 100 % CO_2), 140 (75 °C, 1 atm 15 % CO_2), 107 (105 °C, 50 % CO_2/Ar) and 151 (105 °C, 50 % CO_2/Ar) mg CO_2 per g adsorbent respectively. Given that volatility increases inversely proportional to molecular weight, higher molecular weight PEI would be preferred for the process to minimize the potential loss of the PEI active sorbent phase, however small, under the preferred process conditions.

Amine adsorbents such as diamine grafted SBA-15 (*18*) and APTS-SBA15 (*18*, *44*, *45*); are reported to bind CO_2 at 25 °C via the formation of bicarbonates, carbonates and carbamate species. Bidentate bicarbonate species bind more strongly to diamine grafted SBA-15 than bidentate carbonate species (*18*) and carbamate formation on APTS-SBA15 requires more energy and so was not readily observed at 25 °C (*44*). However it is thought that carbamate formation (refer Equation 1) likely predominates at higher temperatures (> 50 °C) (*14*, *46*, *47*).

$$\text{Equation 1:} \quad 2RNH_2 + CO_2 <-> RNHCOO^- + RNH_3^+$$

Downloaded by CORNELL UNIV on June 14, 2012 | http://pubs.acs.org
Publication Date (Web): May 3, 2012 | doi: 10.1021/bk-2012-1097.ch009

Amine adsorbents also typically exhibit higher heats of adsorption $H_{ads}(CO_2)$ for CO_2 than zeolites. For example, $H_{ads}(CO_2)$ values for surface functionalized amine adsorbents greater than 70 kJ.mol^{-1} have typically been reported (*14*, *17*, *48*). The reported values corresponding to lower partial pressures of CO_2 adsorption and higher adsorption temperatures are higher still; usually over 90 kJ.mol^{-1} (*40*, *46*, *49*, *50*).

By comparison, for zeolite 13X, values of 35-48 kJ.mol^{-1} and 63 kJ.mol^{-1} have been reported at low temperature (*8*) and 120 °C (*8*) respectively.

The requirement for greater heat dissipation means that it will take longer to measure (and achieve) equilibrium adsorption at a fixed temperature. It is thought that this might also impact the CO_2 working capacities that can be achieved in a VSA cycle under adiabatic conditions.

It is noted that the ammonium carbamate species formed by exposure of amine adsorbents to CO_2 are also reported to dehydrate to form highly stable urea linkages (refer Equation 2) at elevated temperature which could ultimately destroy the useful reversible CO_2 capacity of the sorbent (*47*, *51*) and even under milder conditions at a slower rate (*52*) The presence of water however has been found to inhibit such urea formation (*51*, *52*) and so might be effective to preserve the useful cycling capacity of such sorbents under process conditions. Further it is reported that such deactivated amine adsorbents can be fully regenerated by hydrothermal treatment (*52*).

$$\text{Equation 2:} \quad RNCOO^{-} + RNH_3^{+} \text{<->} RNCONR + H_2O$$

The relative performance of different sorbents for CO_2 capture via VSA has typically been interpolated from single gas adsorption isotherms (*53*) collected over a range of different temperatures. This approach however is less than ideal because the isotherms do not account for the kinetic and thermal effects that may be important over the short time scales (1 – 5 min) typically employed in VSA. It was thus proposed that a custom bench scale volumetric gas sorption analyzer (GSA) incorporating a thermally insulated sample vessel to mimic the poor thermal transfer to/from an industrial sorbent bed would better permit assessment of the relative potential of different adsorbents under conditions anticipated for industrial application (*23*, *54*). It was also proposed that the amount of CO_2 adsorbed on an adsorbent from CO_2/Ar mixtures would be directly proportional to the partial pressure of CO_2 (assuming negligible Ar adsorption) akin to the Henry gas law with respect to gas absorption (*55*) such that CO_2 adsorption/desorption isotherms could be more readily obtained with accompanying assessment of $H_{ads}(CO_2)$ via combined thermogravimetric analysis (TGA) and differential thermal analysis (DTA) from mixed CO_2/Ar gas flows for comparison (*23*).

It is noted that the potential of CARiACT G10 solid amine sorbent powder for PCC of CO_2 via pressure swing adsorption (PSA) was more recently assessed via a similar TGA method (CO_2 PPSA) (*38*), employing N_2 as make up gas, 40 minute equilibration steps, sorption studies limited to between 40 and 100 °C and desorption under 100 % N_2. The CARiACT G10 solid amine sorbent was thus found to be suitable for PCC CO_2 via PSA between 40 & 100 °C, with optimal

Downloaded by CORNELL UNIV on June 14, 2012 | http://pubs.acs.org
Publication Date (Web): May 3, 2012 | doi: 10.1021/bk-2012-1097.ch009

Downloaded by CORNELL UNIV on June 14, 2012 | http://pubs.acs.org
Publication Date (Web): May 3, 2012 | doi: 10.1021/bk-2012-1097.ch009

reversible CO_2 capacities at 80 °C (as was the best compromise between kinetic and thermodynamic limitations) and stable over 78 cycles (*38*). Up to 2 vol % H_2O in the gas stream was found to effect a minor reduction to the CO_2 capacity, however did not have any irreversible effect on the adsorbent (*38*).

Here we report the preparation of an SBA-15 type mesoporous silica / polyethyleneimine composite material, S-PEI, and compare its potential for CO_2 capture from flue gas with a commercial zeolite 13X adsorbent. Here we also report the preparation and characterization of the adsorbent in pelletized form, as would be required for a fixed bed configuration in a commercial operation. X-ray diffraction (XRD) was employed to demonstrate the expected periodicity of the silica framework support and to demonstrate loading of the PEI into the mesopores. N_2 adsorption/desorption at 77 K was employed to characterize the surface area, pore volume and pore size distribution of both the silica support and adsorbent materials. Thermogravimetric analysis of air oxidation (combustion) of the hybrid adsorbent and silica framework were conducted to further characterize the PEI loading and thermal stability of the hybrid sorbent. Helium pycnometry further characterized the PEI loading and in addition facilitated correction of the sample manifold volume for the sample volume in the custom gas sorption analyser (ahead). Combined thermogravimetric analysis / differential thermal analysis of CO_2 sorption at various temperatures from both anhydrous and wet gas streams was conducted to investigate the affects of temperature and humidity on the relative potential of the sorbents for CO_2 capture via VSA.

Thus, a custom gas sorption analyzer was constructed and then employed to characterize CO_2 sorption at 105 °C from pure CO_2, to investigate the kinetics of the sorption processes under more realistic VSA conditions and to better assess the relative potential of the different sorbents for CO_2 capture from flue gas via VSA.

Experimental

Chemicals/Supplies

Zeolite 13X pellets (UOP), tetraethylorthosilicate TEOS reagent grade 98 % (Sigma Aldrich #131903), poly(ethylene glycol)-block-poly(propylene glycol)-block-poly(ethylene glycol) “Pluronic P123” (Aldrich #435455), HCl (BDH Analar sg. 1.16), ethanol absolute (Merck), polyethyleneimine 1200 MW in water (Sigma Aldrich #482595), Ar high purity (BOC), CO_2 high purity (BOC), CO_2 food grade (BOC) and He high purity (BOC).

Materials Preparation

A SBA-15 (*56*) type mesoporous silica was prepared via the nonionic templating technique using Pluronic P123 as template and TEOS as silica source as per the method reported by Sayari et al (*57*). The synthesis solution was aged for 24 h sealed within a polypropylene jar that was, in turn, contained within a Hawkins “Big Boy” 22 L pressure cooker placed within an oven maintained at 100°C.

The supported PEI adsorbent S-PEI was prepared by loading 1.0001 g SBA-15 with its approximate pore volume equivalent of PEI (1.9124 g of 50 % PEI/H_2O) as per the "wet impregnation" method (*22*) using ethanol as both solvent and dispersant. The volume of PEI required was determined from the N_2 adsorption isotherm at $p/p_0 = 0.9$, corresponding to pores < 25 nm diameter according to BJH theory. The PEI and silica were first separately dissolved and dispersed, respectively; the silica dispersion and PEI solutions were then combined and continuously stirred for 24 hours at room temperature. The bulk solvent phase was subsequently removed by rotary evaporation over a hot water bath ~40 °C. The product was then heated at 105 °C under N_2 purge to remove residual solvent.

The zeolite 13X pellets were ground to a powder then dried under vacuum at 350 °C (as required to remove all adsorbed water (*8*)).

A pelletized form of the hybrid SBA-15 / PEI adsorbent S-PEIp was prepared by pressing ~0.2 g S-PEI (post N_2 ads/des at 77 K) under vacuum within a Specac 13 mm diameter evacuable pellet die under 8 tons of pressure for 10 mins (Specac 15.000 ton hydraulic press). The S-PEI was initially dried under N_2 purge at 110 °C for ~30 min before it was loaded into the cylinder bore; the sample was then evacuated sealed within the cylinder for 10 mins before the mechanical pressure was applied. The 0.2037 g pellet prepared was 1.317 cm in diameter and 0.128 cm thick (vernier calipers). The volume was thus 0.174 cm^3 ($V = \pi r^2 h$), and the packing density (PD = m/V) was 1.17 $g.cm^3$. It is noted that SBA-15 could not be transformed into a robust pellet via the same procedure.

Downloaded by CORNELL UNIV on June 14, 2012 | http://pubs.acs.org
Publication Date (Web): May 3, 2012 | doi: 10.1021/bk-2012-1097.ch009

Structural Characterization of Materials

X-ray diffraction (0.5 – 2 2θ degrees) was measured with a Philips 1130 powder x-ray diffractometer using Cu K_α radiation (1.5405981 Å). The sample was finely spread on a thin film of Vaseline spread over a silica support.

N_2 adsorption/desorption at 77 K was measured with a Coulter Omnisorp 360CX gas sorption analyzer. The samples were degassed over night at 105 °C to 10^{-5} torr prior to analysis. BET surface areas (SA) were calculated from adsorption data collected over the partial pressure range 0.05 – 0.25, BJH pore size distributions were determined from the desorption data collected over the partial pressure range 1 – 0.15. Pore volumes (PV) were estimated from the amount of N_2 adsorbed at relative pressure 0.90 (pores < 25 nm dia.).

Thermal stability and air oxidation analysis was measured with a Setaram TAG24 simultaneous symmetrical thermogravimetric analyzer. Materials were initially dried to constant mass under 70 $ml.min^{-1}$ Ar at 110 °C then heated from 110 – 1000 °C at 10 $°C.min^{-1}$ under 70 $ml.min^{-1}$ 40 % air/Ar.

Helium pycnometry was conducted via a Micromeritics Accupyc 1330 pycnometer. Samples S-PEI, SBA-15 and 13X were dried under vacuum over night at 110, 110 and 350 °C respectively prior to analysis. S-PEIp was re-dried under N_2 purge at 110 °C for 40 min prior to analysis.

CO_2 Adsorption/Desorption via Thermogravimetric Analyzer

Combined Thermogravimetric analysis and differential thermal analysis of CO_2 adsorption/desorption was characterized via a Setaram TAG24 simultaneous symmetrical thermogravimetric analyzer. High purity Ar and food grade CO_2 were supplied to the instrument via separate molecular sieve moisture traps. The amine adsorbent type and 13X were initially “pre-activated” / dried to constant mass under Ar at 110 °C and 350 °C respectively (~1 h) then re-weighed to determine their dry mass. The samples were then reloaded into the analyzer then re-activated prior to sorption analysis. The samples were again re-activated post sorption analysis then re-weighed to confirm re-generation of the sorbent. A constant 70 $ml.min^{-1}$ gas flow was supplied to the instrument throughout the experiment via Bronkhorst F-201DV-RAD-11-K mass flow controllers. 35 $ml.min^{-1}$ of Ar was continuously supplied to the balance housing from one mass flow controller. The other 35 $ml.min^{-1}$, comprising Ar and/ or CO_2 was supplied to both the reference and sample furnaces, evenly split, from separate mass flow controllers. The Ar and CO_2 supply lines could be separately passed through glass sinters submerged in 200 ml of distilled water (10 °C) prior to mixing to provide a humidified (1 % H_2O) gas stream.

Design/Construction of the Custom Gas Sorption Analyzer

The custom gas sorption analyser “GSA” (refer Figure 1) comprises a classic volumetric fixed volume gas dosing system contained within a HP5890 gas chromatograph fan forced thermal control oven. The dose manifold (DM) and sample manifold (SM) are constructed from 1/8” stainless steel tubing, connectors and adaptors, and are terminated by Swagelock HBSV4 air actuated bellows valves allowing for independent manifold evacuation. The dose manifold incorporates a 25 ml stainless steel gas cylinder reservoir and is plumbed into a Honeywell PPT0020 pressure transducer (externally mounted just above the control oven). The sample manifold incorporates a 2” long, 0.5” od glass sample vessel connected via a ½” Ultra-Torr fitting. Samples were contained under glass wool. A Teflon jacket was fitted to the sample vessel for thermal insulation. The adsorbate and the sorbent bed temperatures were separately measured by stainless steel sheathed non-earthed K-type thermocouples which were vertically suspended into the DM cylinder reservoir and SM sample vessel respectively via stainless steel union crosses. The thermocouples were sealed in place via custom glass packed Teflon ferrule seals. An additional gas conditioning manifold was fitted leading to the DM which incorporated a 50 ml stainless steel gas cylinder to permit pre-heating of the adsorbate, and a metering valve to regulate gas flow into the dose manifold. Pressure and temperature measurements were recorded via a National Instruments USB6008 data acquisition device and LabView v8.0. Calibration of the sample/dose manifold volumes was conducted with He at 40 °C with a stainless steel ball secondary volume standard (calibrated via Helium pycnometry). High purity He, high purity CO_2 and reticulated N_2 were plumbed into the gas manifold, He and CO_2 supplies were plumbed via separate molecular sieve moisture traps.

Downloaded by CORNELL UNIV on June 14, 2012 | http://pubs.acs.org
Publication Date (Web): May 3, 2012 | doi: 10.1021/bk-2012-1097.ch009

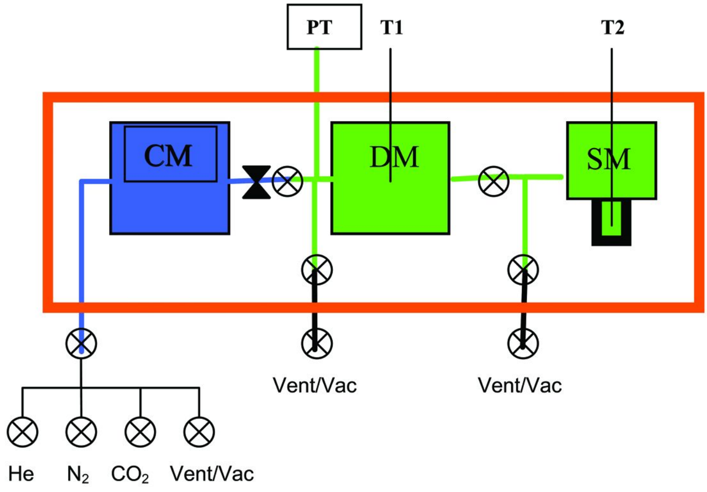

Figure 1. Schematic representation of the custom gas sorption analyzer (GSA): DM-dose manifold, SM-sample manifold, CM-gas conditioning manifold, PT-pressure transducer, T1 & T2 – dose and sample manifold thermocouples,

Downloaded by CORNELL UNIV on June 14, 2012 | http://pubs.acs.org
Publication Date (Web): May 3, 2012 | doi: 10.1021/bk-2012-1097.ch009

CO_2 Adsorption/Desorption via Custom Gas Sorption Analyzer

13X and S-PEI were first weighed into the glass sample vessel, covered with glass wool then dried under vacuum (rotary vane pump) at 350 °C and 110 °C, respectively, for 24 h. The samples were then cooled under N_2 atmosphere, re-weighed, then transferred to the GSA. The samples were then re-degassed in-situ under vacuum at 110 °C for 24 h before the system was thermally equilibrated to 105 °C ready for analysis. CO_2 adsorption (0 – 1 atm), desorption (1 – 0.05 atm) re-adsorption (0.05 – 0.15 atm) and finally re-desorption (0.15 – 0.10 atm) of 13X (~0.7 g) and S-PEI (~0.4 g) were separately conducted, allowing a 20 min thermal equilibration period for each dose. The temperature of the gas volume contained within the insulated sample vessel was assumed to be the same as that of the sorbent bed, the temperature of the remaining dose / sample manifold volume was assumed to be the same as that of the dose manifold. The volume of the samples as determined by their mass amount and helium density was subtracted from the sample manifold volume to facilitate accurate quantification of the amounts of gas adsorbed.

Results

Structural Characterization of Materials

Figure 2 shows the XRD pattern obtained for SBA-15. This exhibits a major peak centered at 0.92 °(2θ) and two minor diffraction peaks at ~1.6 and ~1.8 °(2θ) consistent with the 100, 110 and 200 indexed peaks of calcined SBA-15 type mesoporous silica (p6mm hexagonal symmetry) (*56*). The intense 100 diffraction peak is consistent with a d-space of 96 Å and a unit cell parameter (a=2d*$3^{-0.5}$, average distance between mesopores) of 111 Å.

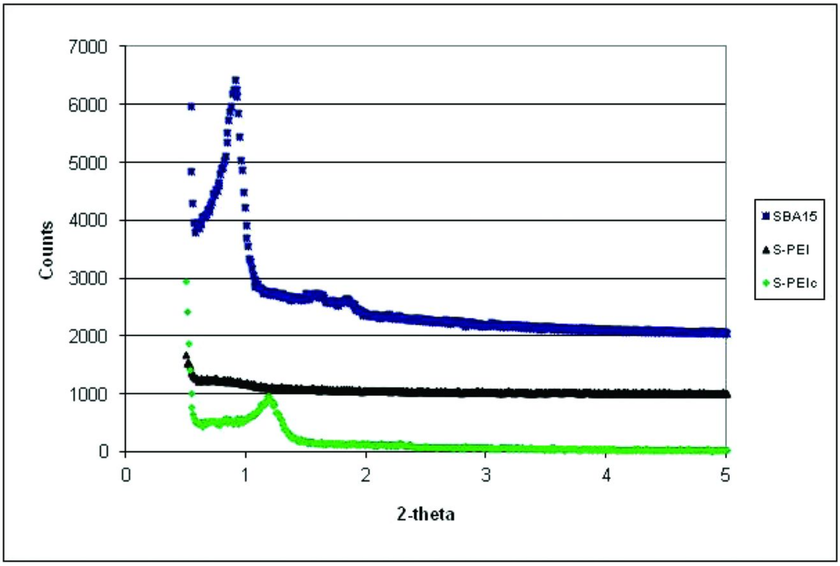

Figure 2. X-ray (Cu-Kα) diffraction obtained for SBA-15, S-PEI and S-PEIc (S-PEI post combustion via TGA).

Figure 2 also shows the XRD patterns obtained for S-PEI both before and after combustion analysis (S-PEIc). The pattern obtained for S-PEI exhibits only very weak broad diffraction over the same 2θ range as SBA-15 and is thought to be consistent with the successful loading of PEI into the substrate mesopores (*22*). The pattern obtained for S-PEIc exhibits a weak diffraction peak at higher 2θ angle consistent with d-space of 74 Å and unit cell parameter of 86 Å. This is thought to be consistent with the subsequent removal / combustion of the PEI component of S-PEI and subsequent dehydroxylation / contraction of the underlying silica framework. These results therefore support the contention that the integrity of the framework was maintained throughout preparation of the S-PEI adsorbent.

Figure 3 shows the N_2 adsorption/desorption isotherms obtained for SBA-15, S-PEI, S-PEIp and 13X. SBA-15 exhibits a Type IV isotherm (*58*), Type H1 hysterisis (*58*) and high mesopore volume as expected for the SBA-15 (*56*). S-PEI exhibits negligible N_2 adsorption and is clearly non-porous, consistent with the successful loading of SBA-15 with a pore volume equivalent of PEI as was intended. S-PEIp likewise exhibits negligible N_2 adsorption consistent with successful compaction of S-PEI without significant loss of PEI. 13X exhibits a Type I isotherm (*58*).

Downloaded by CORNELL UNIV on June 14, 2012 | http://pubs.acs.org
Publication Date (Web): May 3, 2012 | doi: 10.1021/bk-2012-1097.ch009

Downloaded by CORNELL UNIV on June 14, 2012 | http://pubs.acs.org
Publication Date (Web): May 3, 2012 | doi: 10.1021/bk-2012-1097.ch009

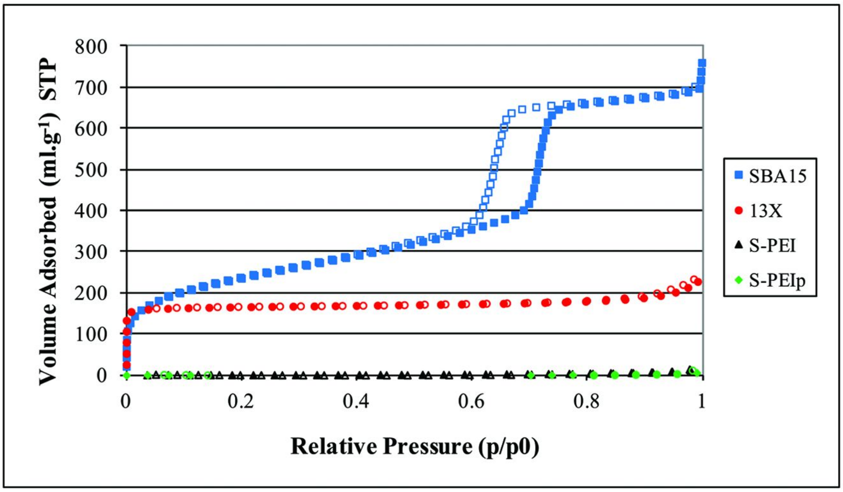

Figure 3. N_2 adsorption/desorption at 77K isotherms obtained for SBA-15, S-PEI, S-PEIp & 13X.

Figure 4 shows the BJH pore size distributions calculated from the desorption isotherms obtained for each of the materials. These results show that the SBA-15 prepared exhibits a narrow distribution of mesopores centered around 5.8 nm consistent with that previously reported (*56*). S-PEI exhibits negligible mesoporosity consistent with the successful loading of SBA-15 with a pore volume equivalent of PEI. 13X likewise exhibits no mesoporosity, as expected for this microporous material.

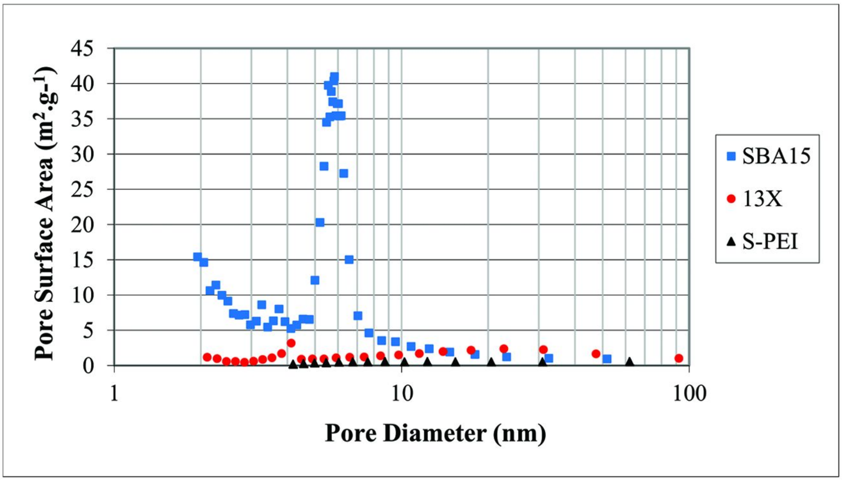

Figure 4. BJH pore size distributions for SBA-15, S-PEI and 13X as calculated from N_2 desorption (77K) isotherms.

Downloaded by CORNELL UNIV on June 14, 2012 | http://pubs.acs.org
Publication Date (Web): May 3, 2012 | doi: 10.1021/bk-2012-1097.ch009

Table 1 lists the BET surface areas (SA), the total pore volumes (PV) and the peak BJH pore diameters (PD) calculated from the relevant isotherm data. These results show that SBA-15 was prepared with 853 $m^2.g^{-1}$ of surface area, 1.04 $ml.g^{-1}$ of pore volume and a narrow distribution of pores centred at 5.8 nm diameter consistent with the highly mesoporous high surface area material reported by Zhao et al (*56*). Given the separation of pore centres determined by XRD (86 Å) it is concluded that SBA-15 exhibits a pore wall thickness of ~53 Å. S-PEI was found to exhibit negligible surface area and negligible pore volume consistent with the loading of SBA-15 with one pore volume equivalent of polyethyleneimine. 13X was found to have a surface area of 523 m^2g^{-1}.

Table 1. Basic physical characteristics of the materials.

	Surface Area *($m^2.g^{-1}$)*	***Pore Volume***^{b} *($ml.g^{-1}$)*	***Pore Diameter*** *(Å)*	***PEI content*** *(wt%)*	***N content*** *(wt%)*	***Helium Density*** *($g.ml^{-1}$)*
std error	11	0.01	0.01			0.01
SBA-15	853	1.04	58	0	0.0	2.23^a
S-PEI	3	0.01	non-porous	50.8	16.5	1.45
S-PEIp	< 3	< 0.01	non-porous	46.7	15.2	1.42
13X	523	0.29	< 20	-	-	2.36

^{a} analogous batch. ^{b} pores less than 25 nm dia. ($p/p_0 = 0.9$).

Figure 5 shows the thermogravimetric analysis records obtained for SBA-15, S-PEI and S-PEIp as they were heated at 10 °C / min from 110 °C to 1000 °C under 40 % air / Ar. SBA-15 exhibits a steady weight loss over the heat ramp losing ~5.2 wt% of its initial dry mass. This is thought to be primarily due to dehydroxylation of the siliceous framework (with possibly a minor contribution from combustion of residual template). S-PEI however exhibits a very different weight loss pattern over the heat ramp losing up to 53.6 wt% (dry basis) due mainly to combustion of the PEI content (and possibly a minor contribution due to dehydroxylation of the silica). The PEI content of S-PEI was calculated to be 50.8 wt% from this data, consistent with an amine N content of 16.5 wt% (assuming PEI MW (43.07 $g.mol^{-1}$) and a 1.00 pore volume equivalent PEI loading into the SBA-15 substrate. S-PEIp was found to comprise only 46.7 wt% PEI (15.2 wt % N), consistent with a 0.86 SBA-15 pore volume equivalent PEI loading. It is therefore concluded that some of the PEI content of S-PEI was lost, either during pelletisation or, more likely, during degassing under ultra low vacuum.

Downloaded by CORNELL UNIV on June 14, 2012 | http://pubs.acs.org
Publication Date (Web): May 3, 2012 | doi: 10.1021/bk-2012-1097.ch009

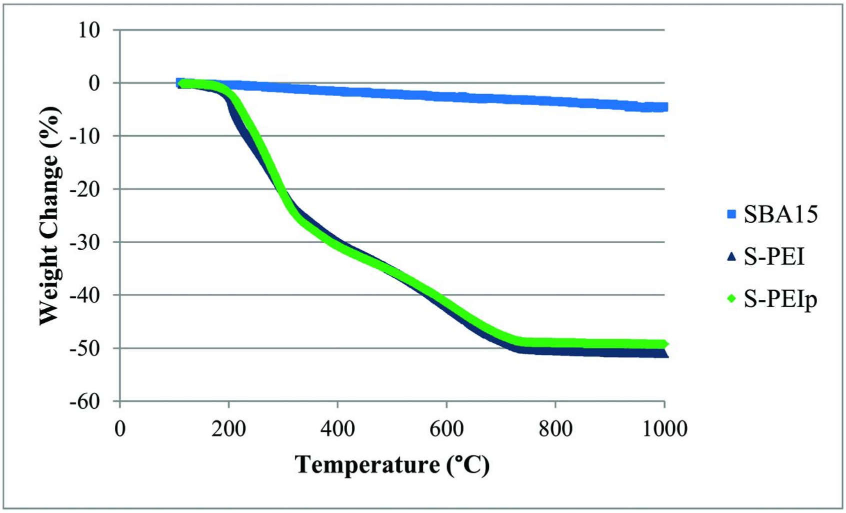

Figure 5. Thermogravimetric analysis of SBA-15, S-PEI and S-PEIp as heated under 70 ml.min^{-1} of 40 % air / Ar.

Table 1 also shows the helium density determined for SBA-15, S-PEI, S-PEIp and 13X. These results show that the SBA-15 had a helium density of 2.23 g.ml^{-1} which is consistent with the density expected for a silicon dioxide (*55*). Likewise the helium density of 13X was found to be 2.36 g.ml^{-1}, i.e. slightly greater than that of SBA-15. The helium density of S-PEI (1.45 g.ml^{-1}) was found to be substantially less than that of SBA-15, as expected, yet even less than that expected for a 50 wt.% loading (~1 pore volume equivelant loading) of PEI in SBA-15 (assuming density of PEI = 1.07 g.ml^{-1}). This is thought due to PEI preventing He access to some of the void space within the material under the experimental conditions (ambient temperature and pressure). S-PEIp had even lower density despite having less PEI content than S-PEI, consistent with compaction preventing He access to even more void space within the material. It is noted that although S-PEI and S-PEIp exhibit negligible porosity at 77K, these results suggest that some of the PEI must be located on the external surface of the SBA-15 leaving some unfilled and inaccesable internal porosity. This porosity which is inaccessible at ambient temperature might, nevertheless, help facilitate good gas diffiusion throughout the PEI phase at the higher temperature at which VSA is evaluated.

CO_2 PPSA via TGA – Anhydrous Atmosphere

Figure 6 shows the thermogravimetric records obtained as the atmospheres surrounding the activated adsorbents S-PEI and 13X were progressively changed from 0 % CO_2/Ar to 2.5, 5, 10, 15, 30, 50, 30, 15, 5, 2.5 and then 0 % CO_2/Ar (allowing 20 min per step for equilibration) at 80, 90, 105, 115 & 125 °C respectively. In each case the weight of the adsorbent increased as the % CO_2 in the atmosphere is increased and then ultimately decreased as the % CO_2 in the surrounding atmosphere was decreased, demonstrating the reversibility of CO_2.adsorption/desorption. At each successive step, the adsorption and desorption of CO_2 appears to reach equilibrium at 105, 115 and 125 °C. However, this does not appear to be so at 80 or 90 °C as the progress towards equilibrium becomes slower as the temperature is reduced. It is noted that the CARiACT G10 solid amine sorbent was found to behave in a similar manner over a slightly lower temperature range (*38*), consistent with its lower PEI loading. The slower adsorption and desorption appears to be due to reduced diffusion of CO_2 through the PEI which, itself, has reduced mobility at the lower temperatures. For 13X, however, CO_2. adsorption and desorption essentially reaches equilibrium at each successive step for all five temperatures studied. Incomplete desorption for each adsorbent is thought to be due to either well bound CO_2 or opportunistic water.

Figure 7 shows the thermogravimetric analysis records obtained for CO_2 adsorption/desorption at 105 °C for S-PEI and 13X accompanied by the DTA records. These show that in each case adsorption was exothermic, desorption was endothermic and the heat flow evolved or released was proportional to the mass adsorbed or desorbed, as expected. Furthermore the DTA records show that S-PEI required more time than 13X to facilitate sorption equilibration over each step, consistent with the TGA records.

Figure 7 also shows the combined TGA/DTA record obtained for S-PEIp. The pelletised adsorbent exhibited a similar thermogravemetric record to its powdered form precursor, however with reduced CO_2 capacity and proportionally reduced heat flow. Thus pelletization was found to lead to a small reduction in sorbent capacity.

Figure 8 shows the $H_{ads}(CO_2)$ estimated from the first 5 minutes of each step of the combined TGA/DTA records for PPSA of CO_2 for both S-PEI and 13X. These results show that $H_{ads}(CO_2)$ on S-PEI is typically within the range 65 – 85 $kJ.mol^{-1}$ over each adsorption step consistent with chemisorption, as expected for carbamate formation. The $H_{ads}(CO_2)$ over the last adsorption step (30-50% CO_2/Ar) is, however, somewhat less (~58 $kJ.mol^{-1}$), possibly due to the lesser significance of additional carbamate formation at this stage. The heat of desorption $H_{des}(CO_2)$ is in most cases similar to the $H_{ads}(CO_2)$ consistent with the reverse reaction, but, it is substantially less for the last desorption step.

Downloaded by CORNELL UNIV on June 14, 2012 | http://pubs.acs.org
Publication Date (Web): May 3, 2012 | doi: 10.1021/bk-2012-1097.ch009

Downloaded by CORNELL UNIV on June 14, 2012 | http://pubs.acs.org
Publication Date (Web): May 3, 2012 | doi: 10.1021/bk-2012-1097.ch009

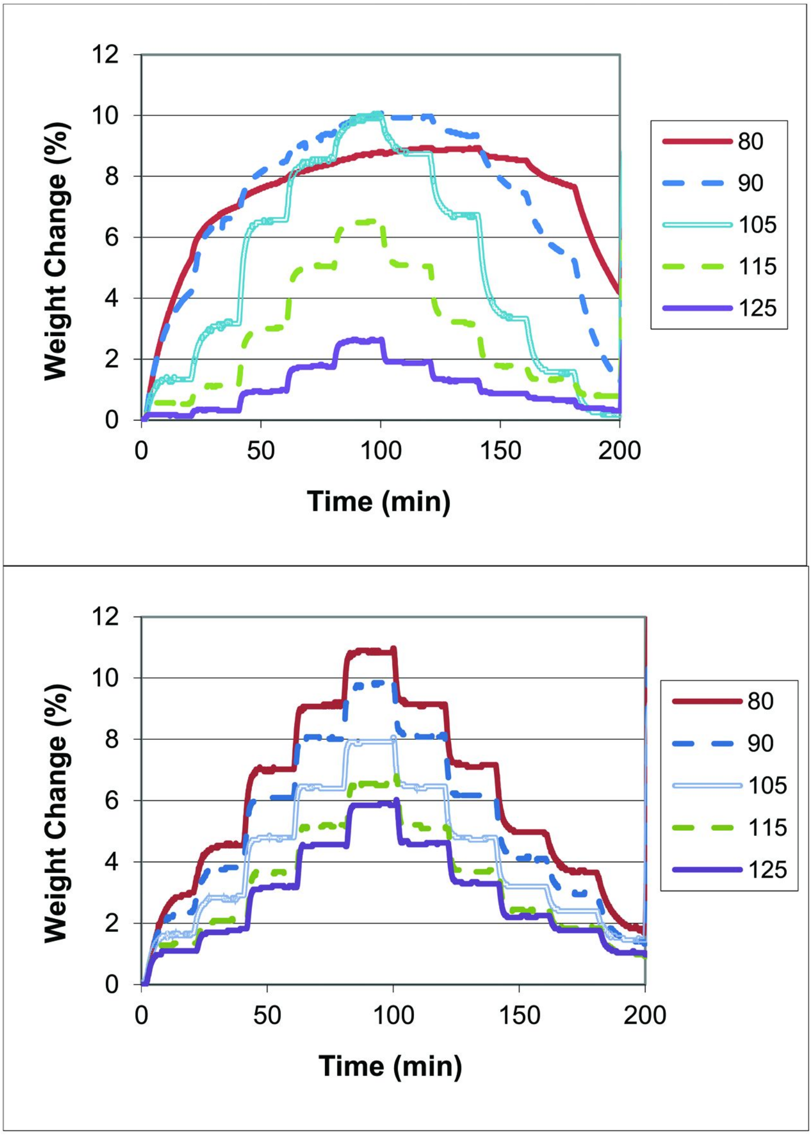

Figure 6. Thermogravimetric analysis of CO_2 adsorption / desorption from 70 ml/min CO_2/Ar mixtures (0, 2.5, 5, 15, 30, 50, 30, 15, 5, 2.5 ,0 % CO_2/Ar) for S-PEI (top) and 13X (btm) at 80, 90, 105, 115 and 125 °C.

Downloaded by CORNELL UNIV on June 14, 2012 | http://pubs.acs.org
Publication Date (Web): May 3, 2012 | doi: 10.1021/bk-2012-1097.ch009

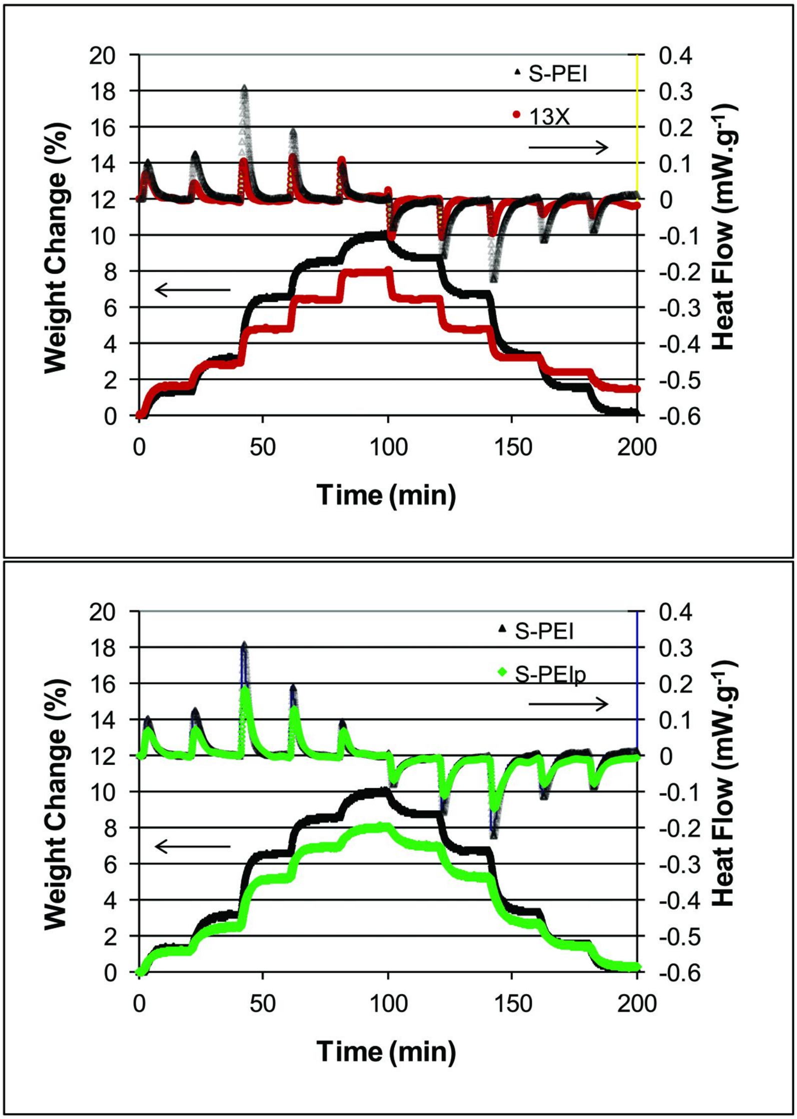

Figure 7. Combined TGA / DTA of CO_2 PPSA for S-PEI & 13X (top) and S-PEI & S-PEIp (btm) at 105 °C from 70 ml.min^{-1} CO_2/Ar mixtures (0, 2.5, 5, 15, 30, 50, 30, 15, 5, 2.5 and 0 % CO_2/Ar).

Downloaded by CORNELL UNIV on June 14, 2012 | http://pubs.acs.org
Publication Date (Web): May 3, 2012 | doi: 10.1021/bk-2012-1097.ch009

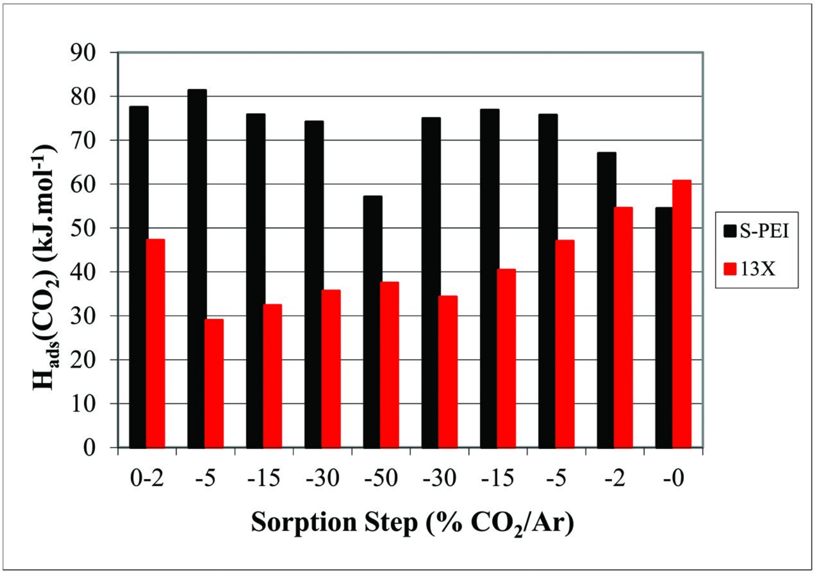

Figure 8. $H_{ads}(CO_2)$ and $H_{des}(CO_2)$ calculated from the combined TGA/DTA records obtained for PPSA of CO_2 for S-PEI and 13X at 105 °C from 70 ml.min^{-1} CO_2/Ar mixtures (0, 2.5, 5, 15, 30, 50, 30, 15, 5, 2.5 and 0 % CO_2/Ar).

The $H_{ads}(CO_2)$ estimated for the 13X is typically within the range 28 – 38 kJ.mol^{-1} which is consistent with the weaker physisorption phenomena expected for this adsorbent. The $H_{ads}(CO_2)$ over the 1st adsorption step (~47 kJ.mol^{-1}) is slightly higher, but this is consistent with the presence of some higher energy sorption sites (*8*). The $H_{des}(CO_2)$ from 13X are within the range observed for adsorption excepting the last two steps; however, this may be a consequence of the greater signficance of measurement errors, due to the smaller amounts of CO_2 desorbed, over these latter steps.

Figure 9 shows the CO_2 adsorption/desorption pseudo isotherms constructed from the thermogravimetric records obtained for S-PEI and 13X (refer Figure 6). Each isotherm point coincides with the weight amount adsorbed at the end of each 20 min equilibration step. The isotherms obtained for 13X are in general linear, exhibit only minor hysteresis at low CO_2 pressure (thought due to the minor presence of opportunistic water) and show that the CO_2 capacity increases in inverse proportion to temperature, as expected, up to 11 wt% (80 °C, 50 % CO_2/Ar).

Downloaded by CORNELL UNIV on June 14, 2012 | http://pubs.acs.org
Publication Date (Web): May 3, 2012 | doi: 10.1021/bk-2012-1097.ch009

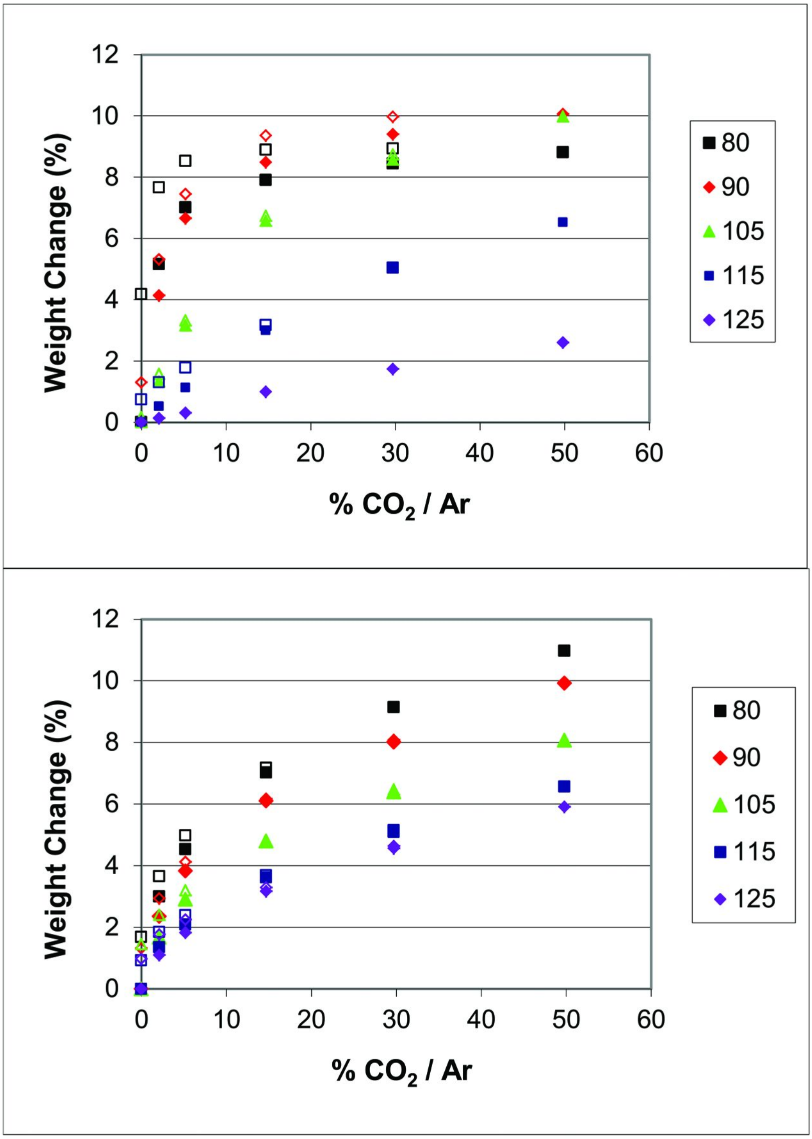

Figure 9. CO_2 pseudo isotherms (105 °C) for S-PEI (top) and 13X (btm) as measured by TGA.

The isotherm obtained for S-PEI at 115 °C is very similar to that observed for 13X at the same temperature. The isotherms obtained at the other temperatures however are very different and, collectively, vary more than those obtained for 13X. The isotherm obtained for S-PEI at 125 °C is more linear but exhibits substantially less CO_2 capacity. The isotherms obtained at 80, 90 and 105 °C are less linear and exhibit a much steeper initial gradient and higher capacity over the CO_2 pressure range (0.05 – 0.15 atm CO_2) targeted for post combustion capture via VSA, thereby suggesting greater CO_2 working capacities. The isotherm obtained at 105 °C appears fully reversible whereas hysteresis is observed at 80 and 90 °C (increasing in inverse proportion to temperature). This is consistent with both carbamate formation and poor PEI mobility being favored at the lower temperatures. Very slight hysterisis is also observed at 115 and 125 °C and this is thought to be due, at least in part, to dehydration of the formed carbamate species into ureas as has previously been reported (*47*, *51*, *52*).

These results show that S-PEI adsorbs up to 10 wt% CO_2 at 105 °C (50 % CO_2/Ar), which is higher than that achieved for 13X at the same temperature, and that adsorption at this temperature is fully reversible. S-PEI exhibits essentially the same CO_2 capacity at 90 °C and, unlike 13X, even less capacity at 80 °C. This reduction in capacity is thought to be due to reduced mobility of the PEI at the lower temperature which thereby reduces the accessiblility of the sorption sites to CO_2. These results also show that the CO_2 capacity of S-PEI is progressively reduced at the higher temperatures of 115 °C to 125 °C, suggesting that about 105 °C is the optimal temperature for VSA processing.

It is noted that S-PEI exhibits greater CO_2 working capacity at 105 °C than does 13X at any of the temperatures at which it was studied. Given that flue gas contains ~0.15 atm CO_2 it is concluded that S-PEI would exhibit greater CO_2 capacity than 13X up to at least 3.3 atm (0.5/0.15 atm) of flue gas. However it is also the case that the reduction in CO_2 capacity from 105 °C to 125 °C is greater for S-PEI than for 13X. This highlights the greater temperature sensitivity of the amine chemisorbent material.

Table 2 lists the CO_2 capacities of S-PEI, S-PEIp and 13X measured under 50 % CO_2/Ar at 105 °C. This shows that the CO_2 capacity of S-PEI (10 wt %) is greater than that of 13X (8.1 wt%) and S-PEIp under these conditions. The S-PEI result is consistent with the capacity reported previously for an analogous but independently prepared material, SBA-15/1200 (*25*) (highlighting synthetic reproducibility), but it is less than the capacity reported for PEI incorporated into mesocellular foam, MCF-y/1200 (~15 wt%)) (*25*), consistent with the higher PEI loading (70 wt%) that can be accommodated within the larger porosity of MCF.

Table 2 also lists the molar ratio of CO_2 adsorbed per amine N (the amine efficiency) for S-PEI, S-PEIp at this loading. These results show that the amine efficiency of S-PEI (0.19 mol.mol^{-1}) was very similar to that for S-PEIp (0.17 mol.mol^{-1}). It is noted, however, that both amine efficiency values are substantially less than 0.5, and therefore that much of the amine content does not effectively bind CO_2 under these conditions. This to some extent is consistent with the contention that the tertiary amine content does not facilitate carbamate formation.

Downloaded by CORNELL UNIV on June 14, 2012 | http://pubs.acs.org
Publication Date (Web): May 3, 2012 | doi: 10.1021/bk-2012-1097.ch009

Table 2 also lists the CO_2 working capacity and associated $H_{ads}(CO_2)$ calculated for both S-PEI, S-PEIp and 13X for the 5 – 15 % CO_2/Ar partial pressure swing at 105 °C. These results show that the working capacity of S-PEI (3.4 wt %) is significantly greater than that of 13X (1.9 wt %) per unit mass, however less than that reported for MCFy/1200 (*25*). These results also show that the $H_{das}(CO_2)$ for S-PEI over this partial pressure swing (76 $kJ.mol^{-1}$) was much greater than that for 13X (32 $kJ.mol^{-1}$) consistent with chemisorptions versus physisorption in the latter case. Since the pellet had a packing density of 1.17 $g.ml^{-1}$, the working capacity of S-PEIp (2.5 wt%) is calculated to be 29.3 g of CO_2 per L of sorbent.

Downloaded by CORNELL UNIV on June 14, 2012 | http://pubs.acs.org
Publication Date (Web): May 3, 2012 | doi: 10.1021/bk-2012-1097.ch009

Table 2. Select CO_2 sorption data for S-PEI, S-PEIh, S-PEIp and 13X as determined by CO_2 PPSA (105 °C) via TGA/DTA.

	CO_2 capacity *[50% CO_2//Ar] (wt%)*	***CO_2 / N*** *[50% CO_2//Ar] ($mol.mol^{-1}$)*	***CO_2 working capacity*** *[5-15% CO_2Ar] (wt%) Ads / Des*	***$H_{ads}(CO_2)$*** *[5-15% CO_2/Ar] (wt%) Ads / Des*
S-PEI	10.0	0.19	3.4 / 3.4	76 / 76
S-PEI-h	8.8	0.17	3.1 / 3.0	80 / 80
S-PEIp	8.0	0.17	2.8 / 2.5	
13X	8.1	n/a	1.9 / 1.6	32 / 47

Figure 10 shows an expanded view of the equilibration records for CO_2 adsorption (0.05 - 0.15 % CO_2/Ar) and CO_2 desorption (0.15 – 0.05 % CO_2/Ar) obtained for S-PEI and 13X via TGA. The data show that 13X exhibits essentially the same initial adsorption rate as S-PEI, despite its overall smaller working CO_2 capacity. In both cases the adsorption rate seems to be limited by the gradual change in CO_2 partial pressure that is a result of the significant gas volume upstream of the sample in the TGA apparatus (ie, the change from 5 – 15 % CO_2 / Ar is not instantaneous). However the fact that the initial rate of CO_2 adsorption for 13X is the same as for the higher capacity S-PEI adsorbent is not inconsistent with better gas diffusion throughout the more porous 13X, as would be expected. The data similarly show that 13X exhibits essentially the same initial desorption kinetics as S-PEI despite its overall smaller working CO_2 capacity. Furthermore these records highlight that desorption proceeds more slowly than adsorption in both cases. Similarly the desorption data are not inconsistent with 13X exhibiting better gas diffusion at this temperature.

Downloaded by CORNELL UNIV on June 14, 2012 | http://pubs.acs.org
Publication Date (Web): May 3, 2012 | doi: 10.1021/bk-2012-1097.ch009

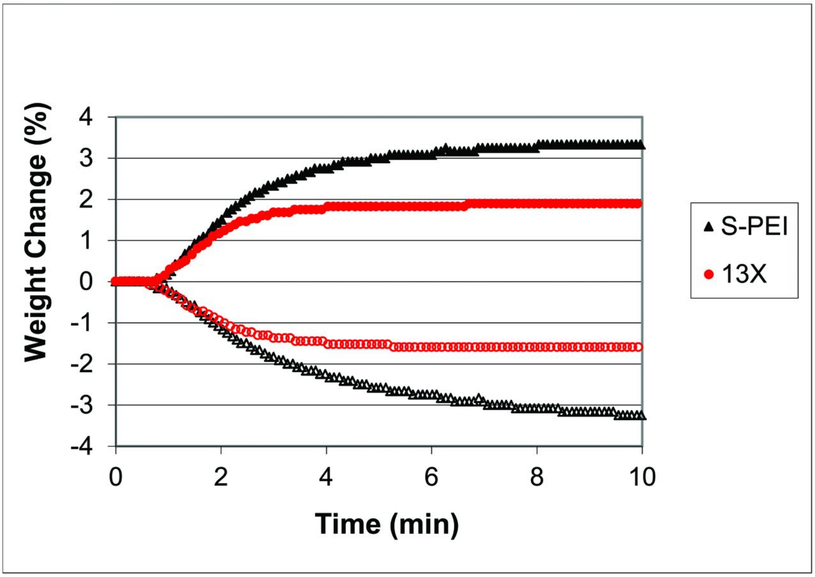

Figure 10. CO_2 PPSA for S-PEI and 13X under anhydrous conditons via TGA; top) adsorption from 5 – 15% CO_2/Ar and bottom) desorption from 15 – 5% CO_2/Ar (70ml/min).

CO_2 PPSA via TGA – Humidified Atmosphere

Figure 11 shows the thermogravimetric records obtained as the atmospheres surrounding the activated adsorbents S-PEI and 13X were first humidified (60 mins) then progressively changed from 0 % CO_2/Ar to 2.5, 5, 10, 15, 30, 50, 30, 15, 5, 2.5 and then 0 % CO_2/Ar (allowing a 20 min equilibration period per step) at 105 °C in the presence of water. These data are plotted together with the data obtained under anhydrous conditions (refer Figure 6). The record obtained for S-PEI under wet conditions is essentially the same as that obtained for S-PEI under anhydrous conditions except for a minor reduction in the amount of mass adsorbed/desorbed over each successive step (refer also Figure 12). It is also noted that a very small amount of weight (0.3 wt%) was found to have become lost from the humidified sample post re-activation. The reduced CO_2 capacity, therefore, may in part be due to loss of some of the low molecular (volatile) PEI fraction due to the presence of water in the gas stream via steam stripping. Should this be the case, steam stripping might then be used as an integral part of sorbent preparation. However, a small reduction in the amount of mass adsorbed was also expected given the reduction of the CO_2 partial pressure due to the addition of water to the gas stream. Nevertheless these results clearly demonstrate that S-PEI exhibits negligible affinity for water under these conditions. Further these results suggest that adsorption to and desorption from S-PEI is not adversely affected by this amount of water in the gas stream at 105 °C, consistent with the affect of 2 vol % water on CO_2 sorption to/from CARiACT G10 solid amine sorbent under similar conditions (*38*).

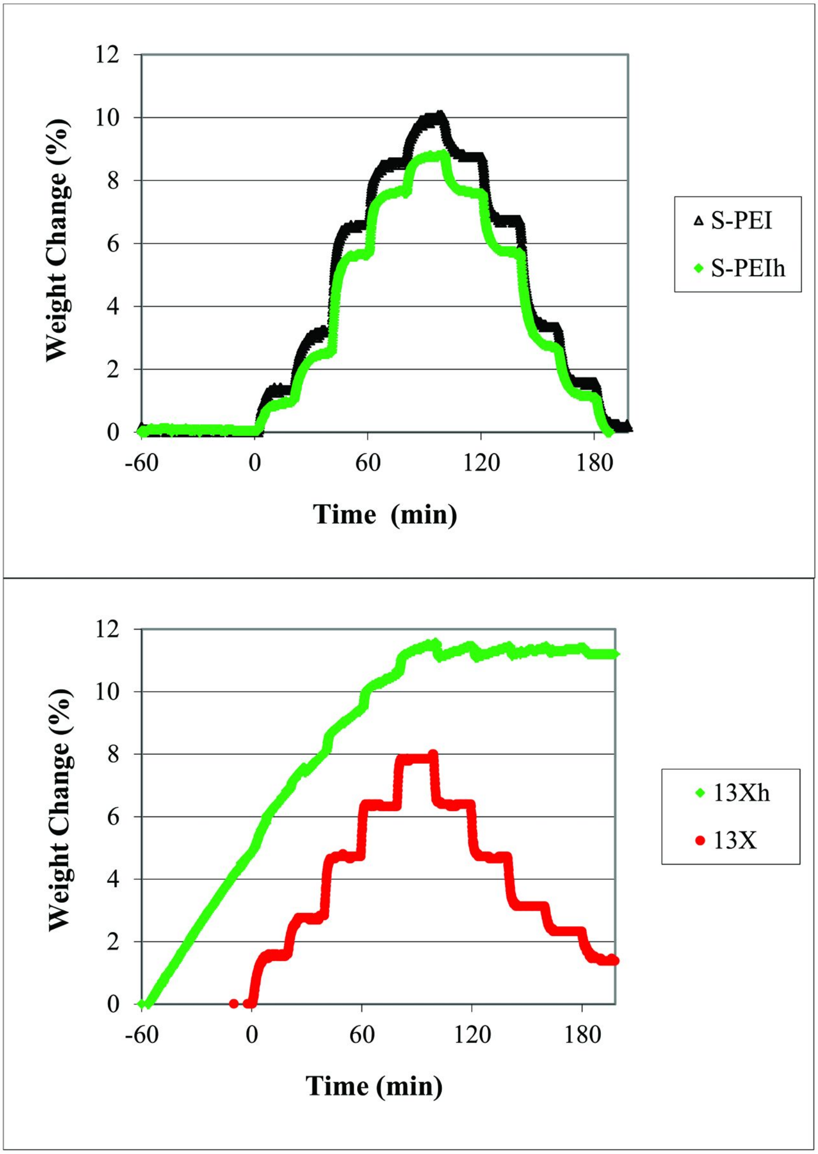

Figure 11. TGA of CO_2 PPSA for S-PEI (top) and 13X (btm) under anhydrous or humidified (h) condions: 70 ml/min of either anhydrous or humidified Ar for 1h followed by 70 ml/min of either anhydrous or humidified CO_2/Ar mixtures (2.5, 5, 15, 30, 50, 30, 15, 5, 2.5, 0 % CO_2/Ar) allowing 20 minutes equilibration per step; gas humidified (~1 % H_2O) by passing 50 % of flow through distilled water (10 °C).

Downloaded by CORNELL UNIV on June 14, 2012 | http://pubs.acs.org
Publication Date (Web): May 3, 2012 | doi: 10.1021/bk-2012-1097.ch009

Downloaded by CORNELL UNIV on June 14, 2012 | http://pubs.acs.org
Publication Date (Web): May 3, 2012 | doi: 10.1021/bk-2012-1097.ch009

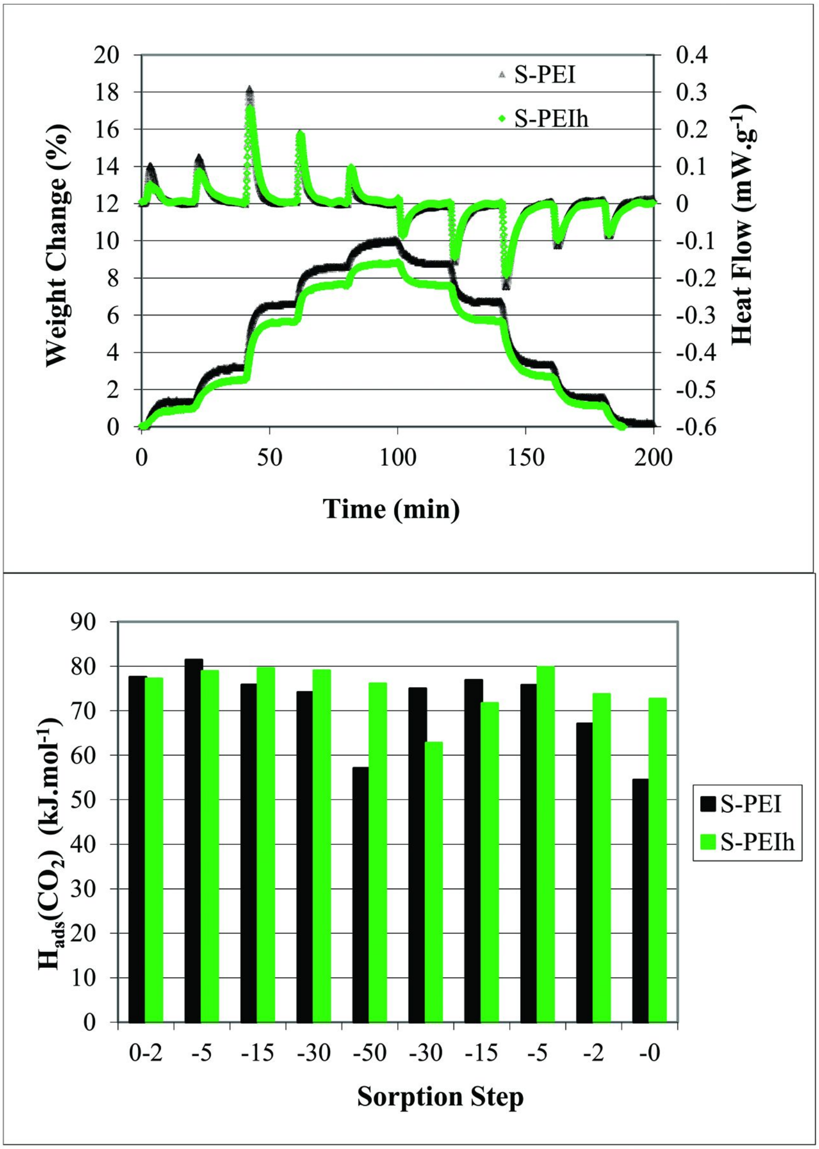

Figure 12. Mass flow and heat flow records (top) and $H_{ads}(CO_2)$ and $[H_{des}(CO_2)]$ estimates (btm) for combined TGA/DTA of CO_2 PPSA for S-PEI at 105 °C under anhydrous and humidified (h) conditons: 70 ml.min^{-1} CO_2/Ar mixtures (0, 2.5, 5, 15, 30, 50, 30, 15, 5, 2.5, 0 % CO_2/Ar), gas humidified (~1 % H_2O) by passing 50% of flow through distilled water (10°C).

The record obtained for 13X under wet conditions, however, is substantially different to that obtained under anhydrous conditions. These data show that 13X adsorbed ~5 wt% H_2O at an essentially constant rate over the initial pre-hydration step and then continued to gain an additional ~6 wt% over the wet CO_2 adsorption cycle. Thus 13X has a much stronger affinity for water than S-PEI. The amount of CO_2 adsorbed under wet conditions cannot be easily determined, because of the competition with H_2O, but it is clearly far less than that observed under anhydrous conditions (~8 wt%). It is noted that 13X exhibits no net mass loss over the subsequent wet desorption cycle which suggests that whatever CO_2 desorption occurred, it was offset by additional water adsorption. It can clearly be concluded that the presence of water has a significant negative impact on CO_2 adsorption on 13X.

Hence these results suggest that S-PEI might be useful to capture CO_2 from higher moisture content gas streams such as would be expected for flue gas without prior removal of the water, whereas they clearly show that 13X would not.

Figure 12 shows both the TGA and DTA records obtained for CO_2 adsorption/desorption at 105 °C for S-PEI under humid (~1 % H_2O) conditions together with those obtained under anhydrous conditions. The records obtained under the humid conditions are very similar to those obtained under the anhydrous conditions in that both exhibit exothermic adsorption, endothermic desorption, heat flow proportional to mass adsorbed/desorbed and similar sorption kinetics. Slightly less heat, however, was evolved/consumed over successive steps under the humid conditions and is thought to be due to the presence of water in the gas stream reducing the effective CO_2 partial pressure in the sample atmosphere.

Figure 12 also shows both the $H_{ads}(CO_2)$ and $[H_{des}(CO_2)]$ estimated from the first 5 minutes of each step of the combined TGA/DTA records for each case. These results show that the enthalpies of adsorption and desorption under the humidified consitions are essentially the same, ranging in general between 70 – 80 $kJ.mol^{-1}$, and so, are consistent with reversible carbamate formation.

Table 2 lists the CO_2 working capacities (5 - 15 % CO_2/Ar) and associated $H_{ads}(CO_2)$ for S-PEI under both anhydrous and humid (S-PEIh) conditions. It can be seen that the CO_2 working capacity of S-PEI under the humid process conditions (3.0 wt%) was only slightly less than that observed under the anhydrous conditions (3.4 wt%). The data also show that S-PEI exhibited $H_{ads}(CO_2)$ of ~80 $kJ.mol^{-1}$, which is essentially the same as that observed under the anhydrous conditions. It is thus concluded that the mechansism of CO_2 adsorption and desorption are the same in each case (carbamate formation), and that the presence of such humidity does not significantly affect the sorption process under these conditions.

CO_2 Adsorption/Desorption via GSA

Figure 13 shows the CO_2 adsorption / desorption (105 °C) isotherms obtained for S-PEI and 13X via the custom Gas Sorption Analyzer GSA. These isotherms show that S-PEI exhibits larger CO_2 capacity than 13X over the range of pressures studied. However, extrapolation of the curves suggests that 13X would have greater CO_2 capacity than S-PEI at higher pressures (> 1.2 atm). The isotherm points up to 0.5 atm are, in each case, essentially the same as those obtained by

In Recent Advances in Post-Combustion CO2 Capture Chemistry; Attalla, M.;
ACS Symposium Series; American Chemical Society: Washington, DC, 2012.

Downloaded by CORNELL UNIV on June 14, 2012 | http://pubs.acs.org
Publication Date (Web): May 3, 2012 | doi: 10.1021/bk-2012-1097.ch009

the thermogravimetric analysis of CO_2 sorption from mixed CO_2/Ar gas streams (~1 atm) and so validate the assumptions made with respect to the application of Henry's Law to gas adsorption and the use of the TGA approach to assess the potential of materials as adsorbents for CO_2 capture via VSA. Furthermore, given that S-PEI was degassed under vacuum at 110 °C (more aggressively than during initial preparation) prior to the GSA experiment, these results further highlight the thermal stability of the sorbent. Given that flue gas contains ~0.15 atm CO_2 these results also suggest that S-PEI will actually exhibit greater CO_2 capacity than 13X up to ~8 atm (1.2/0.15 atm) of flue gas.

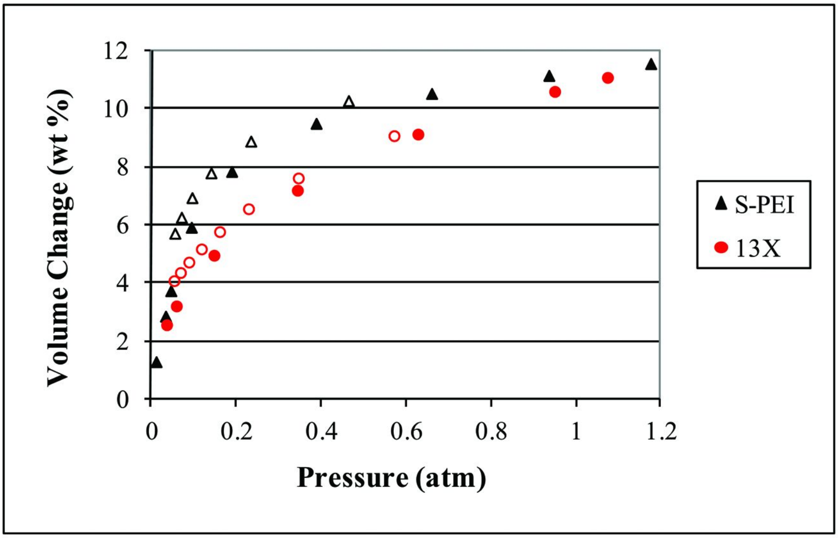

Figure 13. CO_2 adsorption/desorption isotherms (105°C) for S-PEI and 13X via the custom gas sorption analyzer (■-adsorption, □-desorption).

Figure 14 shows the equilibration records (1 – 10 min) obtained for adsorption of CO_2 (0.05 – 0.15 atm, 105 °C) on S-PEI and 13X separately via the custom GSA. These results show that although S-PEI has greater isothermal CO_2 capacity than 13X, it actually exhibits slower initial adsorption kinetics than 13X, only exhibiting greater CO_2 capacity than 13X ~1.5 minutes after the dose was initiated. The 13X bed temperature rises as much as the S-PEI bed temperature despite more initial adsorption consistent with its lower $H_{ads}(CO_2)$.

Downloaded by CORNELL UNIV on June 14, 2012 | http://pubs.acs.org
Publication Date (Web): May 3, 2012 | doi: 10.1021/bk-2012-1097.ch009

Downloaded by CORNELL UNIV on June 14, 2012 | http://pubs.acs.org
Publication Date (Web): May 3, 2012 | doi: 10.1021/bk-2012-1097.ch009

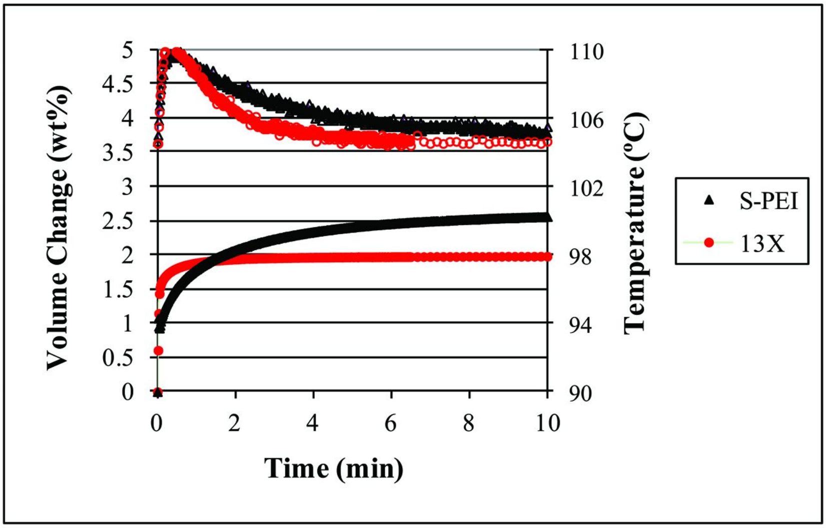

Figure 14. CO_2 adsorption / desorption equilibration record (0.05 - 0.15 atm,105°C) for S-PEI and 13X via the custom gas sorption analyzer (■-adsorbed, □-bed temperature).

Figure 15 shows the equilibration records (1 - 10 mins) obtained for desorption of CO_2 at 105°C from S-PEI (0.15 - 0.10 atm) and from 13X (0.15 - 0.11 atm) via the GSA. Although S-PEI has greater reversible isothermal CO_2 capacity than 13X, it actually exhibits slower desorption kinetics than 13X, only providing greater working capacity than 13X ~1 minute after the step was initiated. Furthermore these results show that the 13X bed temperature drops as much as the S-PEI bed temperature (even slightly more) despite more initial desorption consistent with its lower $H_{ads}(CO_2)$. It is noted that volume of the dose manifold relative to the size of the sample limited the single step desorption from 0.15 atm to only ~0.10 atm; it would be necessary to fit a larger dedicated desorption manifold to the GSA to facilitate characterization of deeper single step desorption.

Conclusions

Highly mesoporous high surface area SBA-15 silica was prepared. The SBA-15 was loaded with one pore volume equivalent of 1200 MW branched polyethyleneimine to prepare a hybrid adsorbent powder, S-PEI, via wet impregnation without compromising the integrity of the support framework. The bulk of the PEI was contained within the framework mesopores, nevertheless some PEI was found to reside external to the mesopores, such that void space existed within the product, permitting good gas diffusion at elevated temperature. The external PEI presumably helped to facilitate compaction of the powder into a robust pellet, S-PEIp.

Downloaded by CORNELL UNIV on June 14, 2012 | http://pubs.acs.org
Publication Date (Web): May 3, 2012 | doi: 10.1021/bk-2012-1097.ch009

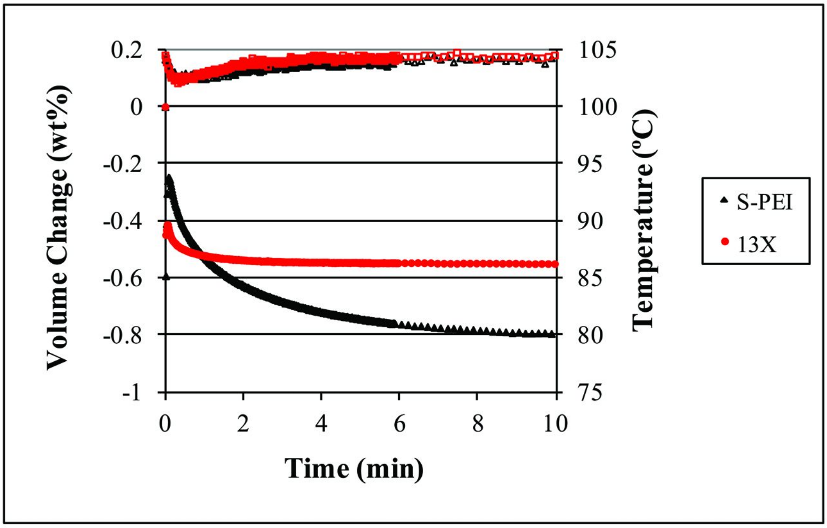

Figure 15. CO_2 desorption equilibration records for S-PEI (0.15 - 0.10 atm, 105 °C) and for 13X (0.15 - 0.11 atm, 105 °C) via the custom gas sorption analyzer (■-adsorbed, □-bed temperature).

S-PEI CO_2 PPSA behavior was found to be highly dependant on temperature. The adsorption was found to be optimal at 105 °C, at which temperature it exhibited 10.0 wt % CO_2 capacity (50 % CO_2/Ar), 3.4 wt% CO_2 working capacity (5 – 15 % CO_2/Ar) and $H_{ads}(CO_2)$ of 70 – 90 kJ.mol^{-1}. (consistent with chemisorption). Adsorption capacities and desorption kinetics were compromised by poorer gas diffusion and the high $H_{ads}(CO_2)$ at lower temperaures. Sorption kinectics were improved by higher process temperatures, however the extent of carbamate formation was compromised. Importantly, S-PEI CO_2 sorption was not adversely affected by the presence of water (1 %) at 105 °C, however 13X was severely compromised.

CO_2 sorption data obtained via the custom gas sorption analyser (GSA) confirmed that PPSA experiments using a TGA to be a valid way to estimate CO_2 sorption under VSA conditions. By both approaches S-PEI was found to exhibit both greater CO_2 working capacity and greater water tolerance than zeolite 13X under key VSA process conditions. The kinetic data collected by the GSA demonstrated that although S-PEI exhibits slower initial sorption kinctics than 13X, consistent with its lower $H_{ads}(CO_2)$, its adsorption/desorption rates are still well suited for the processing of flue gas via VSA.

It was also shown that S-PEI can be readily compacted into a robust pellet with good CO_2 sorption akin to its powder precursor without the need for additional binder. The pellet also exhibited a good CO_2 working capacity (5 – 15 % CO_2/Ar) of 2.5 wt% at 105 °C and with minimal void volume, such that a volumetric working capacity of 29.3 g of CO_2 per L of sorbent was determined. Thus, these results show that amine functionalised mesoporous materials, such as

S-PEI, present a robust, water tolerant and high capacity VSA sorbent option for CO_2 capture from post combustion flue gas.

Acknowledgments

We acknowledge Rod Mackie (School of Physics, Monash University) for obtaining the XRD data. Alan Holland, Roger Bucknell and Rod Cutts (Mechanical Workshop, School of Physics, Monash University) and Antonio Benci, Darren Scott and David Zuidema (Electronics Workshop, School of Physics, Monash University) and Martin Szarszky, King Fung Tze and Hung Tey Nguyen (vacation scholars) are acknowledged for their contributions to the construction and testing of the GSA.

References

1. Stern, N.; Treasury, G. *The economics of climate change: the Stern review*; Cambridge University Press: 2007.
2. Garnaut, R. *The Garnaut Climate Change Review*; Cambridge University Press: Port Melbourne, 2008.
3. Cook, P. J. *Int. J. Environ. Stud.* **2006**, *63* (6), 731–749.
4. Davidson, R.; *Post combustion carbon capture from coal fired plants- solvent scrubbing*; 2007.
5. Davidson, R. *Post-combustion carbon capture- solid sorbents and membranes*; IEA Clean Coal Centre Reports; 2009.
6. Chaffee, A. L.; et al. *Int. J. Greenhouse Gas Control* **2007**, *1* (1), 11–18.
7. Xiao, P.; et al. *Adsorption* **2008**, *14* (4), 575–582.
8. Siriwardane, R. V.; et al. *Energy Fuels* **2005**, *19* (3), 1153–1159.
9. Harlick, P. J. E.; Tezel, F. H. *Microporous Mesoporous Mater.* **2004**, *76* (1−3), 71–79.
10. Choi, S.; Drese, J. H.; Jones, C. W. *ChemSusChem* **2009**, *2* (9), 796–854.
11. Li, G.; et al. *Adsorption* **2008**, *14* (2), 415–422.
12. Li, G.; et al. *Energy Procedia* **2009**, *1* (1), 1123–1130.
13. Belmabkhout, Y.; Serna-Guerrero, R.; Sayari, A. *Ind. Eng. Chem. Res.* **2009**, *49* (1), 359–365.
14. Knowles, G. P.; Delaney, S. W.; Chaffee, A. L. *Ind. Eng. Chem. Res.* **2006**, *45* (8), 2626–2633.
15. Serna-Guerrero, R.; Da'na, E.; Sayari, A. *Ind. Eng. Chem. Res.* **2008**, *47* (23), 9406–9412.
16. Gray, M. L.; et al. *Energy Fuels* **2009**, *23* (10), 4840–4844.
17. Knowles, G. P.; et al. *Fuel Process. Technol.* **2005**, *86* (14−15), 1435–1448.
18. Khatri, R. A.; et al. *Ind. Eng. Chem. Res.* **2005**, *44* (10), 3702–3708.
19. Bollini, P.; et al. *Energy Fuels* **2011**, *25* (5), 2416–2425.
20. Xu, X.; et al. *Proc. - Annu. Int. Pittsburgh Coal Conf.* **2001**, *18*, 820–825.
21. Xu, X.; et al. *Energy Fuels* **2002**, *16* (6), 1463–1469.
22. Xu, X.; et al. *Microporous Mesoporous Mater* **2003**, *62* (1−2), 29–45.

Downloaded by CORNELL UNIV on June 14, 2012 | http://pubs.acs.org
Publication Date (Web): May 3, 2012 | doi: 10.1021/bk-2012-1097.ch009

23. Knowles, G. P.; et al. *Prepr. Symp. - Am. Chem. Soc., Div. Fuel Chem.* **2010**, *55* (1), 683–684.
24. Chen, C.; Ahn, W.-S. *Chem. Eng. J. (Amsterdam, Neth.)* **2011**, *166* (2), 646–651.
25. Subagyono, D. J. N.; et al. *Chem. Eng. Res. Des.* **2011**, *89*, 1647–1657.
26. Yan, X.; et al. *Ind. Eng. Chem. Res.* **2011**, *50* (6), 3220–3226.
27. Liu, S.-H.; et al. *Top. Catal.* **2010**, *53* (3), 210–217.
28. Leal, O.; et al. U.S. Patent 5,087,597, 1992.
29. Kim, S.-N.; et al. *Microporous Mesoporous Mater.* **2008**, *115* (3), 497–503.
30. Osei-Prempeh, G.; et al. *Ind. Eng. Chem. Res.* **2011**, *50* (9), 5510–5522.
31. Huh, S.; et al. *Chem. Mater.* **2003**, *15* (22), 4247–4256.
32. Hicks, J. C.; et al. *J. Am. Chem. Soc.* **2008**, *130* (10), 2902–2903.
33. Harlick, P. J. E.; Sayari, A. *Ind. Eng. Chem. Res.* **2006**, *45* (9), 3248–3255.
34. Li, P.; et al. *Langmuir* **2008**, *24* (13), 6567–6574.
35. Alauzun, J.; et al. *J. Am. Chem. Soc.* **2005**, *127* (32), 11204–11205.
36. Knowles, G. P.; Beyton, V.; Chaffee, A. L. *Prepr. Symp. - Am. Chem. Soc., Div. Fuel Chem.* **2006**, *51* (1), 102–103.
37. Liang, Z.; et al. *Adsorption* **2009**, *15* (5), 429–437.
38. Ebner, A. D.; et al. *Ind. Eng. Chem. Res.* **2011**, *50* (9), 5634–5641.
39. Samanta, A.; et al. *Ind. Eng. Chem. Res.* **2012**, *51*, 1438–1463.
40. Satyapal, S.; et al. *Energy Fuels* **2001**, *15* (2), 250–255.
41. Chatti, R.; et al. *Microporous Mesoporous Mater.* **2009**, *121* (1−3), 84–89.
42. Jadhav, P. D.; et al. *Energy Fuels* **2007**, *21* (6), 3555–3559.
43. Ma, X.; Wang, X.; Song, C. *J. Am. Chem. Soc.* **2009**, *131* (16), 5777–5783.
44. Chang, A. C. C.; et al. *Energy Fuels* **2003**, *17* (2), 468–473.
45. Khatri, R. A.; et al. *Energy Fuels* **2006**, *20* (4), 1514–1520.
46. Pinto, M. s. L.; et al. *Chem. Mater.* **2011**, *23* (5), 1387–1395.
47. Drage, T. C.; et al. *Microporous Mesoporous Mater.* **2008**, *116* (1−3), 504–512.
48. Knowles, G. P.; Delaney, S. W.; Chaffee, A. L. *Stud. Surf. Sci. Catal.* **2005**, 887–896.
49. Belmabkhout, Y.; Sayari, A. *Adsorption* **2009**, *15* (3), 318–328.
50. Knöfel, C.; et al. *Microporous Mesoporous Mater.* **2007**, *99* (1−2), 79–85.
51. Knowles, G. P.; Chaffee, A. L. *Prepr. Pap. - Am. Chem. Soc., Div. Fuel Chem.* **2011**, *56* (1), 265–266.
52. Sayari, A.; Belmabkhout, Y. *J. Am. Chem. Soc.* **2010**, *132* (18), 6312–6314.
53. Pirngruber, G. D.; et al. *Energy Procedia* **2009**, *1* (1), 1335–1342.
54. Knowles, G. P. ; Webley, P. A.; Chaffee, A. L. Novel adsorbents for CO2 separation - adiabatic behaviour. *CO2CRC Research Symposium 2006*; CO2CRC, Australia, 2006.
55. Weast, R. C., Selby, S. M., Eds.; *CRC Handbook of Chemistry and Physics*, 47th ed.; The Chemical Rubber Co.: 1966.
56. Zhao, D.; et al. *J. Am. Chem. Soc.* **1998**, *120* (24), 6024–6036.
57. Sayari, A.; Han, B.-H.; Yang, Y. *J. Am. Chem. Soc.* **2004**, *126* (44), 14348–14349.

Downloaded by CORNELL UNIV on June 14, 2012 | http://pubs.acs.org
Publication Date (Web): May 3, 2012 | doi: 10.1021/bk-2012-1097.ch009

58. Lowell, S.; et al. Characterisation of porous solids and powders: surface area, pore size and density. *Particle Technology*; Scarlett, B., Ed.; Kluwer Academic Publishers: Dordrecht, 2004.

Downloaded by CORNELL UNIV on June 14, 2012 | http://pubs.acs.org
Publication Date (Web): May 3, 2012 | doi: 10.1021/bk-2012-1097.ch009

Downloaded by UNIV OF GUELPH LIBRARY on June 14, 2012 | http://pubs.acs.org
Publication Date (Web): May 3, 2012 | doi: 10.1021/bk-2012-1097.ch010

Chapter 10

Environmental Impacts of Post-Combustion Capture: New Insight

M. I. Attalla,* P. Jackson, and K. Robinson

Energy Transformed Flagship, CSIRO Energy Technology,
10 Murray-Dwyer CCT, Mayfield West NSW 2300, Australia
***e-mail: Moetaz.attalla@csiro.au**

This chapter reports on the propensity of amine-based post combustion CO_2 capture (PCC) solvents to form deleterious nitrosamine compounds in the presence of NO_x. The formation and emission of these materials from the PCC process has not been investigated in detail. The entrainment of these degradation products in the scrubbed flue gas and subsequent release to the environment is an issue that requires attention, particularly because of their hazardous nature. A possible mitigation method that can reduce emissions is the UV treatment of the solvent liquor, scrubbed gas and/or wash water to destroy any $RR'N\text{-}NO_{1,2}$ materials that can form during the PCC process.

Introduction

Despite amine-based post-combustion CO_2 capture (PCC) being an established technology it has been used for decades to remove CO_2 from small volume/flow industrial gas streams many challenges must be overcome before large scale CO_2 capture from power station flue gas can be realized. One challenge involves addressing the degradation of the solvent (by both oxidative and thermal processes) that occurs under typical flue gas conditions i.e. in the presence of O_2, NO_x and SO_x. As well, there is the potential release of volatile solvents and solvent degradation products to the atmosphere via (i) entrainment in droplets

In Recent Advances in Post-Combustion CO2 Capture Chemistry; Attalla, M.;
ACS Symposium Series; American Chemical Society: Washington, DC, 2012.

or (ii) volatilization during the flue-gas scrubbing process. The associated environmental impacts need to be given serious consideration.

If solvent-based PCC technology is deployed at an industrial scale, potentially millions of tonnes of solvent will be used per annum. Hence, the small-scale emission of solvents and solvent degradation products to the environment appears inevitable. Recent reports by Braten *et al.* (*1*) and Stangeland and Shao (*2*) clearly indicate that nitrosamine and nitramine generation is feasible when organic amines are utilized in a PCC process. Nitrosamines, nitramines and other N-centred species are potentially hazardous to both mammals (potential carcinogens) and aquatic life-forms (*3*). The formation and emission of these materials from the PCC process has not yet been fully explored.

Given the potential magnitude of (fugitive) amine release if solvent-based PCC technology is adopted globally, research efforts in areas such as:

i. understanding the photochemistry of slipped nitrosamines and other degradation by-products, their atmospheric half-lives and
ii. understanding the impact of slipped amines and degradation byproducts on the biosphere e.g. organism toxicity,

are warranted and necessary.

This case study demonstrates that secondary amines used in PCC formulations, such as piperazine (PZ) and diethanolamine (DEA), react slowly with NO_x in the presence of O_2 to form nitrosamine derivatives under controlled laboratory conditions. The experimental conditions under which these N-nitrosamine derivatives form are not dissimilar to the conditions found inside a typical CO_2 flue-gas absorption column e.g. P ~ 1 atm; gas composition 81.4 % N_2, 12.8 % CO_2, 0.8 % NO and 5.0 % O_2; temperature of 60 °C. The principal differences between the laboratory-based experiments and those of a typical capture plant are:

i. the absence of sorbent cycling, which is performed at an industrial scale to regenerate the amine from the carbamate derivative and liberate the captured CO_2, and
ii. elevated nitric oxide levels (used as a proxy for NO_x) which are normally present at 300-700 ppm in flue streams derived from black coal (*4*). Elevated levels of nitric oxide and nitrogen dioxide will simply accelerate the rate of amine degradation and the formation of N-nitrosoamines.

The structure of the amines investigated in this study are presented in Figure 1. This chapter focuses mainly on the results for piperazine, which has been studied more exhaustively than the other secondary amines.

Downloaded by UNIV OF GUELPH LIBRARY on June 14, 2012 | http://pubs.acs.org
Publication Date (Web): May 3, 2012 | doi: 10.1021/bk-2012-1097.ch010

Downloaded by UNIV OF GUELPH LIBRARY on June 14, 2012 | http://pubs.acs.org
Publication Date (Web): May 3, 2012 | doi: 10.1021/bk-2012-1097.ch010

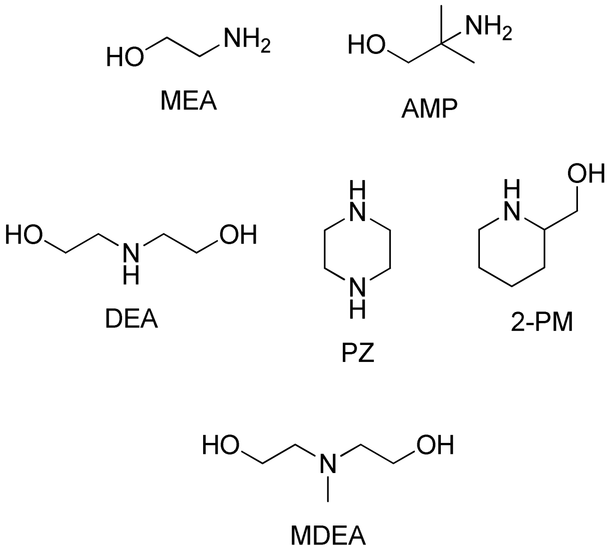

Figure 1. Structures of the amines examined for nitrosamine formation. These amines are commonly used in PCC solvent formulations.

Establishing the Formation of N-Nitrosamine Derivatives

For the investigation of nitrosamine formation from amine-based PCC absorbents, a typical experiment involved bubbling a simulated flue gas stream (of the composition outlined previously) at a flow rate of 1.34 L/min, through a 200 g mass of:

1. 15 wt % aqueous solution of piperazine
2. 30 wt % solutions of monoethanolamine (MEA), 2-amino-2-methyl-1-propanol (AMP), diethanolamine (DEA), methyldiethanolamine (MDEA) and 2-piperidinemethanol (2-PM).

All experiments were carried out at a reaction temperature of 60°C, with a total run time of 15 hours. Reaction mixtures were sampled at 3 hour intervals for analysis by positive ion electrospray ionization-mass spectrometry (ESI-MS). Broad-scan (m/z 50 – m/z 250) ESI-mass spectra were used to screen for the species of interest and optimize mass spectrometer parameters. Measures were adopted to exclude light from the reaction mixture, including the use of aluminium foil and opaque (brown glass) reaction and sample vessels.

Nitrosamine Derivatives of Secondary Amines

N-Nitrospiperazine

The broad scan positive ion ESI-mass spectrum collected for a 15 wt % aqueous piperazine reaction mixture, following exposure to the simulated flue gas stream for 3.5, 7.0 and 15.0 hrs respectively, are shown in Figure 2.

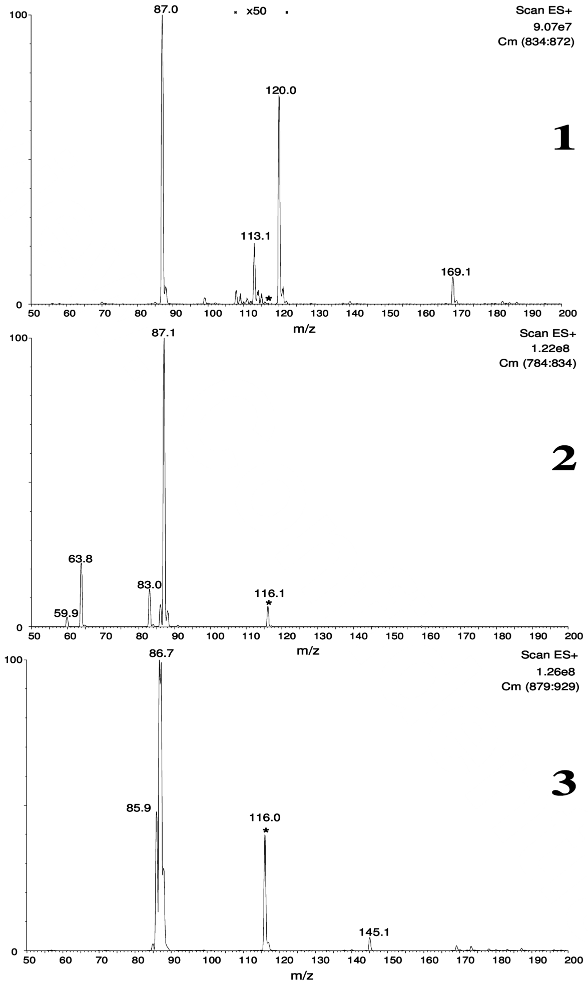

Figure 2. Broad-scan spectra of the aqueous piperazine reaction mixture after exposure to simulated flue gas for ***(1)*** *t = 3.5 hours,* ***(2)*** *t = 7 hours, and* ***(3)*** *t = 15 hours. m/z 116, N-nitrosopiperazine, is labelled with an asterisk. N-nitrosamine can be seen to increase with time relative to the piperazine (m/z 87) peak.*

Downloaded by UNIV OF GUELPH LIBRARY on June 14, 2012 | http://pubs.acs.org
Publication Date (Web): May 3, 2012 | doi: 10.1021/bk-2012-1097.ch010

Downloaded by UNIV OF GUELPH LIBRARY on June 14, 2012 | http://pubs.acs.org
Publication Date (Web): May 3, 2012 | doi: 10.1021/bk-2012-1097.ch010

The broad-scan spectra of the reaction mixtures were quite complex and contained many species. For example, protonated and sodiated peaks identified in the piperazine reaction mixture include $(H_2O)(CH_3CN)H^+$, $(CH_3CN)Na^+$ or $H_2NO_3^+$, $(CH_3CN)_2H^+$, PZH^+, $(CH_3CN)_2Na^+$, $PZ\text{-}OH^+$ (the N-oxide of piperazine), $PZNOH^+$ (N-nitrosopiperazine), $PZ\text{-}CO_2H_2^+$ (piperazine carbamic acid derivative), $PZ\text{-}NO_2H^+$ (piperazine nitramine) and $ON\text{-}PZ\text{-}NOH^+$ (1,4-dinitrosopiperazine). The abundance of the peak at m/z 116 (N-nitrosopiperazine) increases with time in the presence of oxygen, and a peak at m/z 145 also evolves after 15 hrs, which corresponds to protonated N,N-dinitrosopiperazine.

There was found to be no appreciable formation of N-nitrosopiperazine in samples exposed to a simulated flue gas without oxygen (after t = 3.5 hours and t = 14 hours, synthetic flue gas composition 81.4 % N_2, 17.8 % CO_2, 0.8 % NO).

The low energy collision-induced dissociation (CID) spectrum of protonated N-nitrosopiperazine (*m/z* 116) is presented in Figure 3. Peaks corresponding to loss of 30 (NO) and 31 (HNO) mass units dominate the spectrum. Deuterium labelling studies confirmed the identity of these losses, and that m/z 116 is indeed protonated N-nitrosopiperazine (*5*).

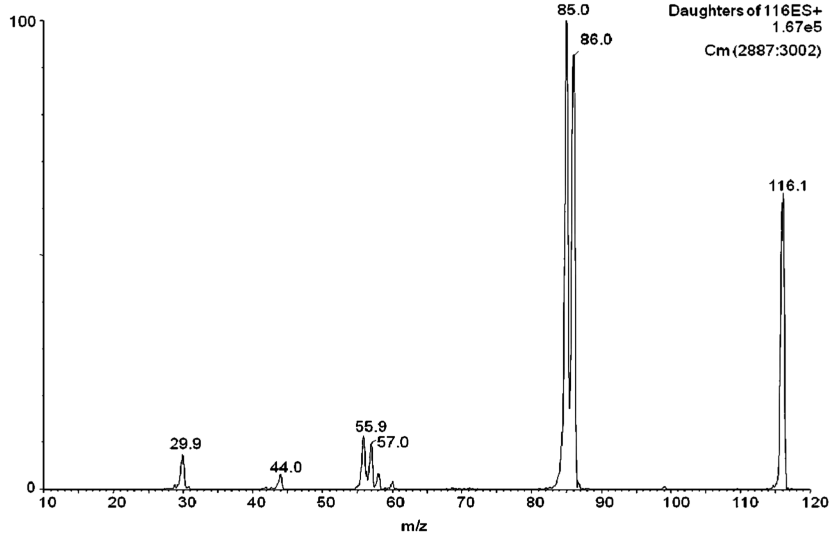

Figure 3. Low energy CID spectrum of putative N-nitrosopiperazine. Two major products are observed corresponding to loss of NO (m/z 86) and HNO (m/z 85).

The mass losses can be rationalised according to Scheme 1, with loss of 31 mass units resulting from protonation of the NO group, whereas protonation of the ring nitrogen at the 4-position leads to loss of $NO^•$. Evidence that the nitrogen in the four position is protonated is the peak corresponding to loss of ammonia (17 mass units, *m/z* 99). The peaks at m/z 56, 57 originate from losses of methanimine from m/z 85, 86 respectively (refer to Scheme 1). The peak at m/z 30 (NO^+) is likely to arise from charge-trapping upon dissociation of the parent ion, to produce neutral piperazine after rearrangement.

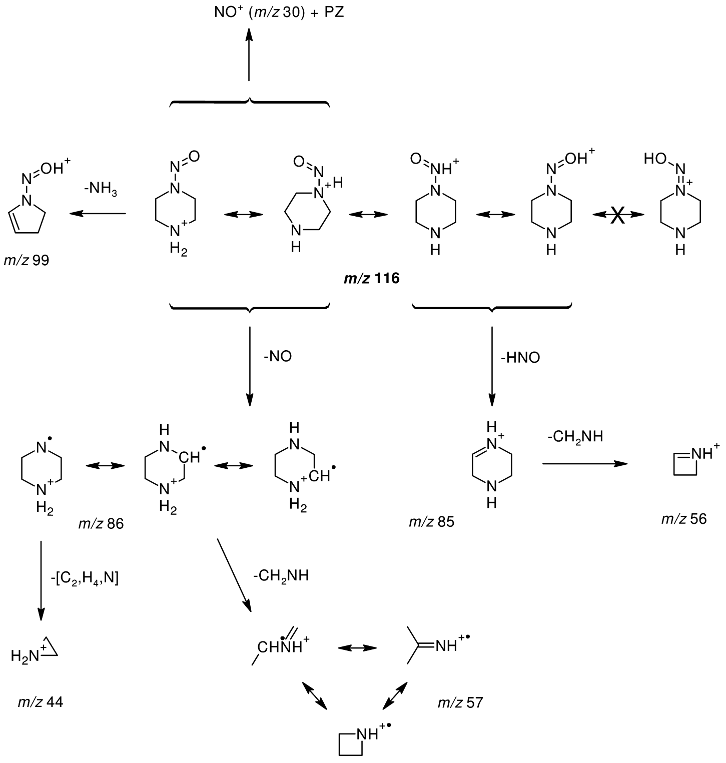

Scheme 1. Fragmentations of N-nitrosopiperazine

Although derived using different ionisation methods, there is excellent agreement between the electron ionisation mass spectrum of N-nitrosopiperazine (*6*) and the ESI-mass spectrum presented in Figure 3.

Downloaded by UNIV OF GUELPH LIBRARY on June 14, 2012 | http://pubs.acs.org
Publication Date (Web): May 3, 2012 | doi: 10.1021/bk-2012-1097.ch010

Downloaded by UNIV OF GUELPH LIBRARY on June 14, 2012 | http://pubs.acs.org
Publication Date (Web): May 3, 2012 | doi: 10.1021/bk-2012-1097.ch010

Detection of the Nitrosoamine Derivatives of Other Secondary Amines: N-Nitrosodiethanolamine and N-Nitroso-2-piperidinemethanol

Analysis of the reaction mixtures (t= 9.0 hrs) for 2-PM and DEA using broad-scan MS revealed the presence of peaks at M/z 145 (putative N-nitroso-2-piperidinemethanol) and M/z 135 (putative N-nitrosodiethanolamine) respectively. The ions were mass-selected and analysed using MS/MS. The low-energy MS/MS spectra are presented in Figure 4.

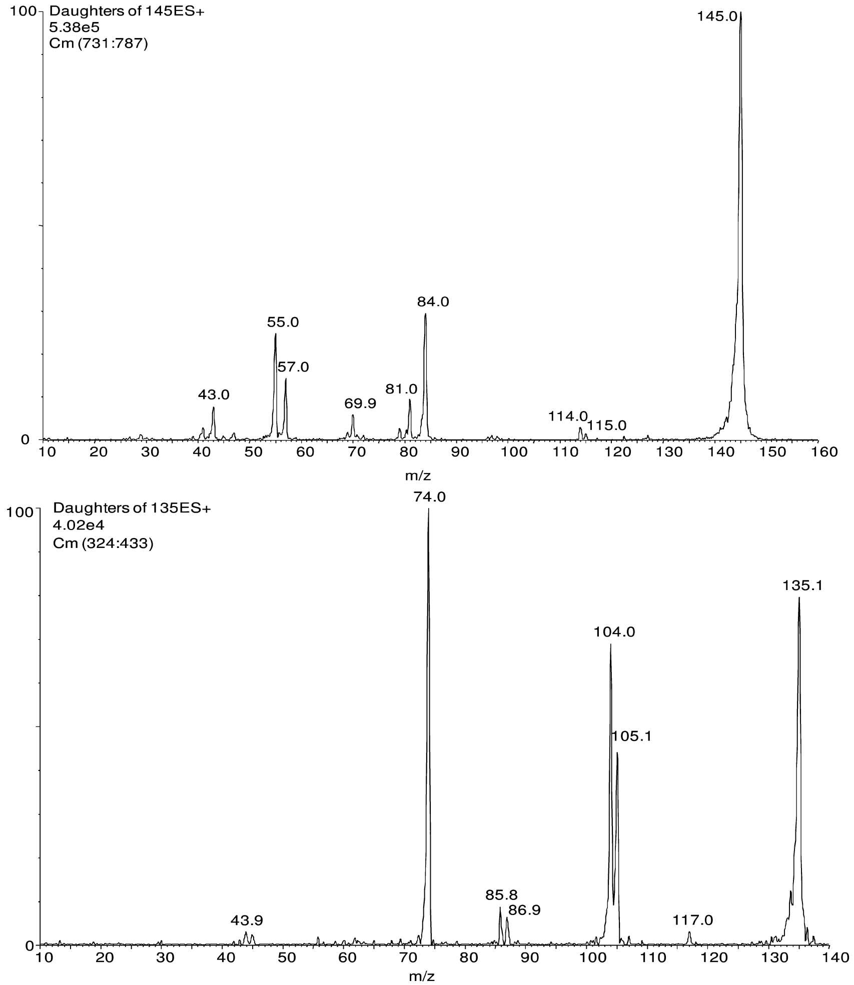

Figure 4. MS/MS spectrum of: (top) m/z 145 (N-nitroso-2-PM), and (bottom) N-nitroso-DEA.

Characteristic losses of 30 Da (NO) and 31 Da (HNO) are evident in both spectra, which identifies these ions as protonated N-nitroso species (albeit these peaks are significantly weaker in the MS/MS spectrum of N-nitroso-2-PM). 2-PM is a "sterically hindered" heterocyclic alkanolamine, and the observation of its N-nitroso derivative suggests that while this aspect of alkanolamine molecular structure may have a small effect on the kinetics, its chemistry with O_2/NO_x is otherwise typical of unhindered alkanolamines i.e. steric hindrance does not preclude the formation of certain derivatives, but the derivatives might be more prone to hydrolysis or other chemistry. This could render the detection of such species difficult.

Downloaded by UNIV OF GUELPH LIBRARY on June 14, 2012 | http://pubs.acs.org
Publication Date (Web): May 3, 2012 | doi: 10.1021/bk-2012-1097.ch010

Nitrosamine Derivative of Primary, Tertiary and 'Hindered' Amines

To determine whether primary, tertiary and 'hindered' amines could form nitrosamines, 30 wt % aqueous solutions of MEA, MDEA and AMP (respectively) were also exposed to the synthetic gas mixture for up to 15 hours. The resulting reaction mixtures were analysed in the same fashion, described *vide infra*. No evidence of nitrosamines were found, although analysis of the MDEA mixture revealed trace amounts of an ion at M/z 106, which was determined to be protonated DEA. The origin of the DEA could be either (i) degradation of MDEA induced by the presence of NO_x in the synthetic gas stream, or (ii) an impurity in the original material. MS analysis of the MDEA purchased from the manufacturer precludes the presence of DEA as an impurity in the stock. A peak at M/z 147 was also detected in negative ion mode for the MDEA reaction mixture (possibly $[MDEA+NO-H]^-$). The MS/MS spectrum of M/z 147 was largely devoid of fragments aside from an intense peak at m/z 62 (spectrum not shown). It is concluded this ion is *not* a nitroso derivative but a nitrate salt, since M/z 62 corresponds to NO_3^-.

Mitigating Methods for the Reduction of Emissions

There are a number of mitigation methods available that can reduce emissions from an amine-based PCC plant, including the removal of NO_x from the flue gas stream prior to the absorption process and minimisation of gaseous emissions by a water wash. However, these methods would have a negative impact on the capital cost of the PCC process and may be viewed as impractical. One approach that is currently being investigated is the UV treatment of the solvent liquor, gaseous emissions and/or wash water to destroy any materials such as nitramines and nitrosamines that can form during the PCC process. This section reports on the thermal- and photo- stability of N-nitrosopiperazine and UV treatment as a possible mitigation strategy in the reduction of these materials from an operational amine-based PCC plant.

Effect of Heat, UV Light and NOx Concentration on the Formation of Nitrosamines

In order to establish the effect of heat and UV light on the formation of nitrosamines, a method was developed for the analysis of N-nitrosopiperazine using HPLC-MS. This method has been published in the journal *Rapid Communications In Mass Spectrometry* (*5*). The results are presented in Figure 5. Figure 5 demonstrates that N- nitrosopiperazine is thermally stable at 150 °C (typical amine regeneration conditions in a CO_2 stripping column), however it does degrade slowly when exposed to UV irradiation between 400-310 nm (maximum irradiance 2.6 μW/cm^2 at 350 nm).

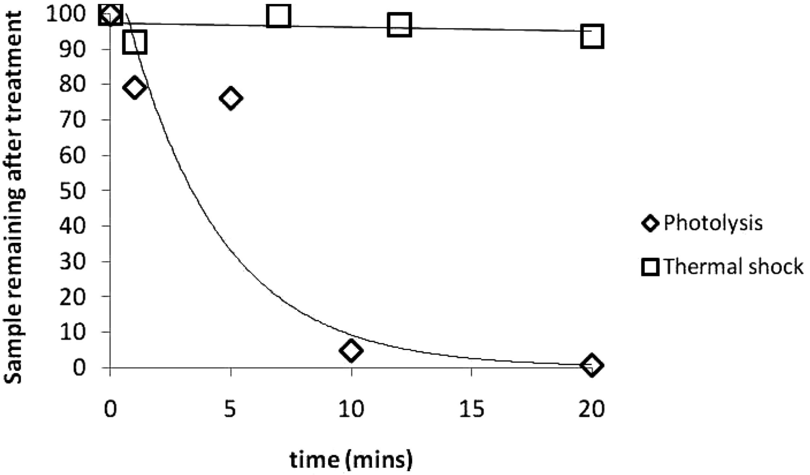

Figure 5. Plot of nitrosopiperazine sample degradation when exposed to UV light (◊) and heat (□).

Effect of Reducing NOx Concentration on the formation of N-Nitrosopiperazine

The detection and formation of the N-nitrosoamine derivatives of secondary amines, discussed at the beginning of this chapter, were investigated in the presence of a high NOx concentration (8000 ppm), much higher than that experienced in a typical flue gas stream form a coal-fired station. For this reason, NO_x concentration was adjusted to resemble Australian flue gas compositions (300-700 ppm (*4*)) and to examine the propensity of N-nitrosopiperazine to form over longer periods of exposure. An aqueous 15 % wt piperazine solution was exposed to a synthetic flue gas with this NO_x concentration (0.07 %), and the N_2 concentration in the stream was adjusted to maintain the gas flow at 1.34 L/min. The experiment was run at 60 °C over 9 days (1215 L NO_x, ~ 50 moles at 298 K). The reaction mixture was then sampled and analysed using multiple reaction monitoring-MS. Both transitions (M/z 86 ← 116, M/z 85 ← 116) recommended above were used in this study. The traces for each transition are shown in Figure

Downloaded by UNIV OF GUELPH LIBRARY on June 14, 2012 | http://pubs.acs.org
Publication Date (Web): May 3, 2012 | doi: 10.1021/bk-2012-1097.ch010

Downloaded by UNIV OF GUELPH LIBRARY on June 14, 2012 | http://pubs.acs.org
Publication Date (Web): May 3, 2012 | doi: 10.1021/bk-2012-1097.ch010

6 for: (i) an N-nitrosopiperazine standard, (ii) a blank injection between the standard and the unknown, and (iii) the reaction mixture. The results demonstrate that N-nitrosopiperazine forms at the lower NO_x concentrations.

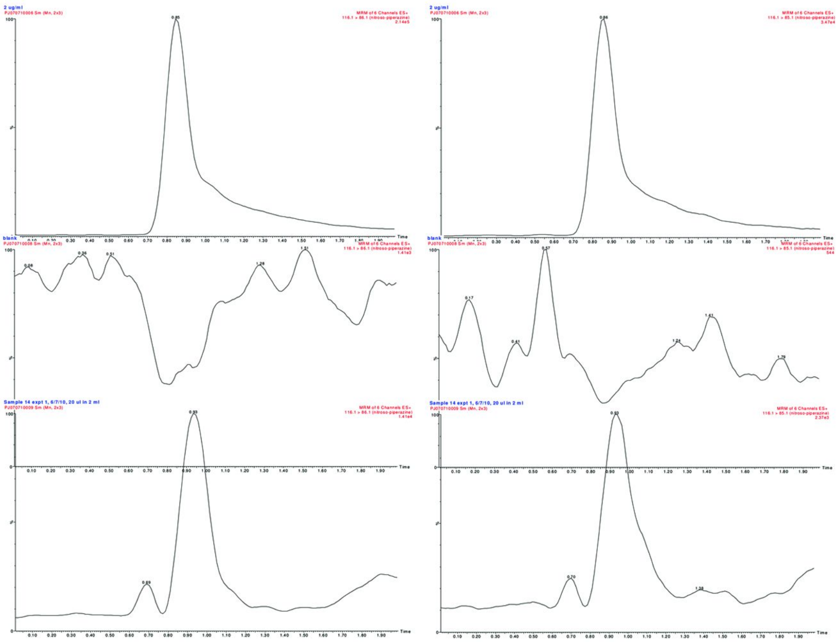

Figure 6. MRM traces for M/z 116 ← 86 ***(left)*** *and M/z 116 ← 85* ***(right)*** *for:* ***(top row)*** *N-nitrosopiperazine standard solution;* ***(centre row)*** *blank injection;* ***(bottom row)*** *PZ reaction mixture exposed to synthetic gas stream containing 700 ppm NOx for 9 days.*

Conclusion

N-nitrosamine formation is facile for secondary amines when exposed to gas streams containing NO_x, however the nitrosamines formed could be destroyed using UV irradiation. While N-nitrosopiperazine appears to be stable at temperatures close to those typically used to regenerate this amine, other nitrosamines formed from alkanolamines may be more thermally labile, and mitigation strategies may not be needed. Work in the area of N-nitrosamine degradation is ongoing. It should be noted that the conditions under which this study was performed did not include solvent cycling; the effect of this process on the N-nitroso species is currently not known, although it is likely to have little effect on N-nitrosopiperazine.

References

1. Bråten, H. B.; Bunkan, A. J.; Bache-Andreassem, L.; Solimannejad, M.; Nielsen, C. J. *Final report on a theoretical study on the atmospheric degradation of selected amines*; Report: NILU: OR 77/2008.
2. Stangeland, A.; Shao, R. *Amines used in CO2 capture – health and environmental impacts*; Report: The Bellona Foundation, Oslo, Norway, 2009. www.bellona.org.
3. Wang, P. G.; Xian, M.; Tang, X.; Wu, X.; Wen, Z.; Cai, T.; Janczuk, A. J. *Chem. Rev.* **2002**, *102*, 1091–1134.
4. Cottrel, A. J.; McGregor, J. M.; Jansen, J.; Artanto, Y.; Dave, N.; Morgan, S.; Pearson, P.; Attalla, M. I.; Wardhaugh, L.; Yu, H.; Allport, A.; Feron, P. H. M. *Energy Procedia* **2009**, *1*, 1003–1010.
5. Jackson, P.; Attalla, M. I. *Rapid Commun. Mass Spectrom.* **2010**, *24*, 3567–3577.
6. Linstrom, P.J.; Mallard, W.G. NIST Chemistry webbook, NIST standard reference database number 69. http://webbook.nist.gov/chemistry/, 2009.

Downloaded by UNIV OF GUELPH LIBRARY on June 14, 2012 | http://pubs.acs.org
Publication Date (Web): May 3, 2012 | doi: 10.1021/bk-2012-1097.ch010

Downloaded by UNIV OF GUELPH LIBRARY on June 14, 2012 | http://pubs.acs.org
Publication Date (Web): May 3, 2012 | doi: 10.1021/bk-2012-1097.ch011

Chapter 11

Oxidation of Aqueous Piperazine: Oxidation Rates, Products, and High-Temperature Oxidation

Stephanie A. Freeman, Fred B. Closmann, and Gary T. Rochelle[*]

Department of Chemical Engineering, The University of Texas at Austin,
Austin TX, 78712
[*]Corresponding author: gtr@che.utexas.edu

The resistance of concentrated PZ to oxidation and thermal degradation under standard CO_2 capture absorption-stripping conditions has been previously identified as an advantage of this solvent. The oxidation rate of concentrated PZ was investigated in bench-scale oxidation reactors from 55 to 125 °C, 48 to 98 kPa O_2, and in the presence of dissolved iron, stainless steel metals (SSM), copper, and Inhibitor A. The generation of total formate was found to predict the expected overall loss of PZ. Total formate is generated with an activation energy 86 ± 16 kJ/mol. PZ loss was found to have a first order relationship with P_{O2}. Cu^{2+} is a strong catalyst for PZ oxidation while Fe^{2+} and SSM were not found to enhance oxidation. Inh A inhibits Cu^{2+}-catalyzed degradation at 55 and 70 °C and in the presence of SSM to levels below a baseline condition. The major, identified oxidation products of PZ are EDA, FPZ, formate, NH_4^+, oxalate and oxalyl amides. Minor products include acetate, acetyl amides, other formyl amides, nitrite, and nitrate when PZ is heavily oxidized.

Using an oxidation model and data gathered from a cycling reactor system, a temperature limit of ~112 °C was estimated to provide 10% dissolved oxygen consumption per pass of solvent through an absorber/stripper system. When the oxygen consumption/pass is allowed to increase to 20%, the temperature limit increases to 123 °C. For a 500 MW power plant and 90% CO_2 capture at a stripper temperature of 120

In Recent Advances in Post-Combustion CO2 Capture Chemistry; Attalla, M.;
ACS Symposium Series; American Chemical Society: Washington, DC, 2012.

°C, the PZ oxidation loss is estimated to be 2.1 moles/ton CO_2 captured, while the annual PZ oxidation loss is estimated to be 8.0 X 105 kg/year.

1. Introduction

Concentrated, aqueous piperazine (PZ) has been identified as the new benchmark solvent for post-combustion absorption-stripping for carbon dioxide (CO_2) capture from coal-fired flue gas (*1–3*). The advantages of this solvent have been studied extensively and include having twice the CO_2 absorption rate and twice the CO_2 capacity of 7 m monoethanolamine (MEA), the baseline solvent for CO_2 capture applications (*4*, *5*).

Solvent management issues important to solvent selection also include amine volatility, heat of absorption, viscosity, thermal degradation, and oxidation. PZ volatility has been shown to be lower than MEA, 2-methyl-2-amino-1-propanol (AMP), and ethylenediamine (EDA) while PZ solutions demonstrate comparable viscosity and a slightly lower heat of absorption than MEA (*6–8*). Comprehensive study of the thermal degradation of PZ has shown the solvent to exhibit thermal stability up to 150 °C, a significant advantage in high temperature stripping operations (*9–11*).

Concentrated PZ was previously identified as resistant to oxidation under absorber conditions in multiple studies (*2*, *5*, *12*). Moderate concentration PZ solutions (2.5 and 5 molal (m)) were screened previously for metal-catalyzed oxidation and PZ was found to be especially resistant iron (II) (Fe^{2+})-catalyzed oxidation and susceptible to copper (II) (Cu^{2+})-catalyzed oxidation at conditions more severe than seen in a typical CO_2 absorber (*12*). Initial work on 8 m PZ, the expected concentration of full-scale PZ systems, has shown PZ to be resistant to oxidation catalyzed by Fe^{2+}, Cu^{2+}, or stainless steel metals (blend of Fe^{2+}, chromium (III) (Cr^{3+}), and nickel (II) (Ni^{2+})) (*2*). Concentrated PZ is more resistant to metal-catalyzed oxidation than MEA, confirming earlier conclusions concerning low concentration PZ systems (*2*, *12*).

An estimate of the expected oxidation of PZ in a full-scale CO_2 capture system has not yet been undertaken in literature. An estimate of this kind relies on first understanding the effect of process conditions and additives on oxidation rates. In this manuscript, the effect of aqueous metals (Fe^{2+}, Cu^{2+}, and a combination of Fe^{2+}, Ni^{2+}, and Cr^{3+}) and Inhibitor A (Inh A) have been expanded upon with new oxidation experiments. Also, the effect of the partial pressure of oxygen (P_{O2}) and temperature has been studied with the aim of extrapolating lab experiments to an estimate of oxidation in a CO_2 capture system. Finally, the oxidation products that have been identified to date are discussed as well as the overall mass balance and potential for as yet unidentified products. Details of this work are reported in the dissertations by Freeman and Closmann (*9*, *13*).

Downloaded by UNIV OF GUELPH LIBRARY on June 14, 2012 | http://pubs.acs.org
Publication Date (Web): May 3, 2012 | doi: 10.1021/bk-2012-1097.ch011

Downloaded by UNIV OF GUELPH LIBRARY on June 14, 2012 | http://pubs.acs.org
Publication Date (Web): May 3, 2012 | doi: 10.1021/bk-2012-1097.ch011

2. Methods and Materials

2.1. Solution Preparation, Total Alkalinity, and Total Inorganic Carbon (TIC)

Concentrated, aqueous PZ solutions were prepared through heating of aqueous PZ mixtures and gravimetric sparging of CO_2 (*2*, *7*, *9*). Anhydrous piperazine (IUPAC: 1,4-diazacyclohexane, CAS 110-85-0, purity 99 %, Acros Organics N.V., Geel, Belgium) and CO_2 (CAS 124-38-9, purity 99.5 %, Matheson Tri Gas, Basking Ridge, NJ) were obtained from commercial sources and used without further purification along with distilled, deionized water for experimental solutions.

The total alkalinity was measured using acid titration (*2*, *5*, *14*). To determine total alkalinity, experimental samples are titrated with 0.1 N sulfuric acid to the automatically detected equivalence point. The CO_2 loading in units of mol CO_2/mol alkalinity (mol CO_2/mol equivalent amine), was quantified using a total inorganic carbon (TIC) assay (*2*, *5*, *14*). Phosphoric acid was used to liberate CO_2 from solution while an infrared detector (Horiba Instruments Inc., Spring, TX) was used to quantify CO_2 concentration. A calibration curve generated from an inorganic carbon standard (Ricca Chemical Company, Pequannock, NJ) was used to calculate CO_2 concentrations.

2.2. Anion and Cation Ion Chromatography (IC)

Anion and cation ion chromatography (IC) were used to track PZ and degradation products (*2*, *5*, *9*). Anion IC was performed using a Dionex ICS-3000 modular Dual Reagent-Free IC system with AS autosampler, 4-mm Anionic Self-Regenerating Suppressor (ASRS), Continuously Regenerated Anion Trap Column (CR-ATC), Carbonate Removal Device (CRD), and conductivity detector. Separation was achieved in an IonPac AG15 guard column (4 x 50 mm) and IonPac AS15 analytical column (4 x 250 mm) using a gradient of potassium hydroxide in analytical grade water.

Cation IC was performed using a Dionex ICS-2100 Integrated Reagent-Free IC system with AS autosampler, 4-mm Cationic Self-Regenerating Suppressor (CSRS), and conductivity detector. Separation was achieved in an IonPac CG17 guard column (4 x 50 mm) and IonPac CS17 analytical column (4 x 250 mm) using a gradient of methanesulfonic acid in analytical grade water.

Amide concentrations were quantified by hydrolyzing experimental samples using 5 N sodium hydroxide (1 g NaOH to 1 g sample) for at least 24 hours to produce the corresponding amine and carboxylate ions (*2*, *9*). Hydrolyzed samples were analyzed using anion and cation IC to determine the increase over experimental samples due to the presence of amides. Anion species are reported as the total concentration resulting from the sum of the carboxylate ion and the carboxylate ion due to the presence of amides quantified in the hydrolyzed sample. The reported total amide concentration represents the total carboxylate product including free carboxylate, amides decomposed by the sodium hydroxide treatment, and any other degradation products that may yield carboxylates upon sodium hydroxide treatment. Concentrations of the other major degradation

Downloaded by UNIV OF GUELPH LIBRARY on June 14, 2012 | http://pubs.acs.org
Publication Date (Web): May 3, 2012 | doi: 10.1021/bk-2012-1097.ch011

products were monitored during sodium hydroxide treatment and were not affected except for increases in amine concentrations (i.e., PZ and EDA) due to the decomposition of amides.

2.3. Teflon® Oxidation Reactor (TOR)

The Teflon® oxidation reactor (TOR) was used to rapidly oxidize PZ solutions through exposure to higher levels of oxygen than expected in a CO_2 absorber. The TOR is an adapted version of the low-gas flow oxidation reactor (*2*, *9*). In the TOR, a glass Schott-style flange, Teflon® lid, Teflon®-coated o-ring, and flange clamp replaced the rubber stopper in the low-gas flow oxidation reactor to reduce chemical interaction of the amine with the rubber stopper. As with previous oxidation experiments, the excess of O_2 and high agitation rate are designed to ensure the maximum amount of oxygen possible absorbs into the amine solution to accelerate PZ oxidation. A schematic of the TOR is shown in Figure 1.

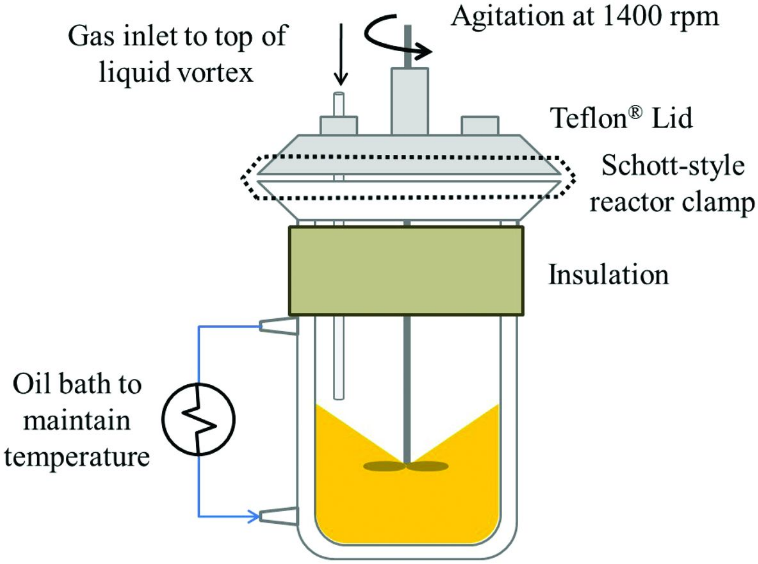

Figure 1. Schematic of Teflon® Oxidation Reactor (TOR)

The TOR retained the overhead agitation at 1400 rpm, circulating oil bath to maintain temperature, 100 mL/minute of gas flow into the headspace of the reactor, pre-saturation in water at the experimental temperature, and insulation on the top portion of the reactor to prevent condensation. Oxidation experiments were conducted using the same procedure as the low-gas flow reactor unless specified. The inlet gas flow contained from 40–98% O_2 and 2–6% CO_2 depending on the experimental condition. In all cases, the CO_2 concentration was adjusted to achieve the desired CO_2 loading at the experimental temperature based on CO_2 solubility curves for 8 m PZ (*4*, *6*).

All metal salts were added as aqueous solutions of sulfate salts in the form of either $FeSO_4 \cdot 7H_2O$, $CuSO_4 \cdot 5H_2O$, $CrK(SO_4)_2 \cdot 12H_2O$, or $NiSO_4 \cdot 6H_2O$. Solutions of 100 mM were created for each metal ion and added to the PZ solution in that form. A standard mixture of stainless steel metals (SSM) was used containing 0.4 mM Fe^{2+}, 0.1 mM Cr^{3+}, and 0.05 mM Ni^{2+}. Liquid samples were taken every two to three days and water was added to maintain the water balance on the reactor contents. Liquid samples were analyzed for PZ, degradation products, and CO_2.

2.4. Integrated Solvent Degradation Apparatus (ISDA)

Solvents were degraded in the Integrated Solvent Degradation Apparatus (ISDA) which alternately creates oxidizing and thermal degradation conditions in a single system and has been described in detail previously (*13*). ISDA simulates degradation conditions observed in an absorber/stripper configuration designed for CO_2 capture. The secondary effects associated with the alternating exposure of solvents to oxidizing and thermal degradation conditions were examined. The ISDA also allows the evaluation of degradation rates when carryover of dissolved oxygen at stripper-like temperatures (≥120 °C) occurs.

The oxidative reactor in the ISDA is a 750 mL flow-through jacketed glass vessel with an actively stirred top section of 400 mL nominal volume, and a 330 mL bottom section which simulates conditions in an absorber. The top section, which is exposed to the atmosphere, is agitated at 1,400 rpm to ensure that degradation is kinetically limited. A 100 mL/min purge gas consisting of 98 % O_2/2 % CO_2 was introduced into the top section above the agitated solvent in all 8 m PZ cycling experiments. Temperature control of the oxidative reactor was achieved by passing water through the jacket-side of the oxidative reactor; all experiments were conducted with the oxidative reactor maintained at 55 °C. A simplified schematic of the ISDA is shown in Figure 2.

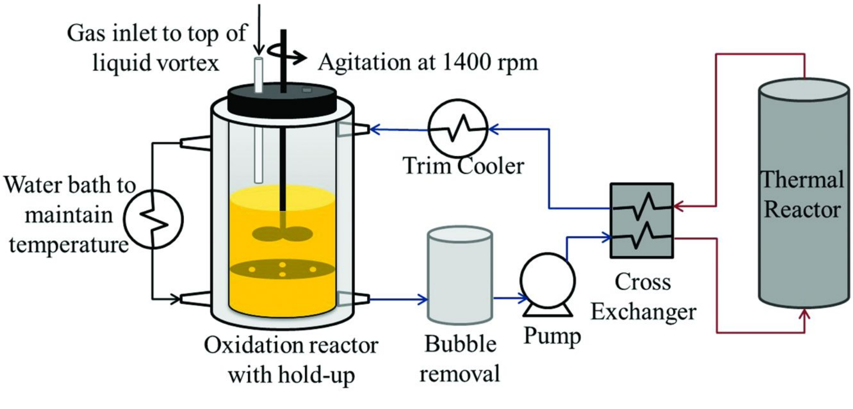

Figure 2. Simplified schematic of the Integrated Solvent Degradation Apparatus (ISDA)

Downloaded by UNIV OF GUELPH LIBRARY on June 14, 2012 | http://pubs.acs.org
Publication Date (Web): May 3, 2012 | doi: 10.1021/bk-2012-1097.ch011

Downloaded by UNIV OF GUELPH LIBRARY on June 14, 2012 | http://pubs.acs.org
Publication Date (Web): May 3, 2012 | doi: 10.1021/bk-2012-1097.ch011

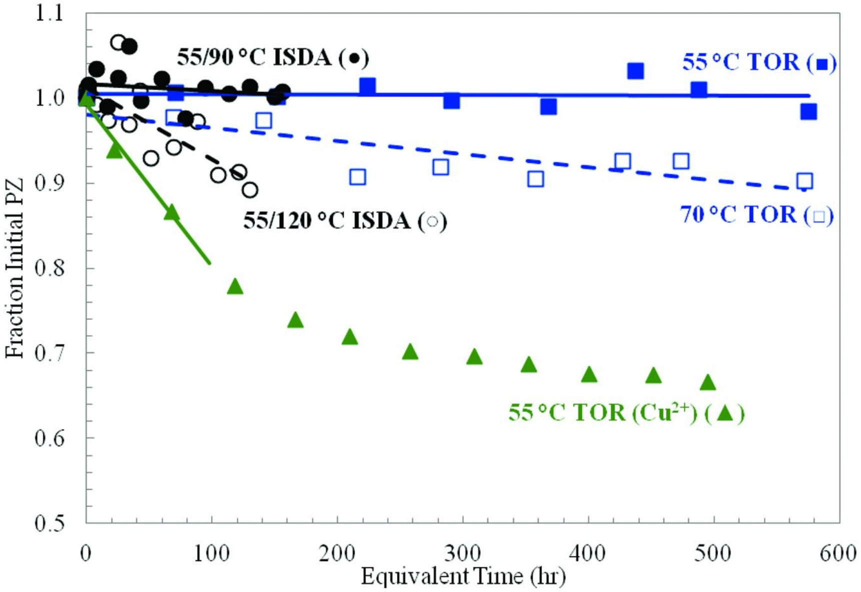

Figure 3. Loss of PZ during oxidation of 8 m PZ in the TOR (■, □, and ▲) and ISDA (●, ○) with SSM or 4 mM Cu^{2+} (▲); TOR data was obtained at 55 (■, ▲) and 70 °C (□); ISDA data is indicated with the oxidation (55 °C) and thermal section temperatures (●, 90; ○, 120 °C); linear regressions for the rate of PZ loss are shown as solid or dashed lines

CO_2-loaded amine was continuously pumped from the bottom section of the oxidative reactor through a positive displacement pump and into the shell side of a counter-currently operated single-pass tube-in-tube cross-exchanger. The amine was then passed through two pre-heaters consisting of stainless steel coiled tubing immersed in oil baths, and entered the internal section of a thermal reactor, which is a 1 L stainless steel tube-in-tube heat exchanger. Dimethyl silicone oil was passed through the jacket side of the thermal reactor to impart heat to the amine. The amine exited the thermal reactor and passed back through the tube side of the cross-exchanger. The amine was then passed through a trim cooler (heat exchanger) where it was cooled before exiting a back-pressure valve (¼-inch metering valve) and returned to the oxidative reactor above the liquid surface at atmospheric pressure. All tubing was ¼-inch outer diameter. Materials of construction included 316 stainless steel for all tubing, compression fittings, cross-exchanger, and thermal reactor, and glass for the oxidative reactor. Solvents were cycled through the reactor system at a nominal liquid flow rate of 200 mL/min, which provided a residence time of 3.5–4.0 minutes in the oxidative reactor and 5–6 minutes in the thermal reactor.

Downloaded by UNIV OF GUELPH LIBRARY on June 14, 2012 | http://pubs.acs.org
Publication Date (Web): May 3, 2012 | doi: 10.1021/bk-2012-1097.ch011

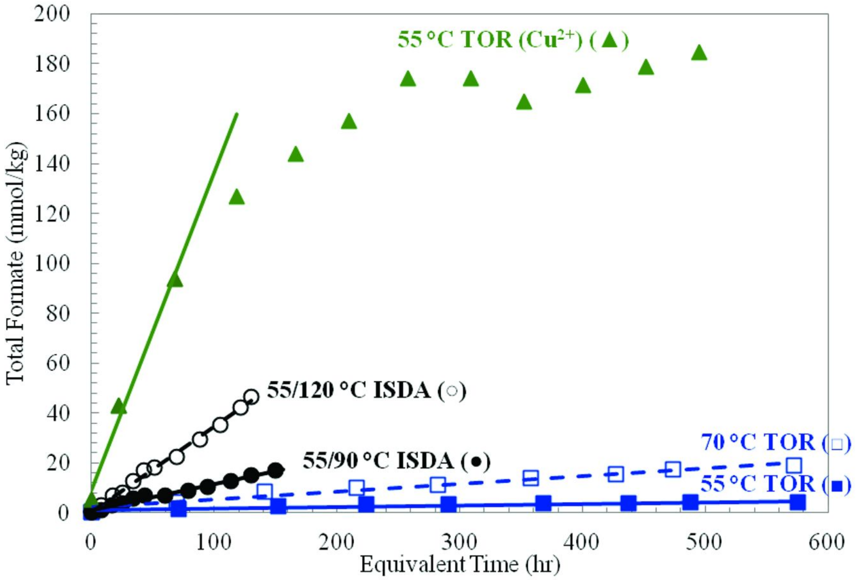

Figure 4. Generation of total formate during oxidation of 8 m PZ in the TOR (■, □, and ▲) and ISDA (●, ○) with SSM or 4 mM Cu^{2+} (▲); TOR data was obtained at 55 (■, ▲) and 70 °C (□); ISDA data is indicated with the oxidation (55 °C) and thermal section temperatures (●, 90; ○, 120 °C); linear regressions for the rate of total formate generation are shown as solid or dashed lines

3. Results and Discussion

3.1. PZ Oxidation Data

The rate of PZ oxidation was investigated over a range of operational conditions in order to assess PZ oxidation in a CO_2 capture system. The oxidation of PZ was observed from 55 to 70 °C in the presence of iron (Fe^{2+}) stainless steel metals (Fe^{2+}, Cr^{3+}, and Ni^{2+}), copper (Cu^{2+}), and a well-studied oxidation inhibitor (Inh A) (*12*, *15*, *16*). Oxidation was examined in the TOR to accelerate oxidation under isothermal and high oxygen conditions. Oxidation with cycling to a high temperature reactor was performed in the ISDA.

The loss of PZ and generation of total formate over the course of a standard experiment was compared for data obtained from the TOR and ISDA in Figure 3 and Figure 4. All data were obtained in the presence of SSM except for the experiment containing only Cu^{2+}, as noted. The ISDA data were normalized to reflect the time spent in the high temperature portion of the system where oxidation is expected to occur to allow direct comparison to the TOR data. The difficulty in accurately quantifying PZ loss with either reactor over the course of long term experiments is evidenced by the scatter seen in the PZ data. Conversely, the generation of total formate, the sum of formate and formyl amides, is seen as a good indicator of the overall level of oxidation.

Downloaded by UNIV OF GUELPH LIBRARY on June 14, 2012 | http://pubs.acs.org
Publication Date (Web): May 3, 2012 | doi: 10.1021/bk-2012-1097.ch011

3.2. Oxidation Rate Analysis

PZ oxidation in the absence of a strong catalyst proceeds too slowly to accurately capture the oxidation rate using cation IC for PZ concentration over a three-week experiment. Because of this limitation, the generation of total formate was used as a marker to indicate PZ oxidation (Figure 4). In previous similar studies, the amines tested oxidized quickly to allow accurate cation IC quantification above baseline error in the experimental and analytical methods without the need of a marker degradation product (*12*, *17*, *18*).

The rate of total formate production (R_{TF}) and the rate of PZ loss (R_{PZ}) were calculated for each oxidation experiment using a least squares fit linear regression of total formate and PZ concentration as shown in Figure 3 and Figure 4. Direct linear correlations of both total formate and PZ were used for data in the absence of Cu^{2+} where oxidation proceeded slowly, such as the four sets of data shown in Figure 3 and Figure 4 with SSM. A linear regression through only the first three data points for total formate and PZ was used for data sets containing Cu^{2+} where oxidation proceeded quickly, such as the data shown in Figure 3 and Figure 4 with Cu^{2+}. The initial data were used to determine the initial rate of oxidation without the effect of depleted PZ in experiments where high levels of oxidation occurred. This effect would not be seen in non-Cu^{2+} experiments because very little PZ oxidation occurred overall. All of the rates were normalized by the partial pressure of O_2 (P_{O2}) to eliminate the effect of P_{O2} change from 40 to 98 kPa.

The R_{PZ} and R_{TF} are plotted in Figure 5 for experiments containing varying aqueous metals and Inh A. A linear regression through all data is shown with a solid line in Figure 5 and the resulting relationship is shown in Equation 1. The regression recognizes that there will be no generation of total formate when there is no PZ loss (i.e., R_{PZ} is zero). The large differences in the magnitudes of rate data result in the Cu^{2+}-containing experiments governing the regression. The experiments with lower overall rates did not strongly influence the linear regression. Despite the differences in magnitude, a linear regression was performed because of the expected relationship during oxidation of PZ loss and marker degradation product generation. The linear fit appears inappropriate for the experiments with low rates of oxidation but, as discussed in Section 3.1, the PZ loss rate is not believed to be quantified with precision in experiments without strong catalysts enhancing oxidation. The correlation between R_{TF} and R_{PZ} is strong for the Cu^{2+} experiments, where the PZ rate is able to be more accurately quantified due to large changes, and indicates a strong correlation between PZ loss and total formate generation during oxidation, making this an appropriate choice of marker compound.

$$R_{TF} = 0.1098 \times R_{PZ} \qquad (1)$$

Downloaded by UNIV OF GUELPH LIBRARY on June 14, 2012 | http://pubs.acs.org
Publication Date (Web): May 3, 2012 | doi: 10.1021/bk-2012-1097.ch011

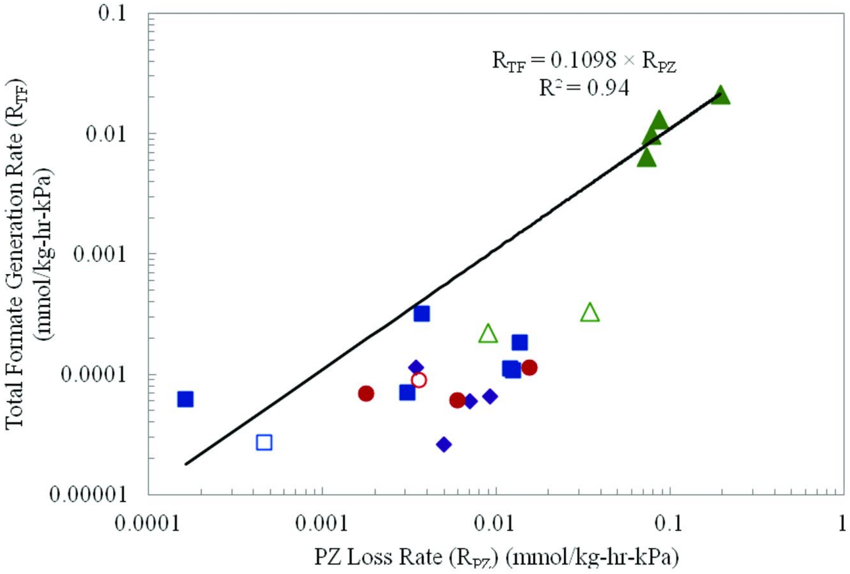

Figure 5. Correlation of R_{PZ} and R_{TF} for all PZ oxidation experiments. Data: ♦, no aqueous metals added; ▴, 4 mM Cu^{2+}; Δ, 4 mM Cu^{2+} and 100 mM Inh A; ■, SSM; □, SSM and 10 mM Inh A; ●, 1 mM Fe^{2+}; ○, 1 mM Fe^{2+} and 100 mM Inh A; a linear regression of all data is shown.

The R_{PZ} observed in experiments without aqueous metals, with Fe^{2+}, or with SSM is mostly overestimated, and is likely the result of some entrainment and scatter in quantifying small changes in a species that is present at over 40 wt %, as in an 8 m solution. The regression shown in Equation 1 represents the expected relationship between PZ loss and total formate generation if quantification could be performed more accurately and if all issues of entrainment were resolved. Therefore, an estimated PZ loss rate ($R_{PZ,est}$) can be calculated based on Equation 1 and the total formate generation in a given experiment. The $R_{PZ,est}$ is meant as a more accurate representation of the oxidation rate expected for concentrated PZ based on the total formate production in each experiment and will be used to compare experimental conditions in this manuscript.

A comparison of R_{TF}, R_{PZ}, and $R_{PZ,est}$ is shown in Table 1 for a variety of additive concentrations for experiments performed in the TOR. The rates shown are averages of experiments conducted at the same conditions with standard deviations shown, when applicable. Rates at 70 °C were extrapolated to 55 °C using an activation energy of oxidation determined for each additive condition as shown previously (*9*).

Downloaded by UNIV OF GUELPH LIBRARY on June 14, 2012 | http://pubs.acs.org
Publication Date (Web): May 3, 2012 | doi: 10.1021/bk-2012-1097.ch011

Table 1. Comparison of average loss or generation rates for each additive condition during oxidation of 8 m PZ with rates at 70 °C adjusted to 55 °C

Additive (mM)[a]	*Aveage Loss or Generation Rate × 10^3 (mmol/kg-hr-kPa)*		
	R_{PZr}	R_{TF}	$R_{PZ,est}$
4 Cu^{2+}	84.4 ± 31	9.7 ± 4.0	107 ± 65
4 Cu^{2+} + 100 A	8.9	0.22	2.0
SSM	3.1 ± 4.3	0.09 ± 0.03	1.2 ± 0.9
SSM + 10 A	0.46	0.03	0.2
1 Fe^{2+}	7.7 ± 7.0	0.08 ± 0.03	0.7 ± 0.3
1 Fe^{2+} + 100 A	1.8 ± 2.6	0.07 ± 0.02	0.7 ± 0.2
None	6.2 ± 2.5	0.07 ± 0.04	0.6 ± 0.3

[a] SSM = stainless steel metal mixture, 0.4 mM Fe^{2+}, 0.1 mM Cr^{3+}, 0.05 mM Ni^{2+}

3.3. Effect of Aqueous Metals and Inh A on Oxidation

The effect of aqueous metals and Inh A on PZ oxidation was evaluated through TOR experiments. Cu^{2+} was investigated as a possible additive for corrosion inhibition while Fe^{2+} and SSM were studied to determine the effect of carbon steel and stainless steel corrosion (*2*, *9*, *12*). The average $R_{PZ,est}$ presented in Table 1 for each additive case elucidates the potential catalyst or inhibitor effect on PZ loss during oxidation.

Cu^{2+} is a strong catalyst with a $R_{PZ,est}$ over 100 times the case without additives. However, the inclusion of 100 mM Inh A lowers the rate 50 times. Inh A is effective at reducing Cu^{2+}-catalyzed PZ oxidation (*2*). Neither SSM or Fe^{2+} were found to be strong catalysts for PZ oxidation, as shown in the low $R_{PZ,est}$ for each. The conclusion that Fe^{2+} is not a catalyst for PZ oxidation is counter to previously published results using the same methods (*2*). The previous results published by the current authors were based on cation IC quantification of PZ. Upon further study, the quantification of degradation products such as formate and total formate was found to be more accurate and conclusions based on these data are made in the current manuscript. Inh A had no effect on oxidation in the presence of Fe^{2+}, while the $R_{PZ,est}$ was reduced slightly for Inh A in the presence of SSM. The combination of SSM and Inh A appeared to have a slight inhibitor effect overall with lower $R_{PZ,est}$ than was the case in the absence of additives.

3.4. Effect of Oxygen Partial Pressure on Oxidation

The effects of oxygen concentration was analyzed through the oxidation of 8 m PZ with 4 mM Cu^{2+} at 55 °C, agitation at 1400 rpm and 100 mL of mixed gas with 2% CO_2, maintaining a loading of 0.3 mole CO_2 per mole alkalinity. The inlet gas also contained either 40 or 98% O_2, with the balance N_2 in the low O_2

case. Provided that copper is a stronger catalyst for amine oxidation, the effect of O_2 was readily observable with this high rate of oxidation.

The PZ loss and generation of total formate for both the low and high O_2 cases are shown in Figure 6. PZ loss and total formate generation are strongly enhanced by an increase in O_2 content. After 450 hours of oxidation, an increase in O_2 content from 40 to 98%, or 245%, enhanced PZ loss by approximately 240% in terms of the fraction of initial loss. PZ loss at 55 °C is therefore approximately first order in O_2 content in the inlet gas as the loss of PZ at the same ratio that O_2 content in the inlet gas increases. The generation of total formate was found to be more than first order in O_2 as an increase of 245% in P_{O2} generated an increase of 340% in total formate concentration. PZ was also confirmed to be first order in P_{O2} for oxidation with Cu^{2+} at 70 °C (details not shown). It is expected that oxidation in the presence of other aqueous metals would proceed with the same behavior although low oxidation rates in the absence of Cu^{2+} made this difficult to confirm positively.

Downloaded by UNIV OF GUELPH LIBRARY on June 14, 2012 | http://pubs.acs.org
Publication Date (Web): May 3, 2012 | doi: 10.1021/bk-2012-1097.ch011

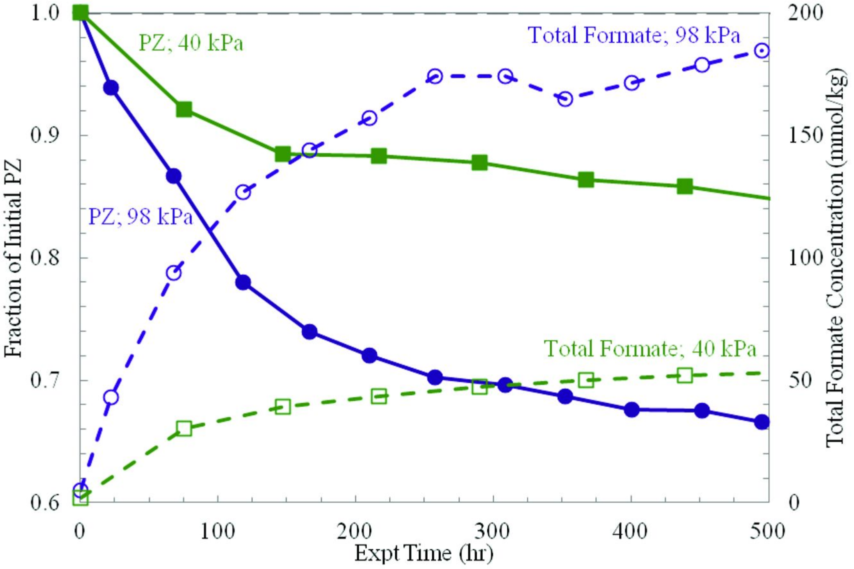

Figure 6. Effect of O_2 on PZ loss for 8 m PZ at 55 °C with 4 mM Cu^{2+} and 100 mL/min inlet gas with 40 (■) or 98 (●) kPa O_2 at 0.3 mol CO_2/mol alkalinity

3.5. Effect of Temperature on Oxidation

The effect of temperature on PZ oxidation was analyzed from 55 to 125 °C using data from both oxidation reactors (TOR and ISDA). In order to compare the ISDA and TOR degradation rates on the same basis, the ISDA rates were normalized to correct for the residence time in the ISDA thermal reactor compared to the total reactor volume. The design of the ISDA reactor is an oxidation section at 55 °C that mimics the TOR reactor, with an additional heated section to allow extended residence time at high temperature. To allow comparison of data between the two reactors, the experiment time for each liquid sampling data point from the ISDA was reduced by the ratio of the volume of the high temperature section to the total volume of the ISDA reactor. In this way, only the time in which the solution resided at the high temperature section was taken into account as it was compared with the TOR data to capture the high temperature effect of the oxidation.

The experiments at 90 and 120 °C were performed with the ISDA configuration where the thermal reactor accounted for 1.2 L of 3.4 L total. The sampling time was adjusted for this data set using a ratio of 1.2 L : 3.4 L. The experiments at 110 and 125 °C were performed using a second ISDA configuration and the data was adjusted using the appropriate ratio of volumes in the same manner (0.13 L : 2.3 L). The data derived from ISDA experiments were also corrected for the P_{O2} content of the inlet gas, as was done for the TOR data in Section 3.2.

An Arrhenius plot of the R_{TF} for data from 55 to 125 °C is shown Figure 7. The generation of total formate is well represented with an Arrhenius relationship between rate and temperature, as demonstrated by the coefficient of determination (R^2) of 0.88 for the linear regression of Ln R_{TF} and T^{-1}. The alignment of the data from the two reactors operated with the same solutions and catalysts demonstrates that the assumptions for data normalization were acceptable. The Arrhenius plot yields an activation energy of total formate generation during oxidation, E_A, of 86 ± 16 kJ/mol. This correlation confirms that high temperature oxidation is successfully being achieved in the ISDA reactor. Also, data from two separate apparatuses have been successfully regressed with the same relationship, bolstering the assumptions that the residence time normalization was appropriate. The value of E_A is in line with previous work on amine oxidation during CO_2 capture processes (*13*).

3.6. Resistance of CO_2 Capture Amines to Oxidation

The resistance to oxidation of concentrated PZ is a significant advantage of this CO_2 capture solvent. The oxidation of numerous CO_2 capture amines including monoethanolamine (MEA), 3-(methylamino)propylamine (MAPA), EDA, 2-methyl-2-amino-1-propanol (AMP), diethanolamine (DEA), and Diglycolamine® (DGA®) has been studied previously for the effect of aqueous metals most likely to be present in CO_2 capture systems on amine oxidation rates (*2*, *12*, *17–19*).

As stainless steel is the most likely material of construction for CO_2 capture systems, the oxidation of 8 m PZ, 7 m MEA, and 9 m (MAPA) in the presence of SSM is compared in Figure 8. All experiments were performed in the TOR at 55 °C with 98 kPa O_2. The amine concentrations differed slightly as each amine has a preferred concentration for CO_2 capture applications (*9*, *12*, *17*). After 350 hours, only 1% of the PZ had oxidized, while the MEA experiment shows a loss of 35%. MAPA is completely oxidized within 120 hours. The resistance of PZ and, to a lesser extent, MEA, to oxidation catalyzed by stainless steel metals is clearly demonstrated.

Downloaded by UNIV OF GUELPH LIBRARY on June 14, 2012 | http://pubs.acs.org
Publication Date (Web): May 3, 2012 | doi: 10.1021/bk-2012-1097.ch011

Downloaded by UNIV OF GUELPH LIBRARY on June 14, 2012 | http://pubs.acs.org
Publication Date (Web): May 3, 2012 | doi: 10.1021/bk-2012-1097.ch011

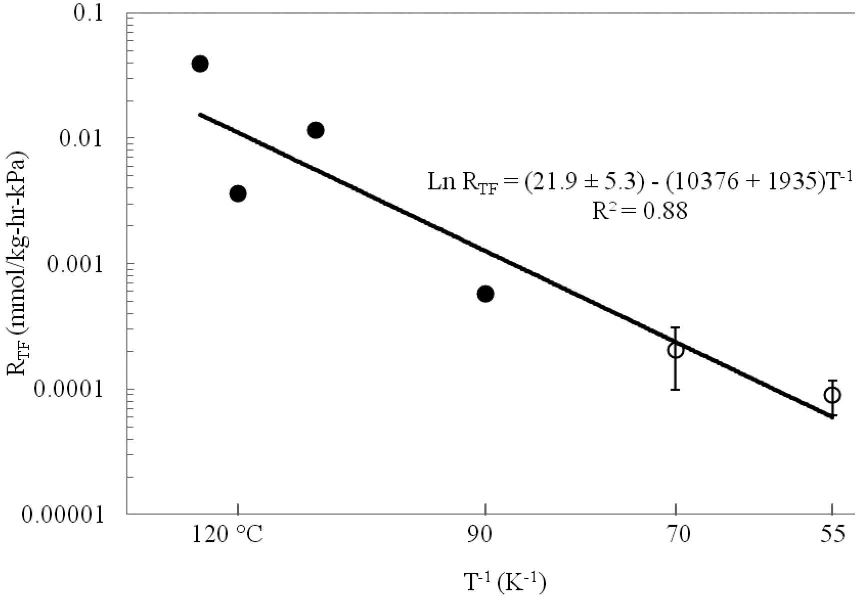

Figure 7. Effect of temperature on R_{TF} for 8 m PZ with SSM oxidized in the ISDA (●) or TOR (○)

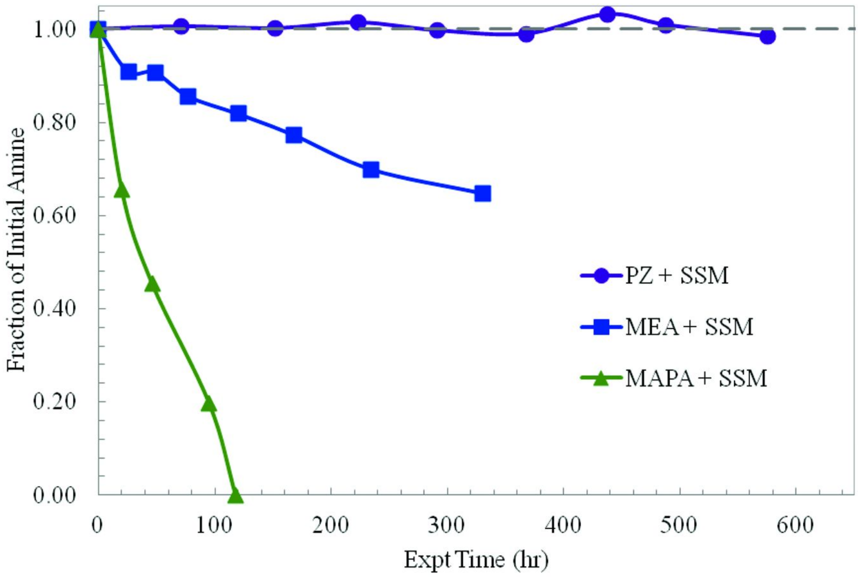

Figure 8. Comparison of PZ, MEA, and MAPA loss in the presence of SSM (55 °C, 1400 rpm, 100 mL/min 98 kPa O_2/2 kPa CO_2) (12, 17)

Concentrated PZ has been shown to be up to 5.5 times more resistant to oxidation in the presence of 1 mM Fe^{2+} compared to MEA (*2*). Sexton found that 7 m DEA also oxidized rapidly in the presence of 1 mM Fe^{2+} while 8 m EDA and 4 m DGA® were found to have resistance similar to that of PZ (*12*). Finally, in the presence of Cu^{2+}, PZ has been shown to have enhanced resistance to oxidation compared to MEA (*2*). Both 4 m AMP and 3.5 m EDA, however, have been found to resist Cu^{2+}-catalyzed oxidation showing nearly negligible losses after exposure to 5 mM Cu^{2+}.

3.7. Estimate of PZ Oxidation in an Industrial CO_2 Capture System

Downloaded by UNIV OF GUELPH LIBRARY on June 14, 2012 | http://pubs.acs.org
Publication Date (Web): May 3, 2012 | doi: 10.1021/bk-2012-1097.ch011

It is expected that PZ will react with dissolved oxygen in the rich solution in the high temperature zone of the heat exchanger and piping before the dissolved oxygen is stripped out at the top of the stripper or flash tank. There is a maximum T at this part of the system that corresponds to a limited amount of oxygen consumption.

Closmann (*13*) showed for 7 m MDEA that 101 °C was the maximum temperature that would provide 10% oxygen consumption with a residence time of 30 seconds. The calculation of the temperature limit for 8 m PZ assumes that the maximum loss of PZ per pass is equal to that of MDEA.

The total formate production rate was estimated from the ratio of amine degradation to total formate production measured in the ISDA experiments with 8 m PZ. Three other underlying assumptions to this calculation are: (A) the incoming flue gas in contact with the solvent has an oxygen concentration of 5 kPa, (B) the solvent residence time in the hotter sections of the system is 30 seconds, and (C) the total formate production rate is a good indicator of overall oxidation in the solvent.

The estimated temperature limit to consume 10% of the dissolved oxygen for 8 m PZ is 112 °C, which is considerably higher than the temperature limit of 101 °C calculated for 7 m MDEA using the same basis. A temperature limit of 108 °C was also calculated for the 20% oxygen consumption basis for 7 m MDEA. On the same basis, the limit calculated for 8 m PZ was 123 °C. The estimated values are compared to the values calculated for 7 m MDEA in Table 2. The resistance to degradation of 8 m PZ is apparent in the considerably higher temperatures at all three oxygen consumption levels, with the estimated tolerance limit at 145 °C for the 50% oxygen consumption level.

An estimate of the amount of PZ loss per ton CO_2 captured in an absorber/stripper configuration was made with assumed stripper temperatures of 120 and 130 °C. The first-order rate constant for total formate production in 7 m MDEA can be related to conversion of PZ to total formate at the temperatures of interest (120 and 150 °C), and through an estimate of solvent CO_2 carrying capacity (0.79 mol CO_2/kg solvent), the amount of PZ loss per unit CO_2 captured can be estimated. Based on the cycling experiments with 8 m PZ, an estimate of 13 mmol PZ lost/mmol total formate produced was used. A flue gas oxygen concentration of 5 kPa (5%) was assumed.

Downloaded by UNIV OF GUELPH LIBRARY on June 14, 2012 | http://pubs.acs.org
Publication Date (Web): May 3, 2012 | doi: 10.1021/bk-2012-1097.ch011

Table 2. Temperature tolerance comparison in 7 m MDEA and 8 m PZ based on total formate production and 30 s of residence time

Oxygen Consumed (%)	*Temperature (°C)*	
	7 m MDEA	*8 m PZ*
10	101	112
20	106	123
50	115	145

For a 500 MW power plant and 90% CO_2 capture at a stripper temperature of 120 °C, the estimated PZ oxidation loss is 2.1 moles PZ lost/ton CO_2 captured, while the annual PZ loss is ~8.0 X 10^5 kg/year. At a stripper temperature of 130 °C, the estimated PZ oxidation is 6.8 mol/ton CO_2, while the annual PZ loss is ~2.6 X 10^6 kg/year.

3.8. Generation of Oxidation Products

The most prominent degradation products of PZ oxidation were formate, oxalate, formyl amides, oxalyl amides, and EDA. Smaller concentrations of acetate, acetyl amides, and glycolate were found inconsistently while NH_4^+, nitrite, and nitrate were found only in heavily oxidized solutions. In general, the quantified degradation products account for a low percentage of the PZ lost during oxidation. This observation is compounded by overestimates of PZ loss through cation IC, as discussed in section 3.2, and the likelihood of volatile, non-ionic, or polymeric products that are not readily detected with the analytical methods employed. A mass balance will be presented that represents the most complete assessment of oxidation products for concentrated PZ oxidation. The experiment discussed is 8 m PZ oxidized at 70 °C with 0.3 mol CO_2/mol alkalinity, 4 mM Cu^{2+}, and 100 mL per minute of 94 kPa O_2/6 kPa CO_2.

The PZ lost and concentrations of oxidation products is presented in Table 3 for the final sample of this experiment. The nitrogen and carbon mass balances based on the species quantified are presented as well. Over 14 days of oxidation, 3170 mmol/kg of PZ is lost while significant concentrations of EDA, FPZ, formate, NH_4^+, oxalate, oxalyl amides, and formyl amides are produced. Based on total nitrogen analysis of this sample (details not shown), the concentration of volatile species was estimated to be 2650 mmol nitrogen/kg. The speciation of this volatile loss is not known but is expected to include NH_3, PZ, and volatile amine oxidation products. Overall, 69% of PZ-nitrogen and 23.4% of PZ-carbon loss is recovered in quantified or estimated products. Discounting the volatile estimate, the recovery of PZ-nitrogen drops to only 27.2%. The unidentified liquid phase oxidation products represent a significant portion of the PZ losses, if the PZ loss quantified as cation IC is accurate. In cases where less PZ was oxidized, as in the presence of Fe^{2+} or SSM, recovery of lost PZ in liquid phase products was usually below 10% for both nitrogen and carbon. N-acetyl piperazine and

Downloaded by UNIV OF GUELPH LIBRARY on June 14, 2012 | http://pubs.acs.org
Publication Date (Web): May 3, 2012 | doi: 10.1021/bk-2012-1097.ch011

N-(2-aminoethyl)glycine are expected stable degradation products, but neither were identified in this effort. Other unstable degradation products are expected to include aldehydes (ex: formaldehyde, acetaldehyde, hydroxyacetaldehyde), imines (ex: 1,2,3,6-tetrahydro pyrazine; CAS 77253-83-9), enamines (ex: 1,2,3,4-tetrahydro pyrazine; 5194-05-8), and hemiaminals (ex: 2-piperazinol; CAS 1104858-53-8).

Table 3. Nitrogen and carbon mass balance in 8 m PZ oxidized at 70 °C for 14 days with 4 mM Cu^{2+} and 100 mL/min 94 kPa O_2/6 kPa CO_2

			Nitrogen Balance		Carbon Balance	
	Structure	Conc. mmol/kg	N Conc.[1] mmol/kg	PZ N Loss %	C Conc. mmol/kg	PZ C Loss %
PZ Lost	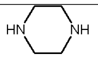	3170	6340	-	12680	-
DEGRADATION PRODUCTS:						
Ethylenediamine (EDA)	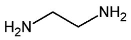	490	980	15.5	980	7.7
N-Formyl PZ (FPZ)	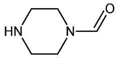	300	600	9.5	1500	11.9
Formate	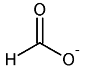	170	NA	-	170	1.3
Ammonium (NH_4^+)		130	130	2.1	NA	-
Oxalate and oxalyl amides	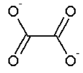	105	NA	-	210	1.7
Formyl amides (non-PZ)	-	90	NA	-	90	0.7
Nitrite and Nitrate (NO_2^- and NO_3^-)		5	5	0.1	NA	-
Acetate and acetyl amides	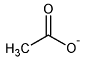	5	NA	-	10	0.1
Volatile N (unknown species)	-	2650	2650	41.8	NA	-
Total PZ Mass Recovered in Products			4365	**69.0**	2960	**23.4**

[1] NA = not applicable

4. Conclusions

Concentrated PZ is resistant to oxidation under conditions expected in an absorber-stripping CO_2 capture system. The oxidation rate of PZ over a range of process conditions has been explored using bench-scale oxidation reactors. Oxidation proceeds slowly and generates analytical limitations to accurately quantifying small changes in PZ concentration. The generation of total formate was determined to closely predict the expected PZ loss due to oxidation.

PZ oxidation generates total formate with an activation energy of 86 ± 16 kJ/mol. PZ loss also has a first order relationship with P_{O2}. Cu^{2+} is a strong catalyst for PZ oxidation while Fe^{2+} and SSM were not found to enhance oxidation. Inh A inhibits Cu^{2+}-catalyzed degradation at 55 and 70 °C and in the presence of SSM to levels below a baseline condition. The major, identified oxidation products of PZ are EDA, FPZ, formate, NH_4^+, oxalate, and oxalyl amides. Minor products include acetate, acetyl amides, other formyl amides, nitrite, and nitrate when PZ is heavily oxidized.

Using an oxidation model and data gathered from the ISDA cycling reactor system, a temperature limit of ~112 °C was estimated based on 10% oxygen consumption per pass of solvent through an absorber/stripper system. When the oxygen consumption/pass is allowed to increase to 20%, the temperature limit increases to 123 °C. These numbers compare favorably to those for 7 m MDEA, which had temperature limits of 101 and 106 °C at 10 and 20% oxygen consumption levels, respectively. For a 500 MW power plant and 90% CO_2 capture at a stripper temperature of 120 °C, the estimated moles PZ lost/ton CO_2 captured is 2.1, while the annual PZ loss is ~8.0 X 10^5 kg/year.

PZ oxidation is a slow phenomenon that should not hinder the application of PZ in industrial CO_2 capture systems containing moderate temperature strippers or flash stripping arrangements. Implementation of full-scale PZ absorption-stripping systems will require further research on the currently unidentified degradation products.

Downloaded by UNIV OF GUELPH LIBRARY on June 14, 2012 | http://pubs.acs.org
Publication Date (Web): May 3, 2012 | doi: 10.1021/bk-2012-1097.ch011

Acknowledgments

The Luminant Carbon Management Program provided support for this work.

Nomenclature and Abbreviations

AMP	2-amino-2-methyl-1-propanol
ASRS	Anionic self-regenerating suppressor; used in anion IC
C	Carbon; total carbon molecules or concentration
CO_2	Carbon dioxide
Cr^{3+}	Chromium (III) ion, added as $CrK(SO_4)_2{\cdot}12H_2O$
CR-ATC	Continuously regenerated anion trap column; used in anion IC
CRD	Carbonate removal device; used in anion IC
CSRS	Cationic self-regenerating suppressor; used in cation IC
Cu^{2+}	Copper (II) ion, added as $CuSO_4{\cdot}5H_2O$
DEA	Diethanolamine
DGA®	Diglycolamine®
EDA	Ethylenediamine
Fe^{2+}	Iron (II) ion, added as $FeSO_4{\cdot}7H_2O$
FPZ	N-Formylpiperazine
IC	Ion chromatography
Inh A	Inhibitor A; trade secret oxidation inhibitor
ISDA	Integrated solvent degradation apparatus
m	Molal; mole of species per kg water
MDEA	Methyldiethanolamine
MEA	Monoethanolamine
MW	Megawatt
N	Nitrogen; total nitrogen molecules or concentration

Ni^{2+}	Nickel (II) ion, added as $NiSO_4 \cdot 6H_2O$
NO_2^-	Nitrite ion
NO_3^-	Nitrate ion
NH_3/NH_4^+	Ammonia or ammonium ion
O_2	Oxygen
P_i	Partial pressure of species i
PZ	Piperazine
R_{PZ}	Rate of PZ loss in units of mmol/kg-hr-kPa
$R_{PZ,est}$	Estimated rate of PZ loss based on rate of total formate production in units of mmol/kg-hr-kPa
R_{TF}	Rate of total formate production in units of mmol/kg-hr-kPa
SSM	Stainless Steel Metal Mixture; 0.4 mM Fe^{2+}, 0.1 mM Cr^{3+}, and 0.05 mM Ni^{2+}
TIC	Total inorganic carbon assay
TOR	Teflon® oxidation reactor

Downloaded by UNIV OF GUELPH LIBRARY on June 14, 2012 | http://pubs.acs.org
Publication Date (Web): May 3, 2012 | doi: 10.1021/bk-2012-1097.ch011

References

1. Rochelle, G. T. *Science (Washington, DC, U. S.)* **2009**, *325* (5948), 1652–1654.
2. Freeman, S. A.; Davis, J.; Rochelle, G. T. *Int. J. Greenhouse Gas Control.* **2010**, *4* (5), 756–761.
3. Rochelle, G. T.; et al. *Chem. Eng. J.* **2011**, *171* (3), 725–733.
4. Dugas, R. E.; Rochelle, G. T. *J. Chem. Eng. Data.* **2011**, *56* (5), 2187–2195.
5. Freeman, S. A.; et al. *Int. J. Greenhouse Gas Control.* **2010**, *4* (2), 119–124.
6. Chen, X.; Rochelle, G. T. *Chem. Eng. Res. Des.* **2011**, *89* (9), 1693–1710.
7. Freeman, S. A.; Rochelle, G. T. *J. Chem. Eng. Data.* **2011**, *56* (3), 574–581.
8. Nguyen, T.; Hilliard, M.; Rochelle, G. T. *Int. J. Greenhouse Gas Control.* **2010**, *4* (5), 707–715.
9. Freeman, S. A. Ph.D. Dissertation, The University of Texas at Austin, Austin, TX, 2011.
10. Freeman, S. A.; Rochelle, G. T. *Energy Procedia* **2011**, *89* (9), 43–50.
11. Freeman, S. A.; Rochelle, G. T. Thermal Degradation of Piperazine and its Structural Analogs. *10th International Conference on Greenhouse Gas Technologies (GHGT)*; International Energy Agency Greenhouse Gas R&D Programme (IEAGHG): Amsterdam, Netherlands, 2010.
12. Sexton, A. J. Ph.D. Dissertation. The University of Texas at Austin, Austin, TX, 2008.
13. Closmann, F. B. Ph.D. Dissertation. The University of Texas at Austin, Austin, TX, 2011.
14. Hilliard, M. D. Ph.D. Dissertation. The University of Texas at Austin, Austin, TX, 2008.
15. Goff, G. S.; Rochelle, G. T. *Ind. Eng. Chem. Res.* **2006**, *45* (8), 2513–2521.
16. Sexton, A. J.; Rochelle, G. T. *Int. J. Greenhouse Gas Control.* **2009**, *3* (6), 704–711.

17. Vevelstad, S. *Norges teknisk-naturvitenskapelige universitet*, Unpublished work, Trondheim, Norway, 2010.
18. Zhou, S.; et al. *ChemSusChem* **2010**, *3* (8), 913–918.
19. Sexton, A. J.; Rochelle, G. T. *Energy Procedia* **2009**, *1* (1), 1179–1185.

Downloaded by UNIV OF GUELPH LIBRARY on June 14, 2012 | http://pubs.acs.org
Publication Date (Web): May 3, 2012 | doi: 10.1021/bk-2012-1097.ch011

Downloaded by OHIO STATE UNIV LIBRARIES on June 14, 2012 | http://pubs.acs.org
Publication Date (Web): May 3, 2012 | doi: 10.1021/bk-2012-1097.ch012

Chapter 12

Identification and Quantification of Degradation Products by Ion Chromatography

**Solrun Johanne Vevelstad,[1] Andreas Grimstvedt,[2]
Hélène Lepaumier,[1,3] Kolbjørn Zahlsen,[2] Marianne Steinsvik Kjos,[2]
Jacob N. Knudsen,[4] and Hallvard F. Svendsen[1,*]**

**[1]Norwegian University of Science and Technology, 7491 Trondheim, Norway
[2]SINTEF Materials and Chemistry, 7465 Trondheim, Norway
[3]Current adress: Laborelec, 1630 Linkebeek, Belgium
[4]DONG Energy Power, 2450 Copenhagen, Denmark
[*]hallvard.svendsen@chemeng.ntnu.no**

CO_2 capture with alkanolamines has been used since the 1930s and monoethanolamine (MEA) is the most studied absorbent for low CO_2 partial pressures and post combustion processes. For optimisation of process conditions, evaluation of new process solvents, modelling of thermodynamics, and for an improved fundamental understanding, it is necessary to know the composition of the liquid phase in detail. There exists several analytical methods, such as Gas Chromatography - Mass Spectrometry (GC-MS) and Liquid Chromatography - Mass Spectrometry (LC-MS), to identify and quantify neutral compounds, but the procedures for ionic compounds in amine samples are less developed and there are special problems related to sample preparation. In the present work, ion chromatography is used to identify and quantify ionic degradation compounds from oxidatively degraded MEA experiments and samples from Esbjerg pilot plant.

Introduction

Ion chromatography (IC) is an old analytical procedure which mainly separates ions on the basis of the electrostatic interactions occurring between charged functional groups present on the stationary phase and the ions present

In Recent Advances in Post-Combustion CO2 Capture Chemistry; Attalla, M.;
ACS Symposium Series; American Chemical Society: Washington, DC, 2012.

in the mobile phase. The mobile phase includes the mobile phase ions and the analyte ions. Separation is also influenced by factors like size and polarisability of the analyte ions, their degree of absorption onto the unfunctionalized portions of the stationary phase and the nature of the fixed group on the stationary phase (*1*). The methods used to influence the separation are rather limited, but separation could be changed using different stationary phases or changing the composition of the eluent. The last of these is time consuming and is mostly used to separate analyte ions of different charge. Thus, the focus has been to develop new stationary phases (*2*, *3*).

Common problems for ion analysis are interference due to the eluent or from the sample matrix. Sample matrix can co-elute with ions of interest, contaminate ions, shift the retention time, disrupt the baseline, overload the column and could be retained irreversibly on the packing (*1*, *2*, *4*). However, ion chromatography is an important technique to determine low levels of ionic impurities in for example lakes/rivers, power plant waste water, waste treatment effluents, etc. (*5–10*).

In an absorption process the liquid phase will normally contain a number of degradation compounds (amines, carboxylic acids, amides, carbonates, carbamates) with varying molecular weight at very different concentrations. Thus, it is not possible to use only one analytical technique to obtain a complete overview of all degradation compounds. On the contrary, it is necessary to combine several methods. GC-MS, LC-MS and IC-EC (Ion Chromatography with Electrochemical Detection) are the most commonly used analytical techniques for identification and quantification (*11–17*). Ion Chromatography has been successfully used for analysing degraded samples with anionic compounds (*5*, *7*, *16*, *18–20*).

Oxidative degradation has been studied by Rooney *et al.* (*21*), Goff, Chi, Sexton and Rochelle (*15*, *22–24*) and Lepaumier *et al.* (*11–13*). Typical degradation products, verified by experiments for monoethanolamine (MEA), are ammonia, aldehydes (formaldehyde, acetaldehyde) and carboxylic acids (acetic acid, formic acid and oxalic acid) (*21*).

Downloaded by OHIO STATE UNIV LIBRARIES on June 14, 2012 | http://pubs.acs.org
Publication Date (Web): May 3, 2012 | doi: 10.1021/bk-2012-1097.ch012

Experimental Section

Degradation Samples

Lab-Scale Experiment Simulating Absorber Conditions

An amine solution, loaded with CO_2 (α= 0.4 mole CO_2 per mole of amine), was introduced into an open-batch reactor. A gas blend of air with 2% CO_2 was sparged into the mixture (0.35 L/min air + 7.5 mL/min CO_2) and the solution was heated at 55 °C. Experiment 1 were in addition added a small amount of ironsulphate (1 mM Fe_2SO_4). Samples were taken regularly from the liquid phase and analyzed by IC. Other liquid phase analysis methods and results are given by Lepaumier (*11*).

MEA Campaign at the Esbjerg Pilot Plant

MEA was used as CO_2 absorbent at the Esbjerg pilot plant, the experiments lasted more than 3300 hours (equivalent to 20 weeks) and liquid samples were taken from different parts of the pilot: lean amine into the absorber, rich amine into the stripper, and the water washes (both of the absorber and stripper) after 11 weeks of operation. Also the final lean MEA was analysed. Other liquid phase analysis methods and results are given by Lepaumier (*11*).

IC Analysis

The IC analyses were carried out on a Dionex DX-500 System equipped with an Autosampler (AS-50), Gradient Pump (GP50), Column Oven (TCC-3000) and Electrochemical Detector (ED40) with a Conductivity Cell with DS3 detector stabilizer. The separation of the different analytes was performed on an IonPac AG11-HC guard column (4*50mm) and AS11-HC analytical column (4*250mm) with a self-regenerating suppressor (ASRS 300, 4mm), trap column (ATC-3) which removed carbonate from the eluent (sodium hydroxide). The mobile phase, sodium hydroxide, was diluted in deoinized water (18.2 MΩ) obtained from a Milli-QPlus Water System from MilliPore: 1mM NaOH for 18 minutes, then increasing to 15mM over 12 minutes, and further increasing to 30mM and then 60mM each over 10 minutes, before reducing to 20mM and 1mM over 7 minutes with a flowrate of 1,5 mL/min. The background conductivity was less than 1 µS and the system pressure was around 1800 psi. Injection volume was 10 µl and the detection limit for all the compounds under these conditions were 5 µg/mL.

All standards used for calibration were purchased from Sigma Aldrich with a purity > 97 % with the exception of DL-Lactic acid (90%). However this was taken into account in the calculations.

All the degraded samples were diluted in deionized water (18,2 MΩ) 1/2 to 1/100 depending on the type of analysis and the level of degradation.

The standards used to investigate the matrix effect were prepared in deionized water (18,2 MΩ), and then spiked with amine solution (5M MEA, 2,5M AMP) giving a dilution of 10 with respect to amine concentration. The standard with amine solution was in addition diluted 10 and 100 times with deionized water (18,2 MΩ) so the total dilution of amine in the sample was 100 and 1000. This gave three samples with different concentration levels of amine to investigate the effect of amine concentration in the sample.

Results and Discussion

Matrix and Eluent Effect on Retention Time

As explained earlier, the retention time could be influenced by the eluent itself and the matrix in the samples. It is known that sodium hydroxide as eluent is not stable and therefore has to be prepared fresh every day, or every second day depending on the analysis. Several tests were performed to investigate the effect

Downloaded by OHIO STATE UNIV LIBRARIES on June 14, 2012 | http://pubs.acs.org
Publication Date (Web): May 3, 2012 | doi: 10.1021/bk-2012-1097.ch012

Downloaded by OHIO STATE UNIV LIBRARIES on June 14, 2012 | http://pubs.acs.org
Publication Date (Web): May 3, 2012 | doi: 10.1021/bk-2012-1097.ch012

of the matrix (both for the retention time and quantification) and the eluent itself. Samples with nitrate and formate in water, 5M MEA (monoethanolamine, diluted 10-1000 times in water) and 2,5M AMP (2-amino-2-methyl-1-propanol, diluted 10-1000 times in water) were analysed at the start of the sequence when the eluent was freshly prepared. The comparison between these three samples is given in Figure 1.

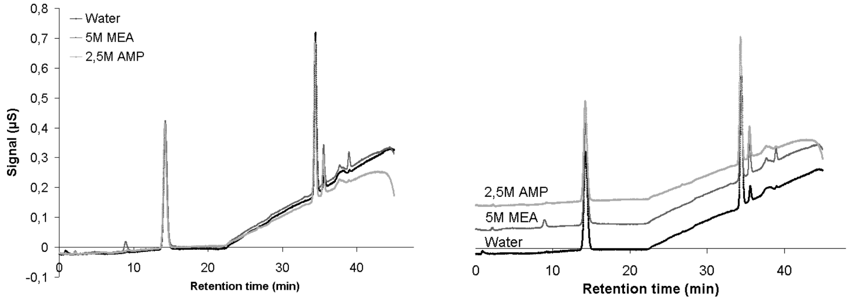

Figure 1. Formate and nitrate in water, MEA and AMP.

Figure 1 shows that the amine content does not seem to have any effect on retention time when the sample is diluted 10-1000 times, where a dilution of 100 seemed to be best for the degradation samples. Quantification of formate and nitrate in the samples in water, 5M MEA and 2,5M AMP respectively suggest that the matrix does not effect the quantification in our samples to any significant extent. However further testing with the rest of the anions and with more amines are necessary to make sure that none of them are affected by the amine.

The effect of eluent was tested running the samples with water and 5M MEA (diluted 10-1000 times in water) one more time at the end of the 48 hours sequence. The comparison between the samples at the beginning and the end of the sequence are given in Figure 2.

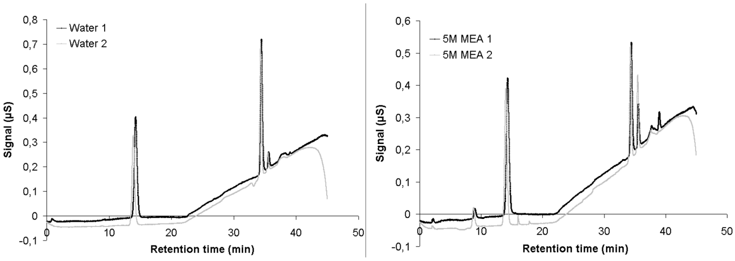

Figure 2. Comparison of retention time for samples run in the beginning and the end of a 48 hours sequence.

Figure 2 shows that the retention time slightly drifts to the left in the 48 hours sequence. It is also visible for the 5M MEA 2 sample that the carbonate content is increasing with time. Sodium hydroxide which is exposed to air will take up CO_2 and produce sodium carbonate over time. This effect is usually not visible because of the trap column, removing carbonate from the eluent. However the ATC-3 trap column has to be regenerated regularly to be able to remove the carbonate from the eluent.

Analysis of MEA Degraded Samples

Liquid samples from different degradation experiments were analysed for anions; lactate, fluoride, acetate, glycolate, propionate, formate, butyrate, nitrite, chloride, bromide, nitrate, sulphate, oxalate and malonate. The chromatograms for two different degradation experiments with 5M MEA are given in Figure 3.

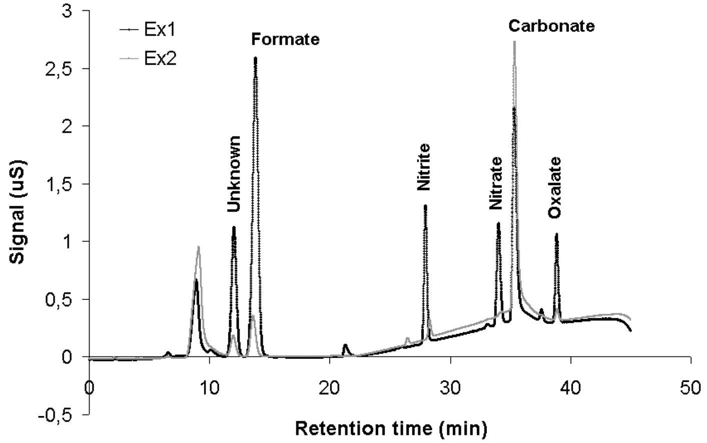

Figure 3. Two degradation experiments with 5M MEA.

The figure shows that the degradation is highest in experiment 1, which was spiked with iron. The unknown peak has the same retention time as propionate, however recent analyses of different MEA samples using another column do not see propionate at all. Recent experiments rather suggest that the unknown peak can be 2-[(2-hydroxyethyl)amino]-2-oxo-acetic acid. However, this has to be verified with a standard of this compound. The first peak without any identifier on it is believed to be caused by loaded MEA as given in Figure 4.

In Recent Advances in Post-Combustion CO2 Capture Chemistry; Attalla, M.;
ACS Symposium Series; American Chemical Society: Washington, DC, 2012.

Downloaded by OHIO STATE UNIV LIBRARIES on June 14, 2012 | http://pubs.acs.org
Publication Date (Web): May 3, 2012 | doi: 10.1021/bk-2012-1097.ch012

Downloaded by OHIO STATE UNIV LIBRARIES on June 14, 2012 | http://pubs.acs.org
Publication Date (Web): May 3, 2012 | doi: 10.1021/bk-2012-1097.ch012

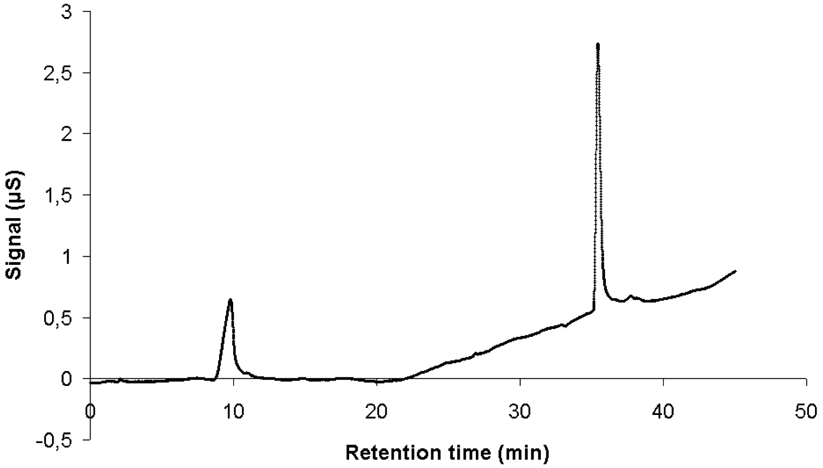

Figure 4. MEA (30 wt%) loaded with CO_2 (α=0,5 mole CO_2 per mole MEA).

This peak could most likely be avoided during analysis connecting a carbonate removal device in the IC-system between the suppressor and before the conductivity detector cell to remove carbonate from the sample. The quantification of the anions shown in Figure 3 is given in Figure 5.

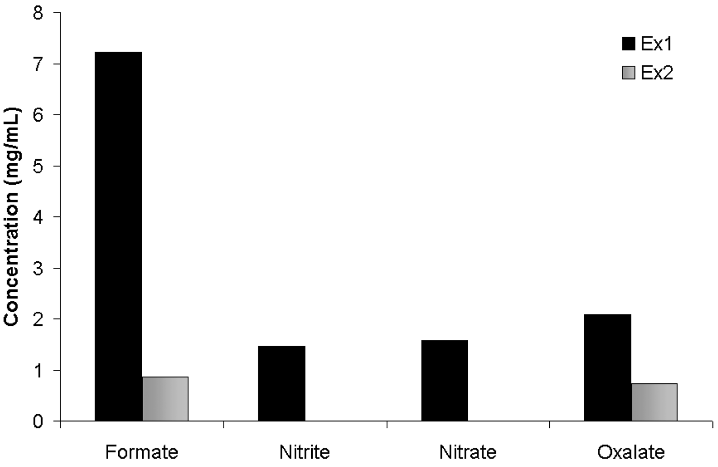

Figure 5. Quantification of anions for the two degradation experiments with 5M MEA.

Experiment 1 also showed nitrite and nitrate in addition to higher amounts of formate and oxalate than in experiment 2. This is probably due to the higher degradation observed for experiment 1 because of additive added to the system. Trace of either acetate or glycolate were also observed for experiment 1. However, the column used does not separate acetate and glycolate from each other and proper

Downloaded by OHIO STATE UNIV LIBRARIES on June 14, 2012 | http://pubs.acs.org
Publication Date (Web): May 3, 2012 | doi: 10.1021/bk-2012-1097.ch012

identification and quantification of these two anions was not successful, see Figure 6.

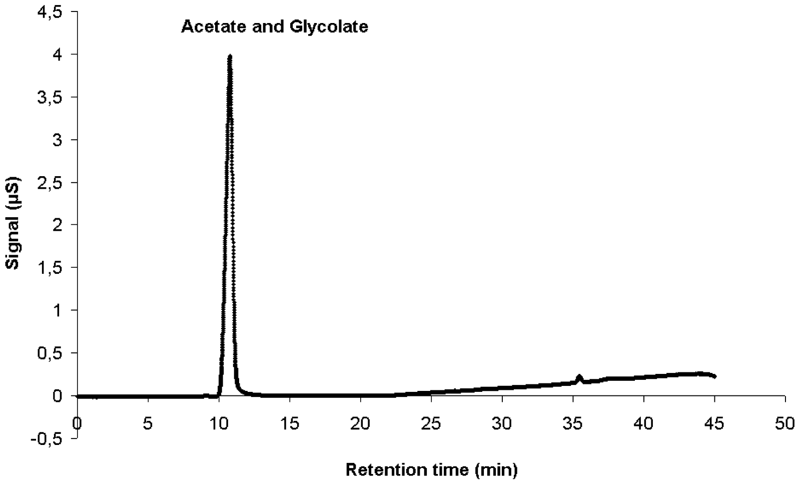

Figure 6. Sample containing 0,01 mg/mL of acetate and glycolate.

There are other columns which could be used to separate acetate and glycolate.

Degraded samples of MEA from the pilot plant at Esbjergværket (ESV) in Denmark were provided by the CESAR project. The details are described in the experimental setup. Anionic compounds in six samples from different locations in the process were identified and quantified - A: lean MEA start-up; B and C: absorber and stripper water washes after 11 weeks; D and E: lean and rich MEA solution after 11 weeks; F: lean MEA solution after 20 weeks, are given in Figure 7.

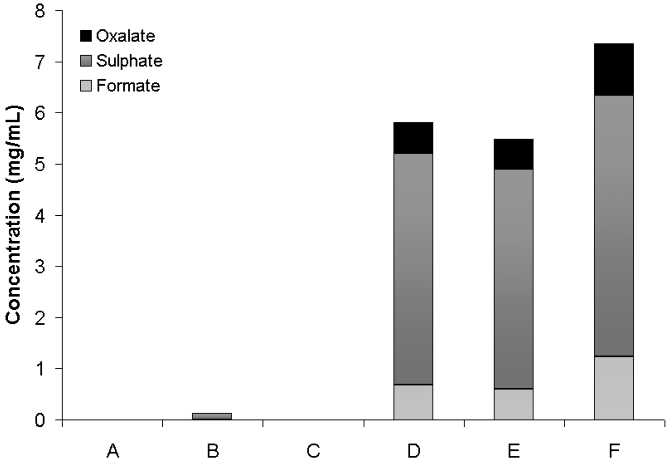

Figure 7. Quantification of ionic degradation compounds observed in the different samples from the MEA campaign at Esbjerg.

It was not possible to separate acetate and glycolate, as shown in figure 6, from each other and these anions have not at this point been identified and quantified. However, there is trace (less than 0,005 mg/mL) of glycolate or acetate in samples C to F. Sample D to F also show the same unknown peak as shown in Figure 3 and traces of chloride and nitrate (less than 0,005mg/mL). Sample B shows trace of nitrite (less than 0,002 mg/mL). The nitrite content in sample B is not verified and could also be caused by background noise since the detection limit of the anion was found to be 0,005 mg/mL with the used system.

Summary

It was shown that quality of eluent influences retention time, while amine content did not seem to effect the retention time or the quantification of the anions tested. However this has to be investigated further with all anions and with different amines and IC-systems. The main anion degradation compounds were formate, oxalate and the unknown compound. The Esbjerg pilot samples also showed high concentration of sulphate in addition to formate, oxalate and the unknown compound.

Acknowledgments

This publication forms a part of the SOLVit project, performed under the strategic Norwegian research program CLIMIT. The authors acknowledge the partners in SOLVit: Aker Clean Carbon, Gassnova, EON, SINTEF, NTNU and the Research Council of Norway for their support.

References

1. Lucy, C. A. *J. Chromatogr., A* **1998**, *804*, 3–15.
2. Haddad, P. R.; et al. *J. Chromatogr., A* **1999**, *856*, 145–177.
3. Weiss, J. *Handbook of Ion Chromatography*, 3rd ed.; Wiley-VCH Verlag GMbH & Co. KGaA: Germany, 2004; Vol. 1, pp 27−278.
4. Henderson, I. K.; et al. *J. Chromatgr.* **1991**, *546*, 61–79.
5. Kadnar, R.; et al. *J. Chromatogr., A* **1995**, *706*, 339–343.
6. Lopez-Ruiz, B. *J. Chromatogr., A* **2000**, *881*, 607–627.
7. Mrklas, O.; et al. *J. Environ. Monit.* **2003**, *5*, 336–340.
8. Singh, R. P.; et al. *J. Chromatogr., A* **1997**, *774*, 1257–1264.
9. Small, H.; et al. *Anal. Chem.* **1975**, *47*, 1801–1809.
10. Toofan, M.; et al. *J. Chromatogr., A* **1997**, *761*, 163–168.
11. Lepaumier, H.; et al. *Energy Procedia* **2011**, *4*, 1652–1659.
12. Lepaumier, H.; et al. *Energy Procedia* **2009**, *1*, 893–900.
13. Lepaumier, H.; et al. *Ind. Eng. Chem. Res.* **2009**, *48*, 9068–9075.
14. Lepaumier, H.; et al. *Ind. Eng. Chem. Res.* **2009**, *48*, 9061–9067.
15. Sexton, A. J.; et al. *Int. J. Greenhouse Gas Control* **2009**, *3*, 704–711.
16. Supap, T.; et al. *Ind. Eng. Chem. Res.* **2006**, *45*, 2437–2451.
17. Straziar, B. R.; et al. *Energy Fuels* **2003**, *17*, 1034–1039.

Downloaded by OHIO STATE UNIV LIBRARIES on June 14, 2012 | http://pubs.acs.org
Publication Date (Web): May 3, 2012 | doi: 10.1021/bk-2012-1097.ch012

18. Kadnar, R. *J. Chromatogr., A* **1999**, *850*, 289–295.
19. Sexton, A. J.; et al. *Energy Procedia* **2009**, *1*, 1179–1185.
20. Supap, T.; et al. *Ind. Eng. Chem. Res.* **2001**, *40*, 3445–3450.
21. Rooney, P. C.; et al. *Hydrocarbon Process.* **1998**, 109–113.
22. Chi, S.; et al. *Ind. Eng. Chem. Res.* **2002**, *41*, 4178–4186.
23. Goff, G. S.; et al. *Ind. Eng. Chem. Res.* **2004**, *43*, 6400–6408.
24. Goff, G. S.; et al. *Ind. Eng. Chem. Res.* **2006**, *45*, 2513–2521.

Downloaded by OHIO STATE UNIV LIBRARIES on June 14, 2012 | http://pubs.acs.org
Publication Date (Web): May 3, 2012 | doi: 10.1021/bk-2012-1097.ch012

Downloaded by PENNSYLVANIA STATE UNIV on June 14, 2012 | http://pubs.acs.org
Publication Date (Web): May 3, 2012 | doi: 10.1021/bk-2012-1097.ch013

Chapter 13

Sequential Degradation of Aqueous Monoethanolamine for CO_2 Capture

Alexander K. Voice, Daniel Wei, and Gary T. Rochelle*

University of Texas at Austin, Dept. of Chemical Engineering, 1 University Station C0400, Austin, TX 78712
***gtr@che.utexas.edu**

Monoethanolamine (MEA) degradation occurs by two parallel pathways: thermal degradation and oxidative degradation. This work examines the stability of products produced by both pathways with a batch-wise sequential degradation experiment.

Oxidation products formate and nitrate were very stable when the solution was heated to 135 °C, whereas hydroxyethyl-imidazole (HEI) degraded over several weeks. Nitrite, oxalate, and oxalyl-amides decomposed after several days at 135 °C. Oxalate species were converted one-to-one into formate, whereas nitrite was rapidly consumed; the fate of the nitrite is unknown. Hydroxyethyl-imidazolidinone (HEIO), a thermal degradation product, was oxidatively stable, whereas hydroxyethyl ethylenediamine (HEEDA) was rapidly oxidized.

Thermal degradation rates of MEA were the same for the neat solution and the oxidized solution. However, oxidation rates were 1.5x–2.5x higher for the thermally degraded solution compared to the neat solution. Oxidation enhancement may be due to the presence of Mn or other metals from corrosion of stainless steel.

Keywords: monoethanolamine (MEA); oxidation; degradation; products; stability; pathways; CO_2 capture

Downloaded by PENNSYLVANIA STATE UNIV on June 14, 2012 | http://pubs.acs.org
Publication Date (Web): May 3, 2012 | doi: 10.1021/bk-2012-1097.ch013

Background

Solvent degradation is a major problem afflicting amine scrubbers using monoethanolamine (MEA) for CO_2 capture. Degradation drives up the cost of operating a CO_2 capture process by reducing the rates and the capacity of the solvent, as well as the capital cost by increasing corrosion rates and decreasing equipment lifetime. A further concern is the environmental fate and toxicity of degradation products.

Previous work has shown that degradation of MEA occurs by two parallel pathways. The first is thermal degradation, which involves dehydrolysis of the MEA-carbamate to form oxazolidinone (OZD), which reacts further to form imidazolidinones, N-substituted ureas, and MEA polymers (Figure 1) (*1–4*).

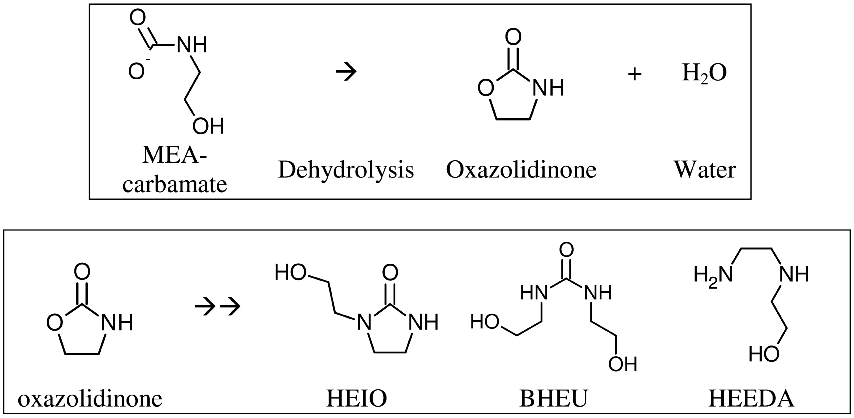

Figure 1. Thermal Degradation Products

The second is oxidative degradation, which involves transition metal-catalyzed fragmentation of MEA-peroxide into ammonia and hydroxyl-acetaldehyde or formaldehyde (Equations 1–3) (*5–8*). Further oxidation produces glyoxal or glyoxylic (from hydroxyacetaldehyde) and formate (from formaldehyde).

$$\mathrm{MEAOOH} \rightarrow \mathrm{MEAO}\bullet \rightarrow \mathrm{MEAOH} \tag{1}$$

$$\mathrm{MEAOH} \rightarrow NH_3 + OHCH_2CHO \text{ (hydroxyacetaldehyde)} \tag{2}$$

$$\mathrm{MEAOH} \rightarrow NH_3 + 2\ CH_2O \tag{3}$$

Downloaded by PENNSYLVANIA STATE UNIV on June 14, 2012 | http://pubs.acs.org
Publication Date (Web): May 3, 2012 | doi: 10.1021/bk-2012-1097.ch013

Aldehydes formed during oxidation can react to form hemi-aminals with MEA, ammonia, or another amine followed by oxidation to produce the amides of formate or oxalate (Figure 2). 1-(2-hydroxyethyl-formamide (HEF) is a known product of MEA oxidation as are several other amides (*9*–*12*).

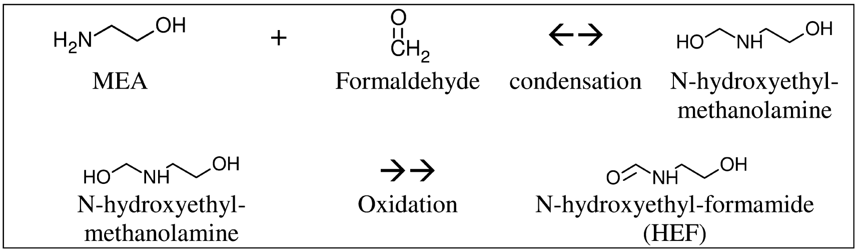
MEA
+
Formaldehyde
condensation
N-hydroxyethyl-methanolamine
N-hydroxyethyl-methanolamine
Oxidation
N-hydroxyethyl-formamide (HEF)

Figure 2. Production of HEF from condensation of formaldehyde and MEA

Hemi-aminals, which are in equilibrium with their respective imines (via dehydrolysis) can further react with each other to form imidazoles such as 1-(2-hydroxyethyl)-imidazole (HEI) (Figure 3) (*13*). HEI was first reported by Sexton (*9*, *10*) as a degradation product of MEA and has since been confirmed in other work (*12*), as have imidazole and some imidazole derivatives (*11*, *12*, *14*).

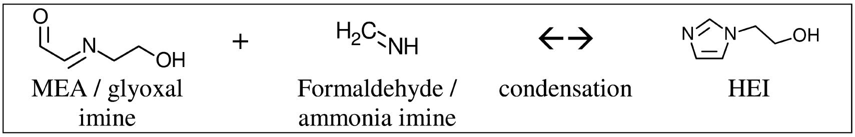
MEA / glyoxal imine
+
Formaldehyde / ammonia imine
condensation
HEI

Figure 3. Production of HEI from condensation of imines

Organic acids (primarily formate and oxalate) are proposed to form by hydrolysis of the corresponding amide (Figure 4) (*15*), rather than by direct oxidation of the corresponding aldehyde. This mechanism is supported by the observation that during oxidation the amide exists in significantly higher concentrations than the acid, however equilibration in the absence of oxygen produces approximately equal concentrations of the two species. Formate and other heat-stable salts are well-known products of MEA degradation (*4*, *16*, *17*).

Downloaded by PENNSYLVANIA STATE UNIV on June 14, 2012 | http://pubs.acs.org
Publication Date (Web): May 3, 2012 | doi: 10.1021/bk-2012-1097.ch013

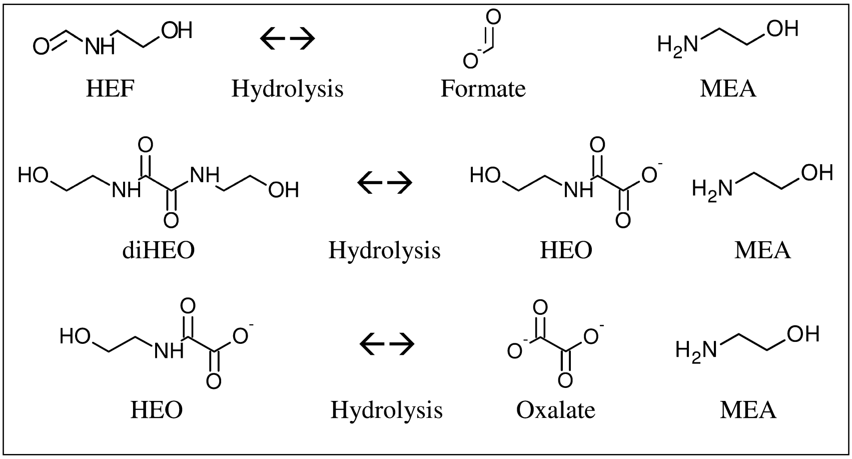

Figure 4. Production of carboxylic acids from amides

In an industrial system, MEA oxidation occurs in the absorber, the absorber hold-up, and the cross exchanger. Any remaining dissolved oxygen flashes out of the solvent as it enters the top of the stripper. Thermal degradation occurs primarily in the reboiler and solvent reclaimer. A number of previous researchers have chosen a single set of experimental conditions to simulate one or more parts of the amine-scrubbing process (*3*, *9*, *10*, *12*, *16–26*).

In the present work, a novel approach is used in which the solvent is sequentially exposed to two separate conditions representing the low temperature, high oxygen environment of the absorber and the high temperature, no oxygen environment of the stripper. Solvent loss and major product formation rates were determined for each experiment.

Experimental Methods

Thermal degradation was conducted using a 2.5” SS316 pipe with plates welded to the ends. One end-plate was fitted with two ¼” MNPT to Swagelok adapters. The reactor was filled with 420 g of CO_2-loaded 7 m MEA, purged with N2, and fitted with a Swagelok endcap. The vessel was placed in a convection oven at 135 °C. Samples were taken periodically by removing the reactor from the oven, quenching it in an ice bath, removing the endcap, and inserting a glass 5 mL pipette into the sampling port. After the sample was taken, the reactor was purged with N_2, resealed, and placed back in the oven. Samples were stored in the dark at 4 °C prior to analysis.

Oxidative degradation was conducted at 55 °C in a glass-jacketed, semi-batch reactor system. Oxygen (98 kPa) and carbon dioxide (2 kPa) passed through a pre-saturator before flowing into the reactor headspace, and exiting around the agitator. The reactor was agitated at 1440RPM to increase oxygen mass transfer. Fe_2SO_4 (0.40 mM), $Cr_2(SO_4)_3$ (0.10 mM) and $NiSO_4$ (0.05 mM) were added to neat

Downloaded by PENNSYLVANIA STATE UNIV on June 14, 2012 | http://pubs.acs.org
Publication Date (Web): May 3, 2012 | doi: 10.1021/bk-2012-1097.ch013

solutions at the beginning of the experiment to simulate real process conditions. This experimental design is the same as that used by Sexton (*10*).

Analysis of amines (MEA and HEEDA) was carried out on a Dionex ICS2100 ion chromatograph with a IonPac CS17 column (4.6x250 mm) using water and aqueous methane sulfonic acid as the eluents. Analysis of formate, oxalate, 1-(2-hydroxyethyl)-oxalamide, nitrate, and nitrite was carried out on a Dionex ICS3000 anion chromatograph with a IonPac AS15 column (4.6x250), suppressor, and CRD using water and aqueous sodium hydroxide as the eluent. Analysis of amides (N-formyl- and N-oxalyl-species) was conducted by hydrolyzing 1 mL of the sample with 2 mL of 5N NaOH at room temperature for 48 hours. Formate- and oxalate-amide concentrations were found by calculating the respective differences of formate and oxalate found before and after the NaOH treatement (as demonstrated by Koike and Sexton (*9*, *10*, *15*)). Anion and cation chromatography methods were the same as those used by Davis (*3*) and Sexton (*9*, *10*).

HEI and HEIO concentrations were determined using reverse-phase chromatography on a Dionex U3000 HPLC with a Phenomenex Luna 3 um unbounded-silica 4x150 mm column, acetonitrile (0-50%) / water (100-50%) eluent, and UV detector (210 nm).

Results

Results are presented for two batch-cycling scenarios. Oxidative degradation followed by thermal degradation (Figures 1–5) and thermal degradation followed by oxidative degradation (Figures 6–10). The dotted line in each plot indicates where the conditions were changed. Key results for each product are given in the figure captions below.

With oxidation followed by thermal degradation, formate, formyl-amides, and nitrate were shown to be thermally stable, whereas oxalate, oxalyl-amides, and nitrite were not. Heating initially resulted in an increase in HEI from the reaction of aldehydes and amines. With continued heating, HEI is slowly degraded; no degradation products were identified. MEA loss was unaffected by the presence of oxidation products.

With thermal degradation followed by oxidation, thermal degradation significantly increased the rate of oxidation, as well as the rates of all oxidation products. HEIO was oxidatively stable, whereas HEEDA degraded rapidly in the presence of oxygen.

Oxidation (55 °C, 98 kPa O_2, 2 kPa CO_2) followed by Thermal Degradation (135 °C)

Figure 5 shows that MEA loss during thermal degradation matches thermal degradation of the neat solution, thus oxidation products have no significant effect on the thermal degradation mechanism. Various oxidation products react differently to the thermal shock. Nitrite is consumed within 24 hours at 135 °C, whereas nitrate concentration does not change after heating to 135 °C (Figure 6).

Formate and formyl-amides equilibrate to approximately 1:1 within 24 hours of heating (from a ratio of 5:1 formyl-amides to formate before heating) (Figure 7). This equilibrium ratio of formyl-amides to formate in loaded MEA at 135 °C is the same as that observed by Freeman (*27*) for loaded piperazine at 175 °C. The total concentration of formyl species in the solution increased by 24 mmol/kg to 111 mmol/kg after heating for ten days (Figure 7).

Some di-oxalamide species hydrolyzed upon heating, resulting in a net increase in mono-oxalamide and oxalate. Equilibrium is never reached because the oxalate is degraded to formate and carbon dioxide (*29*). After heating for ten days, all of the oxalate species (25 mmol/kg) were degraded at a rate of approximately 0.14 mmol/kg/hr (Figure 8). This decrease in oxalate matched the observed increase in formyl-species.

HEI concentration increased immediately by 121 mmol/kg from 70 mmol/kg on heating for 24 hours. After longer times at 135 °C, HEI decreased slowly—the initial rate of HEI degradation, upon heating, was regressed and found to be 1.8 mmol/kg/day. HEI is known to be produced from reaction of equimolar quantities of MEA, glyoxal, ammonia, and formaldehyde (*13*) via a two-step reaction as shown in Figure 3. Formaldehyde and ammonia are known oxidation products of MEA. Glyoxal is highly suspected given the presence of other two-carbon oxidation products such as hydroxyl-acetaldehyde and oxalate (*5–7*, *9*, *10*, *25*, *26*, *28*). The immediate increase in HEI upon heating indicates the likely presence of imines in the solution which condense rapidly to form HEI when heated.

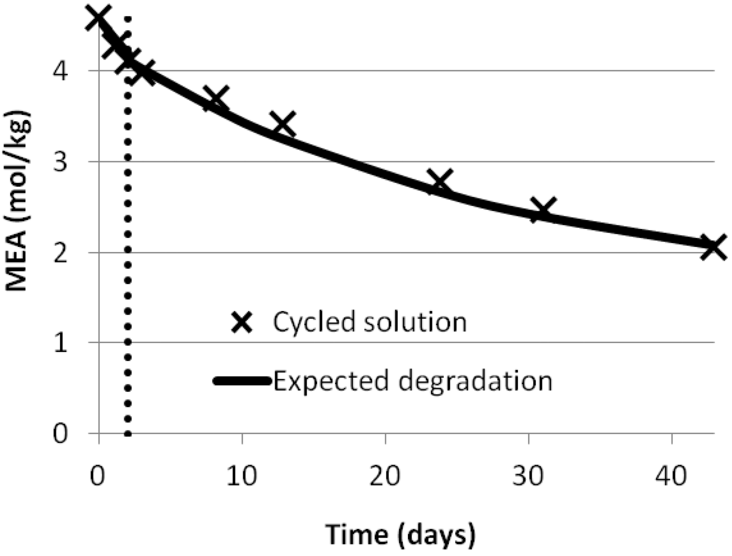

Figure 5. MEA loss during oxidation (55 °C, 98 kPa O_2, 2 kPa CO_2, 0.40 mM Fe, 0.1 mM Cr, 0.05 mM Ni) followed by thermal degradation (135 °C). Expected degradation is the apparent first-order degradation of MEA at 0.4 loading and 135 °C reported by Davis (3)

Downloaded by PENNSYLVANIA STATE UNIV on June 14, 2012 | http://pubs.acs.org
Publication Date (Web): May 3, 2012 | doi: 10.1021/bk-2012-1097.ch013

Downloaded by PENNSYLVANIA STATE UNIV on June 14, 2012 | http://pubs.acs.org
Publication Date (Web): May 3, 2012 | doi: 10.1021/bk-2012-1097.ch013

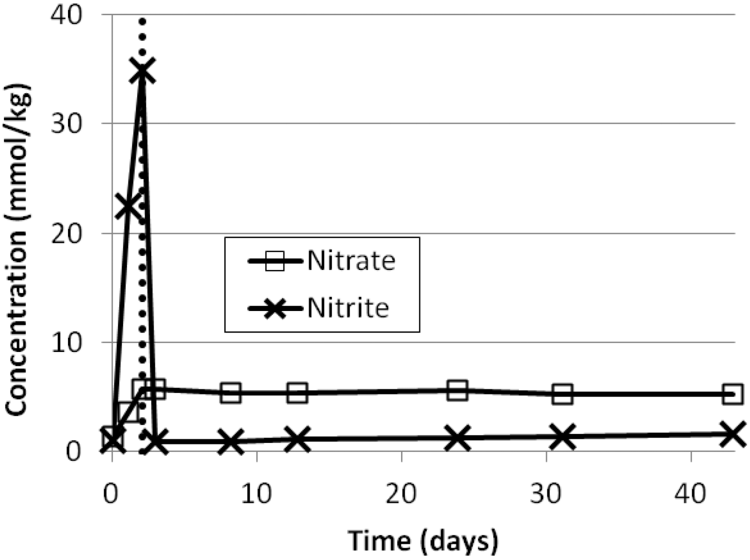

Figure 6. Nitrate and nitrite during oxidation followed by thermal degradation

degradation

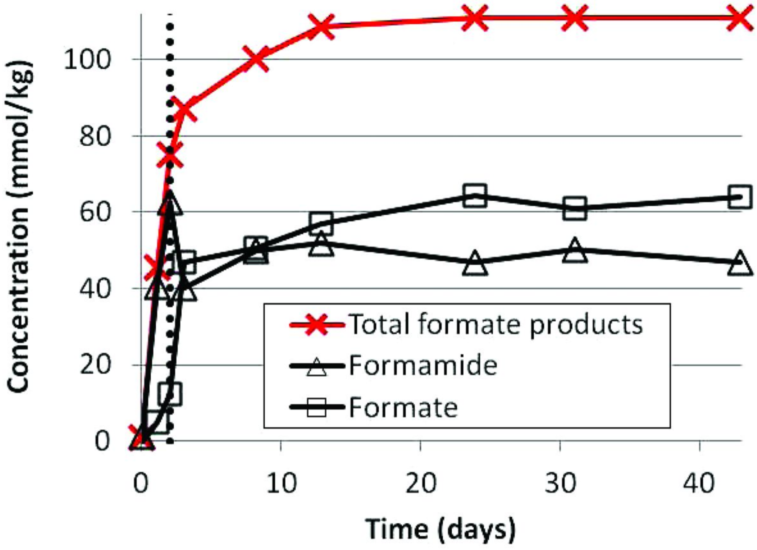

Figure 7. Formate products during oxidation followed by thermal degradation

Downloaded by PENNSYLVANIA STATE UNIV on June 14, 2012 | http://pubs.acs.org
Publication Date (Web): May 3, 2012 | doi: 10.1021/bk-2012-1097.ch013

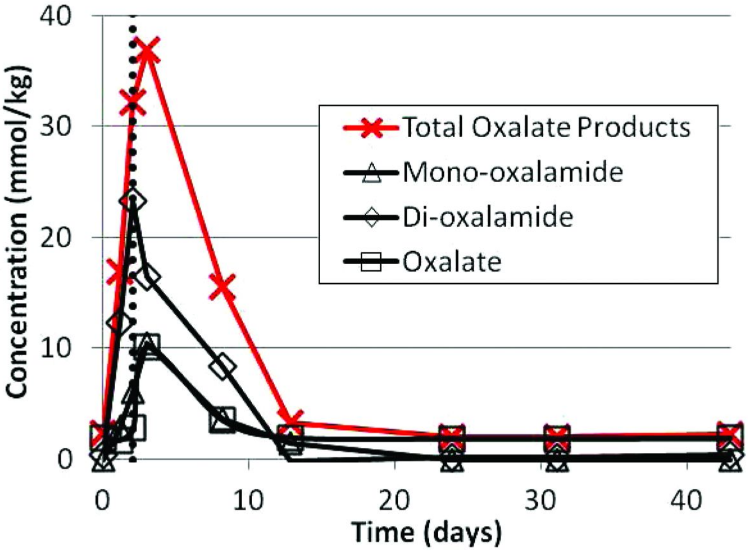

Figure 8. Oxalate products during oxidation followed by thermal degradation

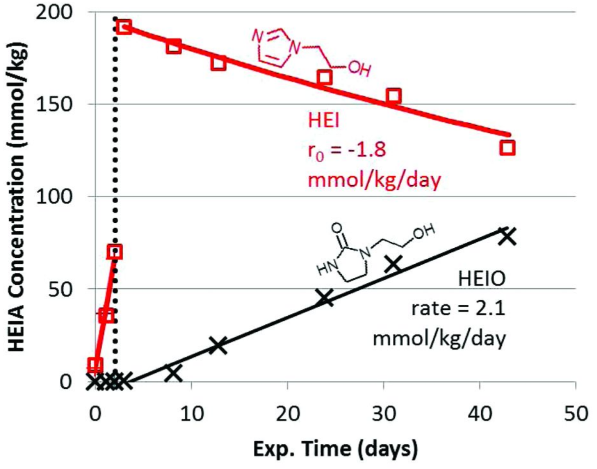

Figure 9. Hydroxyethylimadazole (HEI) and Hydroxyethyl imidazolidinone (HEIO) during oxidation followed by thermal degradation

Thermal Degradation (0.4 loading, 135 °C) followed by Oxidation (55 °C, 98 kPa oxygen, 2 kPa CO_2)

The regressed initial rate of MEA loss in the cycled solution is 14.4 mmol/kg/hr, compared with 8.8 mmol/kg/hr in the neat solution. The initial rate for the neat solution is comparable to that reported by Sexton under similar conditions, however rate for the cycled solution is significantly higher (Figure 10). The difference may be due to the presence of manganese or other metals from corrosion of stainless steel.

HEEDA is produced at an initial rate of 3.6 mmol/kg/hr during at 135 °C; during oxidation, HEEDA is rapidly oxidized at an initial rate of 15.6 mmol/kg/hr (Figure 11). No formate or formyl-species were produced during thermal degradation. During oxidation, total formate production occurred at an initial rate of 2.5 mmol/kg/hr, compared with 1.15mmol/kg/hr in the neat solution (Figure 12).

No oxalate or oxalyl-species were produced during thermal degradation. During oxidation, total formate production occurred at an initial rate of 0.68 mmol/kg/hr, compared with 0.37 mmol/kg/hr in the neat solution (Figure 13).

The regressed initial rate of HEI production in the cycled solution was 1.8 mmol/kg/hr, compared with 0.78 mmol/kg/hr in the neat solution (Figure 14). HEIO is produced at a rate of 16.1mmol/kg/hr during thermal degradation at 135 °C with 0.4 loading. HEIO is stable to oxidation at 55 °C (Figure 15).

Downloaded by PENNSYLVANIA STATE UNIV on June 14, 2012 | http://pubs.acs.org
Publication Date (Web): May 3, 2012 | doi: 10.1021/bk-2012-1097.ch013

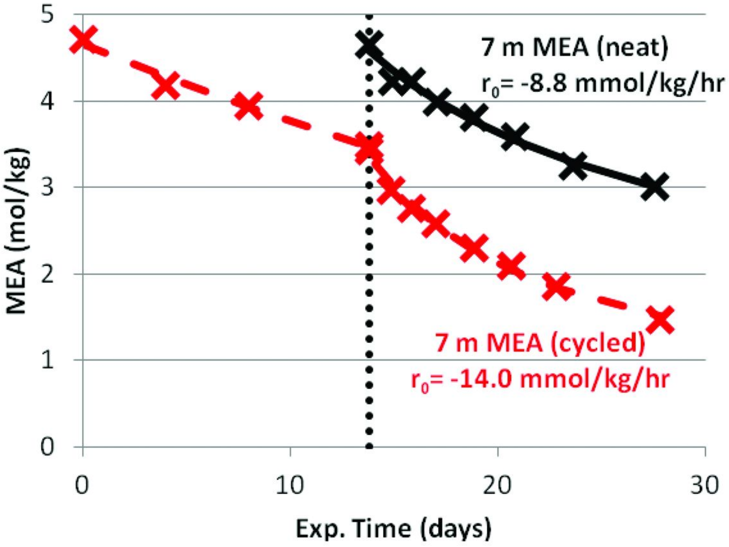

Figure 10. MEA loss during thermal degradation (135 °C, 0.4 loading) followed by oxidation (55 °C, 98 kPa O2, 2 kPa CO_2). Metals added to neat solution – 0.4 mM Fe, 0.1 mM Cr, 0.05 mM Ni

Downloaded by PENNSYLVANIA STATE UNIV on June 14, 2012 | http://pubs.acs.org
Publication Date (Web): May 3, 2012 | doi: 10.1021/bk-2012-1097.ch013

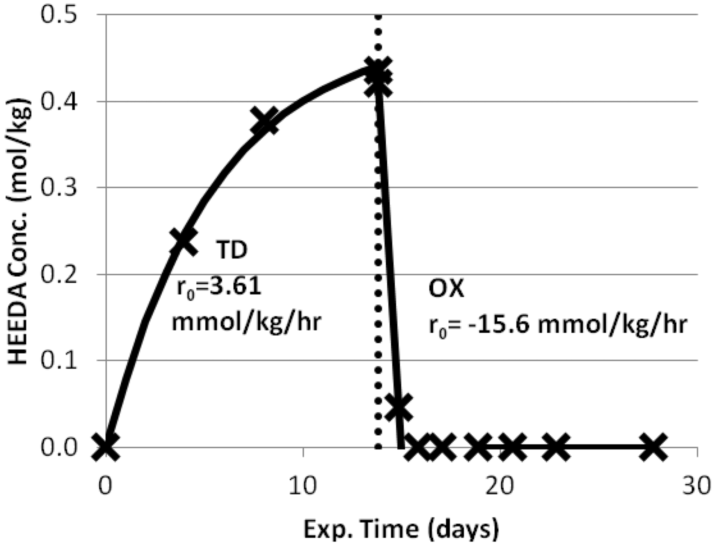

Figure 11. HEEDA during thermal degradation (135 °C, 0.4 loading) followed by oxidation (55 °C, 98 kPa O2, 2 kPa CO_2)

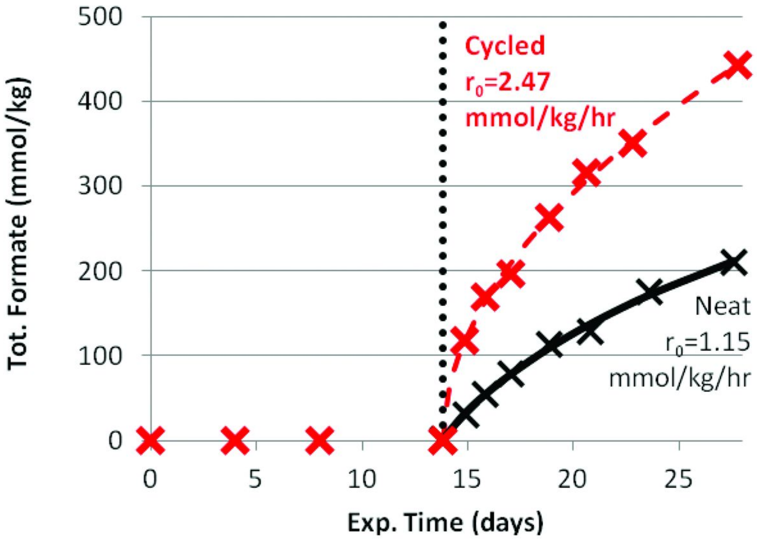

Figure 12. Formate products during thermal degradation followed by oxidation

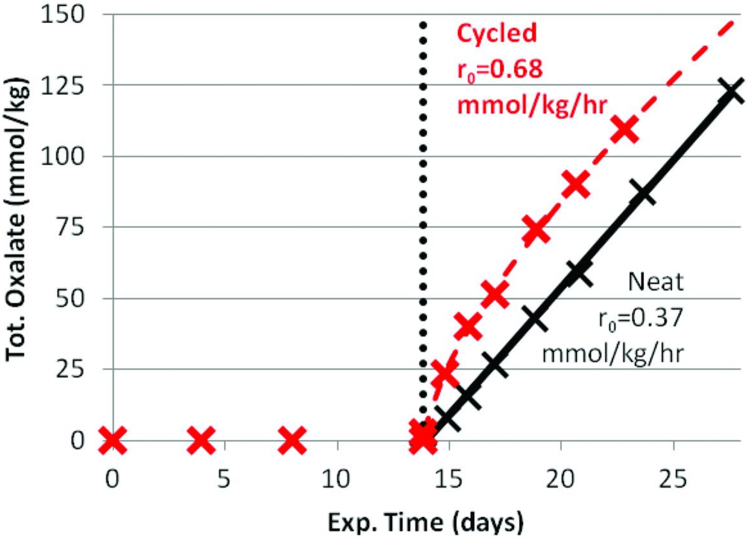

Figure 13. Oxalate products during thermal degradation followed by oxidation

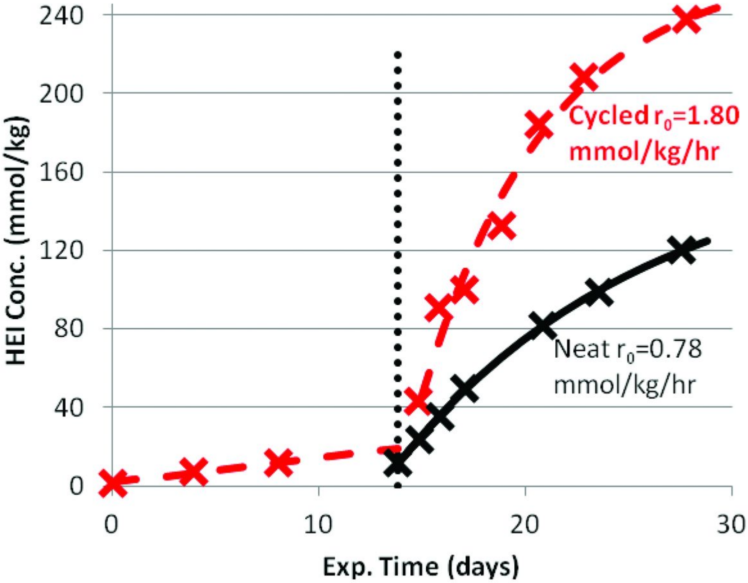

Figure 14. HEI during thermal degradation followed by oxidation

Downloaded by PENNSYLVANIA STATE UNIV on June 14, 2012 | http://pubs.acs.org
Publication Date (Web): May 3, 2012 | doi: 10.1021/bk-2012-1097.ch013

Downloaded by PENNSYLVANIA STATE UNIV on June 14, 2012 | http://pubs.acs.org
Publication Date (Web): May 3, 2012 | doi: 10.1021/bk-2012-1097.ch013

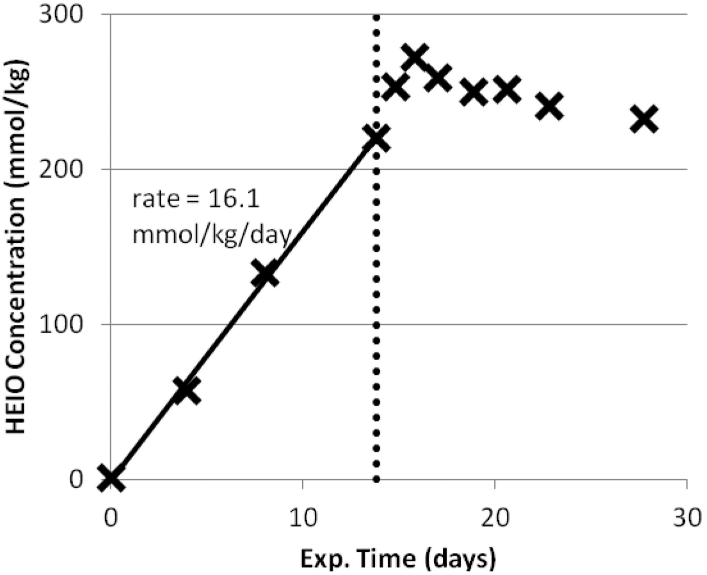

Figure 15. HEIO during thermal degradation followed by oxidation

Conclusions

A variety of degradation products of monoethanolamine are known from previous work to arise from two distinct pathways with regard to carbon capture: oxidation and thermal degradation. The current work has established some of the important interactions between these two mechanisms. The cyclic stability of MEA degradation products is summarized in Table I.

Generally speaking, oxidation is enhanced by prior thermal degradation, in terms of loss of MEA and production of oxidation products. HEEDA, a thermal degradation product, oxidized rapidly whereas HEIO was stable to oxidation.

MEA loss during thermal degradation was not affected by prior oxidation; however, some oxidation products were stable to high temperatures whereas others were not. Formate is produced from hydrolysis of formamide when the oxidized MEA solution was heated, indicating that formamide is the primary oxidation product and not formate. Oxalate is known to decompose to formate (*29*), thus equilibrium is never achieved between oxalyl-amides and oxalate, because oxalate is continuously consumed.

Table I. Summary of MEA Degradation Product Stability

Compound	*CAS*	*Type of Product*	*Stability in cycling*
1-(2-hydroxyethyl)-imidazolidinone (HEIO)	3699-54-5	Thermal	Oxidatively stable
1-(2-Hydroxyethyl) ethylenediamine (HEEDA)	111-41-1	Thermal	Oxidizes rapidly
1-(2-hydroxyethyl) imidazole (HEI)	1615-14-1	Oxidative	Somewhat thermally stable
Formic acid	64-18-6	Oxidative	Equilibrates with formamide
1-(2-hydroxyethyl)-formamide (HEF)	693-06-1	Oxidative	Equilibrates with formate
Oxalic acid	144-62-7	Oxidative	Decomposes to formate
1-(2-hydroxyethyl)-oxalamide (HEO)	5270-73-5	Oxidative	Equilibrates with oxalate
1,4-bis-(2-hydroxyethyl)-oxal-di-amide (BHEO)	1871-89-2	Oxidative	Equilibrates with oxalate
Nitrate	7697-37-2	Oxidative	Thermally stable
Nitrite	7782-77-6	Oxidative	Not thermally stable

Downloaded by PENNSYLVANIA STATE UNIV on June 14, 2012 | http://pubs.acs.org
Publication Date (Web): May 3, 2012 | doi: 10.1021/bk-2012-1097.ch013

All nitrite was consumed in less than 24 hours—the nitrite likely reacted with MEA to form ethylene glycol and N_2 via formation of an unstable diazonium intermediate and subsequent decomposition, a well-known pathway (*30*). However, it is also possible that the nitrite reacted with another MEA degradation product in the solution. Trace amounts of diethanolamine have been shown to react to form N-nitroso-diethanolamine (NDELA) in the presence of MEA and NO_2 (*31*). Nitrosation of other secondary amines and amides present in small quantities is also a possibility (*32*).

Enhancement of oxidation following thermal degradation could be explained in one of two ways. First, the presence of certain metals from corrosion of stainless steel during thermal degradation may have enhanced the oxidation rate. In particular, manganese is known to be a potent oxidation catalyst of similar compounds (*33*, *34*) and may have been present in trace quantities in this experiment. Second, the presence of thermal degradation products may change the redox potential of reactions involving the metal catalysts present, causing them to be more potent (*35*). Determining the exact cause of this enhancement will require further study.

Downloaded by PENNSYLVANIA STATE UNIV on June 14, 2012 | http://pubs.acs.org
Publication Date (Web): May 3, 2012 | doi: 10.1021/bk-2012-1097.ch013

References

1. Polderman, L. D.; Dillon, C. P.; Steele, A. B. *Oil Gas J.* **1955**, *54* (2), 180–183.
2. Yazvikova, N. V.; Zelenskaya, L. G.; et al. *Zh. Prikl. Khim.* **1975**, *48* (3), 674–676.
3. Davis J. D. Ph.D. thesis, The University of Texas, Austin, TX, 2009.
4. Scheiman, M. A. NRL Report 5746; US Naval Research Laboratory: Washington, DC, 1962.
5. Petrayev, E. P.; Pavlov, A. V.; Shadyro, O. T. *Zh. Org. Khim.* **1984**, *20* (1), 29–34.
6. Denisov, E. T. *Russ. Chem. Rev.* **1996**, *65* (6), 505–520.
7. Dennis, W. H.; Hull, L. A. *J. Org. Chem.* **1967**, *32*, 3783–3787.
8. Russell G. A. In *Peroxide Reaction Mechanisms*; Edwards, J. O., Ed.; Interscience Publishers: New York, NY, 1962; pp 107−128.
9. Sexton, A. J.; Rochelle, G. T. *Ind. Eng. Chem. Res.* **2011**, *50*, 667–673.
10. Sexton A. J. Ph.D. thesis, The University of Texas, Austin, TX, 2008.
11. Strazisar, B. R.; Anderson, R. R.; White, C. M. *Energy Fuels* **2003**, *17* (4), 1034–1039.
12. LePaumier, H.; da Silva, E. F.; Einbu, A.; et al. *Energy Procedia* **2011**, *4*, 1652–1659.
13. Speranza, G. P.; Wei-Yang S. U.S. Patent 4927942.
14. Supap, T.; Idem, R.; et al. *Ind. Chem. Eng. Res.* **2006**, *45*, 2437–2451.
15. Koike, L.; Barone, J. S.; et al. *Chem. Ind.* **1987**, 626–627.
16. Rooney, P. C.; Dupart, M. S.; Bacon, T. R. *Hydrocarbon Proc. Int. Ed.* **1998**, *77* (7), 109–113.
17. Hofmeyer, B. G.; Scholten, H. G.; Lloyd, W. G. Presented at the National Meeting of the American Chemical Society, Dallas, TX, 1956.
18. Chi, Q. S. M.S. Thesis, The University of Texas, Austin, TX, 2001.
19. Chi, S.; Rochelle, G. T. *Ind. Eng. Chem. Res.* **2002**, *41* (17), 4178–4186.
20. Goff, G. S. Ph.D. Dissertation, The University of Texas, Austin, TX, 2005.
21. Goff, G. S.; Rochelle, G. T. *Ind. Chem. Eng. Res.* **2004**, *43* (20), 6400–6408.
22. Goff, G. S.; Rochelle, G. T. *Ind. Chem. Eng. Res.* **2006**, *45* (8), 2513–2521.
23. LePaumier, H.; Picq, D.; Carrette, P.-L. *Ind. Eng. Chem. Res.* **2009**, *48*, 9068–9075.
24. Supap, T.; Idem, R.; et al. *Ind. Chem. Eng. Res.* **2001**, *40*, 3445–3450.
25. Kindrick, R. C.; Atwood, K. *Carbon Dioxide Absorbents*; Girdler Report No. T2.15-1-30; Contract NObs-50023; Gas Processes Division, Girdler Corporation: Louisville, KY, 1950.
26. Blachly, C. H.; Ravner H. Accession No. AD609888, NRL-6189; U.S. Naval Research Laboratory: Washington, DC, 1962.
27. Freeman, S. A. Ph.D. Dissertation, The University of Texas, Austin, TX, 2011.
28. Epp, B.; Fahlenkamp, H.; Vogt, M. *Energy Procedia* **2010**, *4*, 2011.
29. Lutgert, I.; Schroer, E. *Z. Phys. Chem. A.* **1940**, *187*, 133–148.
30. Ridd, J. H. *Q. Rev. Chem. Soc.* **1961**, *15*, 418–441.
31. Foståsa, B.; Gangstadb, A.; et al. *Energy Procedia* **2011**, *4*, 1566–1573.

32. Castro, A.; Iglesias, E. *J. Chem. Soc., Perkin Trans.2* **1986**, 1725–1729.
33. Stadtman, E. R.; Berlett, B. S.; Chock, P. B. *Proc. Natl. Acad. Sci. U.S.A.* **1990**, *87*, 384–38.
34. Stadtman, E. R. *Annu. Rev. Biochem.* **1993**, *62*, 797–821.
35. Denisov, E. T.; Afanas'ev, I. B. *Oxidation and antioxidants in organic chemistry and biology*; Taylor and Francis: Boca Raton, FL, 2005; p 620.

Downloaded by PENNSYLVANIA STATE UNIV on June 14, 2012 | http://pubs.acs.org
Publication Date (Web): May 3, 2012 | doi: 10.1021/bk-2012-1097.ch013

Chapter 14

An Investigation into the Photochemistry of Monoethanolamine (MEA) in NOx

Dennys Angove,*[*] Merched Azzi, Anne Tibbett, and Ian Campbell

CSIRO Energy Technology, PO Box 52, North Ryde, NSW 1670, Australia
[*]Corresponding author: dennys.angove@csiro.au

Downloaded by CORNELL UNIV on June 14, 2012 | http://pubs.acs.org
Publication Date (Web): May 3, 2012 | doi: 10.1021/bk-2012-1097.ch014

The capture of CO_2 produced during fossil fuel combustion is problematic. The use of amines, such as monoethanolamine (MEA), to absorb CO_2 is one strategy widely considered to be a viable solution to this problem. Given the scale of the carbon capture process and the mass of MEA required to facilitate CO_2 capture, investigations into the environmental impacts need to be expedited. The literature contains only a small number of studies addressing the atmospheric chemistry of MEA. In this pilot smog chamber study, the formation of formamide and ammonia during the photodecomposition of ~400 ppb of MEA in ~50 ppb NO were observed. The molar yield for the formation of formamide was 0.20 to 0.28 and that of NH_3, 0.33 to 0.40.

Introduction

Monoethanolamine (MEA) or 2-aminoethanol has been used to absorb CO_2 in small applications for many years (*1*). It use as an agent for the capture of CO_2 produced during fossil fuel combustion in power plants is currently being investigated. It is expected that the mass of MEA required to accomplish such a task will be very large. Since MEA will be in contact with the flue gas, the

Published 2012 by the American Chemical Society
In Recent Advances in Post-Combustion CO2 Capture Chemistry; Attalla, M.;
ACS Symposium Series; American Chemical Society: Washington, DC, 2012.

fugitive emission of some MEA is likely. Consequently there are environmental issues that need to be addressed. One such issue is that the mechanism by which MEA photochemically degrades in the atmosphere is not completely known and still requires further experimental investigation.

Compared to hydrocarbons such as volatile alkanes, alkenes and aromatics, the body of literature concerning the photochemistry of amines is relatively small. Some studies have been performed on volatile aliphatic amines such as dimethylamine, diethylamine and triethylamine by Pitts et *al.* (*2*), and Tuazon et *al.* (*3*). Grosjean (*4*) proposed mechanisms for the atmospheric photodecomposition of aliphatic amines initiated by OH radical attack via the C2 and N-atom centres. Schade and Crutzen (*5*) proposed photochemical reaction schemes for mono-, di- and trimethylamine involving the formation of imines. More recently, Murphy et *al.* (*6*) studied aerosol formation from aliphatic amines as well as MEA and concluded that organic aerosol formed was more stable than aerosol composed of nitrate salts.

Malloy et *al.* (*7*) investigated the nitrate radical photochemistry of simple aliphatic amines and observed aerosol formation after rapid nucleation, in all cases. Carter (*8*) performed smog chamber experiments on MEA and 2-amino-2-methyl-1-propanol (AMP) to investigate their potential to form ozone. Reproducibly was problematic since the reported range of amine injection by volume was 5-60% of that expected, probably exacerbated by the low vapour pressure of these amines.

Bråten et *al.* (*9*) recently completed an important review and theoretical study for the Norwegian Institute for Air Research (NILU), on the atmospheric chemistry of amines. As part of this study, they considered OH attack on MEA at the C1, C2 and N-atom centres. Similar to Grosjean (*4*) they predicted that the order of hydrogen-abstraction reactivity from most to least would be C2, N and C1.

Nielsen et *al.* (*10*) and Angove et *al.* (*11*) recently completed MEA/NOx smog chamber studies. The formation of the nitramine, 2-nitroamino-ethanol was observed in the Nielsen et *al.* (*10*) study. A strong correlation (R=0.992) between light dependent NH_3 formation and total aerosol surface area was observed by Angove et *al.* (*11*). The formation of nitroso-compounds were not observed in either study.

As a result of their EUPHORE study, Nielsen et *al.* (*10*) concluded that, >0.8 of MEA photodecomposed principally to formamide and some formaldehyde. Using FTIR, Angove et *al.* (*11*) did not observe formamide spectral features but did measure formaldehyde using DNPH derivitisation as a minor product which represented <0.06 of the photodecomposed MEA.

Since formamide has been observed by Nielsen et *al.* (*10*) as a major product formed during the photodecomposition of MEA, the aim of this study was to determine if the formation of formamide could be observed in CSIRO smog chamber MEA experiments by enhancing FTIR methods used by Angove et *al.* (*11*).

Downloaded by CORNELL UNIV on June 14, 2012 | http://pubs.acs.org
Publication Date (Web): May 3, 2012 | doi: 10.1021/bk-2012-1097.ch014

Downloaded by CORNELL UNIV on June 14, 2012 | http://pubs.acs.org
Publication Date (Web): May 3, 2012 | doi: 10.1021/bk-2012-1097.ch014

Experimental

The CSIRO smog chamber is located in Sydney, Australia. It is used to simulate photochemical reactions in the troposphere and provides a means by which chemical formation mechanisms and the structure and composition of secondary products can be elucidated. The facility is described fully elsewhere (*12*). Briefly, the chamber is 18.1 m^3 and is a low contaminant environment lined with Teflon film which is enclosed in highly reflective aluminium. UVA lights are used to simulate sunlight. Interfaced instruments allow measurement of reactant consumption and product formation. Facilities are available for the sampling of gaseous and aerosol samples. The chamber is cleaned between experiments using a combination of propene/NOx runs and 24 hour clean air flushing at ~850 litres/min between experiments.

The FTIR used in this work was a Nicolet MAGNA 550 fitted with a liquid N_2 cooled, mercury-cadmium-telluride (MCT) detector. Spectra were obtained over a path length of 119.3 metres using a resolution of 1 cm^{-1} and co-addition of 250 to 1000 scans.

Reference spectra for MEA and formamide were obtained by using multiple injections into the chamber of MEA and formamide at different mixing ratios, until a linear concentration law was established for each species. Spectra obtained for the largest MEA and formamide mixing ratios were used as reference spectra on the assumption that 100% injection had occurred. H_2O and H_2O_2 lines were generated using the HITRAN database (*13*) and MALT version 5 was used for spectra least squares fitting (*14*). The reported uncertainty for MEA and formamide mixing ratios are the standard errors calculated by MALT. Preliminary injections of simulated mixtures of MEA and formamide into the smog chamber demonstrated that the spectral features of ~90 ppb of formamide were easily observable in ~340 ppb of MEA, in the IR band 2800 to 2900 cm^{-1}.

MEA (Sigma-Aldrich, 99+%) and formamide ($HCONH_2$) (Sigma, Deionized, 99.5% GC) were injected, always before NO, into a purpose built glass cell mounted close to the chamber. The cell was warmed to 50 to 60°C and the reactants were passed slowly into the chamber over ~1 hour using a pre-warmed (~60°C) nitrogen carrier. MEA loss in the chamber has previously been determined (*11*) to be 2.7±0.6 ppb/hour as worse case. Therefore, it was concluded that MEA wall loss would have little effect in this study since the maximum MEA wall loss would be 13±3 ppb.

NO was always injected last as NO/N_2 (BOC Gases,1.09±0.05%) using the chamber gas panel (*12*). Where required, 1 ml of H_2O_2 /H_2O solution (Riedel-de Haën, 30% extra pure) was injected, always first, using the aforementioned glass cell method over ~2 hours. The reason for injecting H_2O_2 was to generate a continual, liberal supply of OH radicals by H_2O_2 photolysis where needed. Extra care was taken to clean the cell between injections.

Table 1 is the schedule of experiments that were performed in this study. Data for each experiment was collected over 4 hours during which the UV intensity, expressed as the NO_2 photolysis rate, J_{NO2}, was 0.60±0.03 min^{-1}. The initial temperature for all experiments was 21±2 °C.

In Recent Advances in Post-Combustion CO2 Capture Chemistry; Attalla, M.;
ACS Symposium Series; American Chemical Society: Washington, DC, 2012.

Table 1. Schedule of experiments

Expt.	*MEA (ppb)*	*$HCONH_2$ (ppb)*	*H_2O_2 (ppm)*	*NO (ppb)*
E604	-	276±7	-	~50
E605	-	368±10	~15	-
E609	-	220±10	~13	~50
E611	383±15	388±23	-	~50
E613	438±4	-	-	~50

Downloaded by CORNELL UNIV on June 14, 2012 | http://pubs.acs.org
Publication Date (Web): May 3, 2012 | doi: 10.1021/bk-2012-1097.ch014

Experimental Strategy

The strategy employed was to compare the results from two experiments with close to the same MEA and NO initial conditions, one of which had been spiked with formamide to ensure that its spectral features were readily observable in the presence of MEA. Thus, if formamide was produced during the photodecomposition of MEA then, in the case of the spiked experiment, the formamide formed would be added to the initial spiked amount and therefore, able to be measured by FTIR. The success of this strategy was dependent on the degree to which the formamide introduced as the spike would undergo photodecomposition in its own right, since such loss would need to be accounted for.

Formamide is predicted to form from MEA (*9*, *10*). Its experimental, and tropospheric chemistry is not well established. Recently, the formamide reaction with OH radicals was investigated by Barnes et *al.* (*15*). They obtained a k_{OH} for formamide of 3.5±1.0 x 10^{-12} cm^3 $molecule^{-1}$ s^{-1}, which implies that the photodecomposition of formamide would be slow compared to alkenes and substituted aromatics, more like that of *n*-butane.

Figure 1 compares the formamide profiles obtained for experiments E604, E605 and E609 which were performed to investigate the photodecomposition of formamide under increasingly reactive, initial conditions (see Table 1).

No decay of formamide was observed over 4 hours in E604 which used the least reactive initial conditions (~50 ppb NO). In E605, (~15 ppm H_2O_2) there was a mean decay of ~3.3 x 10^{-3} ppb s^{-1} over 4 hours. The most reactive conditions were used in E609, (~13 ppm H_2O_2, ~50 ppb NO). Over the first 2 hours of E609, the mean rate of decay was ~9.2 x 10^{-3} ppb s^{-1} and over the last 2 hours, ~2.9 x 10^{-3} ppb s^{-1}. The latter being similar to that observed for E605. These results indicate that even under very reactive conditions, formamide decay is retarded and, as shown in E604 where no formamide photodecomposition ocurred, significant formamide decay would be unlikely if only ~50 ppb NO were used in a MEA experiment, with or without a formamide spike.

Downloaded by CORNELL UNIV on June 14, 2012 | http://pubs.acs.org
Publication Date (Web): May 3, 2012 | doi: 10.1021/bk-2012-1097.ch014

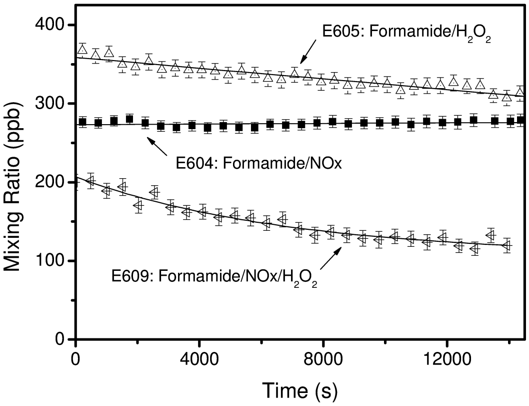

Figure 1. Comparison of formamide profiles measured in E604, E605 and E609

MEA Reaction Results

Figures 2 and 3 show the observed O_3, NO, NOy-NO (~NO_2) and NOy (~NOx) profiles measured during the ~400 ppb MEA and ~50 ppb NO experiments, E611 and E613. The initial 388 ppb formamide spike was performed in E611.

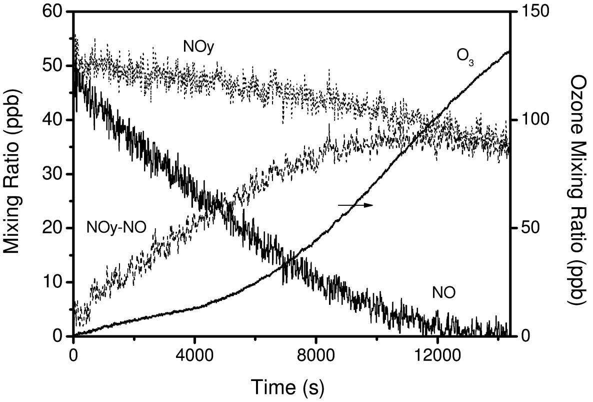

Figure 2. Ozone and NOy (~NOx) profiles obtained for E611 (with initial formamide spike)

Downloaded by CORNELL UNIV on June 14, 2012 | http://pubs.acs.org
Publication Date (Web): May 3, 2012 | doi: 10.1021/bk-2012-1097.ch014

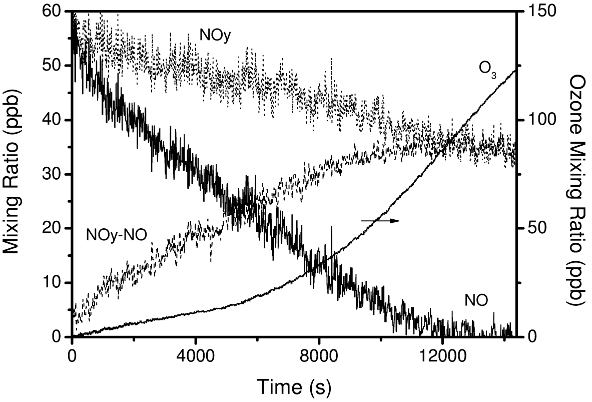

Figure 3. Ozone and NOy (~NOx) profiles obtained for E613

The profiles are very similar which indicates near equivalent reactivity and confirms that the reactivity of formamide with OH radicals is slow compared to that of MEA. The final O_3 mixing ratio for E611 is 132±2 ppb and for E613, 123±2 ppb. This slight difference is attributed to, in part, by the slightly lower initial NO mixing ratio used in E611, as well as a possible small reactivity contribution by the formamide spike, both of which would tend to increase ozone formation in E611 compared to that in E613.

Figures 4 and 5 show the MEA, formamide and NH_3 mixing ratios obtained using FTIR for E611 and E613.

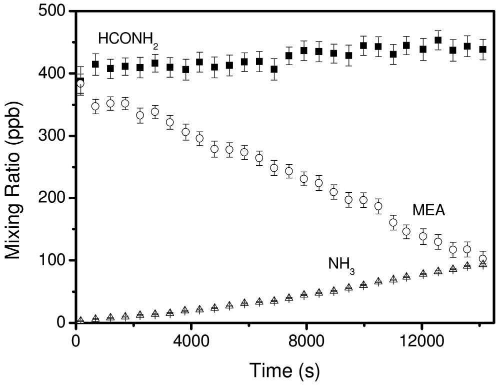

Figure 4. MEA, formamide and NH_3 profiles observed in E611 (with initial formamide spike)

Downloaded by CORNELL UNIV on June 14, 2012 | http://pubs.acs.org
Publication Date (Web): May 3, 2012 | doi: 10.1021/bk-2012-1097.ch014

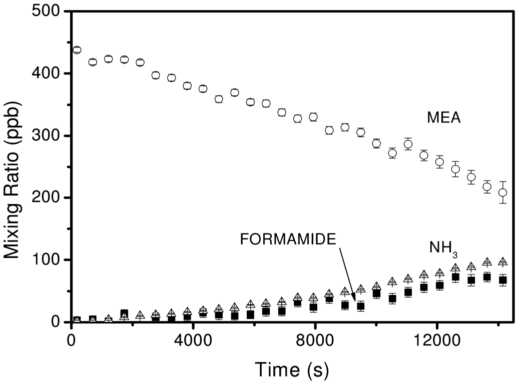

Figure 5. MEA, formamide and NH_3 profiles observed in E613

In E611, the spiked case, the formamide mixing ratio increased by 55 ppb to 438 ppb. The NH_3 mixing ratio increased steadily to 93 ppb as MEA decreased by 281 ppb, reaching 103 ppb at 4 hours. In the E613, the nil-spiked case, formamide increased to 67 ppb, NH_3 increased to 96 ppb and MEA decreased by 238 ppb to 208 ppb at the end of the experiment.

Table 2 summarises the results represented in Figures 4 and 5.

Table 2. Formamide and ammonia yields

Expt	*$HCONH_2$ (ppb)*	*MEA (ppb)*	*$\Delta HCONH_2$ (ppb)*	*ΔMEA^a (ppb*	*ΔNH_3 (ppb)*	*Y_f [b]*	*Y_a [c]*
E611	388	383	55	281	93	~0.20	~0.33
E613	0	438	67	238	96	~0.28	~0.40

[a] *ΔMEA* is the consumed MEA. [b] Y_f is the yield fraction for formamide formation relative to *ΔMEA*. [c] Y_a is the yield fraction for ammonia formation relative to *ΔMEA*.

The consumed MEA (*ΔMEA*) in E611 was 281 ppb compared to 238 ppb observed in E613 which also indicates that overall system reactivity in E611 was marginally faster than E613. The molar yield fraction, Y_f for the formation of formamide, relative to *ΔMEA*, for both experiments ranged from 0.20 to 0.28 which is less than ~0.8 observed by Nielsen et *al.* (*10*). In the case of ammonia formation, Y_a ranged from 0.33 to 0.40. These results indicate that ~0.5 to 0.7 of the MEA consumed occurred as a result of the formation of formamide plus ammonia.

Downloaded by CORNELL UNIV on June 14, 2012 | http://pubs.acs.org
Publication Date (Web): May 3, 2012 | doi: 10.1021/bk-2012-1097.ch014

Comments

The formation of formamide during the photodecomposition of ~400 ppb MEA in ~50 ppb NO has been observed in this study. The application of least squares fitting to determine formamide concentrations in complex IR spectra is only valid if its existence is confirmed by the presence of formamide spectral features or by strategic means if such features are obscured. The reactivity of formamide with respect to attack by OH radicals is much less than that of MEA. Under the conditions used in this study, the observed molar yield fraction for the formation of formamide from MEA was 0.20 to 0.28 and that of NH_3, 0.33 to 0.40.

Acknowledgments

The authors extend their thanks to the organisers of the Pacifichem 2010, ‘Chemistry of Post Combustion Carbon Dioxide Capture’ sessions, in particular, Dr. Moetaz Attalla (CSIRO) for his support and advice.

References

1. Kohl, A.; Nielsen, R. *Gas Purification*, 5th ed.; Gulf Professional Publishing: Houston, TX, 1997; p 1395.
2. Pitts, J. N., Jr.; Grosjean, D.; Cauwenberghe, K. V.; Schmid, J. P.; Fitz, D. R. *Environ. Sci. Technol.* **1978**, *12*, 946–953.
3. Tuazon, E. C.; Carter, W. P. L.; Atkinson, R.; Winer, A. M.; Pitts, J. N., Jr. *Environ. Sci. Technol.* **1984**, *18*, 49–54.
4. Grosjean, D. *J. Air Waste Manage. Assoc.* **1991**, 306–311.
5. Schade, G. W.; Crutzen, P. J. *J. Atmos. Chem.* **1995**, *22*, 319–346.
6. Murphy, S. M.; Sorooshian, A.; Kroll, J. H.; Ng, N. L.; Chhabra, P.; Tong, C.; Surratt, J. D.; Knipping, E.; Flagan, R. C.; Seinfeld, J. H. *Atmos. Chem. Phys.* **2007**, *7*, 2313–2337.
7. Malloy, Q. G. J.; Qi, Li.; Warren, B.; Cocker, D. R., III; Erupe, M. E.; Silva, P. J. *Atmos. Chem. Phys.* **2009**, *9*, 2051–2060.
8. Carter, W. P. L. *Reactivity estimates for selected consumer product compounds*. Final Report to the California Air Resources Board, Contract No. 06-408, 2008.
9. Bråten, H. B.; Bunkan, A. J.; Bache-Andreassem, L.; Solimannejad, M.; Nielsen, C. J. *A theoretical study on the atmospheric degradation of selected amines*; Final Report to NILU: OR 77/2008, 2008.
10. Nielsen, C. J.; D’Anna, B.; Dye, C.; George, C.; Graus, M.; Hansel, A.; Karl, M.; King, S.; Musabila, M.; Muller, M.; Schmidbauer, N.; Stenstrom, Y.; Wisthaler, A. *Atmospheric Degradation of amines: Gas-phase photo-oxidation of 2-aminoethanol (MEA)*; Summary Report to NILU, CLIMIT project no. 193438, 2010.
11. Angove, D. E.; Azzi, M.; Tibbett, A.; White, S.; Cope, M.; Lee, S. *Investigation of the atmospheric photochemistry of the CO_2 capture solvent, monoethanolamine (MEA) under controlled conditions*; Final Report to Norsk Energi and Gassnova SF, CSIRO EP101723, 2010.

12. Hynes, R.; Angove, D.; Saunders, S.; Haverd, V.; Azzi, M. *Atmos. Environ.* **2005**, *39*, 7251–7262.
13. L. S. Rothman, L. S.; Barbeb, A.; Chris Bennerc, D.; Brownd, L. R.; Camy-Peyrete, C.; Carleerf, M. R.; Chancea, K.; Clerbauxf, C; Danae, V.; Devic, V. M.; Fayth, A.; Flaudi, J.-M.; Gamachej, R. R.; Goldmank, A.; Jacquemarta, D.; Jucksa, K. W.; Laffertyl, W. J.; Mandine, J.-M.; Massiem, S. T.; Nemtchinovn, V.; Newnhamo, D. A.; Perrini, A.; Rinslandp, C. P.; Schroederq, J.; Smitho, K. M.; Smithp, M A. H.; Tangq, K.; Tothd, R. A.; Vander Auweraf, J.; Varanasin, P.; Yoshino, K. *J. Quant. Spectrosc. Radiat. Transfer* **2003**, *82*, 5–44.
14. Griffith, D. W. T. *Appl. Spectrosc.* **1996**, *50*, 59–70.
15. Barnes, I.; Solignac, G.; Mellouki, A.; Becker, K. H. *ChemPhysChem* **2010**, *11*, 3844–3857.

Downloaded by CORNELL UNIV on June 14, 2012 | http://pubs.acs.org
Publication Date (Web): May 3, 2012 | doi: 10.1021/bk-2012-1097.ch014

Downloaded by UNIV OF DELAWARE MORRIS LIB on June 14, 2012 | http://pubs.acs.org
Publication Date (Web): May 3, 2012 | doi: 10.1021/bk-2012-1097.ch015

Chapter 15

Surpassing Photosynthesis: High-Efficiency and Scalable CO_2 Utilization through Artificial Photosynthesis

Y.-H. Percival Zhang,[1,2,*] Chun You,[1] Hongge Chen,[1,3] and Rui Feng[2]

[1]Biological Systems Engineering Department, Virginia Tech, 210-A Seitz Hall, Blacksburg, Virginia 24061, USA
[2]Gate Fuels Inc., 3107 Alice Drive, Blacksburg, VA 24060, USA
[3]College of Life Sciences, Henan Agricultural University, 95 Wenhua Road, Zhengzhou, 450002, P. R. China
[*]Corresponding author. Email: ypzhang@vt.edu, Tel: (540) 231-7414 [O], Fax: (540) 231-3199

Plants like solar cells utilize intermittent non-point insolation to biologically fix CO_2 in the form of biomass carbohydrates. However, plant photosynthesis has pretty low solar energy-to-chemical energy conversion efficiencies (e.g., ~0.2-0.3%, global average) and consumes a large amount of water (i.e., at least 500 kg of water per kg of biomass generated). Such low energy efficiencies are mainly attributed to three factors: (i) a narrow light absorption spectrum by chlorophyll, (ii) relatively low efficiencies of carbohydrate synthesis and unmatched reaction rates between fast light-harvesting reactions and slow dark chemical synthesis reactions, and (iii) carbohydrate losses due to the respiration of living plants.

To surpass these limitations in plants, we design a novel scalable bioprocess integrating high-efficiency solar cells, water electrolysis, and biological CO_2 fixation mediated by cascade enzymes for the similar function. This synthetic enzymatic pathway containing *in vitro* numerous enzymes and coenzymes would fix CO_2 into carbohydrates (e.g. starch) and/or ethanol by using electricity or hydrogen. Such *in vitro* synthetic enzymatic pathways are believed to work based on the design principles of synthetic biology, knowledge in the literature, and

In Recent Advances in Post-Combustion CO2 Capture Chemistry; Attalla, M.;
ACS Symposium Series; American Chemical Society: Washington, DC, 2012.

thermodynamics analysis. However, validation experiments and practical application of these systems will require collaborative efforts from biologists, chemists, electrochemists, and engineers. Here we present our latest advances in the proof-of-concept experiment. Large-scale implementation of this artificial photosynthesis would address such sustainability challenges as electricity and hydrogen storage, CO_2 utilization, fresh water conservation, and maintenance of a small closed ecosystem for human survival in emergency situations.

Keywords: artificial photosynthesis; CO_2 utilization; electricity storage; feed and food production; in vitro synthetic biology; sustainability; water conservation

Downloaded by UNIV OF DELAWARE MORRIS LIB on June 14, 2012 | http://pubs.acs.org
Publication Date (Web): May 3, 2012 | doi: 10.1021/bk-2012-1097.ch015

Introduction

Sustainable development is a pattern of resource use that aims to meet human needs from air, water, food to energy, while preserving the environment for next generations. Energy is the only universal currency: one of its many forms must be transformed to another in order to meet these basic needs (*1*, *2*). As the human population grows and its needs and desires expand, the problems of sustaining civilization and improving the quality of life are an urgent challenge for scientists and engineers.

Nonrenewable primary energy sources – crude oil, natural gas and coal – meet approximately 85% of the world's energy demands. As a result, *ca.* 20 billion tons of net CO_2 is emitted into the atmosphere per year. Although solar energy is the most abundant renewable primary energy, solar energy is not really free because of the high hidden costs for its harvesting, conversion, and storage (*2–5*). The transition from the fossil energy- to solar energy-based economy is impossible without the ability to store solar energy in the form of chemical carriers, such as hydrogen, methane, methanol, starch, hydrocarbon species, called "solar fuels" (*6–10*).

Electricity can be generated from different primary energy sources with different conversion efficiencies. Currently approximately two thirds of electricity is generated from carbon-containing fossil fuels, accompanied by large amounts of CO_2 emissions. Electricity generation from renewable non-carbon sources has recently been receiving more attention. In particular, wind electricity generation capacity has the fastest annual growth rates. Solar electricity produced by photovoltaic panels represents the largest clean electricity potential because solar energy is the most abundant renewable primary energy source on the Earth, approximately 6000-fold of all of the energy consumed by humans (*2*, *9*, *11*). But the generation of both wind and solar electricity suffers from large output variations. Therefore, it is very important to find high-efficiency, low-cost, scalable electricity storage approaches; but all current technologies cannot meet such needs (*2*, *12*, *13*).

Downloaded by UNIV OF DELAWARE MORRIS LIB on June 14, 2012 | http://pubs.acs.org
Publication Date (Web): May 3, 2012 | doi: 10.1021/bk-2012-1097.ch015

To solve the large-scale storage challenge of solar or wind electricity, especially off-peak electricity or surplus electricity, and utilization of CO_2, we suggest storing this low-cost or potentially free electricity plus CO_2 as a chemical energy form – carbohydrates (e.g., starch or cellulose) by cascade enzymes. In this book chapter, we briefly review limitations of plant photosynthesis, suggest a novel solution to surpass natural photosynthesis by combining well-known technologies, and present our advances of biological CO_2 fixation through an in vitro synthetic biology platform. Here we do not cover a big picture about CO_2 utilization for the production of a variety of chemicals, such as methanol, hydrocarbons, lactate, urea, succinic acid, polycarbonates (*14–16*).

Plant Photosynthesis

Photosynthesis maintains a biological cycle involving carbon, oxygen, and nitrogen elements out of thermodynamic equilibria. It is the basis of the food supply for most lives on the Earth; it is also the nearly ultimate source of all fossil fuels – petroleum, coal, natural gas, and methane hydrate (*2*). Plants utilize intermittent insolation and low concentration CO_2 in the atmosphere (e.g., 380 ppm) for producing the most abundant renewable bioresource – phytobiomass, some of which have been accumulated as fossil fuel reserves during past billions of years.

Plant photosynthesis is driven by photons, which is absorbed by chlorophyll molecules and then give rise to a charge separation and the release of electrons. These electrons are driving the dissociation of water and generating protons and oxygen. The protons and the associated electrons enable the reduction of carbon dioxide to organic materials, such as carbohydrates, whereby oxygen is essentially a waste product. The stoichiometry of photosynthesis may be written as

$$2\ H_2O + CO_2 \rightarrow [CH_2O] + O_2 + H_2O \qquad [1]$$

where $[CH_2O]$ is commonly used as shorthand for carbohydrates with the same elemental ratio as monosaccharides. In fact, the overall reaction can be divided into two phases: (i) a set of photochemical and redox reactions, called the “light reaction” and (ii) a sequence of enzymatic reactions, called “light-independent reactions”, as they occur both in the light and the dark.

$$\text{Light reaction:} \qquad 2\ H_2O \rightarrow 4\ [H] + O_2 \qquad [2]$$

$$\text{Light-independent reaction:} 4\ [H] + CO_2 \rightarrow [CH_2O] + H_2O\ [3]$$

where the notation [H] refers to the combination of the reduced NAD(P)H and electron. The light reaction operates on very short time scales from femtoseconds to milliseconds, while the light-independent reaction operates over a timespan of seconds to hours (*17*, *18*). This profound mismatch of timescale gives rise to inefficiencies in terms of fluctuating environmental circumstances (e.g., large variations in irradiance, temperature, water, nutrients).

Most plants fix carbon dioxide by using chloroplasts through the reductive pentose-phosphate cycle, i.e., the Calvin-Benson cycle (*19*, *20*). Some plants adapted to arid conditions utilize Crassulacean acid metabolism (CAM photosynthesis) (*21*). In addition, some microorganisms can fix CO_2 through one of the other five discovered pathways: the reductive citric acid cycle (*22*), the reductive acetyl-CoA pathway (Wood-Ljungdahl pathway) (*23*, *24*), the 3-hydroxypropionate pathway (*25*), 3-hydroxypropionate-4-hydroxybutyrate cycle, and dicarboxylate-4-hydroxylbutyrate cycle (*26*).

All of natural biological CO_2 fixation pathways require 12 mol of the reduced cofactor (NADPH) or its equivalents plus several mol of ATP for the generation of one mol of glucose from 6 mol of CO_2. Here ATP works on an extra energy driving force for implementing thermodynamically-unfavorable reactions because most times CO_2 concentrations in the environments are very low. For example, the synthesis of one glucose in plants requires 12 NAD(P)H and 18 or 30 ATP for C3 or C4 plants, respectively (*20*). High concentration CO_2 sources may drastically decrease the ATP number consumed as low as 2 ATP per glucose produced (*26*, *27*). It is noted that low-cost *in vitro* generation of a large amount of ATP technology is not available because ATP generation approaches through substrate phosphorylation or microbial fermentation are too costly for biocommodity production (*27*).

Natural plant photosynthesis has pretty low theoretical energy efficiencies from solar energy to chemical energy of 4.6 and 6.0% for C3 and C4 plants, respectively (*28*). Dedicated crops can have peak efficiencies of ~3-4% with enough irrigation, fertilizer, warm temperature, and ample insolation. On average, plant photosynthesis efficiencies are only 0.2-0.3% (*1*, *9*, *28*, *29*). Such low efficiencies are mainly attributed to three factors (*1*, *17*, *28*, *29*) (Figure 1a):

(i) a narrow light absorption spectrum by chlorophyll molecules (~52% off),
(ii) unmatched reaction rates between light reactions and dark reactions and relatively low efficiencies of carbohydrate synthesis (22.8% only for C4 plants), and
(iii) carbohydrate losses due to the respiration of living entities (~33% off).

Meanwhile, plant photosynthesis has poor water utilization efficiencies: one kg of biomass carbohydrate production requires at least 500 kg of water (*30*). For example, one kg of wheat production needs approximately 1,300 kg of fresh water (*31*). Such high water consumption is mainly used for the prevention of leaf burning.

Downloaded by UNIV OF DELAWARE MORRIS LIB on June 14, 2012 | http://pubs.acs.org
Publication Date (Web): May 3, 2012 | doi: 10.1021/bk-2012-1097.ch015

Downloaded by UNIV OF DELAWARE MORRIS LIB on June 14, 2012 | http://pubs.acs.org
Publication Date (Web): May 3, 2012 | doi: 10.1021/bk-2012-1097.ch015

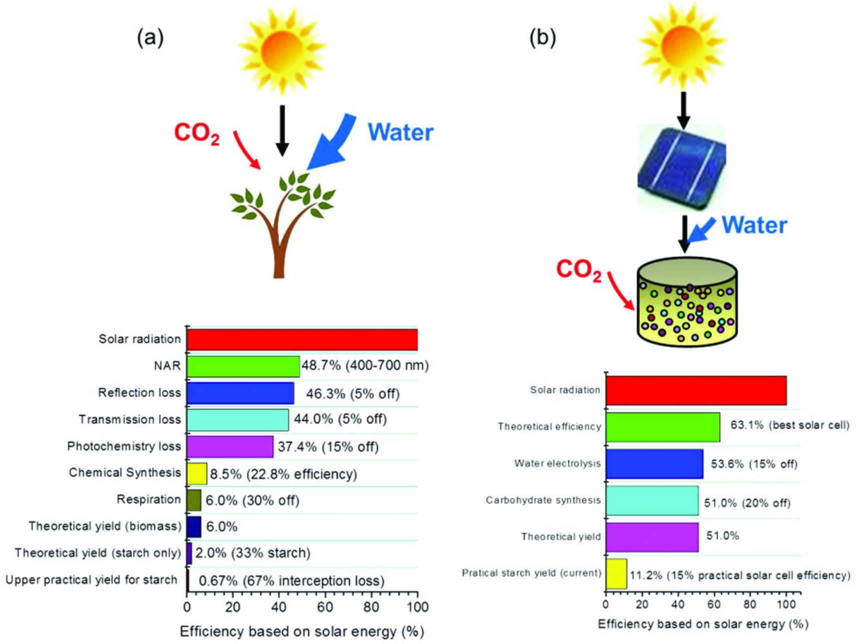

Figure 1. Comparison of natural plant photosynthesis and artificial photosynthesis based on solar cells and artificial biological CO_2 fixation.

Artificial Photosynthesis for Biological CO_2 Fixation

To address above limitations of plant photosynthesis, we propose a novel high-efficiency artificial photosynthesis by integrating solar cells and biological CO_2 fixation process, as shown in Figure 1b. The best future solar cells would have an efficiency of up to 63% (*32*), much higher than those of chlorophylls. Considering efficiency losses in water electrolysis and chemical synthesis, the overall theoretical efficiency would be as high as 51% (Figure 1b). Based on available commercial solar cells with an efficiency of 18% plus 20% discounts in running (i.e., 15% efficiency) (*18*), the hypothetical efficiency of artificial photosynthesis would be 11.2% (Figure 1b). The summarized chemical reaction for CO_2 fixation (eq 4) in artificial photosynthesis is:

$$8\ CO_2\ (g) + 8\ H_2O\ (l)\ (+\ \text{electricity}) \rightarrow C_6H_{10}O_5\ (s) + C_2H_6O\ (l) + 9\ O_2\ (g) \qquad [4]$$

where the inputs are CO_2, water, and electricity; the outputs are amylose (linear starch) or cellulose, ethanol, and oxygen, as shown in Figure 2.

Downloaded by UNIV OF DELAWARE MORRIS LIB on June 14, 2012 | http://pubs.acs.org
Publication Date (Web): May 3, 2012 | doi: 10.1021/bk-2012-1097.ch015

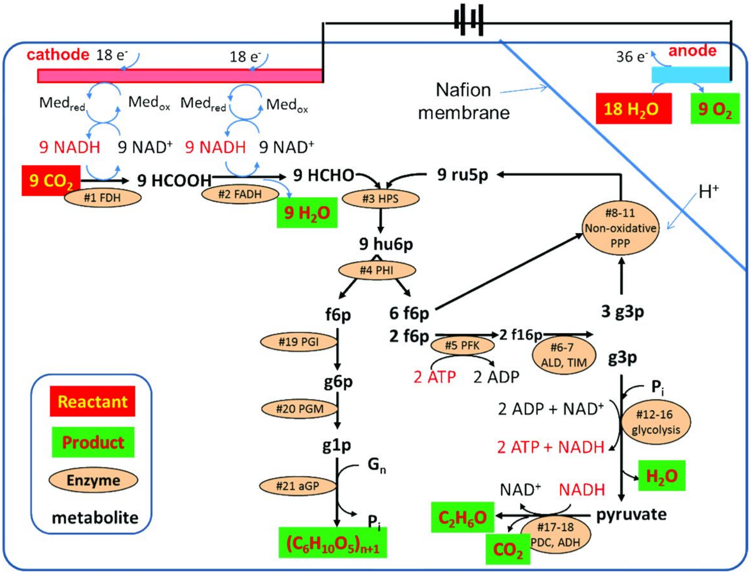
cathode
18 e⁻
18 e⁻
36 e⁻
anode
Med_red
Med_ox
Med_red
Med_ox
Nafion membrane
18 H₂O
9 O₂
9 NADH
9 NAD⁺
9 NADH
9 NAD⁺
9 CO₂
#1 FDH
9 HCOOH
#2 FADH
9 H₂O
9 HCHO
#3 HPS
9 ru5p
H⁺
#8-11 Non-oxidative PPP
9 hu6p
#4 PHI
f6p
6 f6p
3 g3p
#19 PGI
2 f6p
#5 PFK
2 f16p
#6-7 ALD, TIM
g3p
2 ATP
2 ADP
g6p
P_i
#20 PGM
2 ADP + NAD⁺
#12-16 glycolysis
2 ATP + NADH
g1p
G_n
H₂O
#21 aGP
NAD⁺
NADH
P_i
C₂H₆O
pyruvate
#17-18 PDC, ADH
CO₂
(C₆H₁₀O₅)ₙ₊₁
Reactant
Product
Enzyme
metabolite

Figure 2. The synthetic CO_2 utilization pathway powered by electricity. The enzyme list is given in Table I. The listed compounds and metabolites are Med_{red}, reduced mediator; Med_{ox}, oxidized mediator; HCOOH, formic acid; HCHO, formaldehyde; ru5p, ribulose-5-P; hu6p, 3-hexulose-6-P; f6p, fructose-6-phosphate; f16p, fructose-1,6-bisphosphate; g3p, glyceraldehydes-3-phosphate; g6p, glucose-6-phosphate; G_n, linear starch (amylose); P_i, free inorganic phosphate; and C_2H_6O, ethanol.

This hypothetical electricity-to-carbohydrate process contains 21 enzymes. The overall pathway can be organized in six modules (Table I):

(1) electrochemical NADH regeneration for generation of 18 NADH in cathode and 9 dioxygen in anode, which is separated by a Nafion membrane (*33–35*),

$$18\ NAD^+ + 18\ H_2O \rightarrow 18\ NADH + 18\ H^+ + 9\ O_2 \qquad [5]$$

(2) CO_2 fixation to formaldehyde (CH_2O) mediated by formate dehydrogenase and formaldehyde dehydrogenase (*36–38*),

$$9CO_2 + 18NADH + 18H^+ \rightarrow 9CH_2O + 9H_2O + 18NAD^+ \qquad [6]$$

(3) conversion of formaldehyde to fructose-6-phosphate (f6p) by 3-hexulose-6-phosphate synthase and hexulose phosphate isomerase from the ribulose monophosphate pathway (*39*, *40*),

$$9CH_2O + 9\ ru5p \rightarrow 9\ f6p \qquad [7]$$

(4) ribulose-5-phosphate (ru5p) regeneration by the eight enzymes from the non-oxidative pentose phosphate and glycolysis pathways (*19*, *41*),

$$8f6p + 2\ ATP \rightarrow 9ru5p + g3p + 2ADP \quad [8]$$

(5) ethanol production from glyceraldehydes-3-phosphate (g3p) by the seven enzymes from the glycolysis and ethanogenesis pathway (*19*),

$$g3p + P_i + 2ADP \rightarrow C_2H_6O + CO_2 + H_2O + 2ATP \quad [9]$$

(6) starch (amylose, a linear α-1,4-glucosidic bond starch) lengthening reaction mediated by starch phosphorylase along with phosphoglucose isomerase and phosphoglucomutase (*19*, *41*),

$$f6p + (C_6H_{10}O_5)_n \rightarrow (C_6H_{10}O_5)_{n+1} + P_i \quad [10]$$

The Gibbs free energy of eq 4 without electricity input (a reverse starch and ethanol combustion) is +4216.7 kJ/mol, suggesting that this reaction cannot happen. The combination of equations 5-10 results in a stoichiometric reaction of $8CO_2 + 18NADH + 18H^+ \rightarrow C_6H_{10}O_5 + C_2H_5OH + 18NAD^+ + 10H_2O$, with a standard Gibbs free energy of -457.3 kJ/mol, suggesting that the above reaction may occur spontaneously. The reduced NADH can be regenerated by electricity as eq 5 (*33–35*). Reaction 4 plus external electricity input could be technological feasible since (i) nearly every reaction is reversible, except 6-phosphofructokinase and pyruvate kinase, which control the overall reaction direction, (ii) each of the modules (eqs 5-10), involving several enzymatic steps, is validated well, and (iii) a negative Gibbs free energy value for the overall reaction ($8CO_2 + 18NADH + 18H^+ \rightarrow C_6H_{10}O_5 + C_2H_5OH + 18NAD^+ + 10H_2O$) in the aqueous solution. To further decrease the Gibbs free energy so to generate more products, this process would be operated by (i) increasing CO_2 concentration from a power station or a CO_2 storage site, (ii) precipitating amylose in the presence of ethanol, and (iii) stripping ethanol from the aqueous phase.

It is worth noting that numerous artificial and natural pathways might be designed to fix CO_2 and convert it to carbohydrates based on the known or newly-discovered biochemical pathways, but the above pathway developed by us has the highest energy conversion efficiency because it requires NADH only but not ATP. The above design does not involve any membrane protein so that it may be easy for scale-up. The above pathway may be modified for different outputs, for example, lactic acid, acetic acid, sorbitol, and so on.

An alternative pathway by using hydrogen other rather electricity may be preferred because it is very challenging to generate reduced cofactors from electricity directly (*42*, *43*) but it is easier to generate reduced cofactors from hydrogen (*27*, *44–46*).

Downloaded by UNIV OF DELAWARE MORRIS LIB on June 14, 2012 | http://pubs.acs.org
Publication Date (Web): May 3, 2012 | doi: 10.1021/bk-2012-1097.ch015

Downloaded by UNIV OF DELAWARE MORRIS LIB on June 14, 2012 | http://pubs.acs.org
Publication Date (Web): May 3, 2012 | doi: 10.1021/bk-2012-1097.ch015

Table I. The step-by-step chemical reactions and their respective enzymes for artificial photosynthesis powered by electricity.

No.	***E.C.***	***Enzyme Name***	***Reaction***
I. 18 NAD^+ + 18 H_2O → 18 NADH + 18 H^+ + 9 O_2 (by electricity)			
II. CO_2 fixation: 9 CO_2 + 18 NADH + 18 H^+ → 9 CH_2O + 9 H_2O + 18 NAD^+			
#1	1.2.1.2	formate dehydrogenase (FDH)	CO_2 + NADH + H^+ → formate (CH_2O_2) + NAD^+
#2	1.2.1.46	formaldehyde dehydrogenase (FADH)	formate + NADH + H^+ → formaldehyde (CH_2O) + NAD^+ + H_2O
III. Ribulose monophosphate pathway (9 CH_2O + 9 ru5p → 9 f6p)			
#3	4.1.2.43	3-hexulose-6-phosphate synthase (HPS)	ribulose-5-P (ru5p) + formaldehyde → 3-hexulose-6-P (hu6p)
#4	5.3.1.27	hexulose phosphate isomerase (HPI)	3-hexulose-6-P (hu6p) → fructose-6-phosphate (f6p)
IV. Branched pathways for the overall reaction (8 f6p + 2 ATP → 9 ru5p + g3p + 2 ADP)			
2 f6p + 2 ATP → 4 g3p + 2 ADP			
#5	2.7.1.11	6-phosphofructokinase (PFK)	fructose-6-phosphate (f6p) + ATP → fructose-1,6-bisphosphate (f16p)
#6	4.1.2.13	fructose-bisphophate aldolase (ALD)	fructose-1,6-bisphosphate (f16p) → glyceraldehydes-3-phosphate (g3p) + dihydroxacetone phosphate (dhap)
#7	5.3.1.1	triosephosphate isomerase (TIM)	dihydroxacetone phosphate (dhap) → glyceraldehydes-3-phosphate (g3p)
6 f6p + 3 g3p → 9 ru5p			
#8	2.2.1.1	transketolase (TK)	fructose-6-phosphate (f6p)+ glyceraldehyde-3-phosphate (g3p) → xylulose-5-phosphate (x5p) + erythrose-4-phosphate (e4p) sedoheptulose-7-phosphate (s7p) + glyceraldehyde-3-phosphate (g3p)→ xylulose-5-phosphate (xu5p) + ribose-5-phosphate (r5p)

No.	***E.C.***	***Enzyme Name***	***Reaction***
#9	2.2.1.2	transaldolase (TAL)	fructose-6-phosphate (f6p) + erythrose-4-phosphate (e4p)→ sedoheptulose-7-phosphate (s7p) + glyceraldehyde-3-phosphate (g3p)
#10	5.3.1.6	ribose 5-phosphate isomerase (R5PI)	ribose-5-phosphate (r5p) → ribulose-5-phosphate (ru5p)
#11	5.1.3.1	ribulose-5-phosphate 3-epimerase (Ru5PE)	xylulose-5-phosphate (x5p) → ribulose-5-phosphate (ru5p)
V. Glycolysis and ethanogenesis (g3p + P_i + 2 ADP → C_2H_6O + CO_2 + 2 ATP + H_2O)			
#12	1.2.1.12	glyceraldehyde-3-phosphate dehydrogenase (G3PDH)	glyceraldehyde-3-phosphate (g3p) + P_i + NAD + → 1,3-biosphoglycerate + NADH + H^+
#13	2.7.2.3	phosphoglycerate kinase (PGK)	1,3-bisphoglycerate (bpg) + ADP → 3-phosphoglycerate (3pg) + ATP
#14	5.4.2.1	phosphoglycerate mutase (PGCM)	3-phosphoglycerate (3pg) → 2-phosphoglycerate (2pg)
#15	4.2.1.11	enolase (ENO)	2-phosphoglycerate (2pg) → phosphoenolpyruvate (pep) + H_2O
#16	2.7.1.40	pyruvate kinase (PK)	phosphoenolpyruvate (pep) + ADP → pyruvate + ATP
#17	4.1.1.1	pyruvate decarboxylase (PDC)	pyruvate → acetaldehyde + CO_2
#18	1.1.1.1	alcohol dehydrogenase (ADH)	acetaldehyde + NADH +H^+→ C_2H_5OH + NAD^+
VI. starch synthesis (f6p + Glc_n → Glc_{n+1} + P_i)			
#19	5.3.1.9	phosphoglucose isomerase (PGI)	fructose-6-phosphate (f6p) → glucose-6-phosphate (g6p)
#20	5.4.2.2	phosphoglucomutase (PGM)	glucose-6-phosphate (g6p) → glucose-1-phosphate (g1p)
#21	2.4.1.1	starch phosphorylase (αGP)	$(C_6H_{10}O_5)_n$ + glucose-1-phosphate (g1p) → $(C_6H_{10}O_5)_{n+1}$ + P_i

Downloaded by UNIV OF DELAWARE MORRIS LIB on June 14, 2012 | http://pubs.acs.org
Publication Date (Web): May 3, 2012 | doi: 10.1021/bk-2012-1097.ch015

Downloaded by UNIV OF DELAWARE MORRIS LIB on June 14, 2012 | http://pubs.acs.org
Publication Date (Web): May 3, 2012 | doi: 10.1021/bk-2012-1097.ch015

Advances of Proof-of-Concept Experiments

The above *in vitro* synthetic enzymatic pathway is thought to work based on the design principles of synthetic biology, knowledge in the literature, and thermodynamics analysis (*9*, *47*, *48*). However, validation experiments and practical application of these systems will require collaborative efforts from biologists, chemists, electrochemists, and engineers.

One of the largest obstacles to in vitro synthetic biology projects is a lack of thermoenzymes as building blocks (*9*, *27*). Now we are developing a library of thermoenzymes in the past several years. To conduct proof-of-concept experiment, we have expressed and purified most thermoenzymes needed, as shown in Figure 3.

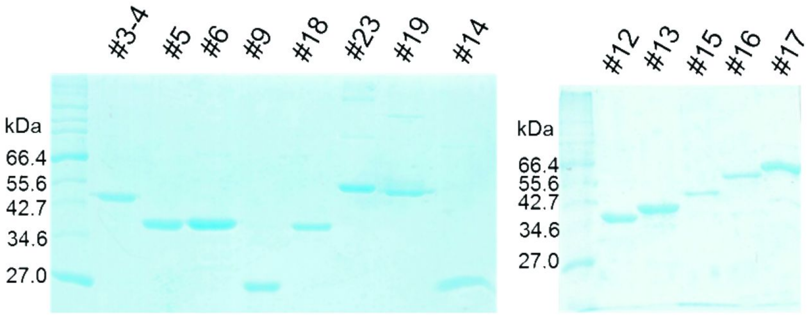

Figure 3. SDS-PAGE of purified enzymes from the proof-of-concept experiments. The enzyme number is listed in Table I.

Furthermore, we attempted to validate some biocatalytic modules before the whole systems integration. Figure 4 shows the profile of fructose-6-phosphate formation from formaldehyde and ribulose-5-phosphate (ru5p) mediated by 3-hexulose-6-phosphate synthase (#3 enzyme) and hexulose phosphate isomerase (#4 enzymes).

Also, we demonstrated the feasibility of starch synthesis from glucose-1-phosphate mediated by potato starch phosphorylase (Figure 5). The presence of starch can be detected by iodine dying. Clearly, two negative controls (neither enzyme addition nor maltotetraose addition) do not show any color change, suggesting that there is no starch formed (Figure 5, Tubes 1 and 2). When the enzyme and maltotetraose were added, starch was synthesized from low degree polymerization maltotetrase to long chain amylose – linear starch, resulting in blue color in Tubes 3-5 (Figure 5). Also, such synthetic ethanol can be precipitated in the presence of ethanol (data not shown). As a result, the separation costs of starch from the aqueous reaction phase would be minimal.

Now we are under way to integrate more parts and modules for implementing the proof-of-concept experiments.

Downloaded by UNIV OF DELAWARE MORRIS LIB on June 14, 2012 | http://pubs.acs.org
Publication Date (Web): May 3, 2012 | doi: 10.1021/bk-2012-1097.ch015

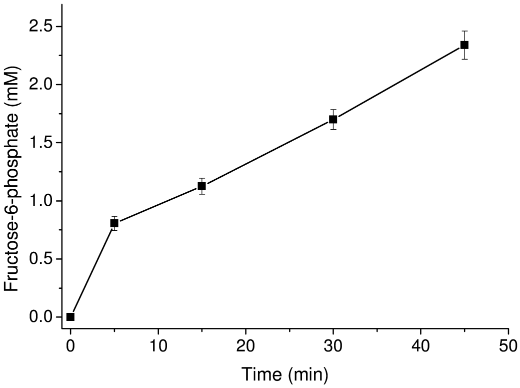

Figure 4. Synthesis of fructose-6-phosphate from formaldehyde and ru5p mediated by #3 and #4 enzymes. The reaction mixture contained 10 mM formaldehyde, 10 mM ru5p, and 0.02 mg/L HPS-HPI in 200 mM HEPES buffer (pH 7.5) containing 10 mM $MgCl_2$ and 0.5 mM $MnCl_2$. The reaction temperature was 37°C.

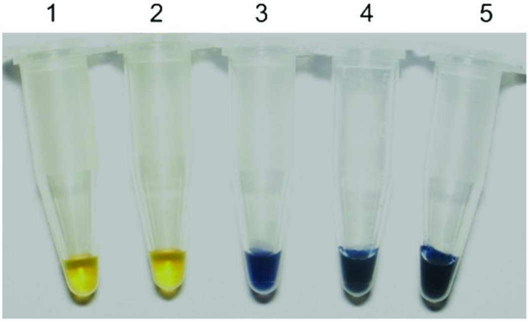

Figure 5. Starch synthesis from glucose-1-phosphate (g1p) mediated by potato starch phosphorylase (PGP). The reaction mixture contains 30 mM HEPES (pH7.3), 25 μM maltotetraose as a seed of starch synthesis, 2~20 mM g1p, and 30 μg/ml potato α-glucan phosphorylase at 42°C. After 16 h reactions, a small amount of iodine reagent was added in each tube. Tube 1, negative control without PGP; Tube 2, negative control without maltotetraose; and Tubes 3-5, positive results with 2, 10 and 20 mM g1p.

Carbon-Neutral Bioeconomy

We wish to suggest a future carbon-neutral bioeconomy (Figure 6). Both natural and this newly-designed artificial photosynthesis will be responsible for fixing CO_2 by utilizing solar energy; while the degradation of carbohydrates and its derivatives will release CO_2 to the atmosphere.

Downloaded by UNIV OF DELAWARE MORRIS LIB on June 14, 2012 | http://pubs.acs.org
Publication Date (Web): May 3, 2012 | doi: 10.1021/bk-2012-1097.ch015

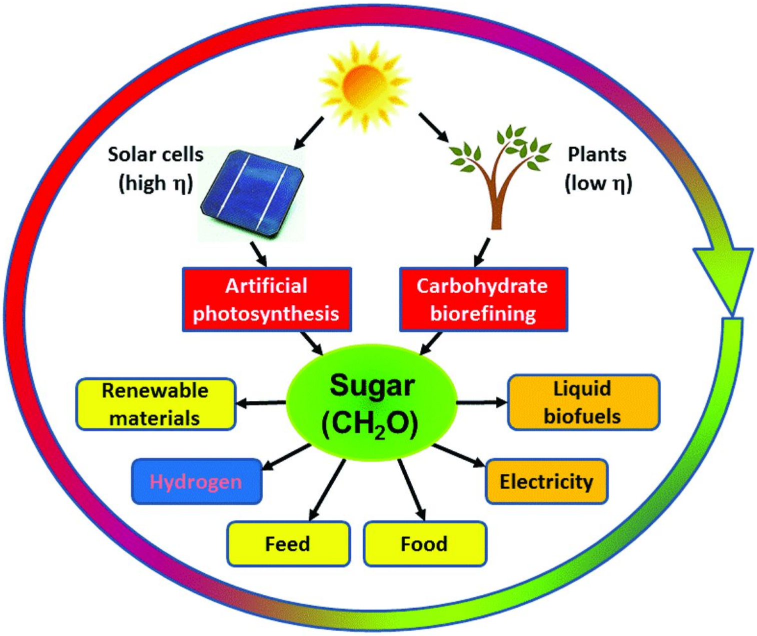

Figure 6. The carbon-neutral cycle based on carbohydrates as food, feed, a source of renewable material precursors (e.g., lactic acid, isoprene, succinic acid), an electricity storage carrier and a hydrogen carrier .

Natural plant photosynthesis is compared with artificial photosynthesis (Table II). Plants can be regarded as self-duplicating, low-efficiency living solar cells that can fix CO_2 by utilizing intermittent non-point solar energy and generate phytobiomass. In our proposed system, carbohydrates from plants will remain a major source of food and animal feed plus some renewable materials (e.g., paper, lumber). After crop growing and harvesting, carbohydrates are processed for different applications (*29*, *49*). Obviously, plant photosynthesis happens in daytime, at modest temperatures, and with enough water supplies and nutrients. However, it suffers from low photosynthesis efficiencies. Consequently, a large fraction of arable lands have to be used to produce food and feed. Meanwhile, plant photosynthesis has poor water utilization efficiencies (*30*, *31*). Also, modern farming requires significantly high energy inputs from nutrients (such as nitrogen and phosphorus), herbicides and pesticides for high biomass productivity (*50*). Only a fraction of fertilizers (e.g., ~30-50%) are utilized by dedicated crops, resulting in non-point runoff pollution from agricultural land (*51*). In addition to food and feed production, the more abundant non-food fraction of biomass has been suggested as a biofuels feedstock. However, potential benefits of second generation biofuels are under debate, mainly due to concerns related to water footprint, fertilizer input, land use change, and so on (*52*, *53*).

Table II. Comparison of artificial photosynthesis and natural photosynthesis by plants.

Feature	*Artificial photosynthesis*	*Natural photosynthesis*
Efficiency[a]	~11-50%	0.2-1%
Land area required	Small	Large
Land quality	Any land	Arable
Water use	One kg of carbohydrate requires only 0.6 kg of water	One kg of carbohydrate requires at least 500 kg of water
Nutrients (N, P) needed	Low	High
Herbicides and pesticides	No	Yes
Operation time	24/7 (whole day)	Daytime only
Growth season	All seasons	Only warm seasons with enough water
Pollutants generated	Point fermentation waste water	Non-point water containing N, P, herbicides and pesticides

[a] based on the overall efficiency of solar energy-to-carbohydrate.

Downloaded by UNIV OF DELAWARE MORRIS LIB on June 14, 2012 | http://pubs.acs.org
Publication Date (Web): May 3, 2012 | doi: 10.1021/bk-2012-1097.ch015

To store a fraction of solar electricity -- off-peak or even waste electricity, solar starch would be synthesized via future low-cost solar cells and artificial photosynthesis. Three major functions of this solar starch would be (i) storing electricity with storage densities of ~10-14 MJ electricity output/kg carbohydrate, (ii) serving as a best biofuel for sugar fuel cell vehicles, and (iii) using as key building blocks for producing liquid jet fuels and renewable materials (*54*). Considering the ultra-high efficiencies of available solar cells (η = ~18-42%), water electrolysis (η = ~85%), and carbohydrate generation from H_2 and CO_2 (η = ~80%, here), it is clear that the overall solar energy-to-carbohydrate efficiency would range from 12 to 29%, much higher than plant photosynthesis. The much higher efficiency of artificial photosynthesis is mainly attributed to (i) higher efficiency of solar cells that can utilize a broader wavelength range solar radiation, (ii) no respiration (energy) loss in cell-free biocatalysis systems, and (iii) higher-energy efficiency of synthetic pathway of carbohydrate. Since electricity can be easily collected by wire and be distributed by grid, it would be feasible to be able to produce solar starch 24/7 at well-controlled reactors. Also due to electricity transportability, electricity generation sites can be separated from carbohydrate generation locations. Even more appealing, artificial photosynthesis, unlike plant photosynthesis, does not require a large amount of water for transpiration, resulting in potential conservation of fresh water by approximately 500-fold or higher. The pollutants generated from bioreactors could be treated more easily than those from agricultural land because they are

Downloaded by UNIV OF DELAWARE MORRIS LIB on June 14, 2012 | http://pubs.acs.org
Publication Date (Web): May 3, 2012 | doi: 10.1021/bk-2012-1097.ch015

point pollution sources (*55*). Except in emergency situations, such as volcanic winter, nuclear winter, a little ice age, or a small closed space ecosystem, synthetic starch would not be used for food.

Approximately 10-60 fold increases in area-specific carbohydrate productivity through this artificial photosynthesis (Figure 1) would drastically decrease land uses for biofuels production and reduce or eliminate land/water competition with food and feed production. Also, the conversion of starch to biofuels is easier than that of non-food biomass (*29*, *49*). This carbon-neutral bioeconomy would never happen without breakthroughs in low-cost carbon-free electricity or hydrogen generation from renewable carbon-free primary energy sources. It is noted that this artificial photosynthesis may be a supplementary tool for mitigating CO_2 emissions if we cannot get rid of most fossil fuel consumption. Because (i) we will not have enough electricity to fix the approximately 20 billion annual tons of CO_2 emissions generated from burning of fossil fuels, and (ii) there would not be a market for this level of solar starch production (e.g., fixing four billion tons of CO_2 means 2.5 billion tons of solar starch). (Note: the current annual global cereal production is about 2.3 billion tons).

Closing Remarks

Experimental validation of this hypothetical artificial photosynthesis system has not yet been finished, but the science behind these novel pathways is crystal clear because each of the key components is well-known and tested in the literature by so many independent groups. The experiment setups are highly complex and require close collaboration among biologists, electrochemists, chemists, and engineers. The obstacles to wide implementation are mainly (i) lack of stable standardized enzymes as building blocks in the pathways (*47*, *48*, *56*), (ii) costly, labile coenzymes (*47*, *48*, *57*), (iii) efficient coenzyme regeneration (*42*, *43*, *58*, *59*) and (iv) careful regulation of metabolite fluxes to different products and in situ product separation.

To address the first obstacle, the discovery and utilization of more (thermo-)stable enzymes suitable for in vitro synthetic biology projects would be a new industrial enzyme gold mine (*60*). As a start, our laboratory has obtained several thermophilic enzymes with enough stability (i.e., high total turn-over numbers (TTN) of $>10^{7-8}$ mol of product per mol of enzyme) (*61–64*). Also, a combination of thermostable enzymes and immobilization would prolong the lifetime of the enzymes by one or two orders of magnitude. For example, immobilized thermophilic glucose isomerase can work at ~55°C for more than two years (*65*). In our laboratory, an immobilized thermophilic phosphoglucose isomerase exhibits TTN values of more than 10^9 mol of product per mol of enzyme at 60°C (*64*). When all enzymes have TTN of more than 10^8 mol of product per mol of enzyme, the carbohydrate (energy) consumed for the synthesis of enzymes would be minimal, less than 1% of total energy consumed (*2*, *47*, *54*, *66*). To decrease the toxic effects of formaldehyde on other enzymes, several enzymes could be further engineered for their ability to tolerate toxic metabolites. Another promising solution is the construction of enzyme complexes, which can rapidly channel toxic formaldehyde generated from #2 enzyme to #3 enzyme. As a result, the level of formaldehyde would be very low. Such substrate channeling has been discovered in nature and been mimicked in the laboratories (*67–71*).

To address the second and third obstacles pertaining to coenzyme regeneration, we expect costly NAD(P) cofactors to be replaced with low-cost and stable biomimetic analogues (*72–75*) plus engineered oxidoreductases that can work on biomimics by using directed enzyme evolution, rational design, or their combination (*57*, *74–76*).

To address the forth obstacle, in silico mathematical models for process simulation must be built for the optimization and redistribution of the synthesis of different end-products. More complicated models for in vivo microorganisms have been developed elsewhere (*77*, *78*). To decrease product separation energy, we designed this pathway that would produce water-insoluble starch and volatile ethanol, which can be stripped by bubbling CO_2. Since ethanol separation energy is closely associated with its concentration (*66*), it is difficult to estimate the percentage of energy loss for ethanol separation now. An alternative way is enzymatic conversion of one ethanol to six reduced coenzymes or their equivalent through the citric acid cycle (*79*) so to produce carbohydrate as a sole product but it could greatly increase the whole enzymatic system complexity.

Additionally, it was worth pointing out that some key reactions in the above artificial photosynthesis pathway may occur on the surface of solid supports, such as nano-materials or membrane-like structures, which help drive some thermodynamically unfavorable reactions at standard conditions to happen (*14*, *15*, *67*).

The implementation of the carbon-neutral bioeconomy would meet humankind's four most basic needs -- air, water, food, and energy, while preserving the Earth. The energy transition from the current fossil fuel-based economy to the future renewable energy-based carbon-neutral bioeconomy will take at least 50 years or longer with intensive international efforts (*2*, *80*).

Downloaded by UNIV OF DELAWARE MORRIS LIB on June 14, 2012 | http://pubs.acs.org
Publication Date (Web): May 3, 2012 | doi: 10.1021/bk-2012-1097.ch015

Acknowledgments

This work cannot be finished without support of the Biological Systems Engineering Department of Virginia Tech. The authors were grateful for support from the USDA Bioprocessing and Biodesign Center (to YPZ), Gate Fuels Inc (to RF) and China Scholarship Council (to HGC).

References

1. Smil, V. *Energy in Nature and Society*; MIT Press: Cambridge, MA, 2008.
2. Zhang, Y.-H. P. *Proc. Biochem.* **2011**, *46*, 2091–2110.
3. Balzani, V.; Credi, A.; Venturi, M. *ChemSusChem* **2008**, *1* (1−2), 26–58.
4. Kalyanasundaram, K.; Graetzel, M. *Curr. Opin. Biotechnol.* **2010**, *21* (3), 298–310.
5. Lewis, N. S. *Science* **2007**, *315* (5813), 798–801.

Downloaded by UNIV OF DELAWARE MORRIS LIB on June 14, 2012 | http://pubs.acs.org
Publication Date (Web): May 3, 2012 | doi: 10.1021/bk-2012-1097.ch015

6. Lewis, N. S.; Nocera, D. G. *Proc. Natl. Acad. Sci. U.S.A.* **2006**, *103* (43), 15729–15735.
7. Esswein, A. J.; Nocera, D. G. *Chem. Rev.* **2007**, *107* (10), 4022–4047.
8. Schlögl, R. *ChemSusChem* **2010**, *3*, 209–222.
9. Zhang, Y.-H. P. *ACS Catal.* **2011**, *1*, 998–1009.
10. Amao, Y. *ChemCatChem* **2011**, *3* (3), 458–474.
11. Hermann, W. A. *Energy* **2006**, *31* (12), 1685–1702.
12. Ibrahim, H.; Ilinca, A.; Perron, J. *Renewable Sustainable Energy Rev.* **2008**, *12* (5), 1221–1250.
13. Chen, H.; Cong, T. N.; Yang, W.; Tan, C.; Li, Y.; Ding, Y. *Prog. Natural Sci.* **2009**, *19* (3), 291–312.
14. Baskaya, F.; Zhao, X.; Flickinger, M.; Wang, P. *Appl. Biochem. Biotechnol.* **2010**, *162* (2), 391–398.
15. Tong, X.; El-Zahab, B.; Zhao, X.; Liu, Y.; Wang, P. *Biotechnol. Bioeng.* **2011**, *108*, 465–469.
16. Aresta, M. *Carbon Dioxide as Chemical Feedstock*; Wiley-VCH Verlag GmbH& Co.: Weinheim, 2010.
17. Williams, P. J. L.; Laurens, L. M. L. *Energy Environ. Sci.* **2010**, *3* (5), 554–590.
18. Blankenship, R. E.; Tiede, D. M.; Barber, J.; Brudvig, G. W.; Fleming, G.; Ghirardi, M.; Gunner, M. R.; Junge, W.; Kramer, D. M.; Melis, A.; Moore, T. A.; Moser, C. C.; Nocera, D. G.; Nozik, A. J.; Ort, D. R.; Parson, W. W.; Prince, R. C.; Sayre, R. T. *Science* **2011**, *332* (6031), 805–809.
19. Berg, J. M.; Tymoczko, J. L.; Stryer, L. *Biochemistry*; W. H. Freeman & Co.: New York, 2002.
20. Nelson, D. L.; Cox, M. M. *Lehninger Principles of Biochemistry*; WH Freeman: New York, 2008.
21. Herrera, A. *Ann. Bot.* **2009**, *103* (4), 645–653.
22. Pereto, J.; Velasco, A.; Becarra, A.; Lazcano, A. *Int. Microbiol.* **1999**, *2*, 3–10.
23. Muller, V. *Appl. Environ. Microbiol.* **2003**, *69* (11), 6345–6353.
24. Wood, H. *FASEB J.* **1991**, *5*, 156–163.
25. Berg, I. A.; Kockelkorn, D.; Buckel, W.; Fuchs, G. *Science* **2007**, *318* (5857), 1782–1786.
26. Berg, I. A.; Kockelkorn, D.; Ramos-Vera, W. H.; Say, R. F.; Zarzycki, J.; Hügler, M.; Alber, B. E.; Fuchs, G. *Nat. Rev. Microbiol.* **2010**, *8* (6), 447–460.
27. Zhang, Y.-H. P.; Myung, S.; You, C.; Zhu, Z. G.; Rollin, J. *J. Mater. Chem.* **2011**, *21* (47), 18877–18886.
28. Zhu, X.-G.; Long, S. P.; Ort, D. R. *Curr. Opin. Biotechnol.* **2008**, *19* (2), 153–159.
29. Zhang, Y.-H. P. *J. Ind. Microbiol. Biotechnol.* **2008**, *35* (5), 367–375.
30. Hightower, M.; Pierce, S. A. *Nature* **2008**, *452*, 285–286.
31. The World Economic Forum Water Initiative. *Water security: the water-food-energy-climate nexus*; Island Press: Washington, DC, 2011.
32. Luque, A.; Martí, A. *Phys. Rev. Lett.* **1997**, *78* (26), 5014–5017.

33. DiCosimo, R.; Wong, C.-H.; Whitesides, G. M. *J. Org. Chem.* **1981**, *46*, 4622–4623.
34. Yoon, S. K.; Choban, E. R.; Kane, C.; Tzedakis, T.; Kenis, P. J. A. *J. Am. Chem. Soc.* **2005**, *127* (30), 10466–10467.
35. Vuorilehto, K.; Lutz, S.; Wandrey, C. *Bioelectrochemistry* **2004**, *65* (1), 1–7.
36. Kuwabata, S.; Tsuda, R.; Yoneyama, H. *J. Am. Chem. Soc.* **1994**, *116*, 5437–5443.
37. Obert, R.; Dave, B. C. *J. Am. Chem. Soc.* **1999**, *121*, 12192–12193.
38. El-Zahab, B.; Donnelly, D.; Wang, P. *Biotechnol. Bioeng.* **2008**, *99* (3), 508–514.
39. Kato, N.; Yurimoto, H.; Thauer, R. K. *Biosci. Biotechnol. Biochem.* **2006**, *70*, 10–21.
40. Orita, I.; Sato, T.; Yurimoto, H.; Kato, N.; Atomi, H.; Imanaka, T.; Sakai, Y. *J. Bacteriol.* **2006**, *188*, 4698–4704.
41. Zhang, Y.-H. P.; Evans, B. R.; Mielenz, J. R.; Hopkins, R. C.; Adams, M. W. W. *PLoS One* **2007**, *2* (5), e456.
42. Zheng, H.; Ohno, Y.; Nakamori, T.; Suye, S.-I. *J. Biosci. Bioeng.* **2009**, *107* (1), 16–20.
43. Kohlmann, C.; Märkle, W.; Lütz, S. *J. Mol. Catal. B: Enzymatic* **2008**, *51* (3−4), 57–72.
44. Mertens, R.; Liese, A. *Curr. Opin. Biotechnol.* **2004**, *15* (4), 343–348.
45. De Lacey, A. L.; Detcheverry, M.; Moiroux, J.; Bourdillon, C. *Biotechnol. Bioeng.* **2000**, *68* (1), 1–10.
46. Sun, J.; Hopkins, R. C.; Jenney, F. E.; McTernan, P. M.; Adams, M. W. W. *PLoS One* **2010**, *5* (5), e10526.
47. Zhang, Y.-H. P.; Sun, J.-B.; Zhong, J.-J. *Curr. Opin. Biotechnol.* **2010**, *21*, 663–669.
48. Zhang, Y.-H. P. *Biotechnol. Bioeng.* **2010**, *105*, 663–677.
49. Lynd, L. R.; Weimer, P. J.; van Zyl, W. H.; Pretorius, I. S. *Microbiol. Mol. Biol. Rev.* **2002**, *66*, 506–577.
50. Smil, V. *Feeding the World: A Challenge for the Twenty-First Century*; MIT Press: Boston, MA, 2000.
51. Braskerud, B. C. *Eco. Eng.* **2002**, *19* (1), 41–61.
52. Service, R. F. *Science* **2009**, *326* (5952), 516–517.
53. Searchinger, T.; Heimlich, R.; Houghton, R. A.; Dong, F.; Elobeid, A.; Fabiosa, J.; Tokgoz, S.; Hayes, D.; Yu, T.-H. *Science* **2008**, *319* (5867), 1238–1240.
54. Wang, Y.; Huang, W.; Sathitsuksanoh, N.; Zhu, Z.; Zhang, Y.-H. P. *Chem. Biol.* **2011**, *18*, 372–380.
55. Grady, G. P. L.; Daigger, G. T.; Love, N. G.; Filipe, C. D. M., *Biological Waste Treatment*, 3rd ed.; CRC Press: Boca Raton, FL, 2011.
56. Zhang, Y.-H. P.; Mielenz, J. R. *Energies* **2011**, *4*, 254–275.
57. Ryan, J. D.; Fish, R. H.; Clark, D. S. *ChemBioChem* **2008**, *9* (16), 2579–2582.
58. Chenault, H. K.; Whitesides, G. M. *Appl. Biochem. Biotechnol.* **1987**, *14* (2), 147–197.
59. Wichmann, R.; Vasic-Racki, D. *Adv. Biochem. Eng. Biotechnol.* **2005**, *92*, 225–260.

Downloaded by UNIV OF DELAWARE MORRIS LIB on June 14, 2012 | http://pubs.acs.org
Publication Date (Web): May 3, 2012 | doi: 10.1021/bk-2012-1097.ch015

60. Zhang, Y.-H. P. *Microbe* **2009**, *4* (12), 560–565.
61. Wang, Y.; Zhang, Y.-H. P. *Microb. Cell Fact.* **2009**, *8*, 30.
62. Wang, Y.; Zhang, Y.-H. P. *J. Appl. Microbiol.* **2010**, *108*, 39–46.
63. Myung, S.; Wang, Y. R.; Zhang, Y.-H. P. *Process Biochem.* **2010**, *45*, 1882–1887.
64. Myung, S.; Zhang, X.-Z.; Zhang, Y.-H. P. *Biotechnol. Prog.* **2011**, *27*, 969–975.
65. Vasic-Racki, D. History of industrial biotransformations -- Dreams and realities. In *Industrial Biotransformations*; Liese, A., Seebald, S., Wandrey, C., Eds.; Wiley-VCH: KGaA: Weinheim, 2006; pp 1−37.
66. Huang, W. D.; Zhang, Y.-H. P. *Energy Environ. Sci.* **2011**, *4*, 784–792.
67. Zhang, Y.-H. P. *Biotechnol. Adv.* **2011**, *29*, 715–725.
68. Winkel, B. S. J. *Annu. Rev. Plant Biol.* **2004**, *55* (1), 85–107.
69. Jørgensen, K.; Rasmussen, A. V.; Morant, M.; Nielsen, A. H.; Bjarnholt, N.; Zagrobelny, M.; Bak, S.; Møller, B. L. *Curr. Opin. Plant Biol.* **2005**, *8* (3), 280–291.
70. Dunn, M. F.; Niks, D.; Ngo, H.; Barends, T. R. M.; Schlichting, I. *Trends Biochem. Sci.* **2008**, *33* (6), 254–264.
71. Huthmacher, C.; Gille, C.; Holzhutter, H.-G. *J. Theor. Biol.* **2008**, *252*, 456–464.
72. Ansell, R. J.; Lowe, C. R. *Appl. Microbiol. Biotechnol.* **1999**, *51* (6), 703–710.
73. Lo, H. C.; Fish, R. H. *Angew. Chem., Int. Ed.* **2002**, *41* (3), 478–481.
74. Nazor, J.; Schwaneberg, U. *ChemBioChem* **2006**, *7* (4), 638–644.
75. Nazor, J.; Dannenmann, S.; Adjei, R. O.; Fordjour, Y. B.; Ghampson, I. T.; Blanusa, M.; Roccatano, D.; Schwaneberg, U. *Protein Eng. Des. Sel.* **2008**, *21* (1), 29–35.
76. Campbell, E.; Wheeldon, I. R.; Banta, S. *Biotechnol. Bioeng.* **2010**, *107* (5), 763–774.
77. Mahadevan, R.; Palsson, B.Ø.; Lovley, D. R. *Nat. Rev. Microbiol.* **2011**, *9* (1), 39–50.
78. Lewis, N. E.; Schramm, G.; Bordbar, A.; Schellenberger, J.; Andersen, M. P.; Cheng, J. K.; Patel, N.; Yee, A.; Lewis, R. A.; Eils, R.; Konig, R.; Palsson, B. O. *Nat. Biotechnol.* **2010**, *28* (12), 1279–1285.
79. Sokic-Lazic, D.; Minteer, S. D. *Biosens. Bioelectron.* **2008**, *24* (4), 939–944.
80. Smil, V. *Energy Transitions: History, Requirements, Prospects*; ABC-CLIO, LLC: Santa Barbara, CA, 2010.

Downloaded by UNIV OF DELAWARE MORRIS LIB on June 14, 2012 | http://pubs.acs.org
Publication Date (Web): May 3, 2012 | doi: 10.1021/bk-2012-1097.ch015

Downloaded by UNIV OF DELAWARE MORRIS LIB on June 14, 2012 | http://pubs.acs.org
Publication Date (Web): May 3, 2012 | doi: 10.1021/bk-2012-1097.ch016

Chapter 16

Developing Efficient Amine-Containing Mesoporous CO_2 Adsorbent

Kun Kun Han and Jian Hua Zhu*

Key Laboratory of Mesosopic Chemistry of MOE, College of Chemistry and Chemical Engineering, Nanjing University, Nanjing 210093, China
***Email: jhzhu@netra.nju.edu.cn. Fax: +86-25-83317761.**
Tel: +86-25-83595848.

To control the increasing atmospheric CO_2 and protect environment, it is feasible to load amines on porous materials forming new and efficient adsorbent. However, how to incorporate a large amount of amine onto the porous host with uniform dispersion is crucial to develop new CO_2 capturers, and this short review highlights some our recent researches on this subject. We tried a new strategy to introduce tetraethylenepentamine (TEPA) into the as-synthesized SBA-15 occluded with P123 template, exploiting the template as the support to disperse amine and preparing new CO_2 adsorbent with high capacity. When the as-synthesized MCM-41 was used to disperse TEPA, the CO_2 adsorptive capability could be enhanced to 210 mg g^{-1}. We also prepared the amine *in situ* coated meso-structured silica monolith, and the TEPA additive in synthesis not only provided the necessary basicity for hydrolysis of silica source, but also directly incorporated into the resulting mesoporous CO_2 adsorbent. Apart from the advantage of saving time and energy in this synthesis, these TEPA containing monoliths owned a mechanistic strength of 64 N cm^{-2}. Finally, the synthesis and CO_2 adsorption performance of mesoporous superbasic materials are also reviewed.

Keywords: CO_2 sorbent; amine-modified as-synthesized mesoporous materials; monolith; mesoporous superbasic materials

In Recent Advances in Post-Combustion CO2 Capture Chemistry; Attalla, M.;
ACS Symposium Series; American Chemical Society: Washington, DC, 2012.

Downloaded by UNIV OF DELAWARE MORRIS LIB on June 14, 2012 | http://pubs.acs.org
Publication Date (Web): May 3, 2012 | doi: 10.1021/bk-2012-1097.ch016

Introduction

The topic of global warming as a result of increased atmospheric CO_2 concentration is arguably the environmental problem facing the whole world. Therefore the capture and sequestration of postcombustion CO_2 are important and imperative. Billion tons of carbon dioxide have been emitted into atmosphere as an ineluctable byproduct of fossil-fuel combustion. For instance there were 2.279 billion metric tons CO_2 emissions alone from coal-fired power plants in United States, 32.4% of the total CO_2 emission for that year (*1*). Consequently, how to control the emission of the greenhouse gas into atmosphere is an urgent concern of governments and energy companies. In fact various adsorptive methods have been tried to reduce CO_2 in exhaust gas and/or natural gas, among them aqueous solutions of amines such as monoethanolamine (MEA), diethanolamine (DEA), and methyldiethanolamine (MDEA), are employed as the absorbents. Nonetheless, their use is limited by the drawbacks such as corrosion, high-energy consumption and limited amine concentration in the aqueous phase due to viscosity and foaming issues (*2–4*). Fortunately, the application of solid adsorbents can overcome these drawbacks. Apart from preparing solid adsorbents such as zeolites and hydrotalcite (*5*, *6*), alkaline earth oxide (*7*), metal-organic frameworks (*8*) and zeolitic imidazolate frameworks (*9*), loading amines on porous materials like silica gel or carbon is a feasible way to get the effective adsorbent (*10–14*). Solid amine adsorbents have the advantages of high selectivity, low causticity and easy regeneration, however, how to incorporate a large amount of amine onto the porous host material while keeping the guest well dispersed is crucial for development of the adsorbents with higher effeciency. There are two main methods to load amine on the porous support, grafting and impregnation. The SBA-15 modified with propylamine was able to adsorb 9-18 mg g^{-1} of CO_2 (*15*), while diamine-grafted SBA-15 showed the enhanced CO_2 adsorption capacity of 44 mg g^{-1} (*16*). Likewise, MCM-41 modified with polyethylenimine (PEI) exhibited a CO_2 adsorption capacity of 114-133 mg g^{-1} at 348 K (*17*). To make a new support to accommodate more amine groups, Sayari and his co-workers used the pore-expanded mesoporous MCM-41 to enhance the adsorptive capacity (*18*, *19*). However, both grafting and impregnation methods have their disadvantages: only the limited amount of amine is able to be grafted on the surface of supports through grafting so that the resulting CO_2 adsorption ability is relatively low. In contrast, more amines can be loaded on the porous support through impregnation, but their distribution is inferior to that with grafting because the guests often conglomerate.

To load large amount of amine on the porous material as that with impregnation meanwhile to keep the amine distribution as that loaded with grafting method, we tried a new post-modification strategy to prepare novel CO_2 adsorbent, directly introducing tetraethylenepentamine (TEPA) into the as-synthesized SBA-15 occluded with P123 [poly (ethylene oxide)-poly (propylene oxide)-poly (ethylene oxide)] through impregnation (*20*). In general the templates (ionic and non-ionic surfactants or amphiphilic block copolymers) that are necessary for inducing the wall structure of mesoporous material through

Downloaded by UNIV OF DELAWARE MORRIS LIB on June 14, 2012 | http://pubs.acs.org
Publication Date (Web): May 3, 2012 | doi: 10.1021/bk-2012-1097.ch016

nanocasting or structure -directing procedure, always need to be removed from the synthetic products by calcination or extraction in order to empty the channel of the mesoporous materials. In fact, however, these micelles have constant chemical composition and relative regular geometric structure therefore the mesopore of as-synthesized mesoporous silica is separated into sub-nanometer rooms by the occluded organic template and thus the as-synthesized mesoporous silica actually is of hierarchical structure. Consequently, we exploited the template in the as-synthesized mesoporous silica as the delicate and soft support to disperse amine, in order to enhance the capacity of the basic guest in CO_2 adsorption. For further pursuing the higher efficiency to capture CO_2, we explored the impact of hydroxyl group on CO_2 adsorption (*21*), and also the as-synthesized MCM-41 was chosen as the support to perform the further studies (*22*).

The convenience of amine-containing CO_2 adsorbents in use is also important for their potential particular application. Most of the mesoporous CO_2 adsorbents are powder-like materials, which hinders their potential application in gas stream such as waste gas of factories, natural gas in the transportation pipeline and the vent gas of building. Thus, a lot of effort has been devoted to develop the porous silica materials with mold appearance (*8*, *9*, *23*, *24*). Toward the aim of developing new CO_2 adsorbent with low cost of synthesis and the convenience in use, we explored a new strategy to prepare the amine *in situ* coated meso-structured silica monolith with adequate mechanical intension to capture CO_2 (*25*). Apart from these amine-containing porous adsorbents, strong basic and superbasic composites are also believed to be the effect capturer of CO_2 since CO_2 is an acidic gas. Among these composites the strong basic or superbasic mesoporous materials attract more attention, because they possess the wide channel to avoid high pressure drop along with the strong basic sites to captur CO_2, so that they can be the competitive candidates to trap the CO_2 from flue gas at relative high temperature. Unfortunately, creation of strong basic or superbasic sites on mesoporous silica is a challenge because of the inherent difficulty in preparation. Through three strategies, we sucessfully obtained the mesoporous superbasic materials and assessed their adsorption performance of CO_2 (*26–28*). The first, magnesia modified mesoporous SBA-15 silica was synthesized directly from strong acidic solution (*26*). The resulting samples had good mesoscopic order and strong basic strengths. Again, this outcome was achieved under milder and simpler synthetic conditions utilizing less time and energy-saving. And the generation of superbasic sites on mesoporous silica SBA-15 was realized through coating neutral salt KNO_3 onto the *in situ* coated material MgO/SBA-15, followed by the thermal activation of the composite (*26*). The second, we tried to directly create the superbasic sites on mesoporous silica through adjusting the guest-host interaction, and thus some alkaline earth metal oxides were selected to modify SBA-15. As expected, superbasic sites (H_- = 27.0) appeared on the SBA-15 modified by CaO, SrO, or BaO, and these alkaline earth metal oxides-modified SBA-15 still exhibited an ordered mesoporous structure (*27*). Finally, we extended the effort of developing superbase to mesoporous alumina by using one-pot synthesis of mesoporous solid superbases. We used K_2CO_3 in this synthetic process to adjust the pH value, promoting the hydrolysis of $Al(NO_3)_3$ to form mesoporous AlOOH (boehmite) walls and producing the base precursor KNO_3. In the succedent calcination process, we conversed both KNO_3 and AlOOH and enabled the strongly basic K_2O species to be directly coated onto the γ-Al_2O_3 formed *in situ* (*28*), resulting in the superbase with high basic strength of $H_- = 27.0$.

CO_2-Capturer Derived from the As-Synthesized SBA-15 Occluded by Template

Downloaded by UNIV OF DELAWARE MORRIS LIB on June 14, 2012 | http://pubs.acs.org
Publication Date (Web): May 3, 2012 | doi: 10.1021/bk-2012-1097.ch016

In general two moles of amine groups in the adsorbent will react with one mol of CO_2 to form carbonate (*29*), for the chemical adsorption of CO_2; and the presence of hydroxyl group can enhance the ratio of CO_2 to N atom so that the additives in rich of hydroxyl group like polyethylene glycol have been adopted to enhance the adsorption capacity (*14*, *17*). This is another reason why we try our new strategy in preparing new efficient capturer of CO_2 by directly coating the amine, TEPA, into the as-synthesized SBA-15 occluded with P123.

Unlike the sample SBA(C) that was calcined at 550 °C for 6h to have the pore size of 9.3 nm and BET specific surface areas of 725 $m^2\ g^{-1}$ as well as the pore volumes of 1.12 $cm^3\ g^{-1}$, the water-washed as-synthesized SBA-15, sample SBA(P), owned about 40% reduced pore volumes and half lowered BET specific surface area because of the presence of P123 that was about 40% by weight in the composite. Besides, its micropore volume was not determined using the t-plot method, due to the differences in low-pressure nitrogen adsorption properties between the reference silica and polymer containing water-washed materials (*30*). P123, poly(ethylene oxide)–poly(propylene oxide)–poly(ethylene oxide) (EO-PO-EO) triblock co-polymers, are used as organic structure-directing agents for synthesizing well-ordered hexagonal mesoporous silica structures (SBA-15). Under acidic conditions, the PO block is expected to display more hydrophobicity than the EO block, thereby increasing the tendency for mesoscopic ordering to occur. Then, positively charged protonated silicate species interact preferentially with the more hydrophilic EO block to promote cooperative self-assembly of a silica-block-polymer–rich mesophase from a dilute water-rich phase. Concurrent and further condensation of the silica species in the presence of the block copolymer surfactant species results in the formation of the mesophase silica composite (*31*). The PO blocks of the P123 spread in the pore of SBA-15 like trees with EO blocks rooting in frameworks, causing the larger reduction in the specific surface areas (~50%) than that in pore volume (~40%), due to the penetration of EO blocks of P123 in the frameworks of silica materials and their occupation in complementary pores (*30*, *32*). We also prepared SBA(CP) sample through impregnation of SBA(C) with the P123 of 40 wt.-% (Figure 1), but it had 70% smaller pore volumes and specific surface area in comparison with SBA(P). Clearly, the P123 micelles in the as-synthesized SBA-15 have the specific dispersion and configration that cannot be repeated by post-modification.

Downloaded by UNIV OF DELAWARE MORRIS LIB on June 14, 2012 | http://pubs.acs.org
Publication Date (Web): May 3, 2012 | doi: 10.1021/bk-2012-1097.ch016

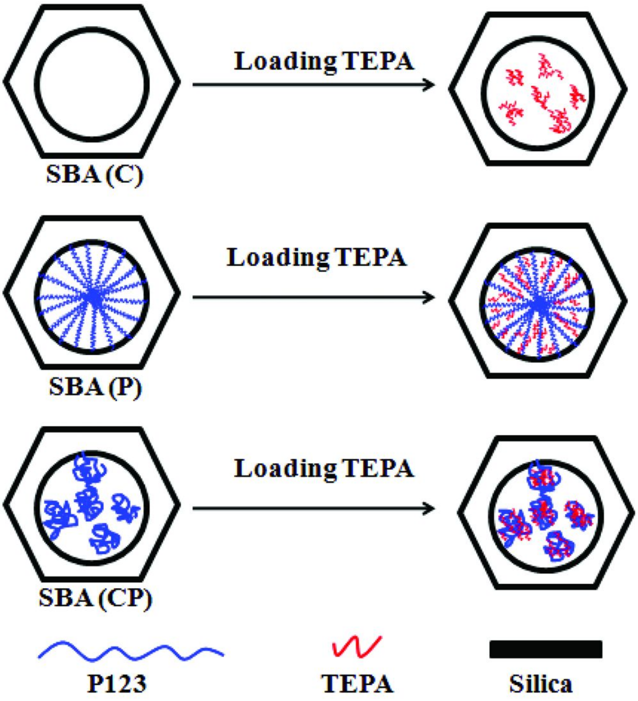

Figure 1. Schematic diagram of the dispersion of TEPA in the channels of SBA-15 samples.

Amine can be coated into the as-synthesized SBA-15 occluded with P123, decreasing the surface area and pore volume obviously (Figure 2). As the TEPA of 50 wt.-% were coated in SBA(P), the resulting sample SBA(P)-50 only owned the surface area of 7 m^2 g^{-1} and the pore volume of 0.02 cm^3g^{-1}. According to the pore volume of SBA(P) host (0.71 cm^3 g^{-1}) and the density of TEPA guest (0.999 g mL^{-1}), the maximum of TEPA to be accommodated inside the SBA(P) should be around 41 wt.-%. In our opinion, the residual pore volume in SBA(P)-50 may result from the new-formed accumulated pore of large particles in the mesoporous host. Coating TEPA on SBA(P) composite dramatically enhances its CO_2 adsorption capacity as expected. SBA(P) itself had a weak CO_2 adsorption capacity (2.23 mg g^{-1}), similar to SBA(C) sample (1.90 mg g^{-1}) but higher than SBA(CP) (0.68 mg g^{-1}). After loading TEPA, the adsorption capacity of SBA(P)-n rose substantially, reaching 62.6, 137 and 144 mg g^{-1} in the case loading 30, 40 and 50 wt.-% of TEPA respectively. When the loading amount of TEPA raised to 60 wt.-%, the composite exhibited a CO_2 adsorption capacity of 164 mg g^{-1}, higher than that of TEPA itself (151 mg g^{-1}). The uniform mesoporous channel of SBA-15 plus the P123 micelles enables these guests to have high accessability for CO_2 because these micelles spread in the pore like trees rooting in frameworks provide the unique support for high dispersion of TEPA, and the inherent affinity of TEPA guests toward CO_2 along with their high dispersion in SBA(P) sample increases the adsorption capacity synergistically. As the TEPA of 70 wt.-% was coated in SBA(P) sample, the adsorption capacity achieved 173 mg g^{-1}. One may question why the TEPA coated composite such as SBA(P)-50 with the pore volume of 0.02 cm^3 g^{-1} can adsorb the CO_2 of 144 mg g^{-1}. This phenomenon, in our opinion, results from the different temperatures used in nitrogen and CO_2 adsorption. The pore volume of SBA(P)-50 is measured at -196°C, at such low temperature the P123 is rigid in the channel so that the probe molecules cannot pass the micelles to enter the channel. Nonetheless, P123 becomes soft when the sample adsorbs CO_2 at the relatively high temperature, thus the adsorbate can enter the channel to contact with the TEPA that coated on the micelles. Figure 3 demonstrates the adsorption temperature on the CO_2 adsorption capability of SBA(P)-50, further supporting the inference of temperature effect. The relatively high temperature in the range of 35 -75°C is favoral for the diffusion of CO_2 in the micelles inside the channel, promoting the adsorption of CO_2 in the SBA(P)-50 composite. Further increase in the temperature fails to linearily enhance the CO_2 adsorption by SBA(P)-50, because of the promoted desorption of CO_2 from adsorbent.

Downloaded by UNIV OF DELAWARE MORRIS LIB on June 14, 2012 | http://pubs.acs.org
Publication Date (Web): May 3, 2012 | doi: 10.1021/bk-2012-1097.ch016

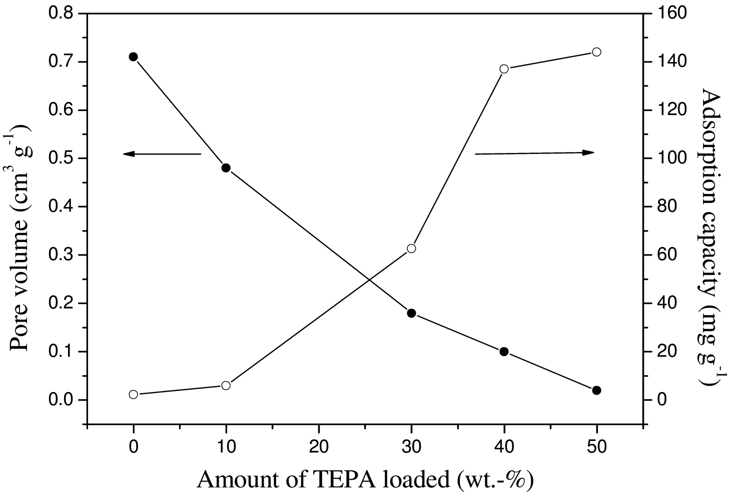

Figure 2. Influence of TEPA loading on the pore volume and CO_2 adsorption in SBA(P) sample, the CO_2 adsorption was performed at 75 °C.

Downloaded by UNIV OF DELAWARE MORRIS LIB on June 14, 2012 | http://pubs.acs.org
Publication Date (Web): May 3, 2012 | doi: 10.1021/bk-2012-1097.ch016

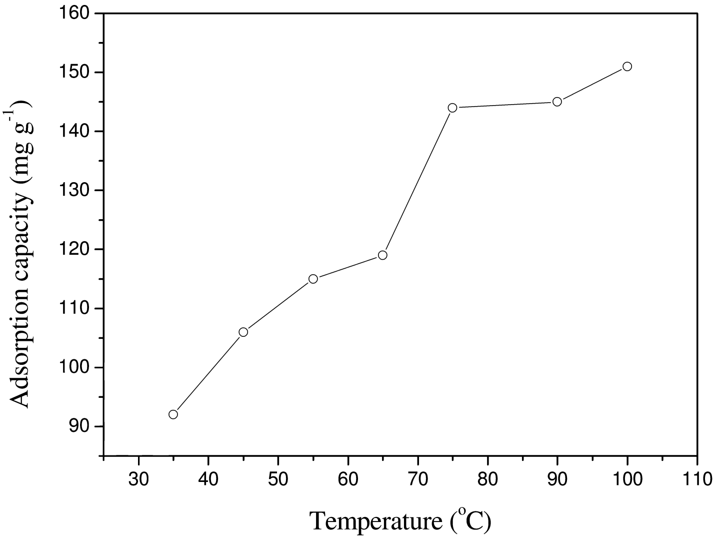

Figure 3. Effect of temperature on the CO_2 adsorption by SBA(P)-50 sample.

We used TG-DSC and MS methods to investigate the adsorption of CO_2 on the sample of SBA(P)-50 at 75 °C. SBA(P)-50 could trap the CO_2 of 110 mg g^{-1} within 2 min, achieving the rate of 50 mg g^{-1}-min^{-1}. However, this rate declined to 0.57 mg g^{-1}-min^{-1} in the following 0.5 h and lowered to 0.14 mg g^{-1}-min^{-1} in the further prolonged 1.5 h. It seems that adsorption of CO_2 in the sample of SBA(P)-50 is a kinetically (diffusion)-controlled process, and CO_2 hardly contacts the affinity sites located inside the clusters of TEPA and those of the TEPA encapsulated in micropore due to the diffusion limitation. Consequently, quite long time is required for CO_2 to reach almost all of the affinity sites in the composite. During the experiment of CO_2 desorption, only 5% of the adsorbed CO_2 slowly desorbed in the range of 35-50 °C, and 14% escaped to 70 °C as the sample was heated at the rate of 2.5 °C min^{-1}. 27% of the CO_2 left the composite once the temperature achieved 80 °C, giving the desorption rate of 3.9 mg g^{-1} °C^{-1}. As the temperature further increased, 20% of the CO_2 desorbed from 80°C to 90°C but the rate lowered to 3.1 mg g^{-1} °C^{-1}. About 23.5% of CO_2 was released in the range of 90-100 °C and the rate rose to 3.4 mg g^{-1} °C^{-1}. When the composite was kept at 100 °C for 0.5 h, about 9% of the trapped CO_2 desorbed from the adsorbent. Unlike the adsorption of CO_2 at 75°C that was hindered by diffusion limitation, almost all of the trapped CO_2 easily desorbed from the adsorbent in the process of temperature-programmed desorption (TPD) up to 100°C.

In Recent Advances in Post-Combustion CO2 Capture Chemistry; Attalla, M.;
ACS Symposium Series; American Chemical Society: Washington, DC, 2012.

Compared with SBA(C) and SBA(CP) samples, SBA(P) has the advantage of low cost due to omitting the calcination in its preparation. These three samples possessed the similar ability to capture CO_2 once they were coated with TEPA of 10~30 wt.-%. However, three supports had different composition. SBA(C) is the mesoporous silica with the empty channel, whereas SBA(P) and SBA(CP) contain porous silica (60 wt.-%) and P123 (40 wt.-%). Besides, PO blocks of the P123 spread in the channel of SBA(P) sample, forming the tree-like configuration, whereas the post-added P123 desultorily occupied the mesopore of SBA(CP) to give a smaller pore volume (*20*). However, different pore volume of three supports did not affect their adsorption performance when they were coated with TEPA of 30 wt.-%. Rather, the adsorption capacity of SBA(CP)-30 (70 mg/g) and SBA(P)-30 (63 mg/g) were slightly higher than that of SBA(C)-30 (57 mg/g), because the hydroxyl groups of P123 influence the chemical adsorption mechanism to compensate the space limitation (*33*): usually each mole of amine reacts with 0.5 mole of CO_2 to form carbamate, however the existence of hydroxyl groups changes the mechanism and the carbamate further reacts with CO_2 to form bicarbonate or carbamate type zwitterions. Therefore the adsorption capacity is enhanced. On the other hand, P123 micelles inside SBA-15 affect the distribution of TEPA to determine the final adsorption of CO_2 on TEPA. When the amine is encapsulated in SBA(P) composite, it is diluted by the P123, felting or interacting with the micelles to get a better accessibility for CO_2 molecules. Moreover, existence of more Si-OH groups in SBA(P) than SBA(C) sample is another factor to promote the dispersion of TEPA, because a large number of surface hydroxyl groups are preserved in the as-synthesized mesoporous silica. They can also improve the adsorption of CO_2 as aforementioned, so the SBA(P)-50 sample exhibited a good adsorptive capability either in the flow with different concentration of CO_2 or the cyclical adsorption-desorption of CO_2. Its capacity kept 136 mg g^{-1} in the 7th cycle of adsorption at 5% CO_2 concentration, representing the attractive potential application.

Enhancement of CO_2 Adsorption by the Hydroxyl Group in the Amine Containing SBA-15

The as-synthesized SBA-15 that preserved template has the pore volume and surface area distinctly different from its template-free analogue, but two composites containing the same weight of amine exhibit the similar adsorption capacity towards CO_2 as aforementioned. One reason to account for this phenomenon, as mentioned above, is the existence of much more hydroxyl groups in the template-preserved sample, which changes the mechanism of amine acting with CO_2 to boost the CO_2 adsorption capacity. This result provides us a valuable clue to improve the efficiency of mesoporous CO_2 capturer through the assistance of hydroxyl group. Apart from exploring the actual function of hydroxyl group in guest compound to improve the CO_2 adsorption capacity of amine-modified SBA-15, we also seek the new way to prepare the adsorbent with a higher efficiency and lower cost. Diethanolamine (DEA) that has two hydroxyl groups and one amine group, and TEPA that owns five amine groups are chosen to be

Downloaded by UNIV OF DELAWARE MORRIS LIB on June 14, 2012 | http://pubs.acs.org
Publication Date (Web): May 3, 2012 | doi: 10.1021/bk-2012-1097.ch016

In Recent Advances in Post-Combustion CO2 Capture Chemistry; Attalla, M.;
ACS Symposium Series; American Chemical Society: Washington, DC, 2012.

supported in the as-synthesized SBA-15, because both of them have been used in aqueous solutions to absorb CO_2. We mix TEPA with DEA then load them on the SBA(P) porous support, examining how the density of hydroxyl group affects the adsorption capacity of the composite. For same purpose, glycerol is also mixed with TEPA to study the promotion of hydroxyl group on the CO_2 adsorption of amine.

We fixed the loading amount of guests at 50 wt.-% on SBA(P) but changed the proportion of TEPA in the mixture of guest to form the sample named as SP-nT-(50-n)D. As more TEPA additives were used, the ultimate of CO_2 desorption peak shifted to higher temperature. For instance it shifted from 62 °C (SP-10T-40D) to 92 °C (SP-40T-10D), and two factors should be taken into account for this variation. The first one is the change of adsorption mechanism caused by the hydroxyl groups of DEA. Without hydroxyl group in the adsorbent, carbamate type zwitterions formation is the main reaction to account for CO_2 removal:

$$CO_2 + 2R_2NH = R_2NH_2^+ + R_2NCOO^-.$$

In case that hydroxyl groups present in the composite, the formation of carbamate type zwitterions can be promoted as follow reaction (*13*, *14*):

$$CO_2 + ROH + R_2NH = ROH_2^+ + R_2NCOO^-$$

Two types of carbamate have different thermal stability so that the mean ultimate temperature of CO_2 desorption varies correspondingly (*34*). The second reason is the diffusion limitation of CO_2 trapped inside of amine clusters that induces the third desorption peak in the CO_2-TPD profiles. For the adsorbed CO_2 molecules, their desorption is affected by the microenvironment around them along with the interaction strength from adsorbent. Clearly, these CO_2 molecules adsorbed at the affinity sites on the surface of TEPA or DEA clusters can easily escape at relatively low temperature, but those to be trapped inside the amine clusters or at the site embedded in the micropores are harder to release due to the diffusion limitations therefore they require a higher temperature to desorb. In the CO_2-TPD profile of SP-10T-40D sample, there were three CO_2 desorption peaks at 50, 62 and 82 °C, respectively, originating from the break of two kinds of amine-CO_2 intermediates and diffusion limitation. As more TEPA components were used in the amine mixture to be supported on SBA(P), the amount of hydroxyl groups in the adsorbent along with the resulting low thermal stability intermediate formed in adsorption was decreased correspondingly. So, the sample of SP-30T-20D exhibited two CO_2 desorption peaks and the CO_2 ultimate desorption peak shifted to a higher temperature (*22*). In contrary, the ultimate of CO_2 desorption peak would shift to low temperature if large amounts of hydroxyl group presented in the mixed amines, since the interaction mechanism of amine with CO_2 was changed. However, all of the trapped CO_2 could be desorbed from the mesoporous adsorbent at 100 °C no matter how the composition of the amine

Downloaded by UNIV OF DELAWARE MORRIS LIB on June 14, 2012 | http://pubs.acs.org
Publication Date (Web): May 3, 2012 | doi: 10.1021/bk-2012-1097.ch016

Downloaded by UNIV OF DELAWARE MORRIS LIB on June 14, 2012 | http://pubs.acs.org
Publication Date (Web): May 3, 2012 | doi: 10.1021/bk-2012-1097.ch016

mixyure varies (*22*), which is beneficial for the regeneration and cycle utilization of this CO_2 capturers. Furthermore, SP-30T-20D sample exhibited a stable adsorption capacity in the gas stream with low concentration of CO_2; keeping the capacity of 159 mg g^{-1} in the 6th cycle with diluted CO_2, which is important for its potential application.

We also use TG-MS method to study desorption of CO_2 from the sample of SP-30T-20D in the range of 35-100 °C. There were two endothermic peaks on the DSC spectrum at 70 and 87 °C respectively, which coincided with the two peaks of CO_2 desorption in the CO_2-TPD experiment. On the other hand, the influence of the hydroxyl group in amine mixture on the CO_2 adsorption capacity was also explored on SBA(C) support. When TEPA alone was used, the resulting CO_2 adsorption capacity was about 142 mg g^{-1} on either SBA(P)-50 and SBA(C)-50 composites. Nonetheless, modification of SBA(P) and SBA(C) with DEA only resulted in the CO_2 adsorption capacity of 20.8 and 9.2 mg g^{-1} respectively, due to the lower amine group density in DEA than TEPA. With the proportion of TEPA rose to 60% in the amine mixture, SP-30T-20D showed the CO_2 adsorption capacity of 163 mg g^{-1}, larger than that using TEPA (144 mg g^{-1}) or DEA (20.8 mg g^{-1}) alone. Supposing two amines were simply added and separately exerted their functions to adsorb CO_2, the corresponding capacity of SP-30T-20D would be 94.7 mg g^{-1} (144×0.6+20.8×0.4), obviously lower than the experimental data (163 mg g^{-1}). This difference indicates the synergy between hydroxyl group and amine in the CO_2 adsorbent. Actually, such synergetic effect had been observed in some SBA(P) samples coated with TEPA alone, characterized with the higher CO_2 adsorptive capability than the template-free analogue SBA(C) (*20*). However, when the SBA(P) sample was coated with TEPA from 40 wt.-% to 50 wt.-%, its CO_2 adsorption capacity rose from 137 to 144 mg g^{-1} (*20*), but the corresponding CO_2/N molar ratio (molar ratio of adsorbed CO_2 to amine groups) declined from 0.29 to 0.25, due to the limit amounts of hydroxyl groups of P123 in the channel. With the groups of guest amine over-increased, the presurved P123 micelles could not afford enough hydroxyl groups to assist them. Consequently, another source inputting enough hydroxyl groups is required in the preparation of CO_2 adsorbent and thus DEA is employed to mix with TEPA to gain the capturer of CO_2 with higher efficiency. The corresponding CO_2/N molar ratio increased from 0.10 (SP-0T-50D) to 0.37 (SP-30T-20D). For the template-free SBA-15, the CO_2/N ratio rose from 0.04 (SC-0T-50D) to 0.38 (SC-30T-20D), and achieving the maximum of 0.39 (SC-35T-15D).

Glycerol with three hydroxyl groups is also mixed with TEPA to modify SBA-15, forming the adsorbent denoted as SP-nT-(50-n)G or SC-nT-(50-n)G, and the relevant CO_2/N molar ratio is enhanced distinctly. For example, SC-30T-20G and SP-30T-20G composites exhibited the CO_2/N molar ratio of 0.32 and 0.33 respectively, considerably higher than TEPA alone modified SC (0.24) and SP (0.25). Besides, we also examined the TG-DSC profiles of CO_2 and H_2O adsorption on the sample of SP-30T-20D, in which the moisture-saturated sample still had a high adsorptive capability towards CO_2, capturing about 140 mg g^{-1} of CO_2 in the presence of water vapor. This result implies the potential application of new CO_2 capturer in controlling CO_2 emission from flue gas.

In Recent Advances in Post-Combustion CO2 Capture Chemistry; Attalla, M.;
ACS Symposium Series; American Chemical Society: Washington, DC, 2012.

Elevating the CO_2-Adsorption by Using As-Synthesized MCM-41 to Disperse Amine

Downloaded by UNIV OF DELAWARE MORRIS LIB on June 14, 2012 | http://pubs.acs.org
Publication Date (Web): May 3, 2012 | doi: 10.1021/bk-2012-1097.ch016

In order to further elevate the efficiency of CO_2 adsorption, we try the as-synthesized MCM-41 to support the amine such as TEPA for two reasons. The first, MCM-41 has the smallest pore size among the mesoporous silica materials available at that time. That is to say, it can provide larger surface area than SBA-15 to disperse the amine guest. The second, cetyltrimethylammonium bromide (CTAB) is ionic surfactant, and its distribution in the as-synthesized MCM-41 is different from that of P123 in as-synthesized SBA-15. In general ionic surfactant has a stronger interaction with silica wall than amphiphilic block copolymers in SBA-15. Consequently, CTAB distributes in the channel of MCM-41 like the spoke in wheel with cation head rooted on the silica wall. Besides, less space between silica wall and template remains in the as-synthesized MCM-41 than that in as-synthesized SBA-15. The hydrophobicity of CTAB carbon tails can enable the additives such as amine and benzene to be incorporated easily into micelle indeed (*35–37*). With this specialty, surfactant-containing MCM-41 has been tried to adsorb organics from solution or gas flow (*38*, *39*). However, it is unknown whether large amount of TEPA can be well dispersed on the micelle inside the channel of as-synthesized MCM-41 because of the incapacious space remained in the composite. And it is also sealed on the influence of CTAB micelle on the TEPA distribution and the succeeding CO_2 adsorption.

The calcined MCM-41 sample (CM) had a large surface area of 1342 $m^2\ g^{-1}$, but its as-synthesized analogue AM owned a very small one of 16 $m^2\ g^{-1}$, slightly larger than that of CM coated with TEPA of 50 wt.-% (CM-50, 7.8 $m^2\ g^{-1}$). This reveals two facts: CTAB micelles strongly interact with silica wall of MCM-41 so that few of them are removed by water wash; thereby, AM composite has a very diminutive pore volume of 0.03 $cm^3\ g^{-1}$. However, TEPA of 50 wt.-% still can be incorporated inside the channel of AM sample, which is confirmed by a simple but powerful experiment. Same amount of TEPA was mixed with quartz, zeolite KA or NaA to give the gel-like product, respectively, since quartz lacks pore and KA and NaA only have small micropores; for zeolite NaY with the pore size of 0.7 nm, the TEPA can enter inside the channel so that the mixture is powder. CM sample has the mesopores of about 2 nm, so its mixture with TEPA was certainly powder-like because the amine entered the channel. However, the mixture of AM and TEPA was also the powder-like (*21*), which indicated the distribution of TEPA inside the channel of support. This indication is confirmed by elemental analysis, in which the C/N molar ratio of AM sample was 19.1, coincided with the inherent C/N molar ratio of CTAB. After modification with TEPA, this data was significantly lowered to 2.92 due to the incorporation of TEPA that possesses the C/N ratio of 1.6.

Once TEPA is encapsulated in the AM composite, it distributes in the palisade of CTAB micelle, perhaps enveloping or interacting with the micelles to acquire better accessibility to the CO_2 molecules. According to results of CO_2-TPD tests (*21*), AM itself was able to adsorb only few CO_2 of 2.4 $mg\ g^{-1}$, but AM-10 trapped 24.7 $mg\ g^{-1}$, AM-30 captured 120.6 $mg\ g^{-1}$, tens times more than the parent. As the

In Recent Advances in Post-Combustion CO2 Capture Chemistry; Attalla, M.;
ACS Symposium Series; American Chemical Society: Washington, DC, 2012.

loading amount of TEPA rose further, AS-50 adsorbed 211 mg g^{-1} while AM-60 trapped 221 mg g^{-1} that was the highest value reported till 2008. At the same time, the climax of CO_2 desorbed from AM-*n* sample shifted to higher temperature as the loading amounts of TEPA increased, from 73 °C (AM-30), 85 °C (AM-50) to 93 °C (AM-60) (*21*), mirroring the elevated CO_2 adsorption capacity of the composite. By the way, most of the trapped CO_2 could be desorbed from AM-*n* sample at 100 °C, which facilitates the regeneration and cycle utilization of the adsorbents. In the test of TG-DSC, AM-50 captured the CO_2 of 100 mg g^{-1} within 1.5 min at 75 °C, achieving the high adsorption rate of 67 mg g^{-1} min^{-1} and inducing an exothermic peak. After another 5 min of exposure to CO_2, the sample trapped 180 mg g^{-1}, and it could reach the capability of 198 mg g^{-1} in 140 min. Clearly the adsorption of CO_2 in AM-50 sample is a kinetically (diffusion) controlled process, similar to other amine modified mesoporous silica (*20*, *24*, *40*), since CO_2 molecules need time to enter the TEPA cluster contacting with the affinity sites that locate inside the cluster. In contrary, desorption of CO_2 from AM-50 composite is quite fast in TPD procedure due to the increasing temperature: Only 2.5% of adsorbed CO_2 was escaped in the 35-60 °C range, and 26.5% desorbed from 60 °C to 80 °C. Upon heating the sample from 80 to 100 °C, about 53% of CO_2 released from the composite and the residual 18% was desorbed by holding the composites at 100°C about 0.5 h.

Existence of CTAB micelles in the AM support is crucial for elevating the efficiency of TEPA guest to adsorb CO_2. With the same TEPA content, AM-10 adsorbed almost doubled more CO_2 (24 mg g^{-1}) than CM-10 (8.8 mg g^{-1}), AM-30 trapped 90% more CO_2 (120 mg g^{-1}) than CM-30 (62 mg g^{-1}). AM-50 owned 211 mg g^{-1} adsorption capacity, obviously larger than CM-50 sample (144 mg g^{-1}). The incorporated TEPA can be equably coated on the preserved micelles that occluded in the channel of mesoporous silica, forming a net inside the pore to capture the CO_2 molecules in flow gas (*20*) and enhancing the efficiency of adsorbent. Another strongpoint of AM-*n* adsorbents is their lower cost than CM-*n* analogues, because the CTAB micelles preserved inside channel are utilized to disperse amine, saving the time and energy of calcination and reducing the proportion of assembled silica in the support. On the other hand, the state of micelles in the channel of MCM-41 also affects the final capability of CO_2 adsorbent. We prepared the sample of M(AS) by impregnating the template-free MCM-41 with CTAB of 50 wt.-% so it contains similar CTAB to AM, but M(AS)-50 trapped less CO_2 (155 mg g^{-1}) than AM-50 (211 mg g^{-1}) though these two composites had the same amount of CTAB and TEPA. Unlike AM sample where CTAB surfactant distribute in the pore like spoke in the wheel with cation head rooted on the silica wall through electrostatic force, CTAB congregates in the pore of M(AS) tangly. It is clear that the amine distribution in M(AS) is not as that in AM, which leads to lower CO_2 adsorption capacity because the dispersion and distribution of CTAB have a strong influence on the accessibility of the amine to be supported and thus the mean CO_2 capture. We also prepared other three samples, EM, the as-synthesized MCM-41 to be extracted with ethanol, PEM, the pore enlarged MCM-41 synthesized using trimethylbenzene (TMB) as swelling agents (*33*) and extracted using ethanol to remove TMB, and DM, the as-synthesized MCM-41 using dodecyltrimethylammonium bromide as template.

Downloaded by UNIV OF DELAWARE MORRIS LIB on June 14, 2012 | http://pubs.acs.org
Publication Date (Web): May 3, 2012 | doi: 10.1021/bk-2012-1097.ch016

Downloaded by UNIV OF DELAWARE MORRIS LIB on June 14, 2012 | http://pubs.acs.org
Publication Date (Web): May 3, 2012 | doi: 10.1021/bk-2012-1097.ch016

With the same TEPA contant, AM-10, DM-10, EM-10, PEM-10 and CM-10 samples exhibited the CO_2 adsorption capacity of 24, 25, 17, 14, 8.8 mg g^{-1} respectively, resulting from different distribution of TEPA guest. When the amine is encapsulated in AM, it distributes in the palisade of CTAB micelle to acquire the better accessibility for CO_2. Likewise, similar distribution of TEPA is in DM support. However, TEPA firstly enters the pore of EM and PEM, similar to that in CM where TEPA conglomerates in the silica pore, and thus their adsorption capacity is decreased. As the amount of TEPA increased to 40 wt.-%, the further loaded TEPA was then introduced into the palisade of micelle and these resulting composites had the similar adsorption capacity around 165 mg g^{-1} except CM-40 (102 mg g^{-1}). Since different micelles existed in AM and DM, their optimal loading of TEPA are different. For DM it is 40 wt.-% while 50 wt.-% is the best one for AM. CTAB has longer carbon chains than DTAB, so that more TEPA can be dispersed in the palisade of CTAB micelle (*21*). With the TEPA loading further increased to 60 wt.-%, the CO_2 adsorption capacity of PEM-60 rises to 237 mg g^{-1} to exceed ASM-60 (221 mg g^{-1}), which results from the special pore structure of the PEM support. Apart from the preserved CTAB micelles, PEM sample possesses the holes by removing the TMB in the core of CTAB micelles in comparison with AM. Consequently, more TEPA can be accommodated and thus this composite has the largest CO_2 adsorption capacity. Similar to the SBA(P)-50 that showed a good stability in cycle adsorption-desorption of CO_2 (*20*), AM-50 exhibited a high adsorption capacity of 200 mg g^{-1} in 5% CO_2 and kept 183 mg g^{-1} in the 6th adsorption cycle, providing a useful candidate for practical applications (*21*). It is interesting to compare four mesoporous CO_2 adsorbent with same TEPA loading amount (Figure 4). SC-50 has the capacity of 142 mg g^{-1}, and this value is enhanced to 144 mg g^{-1} on CM-41 because of the smaller pore size of MCM-41 support. However, SBA(P)-50 sample also exhihit the same capability of 144 mg g^{-1} since the preseved micelles divid the mesoporous pore into numerous tiny spaces so that the amine can be well dispersed. Higher value of 211 mg g^{-1} appears on AM-50 because the support provides the much more tiny spaces than SBA(P) for coating TEPA. In the case that using the as-synthesied PEM with the expanded pore to support TEPA as mentioned above, the corresponding capacity can thus be elevated to 214 mg g^{-1}. On the basis of these results, it is safe to conclude that establishing the optimal dispersion of adsorptive sites is the vital factor to improve the cffienciy of amine-containing mesoporous CO_2 capturer. For this purpose the tiny pore is required to disperse amine so that the baisc guest can be evenly coated rather than interacted on the pore wall. It is very difficult, if not impossible, for the assemble silica to form hierarchical structure with the mesoporous channel consisting the divided sub-nm size tiny pores, but the preserved micelles can compensate this limitation. For this reason, the pores with nm size such as that of SBA-15 or MCM-41 are inferior to that with sub-nm size like that in SBA(P) or AM in dispersing amine, since these as-synthesized composites actually possess the needed hierarchical structure.

In Recent Advances in Post-Combustion CO2 Capture Chemistry; Attalla, M.;
ACS Symposium Series; American Chemical Society: Washington, DC, 2012.

Downloaded by UNIV OF DELAWARE MORRIS LIB on June 14, 2012 | http://pubs.acs.org
Publication Date (Web): May 3, 2012 | doi: 10.1021/bk-2012-1097.ch016

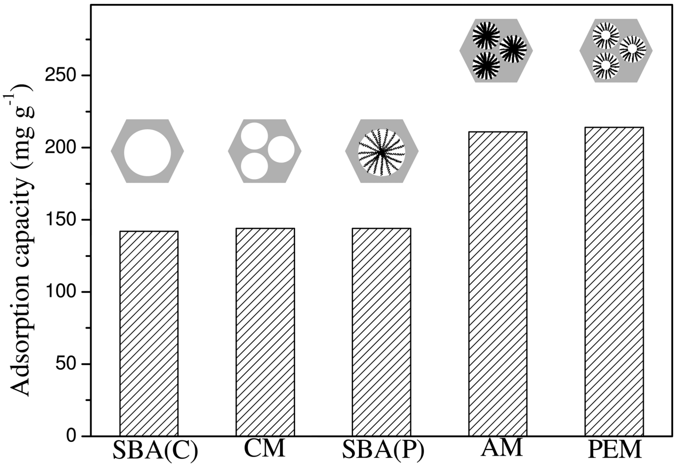

Figure 4. Influence of template state on the CO_2 adsorption by SBA-15 and MCM-41 composites, the weight percentage of TEPA in the composites was 50 wt.-%.

One-Pot Synthesis of Amine-Modified Meso-Structured Monolith CO_2 Adsorbent

Potential industrial application requires the new adsorbents of CO_2 with the advantage of low synthesis cost, high adsorptive capability and the convenience in use. Nonehteless, most of the CO_2 adsorbents derived from molecular sieves are powder-like materials, and thus they are difficult to be applied in gas stream to capture CO_2 so that a lot of effort has been devoted to develop the porous silica materials with mold appearance (*41–44*). We try to combine the synthesis of the silica support, dispersion of TEPA and molding of the products into one-pot process, preparing the amine *in situ* coated meso-structured silica monolith. Utilizing TEPA as the alkali additive along with the organic additive ether (*25*), we alter the composition of initial reaction mixture to control the hydrolysis and condensation of silicate precursor, in order to obtain the mesoporous monolith with adequate mechanical intension and high efficiency in CO_2 adsorption. CTAB was used in the synthesis as template and finally a quarter of the mother solution was remained with solid product, air-dried for several days to get the sample of TSn, where n meant the added amount of TEPA. As expected, TSn composites had the considerable mechanical strength; they were crushed but not pulverized under the press of 65 N. The monolith TS2.2 was proven to be safely used below the pressure of 0.64 MPa cm^{-2}, and TS1.2 could be used as a CO_2 adsorbent under the pressure of 0.44 MPa cm^{-2}.

In the CO_2-TPD test of TSn composites, two strong peaks appeared around 69 °C and 89 °C together with a weak one near 48 °C (Figure 5). For TS1.6 and

TS2.8 samples, two strong peaks shifted to 74-77 °C and 90-95 °C, respectively, but all of the trapped CO_2 could be desorbed at 100 °C. TS1.2 sample adsorbed the CO_2 of 171 mg g^{-1} at 75 °C, same as that trapped by the TEPA (40%) impregnated as-prepared MCM-41 (*21*). In the cyclic adsorption of CO_2, TS1.2 possessed the ability of 157 mg g^{-1} in 5th cycle adsorption, equaling to 92% of the primary capacity (170 mg g^{-1}). This values is comparable to that of TEPA impregnated as-synthesized SBA-15 and MCM-41 where SBA(P)-50 and AM-50 preserved the 87% of the original adsorptive capability under the same experimental conditions (*20*, *21*). According to the TG-DSC analysis (*25*), TS1.2 sample was able to complete CO_2 adsorption within 8 min, giving the adsorptive velocity of 19.7 mg g^{-1} min^{-1}. However, it contained less TEPA (2.06 mmol g^{-1}) than TS1.6 (2.16 mmol g^{-1}), TS2.2 (2.28 mmol g^{-1}), and TS2.8 samples (2.70 mmol g^{-1}) though it really captured more CO_2 than them, which originates from the particular structure of TS1.2 support. In case that these composites were calcined at 550 °C, TS1.2 exhibited the largest surface (811 m^2 g^{-1}) and pore volume (1.01 cm^3 g^{-1}), which redound to disperse TEPA. On the other hand, these calcined samples of TS0.6, TS1.2, TS1.6 and TS2.2 had different micro morphologies; template-free TS0.6 looked like the aggregation of spheres, and the regular sphere originated from the emulsion system used in synthesis. Calcined TS1.2 exhibited similar morphology of collective spheres (Figure 6). Likewise, TS1.6 sample possessed an aggregation-like morphology consisting of various distorted sphere-like hollow particles. These phenomena imply the important role played by the sphere-like structure in the adsorption of CO_2 by amine-dispersed composites. However, calcined TS2.2 composite had a cascade-like one in which many tiny particles formed the accidented surface (*25*). Variation of morphologies is caused by different TEPA proportion in the initial synthetic mixture, since the viscosity and amphipathy of TEPA strongly affect the oil in water emulsion system and change the aggregation of silicate primary particles. The TEPA additive in the mixture also alters the pore structure of the final composites: when the large amount of TEPA is used to synthesize meso-structured monolith, the amine can aggregates on the external surface of micelles to cause the formation of micropore in the silica wall (*25*). Among various compositions of the initial mixture used in the synthesis, the raw material ratio of TS1.6 sample was proven to be favorable producing a relatively ordered structure in the monolith, but TS1.6 composite did not have the highest capacity in the CO_2 adsorption. Contrarily, TS1.2 lacked the symbol of ordered structure in its XRD pattern, but it captured more CO_2 than TS1.6 thanks to its larger surface area and pore volume. This phenomenon indicates the complexity in the design of new CO_2 adsorbent.

Table 1 summarizes the synthesis, surface area and CO_2 adsorption capacity of amine-loaded mesoporous silica adsorbents. Among them some composites consist of the original template micelles inside their channels to lower their cost, promote the dispersion of amine guest and elevate the adsorption efficiency. In the case of loading with amine of 50 wt.-%, they usually exhibit the high capability of adsorbing CO_2 in the range of 144-214 mg g^{-1} at 75 °C, reaching the adsorption efficiency of 13.4-20.5%, and desorb all of the adsorbed CO_2 at 100 °C, achieving the desorption efficiency of 100%.

Downloaded by UNIV OF DELAWARE MORRIS LIB on June 14, 2012 | http://pubs.acs.org
Publication Date (Web): May 3, 2012 | doi: 10.1021/bk-2012-1097.ch016

Downloaded by UNIV OF DELAWARE MORRIS LIB on June 14, 2012 | http://pubs.acs.org
Publication Date (Web): May 3, 2012 | doi: 10.1021/bk-2012-1097.ch016

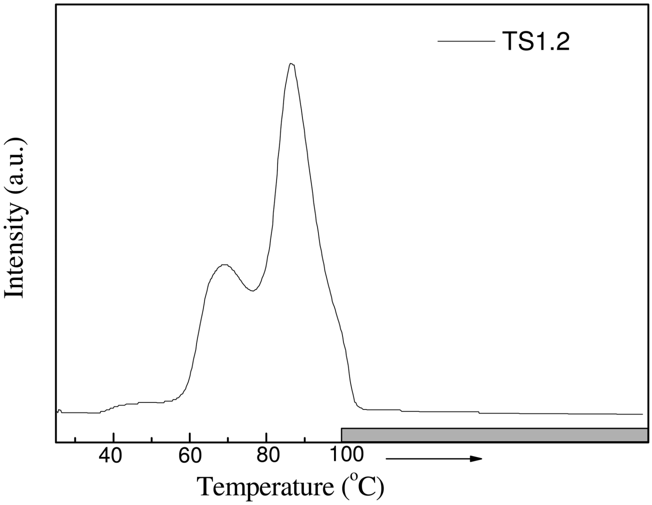

Figure 5. CO_2-TPD profile of TS1.2 sample performed at the rate of 2.5 °C min^{-1} from 35 °C to 100 °C and held at 100 °C for 0.5h.

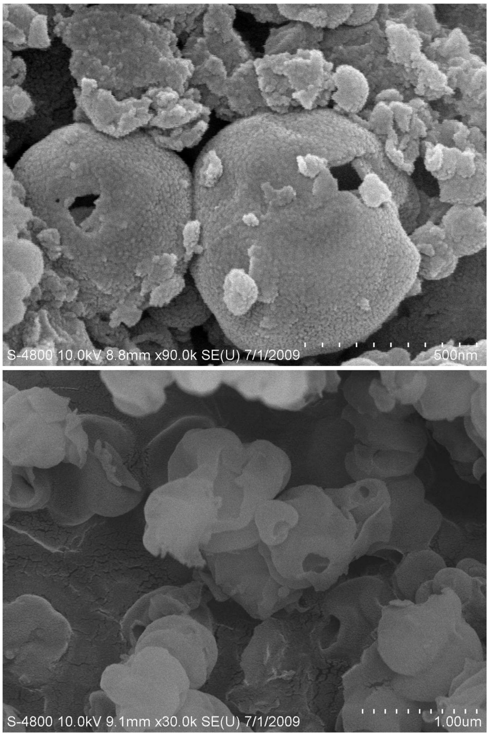
S-4800 10.0kV 8.8mm x90.0k SE(U) 7/1/2009
500nm
S-4800 10.0kV 9.1mm x30.0k SE(U) 7/1/2009
1.00um

Figure 6. SEM images of TS0.6 (upper) and TS1.2 (lower) samples.

Downloaded by UNIV OF DELAWARE MORRIS LIB on June 14, 2012 | http://pubs.acs.org
Publication Date (Web): May 3, 2012 | doi: 10.1021/bk-2012-1097.ch016

Table 1. The preparation, surface area and CO_2 adsorption of amine-modified mesoporous adsorbents CO_2 adsorption: 75°C, 1 atm; Regeneration of adsorbent: 100 °C.

Sample		*Preparation*	*S_{BET} (m^2 g^{-1})*	*TEPA loaded (wt.-%)*	*CO_2 adsorbed (mg g^{-1})[a]*
SBA-15	SBA(P)	Water-washed the as-synthesized SBA-15	345	30	62.6
				40	137
				50	144
				60	164
	SBA(C)	calcined in air at 550 °C for 6h	725	50	142
	SBA(CP)	Impregnation of SBA(C) with P123 of 40 wt %	100	50	128
	SP-30T-20D	50 wt.-% of amine (TEPA and DEA) loaded on SBA(P)	-	TEPA:DEA = 3:2[b]	163
MCM-41	AM	Water-washed as-synthesized MCM-41	16	30	120
				40	167
				50	211
				60	221
	CM	AM calcined in air at 550 °C for 6h to remove template	1342	50	144
	EM	AM extracted with ethanol at 30 °C for 2h to partially remove template	45	50	194
	DM	Small pore size MCM-41 prepared using DTAB as template	-	50	154

Continued on next page.

Downloaded by UNIV OF DELAWARE MORRIS LIB on June 14, 2012 | http://pubs.acs.org
Publication Date (Web): May 3, 2012 | doi: 10.1021/bk-2012-1097.ch016

Table 1. (Continued). The preparation, surface area and CO_2 adsorption of amine-modified mesoporous adsorbents CO_2 adsorption: 75°C, 1 atm; Regeneration of adsorbent: 100 °C.

Sample	*Preparation*	*S_{BET} (m^2 g^{-1})*	*TEPA loaded (wt.-%)*	*CO_2 adsorbed (mg g^{-1})[a]*
PEM	Pore enlarged MCM-41 extracted using ethanol at 30 °C for 2h to remove TMB	76	50	214
M(AS)	impregnating CTAB of 50 wt.-% into CM sample	-	50	155
TS1.2	the TEPA-modified meso-structured monolith synthesized in one-pot process	811[c]	39	170

[a] TEPA-modified-supports are used to adsorb CO_2, for which 75 mg sample was used to adsorb 1.78 mmole CO_2 in the influent. And the ratio of CO_2 to the adsorbent is 1044 mg g^{-1}. [b] mass ratio; [c] the composite was calcined at 550 °C.

Downloaded by UNIV OF DELAWARE MORRIS LIB on June 14, 2012 | http://pubs.acs.org
Publication Date (Web): May 3, 2012 | doi: 10.1021/bk-2012-1097.ch016

The Synthesis and CO_2 Adsorption Performance of Mesoporous Superbasic Materials

Amine-coating CO_2 adsorbents have their limitation in the application at high temperature due to the volatilization of the basic guest, no matter it was encapsulated in mesoporous silica or capsules (*20*, *21*, *44*, *45*). Consequently we try to develop another CO_2 capturer based on strong basic or superbasic mesoporous materials. In another word, we try to replace the amine guest with some basic oxides and form the new guest-host CO_2 adsorbent. Adsorption and catalysis by solid strong bases have been applied for many processes in chemical industry (*46*), but solid superbases are highly desired though lots of effort have been contributed on the synthesis of new superbases (*47–50*). Basic zeolites and related crystalline molecular sieves have the micrпохous pores with sub-nanometer scale, which prevents bulky molecules from reaching the active sites inside the channels (*51*). Contrarily, mesotextured materials have larger surface areas and pore volumes than zeolite (*52*), providing the competitive candidates to develop new superbases. Due to the difficulty in synthesis of mesoporous magnesia or calcium oxide, it is impossible to get the mesoporous super base through simply heating the mesoporous alkaline earth metal oxide in vacuum. Thus, loading basic guest on mesoporous support becomes the only choice. Apart from their high costs, mesoporous alumina or mesoporous zirconia has a relatively low stability therefore we have to seek another mesoporous support materials.

Mesoporous silica is the cheapest one among various mesoporous materials, but silica is easily corroded by alkali metal oxide such as KOH. We use magnesia interlayer to coat on the silica framework, preparing the SBA-15 wrapped with a layer of MgO through one-pot method (*53*): the additive of acetate salt was put into the mother solution in the synthesis of SBA-15, and finally the liquid was evaporated with stirring at 80 °C; through this manner the SBA-15 was *in-situ* coated with magnesia. In fact, incorporation of magnesia in SBA-15 occurs in the evaporation step. If the sample was filtrated and water-washed as usual, it would be free of magnesium (*26*). Magnesia could be well dispersed on SBA-15 up to 30 wt.-%, higher than that by impregnation (20 wt.-%), which enabled the composite to adsorb tens times more CO_2 than SBA-15 and desorbed the CO_2 at 200 °C or above (*53*). Once we disperse the neutral salt KNO_3 on the special support followed by thermal activation to converse the precursor to potassium oxide nanoparticles (*26*), the new superbasic material is produced. This composite possesses the mesoporous structure of SBA-15 and a relatively large surface area that is beneficial for succeeding adsorption. At the same time, an unusual strong basicity with the basic strength (H_-) of 27 appears on the mesoporous composite. The *in situ* coated magnesia consumes the silanol groups of SBA-15 to form the passivation layer, preventing the basic potassium guests from corroding the mesostructure of SBA-15. SBA-15 itself had a small desorption round 80 °C in CO_2-TPD test, but new CO_2 desorption emerged around 600 °C on the composite loaded with KNO_3 of 20 wt.-% (*26*).

To directly generate superbasic sites on mesoporous silica, we select guest to adjust the interaction between the guest and host in order to protect the structure of host. Adjusting the interaction of host-guest is very important because too

In Recent Advances in Post-Combustion CO2 Capture Chemistry; Attalla, M.;
ACS Symposium Series; American Chemical Society: Washington, DC, 2012.

Downloaded by UNIV OF DELAWARE MORRIS LIB on June 14, 2012 | http://pubs.acs.org
Publication Date (Web): May 3, 2012 | doi: 10.1021/bk-2012-1097.ch016

weak host-guest interaction may lead to the difficulty in both dispersion and decomposition of base precursor (*54*), whereas the too strong interaction will damage the mesostructure of host. Alkaline earth metal oxides have the higher electronegativity and Tammann temperature than that of alkali metal oxides, this may affect the host-guest interaction in the resulting composite when they are loaded on support. Again, the electronegativity of metal cation in oxide will affect the interaction between the guest oxide and the support. The value of alkaline earth metal ions (4.45-6.55) is larger than that of alkali metal ions (2.37-2.79), so the metal-oxygen contact in the guest oxide is strong, leading to a weaker interaction of the guest oxide with the host during the thermal activation. The mobility of supported species also affects the structure of the host. Alkaline earth metal oxides have the Tammann temperature higher than the activation temperature (550 °C), so that they will be relatively "stable" in the activation, but alkali metal oxide is very "active" to diffuse or transfer in the pores of host and corrodes the siliceous host during the activation. We tried to introduce calcium nitrate as the guest to modify mesoporous silica SBA-15, by impregnation with solution of $Ca(NO_3)_2$. As expected, $Ca(NO_3)_2$ could be well dispersed on SBA-15 up to 20 wt.-%. And the structure of mesoporous silica was preserved in the composite after activation at high temperature (*27*). The high basic strength of $H_- = 27$ emerged on SBA-15 when the loading amount of $Ca(NO_3)_2$ reached in the range of 20 - 40 wt.-%. CO_2-TPD results confirmed the formation of very strong basic sites, in which new CO_2 desorption appeared at about 370 and 630 °C, and the latter was abundant. Through the similar procedure, super basicity ($H_- = 27.0$) was detected on the composites supported with $Sr(NO_3)_2$ and $Ba(NO_3)_2$ (*27*).

γ-type alumina is a well-known support for a variety of solid superbase (*55–57*). And the occurrence of mesoporous alumina affords a good opportunity to prepare the new mesoporous superbasic materials (*58–60*). However, the stability of mesoporous alumina materials is relatively poor, and their structure will be damaged in the post-synthesis modification. This weak point seriously limits the application of mesoporous alumina in preparing solid super bases. We try to assemble the potassium modified mesoporous γ-alumina by one-pot method. We use K_2CO_3 to adjust the pH value of synthetic system, and get the KNO_3 coated mesoporous boehmite (AlOOH) as the intermediate, and then convert it to the final composite in calcination (*28*). This new route consists of two key-points. The first is the artful application of K_2CO_3, which plays double roles in the synthesis, not only adjusting the pH value of the system to promote the hydrolysis of $Al(NO_3)_3$, but also producing the base precursor KNO_3 at the same time. At this step, KNO_3 coated mesoporous boehmite, KMA-B, is produced. The second is the multifunction of calcination process, in which the conversion of both KNO_3 and boehmite take place, and the strong basic species K_2O directly covers on the *in-situ*-formed γ-Al_2O_3. As is evident from TG-MS analysis (*28*), the dehydration of boehmite to γ-Al_2O_3 occurred from 150 to 500 °C, and the major of supported KNO_3 was decomposed at 500 and 640 °C, mainly producing NO and O_2 rather than NO_2. As the result, the composites denoted as KMA(*n*)-γ was obtained, and the basic sites with high strength (H_-) of 27.0 emerged on the samples with K/Al ratio ranged from 0.11 to 0.27. The results of CO_2-TPD experiment confirmed the generation of strong basic sites on KMA-γ samples, because the large desorption of CO_2 appeared at about 200 °C along with a broad peak centered at 600 °C (*28*). Contrarily, mesoporous alumina itself possessed a weak ability to adsorb CO_2 and gave the desorption around 100 °C in CO_2-TPD profile. These superbasic materials offer the valuable cadidate for the capture of CO_2 at high temperature.

Conclusions

Fossil fuels will be the primary energy source for a quite long period, so the capture and separation of CO_2 in the combustion flue gas and other industrial effluents will also be the serious challenge facing the scientists in the world. Among current technologies used to reduce the emission of CO_2, solid CO_2 adsorbents, especially the host-guest materials are still the promising ones. Mesoporous silica is a versatile and cost-effective support with symmetrical channel, in which either amine or basic metal oxide can be well dispersed to form the CO_2 trapper with high efficiency. Based on our recent researches, it is safe to make following conclusive remarks:

(1) The as-synthesized mesoporous materials can be employed to support amine, forming the efficient CO_2 adsorbent, which not only saves the energy and time to remove template, but also elevates the atomic utilization of these micelles.

(2) The meso-structured monolith CO_2 adsorbents, together with their sphere-like hollow particle, pave a new way to prepare the novel CO_2 trapper with both the high efficiency and the convince in use.

(3) Alkali and alkaline earth metal oxides modified mesoporous materials can have the superbasic sites to adsorb CO_2 at 200 °C or above, which provides a value clue to prepare the adsorbents for trapping CO_2 at high temperature. In order to elevate the actual performance of host-guest CO_2 adsorbents, however, how to decrease the proportion of host meanwhile increasing the ratio of active guest in the composites is of key importance but a long way to go. Furthermore, the application of solid CO_2 adsorbent is often limited by its capacity, especially in the adsorption at the relatively high temperature. So, it is better to endow the adsorptive material with catalytic activity, and the trapped CO_2 can be *in situ* converted. Through the strategy of combining adsorption and catalysis in the functional material, it is hopeful to control the CO_2 emission more efficiently.

Acknowledgments

Financial support from NSF of China (20773601, 20873059 and 21173117), Grant 2008AA06Z327 from the 863 Program of the MST of China, and Analysis Center of Nanjing University is gratefully acknowledged.

Downloaded by UNIV OF DELAWARE MORRIS LIB on June 14, 2012 | http://pubs.acs.org
Publication Date (Web): May 3, 2012 | doi: 10.1021/bk-2012-1097.ch016

Downloaded by UNIV OF DELAWARE MORRIS LIB on June 14, 2012 | http://pubs.acs.org
Publication Date (Web): May 3, 2012 | doi: 10.1021/bk-2012-1097.ch016

References

1. Melillo, J. M.; Mcguire, A. D.; Kicklighter, D. W.; Moore, B.; Vorosmarty, C. J.; Schloss, A. L. *Nature* **1993**, *363*, 234–240.
2. Rinker, E. B.; Ashour, S. S.; Sandall, O. C. *Ind. Eng. Chem. Res.* **2000**, *39*, 4346–4356.
3. Chakma, A. *Energy Convers. Manage.* **1997**, *38*, 51–56.
4. Wilson, M.; Tontiwachwuthikul, P.; Chakma, A.; Idem, R.; Veawab, A.; Aroonwilas, A.; Gelowitz, D.; Barrie, J.; Mariz, C. *Energy* **2004**, *29*, 1259–1267.
5. Siriwardane, R. V.; Shen, M. S.; Fisher, E. P. *Energy Fuel* **2003**, *17*, 571–576.
6. Hutson, N. D. *Chem. Mater.* **2004**, *16*, 4135–4143.
7. Siriwardane, R. V.; Clark, R.; Shen, M.; Simonyi, T. *Energy Fuels* **2007**, *21*, 2088–2097.
8. Walton, K. S.; Millward, A. R.; Dubbeldam, D.; Frost, H.; Low, J. J.; Yaghi, O. M.; Snurr, R. Q. *J. Am. Chem. Soc.* **2008**, *130*, 406–407.
9. Banerjee, R.; Phan, A.; Wang, B.; Knobler, C.; Furukawa, H.; O'Keeffe, M.; Yaghi, O. M. *Science* **2008**, *319*, 939–943.
10. Gray, M. L.; Soong, Y.; Champagnea, K. J.; Baltrus, J.; Stevens, R. W.; Toochinda, P.; Chuang, S. S. C. *Sep. Purif. Technol.* **2004**, *35*, 31–36.
11. Filburn, T.; Helble, J. J.; Weiss, R. A. *Ind. Eng. Chem. Res.* **2005**, *44*, 1542–1548.
12. Satyapal, S.; Filburn, T.; Trela, J.; Strange, J. *Energy Fuel* **2001**, *15*, 250–255.
13. Leal, O.; Bolívar, C.; Ovalles, C.; Carcía, J. J.; Espidel, Y. *Inorg. Chim. Acta* **1995**, *240*, 183–200.
14. Satyapal, S.; Filburn, T.; Trela, J.; Strange, J. *Energy Fuels* **2001**, *15*, 250–255.
15. Chang, A. C. C.; Chuang, S. S. C.; Gray, M.; Soong, Y. *Energy Fuels* **2003**, *17*, 468–473.
16. Khatri, R. A.; Chuang, S. S. C.; Soong, Y.; Gray, M. *Ind. Eng. Chem. Res.* **2005**, *44*, 3702–3708.
17. Xu, X.; Song, C.; Andresen, J. M.; Miller, B. G.; Scaroni, A. W. *Microporous Mesoporous Mater.* **2003**, *62*, 29–45.
18. Franchi, R. S.; Harlick, P. J. E.; Sayari, A. *Ind. Eng. Chem. Res.* **2005**, *44*, 8007–8013.
19. Harlick, P. J. E.; Sayari, A. *Ind. Eng. Chem. Res.* **2006**, *45*, 3248–3255.
20. Yue, M. B.; Chun, Y.; Cao, Y.; Dong, X.; Zhu, J. H. *Adv. Funct. Mater.* **2006**, *16*, 1717–1722.
21. Yue, M. B.; Sun, L. B.; Cao, Y.; Wang, Y.; Wang, Z. J.; Zhu, J. H. *Chem. Eur. J.* **2008**, *14*, 3442–3451.
22. Yue, M. B.; Sun, L. B.; Cao, Y.; Wang, Z. J.; Wang, Y.; Yu, Q.; Zhu, J. H. *Microporous Mesoporous Mater.* **2008**, *114*, 74–81.
23. Xu, X. C.; Song, C. S.; Miller, B. G.; Scaroni, A. W. *Ind. Eng. Chem. Res.* **2005**, *44*, 8113–8119.
24. Xu, X.; Song, C.; Andresen, J. M.; Miller, B. G.; Scaroni, A. W. *Microporous Mesoporous Mater.* **2003**, *62*, 29–45.

25. Wen, J. J.; Gu, F. N.; Wei, F.; Zhou, Y.; Lin, W. G.; Yang, J.; Yang, J. Y.; Wang, Y.; Zou, Z. G.; Zhu, J. H. *J. Mater. Chem.* **2010**, *20*, 2840–2846.
26. Wu, Z. Y.; Jiang, Q.; Wang, Y. M.; Wang, H. J.; Sun, L. B.; Shi, L. Y.; Xu, J. H.; Wang, Y.; Chun, Y.; Zhu, J. H. *Chem. Mater.* **2006**, *18*, 4600–4608.
27. Sun, L. B.; Kou, J. H.; Chun, Y.; Yang, J.; Gu, F. N.; Wang, Y.; Zhu, J. H.; Zou, Z. G. *Inorg. Chem.* **2008**, *47*, 4199–4208.
28. Sun, L. B.; Yang, J.; Kou, J. H.; Gu, F. N.; Chun, Y.; Wang, Y.; Zhu, J. H.; Zou, Z. G. *Angew. Chem., Int. Ed.* **2008**, *47*, 3418–3421.
29. Delaney, W.; Knowles, G.; Chaffee, A. *Prepr. Symp. − Am. Chem. Soc., Div. Fuel Chem.* **2002**, *47*, 65–66.
30. Kruk, M.; Jaroniec, M.; Ko, C. H.; Ryoo, R. *Chem. Mater.* **2000**, *12*, 1961–1968.
31. Zhao, D. Y.; Feng, J. L.; Huo, Q. S.; Melosh, N.; Fredrickson, G. H.; Chmelka, B. F.; Stucky, G. D. *Science* **1998**, *279*, 548–552.
32. Ryoo, R.; Ko, C. H.; Kruk, M.; Antochshuk, V.; Jaroniec, M. *J. Phys. Chem. B* **2000**, *104*, 11465–11471.
33. Delaney, W.; Knowles, G.; Chaffee, A. *Prepr. Symp. − Am. Chem. Soc., Div. Fuel Chem.* **2002**, *47*, 65–66.
34. Caplow, M. *J. Am. Chem. Soc.* **1968**, *90*, 6795–6803.
35. Sayari, A.; Kruk, M.; Jaroniec, M.; Moudrakovski, I. L. *Adv. Mater.* **1998**, *10*, 1376–1379.
36. Ottaviani, M. F.; Moscatelli, A.; Giscard, D. D.; Renzo, F. D.; Kooyman, P. J.; Alonso, B.; Galarneau, A. *J. Phys. Chem. B* **2004**, *108*, 12123–12129.
37. Sayari, A. *Angew. Chem., Int. Ed.* **2000**, *39*, 2920–2922.
38. Denoyel, R.; Rey, E. S. *Langmuir* **1998**, *14*, 7321–7323.
39. Zhao, H.; Nagy, K. L.; Waples, J. S.; Vance, G. F. *Environ. Sci. Technol.* **2000**, *34*, 4822–4827.
40. Xu, X.; Song, C.; Andresen, J. M.; Miller, B. G.; Scaroni, A. W. *Energy Fuels* **2002**, *16*, 1463–1469.
41. Babin, J.; Iapichella, J.; Lefevre, B.; Biolley, C.; Bellat, J. P.; Fajulaa, F.; Galarneau, A. *New J. Chem.* **2007**, *31*, 1907–1917.
42. Huo, Q. S.; Feng, J. L.; Schuth, F.; Stucky, G. D. *Chem. Mater.* **1997**, *9*, 14–17.
43. Lin, H. P.; Mou, C. Y. *Acc. Chem. Res.* **2002**, *35*, 927–935.
44. Chen, C.; Yang, S. T.; Ahn, W. S.; Ryoo, R. *Chem. Commun.* **2009**, 3627–3629.
45. Qi, G.; Wang, Y.; Estevez, L.; Duan, X.; Anako, N.; Park, A.-H. A.; Li, W.; Jones, C. W.; Giannelis, E. P. *Energy Environ. Sci.* **2011**, *4*, 444–452.
46. Ono, Y.; Baba, T. *Catal. Today* **1997**, *38*, 321–334.
47. Arumugam, S.; Verkade, J. G. *J. Org. Chem.* **1997**, *62*, 4827–4828.
48. Matsuhashi, H.; Klabunde, K. J. *Langmuir* **1997**, *13*, 2600–2602.
49. Matsuhashi, H.; Oikawa, M.; Arata, K. *Langmuir* **2000**, *16*, 8201–8205.
50. Li, Z. J.; Prescott, H. A.; Deutsch, J.; Trunschke, A.; Liske, H.; Kemnitz, E. *Catal. Lett.* **2004**, *92*, 175–180.
51. Hattori, H. *Chem. Rev.* **1995**, *95*, 537–550.
52. Soler-Illia, G. J. A. A.; Sanchez, C.; Lebeau, B.; Patarin, J. *Chem. Rev.* **2002**, *102*, 4093–4138.

Downloaded by UNIV OF DELAWARE MORRIS LIB on June 14, 2012 | http://pubs.acs.org
Publication Date (Web): May 3, 2012 | doi: 10.1021/bk-2012-1097.ch016

53. Wei, Y. L.; Wang, Y. M.; Zhu, J. H.; Wu, Z. Y. *Adv. Mater.* **2003**, *15*, 1943–1945.
54. Sun, L. B.; Gu, F. N.; Chun, Y.; Yang, J.; Wang, Y.; Zhu, J. H. *J. Phys. Chem. C* **2008**, *112*, 4978–4985.
55. Ono, Y. *J. Catal.* **2003**, *216*, 406–415.
56. Zhu, J. H.; Wang, Y.; Chun, Y.; Wang, X. S. *J. Chem. Soc., Faraday Trans.* **1998**, *94*, 1163–1169.
57. Wang, Y.; Huang, W. Y.; Chun, Y.; Xia, J. R.; Zhu, J. H. *Chem. Mater.* **2001**, *13*, 670–677.
58. Yang, P.; Zhao, D.; Margolese, D. I.; Chmelka, B. F.; Stucky, G. D. *Nature* **1998**, *396*, 152–155.
59. Zhang, Z.; Pinnavaia, T. J. *J. Am. Chem. Soc.* **2002**, *124*, 12294–12301.
60. Cejka, J. *Appl. Catal., A* **2003**, *254*, 327–338.

Downloaded by UNIV OF DELAWARE MORRIS LIB on June 14, 2012 | http://pubs.acs.org
Publication Date (Web): May 3, 2012 | doi: 10.1021/bk-2012-1097.ch016

Downloaded by UNIV OF DELAWARE MORRIS LIB on June 14, 2012 | http://pubs.acs.org
Publication Date (Web): May 3, 2012 | doi: 10.1021/bk-2012-1097.ch017

Chapter 17

Energy Performance of New Amine-Based Solvents for CO_2 Capture from Blast Furnace Gas

K. Goto,[*] S. Kodama, H. Okabe, and Y. Fujioka

Chemical Research Group, Research Institute of Innovative Technology for the Earth (RITE), 9-2 Kizugawadai, Kizugawashi, Kyoto 619-0292, Japan
[*]goto.ka@rite.or.jp

Energy performances of new amine-based solvents were evaluated in this chapter by three different approaches; a plant test in a 1 $t_{\text{-CO2}}$/d facility, a heat and mass balance analysis based on an equilibrium stage model and a process simulation with Aspen Plus®. The solvents were amine aqueous solutions (Solvent A and Solvent B) developed by RITE in formulation of amine mixtures with 2-Isopropylaminoethanol and additives. A thermal energy requirement to regenerate a solvent in CO_2 removal from blast furnace gas, which was 20 $kPa_{\text{-CO2}}$ in partial pressure, was evaluated in the analyses. The results of the plant test show that thermal energy requirements of Solvent A and Solvent B at the 90% CO_2 recovery were 3.6 GJ/$t_{\text{-CO2}}$ and 4.0 GJ/$t_{\text{-CO2}}$ respectively. Also, the heat and mass balance analysis of equilibrium condition estimates 2.48 GJ/$t_{\text{-CO2}}$ for Solvent A and 2.33 GJ/$t_{\text{-CO2}}$ for Solvent B. To evaluate a potential of each solvent, the process simulation was done in consideration of the optimized process condition, such as installing an intercooler in an absorber and assuming low heat loss from equipments. The result shows that both Solvent A and Solvent B can lead to excellent energy performance of 2.5~2.6 GJ/$t_{\text{-CO2}}$.

1. Introduction

CO_2 capture by chemical absorption for “CO_2 capture and storage (CCS)”, an effective countermeasure against global warming, is regarded as a state-of-art

In Recent Advances in Post-Combustion CO2 Capture Chemistry; Attalla, M.;
ACS Symposium Series; American Chemical Society: Washington, DC, 2012.

Downloaded by UNIV OF DELAWARE MORRIS LIB on June 14, 2012 | http://pubs.acs.org
Publication Date (Web): May 3, 2012 | doi: 10.1021/bk-2012-1097.ch017

technology. Currently, its applications into power plants and industrial CO_2 emission sources are broadly studied. One of key research objectives on the CO_2 capture by chemical absorption is to reduce thermal energy requirement to regenerate a solvent, which is the major part of energy consumption in CO_2 capture. We need to properly evaluate the thermal energy requirement of a solvent for developments of high-performance solvents and energy-saving CO_2 capture.

In the previous papers, Mimura et al. (*1*) studied fundamentals of amine-based solvents in a laboratory and evaluated the solvents in $2t_{-CO_2}$/d pilot plant. They firstly investigated the features of the solvents, such as absorption rate and heat of reaction, and then they evaluated CO_2 capture performance and thermal energy requirement of the solvents in the pilot plant. Hoff et al. (*2*) carried out solvent selection for a post combustion CO_2 capture and characterized solvents by measurements of mass transfer kinetics and equilibrium. In their work, thermal energy requirement was calculated on the basis of the measured equilibrium data. Porcheron et al. (*3*) presented high throughput screening method of amine thermodynamic properties, which was used to calculate thermal energy requirement in their process simulation technique. Mangalaplly et al. (*4*) carried out pilot plant experiments of post combustion CO_2 capture by reactive absorption with Monoethanolamine (MEA) and new solvents. They evaluated solvent performances by the process simulator to compare experimental results with simulation.

RITE has conducted development of high-performance solvents for CO_2 capture from blast furnace gas (BFG) in the steelworks. The steel industry is a major CO_2 emission source as well as power industry. The blast furnace gas is produced at the absolute pressure of about 0.4 MPa, but it is pretreated to use as fuel in the steelworks. The blast furnace gas is finally atmospheric and its CO_2 partial pressure is about 20 kPa_{-CO_2}, which is similar to a post combustion gas. That is, Figure 1 is a process flow diagram of CO_2 capture from BFG. Authors and colleagues have investigated aqueous amine solutions and developed novel solvents (Solvent A and Solvent B) in a previous study (*5*). They were the amine-based mixture solvents containing 2-Isopropylaminoethanol (IPAE) as a major component.

In this study, we evaluated the amine-based solvents by three different approaches; a plant test in a 1 t_{-CO_2}/d facility, a heat and mass balance analysis based on equilibrium stage model and a process simulation with Aspen Plus®. In addition, the potential of the solvents to establish low thermal energy requirement was investigated in the process simulation.

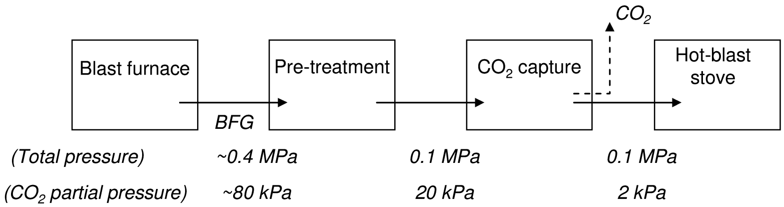

Figure 1. CO_2 capture from BFG and gas pressure conditions.

Downloaded by UNIV OF DELAWARE MORRIS LIB on June 14, 2012 | http://pubs.acs.org
Publication Date (Web): May 3, 2012 | doi: 10.1021/bk-2012-1097.ch017

2. Evaluation Methods

2.1. Novel Amine-Based Solvents

The Solvent A and Solvent B developed by RITE before (*5*) were investigated in this study to clarify the solvent performance for CO_2 capture from BFG. Both the solvents were the mixtures of IPAE and additives. Those had features of low heat of reaction and moderately high absorption rate, and large capacity of CO_2 capture.

Figure 2 shows the relation between heat of reaction and absorption rate. The absorption rates were obtained from a screening test using a 250ml glass scrubbing bottle. They were relative values to compare the conventional amines (MEA, DEA: Diethanolamine, MDEA: Methyldiethanolamine). The heat of reaction was obtained by a reaction calorimetry. From the results of the screening test and the calorimetry, we found that there were trade-off relation between the heat of reaction and the absorption rate, but an aqueous IPAE solution and two novel solvents overcame the trade-off relation.

In addition, the solvents had a large capacity of CO_2 capture as shown in Figure 3. Vapor-liquid equilibrium (VLE) was measured by a semi-batch reactor in the laboratory. Its measurement procedure was presented at the previous paper (*6*). As shown in Figure 3, new solvents had a larger capacity of CO_2 capture than MEA in the case of 40 °C absorption and 120 ° C desorption. CO_2 loading at 40 °C was around 0.7 mol_{-CO2}/mol_{-amine} at 10~20 kPa_{-CO2} in CO_2 partial pressure.

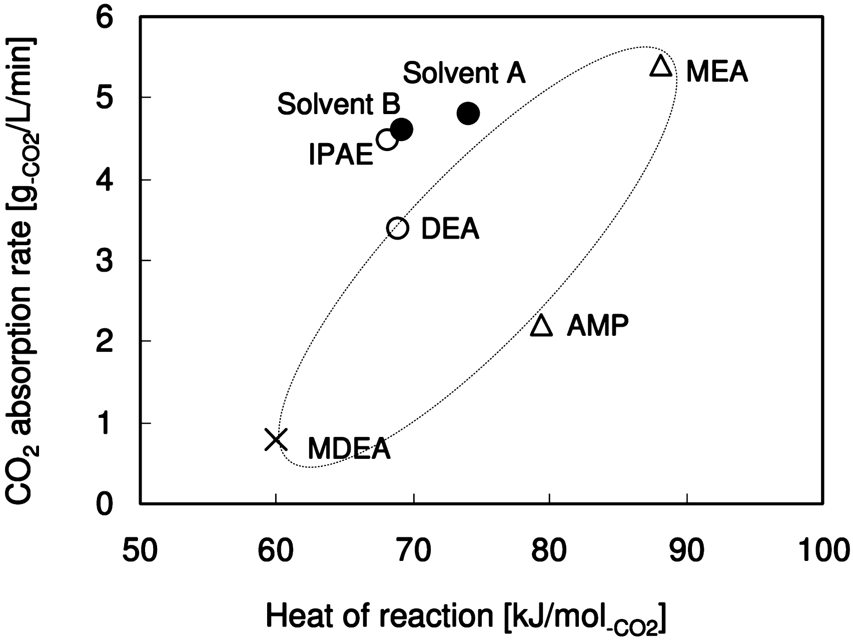

Figure 2. Development of novel amine solvents (5)

Downloaded by UNIV OF DELAWARE MORRIS LIB on June 14, 2012 | http://pubs.acs.org
Publication Date (Web): May 3, 2012 | doi: 10.1021/bk-2012-1097.ch017

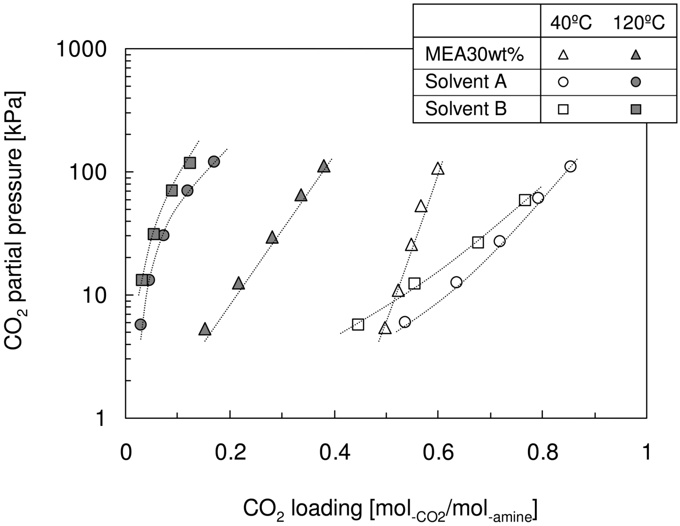

Figure 3. Vapor-liquid equilibrium of MEA and IPAE-based solvents

2.2. Plant Test

The new solvents were tested in a test plant (*5*) installed in Kimitsu works of Nippon Steel Corporation. Figure 4 shows the plant facility, which had one absorber column and one stripper column. The packing section of the absorber was 4.3 m in height and 0.27 m in diameter. The stripper was 2.1 m in height and 0.2 m in diameter. The plant capacity for CO_2 capture from BFG was up to about $1t_{-CO2}$/d. BFG of about 20 kPa_{-CO2} in CO_2 partial pressure, which was supplied from a factory gas line, was blown into the absorber. A BFG feed rate and a solvent circulation rate, a reboiler steam for CO_2 stripping and a stripper pressure were set as an input condition shown in Table 1. The process evaluation of the new solvent in the test plant was carried out in the condition of $55Nm^3/h$ in BFG flow rate.

One or two experimental conditions were investigated in one day. In the test operation, it took about 2 hours to achieve steady state. Research operation was kept for no less than 2 hours. Thermal energy requirement, which was defined as a reboiler heat duty to captured $1t_{-CO2}$, was evaluated by averaging process data and analyzing CO_2 loading of solvent samples. The effect of liquid-to-gas ratio (L/G) on CO_2 recovery and thermal energy requirement was experimentally investigated. Then, solvent evaluation was done at the operation condition of 90 % CO_2 recovery, which was defined as the ratio of removed CO_2 to supplied CO_2.

Downloaded by UNIV OF DELAWARE MORRIS LIB on June 14, 2012 | http://pubs.acs.org
Publication Date (Web): May 3, 2012 | doi: 10.1021/bk-2012-1097.ch017

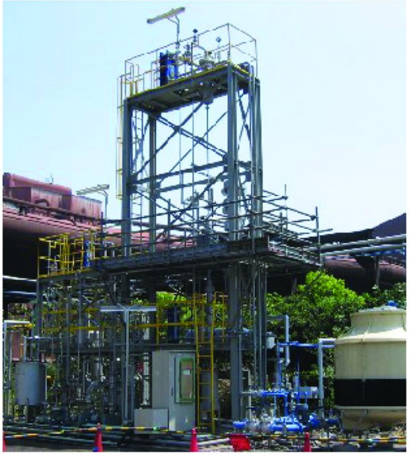

Figure 4. 1 $t_{\text{-}CO2}$/d test plant for CO_2 capture from BFG

Table 1. Experimental condition of the plant test

BFG flow rate	55	[Nm^3/h]
CO_2 partial pressure	20	[kPa]
Liquid-to-gas ratio	2~7	[L/Nm^3]
Absorber liquid inlet temperature	35	[°C]
Stripper bottom temperature	105~125	[°C]
Stripper pressure	0.03~0.15	[MPa gauge]
Reboiler steam feed rate	20~90	[kg/h]

2.3. Heat and Mass Balance Analysis

Thermal energy requirement is the critical factor for chemical absorption. It is defined as the reboiler heat duty divided by the amount of removed CO_2. It consists of the three energy consumptions (reaction, heat loss of solvent and heat loss of steam at stripper top) as shown in Figure 5, if the heat loss from CO_2 capture plant to atmosphere is ignored. This heat balance can be described as eq.(1).

$$Q_T = Q_V + Q_H + Q_R \qquad [\text{MJ/kg}_{\text{-CO2}}]\ (=[\text{GJ/t}_{\text{-CO2}}] \qquad \text{eq.(1)}$$

$$Q_R = \frac{\Delta H_R}{M_{CO2}} \qquad \text{eq.(2)}$$

$$Q_H = W \cdot \overline{Cp_L}\Delta T = \frac{1000/M_{CO2}}{\left(\alpha_{rich} - \alpha_{rich}\right)C_{amine}} \cdot \overline{Cp_L}\Delta T \qquad \text{eq.(3)}$$

$$Q_V = \frac{1000/M_{CO2}}{m^G_{CO2}}\left(m^G_{H2O}\Delta H_V + m^G_{CO2}\Delta H_{CO2}\right) \qquad \text{eq.(4)}$$

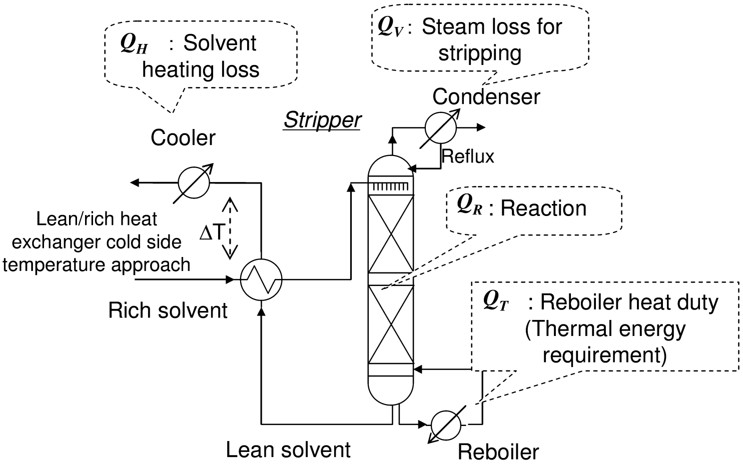
Q_H : Solvent heating loss
Q_V : Steam loss for stripping
Condenser
Stripper
Cooler
Reflux
Q_R : Reaction
Lean/rich heat exchanger cold side temperature approach
ΔT
Rich solvent
Q_T : Reboiler heat duty (Thermal energy requirement)
Lean solvent
Reboiler

Figure 5. Thermal energy requirement and heat consumptions of desorption.

Thermal energy requirement can be estimated with heat and mass balance analysis of the system including stripper and rich/lean heat exchanger (*7*). In this study, equilibrium stage model for stripper was firstly used to obtain the process data. After obtaining the process date of the stripper and the heat exchanger, the three heat consumptions defined in eq.(1) were estimated by the eq.(2), Eq.(3) and Eq.(4), respectively. Consequently, the thermal energy requirement could be evaluated.

The properties of new solvents were gathered from laboratory experiments. For example, heat of reaction and VLE data of a solvent. The heat of reaction for the new solvents was found in the previous paper (*5*) and the VLE data is shown in Figure 3. As for the stripper operation, the absolute pressure was 0.2 MPa and then bottom temperature was around 120 °C. Rich loading was decided as the value of an equilibrium condition at 50 °C in temperature and 20 kPa_{-CO2} in CO_2 partial pressure. This temperature was determined by considering the process data of the plant tests. The performance of the rich/lean heat exchanger was specified by temperature approach on the low temperature side. This was 10 °C in this analysis.

Downloaded by UNIV OF DELAWARE MORRIS LIB on June 14, 2012 | http://pubs.acs.org
Publication Date (Web): May 3, 2012 | doi: 10.1021/bk-2012-1097.ch017

Downloaded by UNIV OF DELAWARE MORRIS LIB on June 14, 2012 | http://pubs.acs.org
Publication Date (Web): May 3, 2012 | doi: 10.1021/bk-2012-1097.ch017

2.4. Process Simulation

In order to mathematically analyze a chemical absorption process, we have applied a process simulation program. This program calculates the stream compositions in the process, temperatures at process units, the necessary reboiler heat duty, and so on. The commercial process simulator, Aspen Plus®, was used for the simulation in this study after modification for the new solvents. The measurement data of equilibrium and heat of reaction for the new solvents were converted into property models in the process simulation. The modification was to take account into the properties of IPAE in the simulation. Correlations for thermodynamics and physical properties were replaced with our laboratory experiment data. A column model block, “Radfrac”, of Aspen Plus® was used.

The basic flowsheet configuration for the simulations is shown in Figure 6. The calculation specifics are as follows: Plant specifications such as packing heights and diameters were the same as the test plant shown in Figure 4. The packing material is FLEXIPAC 1Y HC (Koch-Glitsch). An intercooler was added into the simulation flowsheet to discuss the effect of that. The partially loaded solvent is brought out from the middle stage of the absorber column, cooled to 40 °C in a heat exchanger and returned to the column.

Four different cases of process simulation were done for each the new solvent as shown in Table 2. “Base” case was a simulation of the test plant operation which was conducted at around 90% CO_2 recovery. In this case, heat loss from the stripper was assumed as 10% of reboiler heat duty. “Case 1” was a trial of low liquid circulation to enhance solvent utilization efficiency. “Case 2” was the operation using the intercooler installed to the absorber. “Case 3” was a high heat-efficiency condition, in which heat loss from the stripper was changed from 10% to 5%. For all cases except for Case 1, calculation was done to obtain the thermal energy requirement at the condition of 90% CO_2 recovery. In the calculation of Case 2, the effect of reducing a solvent circulation on a CO_2 recovery was investigated.

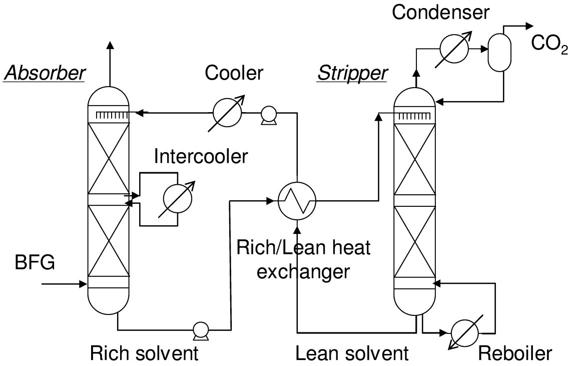

Figure 6. Process flowsheet configurations

Table 2. Case studies of process simulation

Base	*Simulation of 90% CO_2 recovery operation in the plant test*
Case 1	Low liquid circulation to enhance solvent utilization efficiency
Case 2	Intercooler to increase rich loading
Case 3	Reduction of heat loss from stripper (decrease from 10% of total reboiler heat duty to 5% of that)

Downloaded by UNIV OF DELAWARE MORRIS LIB on June 14, 2012 | http://pubs.acs.org
Publication Date (Web): May 3, 2012 | doi: 10.1021/bk-2012-1097.ch017

3. Results and Discussions

3.1. Plant Test

Figure 7 shows the plant test results of Solvent A. With decreasing L/G, thermal energy requirement became small but CO_2 recovery also decreased. At approximately 90% CO_2 recovery, the result was 3.6 GJ/$t_{\text{-CO2}}$ at 4 in L/G. As shown in Figure 8, the result of Solvent B was 4.0 GJ/$t_{\text{-CO2}}$ at 5 in L/G. The reason why Solvent B was inferior to Solvent A is that CO_2 capacity of Solvent B in VLE data was slightly smaller than that of Solvent A as shown in Figure 3. Also absorption rate of Solvent B may be lower than that of Solvent A.

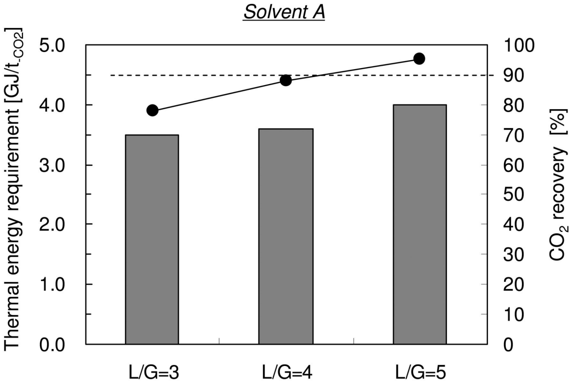

Figure 7. Experimental results of Solvent A in the test plant (bar chart: Thermal energy requirement, line plot: CO_2 recovery)

Downloaded by UNIV OF DELAWARE MORRIS LIB on June 14, 2012 | http://pubs.acs.org
Publication Date (Web): May 3, 2012 | doi: 10.1021/bk-2012-1097.ch017

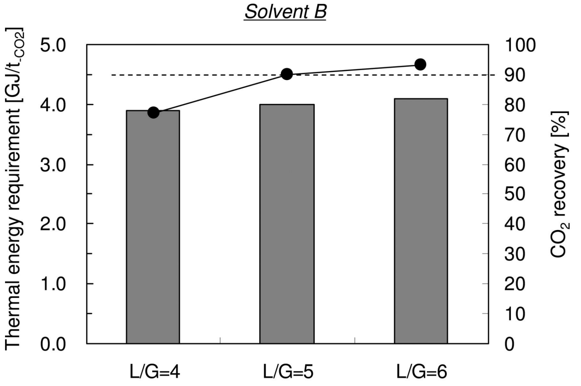

Figure 8. Experimental results of Solvent B in the test plant (bar chart: Thermal energy requirement, line plot: CO_2 recovery)

The regeneration energies of both solvents were high, because the L/G was large at 90% CO_2 recovery operation of both the solvents, because the absorber of the test plant was not optimized specification for each solvent. That is, the plant did not have sufficient packing height for these solvents. In addition, about 10% of reboiler heat duty was consumed as the heat loss from the equipments of this test plant (*5*).

3.2. Calculations

3.2.1. Heat and Mass Balance Analysis

Figure 9 and Table 3 show the calculation results obtained by a mass and heat balance analysis based on equilibrium stage model for a stripper. The bar chart shows the items of heat of reaction, solvent heating loss and steam stripping loss. The heat loss from equipments was ignored in this calculation. MEA as well as the new solvents was also evaluated on the basis of equilibrium data shown in Figure 3. Both the new solvents had a good performance in desorption characteristics and their lean loadings were lower than that of MEA. Also, their capacities of CO_2 capture were larger as indicated in Figure 3. Owing to the new solvents' advantages of low heat of reaction and large capacity of CO_2 capture, all items of the heat consumption were decreased in comparison with the aqueous MEA solution. The results of thermal energy requirement for Solvent A and Solvent B were 2.48 GJ/$t_{\text{-}CO2}$ and 2.33 GJ/$t_{\text{-}CO2}$, respectively.

Downloaded by UNIV OF DELAWARE MORRIS LIB on June 14, 2012 | http://pubs.acs.org
Publication Date (Web): May 3, 2012 | doi: 10.1021/bk-2012-1097.ch017

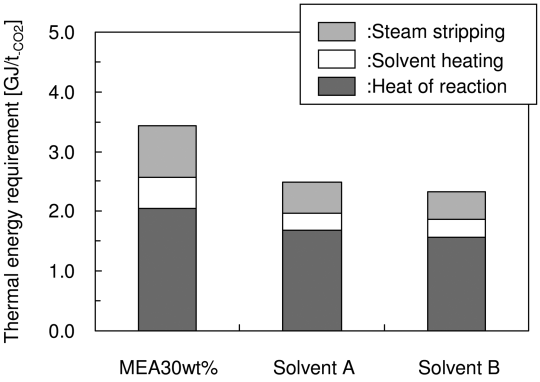

Figure 9. Thermal energy requirement based on equilibrium.

Table 3. Thermal energy requirement estimated by equilibrium model

solvent	*MEA30wt%*	*Solvent A*	*Solvent B*
lean loading [mol-$_{CO2}$/mol-$_{amine}$]	0.20	0.08	0.06
rich loading [mol-$_{CO2}$/mol-$_{amine}$]	0.53	0.57	0.48
capacity of CO_2 capture [mol-$_{CO2}$/L]	1.62	2.40	2.10
L/G [L/Nm^3]*	5.0	3.3	3.8
stripper pressure [MPa-absolute]	0.2	0.2	0.2
stripper top temperature [°C]	123	122	121
stripper bottom temperature [°C]	99	92	92
steam stripping [GJ/t-$_{CO2}$]	0.86	0.52	0.46
solvent heating [GJ/t-$_{CO2}$]	0.53	0.28	0.29
heat of reaction [GJ/t-$_{CO2}$]	2.05	1.68	1.57
Thermal energy requirement [GJ/t-$_{CO2}$]	3.44	2.48	2.33

* Blast furnace gas and 90% recovery.

3.2.2. Process Simulation of Solvent A

Figure 10 and Table 4 shows the simulation results of Solvent A. A result of "Base a" was similar to the operation of plant test at 4 in L/G, shown in Figure 7. Regeneration energies of both plant test and simulation were 3.6 and 3.63 GJ/t-$_{CO2}$, respectively.

In the “Case 1a”, L/G was set at 3.0 and high rich loading was obtained, but CO_2 recovery decreased to 80.9%. In the “Case 2a”, CO_2 recovery returned to 89.6% owing to intercooler of absorber. Because the solvent temperature at absorber bottom decreased to 40.8°C, rich loading could rise and capacity of CO_2 capture increased.

In addition, “Case 3a” shows the effect of reducing heat loss of equipments. thermal energy requirement of the case reached 2.57GJ/t_{-CO2}. The heat loss from equipments was reduced by scale-up of a CO_2 capture plant and 5% was reasonable. This simulation results indicates that Solvent A is an energy efficient solvent.

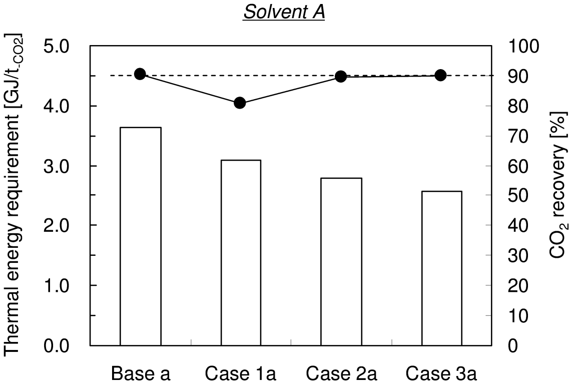

Figure 10. Simulation of process performance of Solvent A (bar chart: thermal energy requirement, line plot: CO_2 recovery)

3.2.3. Process Simulation of Solvent B

Figure 11 and Table 5 shows the simulation results of Solvent B. These results indicate the same as Solvent A. A result of “Base b” was similar to the operation of plant test at 5 in L/G. Regeneration energies of both plant test and simulation were 4.0 GJ/t_{-CO2}.

In the “Case 1b”, L/G was set at 3.5 and high rich loading and low thermal energy requirement were obtained, but CO_2 recovery decreased to 78.4%.

In the “Case 2b”, owing to intercooler of absorber, CO_2 recovery returned to 89.7%. In addition, “Case 3b” shows the effect of reducing heat loss of equipments. The thermal energy requirement of the case reached 2.52GJ/t_{-CO2}, which was lower than that of Solvent A.

Downloaded by UNIV OF DELAWARE MORRIS LIB on June 14, 2012 | http://pubs.acs.org
Publication Date (Web): May 3, 2012 | doi: 10.1021/bk-2012-1097.ch017

Downloaded by UNIV OF DELAWARE MORRIS LIB on June 14, 2012 | http://pubs.acs.org
Publication Date (Web): May 3, 2012 | doi: 10.1021/bk-2012-1097.ch017

Table 4. Simulation summary of Solvent A[a]

case study	*Base a*	*Case 1a*	*Case 2a*	*Case 3a*
feed gas [m^3/h]	55	55	55	55
CO_2 concentration [%]	20	20	20	20
solvent circulation rate [L/h]	213	165	165	165
liquid-to-gas ratio [L/Nm^3]	3.9	3.0	3.0	3.0
(Absorber)				
lean loading [mol_{-CO2}/mol_{-amine}]	0.04	0.04	0.04	0.04
rich loading [mol_{-CO2}/mol_{-amine}]	0.50	0.58	0.63	0.63
capacity of CO_2 capture [mol_{-CO2}/L]	2.03	2.41	2.67	2.68
inlet solvent temp [°C]	35.2	35.2	35.2	35.2
outlet solvent temp [°C]	48.5	43.2	40.8	40.8
intercooler [MJ/h]	-	-	-10.0	-10.0
(Stripper)				
inlet solvent temp [°C]	93.0	93.0	93.0	95.0
reboiler temp [°C]	124.3	124.1	124.1	124.2
reboiler duty [MJ/h]	71.0	54.0	54.0	50.0
heat loss from equipments [%]	10	10	10	5
(Performance)				
CO_2 recovery [%]	90.3	80.9	89.6	90.1
thermal energy requirement [GJ/t_{-CO2}]	3.63	3.09	2.79	2.57

[a] Number of stages in the Radfrac model --- absorber: 10, Stripper: 16

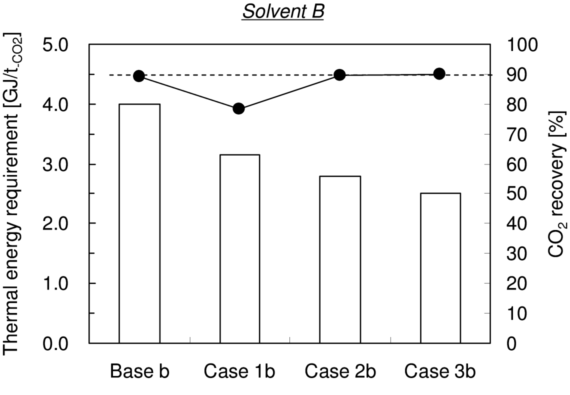

Figure 11. Simulation of process performance of Solvent B (bar chart: thermal energy requirement, line plot: CO_2 recovery)

Table 5. Simulation summary of Solvent B[a]

case study	*Base b*	*Case 1b*	*Case 2b*	*Case 3b*
feed gas [m^3/h]	55	55	55	55
CO_2 concentration [%]	20	20	20	20
solvent circulation rate [L/h]	281	195	195	195
liquid-to-gas ratio [L/Nm^3]	5.1	3.5	3.5	3.5
(Absorber)				
Lean loading [mol_{-CO2}/mol_{-amine}]	0.03	0.03	0.03	0.03
rich loading [mol_{-CO2}/mol_{-amine}]	0.38	0.47	0.53	0.53
capacity of CO_2 capture [mol_{-CO2}/L]	1.56	1.97	2.26	2.27
inlet solvent temp [°C]	35.0	35.0	35.0	35.0
outlet solvent temp [°C]	59.3	50.6	44.2	44.2
intercooler [MJ/h]	-	-	-12.0	-12.0
(Stripper)				
inlet solvent temp [°C]	93.0	93.0	93.0	95.0
reboiler temp [°C]	124.6	124.7	124.9	125.1
reboiler duty [MJ/h]	77.0	53.5	54.0	49.0
heat loss from equipments [%]	10	10	10	5
(Performance)				
CO_2 recovery [%]	89.0	78.4	89.7	90.1
thermal energy requirement [GJ/t_{-CO2}]	4.00	3.16	2.79	2.52

[a] Number of stages in the Radfrac model --- absorber: 10, Stripper: 13)

Downloaded by UNIV OF DELAWARE MORRIS LIB on June 14, 2012 | http://pubs.acs.org
Publication Date (Web): May 3, 2012 | doi: 10.1021/bk-2012-1097.ch017

4. Conclusion

Energy performances of two IPAE-based solvents were evaluated in this chapter by three different approaches; a plant test in a 1 t_{-CO2}/d facility, a heat and mass balance analysis based on an equilibrium stage model and a process simulation with Aspen Plus®. A thermal energy requirement to regenerate a solvent in CO_2 removal from blast furnace gas, which was 20 kPa_{-CO2} in partial pressure, was calculated in the analyses. The results were summarized as follows:

- The results of a plant test shows that the regeneration energies of Solvent A and Solvent B at the 90% CO_2 recovery were 3.6 GJ/t_{-CO2} and 4.0 GJ/t_{-CO2} respectively. These values were high, because the absorber of the test plant was not optimized for each solvent. In addition, about 10% of reboiler heat duty was consumed as the heat loss from the equipments of this test plant.

Downloaded by UNIV OF DELAWARE MORRIS LIB on June 14, 2012 | http://pubs.acs.org
Publication Date (Web): May 3, 2012 | doi: 10.1021/bk-2012-1097.ch017

- The heat and mass balance analysis based on the stage equilibrium model was an effective tool to estimate thermal energy requirement of a solvent at the early stage of solvent development. This calculation can be used on the basis of the laboratory experiments data.
- In order to calculate chemical absorption process using new solvents, the process simulation program, was effectively used with the modification to install property data of new chemicals which was not supported in the original commercial program.
- The evaluations of the solvents at the optimized condition were done using an equilibrium stage model and process simulation. The results of those calculations show that the thermal energy requirements of CO_2 capture form BFG with Solvent A and Solvent B were 2.5~2.6 GJ/t_{-CO2}.

Nomenclature

C_{amine} :	Amine concentration [$kmol_{-amine}/m^3$]
Cp_L :	Specific heat of solvent [$MJ/m^3/K$]
ΔH_{CO2} :	Enthalpy for cooling recovered CO_2 [$MJ/kmol_{-CO2}$]
ΔH_R :	Reaction heat during absorption/desorption [$MJ/kmol_{-CO2}$]
ΔH_V :	Enthalpy of vapor [kJ/mol_{-H2O}]
M :	Molecular weight [kg/kmol]
m :	Mole flow rate of gas phase [kmol/h]
P_T :	Total pressure of stripper [kPa]
Q_T :	Thermal energy requirement [GJ/t_{-CO2}]
Q_H :	Sensible heat of absorbent [GJ/t_{-CO2}]
Q_R :	Reaction heat [GJ/t_{-CO2}]
Q_V :	Latent heat of vapor at the stripper top [GJ/t_{-CO2}]
ΔT :	Temperature difference between rich/lean absorbents [K]
W :	Absorbent flow rate [kg_{-sol}/kg_{-CO2}]
α :	CO_2 loading [mol_{-CO2}/mol_{-amine}]

Acknowledgments

This research was conducted in the COCS Project, which was financially supported by the Ministry of Economy, Trade and Industry (METI), Japan. The COCS project was carried out in collaboration with Nippon Steel Corporation, Nippon Steel Engineering Co. Ltd., Mitsubishi Heavy Industries, Ltd., and The Kansai Electric Power Co., Inc.

References

1. Mimura, T.; Shimojo, S.; Suda, T.; Iijima, M.; Mitsuoka, S. *Kagaku Kogaku Ronbunshu* **1995**, *21* (3), 478–485.
2. Hoff, K. A.; Mejdell, T.; Juliussen, O.; Børresen, E.; Lauritsen, K. G.; Semb, H. T.; Svendsen, H. F. *8th Int. Conf. Greenhouse Gas Control Technologies*,

Trondheim, Norway, June 19−22, 2006; Elsevier Ltd.: Oxford, UK, 2006; paper 01_06_08.pdf (CD-ROM).

3. Porcheron, F; Gibert, A.; Jacquin, M.; Mougin, P.; Faraj, A.; Goulon, A.; Bouillon, P.-A.; Delfort, B.; Le Pennec, D.; Raynal, L. *Energy Procedia* **2011**, *4*, 15–22.
4. Mangalapally, H. P.; Notz, R.; Hoch, S.; Asprion, N.; Sieder, G.; Garcia, H.; Hasse, H. *Energy Procedia* **2009**, *1*, 963–970.
5. Goto, K.; Okabe, H.; Chowdhury, F. A.; Shimizu, S.; Fujioka, Y.; Onoda, M. *Int. J. Greenhouse Gas Control* **2011**, *5*, 1214–1219.
6. Chowdhury, F. A.; Okabe, H.; Shimizu, S.; Onoda, M.; Fujioka, Y. *Energy Procedia* **2009**, *1*, 1241–1248.
7. Goto, K.; Okabe, H.; Shimizu, S.; Onoda, M.; Fujioka, Y. *Energy Procedia* **2009**, *1*, 1083–1089.

Downloaded by UNIV OF DELAWARE MORRIS LIB on June 14, 2012 | http://pubs.acs.org
Publication Date (Web): May 3, 2012 | doi: 10.1021/bk-2012-1097.ch017

Subject Index

A

Absorption capacity, heterocyclic amines, 25*t*
Amine based ionic liquids, 156, 157*f*, 158*f*
Amine based solvents, energy performance
  blast furnace gas, 318*f*, 321*f*
  development, 319*f*
  gas pressure conditions, 318*f*
  heat analysis, 321, 325
  heat consumptions, 322*f*
  mass balance analysis, 321, 325
  overview, 317
  plant test, 320, 321*t*, 324, 324*f*, 325*f*
  process flowsheet configurations, 323*f*
  process simulation, 323, 324*t*, 326, 327*f*, 328*f*, 328*t*, 329*t*
  thermal energy requirement, 322*f*, 326*f*, 326*t*
  vapor-liquid equilibrium, 320*f*
Amine chemical structures influence
  ^{13}C NMR spectroscopy, 31
  chemicals, 31
  CO_2 absorption, 32, 33*t*, 34*f*, 35*f*, 36*f*
  CO_2 desorption, 32, 33*t*, 34*f*, 35*f*, 36*f*
  overview, 29
  reaction apparatus, 31
Amino acid based ionic liquids, 158, 158*f*, 159*f*, 160*f*
2-Amino-2-methylpropanol (AMP), 30, 30*f*
Ammonium bicarbonate, 13*f*
AMP. *See* 2-Amino-2-methylpropanol (AMP)
AMPD. *See* 2-Methyl-2-aminopropanyl-1,3-diol (AMPD)
Aprotic heterocyclic anion based ionic liquids, 164, 164*f*, 165*f*
Aqueous ammonia
  anti-arbamic acid structures, 104*s*
  base-catalysed activation, 116*f*, 117*f*
  carbamate, 104, 107*t*, 127*t*
  carbamic acid, 104, 107*t*, 127*t*
  CO_2 activation, 113, 115*f*
    aqueous activation energies, 118, 119*f*, 122*f*
    bimolecular activation, 114
    carbamate decomposition, 122, 123*f*
    gas-phase activation energies, 117, 118*f*, 121*t*, 124*t*
    reverse aqueous activation energies, 125*f*
    solvent microstructures, 119, 120*f*
  CO_2 capture, 115*f*
  computational methods, 103
  gas phase energetics, 104
  gas phase reaction, 114*f*
  gas phase clustered-anion binding energies, 113*t*
  hypothetical isodesmic reaction, 104*s*
  isodesmic reaction, 108*s*
  lab-scale continuous CO_2 capture
    apparatus, 134, 135*f*
    absorbent, 136
    absorbent flow rate effect, 139, 140*f*
    CO_2 loading, 137
    columns, 135
    feed gas, 136
    feed gas flow rate effect, 139
    heat exchangers, 135
    NH_3 concentration, 137, 138, 139*f*
    reboilers, 135
    regeneration temperature effect, 140, 141, 141*f*, 142*f*
    wash water, 146
  mole fraction calculation, 137
    blocks, 138
    components, 137
    properties, 138
    streams, 138
  NH_2CO_2H isomers, 104
  optimal operating condition selection, 142
    calculated mole fractions, 145*f*
    NH_3 concentration, 149, 150*f*
    optimal operation parameters, 144
    preferred regeneration condition, 142, 143*f*
    regeneration temperature behavior, 147, 148*t*, 149*f*
  overview, 99, 133
  pK$_a$, NH_2CO_2H, 111
  solvation free energies, 106
  syn-arbamic acid structures, 104*s*
  thermochemical values, 105*t*
Aqueous 3-HP, 23*f*
Aqueous 2-MP, 14*f*, 17*f*
Aqueous 3-MP, 20*f*
Aqueous 1-PE, 12*f*, 16*f*
Aqueous 2-PE, 14*f*, 17*f*
Aqueous 4-PE, 22*f*
Aqueous piperazine oxidation
  aqueous metal effect, 228
  CO_2 capture amines resistance, 230, 231*f*

Downloaded by 89.163.35.42 on June 14, 2012 | http://pubs.acs.org
Publication Date (Web): May 3, 2012 | doi: 10.1021/bk-2012-1097.ix002

Downloaded by 89.163.35.42 on June 14, 2012 | http://pubs.acs.org
Publication Date (Web): May 3, 2012 | doi: 10.1021/bk-2012-1097.ix002

  ion chromatography, 221
  ISDA, 223, 223*f*, 224*f*, 225*f*
  nitrogen/carbon mass balance, 234*t*
  overview, 219
  oxidation rate analysis, 226, 227*f*, 228*t*
  oxygen partial pressure effect, 228, 229*f*
  product generation, 233
  PZ oxidation data, 225
  PZ oxidation estimation, 232
  solution preparation, 221
  temperature effect, 229, 231*f*
  temperature tolerance, 233*t*
  TIC, 221
  TOR, 222, 222*f*, 224*f*, 225*f*
  total alkalinity, 221
Aqueous 3-PM, 21*f*
Artificial photosynthesis
  carbon-neutral bioeconomy, 285, 286*f*
  chemical reactions, 282*t*
  CO_2 fixation, 279
  CO_2 utilization, electricity, 280*f*
  experiment advances, 284
  fructose-6-phosphate, 285*f*
  overview, 275
  purified enzymes, 284*f*
  starch synthesis, 285*f*
  vs. plant photosynthesis, 277, 279*f*, 287*t*

B

Base-catalysed activation, aqueous ammonia, 116*f*, 117*f*

C

Carbamate, 104, 107*t*, 127*t*
Carbamate formation, 2*s*
Carbamic acid, 104, 107*t*, 127*t*
CO_2 absorption
  AMPD, 40*f*
  carbamate species, diamines, 37*f*
  MEA, 40*f*
  primary amines, 34*f*
  primary diamines, 36*f*
  secondary diamines, 39*f*
  tertiary diamines, 39*f*
CO_2 absorption, heterocyclic amines
  absorption capacity, 25*t*
  ammonium bicarbonate, 13*f*
  aqueous 3-HP, 23*f*
  aqueous 2-MP, 14*f*, 17*f*
  aqueous 3-MP, 20*f*
  aqueous 1-PE, 12*f*, 16*f*
  aqueous 2-PE, 14*f*, 17*f*
  aqueous 4-PE, 22*f*
  aqueous 3-PM, 21*f*
  carbamate formation, 2*s*
  2-hydroxyalkyl effect, 13
  4-hydroxyalkyl effect, 18
  4-hydroxyl effect, 18
  2-methyl effect, 13
  3-methyl effect, 18
  4-methyl effect, 18
  molecular structural variation effect
    absorption capacity, 24
    absorption rate, 24
    infrared spectral analysis, 5
  overview, 1
  piperazines, 10, 10*f*, 11*f*, 12*f*, 13*f*
  piperidine/hexanol solution, 16*f*
  piperidines, 5*f*, 6, 6*f*, 8*f*, 9*f*, 18*t*
CO_2 activation, aqueous ammonia, 113, 115*f*
  aqueous activation energies, 118, 119*f*, 122*f*
  bimolecular activation, 114
  carbamate decomposition, 122, 123*f*
  gas phase activation energies, 117, 118*f*, 121*t*, 124*t*
  reverse aqueous activation energies, 125*f*
  solvent microstructures, 119, 120*f*
CO_2 adsorbent
  amine-modified mesoporous adsorbents, 309*t*
  CO_2-capturer, 296
  enhancement, 300
  MCM-41, 303, 306*f*
  mesoporous superbasic materials, 311
  one-pot synthesis, 306
  overview, 293
  SBA-15, 306*f*
  temperature effect, 299*f*
  TEPA, 297*f*, 298*f*
CO_2 desorption
  1,5-diaminopentane, 38*f*
  ethylene diamine, 38*f*
  piperazines, 38*f*
  primary amines, 34*f*
  primary diamines, 36*f*
  secondary amines, 35*f*
  secondary diamines, 39*f*
  tertiary diamines, 39*f*
CO_2-philic ionic liquids, 156
  amine based ionic liquids, 156, 157*f*, 158*f*
  amino acid based ionic liquids, 158, 158*f*, 159*f*, 160*f*
  aprotic heterocyclic anion based ionic liquids, 164, 164*f*, 165*f*

- requirements, 156*f*
- superbase based ionic liquids, 161, 161*f*, 162*f*, 163*f*, 164*f*
- transition metal ions, 165, 165*f*

Cyclic amines, 54*t*, 55*f*, 60, 62*t*
- Brønsted plot, 59*f*
- second order reaction constants, 60*t*

D

Dissociation constants (pK_a)
- calculation, 63
- chemical kinetics determination, 45
- computational procedures, 64
- cyclic amines, 60, 62*t*
- overview, 43
- pK_a determination, 47
- prediction, computational chemistry, 63, 63*t*
- results, 65, 65*t*, 66*t*

E

Environmental impacts, post-combustion capture
- emission reduction methods, 214
  - heat effect, 215
  - NOx concentration, 215
  - UV light, 215, 215*f*
- N-nitrosamine derivative formation, 209, 209*f*
  - hindered amines, 214
  - N-nitrosodiethanolamine, 213*f*
  - N-nitroso-2-piperidinemethanol, 213*f*
  - N-nitrospiperazine, 210*f*, 211*f*, 212*s*, 216*f*
  - primary amines, 214
  - secondary amines, 210
  - tertiary amines, 214
- overview, 207

G

Gas sorption analyzer (GSA), 180, 184*f*, 199, 200*f*, 201*f*, 202*f*

GSA. *See* Gas sorption analyzer (GSA)

H

HEEDA. *See* Hydroxyethyl ethylenediamine (HEEDA)

HEI. *See* Hydroxyethyl-imidazole (HEI)

HEIO. *See* Hydroxyethyl imidazolidinone (HEIO)

High pressure CO_2 capture
- absorption *vs.* desorption rate, 91*f*
- amine concentration effects, 94*f*
- amine concentration optimization, 92
- apparatus, 89, 89*f*
- coal gasification gas, 93
- 12-cycle stability test, 97*f*
- data analysis, 90
- energy estimation, 96*f*
- measurement, 89
- one-cycle stability tests, 96*f*
- overview, 87
- pressure-solubility relationships, 95*f*
- reaction heats, 90, 92*f*
- recovery, 92*f*
- separation, 92*t*, 96*f*
- solubility, 90*f*
- stability tests, 90
- tertiary amine solution screening, 91
- total energy estimation, 93
- vapor-liquid equilibria, 93

Hydroxyethyl ethylenediamine (HEEDA), 249, 257, 258*f*

Hydroxyethyl imidazolidinone (HEIO), 256*f*, 260*f*

Hydroxyethyl-imidazole (HEI), 249, 251*f*, 256*f*, 259*f*

I

IGCC gas. *See* Integrated gasification combined cycle (IGCC) gas

Integrated gasification combined cycle (IGCC) gas, 87

Integrated solvent degradation apparatus (ISDA), 223, 223*f*

Ion chromatography
- acetate, 245*f*
- degradation samples, 240
  - IC analysis, 241
  - lab-scale experiment simulating absorber conditions, 240
  - MEA campaign, Esbjerg pilot plant, 241
- formate, 242*f*
- glycolate, 245*f*

Downloaded by 89.163.35.42 on June 14, 2012 | http://pubs.acs.org
Publication Date (Web): May 3, 2012 | doi: 10.1021/bk-2012-1097.ix002

Downloaded by 89.163.35.42 on June 14, 2012 | http://pubs.acs.org
Publication Date (Web): May 3, 2012 | doi: 10.1021/bk-2012-1097.ix002

- ionic degradation compound quantification, 245*f*
- MEA degraded sample analysis, 243, 243*f*, 244*f*
- nitrate, 242*f*
- overview, 239
- retention time, 241, 242*f*

Ionic liquids, 155*f*, 169*t*
- anions, 155*f*
- cations, 155*f*
- CO_2-philic groups, 156
  - amine based ionic liquids, 156, 157*f*, 158*f*
  - amino acid based ionic liquids, 158, 158*f*, 159*f*, 160*f*
  - aprotic heterocyclic anion based ionic liquids, 164, 164*f*, 165*f*
  - requirements, 156*f*
  - superbase based ionic liquids, 161, 161*f*, 162*f*, 163*f*, 164*f*
  - transition metal ions, 165, 165*f*
- Henry's constant, 155*t*
- overview, 153
- polymerised ionic liquids, 166, 167*f*, 168*f*

IPAE. *See* 2-Isopropylaminoethanol (IPAE) aqueous solution

ISDA. *See* Integrated solvent degradation apparatus (ISDA)

2-Isopropylaminoethanol (IPAE) aqueous solution
- amine concentration effect, 82*f*
- ^{13}C NMR spectroscopy, 80, 81*f*
- gas scrubbing test, 73, 74*f*, 75*f*, 77, 77*f*, 83*t*
- NMR spectroscopy, 76
- overview, 71
- piperazine effect, 82*f*
- reaction calorimetry, 76
- reaction heat, 80, 80*t*
- single amine aqueous solutions, 83*t*
- tested amines, 73, 73*t*
- vapor-liquid equilibrium (VLE) measurement, 75, 76*f*, 78, 78*f*

L

Lab-scale continuous CO_2 capture
- apparatus, 134, 135*f*
- absorbent, 136
- absorbent flow rate effect, 139, 140*f*
- CO_2 loading, 137
- columns, 135
- feed gas, 136
- feed gas flow rate effect, 139
- heat exchangers, 135
- NH_3 concentration, 137, 138, 139*f*
- reboilers, 135
- regeneration temperature effect, 140, 141, 141*f*, 142*f*
- wash water, 136

M

MEA. *See* Monoethanolamine (MEA)

2-Methyl-2-aminopropanyl-1,3-diol (AMPD), 40, 40*f*

Molecular structural variation effect
- absorption capacity, 24
- absorption rate, 24
- infrared spectral analysis, 5

Monoethanolamine (MEA), 29, 30*f*
- carboxylic acids, 252*f*
- degradation product stability, 261*t*
- formaldehyde condensation, 251*f*
- HEI, 251*f*, 256*f*
- loss, oxidation, 254*f*, 257*f*
- overview, 249
- oxidation, 253
- photochemistry, NOx
  - ammonia yields, 271*t*
  - experiment schedule, 268*t*
  - formamide, 269*f*, 270*f*, 271*f*, 271*t*
  - NOy, 269*f*, 270*f*
  - overview, 265
  - ozone, 269*f*, 270*f*
- thermal degradation, 257
  - formate, 255*f*, 258*f*
  - HEEDA, 258*f*
  - HEI, 256*f*, 259*f*
  - HEIO, 260*f*
  - nitrate, 255*f*
  - nitrite, 255*f*
  - oxalate, 256*f*, 259*f*
  - products, 250*f*

N

N-Nitrosodiethanolamine, 213*f*

N-Nitroso-2-piperidinemethanol, 213*f*

N-Nitrospiperazine, 210*f*, 211*f*, 212*s*, 216*f*

Downloaded by 89.163.35.42 on June 14, 2012 | http://pubs.acs.org
Publication Date (Web): May 3, 2012 | doi: 10.1021/bk-2012-1097.ix002

P

Partial pressure swing adsorption (PPSA), 177, 189, 191*f*, 192*f*, 195*t*, 196, 196*f*, 197*f*, 198*f*
Photosynthesis, artificial. *See* Artificial photosynthesis
Piperazines, 10, 10*f*, 11*f*, 12*f*, 13*f*
Piperidines, 5*f*, 6, 6*f*, 8*f*, 9*f*, 18*t*
pK_a. *See* Dissociation constants (pK_a)
Polyamines
  CO_2 reaction rates, 52*f*
  cyclic amine screening, 53
  dissociation constants (pK_a)
    chemical kinetics determination, 45
    overview, 43
    pK_a determination, 47
  dissociation constants for aqueous 3-MOPA, 59*t*
  pseudo-first order rate constants, 51*f*
  reaction kinetics
    base catalysis mechanism, 49
    termolecular mechanism, 49
    zwitterion mechanism, 48
  screening, 50
  second order reaction constants
    (1-EPZ + H_2O) solution, 57*t*
    (HEPZ + H_2O) solution, 58*t*
    (3-MOPA + H_2O) solution, 58*t*
    (MPZ + H_2O) solution, 56*t*
    (2-MPZ + H_2O) solution, 57*t*
    (PZ + H_2O) solution, 56*t*
Polymerised ionic liquids, 166, 167*f*, 168*f*
PPSA. *See* Partial pressure swing adsorption (PPSA)
Pseudo-first order rate constants, 51*f*

S

Silica/polyethyleneimine (S-PEI)
  BJH pore size distributions, 186*f*
  chemicals, 181
  CO_2 pseudo isotherms, 193*f*
  gas sorption analyzer, 183
  GSA, 184*f*, 199, 200*f*, 201*f*, 202*f*
  material structural characterization, 182, 184, 187*t*
  materials preparation, 181
  N_2 adsorption, 186*f*
  overview, 177
  PPSA, 189, 191*f*, 192*f*, 195*t*, 196, 196*f*, 197*f*, 198*f*
  supplies, 181
  thermogravimetric analysis, 188*f*, 190*f*, 191*f*, 197*f*, 198*f*
  thermogravimetric analyzer, 183
  X-ray diffraction, 185*f*
Stopped flow instrument, 46*f*
Superbase based ionic liquids, 161, 161*f*, 162*f*, 163*f*, 164*f*

T

Teflon oxidation reactor (TOR), 222, 222*f*
TEPA. *See* Tetraethylenepentamine (TEPA)
Tetraethylenepentamine (TEPA), 294, 297*f*
TIC. *See* Total inorganic carbon (TIC)
TOR. *See* Teflon oxidation reactor (TOR)
Total inorganic carbon (TIC), 221
Transition metal ions, 165, 165*f*

V

Vacuum swing adsorption (VSA), 177
VSA. *See* Vacuum swing adsorption (VSA)